BIOGEOCHEMICAL AND ECOLOGICAL RESPONSES TO WIND- OR TIDE-INDUCED DISTURBANCES OVER MARGINAL SEAS

EDITED BY: Chin-Chang Hung, Bangqin Huang, Wen-Chen Chou, Francois L. L. Muller and Keryea Soong

PUBLISHED IN: Frontiers in Marine Science

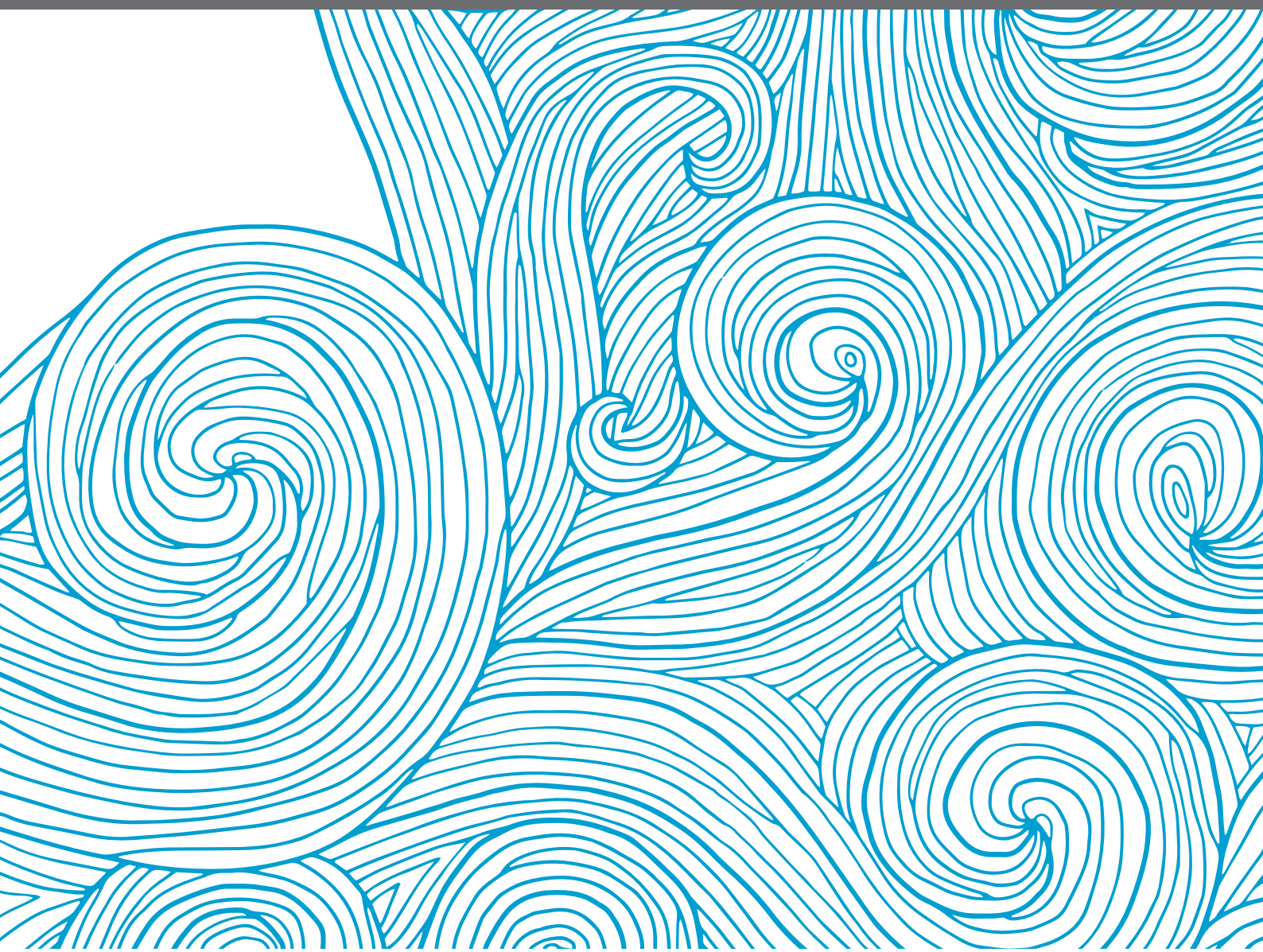

frontiers Research Topics

frontiers

ISSN 1664-8714
ISBN 978-2-83250-809-1
DOI 10.3389/978-2-83250-809-1

About Frontiers

Frontiers is more than just an open-access publisher of scholarly articles: it is a pioneering approach to the world of academia, radically improving the way scholarly research is managed. The grand vision of Frontiers is a world where all people have an equal opportunity to seek, share and generate knowledge. Frontiers provides immediate and permanent online open access to all its publications, but this alone is not enough to realize our grand goals.

Frontiers Journal Series

The Frontiers Journal Series is a multi-tier and interdisciplinary set of open-access, online journals, promising a paradigm shift from the current review, selection and dissemination processes in academic publishing. All Frontiers journals are driven by researchers for researchers; therefore, they constitute a service to the scholarly community. At the same time, the Frontiers Journal Series operates on a revolutionary invention, the tiered publishing system, initially addressing specific communities of scholars, and gradually climbing up to broader public understanding, thus serving the interests of the lay society, too.

Dedication to Quality

Each Frontiers article is a landmark of the highest quality, thanks to genuinely collaborative interactions between authors and review editors, who include some of the world's best academicians. Research must be certified by peers before entering a stream of knowledge that may eventually reach the public - and shape society; therefore, Frontiers only applies the most rigorous and unbiased reviews.
Frontiers revolutionizes research publishing by freely delivering the most outstanding research, evaluated with no bias from both the academic and social point of view. By applying the most advanced information technologies, Frontiers is catapulting scholarly publishing into a new generation.

What are Frontiers Research Topics?

Frontiers Research Topics are very popular trademarks of the Frontiers Journals Series: they are collections of at least ten articles, all centered on a particular subject. With their unique mix of varied contributions from Original Research to Review Articles, Frontiers Research Topics unify the most influential researchers, the latest key findings and historical advances in a hot research area! Find out more on how to host your own Frontiers Research Topic or contribute to one as an author by contacting the Frontiers Editorial Office: frontiersin.org/about/contact

BIOGEOCHEMICAL AND ECOLOGICAL RESPONSES TO WIND- OR TIDE-INDUCED DISTURBANCES OVER MARGINAL SEAS

Topic Editors:
Chin-Chang Hung, National Sun Yat-sen University, Taiwan
Bangqin Huang, Xiamen University, China
Wen-Chen Chou, National Taiwan Ocean University, Taiwan
Francois L. L. Muller, National Sun Yat-sen University, Taiwan
Keryea Soong, National Sun Yat-sen University, Taiwan

The authors declare that the research was conducted in the absence of any commercial or financial relationships that could be construed as a potential conflict of interest.

Citation: Hung, C.-C., Huang, B., Chou, W.-C., Muller, F. L. L., Soong, K., eds. (2022). Biogeochemical and Ecological Responses to Wind- or Tide-Induced Disturbances over Marginal Seas. Lausanne: Frontiers Media SA.
doi: 10.3389/978-2-83250-809-1

Table of Contents

frontiers | Frontiers in Marine Science

TYPE Editorial
PUBLISHED 03 November 2022
DOI 10.3389/fmars.2022.1051194

OPEN ACCESS

EDITED AND REVIEWED BY
Angel Borja,
Technology Center Expert in Marine and Food Innovation (AZTI), Spain

*CORRESPONDENCE
François L. L. Muller
fmuller@mail.nsysu.edu.tw

SPECIALTY SECTION
This article was submitted to Marine Ecosystem Ecology, a section of the journal Frontiers in Marine Science

RECEIVED 22 September 2022
ACCEPTED 30 September 2022
PUBLISHED 03 November 2022

CITATION
Hung C-C, Huang B, Chou W-C, Soong K and Muller FLL (2022) Editorial: Biogeochemical and ecological responses to wind- or tide-induced disturbances over marginal seas.
Front. Mar. Sci. 9:1051194.
doi: 10.3389/fmars.2022.1051194

Editorial: Biogeochemical and ecological responses to wind- or tide-induced disturbances over marginal seas

Chin-Chang Hung[1], Bangqin Huang[2], Wen-Chen Chou[3], Keryea Soong[1] and François L. L. Muller[1]*

[1]Department of Oceanography, National Sun Yat-sen University, Kaohsiung, Taiwan, [2]State Key Laboratory of Marine Environmental Science, Xiamen University, Xiamen, China, [3]Institute of Marine Environment and Ecology, National Taiwan Ocean University, Keelung, Taiwan

KEYWORDS

eddies, South China Sea, Dongsha Island, primary production, tropical cyclone, CO2, biological carbon pump, hypoxia

Editorial on the Research Topic
Biogeochemical and ecological responses to wind- or tide-induced disturbances over marginal seas

Introduction

Global warming caused by sustained increase in radiative forcing over time is known to increase the stratification of the ocean's surface layer. On the other hand, it can also alter the intensity, magnitude and duration of extreme meteorological events (climate warming, storms and typhoons) which are known to induce mixing of the surface layer and thus lead to pulse responses in chemical fluxes, water composition and biology. In the low-latitude marginal seas under consideration here, such disturbances play an especially important role in the summer, i.e. when the initial stratification is more intense than in the winter (Sarmiento et al., 2004; Doney et al., 2012; Shih et al., 2020). The aim of this Research Topic was to take stock of our current understanding of the role played by transient physical disturbances in the surface layer of marginal seas on the transport of chemicals and the productivity and community structure of marine organisms. This was achieved through an interdisciplinary collaboration comprising meteorologists, physical oceanographers, biogeochemists and marine biologists. Most of the papers relate to the South China Sea since a great deal of supporting information was already available for this region.

The studies included in this Research Topic fall into three categories based on the type of marine system considered and the nature of the physical forcing that induces the biogeochemical or ecological response. The first examines the surface ocean variability induced by (a) Kuroshio intrusions and (b) mesoscale eddies in the northern South China Sea (SCS). Mesoscale eddies can persist for many weeks, and their contribution to

chemical and biological variability of the top 100 m of the SCS strongly depends on whether or not they are associated with the meandering of the western-boundary Kuroshio Current (Chow et al.; Wang et al.). The second category of studies focuses on the physical, geochemical and biological responses to wind-induced mixing, ranging from extreme events, such as tropical cyclones (Chowdhury et al.), to low-intensity, seasonal variations in the local wind field (Li et al.). The third group of studies focuses on bays and lagoons situated within the marginal seas of interest and representing hot spots of organic matter production and destruction (Hsieh et al.; Lin et al.) and - in a carbonate shelf lagoon setting - of alkalinity production (Chou et al.).

Eddy-driven vertical mixing: upward flux of nutrients and downward flux of particles

In this Research Topic, three papers address the upward transport of sub-surface waters (> 100 m depth) brought about by cyclonic eddies in the SCS (Chow et al.; Wang et al.) together with the biogeochemical responses to mixing of SCS surface waters with Kuroshio Current waters (Lai et al.). Eddy pumping is a key contributor to vertical mixing and particle export in the SCS (Wang et al., 2018; Shih et al., 2020). In contrast with to wind-induced mixing, it can be long-lasting and also produce noticeable subsurface anomalies. Based on field measurement techniques, bathythermographs and Argo floats, Chow et al. analysed the effects of eddies on thermocline dynamics, nutrient supply and the biological carbon pump in the northern SCS. Interestingly, they found that eddy pumping was strengthened when warmer, lighter water below 100-m depth was advected northwards from the southern SCS by wind-induced Sverdrup transport, but that it was weakened during episodes of Kuroshio water intrusion. Using high-throughput sequencing of both 18S rDNA and rRNA, Wang et al. were able to disentangle the effects of spatial (Kuroshio intrusion) and environmental factors (temperature, nutrients, chlorophyll *a*), so as to show that variations in the nano-eukaryotic community at their northern SCS sites could be significantly explained by the fraction of Kuroshio water present. This may be due to the fact that Kuroshio intrusions lower the nutrient inventory of the upper 100 m and favour small cells such as ammonia oxidising archaea and bacteria. Conversely, Lai et al. found that weather systems associated with the southwest monsoon could drive SCS waters northeastwards to the point where they underwent mixing with the Kuroshio. Their study demonstrates, for the first time, that the pulses of high biomass that periodically occur in the Kuroshio Current are in fact associated with the NE transport of SCS waters.

Wind-driven disturbances: biogeochemical response and CO_2 fluxes

A further five papers examine the effects of surface wind over a very wide range of velocities, time scales and spatial scales. Chowdhury et al. document a relatively rare occurrence, i.e. the simultaneous occurrence of two cyclones in the Indian Ocean, one travelling towards the Arabian Sea and the other into the Bay of Bengal. They provide a thorough and rigorous analysis of the key atmospheric and oceanographic factors responsible for the simultaneous genesis of these two cyclones. They further explain the evolution of each cyclone as it relates to its original strength but also to the host of cyclonic and anticyclonic mesoscale eddies and other surface ocean conditions encountered by each cyclone along its pathway. Li et al. investigated the variations of CO_2 partial pressure in seawater and the air-sea CO_2 flux as it related to the dynamics of the Changjiang river plume during the summer monsoon. They found that the air-sea CO_2 flux is regulated by a combination of biological CO_2 uptake and upwelling events brought about by steady upwelling-favourable winds. At the outset of upwelling, surface plume waters were a carbon source to the atmosphere but they became a carbon sink after one week of sustained upwelling. Satellite remote sensing can be a powerful technique to estimate carbon fixation rate of phytoplankton. As such, Shih et al. compared integrated primary production (PP) derived from ship-based incubations with values derived from the satellite-based vertically generalized production model (VGPM) at the South East Asian Time-series Study (SEATS) station in the SCS from 2003 to 2016. Although they reported a consistent negative relationship between sea surface temperature and either PP or VGPM, they found that PP (*in situ*) estimates were ~50% lower than PP_{VGPM} estimates, likely due to an overestimation of the euphotic depth by the PP_{VGPM} method. Based on shipboard experiments conducted in the SCS over several years, Chen et al. described variations in the picoplankton community, including *Prochlorococcus*, *Synechococcus*, picoeukaryotes, and heterotrophic bacteria. They found that diel-to-seasonal variations of depth-integrated pico-phytoplankton biomass and composition in the euphotic zone was affected by nutrient supply. They report a good linear relationship between sea surface temperature and pico-phytoplankton biomass, suggesting that satellite-derived SST may be used to trace pico-phytoplankton abundance in the SCS. In the face of turbulent mixing, phytoplankton and cyanobacteria must remain suspended in the euphotic zone. Looking at a range of heterocystous cyanobacteria found in the South China Sea (SCS) and the Philippine Sea, Tuo et al. hypothesized that the short trichome length found in *C. rhizosoleniae* and *R. intracellularis* might be what helps them stay in the euphotic zone, regardless of whether they are free-living or associated with symbiotic diatoms.

Benthic processes in shallow water regions

There are four papers in this Research Topic which provide examples of the importance of benthic and/or diagenetic processes in shallow water sediments. Hsieh et al. examine the spatiotemporal variability of eutrophication and hypoxia in the Negombo Lagoon, one of the most productive and sensitive coastal ecosystems in Sri Lanka. Their survey suggests that elevated seawater temperature, sluggish water circulation and high organic matter inputs-partially supported by nutrient pollution-are triggering a sequence of events leading to eutrophication and hypoxia. The work by Chou et al. shows just how much the carbonate system of seawater in shallow semi-enclosed environments can be altered and how a substantial quantity of organic alkalinity may be present in such systems. Chou et al. compared the carbonate chemistry in overlying waters at two seagrass sites, i.e. sheltered site and site located outside the lagoon. They found differences in the variability of carbonate parameters between the two sites on seasonal and diurnal timescales with similar pattern with previous study (Chou et al., 2018). They attributed these differences to enhanced metabolic carbonate dissolution within the sediments of the lagoon. Their finding highlights the importance of taking this process into account when evaluating the 'blue carbon' potential of carbonate-rich coastal ecosystems. The study of Lin et al. reveals that sediment characteristics and carbon fluxes may strongly depend on the ability of benthic microalgae to migrate into the sediment in response to light penetration, nutrients and predation. Focusing on the benthic processes of tidal mudflats, Lin et al. found that net and gross primary production increased with increasing mud content of the sediment. This increase bore little relationship to microalgal biomass but instead was accompanied by a shift in the composition of benthic microalgae when proceeding from sandy to muddy sediments. Their results provide mechanistic evidence of how sediment mud content acts as a critical factor regulating carbon fluxes in tropical and subtropical unvegetated tidal flats. Finally, Darumas et al. investigated variations of nutritional values, carbon–nitrogen contents and renieramycin M concentrations in *Xestospongia* sp. in the Gulf of Thailand. They found that renieramycin M inhibited settlement of acorn barnacle. They argued that there was likely a homogeneous distribution of renieramycin within the sponge which nevertheless retained the ability to limit the metabolism and survival of competing marine organisms.

Future directions

This Research Topic expands our knowledge of the biogeochemical responses to physical disturbances in the surface layer of large marginal seas (Arabian Sea, Bay of Bengal, Philippine Sea, South China Sea). Overall, the collected articles help readers to better understand how climate variability and weather events interact with anthropogenic disturbances (eutrophication, hypoxia, global warming) to affect bacterial and phytoplankton assemblages, primary production, and both the physical and biological carbon pumps in different marine environments. It is apparent that in order to understand and model the complex interplay between forcing factors and biogeochemical responses, future research will need to be directed at the multiple effects of climate warming, storms and ocean acidification on water stratification, oxygen supply, nutrient input, marine ecosystems and food webs in marginal seas.

Author contributions

All authors listed have made intellectual contributions to this Research Topic and approved it for publication.

Funding

This research was supported by the National Sun Yat-sen University and the Ministry of Sciences and Technology (MOST 110-2634-F-019-002, MOST 111-2119-M-019-002).

Acknowledgments

We sincerely thank all the authors and reviewers for their contributions to this Research Topic.

Conflict of interest

The authors declare that the research was conducted in the absence of any commercial or financial relationships that could be construed as a potential conflict of interest.

Publisher's note

References

Chou, W.-C., Chu, H.-C., Chen, Y.-H., Syu, R. W., Hung, C.-C., and Soong, K. (2018). Short-term variability of carbon chemistry in two contrasting seagrass meadows at dongsha island: implications for pH buffering and CO_2 sequestration. *Estuarine Coast. Shelf. Sci.* 210, 36–44. doi: 10.1016/j.ecss.2018.06.006

Doney, S. C., Ruckelshaus, M., Duffy, J. E., Barry, J. P., Chan, F., English, C.A., et al. (2012). Climate change impacts on marine ecosystems. *Annu. Mar. Sci.* 4, 11–37. doi: 10.1146/annurev-marine-041911-111611

Sarmiento, J. L., Slater, R., Barber, R., Bopp, L., Doney, S.C., Hirst, A.C., et al. (2004). Response of ocean ecosystems to climate warming. *Glob. Biogeochem. Cycl.* doi: 10.1029/2003GB002134

Shih, Y., Hung, C., Tuo, S., Shao, H., Chow, C. H., Muller, F. L. L., et al. (2020). The impact of eddies on nutrient supply, diatom biomass and carbon export in the northern south China Sea. *Front. Earth Sci.* 8, 1–17. doi: 10.3389/feart.2020.537332

Wang, L., Huang, B., Laws, E. A., Zhou, K., Liu, X., Xie, Y., et al. (2018). Anticyclonic eddy edge effects on phytoplankton communities and particle export in the northern south China Sea. *J. Geophys. Res. Oceans* 123, 7632–7650. doi: 10.1029/2017JC013623

frontiers in Marine Science

ORIGINAL RESEARCH
published: 17 May 2021
doi: 10.3389/fmars.2021.670180

Effects of Sediment Characteristics on Carbon Dioxide Fluxes Based on Interacting Factors in Unvegetated Tidal Flats

*Wei-Jen Lin[1,2], Ming-Chih Chiu[1,2], Chiao-Wen Lin[1,2] and Hsing-Juh Lin[1,2]**

[1] Department of Life Sciences, National Chung Hsing University, Taichung, Taiwan, [2] Innovation and Development Center of Sustainable Agriculture, National Chung Hsing University, Taichung, Taiwan

The contribution of unvegetated tidal flats to global net primary production is comparable to that of some vegetated coastal habitats. However, compared to carbon flux regulating factors in vegetated habitats, those in unvegetated tidal flats are not well understood, particularly in terms of their cause-effect relationships. Maximum gross primary production (GPP_m), net primary production (NPP) and total respiration (TR) during emersion at noon when the irradiance level was at the saturation level for photosynthesis in nine unvegetated tidal flats across the Taiwan Strait in tropical and subtropical regions were determined in winter and summer from 2011 to 2016 to examine the direct and indirect relationships between sediment characteristics and carbon fluxes by using structural equation models (SEM). Most of the GPP_m and NPP values were higher in winter than in summer. Conversely, the TR values were higher in summer than in winter. The NPP values at some sites shifted to negative values in summer, indicating the sites were carbon sources. The values of GPP_m, TR and NPP for the tidal flats all increased significantly with increasing sediment mud content. The SEM results showed that the sediment mud content directly increased GPP_m or indirectly increased GPP_m via a compositional shift in benthic microalgae. The sediment mud content also directly increased TR or indirectly increased TR via increased organic matter content. The contribution of benthic microalgal and macrofaunal biomass to TR was relatively minor. This result suggests that primary production was stimulated mainly by the organic matter content rather than by increased microalgal biomass. With the integrated SEM framework, our results showed mechanistic evidence of how sediment mud content acted as a critical factor regulating carbon fluxes in unvegetated tidal flats.

Keywords: benthic metabolism, gross primary production, net primary production, respiration, microphytobenthos, structural equation model

OPEN ACCESS

Edited by:
Wen-Chen Chou, National Taiwan Ocean University, Taiwan

Reviewed by:
Dominique Davoult, Sorbonne Université, France
Wei-Jen Huang, National Sun Yat-sen University, Taiwan

***Correspondence:**
Hsing-Juh Lin
hjlin@dragon.nchu.edu.tw

Specialty section:
This article was submitted to Marine Ecosystem Ecology, a section of the journal Frontiers in Marine Science

Received: *20 February 2021*
Accepted: *19 April 2021*
Published: *17 May 2021*

Citation:
Lin W-J, Chiu M-C, Lin C-W and Lin H-J (2021) Effects of Sediment Characteristics on Carbon Dioxide Fluxes Based on Interacting Factors in Unvegetated Tidal Flats. Front. Mar. Sci. 8:670180. doi: 10.3389/fmars.2021.670180

INTRODUCTION

Unvegetated tidal flats (hereafter tidal flats) are the area inundated between the high- and low-tide waterlines, including sandy and muddy sediments (Murray et al., 2012). Tidal flats encompass a large proportion of the coastal zone. The global area of tidal flats has been estimated at 127,921 km^2, with most being distributed in Asia (44% of total; Murray et al., 2019). The estimated global area

of tidal flats is only 16% of that of seagrass beds but is comparable to that of mangroves and 2.3 times that of salt marshes (Davidson and Finlayson, 2019). Although the daily rate of net primary production (NPP) in tidal flats is at most 20% of that of vegetated coastal habitats, the global NPP of tidal flats (11.04 Tg C yr^{-1}), obtained by multiplying the NPP by the global area, might reach approximately 50% of that of salt marshes (Lin et al., 2020). The carbon stock of tidal flats (78.07 Tg C) is nearly four times higher than that of vegetated habitats (20.53 Tg C) along the coast of China (Chen et al., 2020). Currently, anthropogenic activities, such as land development (Koh and Khim, 2014; Chen et al., 2016), oil spills (Junoy et al., 2005; Lee and Lin, 2013; Yu et al., 2013) and heavy metal pollution (Rahman and Ishiga, 2012; Zhang et al., 2013), tend to occur in tidal flats.

Benthic microalgae, also known as microphytobenthos, are generally the major primary producers in tidal flats throughout the year (McIntyre et al., 1996; Underwood and Kromkamp, 1999). These microalgae can contribute up to 65% of the combined production of phytoplankton and benthic microalgae in shallow-water ecosystems (McMinn et al., 2005; Sarker et al., 2009). This production can provide food sources for not only local benthic systems but also nearby pelagic systems. Over 30% of benthic microalgae may be resuspended by the turbulence of tidal currents and wind-generated waves (De Jonge and Van Beuselom, 1992), part of which is exported to nearby coastal ecosystems by tidal currents and further subsidizes secondary production through the outwelling of benthic microalgae (Guarini et al., 2008; Yoshino et al., 2012; Savelli et al., 2019).

The production of benthic microalgae in tidal flats is frequently higher in tropical regions than in temperate regions (Cahoon, 1999). In temperate regions, tidal flats might be either small carbon sinks or carbon sources during emersion (Brotas and Catarino, 1995; Migné et al., 2004; Hubas and Davoult, 2006; Spilmont et al., 2006; Otani and Endo, 2019). In subtropical regions, tidal flats act as carbon sinks during emersion (Lee et al., 2011). Lin et al. (2020) demonstrated a clear latitudinal gradient in winter from 20°N to 40°N in which primary production and respiration in tidal flats during emersion decreased by up to 104% toward higher latitudes, but no clear trend was detected across the latitudinal gradient in summer. It appears that the contribution of NPP from tidal flats to the coastal carbon flux was greater in tropical and subtropical regions than in temperate regions (Lin et al., 2020). Along the latitudinal gradient, sediment temperature is a main factor that regulates carbon fluxes in tidal flats (Lin et al., 2020). The authors also indicated that sediment features might be more prominent in regulating carbon fluxes in tidal flats at a local scale. However, both direct and indirect relationships between sediment characteristics and carbon fluxes in tidal flats are rarely emphasized simultaneously.

There is still no comprehensive quantitative analysis addressing the network of relationships between sediment characteristics and carbon fluxes from benthic microalgae. Some studies have reported no clear relationship between sediment characteristics and the production of benthic microalgae (Davis and McIntire, 1983; Hubas et al., 2006). Others have suggested a negative relationship between sediment mud content and benthic production (Billerbeck et al., 2007; Lee et al., 2011). However, some studies have noted that benthic production was higher in sediments with higher mud content (Colijn and de Jonge, 1984; Hubas et al., 2007; Davoult et al., 2009; Migné et al., 2016; Haro et al., 2020). This inconsistency might be due to different study scales. Most studies have measured only one tidal flat with a limited number of sampling sites; few studies, however, have measured different tidal flats representing a gradient of sediment characteristics. For example, Pratt et al. (2014) compiled data on gross primary production (GPP) and sediment oxygen consumption from nine intertidal flats on the North Island of New Zealand and found that both processes decreased with increases in sediment mud content. However, the range of sediment mud content was between 0 and 30%. It is uncertain whether benthic metabolism would respond in the same way to sediment with mud content > 30%. In this study, because primary production of benthic microalgae mostly occurs on the surface of tidal flats during daytime emersion (Lee et al., 2011), we determined the carbon dioxide (CO_2) fluxes in nine tidal flats during emersion in tropical and subtropical regions along a larger gradient of sediment mud content, between 0 and 90% in summer and winter, respectively. It was hypothesized that the CO_2 fluxes in tidal flats would decrease with increasing sediment mud content. We further explored multiple hypotheses about the direct and indirect relationships between CO_2 fluxes in tidal flats and sediment characteristics by using structural equation models (SEM).

MATERIALS AND METHODS

Sampling Sites

Nine tidal flats in tropical and subtropical regions across the Taiwan Strait (22.48°N∼26.15°N) were chosen as our sampling sites in this study. Five of the sites were in the eastern Taiwan Strait, and four of the sites were located in the western Taiwan Strait (**Figure 1** and **Table 1**). Measurements at each site were conducted separately in summer and in winter. Due to labor constraints and financial difficulties, all the measurements were not necessarily conducted in the same year. The air temperature ranges from 11.2 to 20.0°C in winter and from 27.1 to 30.0°C in summer. The annual precipitation ranges from 908 to 1735 mm. The climate data in the studied years were derived from the local weather station at each sampling site and obtained from the Observation Data Inquiry System of the Central Weather Bureau, Taiwan[1].

Carbon Flux Measurements

The carbon fluxes in the tidal flats were measured during emersion at each sampling site by the benthic closed-chamber method. This method, which was originally developed by Migné et al. (2002) and modified by Lee et al. (2011), was used to measure CO_2 fluxes from the sediment through the photosynthesis of benthic microalgae and through autotrophic and heterotrophic respiration (i.e., total respiration) within the

[1]https://e-service.cwb.gov.tw/HistoryDataQuery

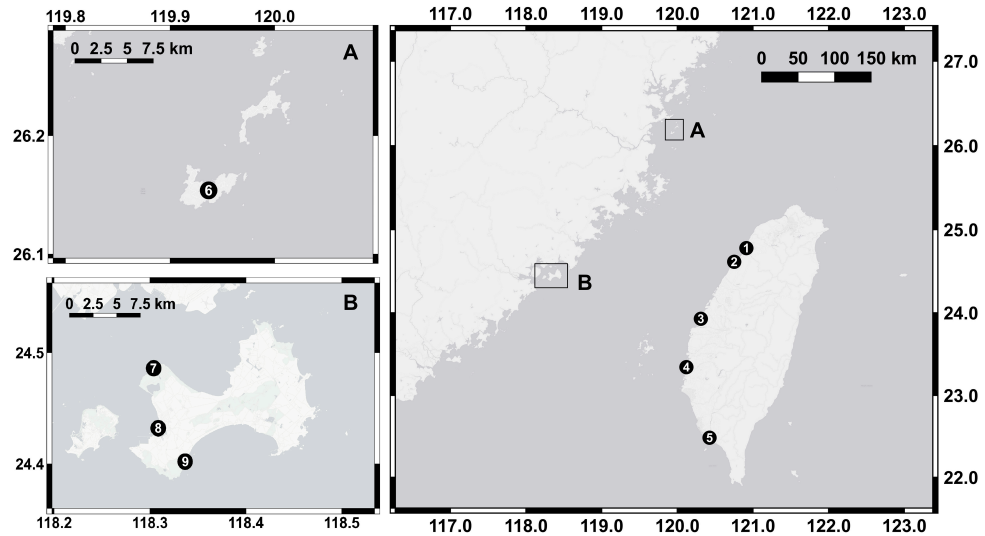

FIGURE 1 | Sampling locations in the nine tidal flats. Five sites were located in the eastern Taiwan Strait, and four sites were in the western Taiwan Strait **(A,B)**. The location numbers and names are given in **Table 1**.

TABLE 1 | Locations, study years, and meteorological conditions in the tidal flats.

	Site	Latitude, longitude	Studied years	Air temperature (°C)		Annual precipitation (mm)
				Winter	Summer	
#1	Siangshan (SS)	24.778°N, 120.913°E	2011∼2012	15.3	28.3	1664
#2	Houlong (HL)	24.614°N, 120.752°E	2014∼2016	15.7	28.7	1502
#3	Fangyuan (FY)	23.928°N, 120.311°E	2014∼2016	17.1	28.8	1160
#4	Haomeiliao (HML)	23.343°N, 120.120°E	2015∼2016	18.3	30.0	1735
#5	Gaoping (GP)	22.484°N, 120.426°E	2014∼2016	20.0	28.9	2108
#6	Nangan (NG)	26.153°N, 119.937°E	2014	11.2	27.1	908
#7	Beishan (BS)	24.485°N, 118.303°E	2011, 2013	13.4	27.6	1091
#8	Wujiang (WJ)	24.415°N, 118.308°E	2011, 2013	13.4	27.6	1091
#9	Oucuo (OC)	24.401°N, 118.336°E	2011, 2013	13.4	27.6	1091

The air temperature in winter and in summer and the annual precipitation were averaged when the study took place over more than one year. The meteorological data are available at https://e-service.cwb.gov.tw/HistoryDataQuery.

chamber. Measurements were conducted *in situ* on sunny days under ambient light conditions at noon (10:00 to 14:00) because the irradiance level was at the saturation level for photosynthesis. The respiration in subtropical tidal flats during nighttime was 50% lower than that during daytime (Lee et al., 2011). However, the main purpose of this study was to examine the relationships between sediment characteristics and carbon fluxes rather than quantifying daily production in the tidal flats. Since the CO_2 fluxes might be affected by tides (Spilmont et al., 2007), emersions during spring tides were selected as the measurement times at all sampling sites to enable cross-site comparisons.

During emersion, a benthic chamber, composed of a semicircular transparent acrylic dome on the top and a stainless steel ring (30 cm in diameter and 16 cm in height) at the bottom, were pushed into the sediment of tidal flats to a depth of 10 cm. The chamber encompassed 10.6 L of air over a sediment area of 0.071 m^2 within the dome. To make the chamber airtight, gas leakage was always excluded prior to each measurement. CO_2 fluxes between the sediment and the air were monitored by an infrared CO_2 gas analyzer (LI-820, LI-COR, Lincoln, NE, United States) and recorded by a data logger (LI-1400, LI-COR) with a 30 s logging frequency for 10 min before the environmental conditions (i.e., air pressure, temperature, and humidity) obviously increased within the chamber compared to outside conditions. The CO_2 fluxes (in mg C m^{-2} h^{-1}) were calculated by the slope of the linear regression line between CO_2 concentration (ppm) and recorded frequency (30 s), assuming a molar volume of 24.5 L mol^{-1} at normal temperature (25°C) and pressure (1 atm) (NTP)and a molar mass of 12 g C mol^{-1} CO_2. To avoid any potential perturbation during initial measurements, only CO_2 fluxes during the last 8 min were regressed against time. The linear regressions were acceptable when the determination coefficient was >0.80. Photosynthetically active radiation (PAR, 400–700 nm, in μmol quanta m^{-2} s^{-1}) and sediment temperature were recorded simultaneously outside the chamber with a quantum sensor

(LI-190SA, LI-COR) and a temperature sensor (LI-1400-101, LI-COR) with the same data logger listed above.

On each measurement, three to five benthic chambers were used. These benthic chambers were placed on the sediment approximately 5 m apart to eliminate any potential interactions between the sediment samples. We performed the measurements on separate days to collect sufficient replicates in each season for each site (**Table 2**). Prior to each measurement, the CO_2 gas analyzers were calibrated with CO_2-free gas and 500 ppm CO_2. The accuracy of the CO_2 gas analyzer was <2.5% of the measurement.

The measurements under ambient light conditions allowed us to estimate the NPP, and the measurements performed in the dark (100% shading) allowed the estimation of total respiration (TR). The GPP describes the total uptake of CO_2 by a tidal flat, which was calculated by adding the NPP to the TR as shown in Equation (1).

$$GPP = NPP + TR \quad (1)$$

whenever the sum of NPP and TR was negative, the tidal flat showed heterotrophic conditions; the GPP was then assumed to be zero. Measurements were considered outliers and excluded for further analysis when they fell outside the interquartile range (i.e., between Q1 – 1.5 × IQR and Q3 + 1.5 × IQR, where Q1 is the first quartile, Q3 is the third quartile, and IQR is the difference between Q1 and Q3, Lin et al., 2020). At each site in each season, at least 10 random and non-repeating replicates of CO_2 flux measurements were obtained.

At each site for each measurement, the chambers were exposed *in situ* to a series of five different irradiances (0, 30, 50, 70, and 100% shading) by covering the chambers with screens with different meshes or an opaque fabric to determine the CO_2 flux as a function of the incident irradiance (i.e., P-I curve) on the sediment. This P-I curve can be described by the equation of Jassby and Platt (1976):

$$GPP = GPP_m \tanh(\alpha E / GPP_m) \quad (2)$$

where GPP_m is the maximum GPP (in mg C m^{-2} h^{-1}) in the absence of photoinhibition under optimal irradiance, α is the initial slope of the P-I curve, and E is the irradiance measured as PAR (in μmol quanta m^{-2} s^{-1}). P-I curves were drawn in Sigmaplot (version 12.5; Systat Software Inc., San Jose, CA, United States) for non-linear regression fitting, and the results were acceptable when the fit was significant ($p < 0.05$) and the determination coefficient was larger than 0.80 (**Supplementary Figure 1**).

Environmental and Biological Variables

After each CO_2 flux measurement, the top 5 cm of the sediment inside each chamber was sampled by a cutoff syringe with a 2.6 cm inner diameter for sediment characterization and interstitial nutrient analyses. The sediment grain size, sorting coefficient, and mud content were determined by the standard wet-sieved method (Bale and Kenny, 2005) and the modified pipette method (Hsieh and Chang, 1991). Fine materials, such as clay and silt, referred to as mud (grain size < 63 μm). The sediment organic matter content was measured by the loss-on-ignition method (Bale and Kenny, 2005). Sediment interstitial water from the top 5 cm layer was collected, filtered through Whatman GF/C glass fiber filters, stored at 4°C, and then brought to the laboratory for nutrient analysis. A spectrophotometer (U-5100, Hitachi, Tokyo, Japan) was used for the determination of nitrite (Bendschneider and Robinson, 1952), nitrate (Jenkins and Medsker, 1964), ammonia (Pai et al., 2001), and phosphate (Murphy and Riley, 1962). The salinity of the interstitial water was measured by a portable conductivity meter (ProfiLine Cond 3310, WTW, Weilheim, Germany).

After each CO_2 flux measurement, the biomasses of benthic microalgae and macrofauna inside the chamber were also determined. The top 1 cm of the sediment, where most benthic microalgae are located (Cadée and Hegeman, 1974), was sampled by a cutoff syringe with a 1 cm inner diameter (six replicates for each chamber). The sediment samples were then frozen until they were brought to the laboratory. The chlorophyll *a*, *b*, and *c* concentrations were measured by the acetone method (Jeffrey and Humphrey, 1975). While the chlorophyll *a* concentration can be a proxy for the total biomass of benthic microalgae, the chlorophyll *b* and *c* concentrations indicate the biomass of green algae and diatoms in tidal flats, respectively (Golterman, 1975). For collecting macrofauna, the top 10 cm of the sediment was sampled by a stainless steel ring corer with a 10 cm inner diameter (one sample for each chamber). The sediment samples were then strained with a 0.5 mm sieve and preserved in 70% ethanol in the field. After being brought back to the laboratory, the macrofauna samples were sorted, counted and weighed by oven-drying (60°C) to a constant weight and then combusted at 500°C for 4 h to determine the ash-free dry weight (AFDW).

Data Analysis

Since our data failed in the normality test and did not meet the assumptions for a one-way ANOVA, the Kruskal–Wallis test was used to examine whether the sediment characteristics differed among the nine study sites. When significant differences ($p < 0.05$) were detected, Dunn's multiple comparisons test was further used to determine which means differed.

Structural equation models (SEM) were used to assess the hypothesized direct and indirect effects of sediment characteristics and the biomasses of benthic microalgae and macrofauna on the primary production and respiration of the tidal flats. To answer such fundamental questions, we needed a mechanistic understanding of the relationships among the potential factors and their relative importance. By testing multivariate hypotheses and considering the direct and indirect effects of multiple interacting variables, SEM is a multivariate technique suitable to test networks of causal models (Eisenhauer et al., 2015).

Since sediment mud content is closely related to other sediment characteristics, such as grain size, organic matter content, sorting coefficient and interstitial nutrient content, sediment mud content was used as the proxy for the sediment characteristics in the conceptual SEM (**Figure 2**).

TABLE 2 | Sediment characteristics of the tidal flats.

Site		Sediment temperature (°C)		Sediment salinity	Sediment organic matter content (%)	Sediment grain size (μm)	Sediment mud content (%)	Sediment sorting coefficient	Benthic chl *a* concentration (mg m^{-2})	Macrofaunal biomass (g AFDW m^{-2})	Interstitial DIN concentration (μM)	Interstitial DIP concentration (μM)
		Winter	Summer									
#1	Siangshan (SS; *n* = 44)	17.5 ~ 34.7 26.2 ± 5.8	33.1 ~ 38.5 36.0 ± 2.0	15.0 ~ 45.5 32.3 ± 5.3^{ab}	0.5 ~ 1.6 0.9 ± 0.3^{cd}	54.9 ~ 208.2 112.2 ± 37.2^{de} (very fine sand)	7.7 ~ 48.2 21.5 ± 10.6^{cd}	0.50 ~ 1.26 1.04 ± 0.16^{b}	44.6 ~ 163.3 84.7 ± 29.9^{bc}	0.00 ~ 62.35 6.19 ± 13.23 ^{ac}	5.6 ~ 322.2 138.1 ± 75.3^{c}	0.50 ~ 8.80 2.45 ± 1.48^{b}
#2	Houlong (HL; *n* = 31)	15.3 ~ 22.2 18.7 ± 2.7	29.8 ~ 34.7 32.5 ± 1.6	17.8 ~ 37.2 30.5 ± 4.4^{ab}	0.9 ~ 2.7 1.6 ± 0.6^{ab}	28.7 ~ 341.5 190.2 ± 89.3b^{cd} (fine sand)	0.1 ~ 64.1 11.4 ± 18.0^{cde}	0.46 ~ 2.06 0.97 ± 0.49^{bc}	1.0 ~ 118.1 22.7 ± 27.0^{e}	0.00 ~ 6.83 0.95 ± 1.92^{de}	15.8 ~ 375.7 124.0 ± 110.9^{cd}	0.07 ~ 3.17 1.60 ± 0.68^{bc}
#3	Fangyuan (FY; *n* = 24)	19.0 ~ 29.2 23.1 ± 3.7	34.5 ~ 36.4 35.3 ± 0.6	13.1 ~ 35.3 25.1 ± 7.0^{b}	1.5 ~ 2.7 2.0 ± 0.3^{a}	35.6 ~ 101.1 57.7 ± 21.0^{f} (silt)	30.6 ~ 87.6 66.7 ± 17.7^{ab}	0.82 ~ 1.49 1.18 ± 0.19^{b}	23.8 ~ 97.0 52.8 ± 17.2^{cde}	0.00 ~ 112.81 16.93 ± 33.03 ^{a}	112.0 ~ 433.4 239.1 ± 110.6^{ac}	1.85 ~ 66.54 11.06 ± 14.98^{a}
#4	Haomeiliao (HML; *n* = 20)	22.8 ~ 29.0 25.7 ± 2.8	34.8 ~ 40.9 36.3 ± 1.7	30.8 ~ 36.0 33.9 ± 1.3^{a}	0.8 ~ 2.1 1.2 ± 0.4^{bc}	39.3 ~ 133.0 81.2 ± 29.8^{ef} (very fine sand)	2.8 ~ 73.6 33.3 ± 21.3^{bc}	0.43 ~ 1.22 0.93 ± 0.21^{b}	5.1 ~ 72.5 29.8 ± 20.0^{de}	0.00 ~ 66.90 14.40 ± 20.44 ^{a}	50.4 ~ 217.0 149.5 ± 78.0^{bcde}	0.52 ~ 1.02 0.83 ± 0.20^{bcd}
#5	Gaoping (GP; *n* = 39)	21.9 ~ 31.5 27.6 ± 3.2	27.6 ~ 35.9 33.1 ± 2.6	2.1 ~ 30.1 14.5 ± 8.0^{c}	0.8 ~ 2.3 1.5 ± 0.3^{ab}	10.2 ~ 339.2 59.0 ± 68.6^{f} (silt)	2.7 ~ 99.9 76.9 ± 24.3^{a}	0.60 ~ 1.76 1.11 ± 0.34^{b}	1.0 ~ 244.0 70.7 ± 58.3^{bcd}	0 ~ 6.19 0.88 ± 1.46 ^{bcd}	2.0 ~ 3942.4 512.0 ± 969.4^{c}	0.05 ~ 3.63 0.84 ± 0.66^{d}
#6	Nangan (NG; *n* = 24)	13.4 ~ 18.8 16.0 ± 1.6	27.8 ~ 34.4 31.2 ± 2.3	12.5 ~ 41.4 30.0 ± 5.1^{b}	0.6 ~ 3.4 1.4 ± 0.7^{bc}	126.2 ~ 567.8 258.7 ± 96.9^{abc} (medium sand)	0.6 ~ 27.9 9.7 ± 8.1^{de}	0.77 ~ 2.23 1.53 ± 0.42^{a}	35.9 ~ 219.3 107.9 ± 43.1^{ab}	0 ~ 76.41 14.07 ± 20.64 ^{a}	171.1 ~ 21915.9 4789.6 ± 6084.1 ^{ab}	0.51 ~ 36.54 5.31 ± 9.45^{b}
#7	Beishan (BS; *n* = 34)	16.2 ~ 34.2 22.7 ± 5.9	34.7 ~ 47.4 40.6 ± 3.6	30.0 ~ 35.3 32.6 ± 1.8^{ab}	0.5 ~ 3.2 1.6 ± 0.6^{ab}	55.3 ~ 395.9 166.7 ± 99.4^{cd} (fine sand)	9.7 ~ 57.2 29.4 ± 12.0^{c}	1.69 ~ 3.08 2.05 ± 0.30^{a}	77.2 ~ 385.6 146.8 ± 66.4^{a}	0 ~ 44.87 8.96±12.63^{a}	11.1 ~ 157.4 49.7 ± 37.6^{df}	0.29 ~ 10.42 3.59 ± 2.79^{abc}
#8	Wujiang (WJ; *n* = 25)	16.7 ~ 26.3 22.2 ± 3.4	34.7 ~ 46.9 40.5 ± 4.3	25.0 ~ 35.0 31.0 ± 2.2^{ab}	0.2 ~ 2.0 0.5 ± 0.5^{de}	323.8 ~ 720.3 552.1 ± 97.1^{a} (coarse sand)	0.0 ~ 3.5 1.0 ± 1.0^{ef}	0.79 ~ 1.44 1.02 ± 0.15^{b}	80.2 ~ 380.3 177.5 ± 80.4^{a}	0 ~ 3.76 0.90 ± 0.99^{c}	27.2 ~ 550.7 127.0 ± 135.6^{cdf}	0.18 ~ 23.17 4.19 ± 5.08^{ab}
#9	Oucuo (OC; *n* = 22)	12.0 ~ 26.3 23.1 ± 5.4	32.2 ~ 46.7 39.1 ± 4.9	15.6 ~ 35.0 29.2 ± 4.0^{b}	0.2 ~ 0.4 0.3 ± 0.1^{e}	207.8 ~ 678.3 319.6 ± 122.4^{ab} (medium sand)	0.0 ~ 0.3 0.09 ± 0.07^{f}	0.33 ~ 0.99 0.66 ± 0.23^{c}	7.2 ~ 42.2 20.6 ± 10.5^{e}	0 ~ 26.54 2.44 ± 6.10^{ce}	4.8 ~ 47.4 22.9 ± 13.0^{ef}	0.37 ~ 3.71 1.52 ± 0.86^{bcd}

Data are presented as the range and mean ± SD.
For each variable, different letters after the data (mean ± SD) indicate significant differences among sites.
chl a, chlorophyll a; AFDW, ash-free dry weight; DIN, dissolved inorganic nitrogen (NO_2 + NO_3 + NH_4); DIP, dissolved inorganic phosphorus (PO_4).

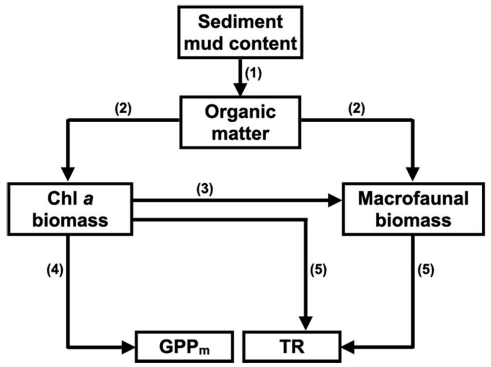

FIGURE 2 | Conceptual structural equation model (SEM) depicting how sediment mud content affects benthic microalgal biomass and macrofaunal biomass and how both of these factors control maximum gross primary production (GPP_m) and total respiration (TR) in tidal flats. **(1)** Fine-grained sediments (e.g., mud) provide more binding sites for organic matter flocculation than coarse-grained sediments (e.g., sand); **(2)** Sediment organic matter is the food sources for benthic microalgae and macrofauna; **(3)** Macrofauna feed on benthic microalgae in the sediment; **(4)** Benthic microalgae contribute most of the GPP in the sediment; **(5)** Both benthic microalgae and macrofauna contribute to the TR in the sediment.

Since sediment characteristics can also affect the composition of benthic microalgae, an alternative conceptual SEM was constructed to assess the potential effects of benthic microalgal composition on the CO_2 fluxes in the tidal flats. We used a composite variable that represented a combination of the chlorophyll *a*, *b*, and *c* concentrations to replace the chlorophyll *a* concentration (the total biomass of benthic microalgae) only for SEM analysis. The composite variable originated from the total combined influence of the measured variables (Grace and Bollen, 2008) and was the sum of all variables involved, depending on the different weights the variables were expected to have. The weights of each variable were derived from the coefficients of the multiple regression of GPP_m with the chlorophyll *a*, *b,* and *c* concentrations of benthic microalgae.

Piecewise SEM was used to test the validity of the conceptual models (Lefcheck, 2016); this approach allowed the fitting of generalized linear mixed models with a hierarchical design (**Figure 2**). We used Shipley's test of direct separation (*d*-test) to assess the overall fit of the models. The model was acceptable when the *p*-value of the chi-square test of Fisher's *C* statistic was higher than the significance level ($p > 0.05$). Fisher's *C* test was related to all the unspecified paths of the conceptual models. When one or more of these unspecified paths presented significant importance, the model did not have a good fit, as the *p*-value of the chi-square test of Fisher's *C* statistic was lower than 0.05. Therefore, these missing paths included required information and needed to be added to the conceptual model. We fitted our conceptual model as a generalized linear model with a Tweedie distribution (Tweedie, 1984) because our data were distributed from zero to positive values. The piecewise SEM was performed by using the 'psem' function from the R package 'piecewiseSEM' (Lefcheck, 2016). The standardized path coefficients were determined using the bootstrap method from the R package 'semEff' (Murphy, 2020). All above statistical analyses were performed with the statistical software R version 4.0.4 (R Core Team, 2021).

RESULTS

Sediment Granulometry

Based on the grain size data, the sediments at the nine tidal flats were classified into five categories: coarse sand (#8 WJ), medium sand (#6 NG, #9 OC), fine sand (#2 HL, #7 BS), very fine sand (#1 SS, #4 HML) and silt (#3 FY, #5 GP) sediment. The median grain size averaged between 57.7 and 552.1 μm, and the mud content averaged from 0.1 to 76.9% (**Table 2**). The increases in sediment mud content were also concomitant with changes in the sorting coefficient and the interstitial dissolved inorganic nitrogen (DIN) concentration (**Table 3**).

Benthic Microalgal and Macrofaunal Biomass

The benthic chlorophyll *a* concentration ranged from 12.5 to 221.3 mg m^{-2}, with an average concentration of 78.8 mg m^{-2} for all the samples analyzed (**Figure 3A**). Of the sites, #8 WJ in summer (221.3 ± 96.2 mg m^{-2}) and #7 BS in winter (168.8 ± 77.4 mg m^{-2}) had the highest observed benthic chlorophyll *a* concentrations. The lowest values of the benthic chlorophyll *a* concentration were observed at #9 OC in both summer and winter (28.8 ± 8.9 mg m^{-2}, 12.5 ± 2.9 mg m^{-2}).

The macrofauna in the top 10 cm of the sediment of the tidal flats were mainly bivalves, decapods, gastropods, amphipods, and polychetes (**Supplementary Table 1**). The macrofaunal biomass in terms of ash-free dry weight (g AFDW m^{-2}) varied among the nine study sites, ranging from 0.1 to 28.6 g AFDW m^{-2}. The macrofaunal biomass showed the highest values at #4 HML (27.7 ± 22.0 g AFDW m^{-2}) in summer and at #6 NG (20.4 ± 27.0 g AFDW m^{-2}) in winter but the lowest values at #5 GP (0.1 ± 0.3 g AFDW m^{-2}) in summer and at #9 OC (0.5 ± 0.5 g AFDW m^{-2}) in winter (**Figure 3B**). The macrofaunal density also varied among the nine study sites, ranging from 0.01 to 0.63 ind. m^{-2}. The highest values of macrofaunal density appeared at #7 BS (0.34 ± 0.40 ind. m^{-2}) in summer and at #1 SS (0.48 ± 0.41 ind. m^{-2}) in winter, while the lowest values appeared at #2 HL (0.01 ± 0.02, 0.01 ± 0.01 ind. m^{-2}) in both summer and winter (**Figure 3C**).

Benthic Carbon Dioxide Fluxes

During emersion, GPP_m showed a clear seasonal pattern with higher values in winter and lower values in summer at most of the study sites except for #8 WJ and #9 OC (**Figure 4A**). Of the sites, #5 GP had the highest values of GPP_m in both summer and winter (76.5 ± 21.2 and 89.7 ± 41.7 mg C m^{-2} h^{-1}, respectively). The lowest values of GPP_m were observed at #3 FY in summer (1.2 ± 1.1 mg C m^{-2} h^{-1}) and at #9 OC in winter (4.4 ± 3.5 mg C m^{-2} h^{-1}). GPP_m was positively correlated with benthic chlorophyll *a* concentration, sorting coefficient and mud content but negatively correlated with interstitial dissolved inorganic phosphorus (DIP) concentration (**Table 3**).

TABLE 3 | Spearman rank correlation coefficients between **(A)** environmental variables and **(B)** environmental variables and carbon fluxes in the tidal flats.

	Temp	Light	Chl *a*	AFDW	Density	Sorting	Mud	DIN	DIP
(A) Environmental variable									
Light	0.08								
Chl *a*	0.08	–0.16*							
AFDW	0.12	–0.13*	0.28***						
Density	0.05	–0.09	0.45***	0.62***					
Sorting	–0.02	–0.03	0.45***	0.20**	0.13*				
Mud	0.02	0.01	0.01	–0.02	–0.01	0.32***			
DIN	0.00	–0.25***	0.25***	0.15*	0.13	0.14	0.19*		
DIP	0.09	0.05	0.19**	0.06	–0.01	0.16*	–0.08	0.10	
(B) Carbon flux									
GPP_m	0.00	–0.02	0.24***	–0.11	0.06	0.21**	0.32***	–0.09	–0.26***
TR	0.36	–0.05	0.22***	0.10	0.19**	0.29***	0.56***	0.29***	–0.01
NPP	–0.10	0.05	0.14*	–0.19**	–0.03	0.18**	0.29***	–0.14*	–0.32***

Temp, sediment temperature; Light, irradiance; Chl a, benthic chlorophyll a concentration; AFDW, macrofaunal biomass in terms of ash-free dry weight; Density, macrofaunal density; Sorting, sediment sorting coefficient; Mud, sediment mud content; DIN, interstitial dissolved inorganic nitrogen (NO_2 + NO_3 + NH_4) concentration; DIP, interstitial dissolved inorganic phosphorus (PO_4) concentration; GPP_m, maximum gross primary production; TR, total respiration; NPP, net primary production.
**p < 0.05, **p < 0.01, ***p < 0.001.*

Total respiration (TR) had an opposite seasonal pattern to that of GPP_m at most of the study sites, with higher values in summer and lower values in winter except at #5 GP (**Figure 4B**). The highest values of TR occurred at #6 NG in summer (17.5 ± 14.2 mg C m^{-2} h^{-1}) and at #5 GP in winter (15.3 ± 7.5 mg C m^{-2} h^{-1}). The lowest values of TR occurred at #8 WJ in summer (1.5 ± 0.4 mg C m^{-2} h^{-1}) and #2 HL in winter (1.0 ± 0.4 mg C m^{-2} h^{-1}). TR was positively correlated with benthic chlorophyll *a* concentration, sorting coefficient, mud content, and interstitial DIN concentration (**Table 3**).

The seasonal pattern of NPP was similar to that of GPP_m (**Figure 4C**). The highest values of NPP appeared at #5 GP in both summer and winter (59.1 ± 26.2 and 68.1 ± 37.0 mg C m^{-2} h^{-1}, respectively). The lowest values of NPP appeared at #3 FY in summer (–17.9 ± 6.4 mg C m^{-2} h^{-1}) and at #9 OC in winter (1.8 ± 3.2 mg C m^{-2} h^{-1}). Notably, the NPP values for the tidal flats at #1 SS, #3 FY, and #6 NG during emersion shifted to negative values in summer, indicating that these sites functioned as carbon sources. The NPP values were positively correlated with benthic chlorophyll *a* concentration, macrofaunal biomass, sorting coefficient and mud content but negatively correlated with interstitial DIN and DIP concentrations.

All values of GPP_m, TR and NPP for the tidal flats during emersion increased significantly with increasing sediment mud content (**Figure 5**). Significant linear increases in GPP_m (y = 0.586x + 5.574, r^2 = 0.386, p < 0.01) and NPP (y = 0.398x + 3.201, r^2 = 0.251, p = 0.034) were apparent when the sediment mud content ranged from 0 to 90%. However, there was high variability in the muddier sediments (**Figures 5A,C**). The TR (y = 0.126x + 2.212, r^2 = 0.400, p < 0.01) curve was similar to the curves of GPP_m and NPP (**Figure 5B**).

SEM Models

Based on the resulting correlations (**Table 3**), the piecewise SEM fit the observed data well (Fisher's C statistic = 8.95, p = 0.062) and revealed that the sediment mud content affected primary production and respiration in tidal flats both directly and indirectly (**Figure 6A**). The sediment mud content directly increased the organic matter content [0.436, 95% confidence interval (CI): 0.356–0.504, p < 0.001]. The sediment mud content also directly increased GPP_m (0.233, 95% CI: 0.154–0.368, p < 0.001) but had an indirect, weak and negative effect on GPP_m via benthic microalgal biomass (–0.180 × 0.117). The sediment mud content also showed a direct and positive effect on TR (0.273, 95% CI: 0.119–0.389, p < 0.001) and indirectly increased TR (0.436 × 0.175) via the organic matter content. Benthic microalgal biomass showed a direct and positive effect on TR. However, there was no direct or indirect effect on TR via benthic macrofaunal biomass.

The alternative SEM replaced with microalgal composition (**Figure 6B**) also fit the observed data well (Fisher's C = 15.52, p = 0.114). The pathways by which sediment mud content influenced TR remained unchanged. In addition to a direct effect on GPP_m (0.208, 95% CI: 0.124–0.347, p < 0.001), the sediment mud content showed an indirect effect on GPP_m (0.381 × 0.053) via a compositional shift in benthic microalgae.

DISCUSSION

Despite the spatial variation in the sediment characteristics, the CO_2 fluxes in the tidal flats during emersion in the tropical and subtropical regions increased with increasing sediment mud content. Our results showed clear positive linear gradients in GPP_m, TR, and NPP from sandy to muddy sediments (**Figure 5**). The SEM further revealed the possible causal pathways by which sediment mud content directly increased GPP_m or indirectly increased GPP_m via a benthic microalgal compositional shift (**Figure 6**). The SEM also revealed that sediment mud content directly increased TR or indirectly increased TR via organic matter content (**Figure 6**). With the integrated SEM framework, our results showed mechanistic evidence of how sediment

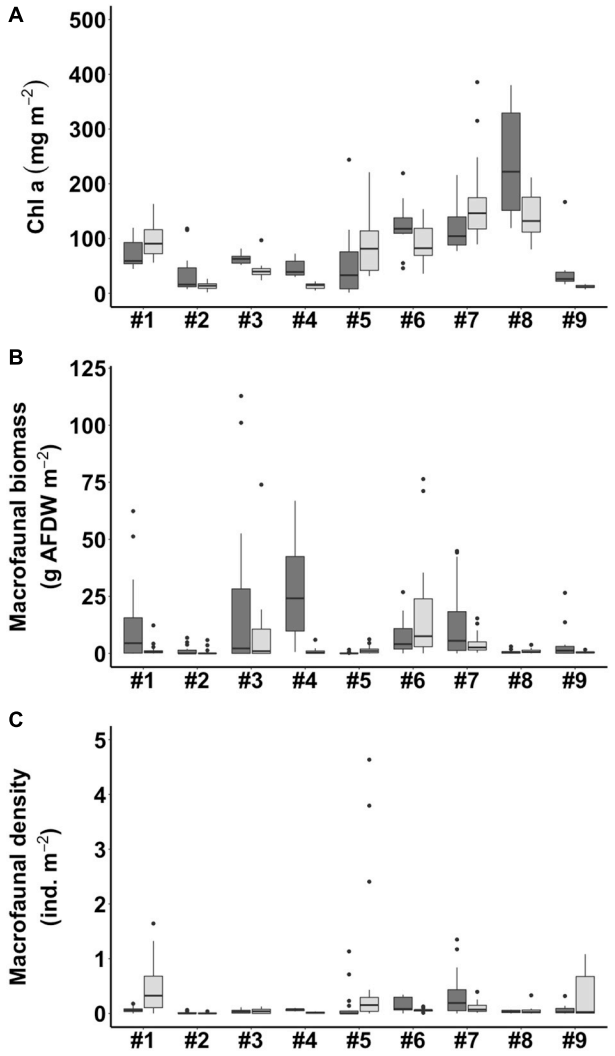

FIGURE 3 | Benthic chlorophyll *a* concentration **(A)**, macrofaunal biomass **(B)**, and macrofaunal density **(C)** in summer (shown in dark gray) and winter (shown in light gray) in the tidal flats. The site numbers are listed in **Table 1**.

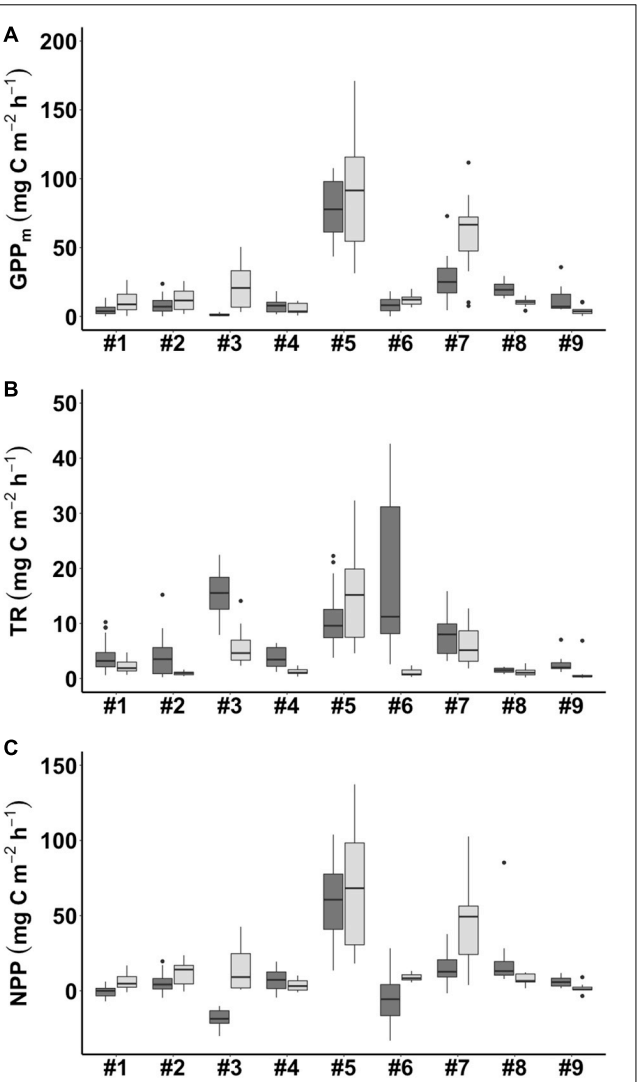

FIGURE 4 | Carbon flux (**A**: GPP_m = maximum gross primary production; **B**: TR = total respiration; **C**: NPP = net primary production) in summer (shown in dark gray) and winter (shown in light gray) in the tidal flats during emersion. The site numbers are listed in **Table 1**.

mud content acted as a critical factor regulating carbon fluxes in tidal flats.

Despite the critical role of sediment mud content in regulating carbon fluxes, prior studies showed inconsistent relationships between benthic chlorophyll *a* concentration and sediment mud content. Both Cahoon et al. (1999) and Cahoon and Safi (2002) reported negative relationships between the proportion of very fine sediments and benthic microalgal biomass in tidal flats in the US and on the North Island of New Zealand. However, both Lee et al. (2011) and Pratt et al. (2015) showed an opposite trend, i.e., that benthic microalgal biomass was positively correlated with sediment mud content. In this study, there was no significant correlation between the benthic chlorophyll *a* concentration and sediment mud content. In fact, the benthic chlorophyll *a* concentration was higher in the sandy sediments at the NG, BS, and WJ sites than at the other sites; in addition, the sediments of these three sites were categorized as medium, fine and coarse sand, respectively. The median grain size at these sampling sites ranged from 166.7 to 552.1 μm, and all the mud content values were lower than 30%. The SEM showed that in comparison to the muddy sediments, the sandy sediments supported more microalgal biomass in the tidal flats.

The greater microalgal biomass in the sandy sediments than in the muddy sediments can be attributed to the thicker photic zone in the sandy sediments. The photic zone in muddy sediments is shallow (<600 μm; Cartaxana et al., 2011, 2006), and benthic microalgae are required to move up and down with diurnal and tidal cycles to maintain photosynthesis. In comparison to algal cells at deeper depths, algal cells that must remain near the sediment surface might be more susceptible to resuspension by tides and waves and

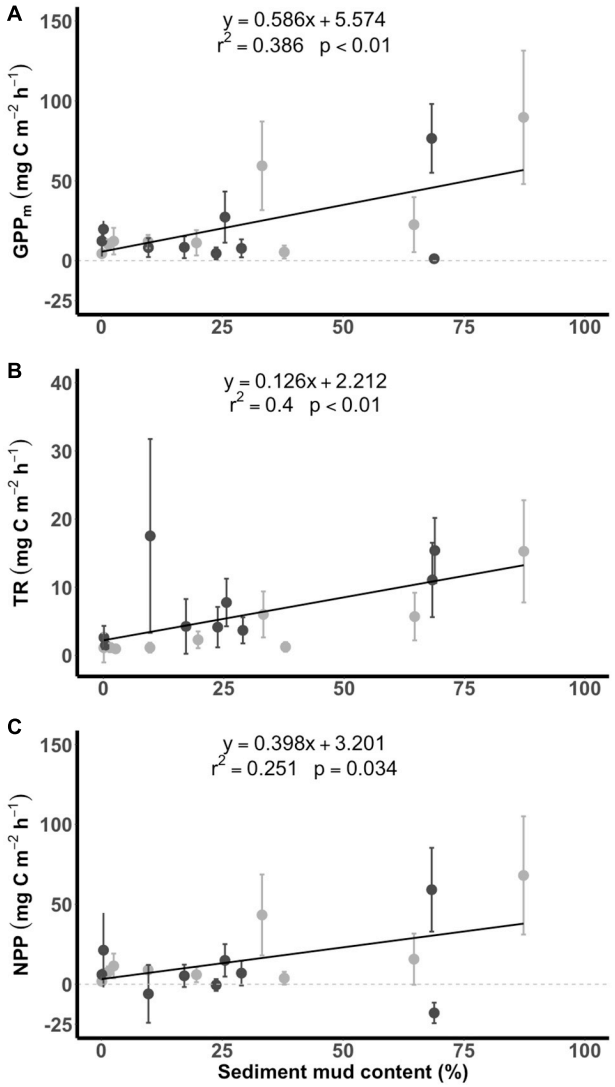

FIGURE 5 | Relationships between carbon flux (**A**: GPP_m, maximum gross primary production; **B**: TR, total respiration; **C**: NPP, net primary production) and sediment mud content in the tidal flats. The dark gray points indicate measurements taken in summer, and the light gray points indicate measurements taken in winter. Data are presented as the mean ± SD.

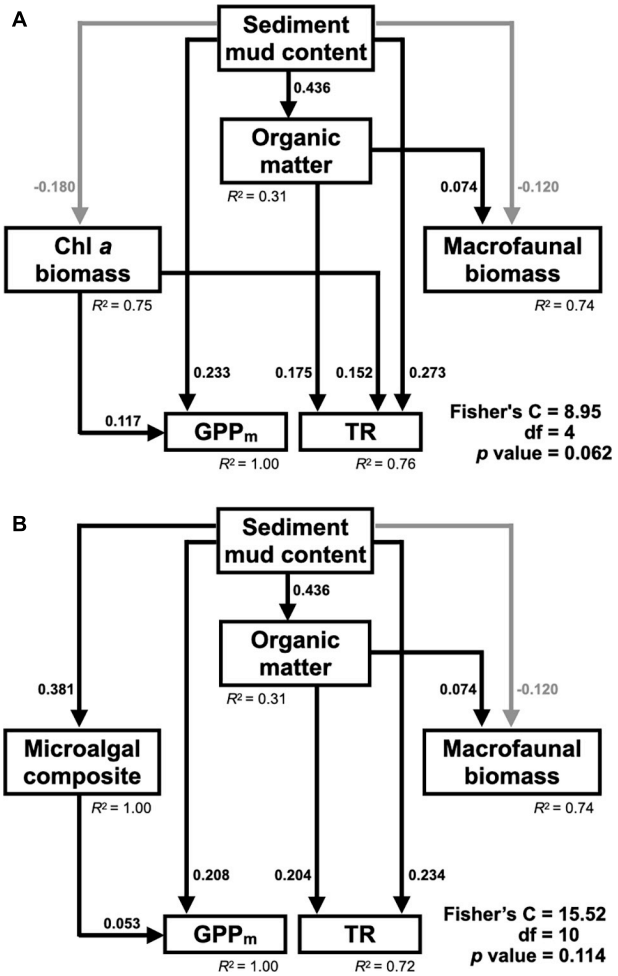

FIGURE 6 | (A) Final piecewise structural equation model (SEM) (Fisher's *C* statistic = 8.95, df = 4, $P = 0.062$) depicting the direct and indirect effects of sediment mud content on GPP_m and TR through benthic microalgal biomass and macrofaunal biomass in tidal flats. **(B)** Final piecewise structural equation model (SEM) (Fisher's *C* statistic = 15.52, df = 10, $P = 0.114$) depicting the direct and indirect effects of sediment mud content on GPP_m and TR through benthic microalgal composition and macrofaunal biomass in the tidal flats. Only significant paths are depicted. Black lines represent positive paths, and gray lines represent negative paths. The standardized coefficients of significant paths and the conditional R^2 values of the response variables are shown.

epifaunal grazing. However, the photic depth can extend to 3 mm in sandy sediments (Cartaxana et al., 2006, 2011). Since light can penetrate deeper into coarse sediments, benthic microalgae can be distributed more evenly throughout the thicker photic layer. The other possibility for this outcome is that the composition of benthic microalgae in the muddy sediments was different from that in the sandy sediments (Du et al., 2009). In muddy sediments, the benthic microalgal community is generally dominated by epipelic benthic diatoms that exhibit endogenous vertical migratory rhythms coupled with diurnal and tidal cycles (Consalvey et al., 2004; Haubois et al., 2005). They often aggregate as a dense and highly productive biofilm at the surface of sediment during low tide in the daytime (Cartaxana et al., 2011). In sandy sediments, the benthic microalgae community composition is generally dominated by epipsammic benthic diatoms that attach to sand particles across the deeper photic layer and do not exhibit migratory patterns (Consalvey et al., 2004). The algal cells near the sediment surface might also be more susceptible than algal cells at deeper depths to grazing by macrofauna. Other factors, such as interstitial space volume, grazing pressure, nutrient fluxes, and light penetration, may confound the relationship between benthic microalgal biomass and sediment granulometry; any combination of these factors might lead to lower or higher benthic microalgal biomass in tidal flats, which might mask the relationship with sediment mud content.

Hydrodynamics might also affect the response of benthic microalgal biomass to sandy sediments. Dalu et al. (2020) conducted a microcosm experiment and found that the benthic chlorophyll *a* concentration was the highest in sediments with coarser particle sizes ranging from 125 to 500 μm, which was comparable to our results. However, the sediment grain sizes at #2 HL and #9 OC both fell into this range, but the chlorophyll *a* concentration at these sites was low (**Table 2**). Compared with those at the #6 NG and #7 BS sites, significantly lower sediment sorting coefficients at #2 HL and #9 OC were also observed. The sediment sorting coefficient was used to assess the distribution of the grain sizes in sediments. Well-sorted sediment indicates that the distribution of grain sizes is even; these sediments might be fully winnowed by waves and tidal currents. Contrary to muddy sediment, where benthic microalgae normally form dense biofilms embedded within a matrix comprised of carbon exudates (commonly known as EPS) that protect them from erosion, such high-energy forces can resuspend or remove not only small particles but also benthic microalgal cells inhabiting the sandy sediment.

Sediment mud content can also influence the density of macrofauna in tidal flats. Pratt et al. (2014) studied nine estuaries on the North Island of New Zealand and found that the densities of a suspension feeder (*Austrovenus stutchburyi*) and a deposit feeder (*Macomona liliana*) decreased significantly with increasing sediment mud content, although the gradient of the mud content ranged only between 0 and 30%. Other studies have indicated that the effects of sediment mud content on macrofaunal abundance were species-dependent (Thrush et al., 2003; Ellis et al., 2006; Anderson, 2008). For example, the relationships between the density of polychetes and sediment mud content can be classified into three types: an increasing curve (*Scolecolepides benhami*), a decreasing curve (*Aonides oxycephala*) and a Gaussian response curve (*Heteromastus filiformis*; Thrush et al., 2003). In this study, benthic macrofaunal biomass was high either in muddy sediments (FY and HML) or in sandy sediments (NG) and did not show a significant correlation with sediment mud content (**Table 3**). The macrofaunal community mainly contained bivalves, decapods, gastropods, amphipods, and polychetes, which might have masked the individual response of each taxon to the sediment mud content. However, the SEM showed that in total, in comparison to the muddy sediments, the sandy sediments supported more macrofaunal biomass in the tidal flats.

The primary production (GPP_m and NPP) was higher in winter than in summer at most of the studied sites except at #8 WJ and #9 OC, while the total respiration (TR) in the tidal flats was higher in summer than in winter at most of the studied sites except at #5 GP. Temperature has been reported to be a major driver of the seasonal variation in the CO_2 fluxes in subtropical tidal flats (Lee et al., 2011). Higher temperatures generally stimulate metabolic processes and photosynthesis rates. Lin et al. (2020) further indicated that the effects of temperature on the CO_2 fluxes in tidal flats were non-linear, showing a quadratic relationship with an optimal temperature at which the CO_2 fluxes were highest. In this study, the sediment temperatures in summer ranged from 31.2°C to 40.6°C, which far exceeded the optimal temperatures (28.7°C for GPP_m, 26.6°C for NPP; Lin et al., 2020) for primary production. Higher temperatures might also result in photoinhibition in benthic microalgae (Laviale et al., 2015). These temperatures can explain the decreases in GPP_m and NPP in summer. In contrast, the sediment temperature in winter ranged from 16.0°C to 27.6°C, which was within the range of optimal temperatures (45°C; Lin et al., 2020) for benthic respiration in tidal flats. This scenario might be the reason that the TR in the tidal flats still increased in summer at most of the study sites.

Hydrodynamics may affect the primary production and respiration in tidal flats during immersion in different ways. Wind- or tide-induced disturbances may increase water turbidity in tidal flats. Increased water turbidity can decrease light availability on the sediment and then reduce the photosynthesis of benthic microalgae (Migné et al., 2009). Drylie et al. (2018) measured GPP in three unvegetated sandflats in Kaipara Harbour, New Zealand and found that the submerged GPP was significantly lower than the emerged GPP due to light limitation. However, respiration was generally higher under immersed condition than under emerged condition due to the elevated activity of infauna during inundation (Migné et al., 2009). Lee et al. (2011) further demonstrated that turbid water increased respiration during immersion in subtropical tidal flats. It is clear that the CO_2 fluxes in tidal flats located in the shallow waters along the coast of marginal seas are prone to disturbances caused by wind or tide.

In the SEM, the direct effect of the sediment mud content on GPP_m was stronger than the indirect effect via benthic chlorophyll *a* content. This result suggests that in comparison to microalgal biomass, the sediment mud content had a more direct influence on GPP_m. Compared to those in sandy sediments, the reduced interstitial volumes in muddy sediments might have allowed more water retention among grain particles (Watermann et al., 1999; Lee et al., 2011), which might have resulted in the accumulation of regenerated nutrients and organic matter that stimulated the growth of benthic microalgae in the sediments (Ehrenhauss et al., 2004). However, in the alternative SEM replaced with the composition of benthic microalgae, there was a weak and indirect effect of sediment mud content on GPP_m via the composition shift of benthic microalgae. In this study, the chlorophyll *c* concentration as a proxy of diatom biomass in the tidal flats decreased with increasing sediment mud content ($y = -0.188x + 12.478$, $r^2 = 0.189$, $p < 0.001$), whereas the chlorophyll *b* concentration as a proxy of green algal biomass remained unchanged. Sediment granulometry has been reported to shift the composition of the benthic microalgal community in tidal flats (Underwood and Barnett, 2006). Some epipelic diatoms with large and long valves occur in finer sediments, whereas small species of diatoms inhabit coarser sediments (Du et al., 2009). In western Taiwan, Shiu (2009) found that the density of benthic diatoms with larger biovolumes was negatively correlated with sediment grain size. Although the biomass of diatoms decreased in muddy sediments, the diatom community may have shifted to diatoms with large biovolumes. Since diatoms with large biovolumes generally have higher photosynthetic rates

(Taguchi, 1976; Geider et al., 1986), the GPP_m is expected to increase with increasing mud content in the sediments.

The SEM showed a significant indirect effect of sediment mud content on TR via organic matter content. However, the contribution of benthic microalgal and macrofaunal biomass to TR was relatively minor. This result is not surprising because in comparison to macrofauna and meiofauna, the bacterial community in tidal flats generally plays a more vital role in benthic respiration and contributes much more to the total respiration (Piepenburg et al., 1995; Hubas et al., 2006). Bacterial respiration can account for 67–88% of the annual benthic respiration in shallow waters (Piepenburg et al., 1995; Hubas et al., 2007). Moreover, the dynamics of bacterial communities are strongly regulated by granulometry (Hubas et al., 2006). Our results further suggest that the sediment mud content influenced the TR in the tidal flats not by increasing the biomasses of benthic microalgae and macrofauna but by influencing the metabolism of the bacterial community.

CONCLUSION

In the nine studied tidal flats in tropical and subtropical regions during emersion at noon, GPP_m and NPP had higher values in winter than in summer due to the sediment temperature in summer deviating from the optimal temperature. In contrast, TR had higher values in summer than in winter because the sediment temperature in summer was still within the optimal temperature range. All the values of GPP_m, TR, and NPP increased significantly with increasing sediment mud content. The SEM further showed mechanistic evidence of how sediment mud content can be a critical factor regulating carbon fluxes in tidal flats. The sediment mud content directly increased GPP_m or indirectly increased GPP_m via a compositional shift in benthic microalgae. The sediment mud content also directly increased TR or indirectly increased TR via increased organic matter content. Considering the large proportion of unvegetated tidal flats in coastal zones, any anthropogenic activity or natural forcing that eventually leads to a change in sediment mud content will likely substantially change the carbon sequestration capacity in those coastal ecosystems.

DATA AVAILABILITY STATEMENT

The original contributions presented in the study are included in the article/**Supplementary Material**, further inquiries can be directed to the corresponding author/s.

AUTHOR CONTRIBUTIONS

W-JL and H-JL conceived the ideas and designed the study. W-JL carried out the field work and sampling quantification. W-JL, C-WL, M-CC, and H-JL contributed to the data analysis and interpretation. W-JL and H-JL drafted the manuscript. All authors read and approved the final manuscript.

FUNDING

This work was funded by (1) Kinmen National Park Headquarters, Ministry of Interior, Taiwan and (2) the "Innovation and Development Center of Sustainable Agriculture" project administered by the "Featured Areas Research Center program" within the framework of Taiwanese Ministry of Education's "Higher Education Sprout Project."

SUPPLEMENTARY MATERIAL

The Supplementary Material for this article can be found online at: https://www.frontiersin.org/articles/10.3389/fmars.2021.670180/full#supplementary-material

Supplementary Figure 1 | Photosynthesis-irradiance (P-I) curves during emersion in summer and winter in the tidal flats. Different symbols represent different samplings in each season at each site. P-I curves with determination coefficients larger than 0.80 are shown. No P-I curve at FY in summer is shown because the GPP values under different light irradiances were zero.

Supplementary Table 1 | Density of each group of macrofauna in the tidal flats. Data are presented as the range and mean ± SD. Zero represents no occurrence of each taxon in the tidal flats. Only samplings with macrofauna were averaged.

Supplementary Table 2 | CO_2 fluxes (in mg C m^{-2} h^{-1}) measured in the tidal flats. Data are presented as the range, mean ± SD and 95% confidence interval.

REFERENCES

Anderson, M. J. (2008). Animal-sediment relationships re-visited: characterising species' distributions along an environmental gradient using canonical analysis and quantile regression splines. *J. Exp. Mar. Bio. Ecol.* 366, 16–27. doi: 10.1016/j.jembe.2008.07.006

Bale, A. J., and Kenny, A. J. (2005). "Sediment analysis and seabed characterisation," in *Methods for the Study of Marine Benthos*, eds A. Eleftheriou and A. McIntyre (Hoboken, NJ: Blackwell Science Ltd), 43–86. doi: 10.1002/9780470995129.ch2

Bendschneider, K., and Robinson, R. J. (1952). A new spectrophotometric method for the determination of nitrite in sea water. *J. Mar. Res.* 11, 87–96.

Billerbeck, M., Røy, H., Bosselmann, K., and Huettel, M. (2007). Benthic photosynthesis in submerged Wadden Sea intertidal flats. *Estuar. Coast. Shelf Sci.* 71, 704–716. doi: 10.1016/j.ecss.2006.09.019

Brotas, V., and Catarino, F. (1995). Microphytobenthos primary production of Tagus estuary intertidal flats (Portugal). *Netherlands J. Aquat. Ecol.* 29, 333–339. doi: 10.1007/BF02084232

Cadée, G. C., and Hegeman, J. (1974). Primary production of the benthic microflora living on tidal flats in the dutch wadden sea. *Netherlands J. Sea Res.* 8, 260–291. doi: 10.1016/0077-7579(74)90020-9

Cahoon, L. (1999). The role of benthic microalgae in neritic ecosystems. *Oceanogr. Mar. Biol. an Annu. Rev.* 37, 47–86.

Cahoon, L. B., Nearhoof, J. E., and Tilton, C. L. (1999). Sediment grain size effect on benthic microalgal biomass in shallow aquatic ecosystems. *Estuaries* 22, 735–741. doi: 10.2307/1353106

Cahoon, L. B., and Safi, K. A. (2002). Distribution and biomass of benthic microalgae in Manukau Harbour, New Zealand. *New Zeal. J. Mar. Freshw. Res.* 36, 257–266. doi: 10.1080/00288330.2002.9517084

Cartaxana, P., Mendes, C. R., Van Leeuwe, M. A., and Brotas, V. (2006). Comparative study on microphytobenthic pigments of muddy and sandy intertidal sediments of the Tagus estuary. *Estuar. Coast. Shelf Sci.* 66, 225–230. doi: 10.1016/j.ecss.2005.08.011

Cartaxana, P., Ruivo, M., Hubas, C., Davidson, I., Serôdio, J., and Jesus, B. (2011). Physiological versus behavioral photoprotection in intertidal epipelic

and epipsammic benthic diatom communities. *J. Exp. Mar. Bio. Ecol.* 405, 120–127. doi: 10.1016/j.jembe.2011.05.027

Chen, J., Wang, D., Li, Y., Yu, Z., Chen, S., Hou, X., et al. (2020). The carbon stock and sequestration rate in tidal flats from coastal China. *Glob. Biogeochem. Cycles* 34:e2020GB006772. doi: 10.1029/2020GB006772

Chen, Y., Dong, J., Xiao, X., Zhang, M., Tian, B., Zhou, Y., et al. (2016). Land claim and loss of tidal flats in the Yangtze Estuary. *Sci. Rep.* 6:24018. doi: 10.1038/srep24018

Colijn, F., and de Jonge, V. (1984). Primary production of microphytobenthos in the Ems-Dollard Estuary. *Mar. Ecol. Prog. Ser.* 14, 185–196. doi: 10.3354/meps014185

Consalvey, M., Paterson, D. M., and Underwood, G. J. C. (2004). The ups and downs of life in a benthic biofilm: migration of benthic diatoms. *Diatom Res.* 19, 181–202. doi: 10.1080/0269249X.2004.9705870

Dalu, T., Cuthbert, R. N., Chavalala, T. L., Froneman, P. W., and Wasserman, R. J. (2020). Assessing sediment particle-size effects on benthic algal colonisation and total carbohydrate production. *Sci. Total Environ.* 710:136348. doi: 10.1016/j.scitotenv.2019.136348

Davidson, N. C., and Finlayson, C. M. (2019). Updating global coastal wetland areas presented in Davidson and Finlayson (2018). *Mar. Freshw. Res.* 70, 1195–1200. doi: 10.1071/MF19010

Davis, M., and Mclntire, C. (1983). Effects of physical gradients on the production dynamics of sediment-associated algae. *Mar. Ecol. Prog. Ser.* 13, 103–114. doi: 10.3354/meps013103

Davoult, D., Migné, A., Créach, A., Gévaert, F., Hubas, C., Spilmont, N., et al. (2009). Spatio-temporal variability of intertidal benthic primary production and respiration in the western part of the Mont Saint-Michel Bay (Western English Channel, France). *Hydrobiologia* 620, 163–172. doi: 10.1007/s10750-008-9626-3

De Jonge, V. N., and Van Beuselom, J. E. E. (1992). Contribution of resuspended microphytobenthos to total phytoplankton in the EMS estuary and its possible role for grazers. *Netherlands J. Sea Res.* 30, 91–105. doi: 10.1016/0077-7579(92)90049-K

Drylie, T. P., Lohrer, A. M., Needham, H. R., Bulmer, R. H., and Pilditch, C. A. (2018). Benthic primary production in emerged intertidal habitats provides resilience to high water column turbidity. *J. Sea Res.* 142, 101–112. doi: 10.1016/j.seares.2018.09.015

Du, G. Y., Son, M., Yun, M., An, S., and Chung, I. K. (2009). Microphytobenthic biomass and species composition in intertidal flats of the Nakdong River estuary, Korea. *Estuar. Coast. Shelf Sci.* 82, 663–672. doi: 10.1016/j.ecss.2009.03.004

Ehrenhauss, S., Witte, U., Janssen, F., and Huettel, M. (2004). Decomposition of diatoms and nutrient dynamics in permeable North Sea sediments. *Cont. Shelf Res.* 24, 721–737. doi: 10.1016/j.csr.2004.01.002

Eisenhauer, N., Bowker, M. A., Grace, J. B., and Powell, J. R. (2015). From patterns to causal understanding: structural equation modeling (SEM) in soil ecology. *Pedobiologia* 58, 65–72. doi: 10.1016/j.pedobi.2015.03.002

Ellis, J., Ysebaert, T., Hume, T., Norkko, A., Bult, T., Herman, P., et al. (2006). Predicting macrofaunal species distributions in estuarine gradients using logistic regression and classification systems. *Mar. Ecol. Prog. Ser.* 316, 69–83. doi: 10.3354/meps316069

Geider, R., Piatt, T., and Raven, J. (1986). Size dependence of growth and photosynthesis in diatoms: a synthesis. *Mar. Ecol. Prog. Ser.* 30, 93–104. doi: 10.3354/meps030093

Golterman, H. L. (ed.) (1975). "Algae and their pigments," in *Physiological Limnology: An Approach to the Physiology of Lake Ecosystems*, (Amsterdam: Elsevier Scientific Publishing Company), 233–247.

Grace, J. B., and Bollen, K. A. (2008). Representing general theoretical concepts in structural equation models: the role of composite variables. *Environ. Ecol. Stat.* 15, 191–213. doi: 10.1007/s10651-007-0047-7

Guarini, J.-M., Chauvaud, L., and Coston-Guarini, J. (2008). Can the intertidal benthic microalgal primary production account for the "Missing Carbon Sink"? *J. Oceanogr. Res. Data* 1, 13–19. doi: 10.3354/meps071013

Haro, S., Lara, M., Laiz, I., González, C. J., Bohórquez, J., Garcia-Robledo, E., et al. (2020). Microbenthic net metabolism along intertidal gradients (Cadiz Bay, SW Spain): spatio-temporal patterns and environmental factors. *Front. Mar. Sci.* 7:39. doi: 10.3389/fmars.2020.00039

Haubois, A. G., Sylvestre, F., Guarini, J. M., Richard, P., and Blanchard, G. F. (2005). Spatio-temporal structure of the epipelic diatom assemblage from an intertidal mudflat in Marennes-Oléron Bay, France. *Estuar. Coast. Shelf Sci.* 64, 385–394. doi: 10.1016/j.ecss.2005.03.004

Hsieh, H. L., and Chang, K. H. (1991). Habitat characteristics and occurrence of the spionid *Pseudopolydora* sp on the tube-caps of the onuphid *Diopatra bilobata* (Polychaeta: Spionidae Onuphidae). *Bull. Inst. Zool. Acad. Sin.* 30, 331–339.

Hubas, C., and Davoult, D. (2006). Does seasonal proliferation of *Enteromorpha* sp. affect the annual benthic metabolism of a small macrotidal estuary? (Roscoff Aber Bay, France). *Estuar. Coast. Shelf Sci.* 70, 287–296. doi: 10.1016/j.ecss.2006.06.019

Hubas, C., Davoult, D., Cariou, T., and Artigas, L. F. (2006). Factors controlling benthic metabolism during low tide along a granulometric gradient in an intertidal bay (Roscoff Aber Bay, France). *Mar. Ecol. Prog. Ser.* 316, 53–68. doi: 10.3354/meps316053

Hubas, C., Lamy, D., Artigas, L. F., and Davoult, D. (2007). Seasonal variability of intertidal bacterial metabolism and growth efficiency in an exposed sandy beach during low tide. *Mar. Biol.* 151, 41–52. doi: 10.1007/s00227-006-0446-6

Jassby, A. D., and Platt, T. (1976). Mathematical formulation of the relationship between photosynthesis and light for phytoplankton. *Limnol. Oceanogr.* 21, 540–547. doi: 10.4319/lo.1976.21.4.0540

Jeffrey, S. W., and Humphrey, G. F. (1975). New spectrophotometric equations for determining chlorophylls *a, b, c1* and *c2* in higher plants, algae and natural phytoplankton. *Biochem. Physiol. Pflanz.* 167, 191–194. doi: 10.1016/S0015-3796(17)30778-3

Jenkins, D., and Medsker, L. L. (1964). Brucine method for determination of nitrate in ocean, estuarine, and fresh waters. *Anal. Chem.* 36, 610–612. doi: 10.1021/ac60209a016

Junoy, J., Castellanos, C., Viéitez, J. M., De La Huz, M. R., and Lastra, M. (2005). The macroinfauna of the Galician sandy beaches (NW Spain) affected by the Prestige oil-spill. *Mar. Pollut. Bull.* 50, 526–536. doi: 10.1016/j.marpolbul.2004.11.044

Koh, C. H., and Khim, J. S. (2014). The Korean tidal flat of the Yellow Sea: physical setting, ecosystem and management. *Ocean Coast. Manag.* 102, 398–414. doi: 10.1016/j.ocecoaman.2014.07.008

Laviale, M., Barnett, A., Ezequiel, J., Lepetit, B., Frankenbach, S., Méléder, V., et al. (2015). Response of intertidal benthic microalgal biofilms to a coupled light-temperature stress: evidence for latitudinal adaptation along the Atlantic coast of Southern Europe. *Environ. Microbiol.* 17, 3662–3677. doi: 10.1111/1462-2920.12728

Lee, L.-H., Hsieh, L.-Y., and Lin, H.-J. (2011). In situ production and respiration of the benthic community during emersion on subtropical intertidal sandflats. *Mar. Ecol. Prog. Ser.* 441, 33–47. doi: 10.3354/meps09362

Lee, L.-H., and Lin, H.-J. (2013). Effects of an oil spill on benthic community production and respiration on subtropical intertidal sandflats. *Mar. Pollut. Bull.* 73, 291–299. doi: 10.1016/j.marpolbul.2013.05.006

Lefcheck, J. S. (2016). piecewiseSEM: piecewise structural equation modelling in r for ecology, evolution, and systematics. *Methods Ecol. Evol.* 7, 573–579. doi: 10.1111/2041-210X.12512

Lin, W.-J., Wu, J., and Lin, H.-J. (2020). Contribution of unvegetated tidal flats to coastal carbon flux. *Glob. Chang. Biol.* 26, 3443–3454. doi: 10.1111/gcb.15107

McIntyre, H. L., Geider, R. J., and Miller, D. C. (1996). Microphytobenthos: the ecological role of the "Secret Garden" of unvegetated, shallow-water marine habitats. I. Disribution, abundance and primary production. *Estuaries* 19, 185–201.

McMinn, A., Hirawake, T., Hamaoka, T., Hattori, H., and Fukuchi, M. (2005). Contribution of benthic microalgae to ice covered coastal ecosystems in northern Hokkaido, Japan. *J. Mar. Biol. Assoc. U.K.* 85, 283–289. doi: 10.1017/S0025315405011173h

Migné, A., Davoult, D., Spilmont, N., Menu, D., Boucher, G., Gattuso, J. P., et al. (2002). A closed-chamber CO_2-flux method for estimating intertidal primary production and respiration under emersed conditions. *Mar. Biol.* 140, 865–869. doi: 10.1007/s00227-001-0741-1

Migné, A., Davoult, D., Spilmont, N., Ouisse, V., and Boucher, G. (2016). Spatial and temporal variability of CO_2 fluxes at the sediment-air interface in a tidal flat of a temperate lagoon (Arcachon Bay, France). *J. Sea Res.* 109, 13–19. doi: 10.1016/j.seares.2016.01.003

Migné, A., Spilmont, N., Boucher, G., Denis, L., Hubas, C., Janquin, M. A., et al. (2009). Annual budget of benthic production in Mont Saint-Michel Bay considering cloudiness, microphytobenthos migration, and variability of respiration rates with tidal conditions. *Cont. Shelf Res.* 29, 2280–2285. doi: 10.1016/j.csr.2009.09.004

Migné, A., Spilmont, N., and Davoult, D. (2004). In situ measurements of benthic primary production during emersion: seasonal variations and annual production in the Bay of Somme (eastern English Channel, France). *Cont. Shelf Res.* 24, 1437–1449. doi: 10.1016/j.csr.2004.06.002

Murphy, J., and Riley, J. P. (1962). A modified single solution method for the determination of phosphate in natural waters. *Anal. Chim. Acta* 27, 31–36. doi: 10.1057/9781137461131

Murphy, M. (2020). *semEff: Automatic Calculation of Effects for Piecewise Structural Equation Models Version 0.5.0*.

Murray, N. J., Phinn, S. R., Clemens, R. S., Roelfsema, C. M., and Fuller, R. A. (2012). Continental scale mapping of tidal flats across east Asia using the landsat archive. *Remote Sens.* 4, 3417–3426. doi: 10.3390/rs4113417

Murray, N. J., Phinn, S. R., DeWitt, M., Ferrari, R., Johnston, R., Lyons, M. B., et al. (2019). The global distribution and trajectory of tidal flats. *Nature* 565, 222–225. doi: 10.1038/s41586-018-0805-8

Otani, S., and Endo, T. (2019). "Blue carbon in shallow coastal ecosystems," in *Blue Carbon in Shallow Coastal Ecosystems*, eds T. Kuwae and M. Hori (Singapore: Springer), 223–250.

Pai, S.-C., Tsau, Y.-J., and Yang, T.-I. (2001). pH and buffering capacity problems involved in the determination of ammonia in saline water using the indophenol blue spectrophotometric method. *Anal. Chim. Acta* 434, 209–216. doi: 10.1016/S0003-2670(01)00851-0

Piepenburg, D., Blackburn, T. H., vonDorrien, C. F., Gutt, J., Hall, P. O., Hulth, S., et al. (1995). Partitioning of benthic community respiration in the Arctic (northwestern Barents Sea). *Mar. Ecol. Prog. Ser.* 118, 199–214. doi: 10.3354/meps118199

Pratt, D. R., Lohrer, A. M., Pilditch, C. A., and Thrush, S. F. (2014). Changes in ecosystem function across sedimentary gradients in estuaries. *Ecosystems* 17, 182–194. doi: 10.1007/s10021-013-9716-6

Pratt, D. R., Pilditch, C. A., Lohrer, A. M., Thrush, S. F., and Kraan, C. (2015). Spatial distributions of grazing activity and microphytobenthos reveal scale-dependent relationships across a sedimentary gradient. *Estuaries Coasts* 38, 722–734. doi: 10.1007/s12237-014-9857-7

R Core Team (2021). *R: A Language and Environment for Statistical Computing*. Vienna: R Foundation for Statistical Computing.

Rahman, M. A., and Ishiga, H. (2012). Trace metal concentrations in tidal flat coastal sediments, Yamaguchi Prefecture, southwest Japan. *Environ. Monit. Assess.* 184, 5755–5771. doi: 10.1007/s10661-011-2379-x

Sarker, J., Yamamoto, T., and Hashimoto, T. (2009). Contribution of benthic microalgae to the whole water algal biomass and primary production in Suo Nada, the Seto Inland Sea, Japan. *J. Oceanogr.* 65, 311–323. doi: 10.1007/s10872-009-0029-5

Savelli, R., Bertin, X., Orvain, F., Gernez, P., Dale, A., Coulombier, T., et al. (2019). Impact of chronic and massive resuspension mechanisms on the microphytobenthos dynamics in a temperate intertidal mudflat. *J. Geophys. Res. Biogeosciences* 124, 3752–3777. doi: 10.1029/2019JG005369

Shiu, J.-W. (2009). *Spatio-Temporal Changes in Biomass and Abundance of Benthic Diatoms in the Kaomei Wetland*. Taichung: National Chung Hsing University.

Spilmont, N., Davoult, D., and Migné, A. (2006). Benthic primary production during emersion: in situ measurements and potential primary production in the Seine Estuary (English Channel, France). *Mar. Pollut. Bull.* 53, 49–55. doi: 10.1016/j.marpolbul.2005.09.016

Spilmont, N., Migné, A., Seuront, L., and Davoult, D. (2007). Short-term variability of intertidal benthic community production during emersion and the implication in annual budget calculation. *Mar. Ecol. Prog. Ser.* 333, 95–101. doi: 10.3354/meps333095

Taguchi, S. (1976). Relationship between photosynthesis and cell size of marine diatoms. *J. Phycol.* 12, 185–189. doi: 10.1111/j.1529-8817.1976.tb00499.x

Thrush, S. F., Hewitt, J. E., Norkko, A., Nicholls, P. E., Funnell, G. A., and Ellis, J. I. (2003). Habitat change in estuaries: predicting broad-scale responses of intertidal macrofauna to sediment mud content. *Mar. Ecol. Prog. Ser.* 263, 101–112. doi: 10.3354/meps263101

Tweedie, M. C. K. (1984). "An index which distinguishes between some important exponential families," in *Statistics: Applications and New Directions. Proceedings of the Indian Statistical Institute Golden Jubilee International Conference*, eds J. K. Ghosh and J. Roy (Calcutta: Indian Statistical Institute), 579–604.

Underwood, G. J. C., and Barnett, M. (2006). "What determines species composition in microphytobenthic biofilms?," in *Functioning of Microphytobenthos In Estuaries*, eds J. Kromkamp, J. F. C. de Brouwer, G. F. Blanchard, R. M. Forster, and V. Créach (Amsterdam: Royal Netherlands Academy of Arts and Sciences), 121–138.

Underwood, G. J. G., and Kromkamp, J. (1999). Primary production by phytoplankton and microphytobenthos in estuaries. *Adv. Ecol. Res.* 29, 93–153. doi: 10.1016/s0065-2504(08)60192-0

Watermann, F., Hillebrand, H., Gerdes, G., Krumbein, W. E., and Sommet, U. (1999). Competition between benthic cyanobacteria and diatoms as influenced by different grain sizes and temperatures. *Mar. Ecol. Prog. Ser.* 187, 77–87. doi: 10.3354/meps187077

Yoshino, K., Tsugeki, N. K., Amano, Y., Hayami, Y., Hamaoka, H., and Omori, K. (2012). Intertidal bare mudflats subsidize subtidal production through outwelling of benthic microalgae. *Estuar. Coast. Shelf Sci.* 109, 138–143. doi: 10.1016/j.ecss.2012.05.021

Yu, O. H., Lee, H. G., Shim, W. J., Kim, M., and Park, H. S. (2013). Initial impacts of the Hebei Spirit oil spill on the sandy beach macrobenthic community west coast of Korea. *Mar. Pollut. Bull.* 70, 189–196. doi: 10.1016/j.marpolbul.2013.02.035

Zhang, R., Zhou, L., Zhang, F., Ding, Y., Gao, J., Chen, J., et al. (2013). Heavy metal pollution and assessment in the tidal flat sediments of Haizhou Bay, China. *Mar. Pollut. Bull.* 74, 403–412. doi: 10.1016/j.marpolbul.2013.06.019

Conflict of Interest: The authors declare that the research was conducted in the absence of any commercial or financial relationships that could be construed as a potential conflict of interest.

frontiers in Marine Science

ORIGINAL RESEARCH
published: 12 July 2021
doi: 10.3389/fmars.2021.678607

Trichome Lengths of the Heterocystous N_2-Fixing Cyanobacteria in the Tropical Marginal Seas of the Western North Pacific

Sing-how Tuo[1,2], Margaret R. Mulholland[2], Yukiko Taniuchi[3], Houng-Yung Chen[1], Wann-Neng Jane[4], Yen-Huei Lin[1] and Yuh-ling Lee Chen[1]*

[1] Department of Oceanography, National Sun Yat-sen University, Kaohsiung, Taiwan, [2] Department of Ocean and Earth Sciences, Old Dominion University, Norfolk, VA, United States, [3] Kushiro Field Station, Fisheries Resources Institute, Japan Fisheries Research and Education Agency, Kushiro, Japan, [4] Institute of Plant and Microbial Biology, Academia Sinica, Taipei, Taiwan

Calothrix rhizosoleniae and *Richelia intracellularis* are heterocystous cyanobacteria found in the tropical oceans. *C. rhizosoleniae* commonly live epiphytically on diatom genera *Chaetoceros* (*C-C*) and *Bacteriastrum* (*B-C*) while *R. intracellularis* live endosymbiotically within *Rhizosolenia* (*R-R*), *Guinardia* (*G-R*), and *Hemiaulus* (*H-R*); although, they occasionally live freely (FL-*C* and FL-*R*). Both species have much shorter trichomes than the other marine filamentous cyanobacteria such as *Trichodesmium* spp. and *Anabaena gerdii*. We investigated the trichome lengths of *C. rhizosoleniae* and *R. intracellularis* in the South China Sea (SCS) and the Philippine Sea (PS) between 2006 and 2014. On average, *H-R* had the shortest trichome lengths (3.5 cells/trichome), followed by *B-C* and *C-C* (4.9–5.2 cells/trichome) and FL-*C* (5.9 cells/trichome), and *R-R*, *G-R*, and FL-*R* had the longest trichome lengths (7.4–8.3 cells/trichome). Field results showed the trichome lengths of *C-C* and *B-C* did not vary seasonally or regionally. However, FL-*C* and *H-R* from the SCS and during the cool season had longer trichomes, where/when the ambient nutrient concentrations were higher. *R-R*, *G-R*, and FL-*R* also showed regional and seasonal variations in trichome length. Ultrastructural analysis found no gas vesicles within the *C. rhizosoleniae* cells to assist in buoyancy regulation. Results suggest that the trichome lengths of *C. rhizosoleniae* and *R. intracellularis* might be regulated by their diatom hosts' symbiotic styles and by ambient nutrients. Short trichome length might help *C. rhizosoleniae* and *R. intracellularis* to stay in the euphotic zone regardless as to whether they are free-living or symbiotic.

Keywords: *Calothrix rhizosoleniae*, *Richelia intracellularis*, diatom diazotroph associations, free-living *Richelia* and *Calothrix*, South China Sea, Philippine Sea, gas vesicles

OPEN ACCESS

Edited by:
Bangqin Huang,
Xiamen University, China

Reviewed by:
Yehui Tan,
South China Sea Institute of Oceanology (CAS), China
Zuozhu Wen,
Xiamen University, China

****Correspondence:***
Sing-how Tuo
singhow.tuo@gmail.com

Specialty section:
This article was submitted to Marine Ecosystem Ecology, a section of the journal Frontiers in Marine Science

Received: *10 March 2021*
Accepted: *08 June 2021*
Published: *12 July 2021*

Citation:
Tuo S, Mulholland MR, Taniuchi Y, Chen HY, Jane WN, Lin YH and Chen YLL (2021) Trichome Lengths of the Heterocystous N_2-Fixing Cyanobacteria in the Tropical Marginal Seas of the Western North Pacific. Front. Mar. Sci. 8:678607. doi: 10.3389/fmars.2021.678607

INTRODUCTION

Marine cyanobacterial dinitrogen (N_2) fixation plays a substantial role in global biogeochemical nitrogen (N) and carbon cycling. Nitrogen fixers (diazotrophs) transform N_2 into bioavailable ammonium (NH_4^+), which can promote primary and secondary production (Carpenter et al., 1999; Sohm et al., 2011) and support large non-diazotrophic diatoms in oligotrophic seawater

(Chen et al., 2011). Diazotrophic cyanobacteria are photoautotrophic, or symbiotic with photoautotrophs, and reside in the upper euphotic zone of the ocean (Carpenter and Capone, 2008). They are classified into several phylogenetic groups that include heterocystous (heterocyst-forming) filamentous (e.g., *Richelia intracellularis*, *Calothrix rhizosoleniae*, and *Anabaena gerdii*), non-heterocystous filamentous (*Trichodesmium* spp.), and unicellular cyanobacteria (*Candidatus* Atelocyanobacterium thalassa, *Crocosphaera watsonii*, and *Cyanothece* spp.) (Carpenter and Janson, 2001; Capone et al., 2005; Foster et al., 2007). While the unicellular representatives can be abundant in both coastal and oligotrophic regions, filamentous groups often occur primarily in oligotrophic oceanic regions and riverine plume-influenced mesohaline waters (Foster et al., 2007; Subramaniam et al., 2008; Grosse et al., 2010; Turk et al., 2011; Chen et al., 2014; Shiozaki et al., 2018, 2020; Mulholland et al., 2019).

Calothrix rhizosoleniae (hereafter *Calothrix*, unless noted) and *Richelia intracellularis* (hereafter *Richelia*) are commonly observed in tropical and subtropical ocean regions and marginal seas (Kimor et al., 1992; Carpenter et al., 1999; Gómez et al., 2005; Bar Zeev et al., 2008; Tuo et al., 2017). Both *Calothrix* and *Richelia* are most often observed in symbiotic relationships with certain diatom species and only occasionally observed free-living (FL) outside of a host (Karsten, 1907; Gómez et al., 2005; White et al., 2007; Foster et al., 2011; Tuo et al., 2017). These diatom diazotroph associations/assemblages (DDAs) are thought to contribute substantial fixed N to oceanic regions where they occur (Mague et al., 1974; Carpenter et al., 1999; Bar Zeev et al., 2008; Grosse et al., 2010).

Calothrix and *Richelia* have different styles of symbiosis. *Calothrix* is often epiphytic with chain-forming *Chaetoceros compressus* and *Bacteriastrum* spp. (both belong to Family Chaetocerotaceae) while *Richelia* most often occurs as an endosymbiont with *Rhizosolenia clevei*, *Guinardia cylindrus* (both belong to Family Rhizosoleniaceae), and *Hemiaulus* spp. (Family Hemiaulaceae) (Sundström, 1984; Gómez et al., 2005; Tuo et al., 2017). More precisely, symbiotic *Richelia* filaments dwell inside the cytosol of *Hemiaulus* hosts or dwell in the periplasmic space between the plasmalemma and frustule of *Rhizosolenia* hosts (Villareal, 1990; Caputo et al., 2019; Nieves-Morión et al., 2020). The actual location of symbiotic *Richelia* inside the *Guinardia* hosts is still unknown. It is also unknown whether the *Richelia* associated with different host diatoms are distinct species or strains (Sundström, 1984; Janson et al., 1999; Foster and Zehr, 2006). *Hemiaulus*-associated *Richelia* (*H-R*) is considered an obligate symbiont due to the fact that its smaller genome (3.2 Mbp) lacks many N-associated metabolic pathways, e.g., glutamine 2-oxoglutarate aminotransferase (GOGAT) and transporters for NH_4^+, nitrate (NO_3^-), nitrite (NO_2^-), and urea (Hilton et al., 2013; Hilton, 2014). The larger genome (5.4 Mbp) of *Rhizosolenia*-associated *Richelia* (*R-R*) also lacks the combined-N transporters (Hilton, 2014; Nieves-Morión et al., 2020). Both the *nifH* gene analysis and morphological examination of FL-*Richelia* (FL-*R*) from field samples suggest that FL filaments originate from *Rhizosolenia* rather than *Hemiaulus* (Zhang et al., 2011; Tuo et al., 2017). However, little is known about the genome of FL-*R* or *Guinardia*-associated *Richelia* (*G-R*). In contrast, *Calothrix* is considered a facultative symbiont or an opportunist. Its genome (6.0 Mbp) is more similar to those of FL heterocystous cyanobacterial species (Hilton et al., 2013; Nieves-Morión et al., 2020), suggesting its ability to live freely (FL-*C*) in nature. In the marginal seas of the low-latitude western North Pacific, FL-*C* comprised about 20–40% of overall *Calothrix* abundance [FL-*C* plus *Chaetoceros*- (*C-C*) and *Bacteriastrum*-associated *Calothrix* (*B-C*), 48–698 $\times$ 10^3 filaments m^{-2}] (Tuo et al., 2017). FL-*R* were occasionally found in the upper water column of the tropical western North Pacific and their abundance (1–29 $\times$ 10^3 filaments m^{-2}) was much lower than symbiotic *Richelia* (403–1,703 $\times$ 10^3 filaments m^{-2}) (Tuo et al., 2017). It has been suggested that FL-*R* are not viable due to their lack of gas vesicles to help them regulate their buoyancy (Janson et al., 1995). However, to date, little is known about how cellular ultrastructure affects the buoyancy regulation of *Calothrix* or whether their symbiotic behavior offer these organisms the ability to stay in the upper water column in the absence of cellular architecture facilitating buoyancy.

It is interesting that both *Calothrix* and *Richelia* have much shorter trichome lengths than other marine filamentous cyanobacteria. According to previous studies from different regions, symbiotic *Calothrix* filaments have no more than 14 cells per trichome (vegetative cells plus one terminal heterocyst) whereas symbiotic *Richelia* have no more than 21 cells per trichome (Schmidt, 1901; Foster and Zehr, 2006; Tuo et al., 2017). Little is known about the trichome lengths of FL-*C* and FL-*R*. In contrast, a filament of *Trichodesmium* may contain more than 100 cells per trichome (Capone et al., 1997; Luo et al., 2012) and a filament of *A. gerdii*, a sparsely distributed heterocystous species, may contain more than 300 cells per trichome (Carpenter and Janson, 2001). These field observations give rise to a question about the trichome length of *Calothrix* and *Richelia*: were the trichome lengths different among the symbionts associated with distinct diatom hosts?

The northern South China Sea (SCS) and the western Philippine Sea (PS), two large and connected marginal seas of the western North Pacific Ocean, harbor diverse N_2-fixing cyanobacteria (Chen et al., 2014, 2019; Shiozaki et al., 2014; Tuo et al., 2017). Both regions are influenced by the Kuroshio western boundary current, in which *Trichodesmium*, *Calothrix*, and *Richelia* are prevalent (Chen et al., 2008; Shiozaki et al., 2014, 2015; Tuo et al., 2014). The Kuroshio originates along the eastern coast of Luzon and flows north across the Luzon Strait where it exchanges waters with the SCS before meandering along the eastern coast of Taiwan and meeting the continental slope of the East China Sea (**Figure 1**; Caruso et al., 2006; Jan et al., 2015). The monsoonal circulation of the SCS results in seasonal variations in the velocity, width, and path of the Kuroshio at the northwestern boundary of the PS (Jan et al., 2015), as well as stronger Kuroshio intrusion from the PS into the SCS during the northeast monsoon (NEM) (Liang et al., 2003). During the NEM, the SCS has cool surface seawater temperatures (SST) and the circulation in the basin is cyclonic, while during the southwest monsoon (SWM), SST is warm and the circulation is anticyclonic in the SCS (Liu et al., 2002). Although monsoon-driven seasonal changes in SST, surface photosynthetically active

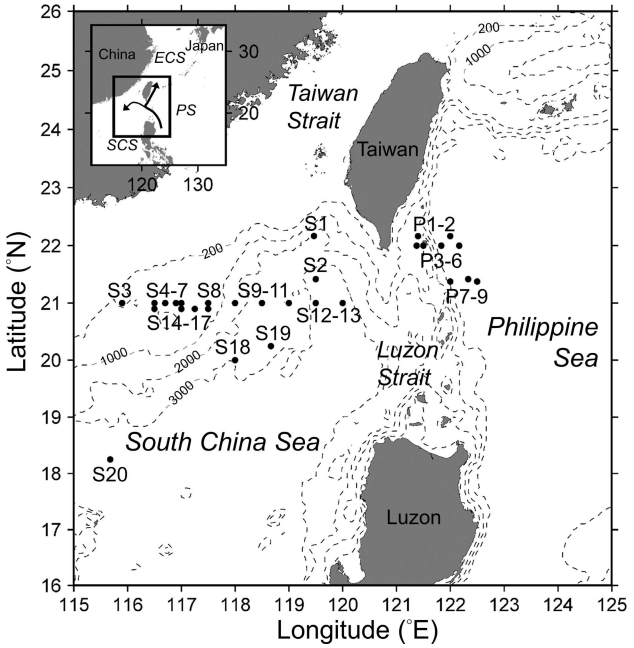

FIGURE 1 | Bottom topography (hatched lines) and locations of sampling stations in the South China Sea (stations S1 to S20) and the Philippine Sea (stations P1 to P9). The arrows in the inset map indicate the path (in the PS) and intrusion (into the SCS) of the Kuroshio (after Caruso et al., 2006).

radiation (SPAR), and stratification index (SI) are observed, the SCS and the PS are both oligotrophic year-round. However, the nutrient distributions in the upper water column differ somewhat between the regions; the SCS generally has shallower nitracline (D_N) and phosphacline depths (D_P) than the PS, suggesting a potential for higher fluxes of nitrate and phosphate from the depth (Chen et al., 2008; Tuo et al., 2017). The two marginal seas provide opportunities to examine whether the trichome length of each distinct host-associated or FL *Calothrix* or *Richelia* was different as the filaments habited in specific regions and seasons.

In this study, we evaluated how trichome length and intracellular characteristics contribute to the distribution of *Calothrix* and *Richelia* in the field. Specifically, we (1) examined whether the trichome lengths were different among the symbionts associated with distinct diatom hosts (and their FL counterparts) and (2) examined whether the trichome length for each *Calothrix*/*Richelia* symbiont was different between the regions and between the seasons. We also used laboratory cultures of an FL-*C* strain isolated from the SCS seawater to examine whether *C. rhizosoleniae* has gas vesicles and other intracellular structures.

MATERIALS AND METHODS

Sampling Strategy

Field samples were collected during 20 cruises between 2006 and 2014 aboard the R/V *Ocean Researcher I* (OR1) and the R/V *Ocean Researcher III* (OR3) (**Table 1**). The cruises were conducted seasonally during the warm SWM (from April to October, 14 cruises) and the cool NEM (from mid-December to January, 6 cruises) seasons (**Table 1**). Samples were collected from 1 to 11 stations per cruise to investigate trichome lengths of *Calothrix* and *Richelia* and environmental parameters (**Figure 1** and **Table 1**). In total, 83 stations were sampled from 29 discrete locations (some stations were revisited) over the 9-year period, and these were categorized into four region–season combinations: SCS-SWM, SCS-NEM, PS-SWM, and PS-NEM. At each station, water samples were collected from seven to nine discrete depths between 5 and 200 m using 20-L Go-Flo bottles attached to a rosette equipped with a Seabird SBE 9 conductivity–temperature–depth sensor and an underwater photosynthetically active radiation (PAR) sensor (OSP200L, Biospherical).

Trichome Length Examination on *Richelia* and *Calothrix*

Samples collected to identify *Richelia* and *Calothrix* and to measure their trichome lengths were prepared as described in Tuo et al. (2017). *Richelia* and *Calothrix*, showing an orange-yellow fluorescence, were identified at ×400 magnification with Zeiss epi-fluorescence microscopes equipped filter set of blue excitation and long pass emission (BP 450–490, FT 510, LP 520). Bright field was also used to distinguish symbionts from FL and to identify their host diatom species.

In total, 12,254 filaments of *Richelia* and 2,697 filaments of *Calothrix*, in free-living (176 filaments of FL-*R* and 1,206 filaments of FL-*C*) or symbiotic forms (12,078 filaments of *Richelia* and 1,491 filaments of *Calothrix*), were examined and their trichome lengths recorded. The morphological examination of 1,382 FL filaments (FL-*R* and FL-*C*) was found at the 83 stations sampled during the 20 cruises. A total of 13,569 symbiont filaments (*H-R*, *R-R*, *G-R*, *C-C*, and *B-C*) were examined from 43 of the 83 stations (from seven of the 20 cruises, conducted between December 2010 and October 2014) (**Table 1**). The general morphological descriptions and the abundances of each DDA and FL were published in Tuo et al. (2017).

Environmental Parameters

At each station, the euphotic depth (D_E, m), surface PAR influx (SPAR, E m^{-2} day^{-1}), stratification index (SI, kg m^{-4}), mixed-layer depth (D_M, m), NO_3^- plus NO_2^- (N+N), soluble reactive phosphorus (phosphate, P), and chlorophyll *a* (mg m^{-3}) concentrations were calculated or measured following Tuo et al. (2017). To better assess the total nutrient inventory in the upper water column at each station, in addition to surface concentrations (N_S and P_S, nM), depth-integrated nutrient inventories (N_I and P_I) and the nutricline depths (D_N and D_P) were calculated for each nutrient (N+N or P). Depth-integrated inventories (N_I and P_I, mmol m^{-2}) were calculated by trapezoidal integration from the surface to 100 m depth. The nutricline is defined as the seawater layer where the greatest change in the nutrient concentration occurs with depth. Based on the definition, the nutricline depth for each nutrient (D_N and D_P) was found from the sampling depths as the depth at which

TABLE 1 | Sampling stations occupied during 20 cruises in the SCS and the PS (see **Figure 1** for station locations).

Season	Cruise	Date	SCS stations	PS stations
SWM	OR3-1217*	April 21–25, 2007		1, 2, 3
	OR3-1234*	July 7–10, 2007		3, 5
	OR1-843*	September 27–October 8, 2007	1, 2	3
	OR3-1284*	April 14–19, 2008	2	3
	OR3-1310*	August 2–7, 2008		3, 6
	OR3-1316*	September 5–10, 2008		3, 6
	OR1-899*	May 17–20, 2009		3
	OR1-910*	August 14–20, 2009	2, 12, 13	4, 7, 9
	OR3-1455*	May 12–17, 2010	4, 7, 8, 9, 12, 13	7, 9
	OR1-973	August 19–28, 2011	3, 4, 7, 8, 9, 11, 12, 13	7, 9
	OR3-1603	May 3–8, 2012	7, 8, 9, 11, 12	
	OR3-1683	May 6–11, 2013	7, 8, 9, 11, 12, 13	
	OR1-1074	May 17–21, 2014	10, 18	
	OR1-1091	October 12–18, 2014	4, 5, 6, 7, 8, 9, 11, 14, 15, 16, 17	
NEM	OR1-819*	December 18–30, 2006	2, 19	8
	OR1-821*	January 12–19, 2007	20	
	OR1-852*	December 10–15, 2007		3, 5, 6
	OR1-886*	December 8–14, 2008	2	3, 5, 6
	OR1-950	December 2–10, 2010	7, 8, 9, 11, 12, 13	9
	OR1-1022	December 7–12, 2012	7	7

**Examinations of free-living filaments only.*

the nutrient gradient increased significantly (57 ± 52 nM m^{-1} for N+N and 4 ± 5 nM m^{-1} for P) in the upper water column. The data for some environmental parameters, including SPAR, SST, SI, D_M, surface salinity (Sal), N_S, P_S, surface chlorophyll *a* (Chl), and depth of chlorophyll *a* maximum (D_{CM}) were previously published in Tuo et al. (2017).

Isolation and Identification of FL-*C* Strain

A unicyanobacterial strain of FL *C. rhizosoleniae* was isolated from the surface water in the SCS collected at 21°25′N, 119°28′E on December 10, 2007 (cruise OR1-852) and enriched with nitrate (10 μM final concentration). After a 1-week incubation in the nitrate-enriched natural seawater, cells were transferred into new polycarbonate (PC) bottles and placed near the window at room temperature (around 19–28°C) in the laboratory. Brownish-yellow clumps appeared at the bottom of the bottles after 3 weeks, and these were transferred into a new PC bottle containing YBCII culture medium (Chen et al., 1996) using a pneumatic micropipette under a Zeiss inverted microscope. Solitary filaments were visible in the bottle a few days later, and these were isolated individually, rinsed several times with YBCII medium, and then transferred to a sterilized Pyrex flask with a cotton stopper containing YBCII medium. A stir bar was placed inside the flask, and the flask was placed on a magnetic stir plate to keep the filaments in suspension. The unicyanobacterial culture was then incubated in a light and temperature-controlled incubator at an illumination intensity of 100–120 μmol quanta m^{-2} s^{-1} on a 12:12-h light:dark cycle at 28°C.

Both molecular phylogenetic and morphological examinations were done to identify the strain of isolated FL-*C*. Phylogenetic analysis based on *nifH* gene sequence (Foster and Zehr, 2006) was applied with several minor modifications (Taniuchi et al., 2012). The *nifH* primers and nested polymerase chain reaction protocol followed Zehr and Turner (2001). Cloned deoxyribonucleic acid (DNA) fragments were sequenced by Tri-I Biotech (Taipei, Taiwan). The sequences were aligned by ClustalW program of DDBJ[1]. A phylogenetic tree was then constructed *via* neighbor-joining by ClustalW. Distance matrix of deduced amino acid sequences of *nifH* were calculated with Kimura's model. The bootstrapped value was based on 1,000 iterations to test for robustness. For the phylogenetic analysis, the *nifH* genes of *Trichodesmium* sp. IMS 101 and *Trichodesmium thiebautii* were used as the outgroups. The identity with close strains was calculated by the identity matrix of BioEdit 4.0 (Hall, 1999). The *nifH* sequences determined in the study have been submitted in the GenBank database[2] under Accession No.: KF284162. Morphological observations included size of heterocysts, the size of heterocysts relative to adjacent vegetative cells, and the tapering of filaments, to distinguish *Calothrix* from *Richelia* (Tuo et al., 2017).

Ultrastructural Analysis on Cultured FL-*C*

To verify whether gas vesicles were present in cells of *Calothrix*, ultrathin sections of cells were examined using a transmission electron microscope (TEM) on April 7, 2015. The examined filaments, harvested from the laboratory cultures in March 2015, were first transferred to 2.5% glutaraldehyde fixative (in YBCII), then postfixed using 1% osmium tetroxide, dehydrated in an acetone series, embedded in Spurr's resin (Spurr, 1969), and

[1]http://clustalw.ddbj.nig.ac.jp/top-e.html
[2]http://www.ncbi.nlm.nih.gov/genbank/

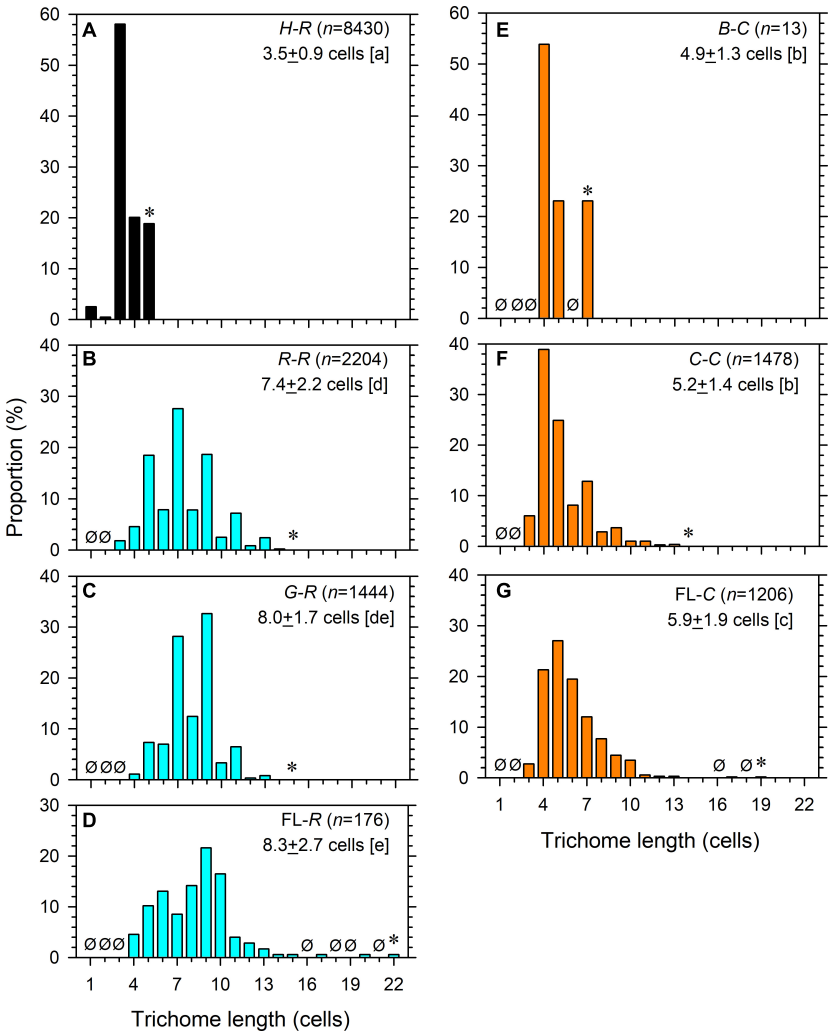

FIGURE 2 | Trichome lengths of **(A)** internal and **(B,C)** partial symbionts *Richelia* and **(D)** free-living *Richelia*, as well as **(E,F)** external symbionts *Calothrix* and **(G)** free-living *Calothrix*. Ø indicates none observed at the length. Asterisk indicates the maximal length observed. *n*, number of filaments examined. The mean ± 1 standard deviation of length is noted. Different lowercase letters in the brackets refer to significant difference ($p < 0.05$) of the mean after ANOVA ($F_{6,14,944} = 3{,}645$, $p < 0.0001$) and Tukey-Kramer test.

sectioned with an ultramicrotome (EM UC7, Leica). Ultrathin sections were double stained with uranyl acetate and lead citrate (Reynolds, 1963) and observed under TEM (Tecnai G2 Spirit TWIN, FEI) at 80 kV.

Statistical Analysis

To compare the trichome lengths among the seven types of *Richelia* and *Calothrix* (*H-R*, *R-R*, *G-R*, FL-*R*, *B-C*, *C-C*, and FL-*C*), one-way analysis of variance (ANOVA) and a *post hoc* Tukey-Kramer test with 0.05 of significance level were used. Before the ANOVA, data from the four region-season classifications were combined for each type, respectively. Differences in trichome lengths of *Calothrix* and *Richelia* and in hydrographic parameters and biogeochemical parameters between regions (SCS vs. PS) and seasons (NEM vs. SWM) were compared using two-way ANOVA. For the unbalanced datasets, a Type II sum-of-square method was applied for the ANOVA. If the interaction effect between region and season was significant ($p < 0.05$), then a *post hoc* Tukey-Kramer test was performed to investigate the difference among the four region–season classifications (SCS-NEM, SCS-SWM, PS-NEM, and PS-SWM). All the data were presented as mean ± 1 standard deviation. SAS program (SAS Institute) was used for all statistical procedures.

RESULTS

Trichome Lengths of *Richelia* and *Calothrix* in the Field

The combined field data showed that trichome lengths were different among the different symbiotic styles of *Calothrix* and *Richelia* (**Figures 2A–G**). On average, *H-R* had the shortest

TABLE 2 | Trichome length of *Richelia* and *Calothrix* in the SCS and the PS during SWM and NEM.

Types	SCS		PS		*F* values in two-way ANOVA		
	SWM	NEM	SWM	NEM	Region × season	Region	Season
Richelia							
H-R	3.5 ± 0.9^{b} (n = 7,453)	3.8 ± 0.8^{c} (n = 687)	2.6 ± 1.2^{a} (n = 241)	3.2 ± 0.4^{b} (n = 49)	9.91** (df = 1, 8,426)		
R-R	7.6 ± 2.1^{b} (n = 1,656)	6.7 ± 2.1^{ab} (n = 39)	6.7 ± 2.5^{a} (n = 460)	7.9 ± 2.2^{b} (n = 49)	18.1** (df = 1, 2,200)		
G-R†	8.0 ± 1.7 (n = 1,397)	11.5 ± 0.7 (n = 2)	7.4 ± 1.6 (n = 45)	ND	–	–	–
FL-*R*	9.0 ± 1.8^{b} (n = 69)	9.3 ± 2.8^{b} (n = 4)	7.6 ± 2.7^{a} (n = 87)	8.8 ± 4.5^{a} (n = 16)	0.35 (df = 1, 172)	10.8**	2.25
Calothrix							
C-C	5.2 ± 1.7^{a} (n = 1,157)	5.0 ± 2.5^{a} (n = 22)	5.3 ± 1.7^{a} (n = 285)	6.0 ± 2.0^{a} (n = 14)	2.05 (df = 1, 1,474)	1.07	0.35
B-C	5.0 ± 1.3 (n = 12)	4 (n = 1)	ND	ND	–	–	–
FL-*C*	6.0 ± 1.9^{b} (n = 512)	8.7 ± 3.3^{d} (n = 45)	5.5 ± 1.5^{a} (n = 531)	6.5 ± 2.0^{c} (n = 118)	22.8** (df = 1, 1,202)	–	–

*n, number of filaments examined; ND, no data; df, degree of freedom. **$p < 0.01$. Different superscript letters indicate significant differences ($p < 0.05$) after Tukey-Kramer tests. †Comparisons for G-R: SCS vs. PS during the SWM, $t_{df = 1,440} = -2.32$, $p < 0.05$ (two-tailed).*

TABLE 3 | Hydrographic and biogeochemical properties in the SCS and the PS during SWM and NEM.

Parameters	SCS		PS		$F_{1,79}$ in two-way ANOVA		
	SWM (n = 44)	NEM (n = 11)	SWM (n = 19)	NEM (n = 9)	Region × season	Region	Season
SPAR (E m^{-2} day^{-1})	62.8 ± 12.5^{b} (n = 40)	27.1 ± 17.1^{a}	63.5 ± 17.6^{b} (n = 14)	31.5 ± 16.0^{a}	0.22 ($F_{1,70}$)	0.25	77.2**
D_E (m)	83 ± 13^{a} (n = 31)	78 ± 4^{a} (n = 5)	113 ± 19^{b} (n = 14)	107 ± 11^{b} (n = 6)	0.01 ($F_{1,52}$)	52.0**	1.14
SST (°C)	28.2 ± 1.2^{c}	25.7 ± 1.0^{a}	28.9 ± 1.0^{d}	26.4 ± 0.9^{b}	0.00	6.37*	76.5**
SI ($\times 10^{-2}$ kg m^{-4})	2.6 ± 0.9^{c}	0.9 ± 0.4^{ab}	1.6 ± 0.5^{b}	0.8 ± 0.6^{a}	5.57*	–	–
D_M (m)	56 ± 31^{a}	100 ± 30^{c}	89 ± 46^{b}	125 ± 37^{d}	0.17	14.2**	19.8**
Sal	33.7 ± 0.3^{a}	34.0 ± 0.2^{b}	34.2 ± 0.3^{c}	34.4 ± 0.2^{d}	0.48	53.0**	8.25**
N_S (nM)	24 ± 23^{a}	360 ± 729^{b}	24 ± 21^{a}	27 ± 18^{a}	5.89*	–	–
P_S (nM)	30 ± 15^{a}	69 ± 40^{b}	30 ± 17^{a}	41 ± 28^{a}	6.19*	–	–
N_S:P_S	0.9 ± 0.7^{a}	3.5 ± 3.8^{b}	1.0 ± 1.2^{a}	0.7 ± 0.5^{a}	11.7**	–	–
N_I (mmol m^{-2})	142 ± 99^{b}	107 ± 77^{b}	15 ± 20^{a}	26 ± 28^{a}	1.20	38.1**	0.58
P_I (mmol m^{-2})	15.0 ± 7.6^{b}	12.4 ± 5.8^{b}	5.5 ± 4.3^{a}	5.9 ± 2.6^{a}	0.83	34.2**	0.70
N_I:P_I	8.7 ± 2.9^{b}	7.9 ± 2.3^{b}	2.8 ± 2.4^{a}	4.1 ± 2.8^{a}	2.04	71.9**	0.01
D_N (m)	45 ± 15^{a}	43 ± 24^{a}	87 ± 26^{b}	73 ± 26^{b}	1.47	67.4**	1.74
D_P (m)	38 ± 17^{a}	54 ± 30^{a}	75 ± 42^{b}	69 ± 27^{b}	2.35	24.1**	1.08
Chl (mg m^{-3})	0.16 ± 0.12^{a}	0.45 ± 0.12^{b}	0.10 ± 0.05^{a}	0.21 ± 0.12^{a}	11.6**	–	–
D_{CM} (m)	63 ± 19^{c}	15 ± 24^{a}	89 ± 22^{d}	60 ± 30^{b}	2.75	35.8**	50.7**

*n, number of stations; df, degree of freedom. *$p < 0.05$; **$p < 0.01$. Different superscript letters indicate significant differences ($p < 0.05$) after Tukey-Kramer tests.*

trichome length (3.5 ± 0.9 cells), followed by *B-C* (4.9 ± 1.3 cells) and *C-C* (5.2 ± 1.4 cells), and *R-R* (7.4 ± 2.2 cells) and *G-R* (8.0 ± 1.7 cells) had the longest trichome length ($p < 0.05$). The differences between *B-C* and *C-C* and between *R-R* and *G-R* were not significant ($p > 0.05$). FL-*C* showed longer average trichome length (5.9 ± 1.9 cells) than its symbiotic counterparts *B-C* and *C-C* ($p < 0.05$). FL-*R* also showed longer trichome length (8.3 ± 2.7 cells) than its symbiotic counterpart *R-R* ($p < 0.05$); however, it showed comparable ($p > 0.05$) trichome lengths with *G-R*. The FL cyanobacteria were able to develop longer trichomes than their symbiotic counterparts, according to the maximum observed cells per trichome (22 cells for FL-*R* and 19 cells for FL-*C*) (**Figures 2B–G**).

Among the host-associated and FL filaments, some of them showed significant seasonal and/or regional differences in their average trichome length, although the difference was only around 1 cell per trichome (**Table 2**). *H-R* had longer trichomes during the NEM than the SWM in both regions and had longer trichomes in the SCS than in the PS during both seasons ($p < 0.05$) (**Table 2** and **Supplementary Figure 1**). The trichome length of *R-R* was longer in the SCS than the PS during the SWM and was longer during the NEM than during the SWM in the PS ($p < 0.05$) (**Table 2** and **Supplementary Figure 2**). Similarly, the trichome length of *G-R* was also longer in the SCS than the PS during the SWM ($p < 0.05$) (**Table 2** and **Supplementary Figure 3**). However, FL-*R* had longer trichomes in the SCS than the PS during both seasons ($p < 0.05$), but the seasonal differences were not significant ($p > 0.05$) (**Table 2** and **Supplementary Figure 4**). On the other hand, the symbiotic *Calothrix* samples did not show regional and seasonal differences. Specifically, the trichome length of *C-C* was comparable ($p > 0.05$) between the regions and/or between the seasons (**Table 2** and **Supplementary Figure 5**). The data of *B-C* were too few for statistical tests (**Table 2** and **Supplementary Figure 6**). However, FL-*C* had

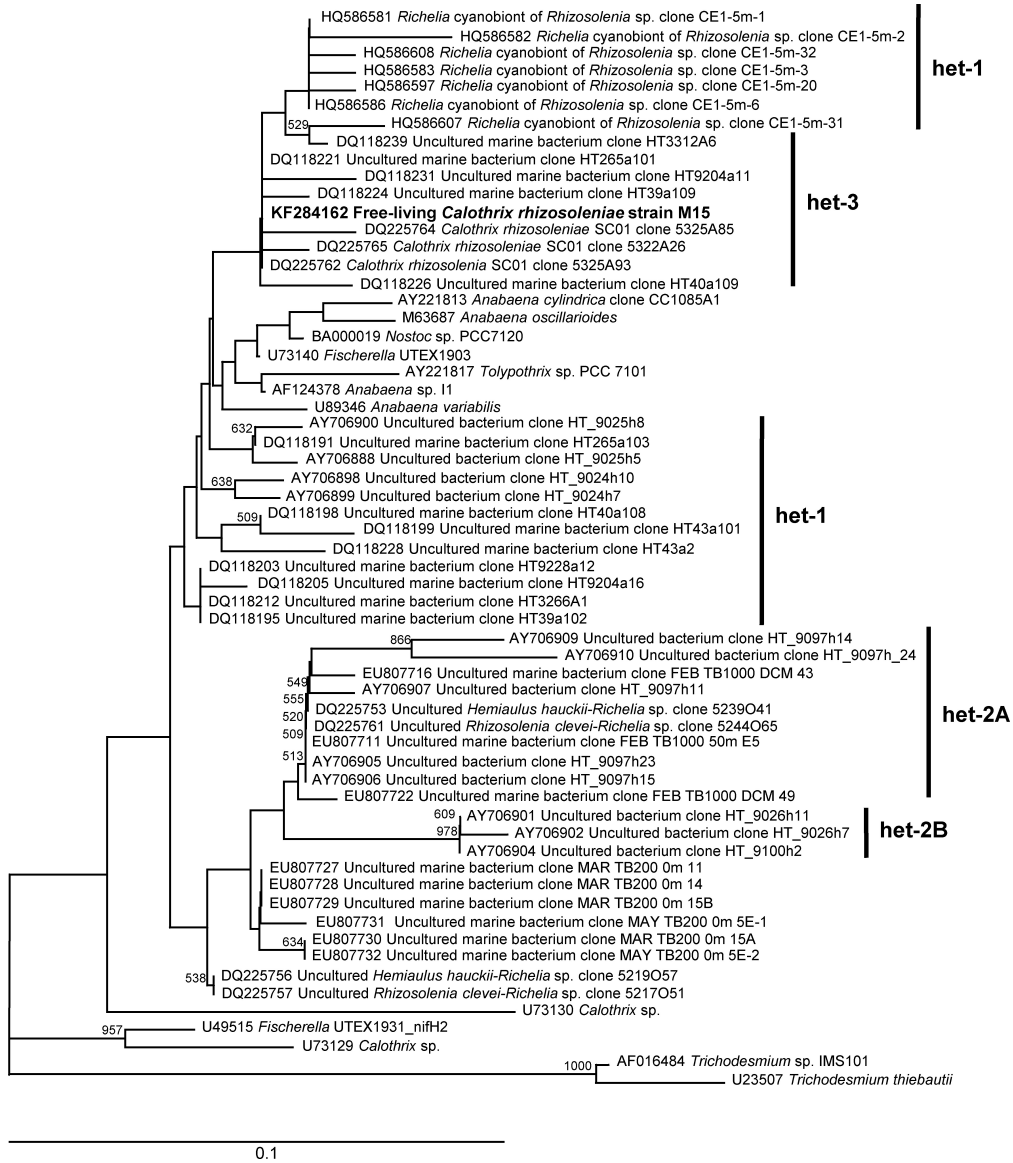

FIGURE 3 | Neighbor-joining phylogenetic tree for partial *nifH* amino acid sequences. The sequence obtained from *Calothrix rhizosoleniae* strain M15 (KF284162) is indicated in boldface. The bootstrap values (>500) are indicated at the nodes. The scale bar represents 0.1 substitutions per site, and the *nifH* genes *of Trichodesmium* sp. IMS 101 (AF016484) and *Trichodesmium thiebautii* (U23507) were used as the outgroups.

longer trichomes during the NEM than the SWM in both regions and had longer trichomes in the SCS than the PS during both seasons ($p < 0.05$) (**Table 2** and **Supplementary Figure 7**).

Hydrographic and Biogeochemical Properties in the Study Areas

Hydrographic characteristics, including SPAR, SST, SI, and D_M, differed significantly ($p < 0.05$) between seasons in both the SCS and the PS. The first three parameters were higher during the SWM than during the NEM. SST was also higher in the PS than the SCS during both seasons ($p < 0.05$). On the other hand, D_M was deeper during the NEM than during the SWM in both regions ($p < 0.01$) and was deeper in the PS than the SCS during both seasons ($p < 0.05$). The SI was higher in the SCS than the PS during the SWM ($p < 0.05$), but during the NEM, it was comparable between the regions ($p > 0.05$) (**Table 3**).

The SCS had significantly higher N_I and P_I ($p < 0.01$) than the PS during both seasons. The SCS also had significantly ($p < 0.05$) higher N_S and P_S than the PS during the NEM. However, there were no differences in N_S and P_S between the two regions during the SWM (**Table 3**). Both D_N and D_P were deeper in the PS than the SCS during both seasons ($p < 0.01$). In the SCS, N_S, and P_S were significantly ($p < 0.05$) higher during the NEM than the SWM. In contrast, seasonal variations in N_S and P_S in the PS were not significant ($p > 0.05$) (**Table 3**). Significant differences

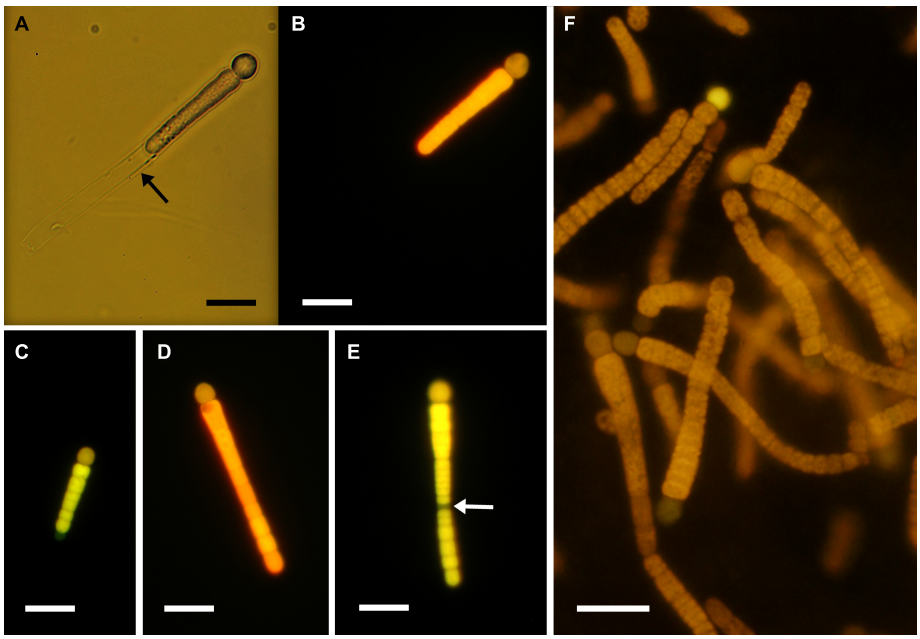

FIGURE 4 | (A–E) Solitary or **(F)** clumping filaments of *Calothrix rhizosoleniae* strain M15 under **(A)** bright field and **(B–F)** epi-fluorescence microscopy. Black and white arrows indicate empty sheath and necridium, respectively. Scale bar: 10 μm.

in D_{CM} were observed seasonally or regionally ($p < 0.01$). Seasonal differences in Chl were also observed in the SCS but not in the PS. Ratios of N:P (N_S:P_S and N_I:P_I) were consistently below the Redfield ratio of 16 (Redfield, 1958), suggesting that phytoplankton growth was limited by N in both regions (**Table 3**).

In summary, the SCS-NEM stations had the lowest SST, the highest N_S, P_S, and Chl, and the shallowest D_{CM}. On the other hand, there were significant regional differences in nutrient concentrations; i.e., higher N_I and P_I and shallower D_N and D_P in the SCS than the PS (**Table 3**).

Identification of the Cultured FL-*C*

The isolated FL-*C* strain, M15, was positively identified as *C. rhizosoleniae* according to phylogenetic (**Figure 3**) and morphological examinations (**Figure 4**). Phylogenetic trees reconstructed from *nifH*-deduced amino acid sequences revealed that the isolated strain was included in the het-3 clade (**Figure 3**) that contained *C. rhizosoleniae* strain SC01, which was isolated from the North Pacific (Foster and Zehr, 2006). In the analysis of *nifH* DNA sequence, the strain showed high identity to *C. rhizosoleniae* SC01 (het-3) (99.6–100%). In contrast, its identity to *Richelia* associated with *Rhizosolenia* (het-1) or *Hemiaulus* (het-2) was ≤91.3% (**Supplementary Table 1**). Morphologically, a filament of the isolate consisted of several vegetative cells followed by one basal heterocyst covered with thin hyaline sheath and lacked hair formation (**Figures 4A,B**). The trichome length in maximum and in minimum recorded two and 114 cells, respectively. The heterocyst was often smaller (**Figures 4C,D**) or equal in diameter to its adjacent vegetative cell (**Figures 4A,B,E,F**). Most of the newly divided filaments had slightly tapering ends and sometimes empty sheaths near their ends (**Figures 4A–C**). Some longer filaments tapered in the center and had a developing rounded end-cell at its opposite end suggesting the filament was getting ready to divide (**Figures 4D,E**). The narrowest cell at the middle part would become a necridium (**Figure 4E**) from which a filament would divide into the longer mother filament the shorter hormogonium.

Ultrastructure of Cultured FL-*C*

The images of thin sections showed no gas vesicles in either vegetative cells or heterocysts in the cultured FL-*C* (**Figure 5**). The photosynthetic thylakoids were more abundant and denser in vegetative cells (**Figures 5D,E**) but distributed sparsely in heterocysts (**Figures 5B,C**) and necridia (**Figure 5A** and **Supplementary Figure 8**). The difference in thylakoid abundance among vegetative cells, heterocysts, and necridia was apparent from epifluorescence microscopy, i.e., vegetative cells often had brighter fluorescence than heterocysts and necridia (**Figures 4B–F**). Carboxysomes, cyanophycin granules, osmiophilic granules, and electron-transparent areas were found in both heterocysts and vegetative cells (**Figure 5**).

DISCUSSION

Different Trichome Lengths Among Host-Specific Symbionts

The field results showed that the trichome lengths were different among the three types of *Richelia*/*Calothrix* symbionts, classified by Nieves-Morión et al. (2020). The internal symbiont (*H-R*) had the shortest trichome lengths, followed by the external symbiont (*Calothrix*). The partial/periplasmic symbiont (*R-R*, FL-*R*, and

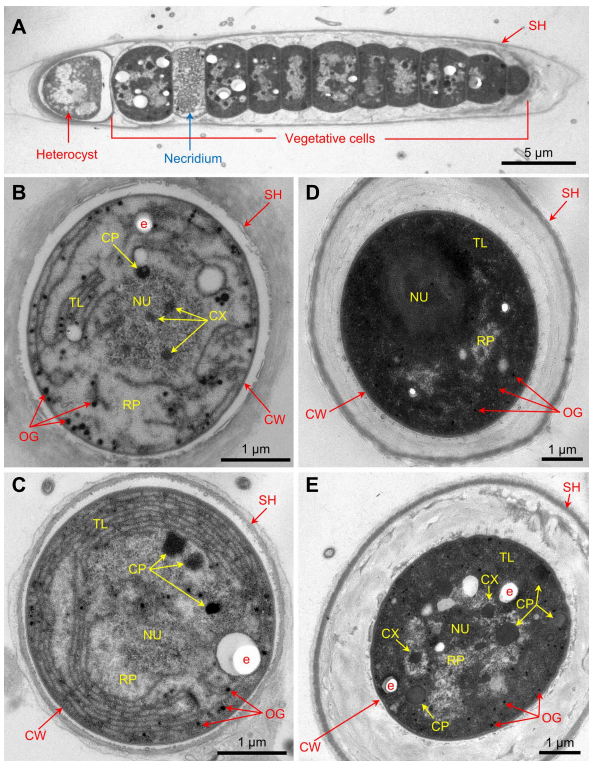

FIGURE 5 | Thin sections of **(A)** a filament, **(B,C)** heterocysts, and **(D,E)** vegetative cells of the FL-*C* strain. SH, sheath; CW, cell wall; TL, thylakoids; RP, riboplasm; NU, nucleoid; CP, cyanophycin granule; CX, carboxysome; OG, osmiophilic granule; e, electron-transparent area.

perhaps *G-R*) had the longest trichome lengths (**Figure 2**). According to a coarse-grained cell flux model of the *Hemiaulus-Richelia* symbiosis (CFM-DDA), the *Hemiaulus* host provided its symbiont with two-thirds of its fixed carbon (C) requirement (Inomura et al., 2020). Because the *Hemiaulus* host can provide such a large proportion of their fixed C requirement, an *H-R* symbiont may not need to maintain as many vegetative cells and so form shorter trichomes (Sundström, 1984; Villareal, 1994; Foster and Zehr, 2006; Foster et al., 2007; Bar Zeev et al., 2008; Lyimo, 2011; Hilton et al., 2013), consistent with our field observations (**Table 4**). In addition, a reduction in *H-R* symbiont vegetative cells/trichome length may facilitate their dwelling in the compact cytoplasm of their *Hemiaulus* hosts (Caputo et al., 2019). On the other hand, external symbionts (*C-C* and *B-C*) (Lemmermann, 1905; Janson et al., 1999; Foster and Zehr, 2006) and periplasmic symbionts (*R-R*) (Schmidt, 1901; Janson et al., 1999; Zehr et al., 2007; Bar Zeev et al., 2008; Kulkarni et al., 2010; Padmakumar et al., 2010; Lyimo, 2011; Jabir et al., 2013; Madhu et al., 2013; **Table 4**) may require more vegetative cells to satisfy their fixed C demand as their symbiotic locations lead to less-efficient exchange of molecules (e.g., fixed C and N) than internal symbionts. The comparable trichome lengths between *R-R* and *G-R* (**Figures 2B,C**) suggest that *G-R* is also a periplasmic symbiont. The fact that both FL-*R* and FL-*C* showed longer trichomes (both average and maximum trichome lengths) than their symbiotic counterparts (*R-R* and *C-C*) (**Figure 2**) was also predicted by the CFM-DDA (Inomura et al., 2020). This study reports the first quantification of *G-R*, FL-*R*, *B-C*, and FL-*C* trichome lengths from natural waters. For *H-R*, *R-R*, and *C-C*, our observations of trichome length from the SCS and PS were comparable with those reported from other oceanic regions (**Table 4**). In a previous global model study, the C biomass of *Calothrix* and *Richelia* were calculated by using a fixed number of vegetative cells per trichome (trichome length minus 1) without considering variations in trichome length for symbionts associated with different diatom hosts (Luo et al., 2012). Our results suggest that trichome length varies based on the nature of the DDA, and this should be considered in future models.

The exceptionally short trichome length of *H-R* observed in this study (**Figure 2A**) was similar to an earlier study (**Table 4**; Foster et al., 2007). The short trichomes of *H-R* are thought to be strongly manipulated or restricted by their hosts; they have an extremely slimmed genome and are located in the host's cytosol (Hilton et al., 2013; Caputo et al., 2019). Unlike *Calothrix*, which is considered a facultative symbiont or an opportunist, *H-R* is unable to live alone without its host. The limited field data from this study suggests that all of the observed FL-*R* filaments were similar in length to those associated with *Rhizosolenia* and *Guinardia*. In a previous study, it was found that none of the FL-*R* filaments were derived from *Hemiaulus* (Tuo et al., 2017). *Rhizosolenia*-associated *Richelia* may be able to live outside of its host for at least a short time because its genome is larger than that of *Hemiaulus*-associated *Richelia*, probably of metabolic necessity since its symbiotic location is just outside the host's cytosol (Villareal, 1990; Hilton, 2014; Caputo et al., 2019). Microscopic evidence from field samples have shown *Richelia* filaments escaping from moribund or dead *Rhizosolenia* hosts by direct penetration through the frustule or attached on the plasmalemma of *Rhizosolenia* lacking a frustule (Villareal, 1989; Gómez et al., 2005) supporting this assertion.

Although the average trichome lengths between FL and symbiotic *Calothrix* were comparable, the maximum lengths of the FL-*C* trichomes were much longer than *B-C* and *C-C* (**Figures 2E–G**), implying that *Bacteriastrum* and *Chaetoceros* hosts prefer their epiphytic symbionts to be short. In addition, with only a single heterocyst, a long filament might not be as beneficial to their host in providing fixed N (Foster et al., 2011). As an epiphyte, a long filament might also increase N loss to the surrounding seawater due to the inefficiency of a long-trichome N transport. In addition, longer filaments have more vegetative cells thereby increasing the N demand of the cyanobacterial symbiont itself. Overall, shorter *Calothrix* seemed to benefit their *Chaetoceros* and *Bacteriastrum* hosts by not weighing them down and providing better transfer efficiency for the recently fixed N.

Spatiotemporal Variations of Trichome Lengths

Field results showed significant regional and seasonal differences in the trichome lengths of *H-R* and FL-*C*; they were longer in the SCS than the PS and longer during the NEM than the SWM.

TABLE 4 | Trichome lengths of *Calothrix* and *Richelia* symbionts by region.

Type	Study area	Trichome length (cells/trichome)			References
		Minimal	Maximal	Average	
Richelia	Subtropical North Pacific Ocean	2	7	–	Zehr et al. (2007)†
H-R	Western Philippine Sea	1	5	3*	**This study**
	Northern South China Sea	1	5	4*	**This study**
	Malacca Strait	2	6	–	Sundström (1984)
	Western Indian Ocean	–	–	5	Lyimo (2011)
	Eastern Mediterranean Sea	4	7	–	Bar Zeev et al. (2008)
	Western North Atlantic Ocean and Caribbean Sea	6	11	–	Villareal (1994)
	Western tropical North Atlantic Ocean	1	5	4	Foster et al. (2007)
	Tropical North Atlantic Ocean	2	3	–	Foster and Zehr (2006)
	Laboratory cultures (Gulf of Mexico)	4	6	–	Hilton et al. (2013)
R-R	Subtropical North Pacific Ocean	4	5	–	Foster and Zehr (2006)
	Western Philippine Sea	3	15	7*	**This study**
	Northern South China Sea	3	15	8*	**This study**
	Malacca Strait and Gulf of Thailand	7	20	–	Schmidt (1901)
	Bay of Bengal	9	11	–	Kulkarni et al. (2010)
	Palk Bay	15	24	–	Madhu et al. (2013)
	Southeastern Arabian Sea	13	20	–	Jabir et al. (2013)
	Northern Arabian Sea	10	15	–	Padmakumar et al. (2010)
	Western Indian Ocean	5	15	–	Lyimo (2011)
	Eastern Mediterranean Sea	–	11	–	Bar Zeev et al. (2008)
	Western tropical North Atlantic Ocean	–	–	5	Foster et al. (2007)
	The Bahamas and northern Caribbean Sea	5	11	–	Janson et al. (1999)
G-R	Western Philippine Sea	5	11	7*	**This study**
	Northern South China Sea	4	15	8*	**This study**
FL-R	Western Philippine Sea	4	22	8*	**This study**
	Northern South China Sea	5	15	9*	**This study**
Calothrix	Subtropical North Pacific Ocean	4	8	–	Lemmermann (1905)‡
C-C	Subtropical North Pacific Ocean	4	5	–	Foster and Zehr (2006)
	Western Philippine Sea	3	12	5*	**This study**
	Northern South China Sea	3	14	5*	**This study**
	The Bahamas and northern Caribbean Sea	5	11	–	Janson et al. (1999)
B-C	Northern South China Sea	4	7	5*	**This study**
FL-C	Laboratory cultures (North Pacific strain)	–	>11	–	Foster et al., 2010
	Laboratory cultures (North Pacific strain)	2	4	–	Nieves-Morión et al. (2020)
	Western Philippine Sea	3	17	6*	**This study**
	Northern South China Sea	3	19	6*	**This study**
	Laboratory cultures (South China Sea strain)	2	114	–	**This study**

SWM and NEM data combined, see **Table 3 for the seasonal differences. †Not host specific. ‡Reported as epiphytes on Rhizosolenia and Hemiaulus.*

Similarly, FL-*R* trichomes were longer in the SCS than in the PS during both seasons, whereas *R-R* and *G-R* trichomes were longer in the SCS than the PS only during the SWM. The trichomes of *R-R* and *G-R* were also longer during the NEM than the SWM in the PS and the SCS, respectively. Such spatiotemporal differences in trichome lengths were accompanied by variations in nutrient supplies among regions and seasons. Both higher nutrient inventories (N_I and P_I) and shallower nutriclines (D_N and D_P) were observed in the SCS than in the PS during both seasons. In the SCS, higher surface nutrient concentrations (N_S and P_S) seemed related to longer trichome lengths during the NEM than the SWM. In the PS, although N_S and P_S were seasonally comparable, relatively high nutrient fluxes, reflected in the lower SI and deeper D_M, may have contributed to the longer trichome lengths during the NEM. Furthermore, higher Chl and shallower D_{CM} also reflected the relatively high nutrient supplies in the SCS and during the NEM. The correlation matrix also showed positive relationships between trichome length of *H-R* and nutrients (N+N or P); however, the correlation coefficients were very low ($r < 0.10$) (**Supplementary Table 2**). Like nutrients, certain physical variables including SST and SPAR also showed significant regional and seasonal differences (**Table 2**). The correlation matrix also showed negative relationships between trichome lengths of *H-R*, *R-R*, and FL-*C* and temperature (**Supplementary Table 2**). However, temperature (or SST) was usually highly correlated with nutrients

TABLE 5 | Similarities of gas vesicle structural proteins (Gvp) between cyanobacterial diazotrophs and *Dolichospermum flos-aquae* CCAP 1403/13F (GenBank: U17109.1) by BLASTp.

Strain†	GvpA	GvpC	GvpN	GvpA/J	GvpK	GvpF/L	GvpG	GvpV	GvpW	GvpP
Aphanizomenon flos-aquae MDT14a	96.8	88.1	93.9	71.9	93.1	91.1	88.3	84.9	90.2	88.4
Aphanizomenon flos-aquae NIES-81	95.5	72.3	75.3	72.4	74.0	84.3	91.9	81.8	79.0	88.7
Aphanizomenon flos-aquae WA102	98.7	99.5	99.4	94.6	99.2	98.8	99.3	99.1	98.7	88.7
Calothrix sp. NIES-2098	81.2	29.4	50.2	32.6	63.2	47.7	45.8	48.4	50.9	69.9
Calothrix sp. NIES-2100	92.4	64.0	74.5	43.2	81.1	76.7	55.4	65.1	69.3	69.1
Calothrix sp. NIES-3974	na	na	na	na	na	na	na	na	na	62.6
Calothrix sp. NIES-4071	na	na	na	na	na	na	na	na	na	58.3
Calothrix sp. NIES-4105	na	na	na	na	na	na	na	na	na	58.3
Calothrix brevissima NIES-22	88.5	67.5	76.6	40.7	77.6	73.8	60.1	56.2	32.6	68.0
Calothrix desertica PCC 7102	na	na	na	na	na	na	na	na	na	59.9
Calothrix elsteri CCALA 953	na	na	na	na	na	na	na	na	na	62.9
Calothrix parasitica NIES-267	na	na	na	na	na	na	na	na	na	59.4
Calothrix rhizosoleniae SC01	na	na	na	na	na	na	na	na	na	69.3
Nostoc punctiforme PCC73102	82.2	28.0	49.4	33.5	63.0	60.8	48.2	49.1	51.1	65.9
Nostoc punctiforme NIES-2108	89.5	48.1	59.3	41.6	78.8	73.9	56.6	57.5	67.4	69.1
Richelia intracellularis RC01	na	na	na	na	na	na	na	na	na	60.2
Tolypothrix sp. PCC 7601	91.4	67.5	73.4	68.9	76.7	76.0	57.8	65.4	69.9	68.5
Tolypothrix sp. NIES-4075	79.9	na	63.1	38.6	70.7	70.3	50.1	56.0	na	68.5
Tolypothrix bouteillei VB521301	81.8	na	63.8	34.5	68.8	68.0	51.6	55.7	57.0	67.5
Tolypothrix tenuis PCC 7101	91.7	67.1	73.4	41.1	77.5	75.4	55.2	65.1	70.5	68.5
Trichodesmium erythraeum IMS101	31.2	na	64.0	35.1	63.0	56.7	50.1	na	50.8	49.7

†*See* ***Supplementary Tables 3, 4*** *for genome information and Gvp accession numbers, respectively.*

(**Supplementary Table 3**; Tuo et al., 2017). Nutrient stress has been considered a cause of short trichome length in cyanobacteria (Smith and Gilbert, 1995). For example, when a freshwater cyanobacterium *Oscillatoria agardhii* was under a period of P limitation, its cell phosphorus content declined and its trichomes became progressively shorter (Gibson and Stevens, 1979). Our results imply that higher nutrient concentrations (especially P) might support the production of longer trichomes of both *Richelia* and *Calothrix*.

In contrast to the other associations and free-living *Richelia* and *Calothrix*, *C-C* had comparable trichome lengths regardless of the region or season. Unlike endosymbiotic *Richelia*, which inhabit space inside the host cells, *C-C* attach to the hosts' apertures and are oriented transversely to the long axis of the chains (Gómez et al., 2005; Tuo et al., 2014). As a facultative symbiont or an opportunist, a filament of *C-C* could easily detach from its host and lengthen, especially under replete nutrient conditions (Tuo et al., 2017). The clear spatiotemporal length variations of the FL-*C* trichome relative to *C-C* and *B-C* are reflected in **Table 4**.

It should be noticed that regional and/or seasonal differences in the mean trichome length was around one vegetative cell for most types of *Calothrix* (∼1.0 cells) and *Richelia* (0.3–1.7 cells), except FL-*C* and *G-R* (**Table 2**). The larger difference for *G-R* (4.1 cells) was likely due to the very small sample size at the SCS-NEM stations ($n = 2$). When ignoring the SCS-NEM sample, the regional difference during the SWM for *G-R* was also around one cell. On the other hand, FL-*C* showed larger spatiotemporal differences (0.5–3.2 cells), implying stronger influences from ambient nutrient availability. However, the small variation in symbiotic *Calothrix* and *Richelia* trichome length (i.e., one cell) implies that nutrient availability in this study area was not a primary control on trichome length in the SCS and PS.

Lack of Gas Vesicles in *C. rhizosoleniae* Cells

Gas vesicles are common cellular components in freshwater species of heterocystous cyanobacteria such as *Dolichospermum* spp., *Aphanizomenon* spp., *Nostoc* spp., and *Calothrix epiphytica*, which usually have elongated trichomes with tens to hundreds of cells per trichome (West and West, 1897; Walsby, 1994; Wacklin et al., 2009). We found that *C. rhizosoleniae* lacks gas vesicles (**Figure 5**), similar to *Richelia*, suggesting poor buoyancy regulation or an inclination to sink (Janson et al., 1995). The lack of gas vesicles in cultured *C. rhizosoleniae* might have been the result of acclimation to cultivation; cultures were isolated in December 2007 and harvested for TEM in March 2015. To support our ultrathin section results (**Figure 5**), we also examined gas vesicle structural proteins (Gvp) in the genomes of *C. rhizosoleniae*, *R. intracellularis*, and other representative filamentous cyanobacteria to those of *Dolichospermum flos-aquae* CCAP 1403/13F (GenBank: U17109.1). The similarity comparisons showed that *C. rhizosoleniae* (SC01, a FL strain isolated from *Chaetoceros* hosts), *R. intracellularis* (RC01, associated with *Rhizosolenia* hosts), and certain species of *Calothrix* lacked the sequences of the structural protein (GvpA), large outer surface protein (GvpC), and putative gas vesicle protein (GvpN, GvpA/J, GvpK, GvpF/L, GvpG, GvpV, and GvpW) (**Table 5** and **Supplementary Tables 4, 5**). While

GvpP was found and is also a putative protein related to gas vesicles, it showed no obvious amino acid identity to the other *gvp* gene products (especially GvpA) (Li and Cannon, 1998). Thus, the genomic information supported the observation that *C. rhizosoleniae* and *R. intracellularis* cells lacked gas vesicles. Without the ability to produce gas vesicles, cyanobacterial species must regulate their buoyancy by turgor collapse and accumulation of condensed carbohydrate (Reynolds et al., 1987), and/or they might decrease their filament volume by shortening trichome length to control their buoyancy/sinking, if the Stokes' Law worked for them.

SUMMARY

The trichome length of diatom host-associated symbionts may be controlled by their hosts/symbiotic styles. On average, the internal *Richelia* symbiont (*H-R*) produced the shortest trichomes, followed by the external *Calothrix* symbionts (*C-C* and *B-C*); the periplasmic *Richelia* symbionts (*R-R* and perhaps *G-R*) produced the longest trichomes. The trichome lengths of FL-*C* and FL-*R* were comparable with their symbiotic counterparts *C-C* and *R-R*, respectively. Regional and/or seasonal differences in trichome length were observed for various types of *Richelia* and FL-*C*. However, the difference in length was only about one cell per trichome. Both *Richelia* and *Calothrix* (*rhizosoleniae*) may have limited buoyancy regulation due to their lack of gas vesicles and the ability to produce them. This may require them to maintain shorter trichome lengths unlike other filamentous cyanobacterial species that have gas vacuoles.

DATA AVAILABILITY STATEMENT

The datasets presented in this study can be found in online repositories. The names of the repository/repositories and accession number(s) can be found in the article/ **Supplementary Material**.

AUTHOR CONTRIBUTIONS

ST and YLLC conceived the idea. ST, MRM, and YLLC wrote the manuscript with contributions from YT. ST, YT, WNJ, and YHL performed the experiments and created the figures and tables. ST, MRM, YLLC, YT, and HYC revised the manuscript. All authors reviewed the manuscript.

FUNDING

This research was in part supported by the Taiwan Ministry of Science and Technology (formerly, National Science Council) through the grants NSC (94-2611-M-110-009, 95-2611-M-110-002, 95-2611-M-110-004, 96-2628-M-110-005, 97-2628-M-110-002, 98-2628-M-110-002, 99-2611-M-110-015, 100-2611-M-110-001, 101-2611-M-110-001, and 102-2611-M-110-001); MOST (103-2611-M-110-001, 104-2611-M-110-005, 104-2811-M-110-009, and 108-2917-I-564-017), and in part from the Asia-Pacific Ocean Research Center, National Sun Yat-sen University, Kaohsiung, Taiwan.

ACKNOWLEDGMENTS

We thank Mei-Ling Tsai for the DNA cloning, Takuhei Shiozaki, Hsiao-Hsueh Shen, Yuan Ju Liao, Tze Ching Yong, Chien-Chih Huang, Bo-Ruei Huang, Yi-Xain Liu, Lian-Fen Jian, Hong Jun Ma, Jiunn Lin Tzeng, Hanlin Lai, Tien Yi Chen, and Che-Chen Chuang, as well as the captains, crews, and technicians on R/Vs *Ocean Researcher I* and *III* for assistance in field collections.

SUPPLEMENTARY MATERIAL

The Supplementary Material for this article can be found online at: https://www.frontiersin.org/articles/10.3389/fmars.2021.678607/full#supplementary-material

REFERENCES

Bar Zeev, E., Yogev, T., Man-Aharonovich, D., Kress, N., Herut, B., Béja, O., et al. (2008). Seasonal dynamics of the endosymbiotic, nitrogen-fixing cyanobacterium *Richelia intracellularis* in the eastern Mediterranean Sea. *ISME J.* 2, 911–923. doi: 10.1038/ismej.2008.56

Capone, D. G., Burns, J. A., Montoya, J. P., Subramaniam, A., Mahaffey, C., Gunderson, T., et al. (2005). Nitrogen fixation by *Trichodesmium* spp.: an important source of new nitrogen to the tropical and subtropical North Atlantic Ocean. *Glob. Biogeochem. Cycles* 19:GB2024.

Capone, D. G., Zehr, J. P., Paerl, R. W., Bergman, B., and Carpenter, E. J. (1997). Trichodesmium, a globally significant marine cyanobacterium. *Science* 276, 1221–1229. doi: 10.1126/science.276.5316.1221

Caputo, A., Nylander, J. A., and Foster, R. A. (2019). The genetic diversity and evolution of diatom-diazotroph associations highlights traits favoring symbiont integration. *FEMS Microbiol. Lett.* 366:fny297.

Carpenter, E. J., and Capone, D. G. (2008). "Dinitrogen fixation," in *Nitrogen in the Marine Environment*, eds D. G. Capone, M. R. Mulholland, and E. J. Carpenter (Amsterdam: Elsevier), 141–198.

Carpenter, E. J., and Janson, S. (2001). *Anabaena gerdii* sp. nov., a new planktonic filamentous cyanobacterium from the South Pacific Ocean and Arabian Sea. *Phycologia* 40, 105–110.

Carpenter, E. J., Montoya, J. P., Burns, J., Mulholland, M. R., Subramaniam, A., and Capone, D. G. (1999). Extensive bloom of a N2-fixing diatom/cyanobacterial association in the tropical Atlantic Ocean. *Mar. Ecol. Prog. Ser.* 185, 273–283. doi: 10.3354/meps185273

Caruso, M. J., Gawarkiewicz, G. G., and Beardsley, R. C. (2006). Interannual variability of the Kuroshio Intrusion in the South China Sea. *J. Oceanogr.* 62, 559–575. doi: 10.1007/s10872-006-0076-0

Chen, T. Y., Chen, Y. L. L., Sheu, D. S., Chen, H. Y., Lin, Y. H., and Shiozaki, T. (2019). Community and abundance of heterotrophic diazotrophs in the northern South China Sea: revealing the potential importance of a new alphaproteobacterium in N2 fixation. *Deep Sea Res. I* 143, 104–114. doi: 10.1016/j.dsr.2018.11.006

Chen, Y. B., Zehr, J. P., and Mellon, M. (1996). Growth and nitrogen fixation of the diazotrophic filamentous nonheterocystous cyanobacterium *Trichodesmium* sp. IMS 101 in defined media: evidence for a circadian rhythm. *J. Phycol.* 32, 916–923. doi: 10.1111/j.0022-3646.1996.00916.x

Chen, Y. L. L., Chen, H. Y., Lin, Y. H., Yong, T. C., Taniuchi, Y., and Tuo, S. (2014). The relative contributions of unicellular and filamentous diazotrophs to N2 fixation in the South China Sea and the upstream Kuroshio. *Deep Sea Res. I* 85, 56–71. doi: 10.1016/j.dsr.2013.11.006

Chen, Y. L. L., Chen, H. Y., Tuo, S., and Ohki, K. (2008). Seasonal dynamics of new production from Trichodesmium N2 fixation and nitrate uptake in

the upstream Kuroshio and South China Sea basin. *Limnol. Oceanogr.* 53, 1705–1721. doi: 10.4319/lo.2008.53.5.1705

Chen, Y. L. L., Tuo, S.-H., and Chen, H. Y. (2011). Co-occurrence and transfer of fixed nitrogen from *Trichodesmium* spp. to diatoms in the low-latitude Kuroshio Current in the NW Pacific. *Mar. Ecol. Prog. Ser.* 421, 25–38. doi: 10.3354/meps08908

Foster, R. A., Goebel, N. L., and Zehr, J. P. (2010). Isolation of *Calothrix rhizosoleniae* (Cyanobacteria) strain SC01 from *Chaetoceros* (Bacillariophyta) spp. diatoms of the subtropical North Pacific Ocean. *J. Phycol.* 46, 1028–1037. doi: 10.1111/j.1529-8817.2010.00885.x

Foster, R. A., Kuypers, M. M., Vagner, T., Paerl, R. W., Musat, N., and Zehr, J. P. (2011). Nitrogen fixation and transfer in open ocean diatom-cyanobacterial symbioses. *ISME J.* 5, 1484–1493. doi: 10.1038/ismej.2011.26

Foster, R. A., Subramaniam, A., Mahaffey, C., Carpenter, E. J., Capone, D. G., and Zehr, J. P. (2007). Influence of the Amazon River plume on distributions of free-living and symbiotic cyanobacteria in the western tropical north Atlantic Ocean. *Limnol. Oceanogr.* 52, 517–532. doi: 10.4319/lo.2007.52.2.0517

Foster, R. A., and Zehr, J. P. (2006). Characterization of diatom-cyanobacteria symbioses on the basis of nifH, hetR and 16S rRNA sequences. *Environ. Microbiol.* 8, 1913–1925. doi: 10.1111/j.1462-2920.2006.01068.x

Gibson, C. E., and Stevens, R. J. (1979). Changes in phytoplankton physiology and morphology in response to dissolved nutrients in Lough Neagh, N. Ireland. *Freshw. Biol.* 9, 105–109. doi: 10.1111/j.1365-2427.1979.tb01494.x

Gómez, F., Furuya, K., and Takeda, S. (2005). Distribution of the cyanobacterium *Richelia intracellularis* as an epiphyte of the diatom Chaetoceros compressus in the western Pacific Ocean. *J. Plankton. Res.* 27, 323–330. doi: 10.1093/plankt/fbi007

Grosse, J., Bombar, D., Doan, H. N., Nguyen, L. N., and Voss, M. (2010). The Mekong River plume fuels nitrogen fixation and determines phytoplankton species distribution in the South China Sea during low and high discharge season. *Limnol. Oceanogr.* 55, 1668–1680. doi: 10.4319/lo.2010.55.4.1668

Hall, T. A. (1999). BioEdit: a user-friendly biological sequence alignment editor and analysis program for Windows 95/98/NT. *Nucleic Acids Symp. Ser.* 41, 95–98.

Hilton, J. A. (2014). *Ecology and Evolution of Diatom-Associated Cyanobacteria Through Genetic Analyses*. PhD Thesis. Santa Cruz, CA: University of California Santa Cruz.

Hilton, J. A., Foster, R. A., Tripp, H. J., Carter, B. J., Zehr, J. P., and Villareal, T. A. (2013). Genomic deletions disrupt nitrogen metabolism pathways of a cyanobacterial diatom symbiont. *Nat. Commun.* 4:1767.

Inomura, K., Follett, C. L., Masuda, T., Eichner, M., Prášil, O., and Deutsch, C. (2020). Carbon transfer from the host diatom enables fast growth and high rate of N2 fixation by symbiotic heterocystous cyanobacteria. *Plants* 9:192. doi: 10.3390/plants9020192

Jabir, T., Dhanya, V., Jesmi, Y., Prabhakaran, M. P., Saravanane, N., Gupta, G. V. M., et al. (2013). Occurrence and distribution of a diatom-diazotrophic cyanobacteria association during a *Trichodesmium* bloom in the southeastern Arabian Sea. *Int. J. Oceanogr.* 2013:350594. doi: 10.1155/2013/350594

Jan, S., Yang, Y. J., Wang, J., Mensah, V., Kuo, T. H., Chiou, M. D., et al. (2015). Large variability of the Kuroshio at 23.75°N east of Taiwan. *J. Geophys. Res. Oceans* 120, 1825–1840. doi: 10.1002/2014jc010614

Janson, S., Rai, A. N., and Bergman, B. (1995). Intracellular cyanobiont *Richelia intracellularis*: ultrastructure and immuno-localisation of phycoerythrin, nitrogenase, Rubisco and glutamine synthetase. *Mar. Biol.* 124, 1–8. doi: 10.1007/bf00349140

Janson, S., Wouters, J., Bergman, B., and Carpenter, E. J. (1999). Host specificity in the *Richelia*-diatom symbiosis revealed by hetR gene sequence analysis. *Environ. Microbiol.* 1, 431–438. doi: 10.1046/j.1462-2920.1999.00053.x

Karsten, G. (1907). "Das indische Phytoplankton nach dem Material der deutschen Tiefsee-Expedition 1898-1899," in *Wissenschaftliche Ergehniss der deutschen Tiefsee-Expedition auf dem Dampfer "Valdivia" 1898-1899*, ed. C. Chun (Jena: Gustav Fischer Verlag), 221–548.

Kimor, B., Gordon, N., and Neori, A. (1992). Symbiotic associations among the microplankton in oligotrophic marine environments, with special reference to the Gulf of Aqaba, Red Sea. *J. Plankton. Res.* 14, 1217–1231. doi: 10.1093/plankt/14.9.1217

Kulkarni, V. V., Chitari, R. R., Narale, D. D., Patil, J. S., and Anil, A. C. (2010). Occurrence of cyanobacteria-diatom symbiosis in the Bay of Bengal: implications in biogeochemistry. *Curr. Sci.* 99, 736–737.

Lemmermann, E. (1905). Die Algenflora der Sandwich Inseln. Ergebnisse einer Reise nach dem Pacific, H. Schauinsland 1896/97. *Bot. Jahrb. Syst., Pflanzengesch. Pflanzengeogr.* 34, 607–633.

Li, N., and Cannon, M. C. (1998). Gas vesicle genes identified in Bacillus megaterium and functional expression in *Escherichia coli*. *J. Bacteriol.* 180, 2450–2458. doi: 10.1128/jb.180.9.2450-2458.1998

Liang, W. D., Tang, T. Y., Yang, Y. J., Ko, M. T., and Chuang, W. S. (2003). Upper-ocean currents around Taiwan. *Deep Sea Res. II* 50, 1085–1105. doi: 10.1016/s0967-0645(03)00011-0

Liu, K. K., Chao, S. Y., Shaw, P. T., Gong, G. C., Chen, C. C., and Tang, T. Y. (2002). Monsoon-forced chlorophyll distribution and primary production in the South China Sea: observations and a numerical study. *Deep Sea Res. I* 49, 1387–1412. doi: 10.1016/s0967-0637(02)00035-3

Luo, Y.-W., Doney, S. C., Anderson, L. A., Benavides, M., Berman-Frank, I., Bode, A., et al. (2012). Database of diazotrophs in global ocean: abundance, biomass and nitrogen fixation rates. *Earth Syst. Sci. Data* 4, 7–73. doi: 10.5194/essd-4-47-2012

Lyimo, T. J. (2011). Distribution and abundance of the cyanobacterium *Richelia intracellularis* in the coastal waters of Tanzania. *J. Ecol. Nat. Environ.* 3, 85–94.

Madhu, N. V., Meenu, P., Ullas, N., Ashwini, R., and Rehitha, T. V. (2013). Occurrence of cyanobacteria (*Richelia intracellularis*)-diatom (*Rhizosolenia hebetata*) consortium in the Palk Bay, southeast coast of India. *Indian J. Mar. Sci.* 42, 453–457.

Mague, T. H., Weare, N. M., and Holm-Hansen, O. (1974). Nitrogen fixation in the north Pacific Ocean. *Mar. Biol.* 24, 109–119. doi: 10.1007/bf00389344

Mulholland, M. R., Bernhardt, P. W., Widner, B. N., Selden, C. R., Chappell, P. D., Clayton, S., et al. (2019). High rates of N2 fixation in temperate, western North Atlantic coastal waters expand the realm of marine diazotrophy. *Glob. Biogeochem. Cycles* 33, 826–840. doi: 10.1029/2018GB006130

Nieves-Morión, M., Flores, E., and Foster, R. A. (2020). Predicting substrate exchange in marine diatom-heterocystous cyanobacteria symbioses. *Environ. Microbiol.* 22, 2027–2052. doi: 10.1111/1462-2920.15013

Padmakumar, K. B., Menon, N. R., and Sanjeevan, V. N. (2010). Occurrence of endosymbiont *Richelia intracellularis* (Cyanophyta) within the diatom Rhizosolenia hebetata in Northern Arabian Sea. *Int. J. Biodivers. Conserv.* 2, 70–74.

Redfield, A. C. (1958). The biological control of chemical factors in the enviroment. *Am. Sci.* 46, 205–221.

Reynolds, C. S., Oliver, R. L., and Walsby, A. E. (1987). Cyanobacterial dominance: the role of buoyancy regulation in dynamic lake environments. *N. Z. J. Mar. Freshw. Res.* 21, 379–390. doi: 10.1080/00288330.1987.9516234

Reynolds, E. S. (1963). The use of lead citrate at high pH as an electron-opaque stain in electron microscopy. *J. Cell. Biol.* 17, 208–212. doi: 10.1083/jcb.17.1.208

Schmidt, J. (1901). Über *Richelia intracellularis*, eine neue in Plankton-Diatomeen lebende Alge. *Hedwigia* 40, 112–115.

Shiozaki, T., Chen, Y. L. L., Lin, Y. H., Taniuchi, Y., Sheu, D. S., Furuya, K., et al. (2014). Seasonal variations of unicellular diazotroph groups A and B, and *Trichodesmium* in the northern South China Sea and neighboring upstream Kuroshio Current. *Cont. Shelf Res.* 80, 20–31. doi: 10.1016/j.csr.2014.02.015

Shiozaki, T., Fujiwara, A., Ijichi, M., Harada, N., Nishino, S., Nishi, S., et al. (2018). Diazotroph community structure and the role of nitrogen fixation in the nitrogen cycle in the Chukchi Sea (western Arctic Ocean). *Limnol. Oceanogr.* 63, 2191–2205. doi: 10.1002/lno.10933

Shiozaki, T., Fujiwara, A., Inomura, K., Hirose, Y., Hashihama, F., and Harada, N. (2020). Biological nitrogen fixation detected under Antarctic sea ice. *Nat. Geosci.* 13, 729–732. doi: 10.1038/s41561-020-00651-7

Shiozaki, T., Takeda, S., Itoh, S., Liu, X., Hashihama, F., and Furuya, K. (2015). Why is *Trichodesmium* abundant in the Kuroshio? *Biogeosciences* 12, 6931–6943. doi: 10.5194/bg-12-6931-2015

Smith, A. D., and Gilbert, J. J. (1995). Spatial and temporal variability in filament length of a toxic cyanobacterium (*Anabaena affinis*). *Freshw. Biol.* 33, 1–11. doi: 10.1111/j.1365-2427.1995.tb00381.x

Sohm, J. A., Subramaniam, A., Gunderson, T. E., Carpenter, E. J., and Capone, D. G. (2011). Nitrogen fixation by *Trichodesmium* spp. and unicellular diazotrophs in the North Pacific Subtropical Gyre. *J. Geophys. Res.* 116:G03002.

Spurr, A. R. (1969). A low-viscosity epoxy resin embedding medium for electron microscopy. *J. Ultrastruct. Res.* 26, 31–43. doi: 10.1016/s0022-5320(69)90033-1

Subramaniam, A., Yager, P. L., Carpenter, E. J., Mahaffey, C., Björkman, K., Cooley, S., et al. (2008). Amazon River enhances diazotrophy and carbon sequestration in the tropical North Atlantic Ocean. *Proc. Natl. Acad. Sci. U.S.A.* 105, 10460–10465. doi: 10.1073/pnas.0710279105

Sundström, B. G. (1984). Observations on *Rhizosolenia clevei* Ostenfeld (Bacillariophyceae) and *Richelia intracellularis* Schmidt (Cyanophyceae). *Bot. Mar.* 27, 345–356.

Taniuchi, Y., Chen, Y. L. L., Chen, H. Y., Tsai, M. L., and Ohki, K. (2012). Isolation and characterization of the unicellular diazotrophic cyanobacterium Group C TW3 from the tropical western Pacific Ocean. *Environ. Microbiol.* 14, 641–654. doi: 10.1111/j.1462-2920.2011.02606.x

Tuo, S., Chen, Y. L. L., and Chen, H. Y. (2014). Low nitrate availability promotes diatom diazotroph associations in the marginal seas of the western Pacific. *Aquat. Microb. Ecol.* 73, 135–150. doi: 10.3354/ame01715

Tuo, S., Chen, Y. L. L., Chen, H. Y., and Chen, T. Y. (2017). Free-living heterocystous cyanobacteria in the tropical marginal seas of the western North Pacific. *J. Plankton. Res.* 39, 404–422. doi: 10.1093/plankt/fbx023

Turk, K. A., Rees, A. P., Zehr, J. P., Pereira, N., Swift, P., Selley, R., et al. (2011). Nitrogen fixation and nitrogenase (nifH) expression in tropical waters of the eastern North Atlantic. *ISME J.* 5, 1201–1212. doi: 10.1038/ismej.2010.205

Villareal, T. A. (1989). Division cycles in the nitrogen-fixing Rhizosolenia (Bacillariophyceae)-*Richelia* (Nostocaceae) symbiosis. *Eur. J. Phycol.* 24, 357–365. doi: 10.1080/00071618900650371

Villareal, T. A. (1990). Laboratory culture and preliminary characterization of the nitrogen-fixing Rhizosolenia-*Richelia symbiosis*. *Mar. Ecol.* 11, 117–132. doi: 10.1111/j.1439-0485.1990.tb00233.x

Villareal, T. A. (1994). Widespread occurrence of the Hemiaulus-cyanobacterial symbiosis in the southwest North Atlantic Ocean. *Bull. Mar. Sci.* 54, 1–7.

Wacklin, P., Hoffmann, L., and Komárek, J. (2009). Nomenclatural validation of the genetically revised cyanobacterial genus *Dolichospermum* (Ralfs ex Bornet et Flahault) comb. nova. *Fottea* 9, 59–64. doi: 10.5507/fot.2009.005

Walsby, A. E. (1994). Gas vesicles. *Microbiol. Mol. Biol. Rev.* 58, 94–144. doi: 10.1128/mmbr.58.1.94-144.1994

West, W., and West, G. S. (1897). Welwitsch's African freshwater algae. *J. Bot. Br. For.* 35, 235–243.

White, A. E., Prahl, F. G., Letelier, R. M., and Popp, B. N. (2007). Summer surface waters in the Gulf of California: prime habitat for biological N2 fixation. *Glob. Biogeochem. Cycles* 21:GB2017.

Zehr, J., and Turner, P. (2001). "Nitrogen fixation: nitrogenase genes and gene expression," in *Methods in Microbiology*, ed. J. H. Paul (St. Petersburg, FL: Academic Press), 271–286. doi: 10.1016/s0580-9517(01)30049-1

Zehr, J. P., Montoya, J. P., Jenkins, B. D., Hewson, I., Mondragon, E., Short, C. M., et al. (2007). Experiments linking nitrogenase gene expression to nitrogen fixation in the North Pacific subtropical gyre. *Limnol. Oceanogr.* 52, 169–183. doi: 10.4319/lo.2007.52.1.0169

Zhang, Y., Zhao, Z., Sun, J., and Jiao, N. (2011). Diversity and distribution of diazotrophic communities in the South China Sea deep basin with mesoscale cyclonic eddy perturbations. *FEMS Microbiol. Ecol.* 78, 417–427. doi: 10.1111/j.1574-6941.2011.01174.x

Conflict of Interest: The authors declare that the research was conducted in the absence of any commercial or financial relationships that could be construed as a potential conflict of interest.

frontiers in Marine Science

ORIGINAL RESEARCH
published: 03 August 2021
doi: 10.3389/fmars.2021.707807

Phytoplankton and Bacterial Responses to Monsoon-Driven Water Masses Mixing in the Kuroshio Off the East Coast of Taiwan

Chao-Chen Lai[1], *Chau-Ron Wu*[2], *Chia-Ying Chuang*[1], *Jen-Hua Tai*[1], *Kuo-Yuan Lee*[1], *Hsiang-Yi Kuo*[1] *and Fuh-Kwo Shiah*[1,3,4]*

[1] Research Center for Environmental Changes, Academia Sinica, Taipei, Taiwan, [2] Department of Earth Sciences, National Taiwan Normal University, Taipei, Taiwan, [3] Institute of Oceanography, National Taiwan University, Taipei, Taiwan, [4] Institute of Marine Environment and Ecology, National Taiwan Ocean University, Keelung, Taiwan

Biogeochemical responses to mixing were examined in two cruise surveys along a transect across the Kuroshio Current (KC) in May and July 2020. Two stations located at the South China Sea (SCS)–KC mixing and the KC waters were chosen for the diel study. In the euphotic zone (~100 m depth), the average values of nitrate (0.97–1.62 μM), chlorophyll-*a* (Chl-*a*, 0.36–0.40 mg/m^3), and primary production (PP; 3.46 ± 1.37 mgC/m^3/day) of the mixing water station (MWS) of the two cruises were several folds higher than those of the KC station (KCS; nitrate, 0.03–0.10 μM; Chl-*a*, 0.14–0.24 mg/m^3; and PP, 0.91 ± 0.47 mgC/m^3/day). In the July cruise, the maximal bacterial production (BP) at the MWS (3.31 mgC/m^3/day) was 82% higher in comparison with that of the KCS (1.82 mgC/m^3/day); and the readings of Chl-*a* showed no trend with BP in the oligotrophic KCS, but a positive relationship was found among these measurements at the mesotrophic MWS. This implies that the trophic status of the system might affect phytoplankton–bacteria interactions. The backward-trajectory analyses conducted by an observation-validated three-dimensional model identified that the prevailing southwest monsoon drove a northeastward "intrusion" of the SCS waters in July 2020, resulted in mixing between SCS and Kuroshio (KC) waters off the east coast of southern Taiwan. For the first time, this study demonstrates that the high biological biomass and activities that occur in the KC are induced by the northward intrusion of the SCS waters.

Keywords: NW-Pacific, Kuroshio, southwest monsoon, phytoplankton, primary production, bacterial production

OPEN ACCESS

Edited by:
Wen-Chen Chou, National Taiwan Ocean University, Taiwan

Reviewed by:
Xin Liu, Xiamen University, China
Hung-Yen Hsieh, National Dong Hwa University, Taiwan

***Correspondence:**
Fuh-Kwo Shiah
fkshiah@rcec.sinica.edu.tw

Specialty section:
This article was submitted to Marine Ecosystem Ecology, a section of the journal Frontiers in Marine Science

Received: *10 May 2021*
Accepted: *29 June 2021*
Published: *03 August 2021*

Citation:
Lai C-C, Wu C-R, Chuang C-Y, Tai J-H, Lee K-Y, Kuo H-Y and Shiah F-K (2021) Phytoplankton and Bacterial Responses to Monsoon-Driven Water Masses Mixing in the Kuroshio Off the East Coast of Taiwan. Front. Mar. Sci. 8:707807. doi: 10.3389/fmars.2021.707807

INTRODUCTION

Planktons play a significant role in affecting the transformation and distribution of materials in aquatic ecosystems. Biological activities can be categorized into autotrophic (i.e., the formation of organic from inorganic) and heterotrophic (i.e., the consumption of organic to form inorganic) processes. For autotrophic processes, primary production (PP) is the formation rate of biogenic organic materials performed by phytoplankton in the ocean. In terms of C-cycling, the "biological pump" extracts carbon (through photosynthesis) from the "surface skin" of the ocean that interacts with the atmosphere, presenting a lower partial pressure of CO_2 to the atmosphere and thus lowering its CO_2 content (Sigman and Haug, 2006). This sequestration of CO_2 from the atmosphere to the ocean interior highlights the importance of studying PP.

The dissolved organic carbon (DOC) inventory (∼660 Giga-ton C) of the ocean roughly equals that of CO_2 in the atmosphere (Hansell et al., 2009; Lønborg et al., 2020, and citations therein). Most oceanic DOC results from autochthonous food-web processes such as phytoplankton exudation, zooplankton/metazoans excretions, bacteriovory, and viral lysis. Prokaryotic heterotrophic bacteria (i.e., bacteria) are the key microorganisms responsible for the decomposition of DOC (Cho and Azam, 1988). This makes bacteria act as an "anti-biological pump" in the ocean (Azam, 1998; Azam and Malfatti, 2007).

The Kuroshio Current (KC), originating from the North Equatorial Current, is a western boundary current in the North Pacific Ocean. After bifurcating east of Mindanao, the north branch of the North Equatorial Current forms the KC, which flows along the east coasts of Luzon and Taiwan and trends northward along the continental slope of the East China Sea. The KC makes an important contribution to the thermohaline and momentum budgets of the North Pacific Ocean. At an annual scale, the KC frequently intrudes into the northern SCS (NSCS) through the Luzon Strait (Wu et al., 2017, and citations therein). The vertical distribution of the KC through the Strait mimics a sandwich structure: Water of KC enters the northern SCS at depths of 0–400 and ∼1,500–3,000 m, and it returns to the western Pacific Ocean at intermediate depths of ∼500–1,500 m (Nan et al., 2015). The annually averaged net volume flux through the Luzon Strait is ∼2 Sv into the northern south china sea (NSCS) from May to January of the next year. From February to April, the net transport reverses from the NSCS to the Pacific (Xue et al., 2004). It is noted that the SCS–KC intrusion in the east–west direction has been addressed by many studies (Chou et al., 2007; Sheu et al., 2009), while the northward intrusion of SCS into KC has rarely been mentioned if it can be done.

From chemical and biological perspectives, the warm KC flow along the east coast of Taiwan had been viewed as an oligotrophic biome due to the limited supply of inorganic nutrients and low biological production in the euphotic zone (Shiah, 1999; Shiah et al., 2000; Tseng et al., 2005). Recent studies revealed satellite images showing high chlorophyll-*a* (Chl-*a*) concentration in this area (Cheng et al., 2020). However, the availability of primary and bacterial production (PP and BP) data in this area has been limited. Our two surveys were a biogeochemistry-oriented pilot study for designing a long-term project, which intends to study the potential contribution of the high chlorophyll areas to biogenic carbon production/export, local fishery (e.g., larvae and flying fishes), and dolphin sightseeing business. In addition, conducting surveys across KC enables us to compare phytoplankton–bacteria interactions under mesotrophic and oligotrophic conditions. It is noted that organic carbon export (or the biological pump) on the east coast of Taiwan could be unique since it has a very narrow shelf and steep slope, which might quicken the export into the deep sea. The Chl-*a* and PP data measured during cruise surveys can further be used for the ground truth of the satellite ocean color data.

Our previous temperature–salinity diagrams (Shiah, data not shown) indicated a mixing of the SCS and KC waters occurred around this area, and we suspected that the vertical shear/mixing between the two abovementioned water masses could generate the changes of physical, chemical, and thus biological properties in this area.

MATERIALS AND METHODS

Stations and Sampling

Two surveys (May 12–16, 2020 and July 21–25, 2020) were performed at a transect across the KC east of Taiwan (**Figure 1**). The sampling schedule in the May cruise was impeded by an unexpected artillery fire drill. Therefore, water samples were repeatedly sampled every 12 h at stations 2 (4 hydrocasts) and 6 (3 hydrocasts), which represented the mixing water and KC water stations, respectively. In the July cruise, hydrocasts were deployed two times from stations 1–8 at the beginning and end of the cruise. Repeated sampling with ≥7 hydrocasts every 12 h for each station was conducted at these two diel stations. Water samples were taken within the upper 200 m by 20-L Go-Flo bottles from eight depths (10, 20, 30, 50, 80, 100, 150, and 200 m). The profiles of temperature (T), salinity (S), fluorescence, and underwater photosynthetic available radiance (PAR) were recorded by sensors attached to a CTD Rosette (General Oceanic Model 1015; General Oceanics, Miami, FL, USA). The typical T–S diagrams of the SCS and KC waters were derived from the averages of more than 200 historical hydrocasts in these two areas (data source, the Ocean Data Bank, Taiwan; http://www.odb.ntu.edu.tw/).

Numerical Modeling on Backward-Trajectory and Flow Pattern Analyses

The shipboard acoustic Doppler current profiler (ADCP; to measure current speed and direction) was out of order during both cruises. We used the numerical modeling method to simulate the most likely current flow pattern for this area when the July survey was conducted. A 14-day backward-trajectory floater simulation based on the current field at 15 m depth was obtained by the Hybrid Coordinate Ocean Model (HYCOM; GLBv0.08/expt_93.0). The release period was set as July 21–31, 2020, and releases were staggered at 3-h intervals. The velocity data are based on the HYCOM analysis. Furthermore, an observation-validated, three-dimensional model [Global Ocean Flux Study (GOFS) 3.1: 41-layer HYCOM + Navy Coupled Ocean Data Assimilation Global 1/12° Analysis; https://hycom.org] was used to simulate the flow pattern on July 22, 2020, in the vicinity of the study area. Temporal and spatial resolutions were 3-h and 1/10°, respectively. The data assimilation schemes such as the three-dimensional variation scheme and the improved synthetic ocean profiles were applied. Simulation plots were generated with MATLAB (R2019b, https://www.mathworks.com/).

Inorganic Nutrients, Chlorophyll-*a*, and Total Organic Carbon Concentrations

Inorganic nutrients (i.e., nitrate, phosphate, and silicate) and Chl-*a* concentrations were determined according to the methods of Parsons et al. (1984). Total organic carbon (TOC) was derived from the sum of particulate and dissolved organic carbon (POC

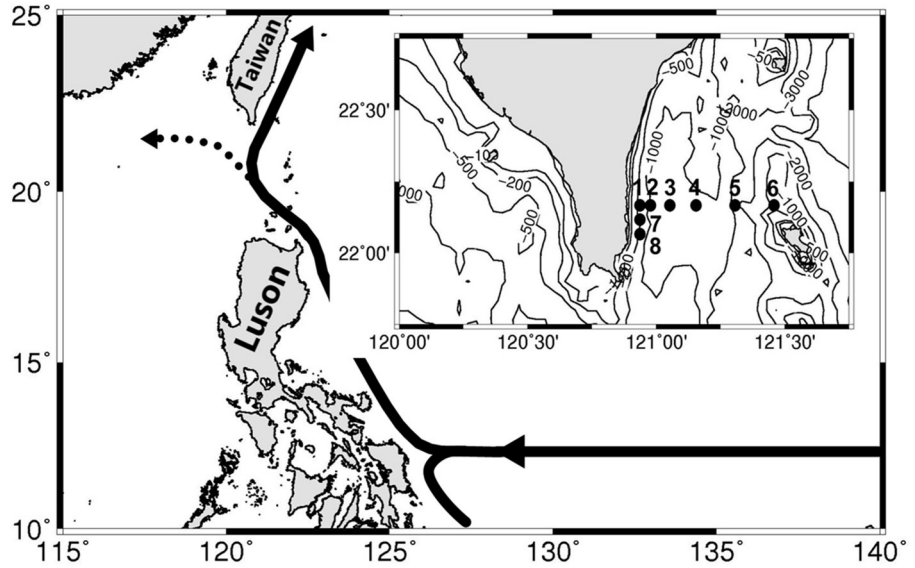

FIGURE 1 | Map of southern Taiwan shows the sampling stations across the mainstream of the Kuroshio. The isovalue lines of bottom depth are also shown. Diel sampling was conducted at stations 2 and 6. The solid and dashed lines with arrows in the upper-left corner indicate the axes of the Kuroshio mean flow.

and DOC). For POC, water samples (1–2 L) were filtered through a 200-μm mesh to remove zooplankton and then through 25-mm GF/F filters. POC concentrations were measured by a CHN analyzer (Fisons; NA1500). Samples for DOC were filtered through a GF/F filter. Filtrates were filled into precombusted 40-mL glass vials (Kimble). Samples were analyzed by a high-temperature catalytic oxidation method using a Shimadzu TOC 5000. The details of DOC measurement can be found in the study of Austria et al. (2018).

Bacterial Abundance, Production, and Growth Rate

The procedures of Gaso and Giorgio (2000) and Brussaard (2004) were followed for heterotrophic bacteria and other picophytoplankton counts. Water samples were fixed with the final concentrations of 1% paraformaldehyde (for viruses) and 0.1% glutaraldehyde (for bacteria) and then frozen with liquid nitrogen and stored at −80°C. Samples were stained with SYBR Green I and then incubated for 15 min at room temperature in the dark. The samples were run in a flow cytometer of CyFlow® Space (PARTEC) at a rate allowing <1,000 events per second to avoid particle coincidence. The bacterial activity was determined by ^{3}H-thymidine incorporation (Fuhrman and Azam, 1982). After the injection of ^{3}H-thymidine, water samples were incubated at *in situ* temperature for 2 h. Bacterial biomass (BB) and BP in C units were derived with thymidine and carbon conversion factors of 1.18×10^{18} cell/mole and 2×10^{14} gC/cell (Ducklow and Carlson, 1992), respectively. Bacterial (per cell) growth rate (Bμ) was calculated by diving production with biomass. The details of bacterial parameters can be found in the study of Austria et al. (2018).

Primary Production

Primary production (PP) was measured by the ^{14}C assimilation method (Parsons et al., 1984) on board with seawater samples taken during the dawn. In brief, the 2:1 light/dark 250-mL clean polycarbonate bottles were filled with water samples. After $H^{14}CO_3^{-1}$ (final concentration, 10 μCi or 370 kBq/ml) inoculation, samples were wrapped with 10 neutral density LEE filters and incubated in a self-designed tank with an artificial light source (∼2,000 μE/m^2/s). Following retrieval, samples were filtered through GF/F filters, and the radioactivity was counted in a liquid scintillation counter (Packard 2000). The details of PP calculation can be found in the study of Austria et al. (2018). Three and two sets of PP measurements were conducted in the dawn at only stations 2 and 6, respectively. This was based on the protocols of the Joint Global Ocean Flux Study (JGOFS) (Knap et al., 1996) which recommend that PP should be measured using a water sample taken at dawn. The euphotic zone was defined as the depth to which 1% of surface light reaches.

Data Management and Statistical Analysis

For the May cruise, only the data of inorganic nutrients, Chl-*a*, and BB, were available. The bulk properties of measured variables were compared in terms of tempo-spatial (horizontal) variation by deriving depth-integrated (i.e., trapezoidal method) averaged values. The statistical analysis was performed using SPSSVR software version 12.0 (IBM, Armonk, NY, USA).

RESULTS

Backward-Trajectory and Flow Pattern Analyses

Figure 2A shows the major current paths arriving at the south end of Taiwan in July. In the central path, floaters passed through

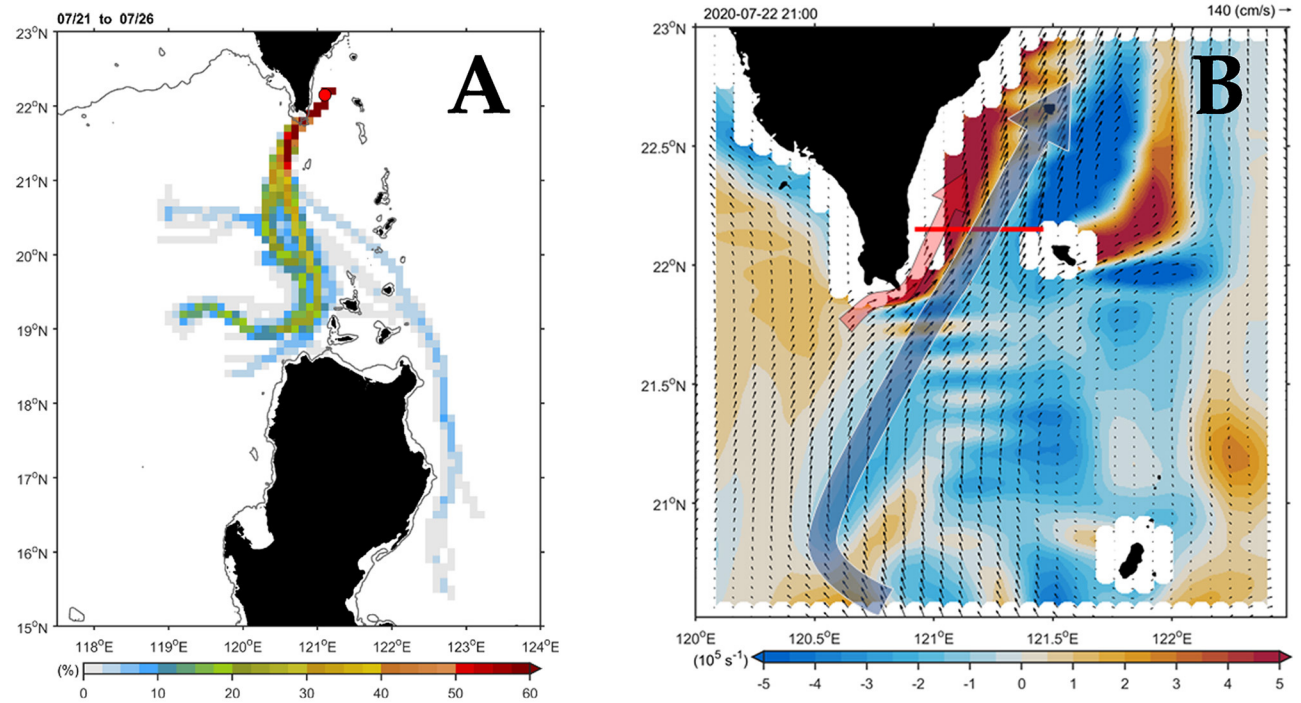

FIGURE 2 | Three-dimensional numerical simulation of flow patterns in the study area. **(A)** Paths of the currents based on the backward-trajectory analyses. The horizontal color bar indicates the percentage for the arrival of the floater. The percentage is 100% in the releasing position (station 2; red dot; 22.15°N, 121.1°E). **(B)** Simulated flow patterns of the 15-m depth velocity (vector) and vorticity (shading) on July 22, 2020. The red line in **(B)** indicates the sampling transect.

the study area with a high percentage (i.e., >50%), which could be traced back to their source upstream in the Luzon Strait. The numerically simulated flow pattern (**Figure 2B**) presented a typical summer circulation regime when the southwest monsoon prevailed over the study area. After leaving the northern tip of Luzon Island, the northward-flowing Kuroshio (i.e., KC) mainstream followed a relatively straight pathway bypassing the Luzon Strait with less westward intrusion into the South China Sea (SCS). That is, most of the KC water returned to the east and continued its northward flow along the east coast of Taiwan (blue arrow). Meanwhile, a northeastward-flowing branch originating from the SCS (red arrow) joined the western flank of the KC off southeast Taiwan.

Physical and Chemical Hydrography

In May, the temperature–salinity (T–S) diagrams of St. 2 indicated that the water mass was a mixture of the SCS and KC waters (**Figures 3A–D**). In contrast, the water properties of St. 6 were imaged with those of KC (**Figures 3E–G**). In the July cruise, similar to the findings recorded in May, the T–S diagrams of Sts. 8, 7, 1, and 2 were closest to the east coast of Taiwan, indicating that at the beginning of the sampling period, the water masses were a mixture of the SCS–KC waters (**Figures 4A–D**). Additionally, the signal of the SCS–KC mixing extended to Sts. 3 and 4 (**Figures 4E,F**). Stations 5 and 6 at the easternmost side were typical KC water (**Figures 4G,H**). For the ending-cast, the T–S properties of Sts. 7, 8, 1, 2, and 3 (**Figures 4I–M**) retained the SCS–KC mixing characteristics, while that of St. 6 (**Figure 4P**) was comparable to that of KC. The water masses of Sts. 4 and 5 (**Figures 4N,O**) tended to be more like KC water but still possessed some of the SCS–KC mixing signals in the deep water. Overall, the T–S results indicated that St. 4 (∼33 km off the east coast) could be viewed as the east boundary of the SCS–KC mixing zone. Temperature profiles in May showed that the 25°C isotherm at St. 6 (**Figure 5A**) was located at depths of 80–100 m, while that of St. 2 (**Figure 5E**) fluctuated at depths of 50–60 m. Nitrate concentrations (NO_3) at St. 6 (**Figure 5B**) and St. 2 (**Figure 5F**) ranged from <0.1 to 4.8 μM and from <0.1 to 10.6 μM, respectively. The area of the NO_3-depletion zone at St. 6 (>120 m deep) was two times deeper than that of St. 2, which was ∼50–60 m deep. In July, temperature profiles showed that the 25°C isotherm at St. 6 (**Figure 6A**) was located at depths of ∼100 m, while that of St. 2 (**Figure 7A**) was positioned at depths of 40–60 m. NO_3 concentrations at St. 6 (**Figure 6B**) and St. 2 (**Figure 7B**) ranged from <0.1 to 4.1 μM and from <0.1 to 14.0 μM, respectively. The area of the NO_3-depletion zone at St. 6 (∼100 m deep) was two times deeper than that of St. 2, which was ∼50 m deep. It is noted that NO_3 dropped to low values at the sixth sampling point at St. 2. Therefore, NO_3 at 200 m depth was 0.78 μM, which was ∼10 times lower than the 200-m readings (8.6–14.0 μM) of the other sampling points. Phosphate concentrations (i.e., SRP) collected from these two stations changed proportionally with NO_3 with a relationship of $NO_3 = -0.24 + 13.45 \times \mathrm{SRP}$, $R^2 = 0.99$, $n = 111$, where

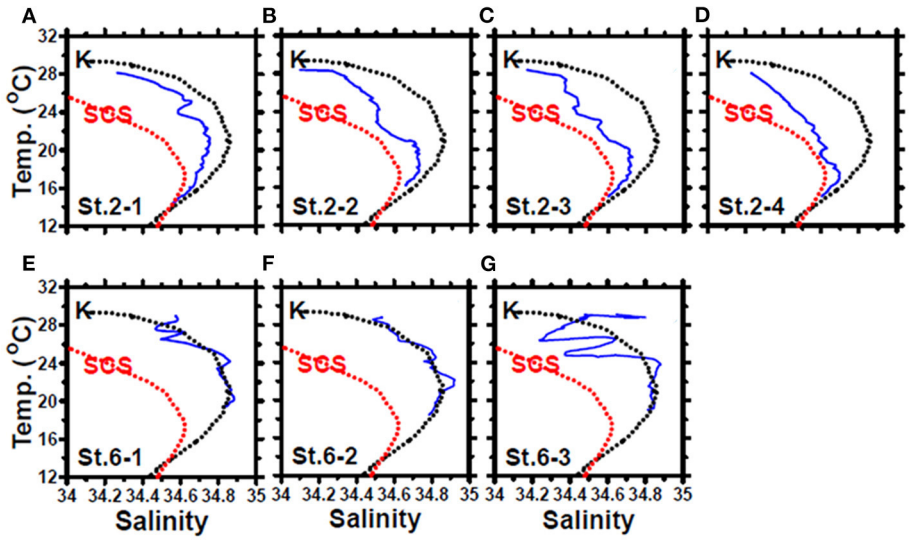

FIGURE 3 | The temperature–salinity diagrams of the casts deployed at stations 2 **(A–D)** and 6 **(E–G)** of the May cruise. The black and red dashed lines represent the typical Kuroshio Current (KC) and South China Sea (SCS) waters, respectively. The data were collected from the Ocean Data Bank, Taiwan (http://www.odb.ntu.edu.tw/). The first and second numbers of the abbreviation St. x–x in each panel indicate the sampling station and the hydrocast deployed at that station, respectively.

R^2 and n are the coefficients of determination and sampling size, respectively.

Spatial and Temporal Variation of Phytoplankton Biomass and Production

The satellite-derived data (**Figure 8**) of the July cruise indicated the daily evolution of the sea-surface Chl-*a* concentrations during the sampling period. Sts. 1, 2, 7, and 8 were occupied by high Chl-*a* while Sts. 4, 5, and 6 were continuously typified by a low Chl-*a* condition. Spatially (i.e., vertically and horizontally), we found that the distribution of high surface Chl-*a* values with shallow subsurface Chl-*a* maximum (SCM; ∼50 m depth; **Figure 9A**) echoed the area (e.g., Sts. 7, 8, 1, 2, and 3) with the SCS–KC mixing signals (**Figures 4A–E,I–M**). In contrast, much lower Chl-*a* values and deep SCM at ∼100 m were found at KC stations (e.g., Sts. 5 and 6). The spatial variation of Chl-*a* and SCM of the ending-cast (**Figure 9B**) generally followed those of the beginning-cast with one modification. The SCM concentrations recorded at Sts. 1–3 increased at least 3-fold in the ending-cast.

In May, low-surface Chl-*a* values (0.04–0.58 mgChl-*a*/m^3) with significant SCM mostly located at ∼100 m depth were observed at St. 6 (**Figure 5C**). In contrast to that, Chl-*a* at St. 2 (0.04–0.85 mgChl-*a*/m^3, **Figure 5G**) was much higher and its SCM was located at depths <50 m. In July, low-surface Chl-*a* values (0.03–0.52 mgChl-*a*/m^3) with significant SCM located at ∼100 m depth were observed at St. 6 (**Figure 6C**). In contrast to that, Chl-*a* at St. 2 (0.02–1.74 mgChl-*a*/m^3, **Figure 7C**) was much higher and its SCM was located at depths <50 m. Ranges and depth distributions of TOC recorded at St. 6 (**Figure 6D**; 49–101 μM) and St. 2 (**Figure 7D**; 45–109 μM) were similar to each other. The depth-integrated primary productions (PP) recorded at St. 6 were 57 and 124 mgC/m^2/day and at St. 2 were 197, 367, and 465 mgC/m^2/day.

Temporal Variation of Bacterial Biomass and Productions

Bacterial biomass (BB) at St. 6 (**Figure 5D**; 2.9–16.0 mgC/m^3) and St. 2 (**Figure 5H**; 1.6–22.7 mgC/m^3) in the May cruise showed similar patterns with higher values on the surface and then decreased with depth. In July at St. 6, BB (**Figure 6E**; 3.8–16.5 mgC/m^3) varied 4-fold with higher values on the surface, but with subsurface BB maximum recorded at depths of 40–70 m. In contrast, rate parameters, such as production (BP; **Figure 6F**; 0.37–1.82 mgC/m^3/day) and growth rate (Bμ; **Figure 6G**; 0.04–0.17 per day), were out of phase with BB. That is, higher BB occurred during the first half of the survey period (e.g., sampling points 1–5), while BB and Bμ elevated during the late phase (i.e., sampling points 5–7).

Spatially, the BP and Bμ data were higher on the surface and then decreased with depth. The only exception was that a subsurface Bμ maximum occurred at the depth of 150 m at the last sampling point. At St. 2, bacterial rate parameters (**Figures 7F,G**) were almost in phase with each other, with higher readings occurring on the surface and decreasing with depth. Similar to that of St. 6, higher BP (and Bμ) occurred later than those of BB at St. 2 (**Figure 7E**), and subsurface high Bμ values were recorded for these two stations at the depths of 150 m in the earliest and latest phases (**Figure 7G**).

Correlation Among Measurements

The correlation analysis (**Table 1**) of the July cruise data indicated that at St. 6, Chl-*a* did not correlate with any measurement, while at St. 2, we observed positive correlations

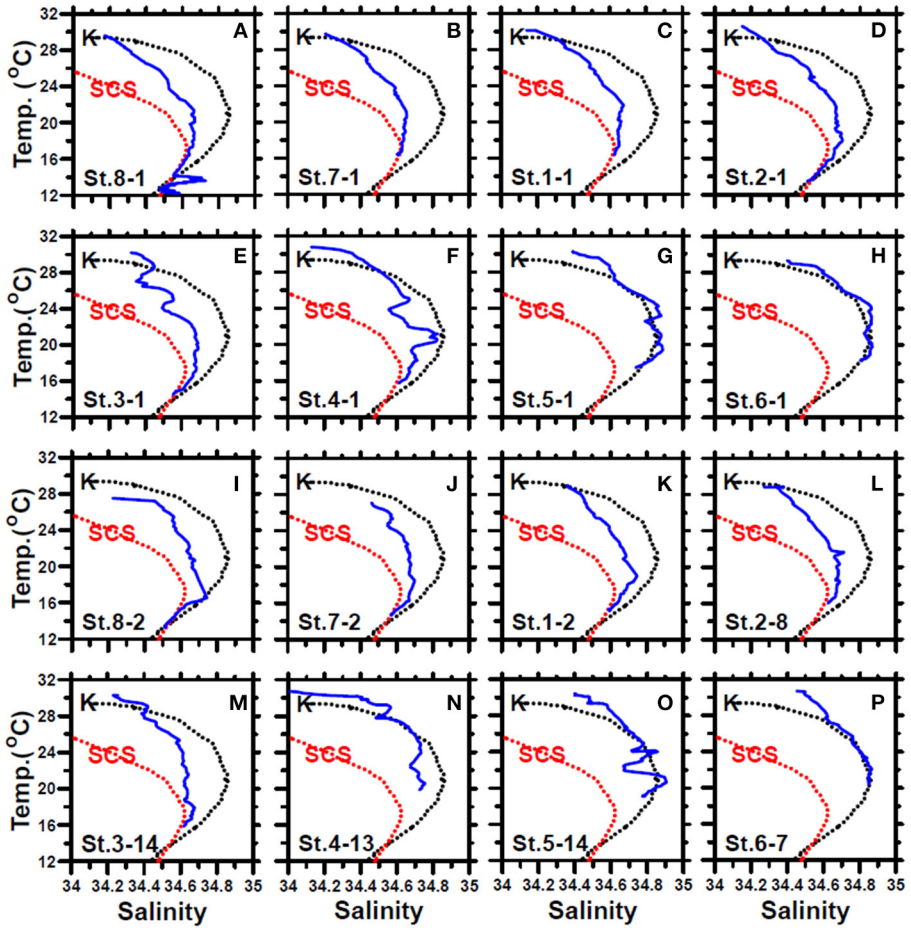

FIGURE 4 | The temperature–salinity diagrams of the first-cast (blue lines) **(A–H)** and last-cast **(I–P)** deployed at stations 8, 7, and 1–6 of the July cruise. The black and red dashed lines represent the typical KC and SCS waters, respectively. The data were collected from the Ocean Data Bank, Taiwan (http://www.odb.ntu.edu.tw/). The first and second numbers of the abbreviation St. x–x in each panel indicate the sampling station and the hydrocast deployed at that station, respectively.

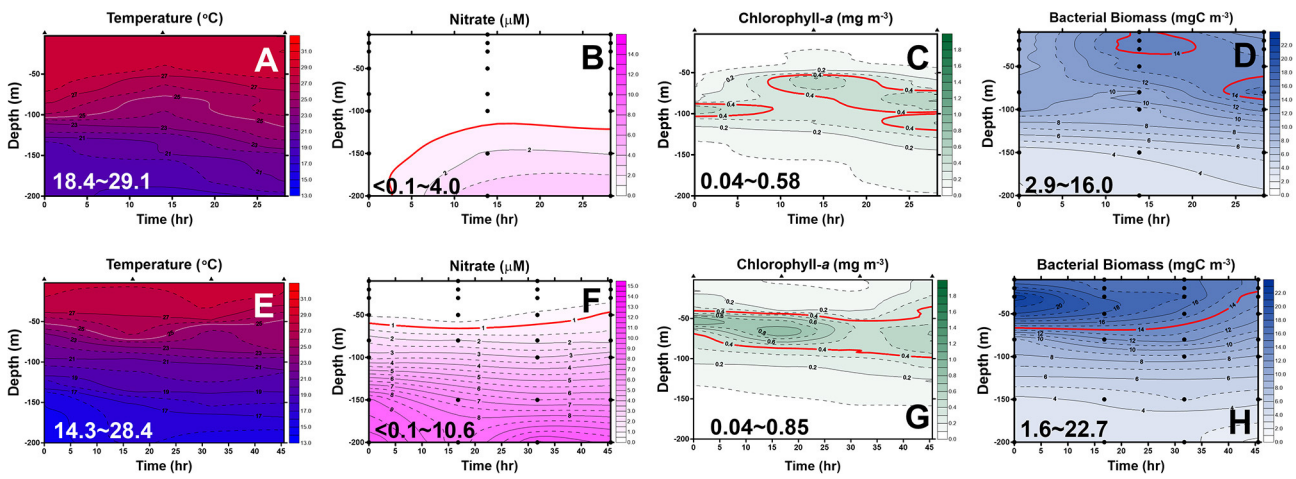

FIGURE 5 | Diel changes of the contour plots of the measurements in the upper 200 m of station 6 **(A–D)** and station 2 **(E–H)** of the May cruise. The ranges for each measurement are shown in each panel. The lines represent an isotherm of 25°C **(A,E)**, isovalue lines of 1.0 μM nitrate **(B,F)**, 0.4 mg/m^3 chlorophyll-*a* (Chl-*a*) **(C,G)**, and 14 mgC/m^3 bacterial biomass (BB) **(D,H)**, respectively.

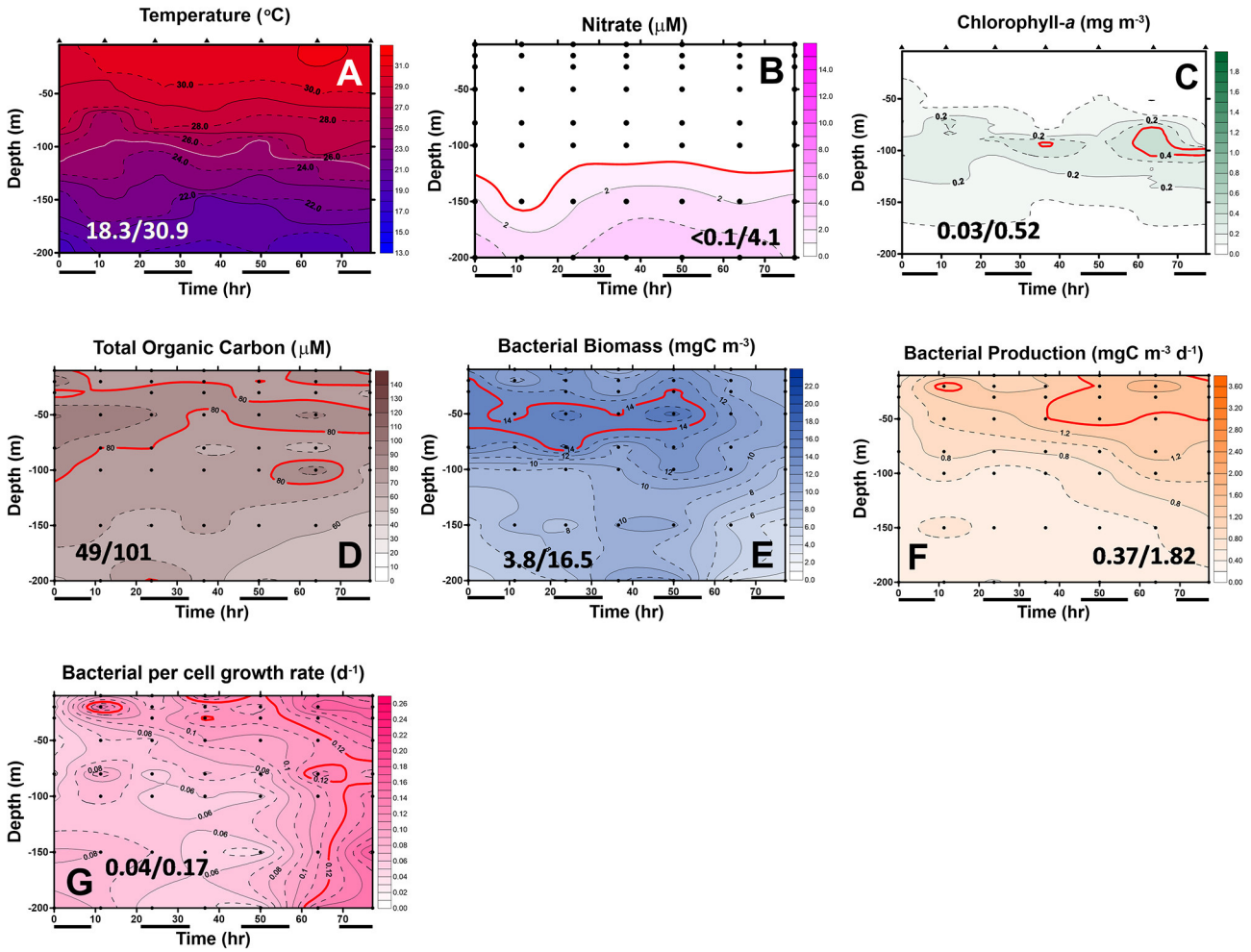

FIGURE 6 | Diel changes of the contour plots of the measurements in the upper 200 m of station 6 of the July cruise. The values in slash indicate the minimum and maximum in each panel. The lines in **(D–G)** represent the isovalue lines of 80 μMC total organic carbon (TOC), 14 mgC/m^3 BB, 1.4 mgC/m^3/day bacterial production (BP), and 0.12 bacterial growth rate (Bμ) per day, respectively. The isovalue lines for **(A–C)** are the same as mentioned in **Figure 5**. Black bars below the *X*-axis denote nighttime.

for Chl-*a* on all measurements except NO_3, which showed a negative trend. Positive correlations between TOC and BB were significant at both sampling sites. The coupling between bacterial measurements and their substrate source (e.g., Chl-*a*) was unseen at St. 6 and then became strong at St. 2. Similarly, the correlations for TOC with BP and Bμ at St. 6 were insignificant, but their relationships changed to positive ones at St. 2.

Comparison Between SCS–KC Mixing and KC Waters

In May, chemical (NO_3), and biological measurements (Chl-*a* and BB) at St. 2 were all higher than those recorded at St. 6 (**Table 2**). In July, NO_3 inventories in the euphotic zone (Z_e) of St. 2 were 4- to 5-fold higher than those of St. 6 (**Table 2**). Autotrophic measurements including Chl-*a* and PP were doubled and tripled, respectively, within the Z_e of St. 2. The depth-integrated averages of heterotrophic properties including BB, BP, and Bμ at St. 2 were slightly higher with percentages increasing <20%. Still, it was noted that the individual-depth BP maximum recorded at St. 2 (3.31 mgC/m^3/day; **Figure 7F**) was 82% higher when compared with that of St. 6 (1.82 mgC/m^3/day; **Figure 6F**). The depth-integrated averaged BP within Z_e were positively correlated with those of PP with a slope of ∼0.39 (±0.12) when the data of both stations were used (**Figure 10**).

DISCUSSION

For convenience, we categorized the KC into three sections, namely, the downstream, midstream, and upstream, which covered the areas north of 25°N, 22–25°N, and south of 22°N, respectively. The physical–chemical–biological coupling has long been a major research issue in the field of biological oceanography. Being the west-boundary current of the Pacific Ocean, the KC has been viewed as an oligotrophic biome. Recent

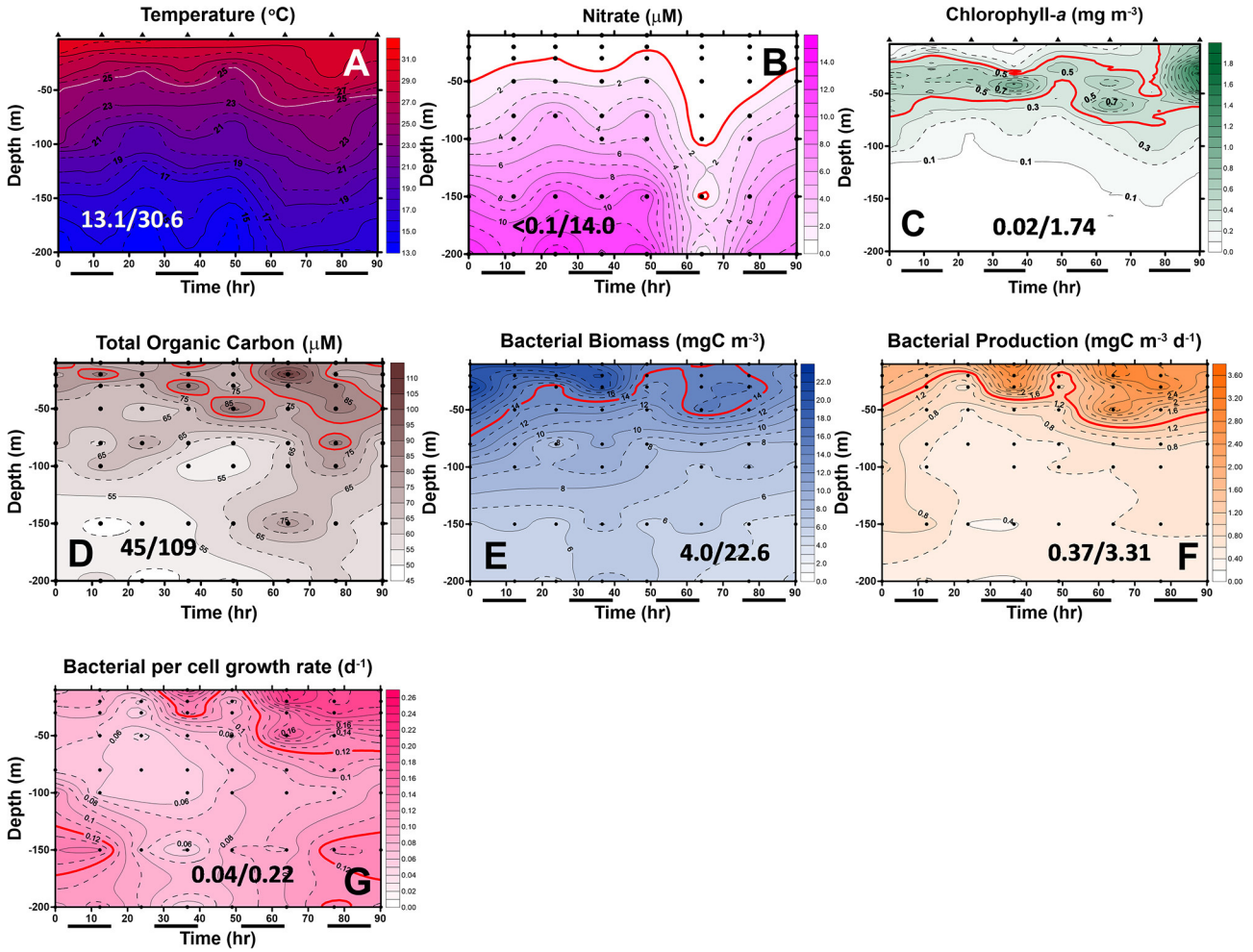

FIGURE 7 | Diel changes of the contour plots of the measurements in the upper 200 m of station 2 of the July cruise. The values in slash indicate the minimum and maximum in each panel. The lines in **(D–G)** represent the isovalue lines of 80 μMC TOC, 14 mgC/m^3 BB, 1.4 mgC/m^3/day BP, and 0.12 Bμ per day, respectively. The isovalue lines for **(A–C)** are the same as mentioned in **Figure 5**. Black bars below the *X*-axis denote nighttime.

studies have recommended several physical mechanisms that might transport deep-water nutrients to the surface waters and trigger high plankton biomasses and activities in the KC. In the downstream area, the intrusion of nutrient-rich KC subsurface water onto the continental shelf (Liu et al., 2013; Hasegawa et al., 2019), the mesoscale lateral mixing of KC water with Oyashio water (Clayton et al., 2014), and the topographically induced turbulence mixing (Kobari et al., 2020) have been proposed as the mechanisms that might intensify biological biomass and production in the surface water. At the KC upstream area (Tsutsumi et al., 2020), findings have demonstrated that the high minerals fluxes and high surface Chl-*a* concentrations observed in the Luzon Strait could be ascribed to the strong turbulence mixing induced by the interaction of topography (i.e., steep oceanic ridges) and tidal current.

In fact, some of the sampling stations (i.e., Sts. 1, 2, 7, and 8) are very close to the coast. However, they cannot be categorized as coastal/nearshore stations. The east coast terrain has cliff topography, which gives the area a very steep slope and almost no continental shelf. The bottom depths for the abovementioned stations are all greater than 200 m (**Figure 1**). In particular, St. 2 has a bottom depth of ∼760 m. Therefore, the mixing caused by the wind-blown and/or wave-breaking processes that commonly occur in shallow coastal areas is not applicable in this study. At the east coast of Taiwan (i.e., midstream area), biogenic processes such as the new nutrient (i.e., ammonium) produced *via* the high-density N_2-fixing *Trichodesmium* have been proposed as a cause for higher phytoplankton and bacterial growth/production in the KC in summer (Tseng et al., 2005). With satellite-derived Chl-*a*, sea-surface temperature maps, a drifter trajectory, and numerical model simulations, Cheng et al. (2020, see their Figure 11) indicated that at the southernmost end of Taiwan, the formation of submesoscale cyclonic eddies could trap cold and high Chl-*a* water every day and could form frontal waves between the free-stream and the wake-flow. It was suggested that the inorganic nutrient derived from eddy processes could

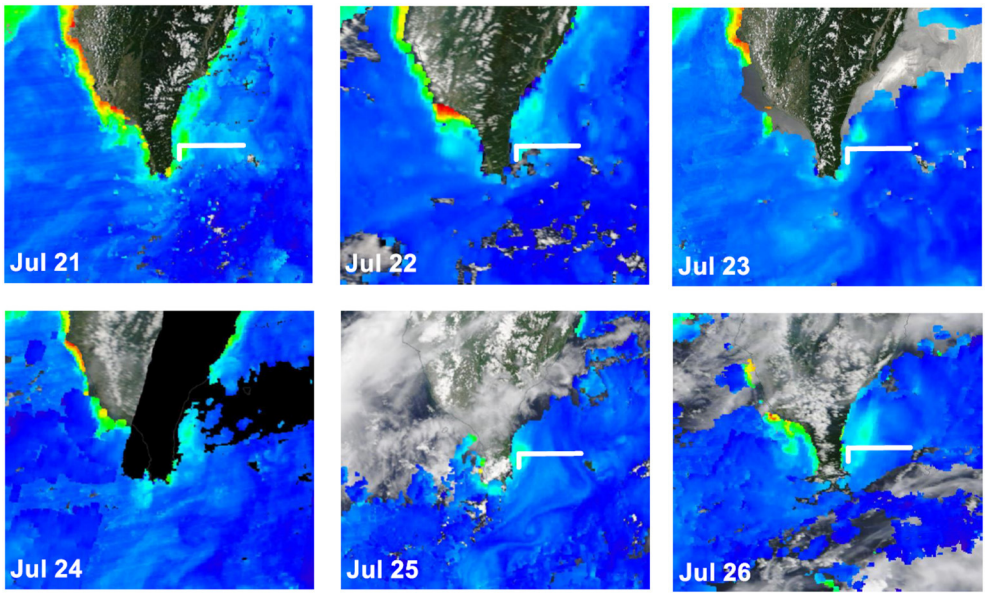

FIGURE 8 | Sequential changes of satellite-derived sea-surface Chl-*a* concentrations of the investigation period of July 21–25, 2020 (https://oceancolor.gsfc.nasa.gov/). The white line indicates the sampling transect.

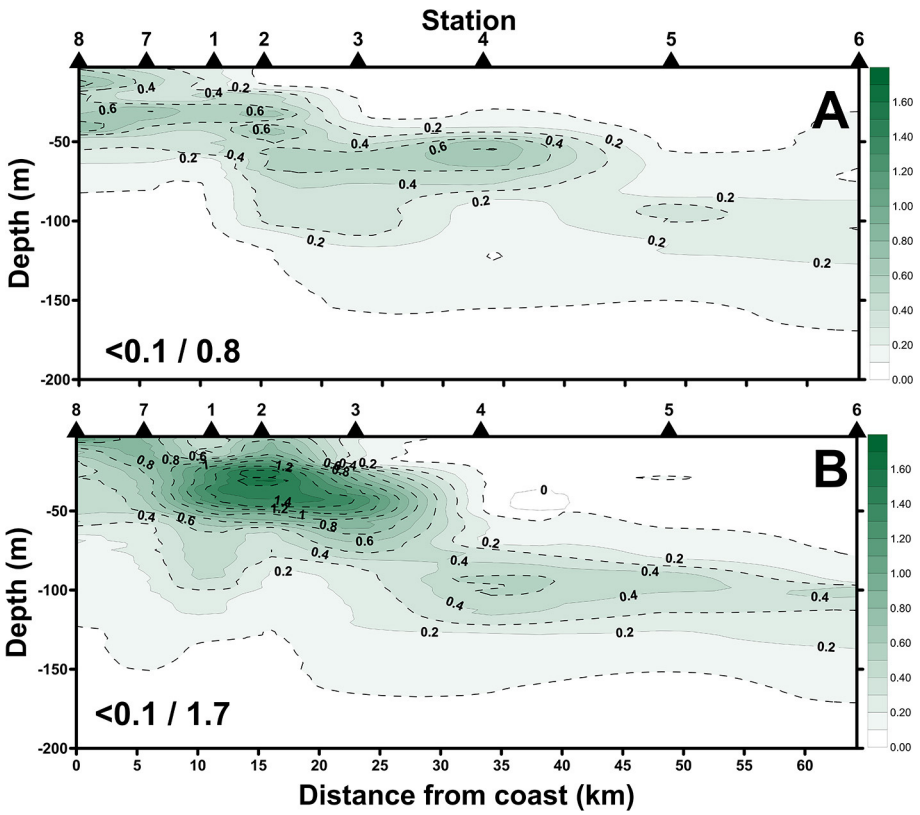

FIGURE 9 | Spatial changes of Chl-*a* concentrations along the sampling transect of the beginning-cast **(A)** and ending-cast **(B)** of the July cruise. Values in slash indicate the minimum and maximum in each panel.

TABLE 1 | Correlation matrix for measurements collected from stations 6 and 2 of the July cruise.

Items (units)	T (°C)	NO_3 (μM)	Chl-*a* (mg\m^3)	TOC (μM)	BP (mgC\m^3\day)	BB (mgC\m^3)	Bμ (day^{-1})
T		*−0.92*	*ns*	*+0.57*	*+0.79*	*+0.63*	*ns*
NO_3	−0.93		*ns*	*−0.61*	*−0.65*	*−0.62*	*ns*
Chl-*a*	+0.55	−0.55		*ns*	*ns*	*ns*	*ns*
TOC	+0.74	−0.71	+0.38		*ns*	*+0.59*	*ns*
BP	+0.78	−0.65	+0.42	+0.67		*+0.36*	*+0.67*
BB	+0.86	−0.76	+0.36	+0.59	+0.72		*−0.41*
Bμ	+0.37	*ns*	+0.35	+0.43	+0.77	ns	

Station 6 (upper right; in Italic) and station 2 (lower left). All were significant at the level of p = 0.01. ns, not significant. T, NO_3, Chl-a, TOC, BP, BB, and Bμ represented temperature, nitrate, chlorophyll-a, total organic carbon concentrations, bacterial production, bacterial biomass, and bacterial growth rate, respectively.

TABLE 2 | The euphotic zone (0–100 m) depth-integrated averages ± SDs of the measurements collected from stations 6 and 2 of the May and July cruises.

Month	Station	NO_3 (μM)	Chl-*a* (mg\m^3)	TOC (μM)	BP (mgC\m^3\day)	BB (mgC\m^3)	Bμ (day^{-1})	PP (mgC\m^3\day)
May	St. 6	0.10 ± 0.15	0.24 ± 0.07	na	na	11.9 ± 1.9	na	na
	St. 2	0.97 ± 0.37	0.40 ± 0.07	na	na	14.5 ± 2.1	na	na
July	St. 6	0.03 ± 0.03	0.14 ± 0.04	73 ± 8	1.00 ± 0.22	10.9 ± 1.6	0.09 ± 0.03	0.91 ± 0.47
	St. 2	1.62 ± 0.89	0.36 ± 0.14	65 ± 5	1.17 ± 0.40	11.3 ± 2.1	0.09 ± 0.03	3.46 ± 1.37

na, not available. NO_3, Chl-a, TOC, BP, BB, Bμ, and PP represented nitrate, chlorophyll-a, total organic carbon concentrations, bacterial production, bacterial biomass, bacterial growth rate, and depth-integrated averaged primary production, respectively.

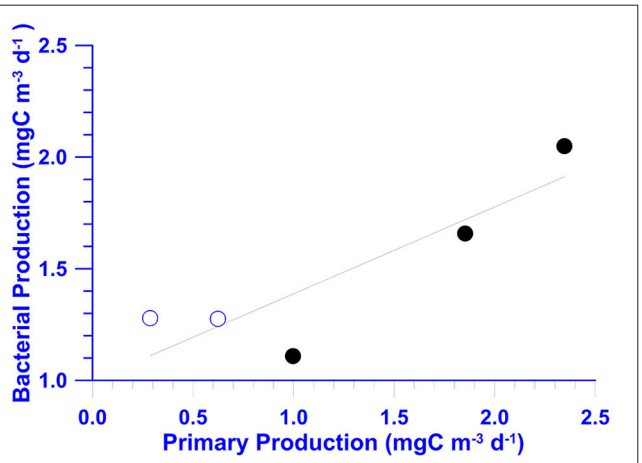

FIGURE 10 | A scatter plot of the euphotic zone (0–100 m) depth-integrated averages of BP vs. PP at stations 2 (solid dots) and 6 (open dots) of the July cruise. The linear regression equation is shown.

enhance the growth of phytoplankton, and the high Chl-*a* could be transported further northward.

In addition to the submesoscale eddy process, we argued that the monsoon-driven mixing of the SCS and KC waters (**Figure 2**) could be important in explaining the high algal biomass and PP in the nearshore area. The T–S signature (**Figures 3A–D**, **4D,L**) indicated that the water at St. 2 (also at Sts. 7, 8, 1, and 3) was a mixture of the SCS and KC waters. Three points were particularly noted. First, in the panels of **Figures 5A–E,I–M**, the starting point of the blue line at the bottom of each panel was linked to the red line, which represented the SCS water; the head of the blue line in each panel was bonded with the typical KC water as indicated by the black dashed line. If it were eddy effects, then the abovementioned T–S diagrams could not be generated. Second, shallower (<50 m) SCM with high Chl-*a* concentrations occurred only at the area west of St. 4 (**Figures 9A,B**), and all the T–S diagrams of the stations (Sts. 8, 7, 1, 2, and 3) in this area were characterized with SCS–KC mixing sign (**Figure 4**). The very shallow nitrocline (**Figures 5B**, **7B**; <50 m) implied that St. 2 could be viewed as a mesotrophic system. Finally, the numerical simulation of the backward-trajectory and flow pattern (**Figure 2**) processes highlighted a plausible physical mechanism for the SCS–KC mixing processes.

Mixing in deep water areas can occur due to shear stress. Shear stress is the pulling force of a fluid moving in one direction as it passes close to a fluid or object moving in another direction. The shear stress–generated pulling force can bring nutrient-rich water from deep water toward the ocean surface, which is usually nutrient-depleted. The nutrient-rich water stimulates the growth and reproduction of primary producers such as phytoplankton. In summer, the prevailing southwest monsoon invites the outflow from the SCS, joining the western flank of the KC off southeast Taiwan. The collision and velocity shear between the SCS and KC induces the mixing between the two water masses, as shown in **Figures 3**, **4**. The phenomenon of annual mean wind from the southwest inviting the outflow from the SCS to the southeastern coast of Taiwan in summer follows both *in situ* measurements and satellite observation, e.g., the long-term observations from both surface drifter trajectories (Centurioni et al., 2004) and shipboard ADCP velocity composites (Liang et al., 2003) as well as a satellite altimeter-based geostrophic current (Hsin et al., 2013). The high-resolution numerical model simulation of this study further confirmed a northeastward flow originating from the SCS that joined the western flank of the KC off southeast

Taiwan in late July 2020 (**Figure 2**). The T–S diagram of St. 2 exhibited the consequential mixing between the SCS and Kuroshio waters (**Figures 3**, **4**). The flow pattern lent further support, indicating that the water near Sts. 1 and 2 was a mixture of the SCS and KC waters. Furthermore, the velocity–vorticity (shear) off southeast Taiwan was positive, which was favorable for local upwelling, resulting in higher Chl-*a* concentrations (**Figure 8**) recorded in our studies.

In addition to the atmospheric force (i.e., the southwest monsoon), the driving force from the ocean interior might also cause SCS water intrusion. By analyzing the moored current velocities in the central Luzon Strait, Tai et al. (2010 and citations therein) revealed a Kuroshio frontal instability wave (KFIW) propagating northward over a 5-day period, and its wave amplitude was increasing northward. Their results of the two-layered model suggested that the flow was stabilized for the long-wave mode but destabilized for the short-wave mode, due to increasing vertical shear in the horizontal velocity. Therefore, the possibility that the eastward skew of the KFIW might also cause the SCS–KC mixing by the east coast of Taiwan cannot be ruled out.

In a cross-system review, Cole et al. (1988) observed strong positive BB–Chl-*a* and BP–PP relationships, suggesting that bacterial biomass/activity is controlled by the bottom-up (i.e., substrate supply) processes. In several cross-shelf analyses, positive BP–PP relationships were found in the mid- to outer-shelf (i.e., the KC water) areas of the East China Sea (Shiah et al., 2001) and the SCS (Lai et al., 2014; Austria et al., 2018). Our results (**Figure 10**) also indicated that when the data of two different water masses were pooled together, BP also showed a positive trend with PP.

It is particularly important to note that the positive relationships of BB vs. Chl-*a* and/or BP vs. PP observed in the cross-system analyses shown above were not necessarily observed in a single water mass, even an oligotrophic one. Our BP data showed no relationship with autotrophic biomass (i.e., Chl-*a*) in the oligotrophic KC water, but their relationship changed to a positive one in mesotrophic productive water (**Table 1**). It has been suggested that heterotrophic bacteria could compete with phytoplankton for mineral nutrients such as N, P, or Fe (Currie and Kalff, 1984; Thingstad, 2000; Wambeke et al., 2008; Chen et al., 2016 and citations therein). The mineral uptake by bacteria might place bacteria and phytoplankton in competition for growth-limiting nutrients, rather than in their traditional roles as the respective "source" and "sink" for these nutrients in the plankton (Caron et al., 2000). Additionally, the study of Armengol et al. (2019) denoted the classic paradigm of a shorter food web, and more efficient energy transfer toward upper food-web levels in productive regions, but longer a microbe-dominated food web, which could be more efficient at recycling in oligotrophic regions.

These two abovementioned viewpoints highlight the possibility that bacteria could receive substrate sources from the nonalgal components and result in a noncorrelation situation between autotrophs and heterotrophs in oligotrophic KC (**Table 1**). In a sense, we deduced that the KC water is a "mature and stable" ecosystem, while that of the mixing water is a "new and unsteady" one. The abundant supplies of new nutrients (from deep-water mixing) and new substrates (from enhanced PP) might facilitate the coupling of phytoplankton and bacteria within the water column over a timescale of days (**Table 1**).

A certain amount of photosynthetic product could be excreted to the surrounding environment in the dissolved phase by phytoplankton. This process is known as exudation, and its rate is defined as dissolved primary production (DPP). The PP derived from the ^{14}C–assimilation–filtration method was an estimate of particulate PP (PPP) and did not take DPP into account. Chen et al. (2020) showed that DPP in the KC in northern Taiwan could be equivalent to that of PPP. The slope (0.39 ± 0.12) shown in **Figure 10** indicated a BP/PP ratio of ∼40% in our study, which is within the range that has been reported (Ducklow and Carlson, 1992). Additionally, the BP/PP ratio reported in this study could drop to 20% when DPP was included.

CONCLUSION

This study proposes a novel physical mechanism of water mass mixing induced by the prevailing southeast monsoon at the cape of southern Taiwan. It appears that there are at least two physical processes that might enhance the biological biomass/production in the study site: One is the eddy process and the other is the mixing process. These two physical processes might be acting additively (on the nutrients supply and biological activities) but at different time scales. The eddy process is operating daily as affected by tidal movement, and the mixing caused by the northeastward intrusion of the SCS waters is approximately at a seasonal scale. However, the relative effectiveness of these two processes in boosting biological biomass/production in the summer season cannot be differentiated at this stage. It is noted that the "new production" probably driven by the new nutrients from mixing/eddy processes in this region is particularly important since there is almost no shelf at the east coast of Taiwan. The sinking particles in the productive areas could be transported to the deep sea very quickly. This study further provides microbial evidence suggesting an uncoupling bacteria–phytoplankton relationship in the oligotrophic Kuroshio water. The heterotrophic and autotrophic planktons then become highly coupled in adjacent productive water resulted from the mixing process.

DATA AVAILABILITY STATEMENT

The raw data supporting the conclusions of this article will be made available by the authors, without undue reservation.

AUTHOR CONTRIBUTIONS

J-HT, K-YL, and H-YK: data collection and measurements. C-CL, C-RW, and F-KS: discussion in manuscript preparation and writing. F-KS: experiment design. All authors contributed to the article and approved the submitted version.

FUNDING

This study was supported by the Ministry of Sciences and Technology, Taiwan, Grant No. 107-2611-M-001-005-MY3.

ACKNOWLEDGMENTS

The cruise assistance from the crew of research vessel OR-III is highly appreciated.

REFERENCES

Armengol, L., Calbet, A., Franchy, G., Rodríguez-Santos, A., and Hernández-León, S. (2019). Planktonic food web structure and trophic transfer efficiency along a productivity gradient in the tropical and subtropical Atlantic Ocean. *Sci. Rep.* 9:2044. doi: 10.1038/s41598-019-38507-9

Austria, E. S., Lai, C. C., Ko, C. Y., Lee, K. Y., Kuo, H. Y., Chen, T. Y., et al. (2018). Growth-controlling mechanisms on heterotrophic bacteria in the South China Sea shelf: summer and winter patterns. *Terr. Atmos. Ocean Sci.* 29, 441–453. doi: 10.3319/TAO.2018.01.19.01

Azam, F. (1998). Microbial control of oceanic carbon flux: the plot thickens. *Science* 280, 694–696. doi: 10.1126/science.280.5364.694

Azam, F., and Malfatti, F. (2007). Microbial structuring of marine ecosystems. *Nat. Rev.* 5, 782–792. doi: 10.1038/nrmicro1747

Brussaard, C. P. D. (2004). Optimization of procedures for counting viruses by flow cytometry. *Appl. Environ. Microbiol.* 70, 1506–1513. doi: 10.1128/AEM.70.3.1506-1513.2004

Caron, D. A., Lim, E. L., Sanders, R. W., Dennett, M. R., and Berninger, U. (2000). Responses of bacterioplankton and phytoplankton to organic carbon and inorganic nutrient additions in contrasting oceanic ecosystems. *Aquat. Microb. Ecol.* 22, 175–184. doi: 10.3354/ame022175

Centurioni, L. R., Niiler, P. P., and Lee, D. K. (2004). Observation of inflow of Philippine Sea surface water into the South China Sea through the Luzon Strait. *J. Phys. Oceanogr.* 34, 113–121.2.0.CO;2. doi: 10.1175/1520-0485(2004)034andlt;0113:OOIOPSandgt;2.0.CO;2

Chen, T. Y., Lai, C. C., Shiah, F. K., and Gong, G. C. (2020). Dissolved and particulate primary production and subsequent bacterial C consumption in the Southern East China Sea. *Front. Mar. Sci.* 7:713. doi: 10.3389/fmars.2020.00713

Chen, T. Y., Ta, J. H., Ko, C. Y., Hsieh, C., Chen, C. C., Jiao, N., et al. (2016). Nutrient pulses driven by internal solitary waves enhance heterotrophic bacterial growth in the South China Sea. *Environ. Microbiol.* 18, 4312–4323. doi: 10.1111/1462-2920.13273

Cheng, Y. H., Chang, M. H., Ko, D. S., Jan, S., Andres, M., Kirincich, A., et al. (2020). Submesoscale eddy and frontal instabilities in the Kuroshio interacting with a Cape South of Taiwan. *J. Geophys. Res. Oceans* 125:e2020JC016123. doi: 10.1029/2020JC016123

Cho, B. C., and Azam, F. (1988). Major role of bacteria in biogeochemical fluxes in the ocean's interior. *Nature* 332, 441–443. doi: 10.1038/332441a0

Chou, W. C., Sheu, D. D., Chen, C. T. A., Wen, L. S., Yang, Y., and Wei, C. L. (2007). Transport of the South China Sea subsurface water outflow and its influence on the carbon chemistry of Kuroshio waters off southeastern Taiwan. *J. Geophys. Res.* 112:C12008, doi: 10.1029/2007JC004087

Clayton, S., Nagai, T., and Follows, M. J. (2014). Fine scale phytoplankton community structure across the Kuroshio Front. *J. Plankton Res.* 36, 1017–1030. doi: 10.1093/plankt/fbu020

Cole, J. J., Findlay, S., and Pace, M. L. (1988). Bacterial production in fresh and saltwater ecosystems: a cross-system overview. *Mar. Ecol. Prog. Ser.* 43, 1–10. doi: 10.3354/meps043001

Currie, D., and Kalff, J. (1984). The relative importance of bacterioplankton and phytoplankton in phosphorus uptake in freshwater. *Limnol. Oceanogr.* 29, 311–321. doi: 10.4319/lo.1984.29.2.0311

Ducklow, H. W., and Carlson, C. A. (1992). "Oceanic bacterial production," in *Advance in microbial ecology,* ed K. C. Marshall (NY: Plenum), 113–181.

Fuhrman, J. A., and Azam, F. (1982). Thymidine incorporation as a measurement of heterotrophic bacterioplankton production in marine surface waters: evaluation and field results. *Mar. Biol.* 66, 109–120. doi: 10.1007/BF00397184

Gaso, J. M., and Giorgio, P. A. D. (2000). Using flow cytometry for counting natural planktonic bacteria and understanding the structure of planktonic bacterial communities. *Sci. Mar.* 64, 197–224. doi: 10.3989/scimar.2000.64n2197

Hansell, D. A., Carlson, C. A., Repeta, D. J., and Schlitzer, R. (2009). Dissolved organic matter in the ocean: a controversy stimulates new insights. *Oceanography* 22, 203–211. doi: 10.5670/oceanog.2009.109

Hasegawa, T., Kitajima, S., and Kiyomoto, Y. (2019). "Phytoplankton distribution in the Kuroshio Region of the Southern East China Sea in early spring," in *Kuroshio Current: Physical, Biogeochemical, and Ecosystem Dynamics, Geophysical Monograph 243,* eds T. Nagai, H. Saito, K. Suzuki, and M. Takahashi (New York, NY: Wiley and Sons, Inc.), 191–204.

Hsin, Y. C., Qiu, B., Chiang, T. L., and Wu, C. R. (2013). Seasonal to interannual variations in the intensity and central position of the surface Kuroshio east of Taiwan. *J. Geophys. Res. Oceans* 118, 4305–4316. doi: 10.1002/jgrc.20323

Knap, A., Michaels, A., Close, A., Ducklow, H., and Dickson, A. (1996). "Protocols for the Joint Global Ocean Flux Study (JGOFS) Core Measurements", in *Intergovernmental Oceanographic Commission Manu*als and Guides: 29. JGOFS Report; 19.

Kobari, T., Honma, T., Hasegawa, D., Yoshie, N., Tsutsumi, E., Matsuno, T., et al. (2020). Phytoplankton growth and consumption by microzooplankton stimulated by turbulent nitrate flux suggest rapid trophic transfer in the oligotrophic Kuroshio. *Biogeosciences* 17, 2441–2452. doi: 10.5194/bg-17-2441-2020

Lai, C. C., Fu, Y. W., Liu, H. B., Kuo, H. Y., Wang, K. W., Lin, C. H., et al. (2014). Distinct bacterial-production–DOC–primary-production relationships and implications for biogenic C cycling in the South China Sea shelf. *Biogeosciences* 11, 147–156. doi: 10.5194/bg-11-147-2014

Liang, W. D., Tang, T. Y., Yang, Y. J., Ko, M. T., and Chuang, W. S. (2003). Upper-ocean currents around Taiwan. *Deep-Sea Res. II* 50, 1085–1105. doi: 10.1016/S0967-0645(03)00011-0

Liu, X., Furuya, K., Shiozak, T., Masuda, T., Kodama, T., Sato, M., et al. (2013). Variability in nitrogen sources for new production in the vicinity of the shelf edge of the East China Sea in summer. *Cont. Shelf Res.* 61–62, 23–30. doi: 10.1016/j.csr.2013.04.014

Lønborg, C., Carreira, C., Jickells, T., and Álvarez-Salgado4, X. A. (2020). Impacts of global change on ocean dissolved organic carbon (DOC) cycling. *Front. Mar. Sci.* 7:466. doi: 10.3389/fmars.2020.00466

Nan, F., Xue, H., and Yu, F. (2015). Kuroshio intrusion into the South China Sea. *Prog. Oceanogr.* 137, 314–333. doi: 10.1016/j.pocean.2014.05.012

Parsons, T. R., Maita, Y., and Lalli, C. M. (1984). *A Manual of Chemical and Biological Methods for Seawater Analysis.* New York, NY: Pergamon.

Sheu, D. D., Chou, W. C., Chen, C. T. A., Wei, C. L., Hsieh, H. L., Hou, W. P., et al. (2009). Riding over the Kuroshio from the South to the East China Sea: mixing and transport of DIC. *Geophys. Res. Lett.* 36:L07603. doi: 10.1029/2008GL037017

Shiah, F. K. (1999). Diel cycles of heterotrophic bacterioplankton abundance and production in the ocean surface waters. *Aquat. Microb. Ecol.* 17, 239–246. doi: 10.3354/ame017239

Shiah, F. K., Chen, T. Y., Gong, G. C., Chen, C. C., Chiang, K. P., and Hung, J. J. (2001). Differential coupling of bacterial and primary production in mesotrophic and oligotrophic systems of the East China Sea. *Aquat. Microb. Ecol.* 23, 273–282. doi: 10.3354/ame023273

Shiah, F. K., Liu, K. K., Kao, S. J., and Gong, G. C. (2000). The coupling of bacterial production and hydrography in the southern East China Sea: spatial patterns in spring and fall. *Continent. Shelf Res.* 20, 459–477. doi: 10.1016/S0278-4343(99)00081-3

Sigman, D. M., and Haug, G. H. (2006). "The biological pump in the past," in *Treatise on Geochemistry,* eds H. Elderfield, H. D. Holland, and K. K. Turekian (Amsterdam: Elsevier), 625.

Tai, J. H., Tang, T. Y., and Gawarkiewicz, G. (2010). Instability of the Kuroshio in Luzon Strait: effects of ridge topography and stratification. *J. Oceanogr.* 66, 523–538. doi: 10.1007/s10872-010-0044-6

Thingstad, T. F. (2000). Elements of a theory for the mechanisms controlling abundance, diversity, and biogeochemical role of lytic bacterial viruses in aquatic systems. *Limnol. Oceanogr.* 45, 1320–1328. doi: 10.4319/lo.2000.45.6.1320

Tseng, Y. F., F. J., Lin, Chiang, K. P., Kao, S. J., and Shiah, F. K. (2005). Potential impacts of N2-fixing *Trichodesmium* on heterotrophic bacterioplankton turnover rates and organic carbon transfer efficiency in the subtropical oligotrophic ocean system. *Terrest. Atmos. Ocean. Sci.* 16, 361–376. doi: 10.3319/TAO.2005.16.2.361(Oc)

Tsutsumi, E., Matsuno, T., Itoh, S., Zhang, J., Senjyu, T., Sakai, A., et al. (2020). Vertical fluxes of nutrients enhanced by strong turbulence and phytoplankton bloom around the ocean ridge in the Luzon Strait. *Sci. Rep.* 10:17879. doi: 10.1038/s41598-020-74938-5

Wambeke, F. V., Bonnet, S., Moutin, T., Raimbault, P., Alarcoń, G., and Guieu, C. (2008). Factors limiting heterotrophic bacterial production in the southern Pacific Ocean. *Biogeosciences* 5, 833–845. doi: 10.5194/bg-5-833-2008

Wu, C. R., Wang, Y. L., Lin, Y. F., and Chao, S. Y. (2017). Intrusion of the Kuroshio into the South and East China Seas. *Sci. Rep.* 7:7895. doi: 10.1038/s41598-017-08206-4

Xue, H., Chai, F., Pettigrew, N., Xu, D., Shi, M., and Xu, J. (2004). Kuroshio intrusion and the circulation in the South China Sea. *J. Geophys. Res. Oceans* 109:C02017. doi: 10.1029/2002JC001724

Conflict of Interest: The authors declare that the research was conducted in the absence of any commercial or financial relationships that could be construed as a potential conflict of interest.

Publisher's Note: All claims expressed in this article are solely those of the authors and do not necessarily represent those of their affiliated organizations, or those of the publisher, the editors and the reviewers. Any product that may be evaluated in this article, or claim that may be made by its manufacturer, is not guaranteed or endorsed by the publisher.

frontiers in Marine Science

ORIGINAL RESEARCH
published: 19 August 2021
doi: 10.3389/fmars.2021.717576

The Wind Effect on Biogeochemistry in Eddy Cores in the Northern South China Sea

*Chun Hoe Chow[1], Yung-Yen Shih[2], Ya-Tang Chien[1,3], Jing Yi Chen[4], Ning Fan[2], Wei-Chang Wu[1,5] and Chin-Chang Hung[4]**

[1] Department of Marine Environmental Informatics, National Taiwan Ocean University, Keelung, Taiwan, [2] Department of Applied Science, Republic of China Naval Academy, Kaohsiung, Taiwan, [3] Research Center for Environmental Changes, Academia Sinica, Taipei, Taiwan, [4] Department of Oceanography, National Sun Yat-sen University, Kaohsiung, Taiwan, [5] Institute of Oceanography, National Taiwan University, Taipei, Taiwan

Cyclonic and anticyclonic eddies are usually characterized by upwelling and downwelling, respectively, which are induced by eddy pumping near their core. Using a repeated expendable bathythermograph transect (XBT) and Argo floats, and by cruise experiments, we determined that not all eddies in the northern South China Sea (NSCS) were accompanied by eddy pumping. The weakening of background thermocline was attributed to the strengthening of eddy pumping, affected by (1) wind-induced meridional Sverdrup transports and (2) Kuroshio intrusion into the NSCS. Higher particulate organic carbon (POC) fluxes (> 100 mg-C m^{-2} day^{-1}) were found near the eddy cores with significant eddy pumping (defined by a depth change of 22°C isotherm near the thermocline for over 10 m), although the satellite-estimated POC fluxes were inconsistent with the *in-situ* POC fluxes. nitrogen limitation transition and high POC flux were even found near the core of a smaller mesoscale (diameter < 100 km) cyclonic eddy in May 2014, during the weakening of the background thermocline in the NSCS. This finding provides evidence that small mesoscale eddies can efficiently provide nutrients to the subsurface, and that they can remove carbon from the euphotic zone. This is important for global warming, which generally strengthens upper ocean stratification.

Keywords: eddy pumping, ocean stratification, nutrients, carbon flux, carbon removal, Sverdrup transport, northern South China Sea

OPEN ACCESS

Edited by:
Angel Borja,
Technological Center Expert in Marine and Food Innovation (AZTI), Spain

Reviewed by:
Peter Strutton,
University of Tasmania, Australia
Wenxia Zhang,
East China Normal University, China

***Correspondence:**
Chin-Chang Hung
cchung@mail.nsysu.edu.tw

Specialty section:
This article was submitted to Marine Ecosystem Ecology, a section of the journal Frontiers in Marine Science

Received: *31 May 2021*
Accepted: *19 July 2021*
Published: *19 August 2021*

Citation:
Chow CH, Shih Y-Y, Chien Y-T, Chen JY, Fan N, Wu W-C and Hung C-C (2021) The Wind Effect on Biogeochemistry in Eddy Cores in the Northern South China Sea. Front. Mar. Sci. 8:717576. doi: 10.3389/fmars.2021.717576

INTRODUCTION

The Southeast Asia monsoon largely determines the ocean circulation in the South China Sea (SCS), the largest semi-closed marginal sea in the northwest Pacific. During the northeast (NE) monsoon, ocean circulation is mainly occupied by a basin-wide cyclonic gyre in the upper layer of the SCS (Su, 2004), with Kuroshio intrusion through the Luzon Strait (Hu et al., 2000; Nan et al., 2015). In general, the Kuroshio intrudes warmer and saltier water from the Pacific into the northern SCS (NSCS). During the southwest (SW) monsoon, ocean circulation is characterized by two basin-wide gyres in the upper layer of the SCS: one is cyclonic in the NSCS, and the other is anticyclonic in the southern South China Sea (SSCS) (Su, 2004).

According to *in situ* and satellite observations, the seawater in the region of the SCS basin is strongly stratified and oligotrophic, with a low chlorophyll-a (Chl) concentration (< 0.1 mg/m^3)

near the surface (Liu et al., 2002; Chen, 2005; Chen et al., 2006; Shen et al., 2008; Zhang et al., 2016). Phytoplankton growth near the surface is limited because of nearly undetectable nitrogen concentration, corresponding to the deep nitracline (Liu et al., 2002; Chen et al., 2004, 2006; Zhang et al., 2016). However, in the region of the basin, during the NE monsoon, surface Chl concentration can reach as high as 0.3 mg/m^3 (Liu et al., 2002; Shen et al., 2008). This is because the shallower nitracline causes an increase in nitrate-based new production (Chen, 2005). Physical factors that support phytoplankton growth in marginal seas include monsoons (Liu et al., 2002), dust deposition (Wu et al., 2003; Hung et al., 2009), typhoons (Siswanto et al., 2007, 2008; Hung et al., 2010b; Chen et al., 2013; Shih et al., 2013, 2020), ocean eddies (Chen et al., 2007, 2015; Shih et al., 2015), and internal waves (Li et al., 2018a; Tai et al., 2020). These provide nutrient supplies in the sunlit layer *via* surface fluxes, horizontal advection, vertical upwelling, and vertical mixing.

The South China Sea is full of ocean mesoscale eddies (Hwang and Chen, 2000; Wang et al., 2003; Chow et al., 2008; Xiu et al., 2010; Du et al., 2016; Chu et al., 2020), which have a mean radius of ∼132 km and a lifetime of ∼8.8 weeks (Chen et al., 2011). Ocean cooling and warming can form near the core of cyclonic eddies (CEs) and anticyclonic eddies (AEs), respectively, induced by eddy pumping (Soong et al., 1995; Li et al., 1998; Chow et al., 2008; Xiu and Chai, 2011). However, eddy-induced cooling and warming were not found universally in mesoscale eddies near the ocean surface. Liu et al. (2020) found that only ∼60% of AEs and CEs corresponded to the positive and negative anomalies of sea surface temperature (SST), respectively, based on satellite observation of the SCS. Namely, ∼40% of eddies had warm-core CEs and cold-core AEs, reversed to a generally known situation that CEs and AEs are usually characterized by cold and warm cores, respectively. Indeed, warm-core CEs and cold-core AEs have been detected in the Pacific and the Atlantic using a satellite and by *in-situ* observation (Flagg et al., 1998; Itoh and Yasuda, 2010; Shih et al., 2015; Sun et al., 2019). Huang and Xu (2018) suggested that when studying eddy-related biogeochemistry by satellite observation, the upper-ocean vertical structure should be carefully considered. Subsurface Chl variability cannot be fully detected from the surface *via* satellite measurements in mesoscale eddies.

Cold-core cyclonic eddies and warm-core anticyclonic eddies can contribute to local biogeochemical budgets *via* strong vertical upwelling (Chen et al., 2007) and deep vertical mixing (Chen et al., 2015), respectively. The mechanisms of global eddy-induced Chl variation can be classified into several types (Siegel et al., 2011; McGillicuddy, 2016): (1) eddy pumping (a general type), (2) eddy-wind interaction (eddy-Ekman pumping), (3) eddy stirring/advection (Chelton et al., 2011a; Chow et al., 2017), (4) strain-induced submesoscale upwelling along eddy peripheries (McGillicuddy, 2016; Chow et al., 2019; Zhang et al., 2019), (5) eddy trapping (McGillicuddy, 2016), and (6) eddy-induced mixed-layer deepening (Gaube et al., 2014; McGillicuddy, 2016). Moreover, high fluxes of particulate organic carbon (POC), ranging from 83 to 194 mg-C m^{-2}day^{-1}, were observed around the eddies in the western North Pacific (Shih et al., 2015). In the SCS, eddy currents were found to be controlling the particle movement within eddies. With a sinking rate of below 80 m day^{-1}, particles can be transported from the eddy edge to the eddy core (Ma et al., 2021).

In this study, we observed the ocean vertical structure in several mesoscale eddies by analyzing the ocean profiles obtained *via* expendable bathythermographs (XBTs), Argo floats, and cruise measurements. We found that not all eddies were accompanied by eddy pumping. What was the condition required for significant eddy pumping near the core of eddies in the NSCS? What was the biogeochemical response to eddies with and without eddy pumping? To answer these scientific questions, we studied the variability in the ocean vertical structure, nutrients, and POC flux corresponding to eddies in the NSCS, where the temperature-salinity (TS) properties of seawater are largely affected by ocean currents from its boundary, such as the Kuroshio intrusion. We defined the significant eddy pumping in the Data and Methods section. Then, we showed the significant eddy pumping that is related to the weakening of ocean stratification, combined with the results of nutrient dynamics, POC flux, and wind-related mechanisms. Last, we showed that the Kuroshio intrusion may depress the eddy pumping.

DATA AND METHODS

Ocean Profile Data

To observe the vertical motion near the eddy cores, we used the temperature-profile data, provided by the Coriolis Operational Oceanography, of expendable bathythermographs (XBTs) along the PX44 transect (shown by the black dots in **Figure 1**) that repeatedly passed through the northern South China Sea (NSCS) from 2000 to 2010 (43 transects of PX44). In addition, we applied the available hydrographic data of Argo floats from 2005 to 2017 that were collected and made available by the Coriolis Operational Oceanography. There were a total of 109 Argo floats found. We only used those flagged as good-quality Argo data of temperature, salinity, and pressure from eddy cores in the basin of the NSCS, where the ocean bottom is over 1,000 m. The Argo data selected in this study had a time resolution ranging from 3 to 4 days.

To study the background temperature and salinity fields, assuming there were no eddy effects, we used the dataset from synoptic monthly gridded three-dimensional World Ocean Database version 2013 (WOD13) (Chu and Fan, 2017) and World Ocean Atlas version 2013 (WOA13), at 1° resolution, provided by the National Oceanic and Atmospheric Administration (NOAA). The monthly dataset of the former was available from 1945 to 2014. The anomalies of ocean profiles analyzed in this study were defined by referring to deviations from climatological means, which were obtained from WOA13. The WOA dataset included the 1°-gridded climatological profiles of temperature, salinity, and nutrients, which were linearly interpolated to the locations of the Argo floats and the stations of cruise measurements. Note that the results obtained in this study show no significant difference when the dataset of World Ocean Atlas version 2018 (WOA18) was used.

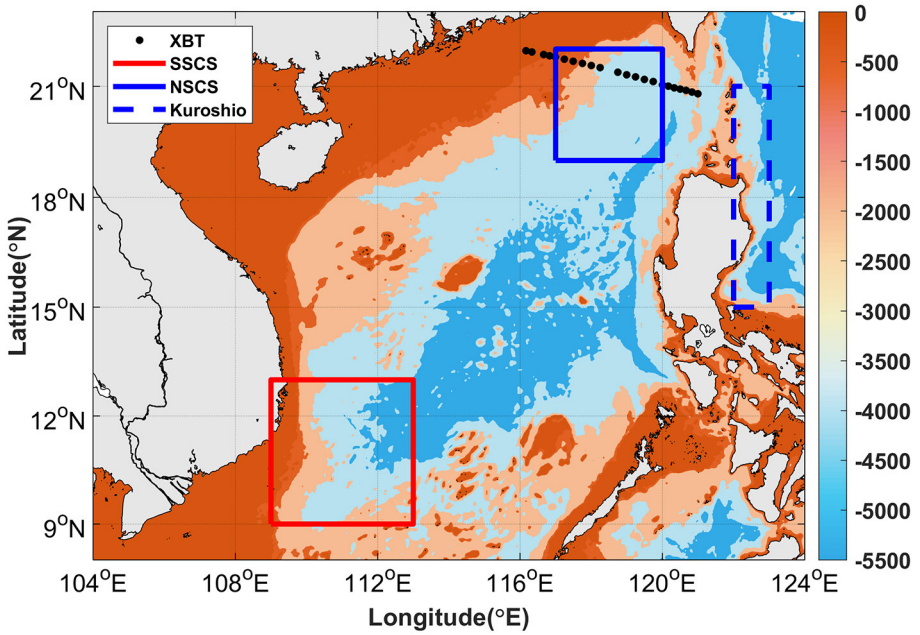

FIGURE 1 | Bathymetry in the South China Sea (SCS). The black dots show the PX44 transect, which is the repeated hydrographic surveys of expendable bathythermographs (XBTs). The solid blue, dashed blue, and solid red rectangles show the region of northern South China Sea (NSCS), Kuroshio, and southern South China Sea (SSCS) used to show the long-term temperature-salinity (TS) properties of seawater.

Eddy Detection

To detect the ocean eddies, we used the daily satellite-altimetry data of sea-level anomalies (SLAs) at 1/4° resolution obtained from the Copernicus Marine Environment Monitoring Service (CMEMS), available since the end of 1992. We derived the geostrophic velocity anomalies (u′, v′) from the zonal and meridional gradients of the daily SLAs (Hwang and Chen, 2000). Then, we calculated the Okubo–Weiss (OW) parameter (Okubo, 1970; Weiss, 1991; Faghmous et al., 2015) from the derived geostrophic velocity anomalies (u', v') using

$$OW = {S_{sh}}^2 + {S_{st}}^2 - {\xi}^2 \ldots \quad (1)$$

where S_{sh} is the shear deformation rate estimated as $\partial v'/\partial x + \partial u'/\partial y$, S_{st} is the stretch deformation rate estimated as $\partial u'/\partial x - \partial v'/\partial y$, and ξ is the current vorticity estimated as $\partial v'/\partial x - \partial u'/\partial y$.

The general flow in eddies is characterized by rotation, namely, a large magnitude of vorticity, around a background circulation (such as the SCS circulation or the Kuroshio intrusion) with flow dominated by the shear and stretch deformations. The OW parameter compares the deformation-dominated circulation ($OW > 0$) with the rotation-dominated eddies ($OW < 0$). Thus, in this study, we identified the ocean eddies according to the negative OW parameter at the local maxima and minima of two-dimensional SLAs, which could also be induced by background circulation (Chow et al., 2015) or planetary Rossby waves (Chelton et al., 2011b).

To study the eddy vertical structure obtained from the ocean profiles of the Argo floats and XBTs, the daily gridded values of SLAs and OW parameter were linearly interpolated onto the profile locations that passed through the eddy cores. If the profile locations were in the closed SLA contours with a negative OW parameter near the eddy cores (Ma et al., 2021), then we assumed that the ocean profiles were in the region of eddy cores, which were defined by the local maxima and minima of two-dimensional SLAs for the AEs and CEs, respectively (Faghmous et al., 2015). We used the MATLAB program for eddy detection written by Faghmous et al. (2015) to detect eddy cores. If the distance between the profile location and the eddy core was shorter than the length of the eddy minor axis, which was an eddy parameter provided by eddy detection codes (Faghmous et al., 2015), an ocean profile was confirmed to pass through an eddy core. We studied the eddy vertical structure observed with at least three ocean profiles, which were measured by an Argo float or along an XBT transect.

In this study, we included new-born/short-lived eddies that could be traced back for at least 10 days and were confirmed with the negative OW parameter (**Supplementary Figures S1, S2**). Globally, ∼55% of eddies were short lived (<30 days) ones (Chen and Han, 2019), highlighting the considerable effects of short-lived eddies on the variability in marine environments. However, we excluded the eddies with a lifetime shorter than 10 days because of the higher uncertainty of eddy detection using satellite altimeters (Faghmous et al., 2015). Note that the misclassification rate for eddies with a 10-day-lifetime can reach up to 7% of global satellite-detected eddies. Overall, we analyzed the ocean profiles

of six repeated-XBT transects (14% of 43 transects) and 10 Argo floats (9% of 109 Argo floats) that passed through the eddy cores (**Supplementary Figures S1, S2**) based on the above criteria.

Additionally, we used the satellite dataset of Chl concentration, SST, and surface wind. The Chl data were the daily interpolated cloud-free glob-color product, at a spatial resolution of 4 km, provided by the CMEMS. The SST and wind data were the daily product of microwave optimally interpolated (OI) SST and cross-calibrated multi-platform (CCMP) gridded surface vector winds, at a spatial resolution of 0.25°, provided by Remote Sensing Systems (RSS).

Eddy Pumping and Ocean Vertical Structure

To confirm eddy pumping near the eddy cores, we studied the profiles of XBTs and Argo floats that passed through the eddy cores, detected with the satellite altimeters. We defined the significant upwelling and downwelling of eddies according to the 22°C *in situ* isothermal depth (hereafter, D22) that varies at least 10 m upward and downward, respectively, from the depth of a climatological 22°C isotherm. The significant upwelling and downwelling were confirmed by two to four ocean profiles with a 10-m departure of D22 from the climatology.

Based on the repeated XBT transects, we found two anticyclonic eddies (AEs) and four cyclonic eddies (CEs) (AE1, AE4, and CE8 to CE11 in **Supplementary Table S1**). For Argo observation, we identified four AEs and six CEs. **Supplementary Table S1** includes the dates of when the ocean profiles were closest to the eddy cores and the World Meteorological Organization (WMO) numbers of the Argo floats and XBT transects. The Argo floats are identified by their WMO numbers, hereafter. Interestingly, Argo 2900825 passed through the same anticyclonic eddy (AE1) observed along the XBT-WDD6033 transect in September 2008. Moreover, Argo 2901123 and Argo 2901382 co-observed the vertical profile of AE2 in December 2010. Argo 5902165 passed through the same CE5 observed during a cruise experiment in May 2014 (**Supplementary Figure S3B**). Two cruises were conducted onboard the R/V *Ocean Researcher V* (OR-V 0038) and R/V *Ocean Researcher III* (OR-III 1679) from 20th to 28th May 2014 and 14th to 17th April 2013, respectively

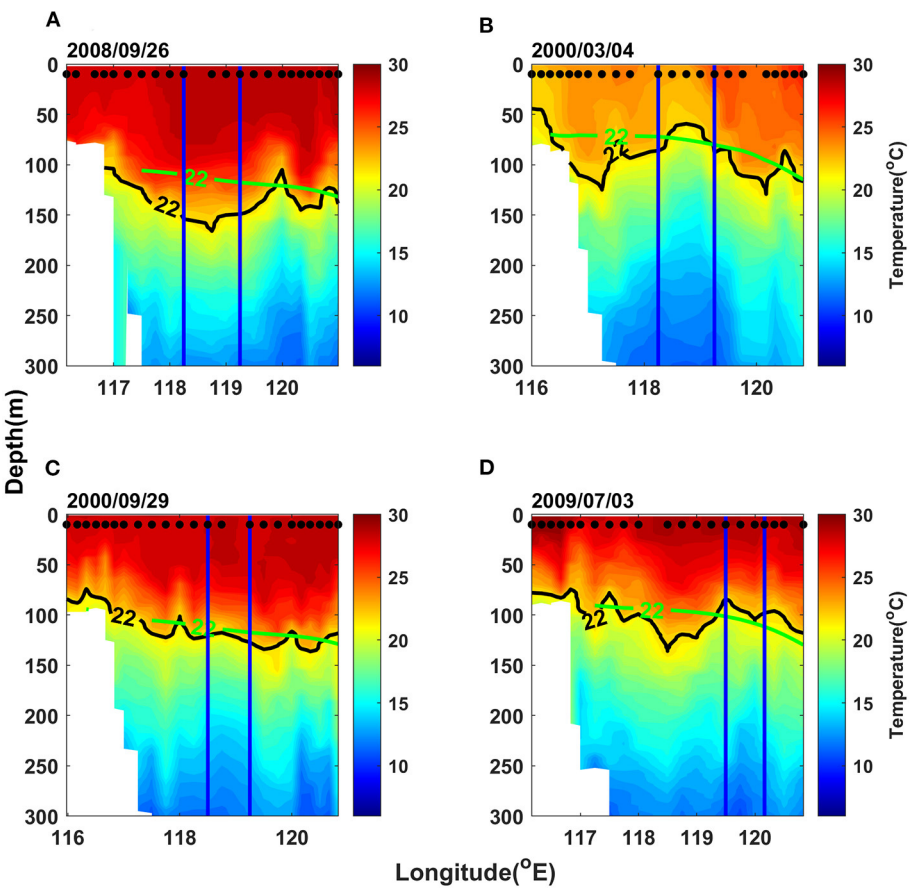

FIGURE 2 | The temperature profiles along the PX44 section on **(A)** September 26, 2008 (AE1), **(B)** March 4, 2000 (CE8), **(C)** September 29, 2000 (AE4), and **(D)** July 3, 2009 (CE10). The two blue vertical lines in each sub-figure show the region within an eddy confirmed with satellite altimeters. The green curves show the climatological temperature contours at 22°C. The dots near the surface show the locations of expendable bathythermographs (XBTs). The left (right) panel is for the cases of anticyclonic (cyclonic) eddies, while the upper (lower) panel is for the cases with (without) significant eddy pumping.

(Shih et al., 2020). The former cruise (OR-V 0038) was along 116.2°E within 19°N and 18°N, observing CE5 with significant upwelling. While the latter cruise (OR-III 1679) was along 120.33°E within 22°N and 20°N, observing CE6 but without significant upwelling. Information on all eddy cases with and without significant eddy pumping is given in **Supplementary Table S1**.

We compared the biogeochemistry obtained between the two cruises. Water samples were collected together with CTD casts at Stations S1 and S2 for OR-III 1679, and Stations S3 and S4 for OR-V 0038 (**Supplementary Figures S3A,B**). To measure the concentration of nitrate + nitrite (N), phosphorus (P), and Chl from the water samples, we used the methods described in Shih et al. (2020). We also used the TS data provided by the ocean data bank (ODB) of Taiwan and from Argo 2901180, to study the TS properties of seawater near the XBT transects, which did not measure ocean salinity.

To observe ocean vertical structure in the time and space domain, we combined the ocean profiles obtained from the Argo floats, XBTs, and CTD casts near and around the eddy cores by calculating the squared buoyancy frequencies (N^2) using (Gill, 1982).

$$N^2 = -\frac{g}{\rho_0}\frac{\partial \rho}{\partial z} \ldots \tag{2}$$

where ρ is the ocean potential density, z is the depth (positive upward), ρ_0 is the mean ocean potential density between each depth, and g is gravity acceleration (=9.8 m/s^2). To study the background ocean stratification, the average of squared buoyancy

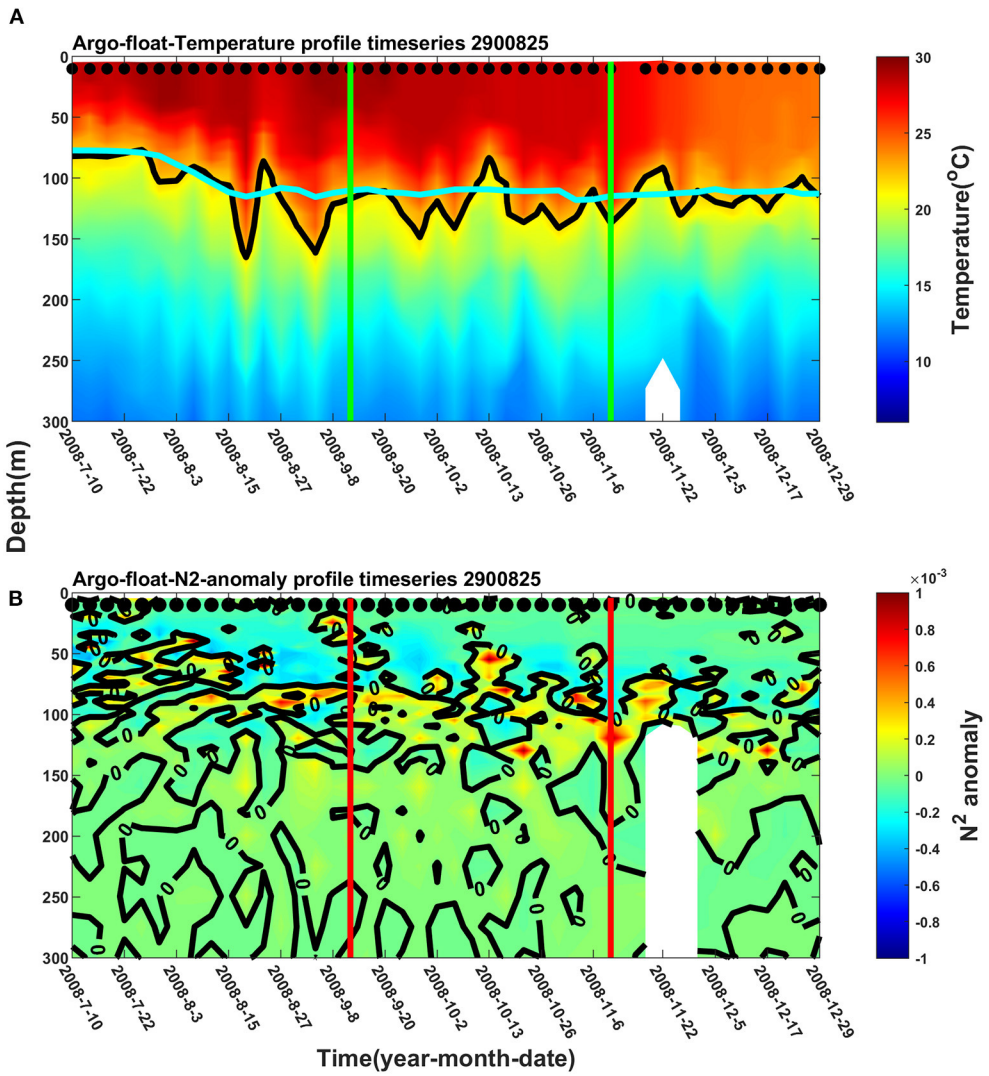

FIGURE 3 | Profiles of **(A)** temperature and **(B)** N^2 anomalies obtained from Argo 2900825 from July 10 to December 29, 2008. The two vertical lines in each subfigure show the region of anticyclonic eddy confirmed with satellite altimeters. The dots near the surface show the observed times of the Argo float.

frequencies was calculated from the mixed-layer depth at ∼50 m to the thermocline bottom at ∼162 m (Peng et al., 2018).

Since expendable bathythermograph transects do not measure salinity, we reconstructed the salinity profiles at the stations of XBTs using the method of Vignudelli et al. (2003). We interpolated the TS profiles of WOD13 into the grids of XBT temperature data. Then, the WOD13 salinity in which the corresponding WOD13 temperature is closest to the XBT temperature was taken as salinity at the grids of the XBT temperature. We tested the salinity-reconstructed method using the temperature profile of Argo 2900825 near the core of AE1, comparing it with the salinity observed by the Argo float itself. For the salinity profile near the eddy core on September 28, 2008, the correlation coefficient between the reconstructed and observed salinity was ∼0.98, with a root-mean-squared error of ∼0.09 psu, showing acceptable performance of the salinity reconstruction method.

To study the effect of wind on oceanic variability, we further calculated the meridional Sverdrup transport (M_y), based on the CCMP wind product, using

$$M_y = \frac{curl_z\vec{\tau}}{\beta} = \frac{R}{2\Omega\cos\varphi}\left(\frac{\partial\overline{\tau_y}}{\partial x} - \frac{\partial\overline{\tau_x}}{\partial y}\right)\ldots \quad (3)$$

In Equation (3), β is the change rate of coriolis force (f) due to latitude ($\partial f/\partial y$), R is the earth radius (= 6371 km), Ω is earth rotation angular speed (= 7.29×10^{-5} s^{-1}), φ is the latitude, and $curl_z\vec{\tau}$ is the curl of the wind-stress vector $\vec{\tau}(\overline{\tau_x}, \overline{\tau_y})$. In this study, $(\overline{\tau_x}, \overline{\tau_y})$ was calculated using

$$\bar{\tau}_x = \rho_a \times C_d \times spd_w \times u_w \ldots \quad (4)$$

$$\bar{\tau}_y = \rho_a \times C_d \times spd_w \times v_w \ldots \quad (5)$$

$$C_d = \frac{\mathbf{2.7}}{spd_w} + \mathbf{0.142} + \mathbf{0.0764} \times spd_w \ldots \quad (6)$$

where the air density ρ_a = 1.2 kg/m^3, spd_w is the wind speed, and C_d is the drag coefficient, which was computed by following, Large and Pond (1982).

Measurement of POC Fluxes Near Eddy Cores

The particulate organic carbon fluxes were obtained near the eddy cores by *in situ* observation and satellite estimation. For

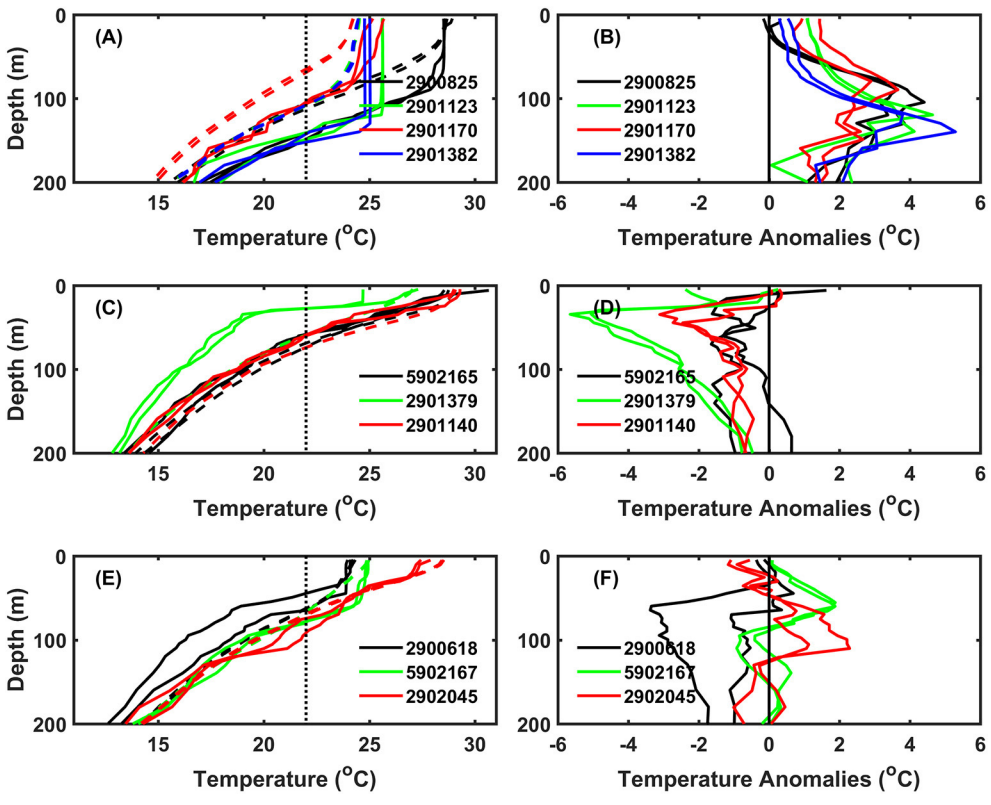

FIGURE 4 | Profiles of temperature (left) and temperature anomalies (right) observed *via* Argo floats near the eddy cores for the cases of **(A,B)** anticyclonic eddies with significant downwelling, **(C,D)** cyclonic eddies with significant upwelling, and **(E,F)** cyclonic eddies without significant upwelling. The dashed curves in the left panel show the climatological temperature profiles corresponding to the Argo profiles in the same month. The vertical dotted line in the left panel shows the temperature at 22°C.

in situ observation, we used buoy-tethered drifting sediment traps at ∼150 m to collect sinking particles at cyclonic eddies in 2013 and 2014. The detailed method of buoy-tethered drifting traps can be found in Shih et al. (2019). Next, we followed the procedure of a POC analysis described by Shih et al. (2020) to determine the POC fluxes (Hung et al., 2010a) after collection from the traps. For satellite-derived POC flux estimation, we used the method given by Dunne et al. (2005):

$$F_{POC} = NPP \times \left[-0.0101^{\circ}C^{-1} \times SST + 0.0582 \times \ln\left(\frac{NPP}{Z_{eu}}\right) + .419 \right] \quad ..(7)$$

where Z_{eu} is euphotic depth, and *NPP* is net primary production, which can be obtained *via* the satellite-derived vertically generalized production model (VGPM) first described by Behrenfeld and Falkowski (1997). Note that the VGRM assumed a homogeneous vertical distribution of Chl in the euphotic zone (Behrenfeld and Falkowski, 1997).

RESULTS

Significant and Insignificant Eddy Pumping

This section represents the significant and insignificant eddy pumping observed *via* XBTs, Argo floats, and cruises,

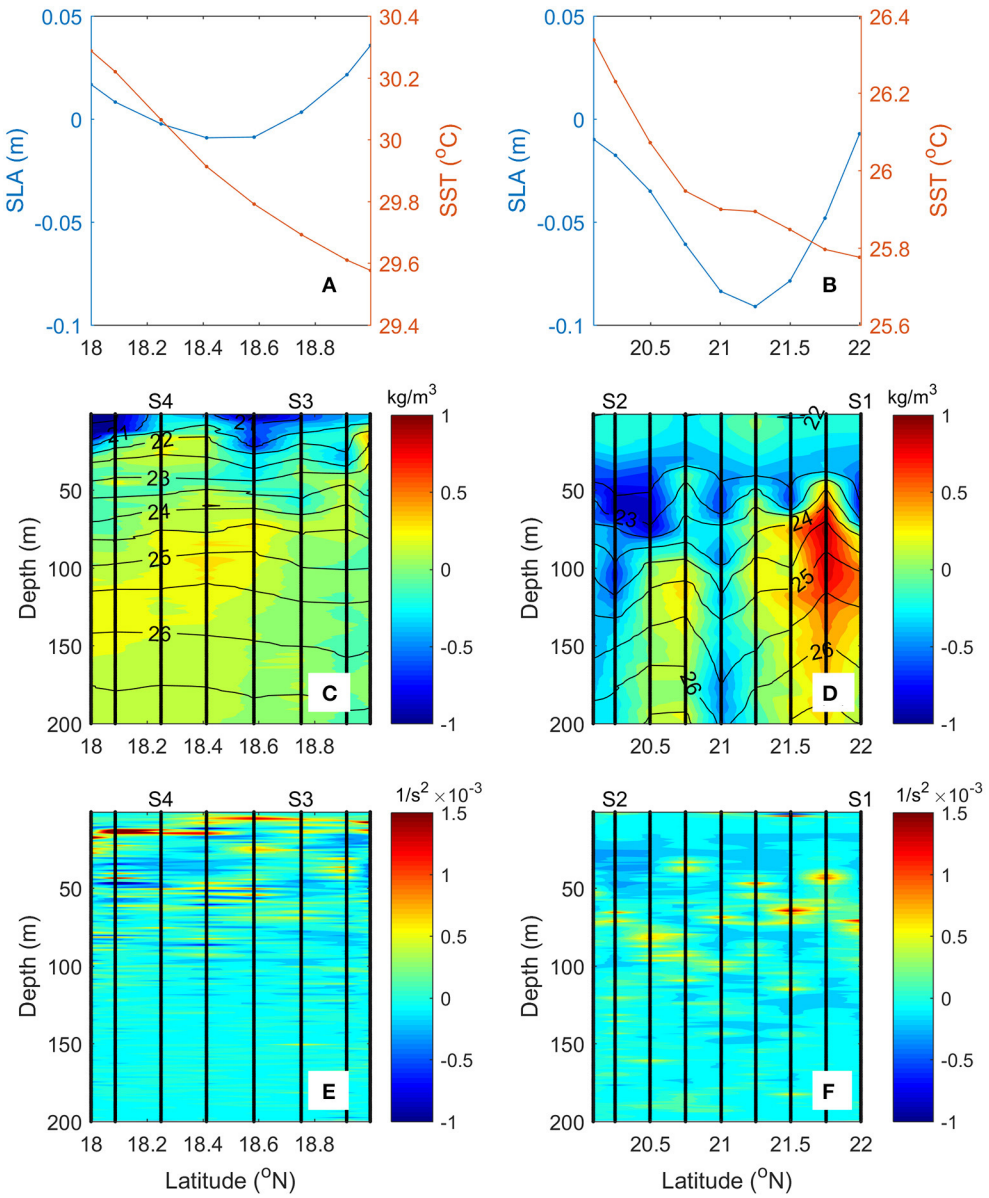

FIGURE 5 | (A,B) Sea-level anomaly (SLA), sea surface temperature (SST), **(C,D)** density anomalies, and **(E,F)** N^2 anomalies observed along 116.17°E within 18°N and 19°N from May 20 to 28, 2014 (left) and along 120.33°E within 22°N and 22°N from April 14 to 17, 2013 (right). The stations, with water sample collection, are noted by "S1," "S2," "S3," and "S4." Contours in **(C)** and **(D)** show the density profiles.

sequentially. **Figure 2** shows the temperature profiles obtained *via* the XBT transect passing through the AEs in September of 2000 (AE4) and 2008 (AE1), and the CEs in April 2000 (CE8) and July 2009 (C10). As shown in **Figure 2A**, the downwelling is significant with the increase in D22 reaching 50 m (from 100 to 150 m) near the core of AE1. However, as shown in **Figure 2C**, no significant downwelling is observed near the core of AE4, according to the small changes in D22 ($<$ 10 m), which are insignificant. For the satellite-detected CEs, **Figure 2B** shows the significant upwelling in CE8 according to D22 shallowing to 50 m. The outcropping of the isotherm can be seen near the surface in the eddy core, confirming the occurrence of upwelling. However, no significant upwelling can be found in the other three CE cases (CE9, CE10, and CE11) along the XBT transect (only CE10 is shown in **Figure 2D**, similar results were obtained for CE9 and CE11).

Based on Argo observation, **Figure 3** shows the temporal variation of ocean profiles in the AE1 observed along the XBT transect in September 2008. The significant downwelling can be seen from the Argo-obtained temperature profiles, represented by the increase in D22 reaching 50 m (from 100 to 150 m) from September 20 to November 6, 2008, when observing the AE1 profiles (**Figure 3A**). Note that D22 is shallower than the climatological field from one of the profiles on October 13, 2008 (**Figure 3A**), likely because of a different natural phenomenon with a shorter time scale, such as internal waves. **Figure 3B** also shows the relative variation in ocean stratification represented by N^2 anomalies. The negative N^2 anomalies can be found above

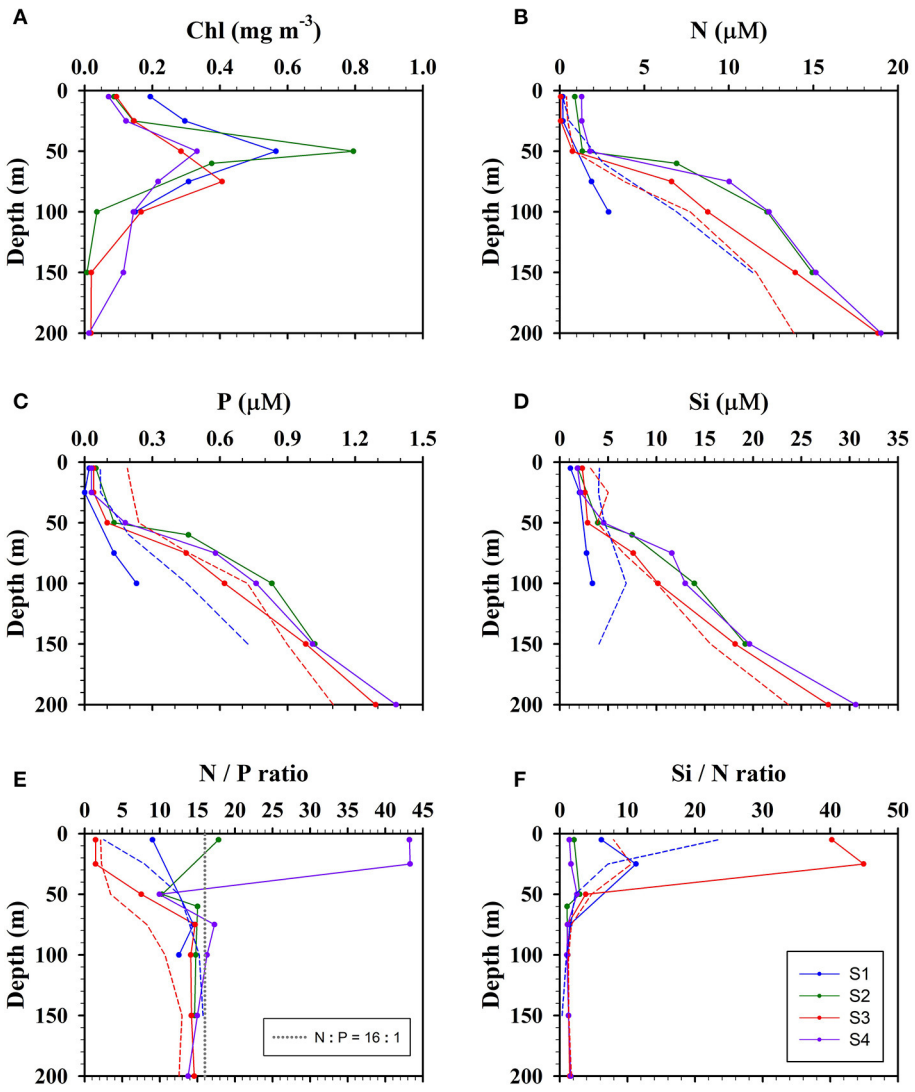

FIGURE 6 | The concentration profiles of **(A)** chlorophyll-a (Chl), **(B)** nitrate + nitrite (N), **(C)** phosphate (P), **(D)** silicate (Si), **(E)** N:P ratio and **(F)** Si:N ratio, observed at Stations S1 (blue) and S2 (green) from April 14 to 17, 2013 and at Stations S3 (red) and S4 (purple) from May 20 to 28, 2014. Blue and red dashed curves show the relative climatological profiles for April and May, respectively, obtained from WOA13.

100 m (**Figure 3B**), showing a weaker stratification in the upper ocean. More studies exploring the weaker ocean stratification are given in Upper ocean stratification in the eddy cores Section.

For all the Argo-observed ocean profiles corresponding to significant and insignificant eddy pumping, **Figure 4** displays the temperature and temperature anomaly profiles near the

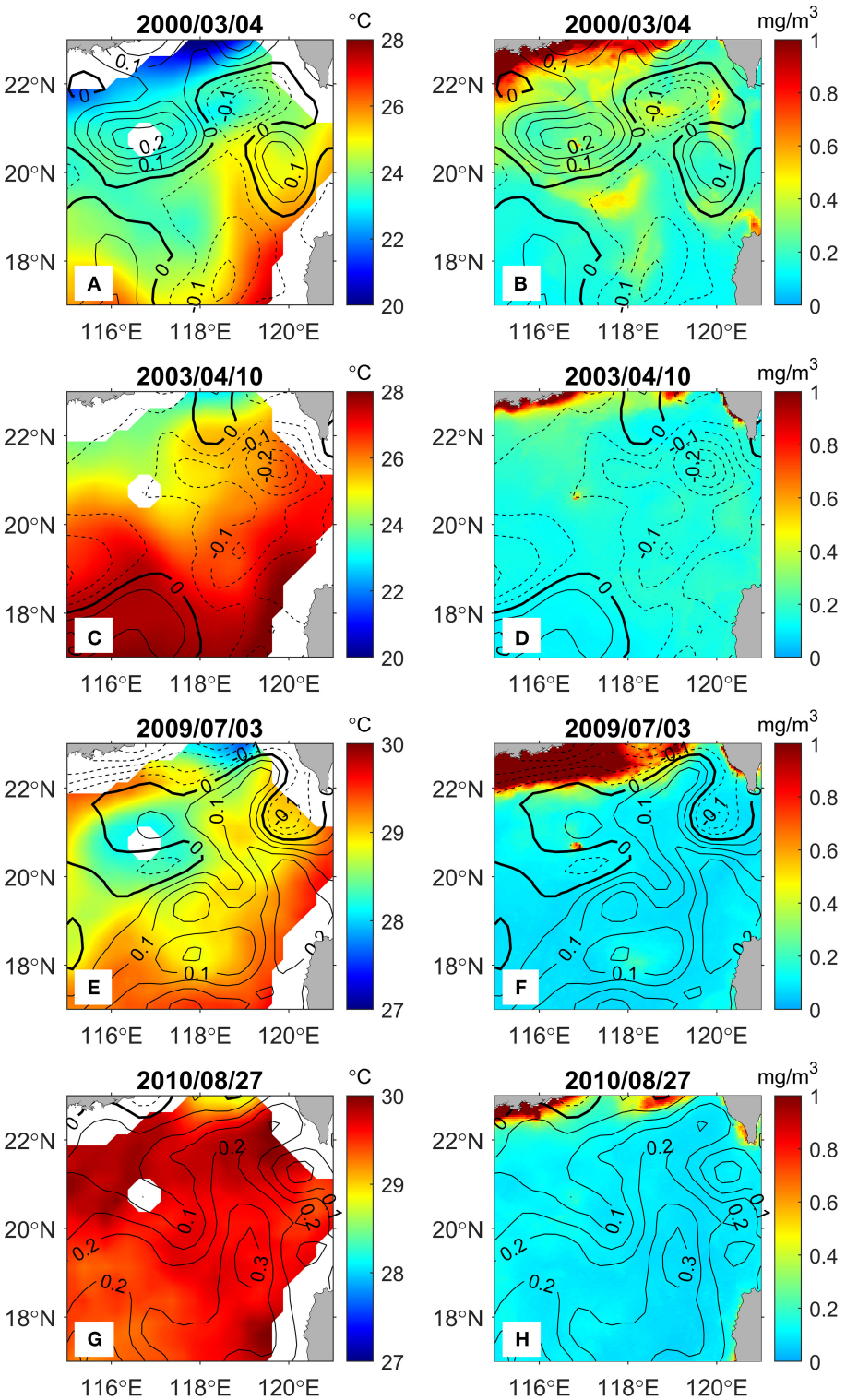

FIGURE 7 | (Left) Spatial distribution of SST on March 4, 2000, April 10, 2003, July 3, 2009, and August 27, 2010. (Right) Same as the left-panel subfigures but are for the chlorophyll-a (Chl) distribution.

eddy cores obtained with the 10 Argo floats used in this study (**Supplementary Table S1**). **Figures 4A,C** show the significant downwelling and upwelling, respectively, with a change in D22 over 10 m confirmed by two vertical profiles observed with each Argo float. In **Figures 4B,D**, the magnitude of temperature anomalies can reach as high as 4°C near the thermocline, showing a deeper and shallower depth of local maximum changes in temperature for the downwelling and upwelling, respectively. Similar results were obtained by Sun et al. (2018) who showed that the local maximum changes in density could be found within 50 and 110 m. For the cases with insignificant eddy upwelling, **Figure 4E** shows that D22 is similar to that of the climatological field, even with warming at some depths of observed CEs *via* Argo 2902045 and Argo 5902167 (**Figure 4F**). For the case observed *via* Argo 2900618, since there was only one profile that observed the changes in D22 over 10 m, it was not considered as significant eddy upwelling to avoid confusion with other natural phenomena.

For the cruise experiments, **Figure 5** shows the significant and insignificant upwelling in CE5 and CE6, respectively, which are characterized by the trough of sea-level anomalies (SLAs) along the cruise section (**Figures 5A,B**; **Supplementary Figures S3A,B**). Note that CE5 is a smaller eddy compared with the others in this study. However, in CE5, denser water (density maximum changes) can be found especially around 100 m near Station S4, compared with the surroundings (**Figure 5C**). In contrast to CE5, the maximum changes in ocean density were not found around 100 m near the core of CE6 (**Figure 5D**) but in the north boundary of CE6 near Station S1. **Figures 5C,D** show a large difference in ocean stratification between these two cases. Denser water is below 100 m in CE6 (**Figure 5D**), being depressed by lighter water from the surface to ∼50 m. Thus, stronger stratification can be found within 50 to 100 m around CE6 (**Figure 5F**), in contrast to the weaker stratification around CE5 (**Figure 5E**). Moreover, no surface cooling can be detected in CE5 and CE6 along the cruise section *via* satellites (**Figures 5A,B**).

Observed Biogeochemical Variability

Figure 6 shows the profiles of Chl, N, P, Si, N:P ratio, and Si:N ratio at Stations S1 and S2 near CE6, and Stations S3 (located at edge between CE5 and an AE) and S4 near CE5 during the cruise experiments. More nutrients are found at Stations S2 (green) and S4 (purple), compared with the climatological fields. However, Station S4 is closer to the core of CE5, while Station S2 is farther from the core of CE6. At Station S4, the depth of subsurface Chl maximum (SCM) is as shallow as 50 m (**Figure 6A**, purple), while the SCM depth at Station S3 (red) is deeper (75 m), indicating that the nutrient-rich water was upwelled toward the surface at Station 4 (Hung et al., 2003). The N and Si concentration at Station S4 is at least twice larger than the climatological profiles, reaching 10 and 11.6 μM, respectively, at 75 m (**Figures 6B,D**). In **Figure 6E**, the N:P ratios are generally smaller than 16:1 based on the climatological fields in the NSCS, highlighting the limitation of N. In contrast, at Station S4 near the CE5 core, the N:P ratios are larger than 16:1 at depths near the surface, reflecting the fact that P concentrations are insufficient to support phytoplankton growth (**Figure 6E**); while the Si:N ratios are maintained at 1∼2 near the surface (**Figure 6F**).

What potential mechanisms result in low Chl values at Stations 3 and 4 (i.e., near CE5)? The Chl concentration is ∼0.33 mg m^{-3} at 50 m at Station 4 (the core of CE5), lower than that at Station 3 (∼0.41 mg m^{-3}). Previously, it has been shown that the warm and P-depleted water at Stations 3 and 4 were mainly from the mixed water of SCS and Kuroshio, based on the TS diagram (see **Figure 1D** from Shih et al., 2020). Shih et al. (2020) observed diatoms that are the predominant phytoplankton assemblages in the surface water near the CE5 core and reported that both POC flux (166 mg m^{-2} day^{-1}) and diatom inventory (56 × 10^6 cells m^{-2}) at Station 3 were higher than those (POC flux = 50 mg m^{-2} day^{-1} and diatoms = 26 × 10^6 cells m^{-2}) at Station 4. These results suggest that various phytoplankton species and their cellular fluorescence signals may affect Chl inventories and POC fluxes (Shih et al., 2020; Zhou et al., 2020).

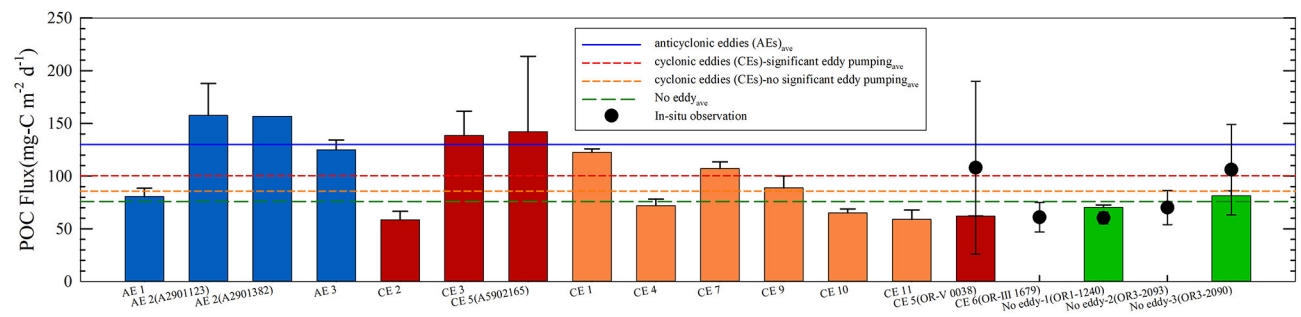

FIGURE 8 | Particulate organic carbon (POC) fluxes for the eddy cases based on *in situ* observation (solid circles) and satellite estimation (color-shaded bars). The bars in blue, red, orange, and green show the POC fluxes corresponding to the cases with significant anticyclonic eddies (AEs) pumping, significant cyclonic eddies (CEs) pumping, insignificant CEs pumping, and no eddies, respectively. All error bars show the standard deviation of the POC fluxes. The horizontal solid and dashed lines show the total mean of POC flux for each case based on satellite estimation. We performed direct measurement of the POC flux given by Shih et al. (2020) for CE5 (OR-V 0038) and CE6 (OR-III 1679).

Besides examining diatoms contributing to phytoplankton biomass in the water column, we did not know of other small phytoplankton such as synechococcus, prochlorococcus, and picoeukaryotes. Hung et al. (2003) reported that some phytoplankton assemblages of prymnesiophyte, prasinophytes, and prochlorophyte were dominant species within the cold core ring (i.e., cyclonic eddy) in the Gulf of Mexico. Wu et al. (2014) reported that prasinophytes and prymnesiophytes accounted for 19% and 42%, respectively, of the Chl levels in the SCS. Based on the changes in nutrient ratio, the phytoplankton species in the oligotrophic water of the NSCS might shift from diatoms to tricodizmia (Liu et al., 2002) or other small phytoplankton (Wu et al., 2014). Moreover, Si and N played important roles in the population dynamics of diatoms (Kudo, 2003). The marine environment with Si:N ratios of 1–2 near the surface was favorable for the diatoms, but the diatom abundance in surface water at Stations 3 and 4 were below 0.5×10^3 (cells L^{-1}), which could be due to P limitation.

Figure 7 shows the satellite-observed SST and Chl on the days when the CEs were observed along the repeated XBT transects. In **Figure 7**, the CEs are all located southwest of Taiwan where the XBT transects passed by. By comparing with the eddy vicinity (**Figure 7**), colder SST and higher Chl are likely found near the core of CE8 with a lower sea surface height on March 4, 2000 (**Figures 7A,B**), when significant upwelling was observed *via* the XBT transect. However, for those cases without significant upwelling, neither colder SST nor higher Chl can be found near the cores of CEs. These comparisons suggest that the biological field only varies near the core of CEs with significant upwelling.

Figure 8 shows the particulate organic carbon fluxes obtained by *in-situ* observation and satellite estimation for the eddy cases in this study. Based on the satellite-derived POC fluxes, both AEs and CEs with significant eddy pumping (defined by the 10-m departure of D22 from the climatology) correspond to higher POC fluxes, compared with those with insignificant eddy pumping (20 ± 7 mg-C $m^{-2}day^{-1}$). Specifically for the cases of AE2, AE3 and CE3 which have significant eddy pumping under the NE monsoon (December to May), the satellite-derived POC fluxes exceed 100 mg-C m^{-2} day^{-1} (**Figure 8**). The high POC flux could arise from a combination of eddy pumping and deepening of the wind-induced mixed layer (Zhou et al., 2020). In the core of AEs with significant downwelling, strong mixed-layer deepening could reach the nitracline (McGillicuddy, 2016), then

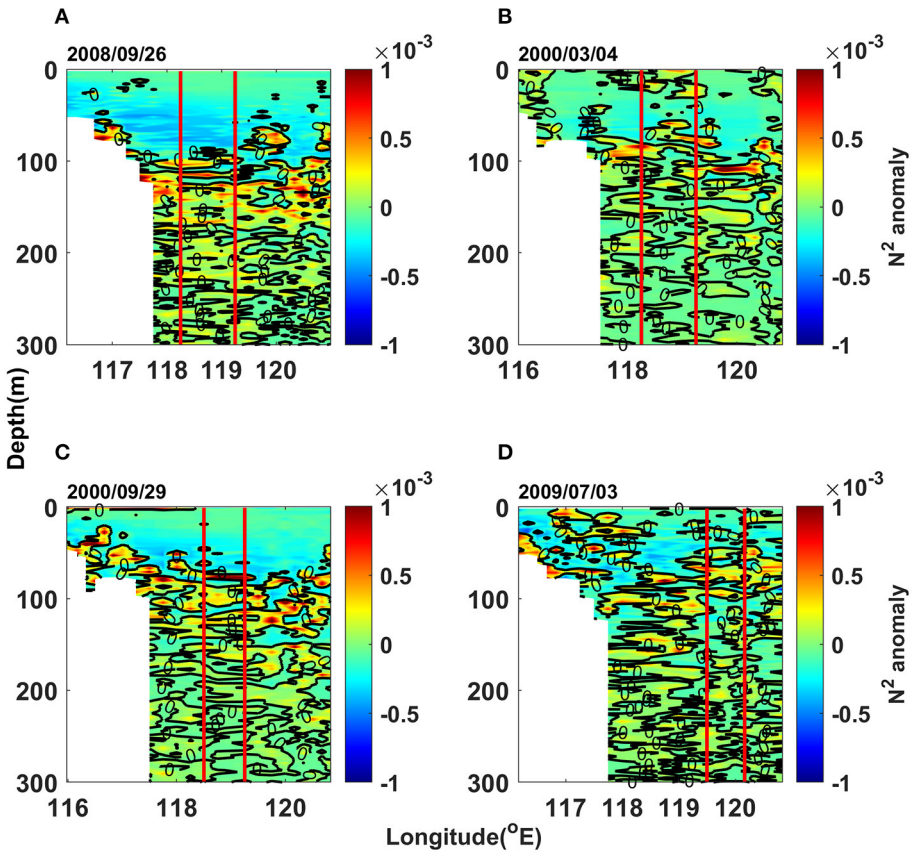

FIGURE 9 | Anomalies of squared buoyancy frequency on **(A)** September 26, 2008 (AE1), **(B)** March 4, 2000 (CE8), **(C)** September 29, 2000 (AE4), and **(D)** July 3, 2009 (CE10), showing the background situation of ocean stratification around the eddies. The two red vertical lines show the region of eddies confirmed with satellite altimeters. The left (right) panel is for the cases of anticyclonic (cyclonic) eddies, while the upper (lower) panel is for the cases with (without) significant eddy pumping.

increase Chl and POC fluxes near the surface. A positive correlation of Chl anomalies with the AEs could be found globally in nutrient-limited regions (McGillicuddy, 2016), such as the oligotrophic South Indian Ocean and subtropical Pacific (Gaube et al., 2014). Thus, we observed AEs with higher Chl and POC fluxes.

Based on the *in-situ* observation conducted in spring (March to May), the POC flux is higher near CE5 (May 2014) with significant upwelling than that near CE6 (April 2013) with insignificant upwelling. In addition, the CE5 POC flux was higher than that observed from the cruise experiment, OR-III 2093 (April 2019), which did not detect eddies in a similar region (**Supplementary Figure S3D**). The POC flux near CE5 was ∼108 mg-C m^{-2} day^{-1} (Shih et al., 2020), the highest among the cruise experiments performed in this study, which were executed in the NSCS during spring. The estimation of POC fluxes near the eddy cores with significant eddy pumping in the NSCS was comparable with the high POC fluxes ranging from 83 to 194 mg-C $m^{-2}day^{-1}$ observed around the eddies in the western North Pacific (Shih et al., 2015).

Overall, the particulate organic carbon (POC) fluxes are higher than 100 mg-C m^{-2} day^{-1} near the eddy cores with significant eddy pumping, but are smaller than 100 mg-C m^{-2} day^{-1} near the eddy cores with insignificant eddy pumping or regions with no detected eddies in the northern South China Sea (NSCS) (**Figure 8**). It is worth noting that the satellite-obtained POC fluxes may be underestimated when using the satellite-obtained Chl to calculate the NPP value in the NSCS (Li et al., 2018b). Based on three cruise experiments (**Supplementary Figures S3B,C,E**) with satellite POC-flux estimation, the difference between the satellite-obtained POC fluxes and the *in-situ* POC fluxes ranges from −42 to 17% (minus is for underestimated), showing the inconsistency of the satellite-estimated POC fluxes compared with the *in situ*-measured POC fluxes. The causes of these inconsistencies are complex, since the model-derived POC fluxes are based on three parameters, NPP, SST, and Z_{eu} that are obtained from the satellite data bank, suggesting more *in situ*-measured POC fluxes are needed to evaluate those model-derived values of POC fluxes in the NSCS.

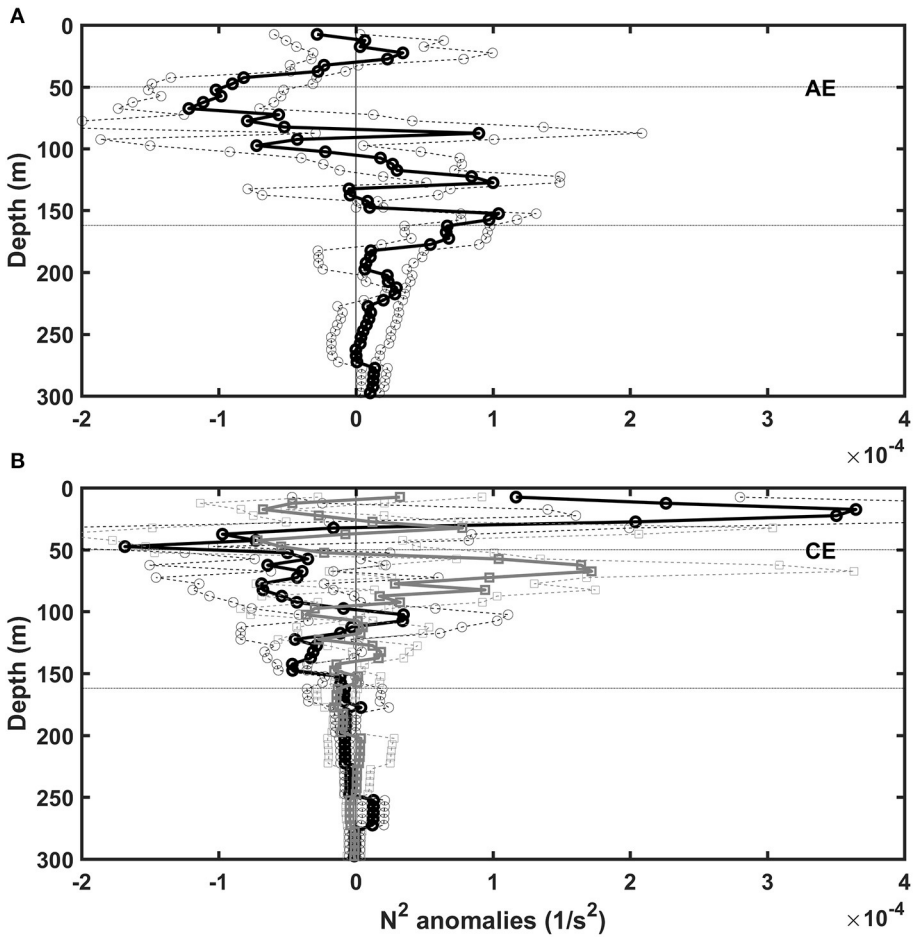

FIGURE 10 | Mean (solid curve) and standard deviation (dashed curves) of N^2 anomalies at the location of Argo floats observing **(A)** four anticyclonic eddies with significant downwelling and **(B)** three cyclonic eddies with (black curve) and without (gray curve) significant upwelling.

Upper Ocean Stratification in the Eddy Cores

We hypothesized that when ocean stratification is weakened (smaller N^2), eddy pumping is stronger according to the indirect estimation of vertical velocity (w) *via* the eddy pumping (McGillicuddy and Robinson, 1997; Sun et al., 2017):

$$w = \frac{g}{\rho_0 N^2}\left(\frac{\partial \rho}{\partial t} + u_r\frac{\partial \rho}{\partial r} + u_\theta\frac{1}{r}\frac{\partial \rho}{\partial \theta}\right) \ldots \quad (8)$$

where t is the time, u_r and u_θ are the horizontal components of ocean currents in the r and θ direction, respectively, and other variables are the same as those in Equation (2). Besides the density evolution induced by the ocean eddies, the background N^2 could also affect the amplitude of w. The smaller the N^2, the larger the amplitude of w. Moreover, water column stability was found to determine the formation of subtropical phytoplankton blooms in the northwestern Pacific (Matsumoto et al., 2021).

Figure 9 shows the anomaly profiles of squared buoyancy frequencies obtained *via* the expendable bathythermograph (XBT) transect that passed through the cyclonic eddies (CEs) and anticyclonic eddies (AEs). In **Figures 9A,B**, the anomaly profiles of squared buoyancy frequencies are mostly negative above 100 m around the cores of AE1 and CE8 with significant eddy pumping. To the west and east of these eddies, the squared buoyancy frequencies are lower than the climatological field above 100 m (**Figures 9A,B**), showing background weakening of upper ocean stratification. Averaged from the mixed layer depth at ∼50 m to the thermocline bottom at ∼162 m (Peng et al., 2018), the anomalies of squared buoyancy frequencies are -2×10^{-5} and -13×10^{-5} s^{-2} around CE8 and AE1, respectively, in March 2000 and September 2008. For the eddies with insignificant vertical motion (**Figures 9C,D**), the anomalies of squared buoyancy frequencies are 4×10^{-5} and 8×10^{-5} s^{-2} around AE4 and CE10, respectively, in September 2000 and July 2009. For the other two cases of CEs (CE9 and CE11) without significant upwelling observed in April 2003 and August 2010,

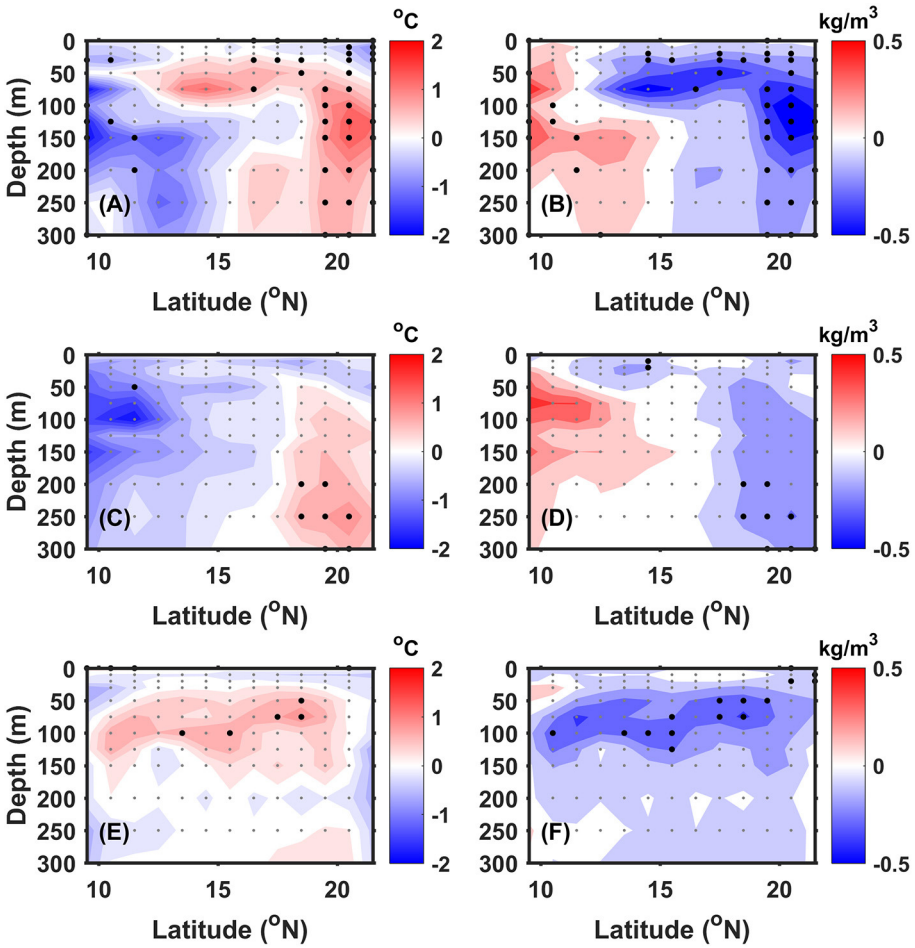

FIGURE 11 | Meridional distribution of the anomalies in temperature (left) and potential density (right) averaged within 108°E and 121°E during the month and a month before observing the ocean eddies, using the temperature-salinity (TS) gridded data of World Ocean Database version 13 (WOD13). **(A,B)** For the anticyclonic eddies with significant downwelling. **(C,D)** For the cyclonic eddies with significant upwelling. **(E,F)** For all the eddies without significant upwelling or downwelling. The gray dots show the data points to plot the contours, and the black dots shows the data points significant to the 95% confidence level based on *t*-testing. Note that the statistical analysis in **(E,F)** does not include the case of Argo 2902045 in May 2017 because of the data availability of TS gridded data of WOD13 up to 2014.

the anomalies of squared buoyancy frequencies have a positive value, which is over 5×10^{-5} s^{-2}. This comparison suggests that weaker stratification from 50 to 162 m is the condition required for significant eddy vertical motion in the NSCS.

In addition to the expendable bathythermograph (XBT) observations, weaker stratification can also be found *via* the Argo floats that observed eddies with significant eddy pumping. **Figure 3B** shows a time series of N^2 anomaly profiles obtained from Argo 2900825 that observed the same anticyclonic eddy (AE1) that passed by the XBT transect in September 2008. Before and after observing AE1, the anomalies of N^2 are mostly negative above 100 m (**Figure 3B**), suggesting weaker stratification near the thermocline. Furthermore, to highlight the ocean background with weakened stratification at the Argo floats (**Supplementary Table S1**), **Figure 10** represents the composite analysis of N^2 anomalies at the Argo locations during the months when the eddies were observed. The N^2 anomalies are generally negative around the depths from 50 and 162 m (around the thermocline depth) during the months when significant eddy pumping was observed near the core of AEs (**Figure 10A**) and CEs (**Figure 10B**). However, for the cases of CEs without significant upwelling, **Figure 10B** (gray curve) shows that the profiles of N^2 anomalies are positive around the depths from 50 to 162 m. This comparison suggests that ocean stratification is weaker than the climatological field from 50 to 162 m during the months when significant eddy pumping was observed in the NSCS.

Mechanism of Stratification Weakening

It is natural to ask what causes the stratification changes near the thermocline in the NSCS. We hypothesized that (1) the stratification is weakened when the lower ocean becomes lighter or the upper ocean becomes denser, and (2) the Kuroshio intrusion that brings lighter surface waters *via* the Luzon Strait strengthens the ocean stratification, which tends to suppress eddy pumping. To prove these hypotheses, **Figure 11** shows the background temperature changes in ocean vertical profiles in the SCS during the month and a month before the observation

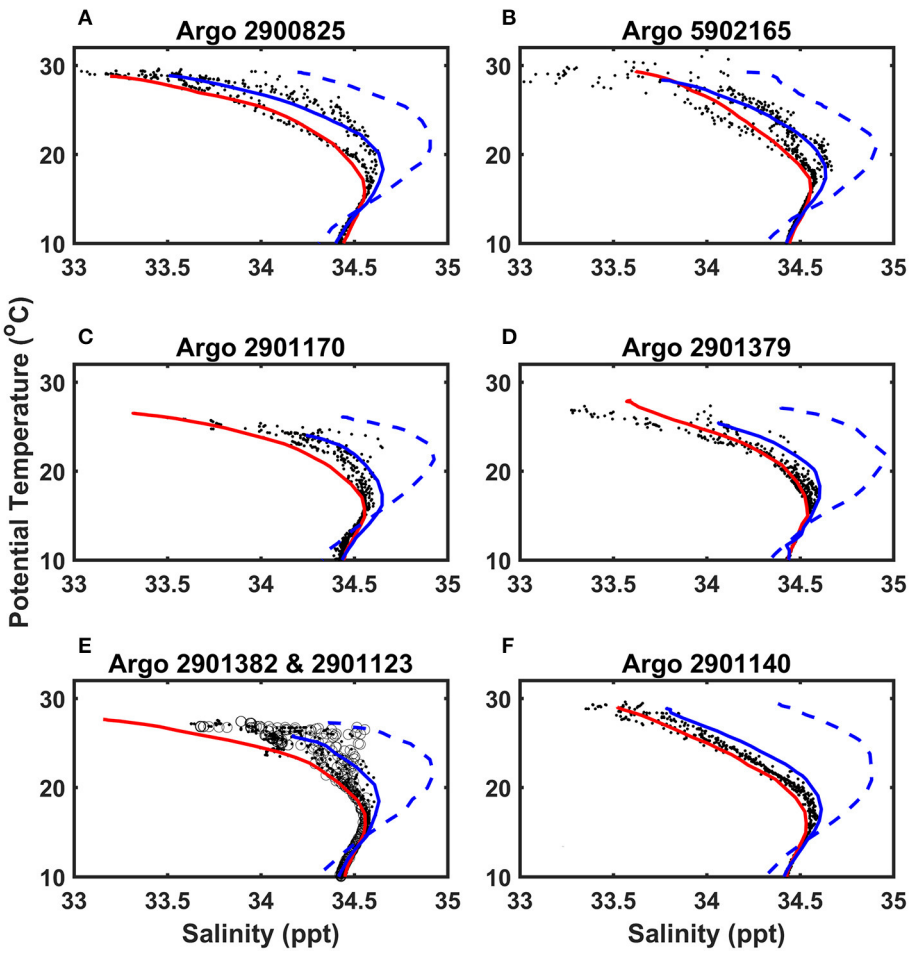

FIGURE 12 | Temperature-salinity (TS) diagrams during the month and a month before observing the ocean eddies *via* Argos **(A)** 2900825, **(B)** 5902165, **(C)** 2901170, **(D)** 2901379, **(E)** 2901382, 2901123, and **(F)** 2901140. The left and right panels are for anticyclonic and cyclonic eddies, respectively. The solid red and dashed blue curve represents the TS properties of water masses in the southern South China Sea (SCS) and in the Kuroshio region, respectively. In **(E)**, the dots are for the TS obtained from Argo 2901123 and the circles are for Argo 2901382, observing the same anticyclonic eddy with significant downwelling.

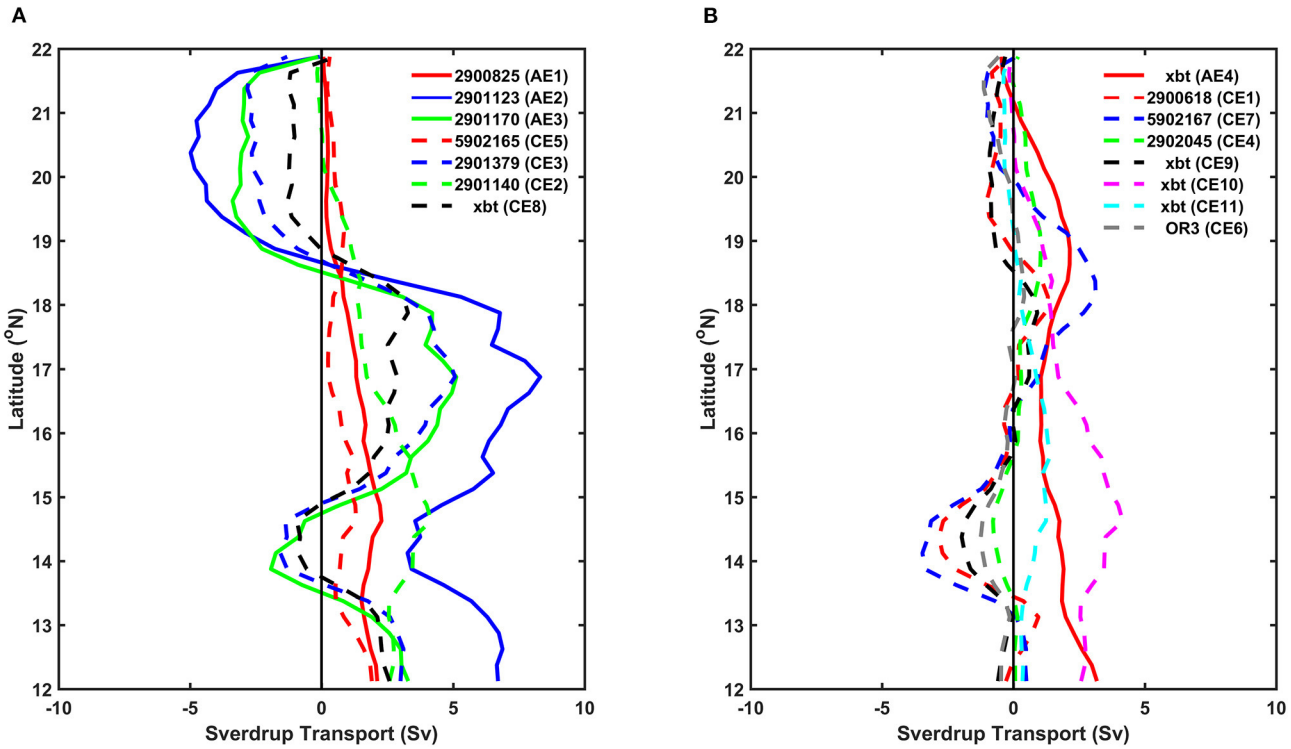

FIGURE 13 | Meridional distribution of Sverdrup transport averaged within 109°E and 120°E during the month and a month before observing the ocean eddies *via* Argo floats and expendable bathythermographs (XBTs). **(A)** Cases with significant eddy pumping. **(B)** Cases without significant eddy pumping. Solid and dashed curves are for the anticyclonic and cyclonic eddies, respectively. Only considering depth larger than 100 m.

of the ocean eddies. Compared with the climatological fields below 100 m, the water is warmer and lighter in the NSCS but is colder and denser in the SSCS for both AEs (**Figures 11A,B**) and CEs (**Figures 11C,D**) with significant eddy pumping. However, for the eddy cases without significant eddy pumping (**Figures 11E,F**), the water is warmer and lighter from 50 to 100 m in the whole SCS. This comparison suggests that when the NSCS is lighter and warmer below the thermocline, the stratification near the thermocline becomes weak and forms a background condition favorable for significant eddy pumping to occur near eddy cores.

To examine the causes of warming in the northern South China Sea (NSCS), **Figure 12** shows the TS properties of seawater obtained from the Argo floats that observed significant eddy pumping, compared with the background TS in the SSCS (east of Vietnam coast) and the region east of Luzon island (for the Kuroshio). In **Figure 12A**, the TS properties, which were observed *via* Argo 2900825 in the NSCS between August and September 2008, are occasionally similar to those observed in the SSCS. TS properties similar to those of the SSCS can be found in the other cases with significant downwelling (**Figure 12**, left) and upwelling (**Figure 12**, right). These TS diagrams suggest that the warm water in the NSCS comes from the SSCS.

To show the northward transport of South China Sea (SCS) water, **Figure 13** shows the Sverdrup transports in the SCS averaged within 109°E and 120°E during the month and a month before observing the eddies *via* the Argo floats and XBTs. As shown in **Figure 13A**, the Sverdrup transports are mostly positive (northward) south of 18°N for all the cases with significant eddy pumping. In contrast, **Figure 13B** shows that most cases with insignificant eddy pumping (except AE4, CE10, and CE11) are accompanied by negative (southward) or small positive Sverdrup transports south of 17°N. Within 12°N and 22°N, the net Sverdrup transports for cases with significant eddy pumping range from 0.7 to 2.6 Sv, larger than those with insignificant eddy pumping (−0.4 to 1.8 Sv). This comparison suggests that the wind-induced Sverdrup transports bring the SSCS water northward into the NSCS during the month and a month before observing the ocean eddies with significant eddy pumping.

Even with the positive Sverdrup transports, the eddy pumping of AE4, CE10, and CE11 was insignificant along the XBT transects near the Luzon Strait in September 2000, July 2009, and August 2010, respectively. To determine why this is the case, we searched for all the available historical data of ocean profiles from Argo and CTD observations. Fortunately, Argo 2901180 was close to the XBT transect on July 8, 2009 (**Supplementary Figure S3F**), 5 days after the CE10 core was observed *via* the XBTs. Besides, CTD casting was found near the XBT transect on September 17, 2000 and August 16, 2010, about 10 days before the core of AE4 and CE11, respectively, were observed (**Supplementary Figure S3F**). Based on these ocean profiles, **Figure 14** shows that warmer and more saline water coming from the Kuroshio can be found near the XBT transect, showing the Kuroshio intrusion into the Luzon Strait at the time

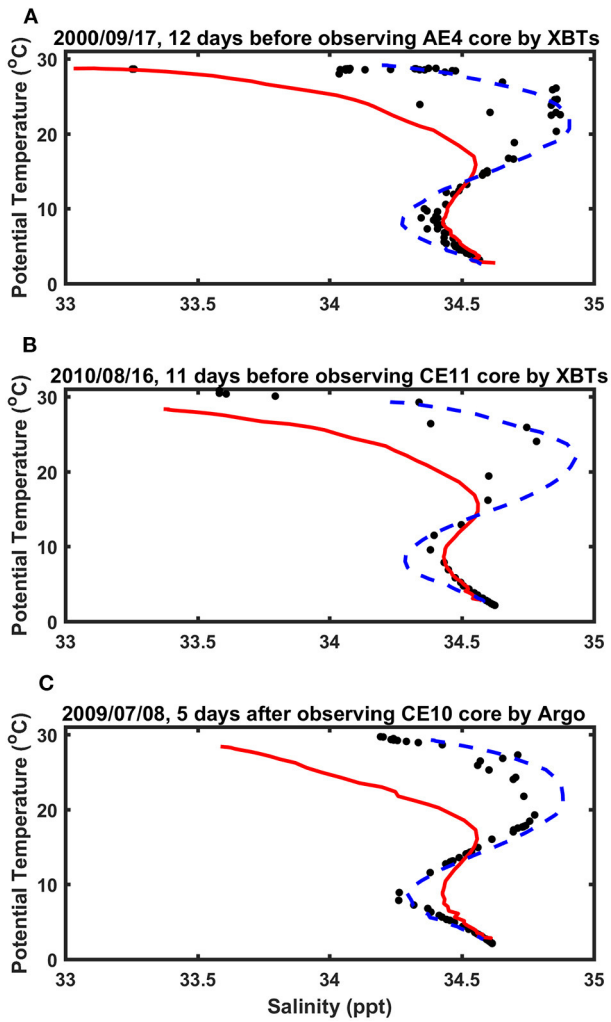

FIGURE 14 | Temperature-salinity (TS) diagrams corresponding to the cases with insignificant eddy pumping and the positive Sverdrup transport, on a particular date closest to day when observing the eddy core *via* expendable bathythermographs (XBTs). The TS data obtained from **(A)** the ODB-CTD data for September 17, 2000, **(B)** the ODB-CTD data for August 16, 2010, and **(C)** the Argo 2901180 data for July 8, 2009. The solid red and dashed blue curve represents the TS properties of water masses in the southern South China Sea (SCS) and in the Kuroshio region, respectively.

the eddy cores without significant eddy pumping were observed. The Kuroshio intrusion causes lighter water in the upper layer enhancing the ocean stratification near the thermocline; thus, it may depress the eddy pumping of AE4, CE10, and CE11 even though the Sverdrup transports are positive in the SCS.

SUMMARY

In general, cyclonic eddies and anticyclonic eddies can be accompanied by upwelling and downwelling, respectively, near the eddy core. However, we observed eddies with and without significant eddy pumping *via* a repeated XBT transect, Argo floats, and cruise experiments in the NSCS.

By studying the ocean vertical structure case by case from 2000 to 2017, eddies with and without significant pumping were found in different monsoons. The analysis showed that the ocean stratification near the thermocline was an important factor in determining eddy pumping in the NSCS. When the ocean stratification was weaker than the climatological field, significant upwelling (downwelling) was observed near the cores of CEs (AEs), although the eddies could only be traced back for 10 days. However, in the same trace-back period, some eddies had no significant upwelling and downwelling near their cores when the ocean stratification was stronger than the climatological field. When waters were transported northward into the NSCS, the thermocline became weaker because of decreasing density vertical gradients (the weakening of the ocean stratification) caused by the lighter and warmer waters transported from the SSCS. Under such conditions with thermocline weakening, significant upwelling and downwelling were observed near the cores of CEs and AEs, respectively.

The biogeochemical response to significant upwelling near a cyclonic eddy (CE5) was observed *via* a cruise experiment executed in May 2014, although the cyclonic eddy (CE5) had a small diameter (50 to 100 km), compared with the mean radius of eddies in the SCS. A higher concentration of nutrients was found near the core of the cyclonic eddy (CE5) where the upwelling occurred. With an increasing concentration of N near the eddy core, the N:P ratio became larger than 16:1 (the Redfield ratio) at some depths above the thermocline, in contrast to the marine environment in the background NSCS. The POC flux was higher than 100 mg-Cm^{-2} day^{-1} near the eddy cores with significant eddy pumping, obtained by *in situ* measurement and satellite estimation. although the satellite-estimated POC fluxes were inconsistent compared with the measured POC fluxes.

DATA AVAILABILITY STATEMENT

The raw data supporting the conclusions of this article will be made available by the authors, without undue reservation, to any qualified researcher.

AUTHOR CONTRIBUTIONS

C-CH and CC wrote the manuscript. Y-YS executed the experiments and collected water samples for the biogeochemical part of this study. CC and Y-TC detected eddies and studied ocean vertical structure. JC and NF analyzed the nutrient samples and provided **Figures 7**, **9**. W-CW analyzed satellite images and provided **Figure 8**. CC, Y-YS, and C-CH revised the manuscript. All authors contributed to the article and approved the submitted version.

FUNDING

This study is supported by the Ministry of Science and Technology (MOST), Taiwan (ROC), under the project Eddy roles in marine environmental variability near Taiwan (105-2119-M-110-011-MY2, 105-2119-M-019-009-MY2, 107-2611-M-019-020-MY2, and 109-2611-M-019-013), I-Taiwan grants from

MOST (107-2611-M-019-020-MY2, 108-2611M-110-019-MY3, 108-2917-I-564-017, and 109-2611-M-019-013) and Influences of typhoons and internal waves on *in situ* and remote carbon fixation of phytoplankton in the northern South China Sea (II)(III) (109-2611-M-012-001 and 110-2611-M-012-002).

ACKNOWLEDGMENTS

We thank the Coriolis Operational Oceanography (http://www.coriolis.eu.org), NOAA, and Taiwan ODB for providing the data of ocean profiles based on the Argo floats, XBTs, CTD, WOD13, and WOA13. We also thank CMEMS and RSS (https://www.remss.com/) for the satellite data of SLAs, ocean color, and SST. We are grateful to the captains and crews of the R/Vs OR-I, OR-III, and OR-V for their efforts in executing the sea-going experiments in the NSCS.

SUPPLEMENTARY MATERIAL

The Supplementary Material for this article can be found online at: https://www.frontiersin.org/articles/10.3389/fmars.2021.717576/full#supplementary-material

REFERENCES

Behrenfeld, M. J., and Falkowski, P. G. (1997). Photosynthetic rates derived from satellite-based chlorophyll concentration. *Limnol. Oceanogr.* 42, 1–20. doi: 10.4319/lo.1997.42.1.0001

Chelton, D. B., Gaube, P., Schlax, M. G., Early, J. J., and Samelson, R. M. (2011a). The influence of nonlinear mesoscale eddies on near-surface oceanic chlorophyll. *Science* 334, 328–332. doi: 10.1126/science.1208897

Chelton, D. B., Schlax, M. G., and Samelson, R. M. (2011b). Global observations of nonlinear mesoscale eddies. *Prog. Oceanogr.* 91. 167–216. doi: 10.1016/j.pocean.2011.01.002

Chen, C. C., Shiah, F. K., Chung, S. W., and Liu, K. K. (2006). Winter phytoplankton blooms in the shallow mixed layer of the South China Sea enhanced by upwelling. *J. Mar. Syst.* 59, 97–110. doi: 10.1016/j.jmarsys.2005.09.002

Chen, G., and Han, G. (2019). Contrasting short-lived with long-lived mesoscale eddies in the global ocean. *J. Geophys. Res. Oceans*. 124, 3149–3167. doi: 10.1029/2019JC014983

Chen, G., Hou,Y., and Chu, X. (2011). Mesoscale eddies in the South China Sea: mean properties, spatiotemporal variability, and impact on thermohaline structure. *J. Geophys. Res.* 116, C06018. doi: 10.1029/2010JC006716

Chen, K. S., Hung, C. C., Gong, G. C., Chou, W. C., Chung, C. C., and Shih, Y. Y. (2013). Enhanced POC export in the oligotrophic northwest Pacific Oceanafter extreme weather events. *Geophys. Res. Lett.* 40, 5728–5734. doi: 10.1002/2013GL058300

Chen, Y. L., Chen, H. Y., Lin,I. I., and Lee,M. A., Chang,J. (2007). Effects of cold eddy on phytoplankton production and assemblages in LuzonStrait bordering the South China Sea. *J. Oceanogr.* 63, 671–683. doi: 10.1007/s10872-007-0059-9

Chen, Y. L. L. (2005). Spatial and seasonal variations of nitrate-based new production and primary production in the South China Sea. *Deep-Sea Res. I.* 52, 319–340. doi: 10.1016/j.dsr.2004.11.001

Chen, Y. L. L., Chen, H. Y., Jan, S., Lin, Y. H., Kuo, T. H., and Hung, J. J. (2015), Biologically active warm-core anticyclonic eddies in the marginal seas of the western pacific ocean. *Deep Sea Res. Part I Oceanogr. Res. Pap*. 106, 68–84. doi: 10.1016/j.dsr.2015.10.006

Chen, Y. L. L., Chen,H. Y., Karl,D. M., and Takahashi M (2004). Nitrogen modulates phytoplankton growth in spring in the South China Sea. *Cont. Shelf Res.* 24, 527–541. doi: 10.1016/j.csr.2003.12.006

Chow, C.-H., Hu,J.-H., Centurioni, L. R., and Niiler, P. P. (2008). Mesoscale Dongsha cyclonic Eddy in the northern South China Sea by drifter and satellite observations. *J. Geophys. Res.* 113:C04018. doi: 10.1029/2007JC004542

Chow, C. H., Cheah, W., and Tai, J.-H. (2017). A rare and extensive summer bloom enhanced by ocean eddies in the oligotrophic western North Pacific Subtropical Gyre. *Sci. Rep.* 7:6199. doi: 10.1038/s41598-017-06584-3

Chow, C. H., Cheah, W., Tai, J.-H., and Liu, S.-F. (2019). Anomalous wind triggered the largest phytoplankton bloom in the oligotrophic North Pacific Subtropical Gyre. *Sci. Rep.* 9:15550. doi: 10.1038/s41598-019-51989-x

Chow, C. H., Liu, Q., and Xie, S.-P. (2015). Effects of Kuroshio Intrusions on the atmosphere northeast of Taiwan Island. *Geophys. Res. Lett.* 42, 1465–1470. doi: 10.1002/2014GL062796

Chu, P. C., and Fan, C. W. (2017). Synoptic monthly gridded global and regional four dimensional WOD and GTSPP (T, S, u, v) fields with the optimal spectral decomposition (OSD) and P-vector methods. *Geosci. Data J.* 4, 50–71. doi: 10.1002/gdj3.48

Chu, X., Chen, G., and Qi, Y. (2020). Periodic mesoscale Eddies in the South China Sea. *J. Geophys. Res. Oceans*. 125:e2019JC015139. doi: 10.1029/2019JC015139

Du, Y., Wu, D., Liang, F., Yi, J., Mo, Y., He, Z., et al. (2016). Major migration Corridors of Mesoscale Ocean Eddies in the South China Sea from 1992 to 2012. *J. Mar. Syst.* 158, 173–181. doi: 10.1016/j.jmarsys.2016.01.013

Dunne, J. P., Armstrong, R. A., Gnanadesikan, A., and Sarmiento, J. L. (2005). Empirical and mechanistic models for the particle export ratio. *Global Biogeochem. Cy.* 19:GB4026. doi: 10.1029/2004GB002390

Faghmous, J. H., Frenger, I., Yao, Y., Warmka, R., Lindell, A., and Kumar, V. (2015). A daily global mesoscale ocean eddy dataset from satellite altimetry. *Sci. Data.* 2:150028. doi: 10.1038/sdata.2015.28

Flagg, C. N., Wallace, D., and Kolber, Z. (1998). Cold anti-cyclonic eddies formed from cold pool water in the southernmiddle Atlantic bight. *Cont. Shelf Res.* 15, 1839–1867. doi: 10.1016/S0278-4343(97)00038-1

Gaube, P., McGillicuddy Jr, D. J., Chelton, D. B., Behrenfeld, M. J., and Strutton, P. G. (2014). Regional variations in the influence of mesoscale eddies on near-surface chlorophyll. *J. Geophys. Res. Oceans* 119, 8195–8220, doi: 10.1002/2014JC010111

Gill, A. (1982), *Atmosphere–Ocean Dynamics*. New York, NY: Academic Press.

Hu, J. Y., Kawamura, H., Hong, H. S., and Qi, Y. Q. (2000). A review on the currents in the South China Sea: seasonal circulation, South China Sea warm current and Kuroshio intrusion. *J. Oceanogr.* 56, 607–624. doi: 10.1023/A:1011117531252

Huang, J., and Xu, F. (2018). Observational evidence of subsurface chlorophyll response to mesoscale eddies in the North Pacific. *Geophys. Res. Lett.* 45, 8462–8470. doi: 10.1029/2018GL078408

Hung, C.-C., Gong, G.-C., Chou, W.-C., Chung, C.-C., Lee, M.-A., and Chang, Y. (2010b). The effect of typhoon on particulateorganic carbon flux in the southern East China Sea. *Biogeosciences* 7, 3521–3550. doi: 10.5194/bg-7-3007-2010

Hung, C.-C., Gong, G.-C., Chung, W.-C., Kuo, W.-T., and Lin, F.-C. (2009). Enhancement of particulate organic carbon export flux induced by atmospheric forcing in the subtropical oligotrophic northwest Pacific Ocean. *Mar. Chem.* 113, 19–24 doi: 10.1016/j.marchem.2008.11.004

Hung, C.-C., Guo, L., Schultz Jr, G. E., Pinckney, J. L., and Santschi, P. H. (2003). Production and flux of carbohydrate species inthe Gulf of Mexico. *Global Biogeochem. Cy.* 17:1055. doi: 10.1029/2002GB001988

Hung, C.-C., Xu, C., Santschi, P. H., Zhang, S.-J., Schwehr, K. A., Quigg, A., et al. (2010a). Comparative evaluation of sediment trap and ^{234}Th-derived POC fluxes from the upper oligotrophic waters of the Gulf of Mexico and the subtropical northwestern Pacific Ocean. *Mar. Chem.* 121, 132–144. doi: 10.1016/j.marchem.2010.03.011

Hwang, C., and Chen, S. A. (2000). Circulations and eddies over the South China Sea derived from TOPEX/Poseidon altimetry. *J. Geophys. Res.* 105, 23943–23965. doi: 10.1029/2000JC900092

Itoh, S., and Yasuda, I. (2010). Water mass structure of warm and cold anticyclonic eddies in the western boundary region of the Subarctic North Pacific. *J. Phys. Oceanogr.* 40, 2624–2642. doi: 10.1175/2010JPO4475.1

Kudo, I. (2003). Change in the uptake and cellular Si:N ratio in diatoms responding to the ambient Si:N ratio and growth phase. *Mar. Biol.* 143, 39–46. doi: 10.1007/s00227-003-1063-2

Large, W. G., and Pond, S. (1982). Sensible and latent heat flux measurements over the ocean. *J. Phys. Oceanogr.* 12, 464–482. doi: 10.1175/1520-0485(1982)012andlt;0464:SALHFMandgt;2.0.CO;2

Li, D., Chou, W.-C., Shih, Y.-Y., Chen, G.-Y., Chang, Y., Chow, C. H., et al. (2018a). Elevated particulate organic carbon export flux induced by internal waves in the oligotrophic northern South China Sea. *Sci. Rep.* 8:2042. doi: 10.1038/s41598-018-20184-9

Li, L., Worth, D. N., and Su, J. (1998). Anticyclonic rings from the Kuroshio in the South China Sea. *Deep Sea Res. Part I.* 45, 1469–1482. doi: 10.1016/S0967-0637(98)00026-0

Li, T., Bai, Y., He, X., Xie, Y., Chen, X., Gong, F., et al. (2018b). Satellite-based estimation of particulate organic carbon export in the northern South China Sea. *J. Geophys. Res. Oceans.* 123, 8227–8246. doi: 10.1029/2018JC014201

Liu, K. K., Chao, S. Y., Shaw, P. T., Gong, G. C., Chen, C. C., and Tang, T. Y. (2002). Monsoon-forced chlorophyll distribution and primary production in the South China Sea: observations and a numerical study. *Deep Sea Res. I.* 49, 1387–1412. doi: 10.1016/S0967-0637(02)00035-3

Liu, Y., Yu, L., and Chen, G. (2020). Characterization of sea surface temperature and air-sea heat flux anomalies associated with mesoscale eddies in the South China Sea. *J. Geophys. Res. Oceans* 125:e2019JC015470. doi: 10.1029/2019JC015470

Ma, W., Xiu,. P., Chai, F., Ran, L., Wiesner, M. G., Xi, J., et al. (2021). Impact of mesoscale eddies on the source funnel of sediment trap measurements in the South China Sea. *Prog. Oceanogr.* 194:102566. doi: 10.1016/j.pocean.2021.102566

Matsumoto, K., Sasai, Y., Sasaoka, K., Siswanto, E., and Honda, M. C. (2021). The formation of subtropical phytoplankton blooms is dictated by water column stability during winter and spring in the oligotrophic northwestern North Pacific. *J. Geophys. Res. Oceans* 126:e2020JC016864. doi: 10.1029/2020JC016864

McGillicuddy, D. J. (2016),Mechanisms of physical-biological-biogeochemical interaction at the oceanic mesoscale. *Ann. Rev. Mar. Sci.* 8, 125–159. doi: 10.1146/annurev-marine-010814-015606

McGillicuddy, D. J., and Robinson, A. R. (1997). Eddy-induced nutrient supply and new production in the Sargasso Sea. *Deep Sea Res. Part I* 44, 1427–1450. doi: 10.1016/S0967-0637(97)00024-1

Nan, F., Xue, H. J., and Yu, F. (2015). Kuroshio intrusion into the South China Sea: a review. *Prog. Oceanogr.* 137, 314–333. doi: 10.1016/j.pocean.2014.05.012

Okubo, A. (1970). Horizontal dispersion of floatable particles in the vicinity of velocity singularities such as convergences. *Deep Sea Res. Oceanogr. Abstr.* 17, 445–454. doi: 10.1016/0011-7471(70)90059-8

Peng, H., Pan, A., Zheng, Q. A., and Hu, J. (2018). Analysis of monthly variability of thermocline in the South China Sea. *J. Oceanol. Limnol.* 36, 205–215. doi: 10.1007/s00343-017-6151-0

Shen, S., Leptoukh, G. G., Acker, J. G., Yu, Z., and Kempler, S. (2008). Seasonal variations of chlorophyll a concentration in the Northern South China Sea. *IEEE Geosci. Remote Sens. Lett.* 5, 315–319. doi: 10.1109/LGRS.2008.915932

Shih, Y.-Y., Hung, C.-C., Gong, G.-C., Chung, W. C., Wang, Y.-H., Lee, I.-H., et al. (2015). Enhanced particulate organic carbon export at Eddy edges in the oligotrophic Western North Pacific Ocean. *PLoS ONE* 10:e0131538. doi: 10.1371/journal.pone.0131538

Shih, Y.-Y., Hung, C.-C., Huang, S.-Y., Muller, F. L. L., and Chen, Y.-H. (2020). Biogeochemical variability of the upper ocean response to typhoons and storms in the northern South China Sea. *Front. Mar. Sci.* 7:151. doi: 10.3389/fmars.2020.00151

Shih, Y.-Y., Lin, H.-H., Li, D., Hsieh, H.-H., Hung, C.-C., and Chen, C.-T. A. (2019). Elevated carbon flux in deep waters of the South China Sea. *Sci. Rep.* 9:1496. doi: 10.1038/s41598-018-37726-w

Shih, Y. Y., Hsieh, J. S., Gong, G. C., Chou, W. C., Lee, M. A., Hung, C. C., et al. (2013). Field observations of changes in SST, chlorophyll and POC flux in the southern East China Sea before and after the passage of typhoon Jangmi. *Terr. Atmos. Ocean. Sci.* 24, 899–910. doi: 10.3319/TAO.2013.05.23.01(Oc)

Siegel, D. A., Peterson, P., McGillicuddy, D. J., Maritorena, S., and Nelson, N. B. (2011). Bio-optical footprints created by mesoscale eddies in the Sargasso Sea. *Geophys. Res. Lett.* 38:L13608. doi: 10.1029/2011GL047660

Siswanto, E., Ishizaka, J., Morimoto, A., Tanaka, K., Okamura, K., and Kristijono, A. (2008).Ocean physical and biogeochemical responses to the passage of Typhoon Meari in the East ChinaSea observed from Argo float and multiplatform satellites. *Geophys. Res. Lett.* 35:L15604. doi: 10.1029/2008GL035040

Siswanto, E., Ishizaka, J., Yokouchi, K., Tanaka, K., and Tan, C. K. (2007). Estimation of interannual andinterdecadal variations of typhoon-induced primary production: a cases study for the outer shelfof the East China Sea. *Geophys. Res. Lett.* 34:L03604. doi: 10.1029/2006GL028368

Soong, Y. S., Hu, J. H., Ho, C. R., and Niiler, P. P. (1995). Cold cool eddy detected in South China Sea. *Eos Trans. AGU.* 76, 345–347. doi: 10.1029/95EO00209

Su, J. (2004). Overview of the South China Sea circulation and its influence on the coastal physical oceanography outside the Pearl River Estuary. *Cont. Shelf Res.* 24, 1745–1760. doi: 10.1016/j.csr.2004.06.005

Sun, W., Dong, C., Tan, W., and He, Y. (2019). Statistical characteristics of cyclonic warm-core eddies and anticyclonic cold-core eddies in the North Pacific based on remote sensing data. *Remote Sens.* 11:208. doi: 10.3390/rs11020208

Sun, W., Dong, C., Tan, W., Liu, Y., He, Y., and Wang, J. (2018), Vertical structure anomalies of oceanic Eddies and Eddy-induced transports in the South China Sea. *Remote Sens.* 10:795. doi: 10.3390/rs10050795

Sun, W., Dong, C., Wang, R., Liu, Y., and Yu, K. (2017). Vertical structureanomalies of oceanic eddies in the Kuroshio Extension region. *J. Geophys. Res. Oceans* 122, 1476–1496. doi: 10.1002/2016JC012226

Tai, J. H., Chou, W. C., Hung, C. C., Wu, K. C., Chen, Y. H., Chen, T. Y., et al. (2020).Short-term variability of biological production and CO_2 system around dongsha atoll of the Northern South China sea: impact of topography-flow interaction. *Front. Mar. Sci.* 7:511. doi: 10.3389/fmars.2020.00511

Vignudelli, S., Cipollini, P., Reseghetti, F., Fusco, G., Gasparini, G. P., and Manzella, G. M. R. (2003).Comparison between XBT data and TOPEX/Poseidon satellite altimetry in the Ligurian-Tyrrhenian area. *Ann. Geophys.* 21, 123–135. doi: 10.5194/angeo-21-123-2003

Wang, G. H., Su, J. L., and Chu, P. C. (2003). Mesoscale eddies in the South China Sea observed with altimeter data. *Geophys. Res. Lett.* 30:2121. doi: 10.1029/2003GL018532

Weiss, J. (1991). The dynamics of enstrophy transfer in 2-dimensional hydrodynamics. *Phys. D.* 48, 273–294. doi: 10.1016/0167-2789(91)90088-Q

Wu, J., Chung, S.-W., Wen, L.-S., Liu, K.-K., Chen, Y.-L. L., Chen, H.-Y., et al. (2003). Dissolved inorganic phosphorus, dissolved iron, and Trichodesmium in the oligotrophic South China Sea. *Global Biogeochem. Cy.* 17:1008. doi: 10.1029/2002GB001924

Wu, W., Huang, B., and Zhong, C. (2014). Photosynthetic picoeukaryote assemblages in the South China Sea from the Pearl River estuary to the SEATS station. *Aqua. Microb. Ecol.* 71, 271–284. doi: 10.3354/ame01681

Xiu, P., and Chai, F. (2011). Modeled biogeochemical responses to mesoscale eddies in the South China Sea. *J. Geophys. Res.* 116:C10006. doi: 10.1029/2010JC006800

Xiu, P., Chai,. F., Shi, L., Xue, H., and Chao, Y. (2010). A census of eddy activities in the South China Sea during 1993–2007. *J. Geophys. Res.* 115:C03012. doi: 10.1029/2009JC005657

Zhang, W.-Z., Wang, H., Chai, F., and Qiu, G. (2016). Physical drivers of chlorophyll variability in the open South China Sea.

J. Geophys. Res. Oceans 121, 7123–7140. doi: 10.1002/2016JC011983

Zhang, Z., Qiu, B., Klein, P., and Travis, S. (2019). The influence of geostrophic strain on oceanic ageostrophic motion and surface chlorophyll. *Nat. Commun.* 10:2838. doi: 10.1038/s41467-019-10883-w

Zhou, K., Dai, M., Maiti, K., Chen, W., Chen, J., Hong, Q., et al. (2020). Impact of physical and biogeochemical forcing on particle export in the South China Sea. *Prog. Oceanogr*. 187:102403. doi: 10.1016/j.pocean.2020.102403

Conflict of Interest: The authors declare that the research was conducted in the absence of any commercial or financial relationships that could be construed as a potential conflict of interest.

Publisher's Note: All claims expressed in this article are solely those of the authors and do not necessarily represent those of their affiliated organizations, or those of the publisher, the editors and the reviewers. Any product that may be evaluated in this article, or claim that may be made by its manufacturer, is not guaranteed or endorsed by the publisher.

frontiers in Marine Science

ORIGINAL RESEARCH
published: 31 August 2021
doi: 10.3389/fmars.2021.658233

Diversity, Composition, and Activities of Nano- and Pico-Eukaryotes in the Northern South China Sea With Influences of Kuroshio Intrusion

Feipeng Wang[1,2], Bangqin Huang[1,3], Yuyuan Xie[1], Shujie Cai[1], Xiuxiu Wang[1] and Jingli Mu[2]*

[1] State Key Laboratory of Marine Environmental Science, Fujian Provincial Key Laboratory of Coastal Ecology and Environmental Studies, Xiamen University, Xiamen, China, [2] Institute of Oceanography, Minjiang University, Fuzhou, China, [3] Southern Marine Science and Engineering Guangdong Laboratory (Zhuhai), Zhuhai, China

Nano- and pico-eukaryotes play important roles in the diversity and functions of marine ecosystems. Warm, saline, and nutrient-depleted water that originates in the Kuroshio Current seasonally intrudes into the northern South China Sea (NSCS) from autumn to spring. To clarify the mechanisms in shaping the community structure of nano- and pico-eukaryotes as well as impacts of the Kuroshio intrusion on the NSCS ecosystem, genomic DNA and RNA were co-extracted from samples collected at two depths from nine stations, and then the V9 region of 18S rDNA and rRNA was sequenced with high-throughput sequencing. Our results showed that Dinophyceae was the most diverse and abundant nanoeukaryotic group during the study period revealed by both DNA and RNA surveys. In contrast, the relative read abundance of MAST, Pelagophyceae, and Dinophyceae in the size fraction of picoeukaryotes might be largely underestimated by the DNA survey. The RNA survey was the more reliable method to investigate the eukaryotic community structure. Environmental filtering played an important role in shaping the community structure, and the sampling depth became the governing factor of the beta diversity under the environmental setting of stratification during the study period. The spatial variations in the diversity of nanoeukaryotes were subject to the dispersal limitation under the size rule. The effects of the Kuroshio intrusion on the nanoeukaryotic community structure might also be explained by the dispersal limitation. Overall, neutral processes are critical in shaping the community structure of nanoeukaryotes. The relative metabolic activities of nanoeukaryotes were relatively stable in accordance with the high similarity of community structure between sampling sites. The responses of the relative metabolic activities of picoeukaryotes to environmental factors displayed two distinct patterns: positive correlations with salinity and nutrients and negative with temperature for Dinophyceae, MAST, and Pelagophyceae, while reversed patterns for Mamiellophyceae and Radiolaria. Our findings improve the understanding of the nano- and pico-eukaryotic communities in the NSCS and the mechanisms of their assembly.

Keywords: nano- and pico-eukaryotes, RNA/DNA comparison, neutral process, Kuroshio intrusion, northern South China Sea

OPEN ACCESS

Edited by:
Xavier Pochon, The University of Auckland, New Zealand

Reviewed by:
Margaret Anne Mars Brisbin, Okinawa Institute of Science and Technology Graduate University, Japan
Franck Lejzerowicz, University of California, San Diego, United States

****Correspondence:***
Bangqin Huang
bqhuang@xmu.edu.cn

Specialty section:
This article was submitted to Marine Ecosystem Ecology, a section of the journal Frontiers in Marine Science

Received: *25 January 2021*
Accepted: *10 August 2021*
Published: *31 August 2021*

Citation:
Wang F, Huang B, Xie Y, Cai S, Wang X and Mu J (2021) Diversity, Composition, and Activities of Nano- and Pico-Eukaryotes in the Northern South China Sea With Influences of Kuroshio Intrusion. Front. Mar. Sci. 8:658233. doi: 10.3389/fmars.2021.658233

INTRODUCTION

Nano- and pico-eukaryotes (size fractions of 3–20 and 0.2–3 μm, respectively) are present worldwide, abundantly, and persistently in various marine ecosystems (Massana et al., 2015). Much attention has been paid to their astonishing diversity (Caron et al., 2012; Piwosz et al., 2015; de Vargas et al., 2015; Caron et al., 2016) and more recently to their trophic modes and interactions (Piwosz et al., 2018; Adl et al., 2019; Sassenhagen et al., 2019). The photosynthetic groups of nano- and pico-eukaryotes are important contributors to primary production (Grob et al., 2007; Jardillier et al., 2010; Hartmann et al., 2012), which link trophic levels in the microbial food web (Massana et al., 2009), and mixotrophic groups are important bacterial grazers and have the potential to dominate the primary production and bacterivory in marine ecosystems (Unrein et al., 2014). Understanding the diversity, composition, and functions of these groups is therefore important to unveil critical biogeochemical cycles in the sea.

The main goal of microbial ecology is to reveal the mechanisms shaping and maintaining community assembly (Zhou and Ning, 2017). The framework described by Sloan et al. (2006) proposed four main processes for regulating the distribution patterns of microbial communities, including: selection, ecological drift, dispersal, and speciation. These four processes can be further grouped into two categories: deterministic processes (or selective processes) and neutral processes (or stochastic processes) (Sloan et al., 2006; Logares et al., 2013). The deterministic process refers to the governing of the microbial community structure by environmental conditions (e.g., temperature, salinity, and nutrient concentration) and biotic interactions (e.g., predation, competition, and mutualism) (Stegen et al., 2012; Yu et al., 2015; Zhou and Ning, 2017). The neutral process refers to the governing of the microbial community structure by the stochastic process of birth, death, extinction, colonization, and speciation (Hubbell, 2011). The neutral community model (NCM) is an adaptation of the neutral theory, which is very useful in quantifying the importance of neutral process in diverse environments (Logares et al., 2013; Chen et al., 2017). Normalized stochasticity ratio (NST), proposed by Ning et al. (2019), is also powerful in evaluating the community assembly processes (Li et al., 2020). The relative importance of deterministic and neutral processes varies among regions, taxa, and ecosystems (Bahram et al., 2016; Wu et al., 2017b).

Eukaryotic diversity in the ocean has been extensively studied. Most studies targeted one specific size fraction, while a few studies explored diversity across size, usually in four size classes: picoplankton (0.2–3 μm), nanoplankton (3–20 μm), microplankton (20–200 μm), and mesoplankton (200–2000 μm) (de Vargas et al., 2015; Massana et al., 2015; Ramond et al., 2019). These studies disclosed cryptic diversity across oceans with many parasitic and phagotrophic species unseen by traditional methods. The deeply sequenced samples help reacquaint the trophic modes of eukaryotes in the ocean (Ramond et al., 2019). In spite of the dominance of heterotrophs in every size fraction, the ratio between heterotrophs and autotrophs increases with the nominal size of fractions (de Vargas et al., 2015), and cell size constrains fundamental requirements and physiological rates (e.g., growth rate) of plankton as well as biotic interactions (e.g., grazing and competition) between them (Barton et al., 2013). In contrast with picoplankton studied by most research, nanoplankton have higher requirements for nutrients and food, in turn, nanoplankton contribute more to carbon export than picoplankton (Ward and Follows, 2016; Leblanc et al., 2018). Cell size is also an important factor for dispersal limitation to shape community structure. Dispersal limitation was reported to increase with cell size (de Vargas et al., 2015).

High-throughput sequencing (HTS) has revealed the astonishing diversity of protist (microbial eukaryotes) and greatly improved our understanding of their community composition in environmental samples (Edgcomb et al., 2011; Parris et al., 2014; Massana et al., 2015; de Vargas et al., 2015; Piwosz et al., 2018; Liu et al., 2019). Moreover, protistologists have generally accepted that protist assemblages inferred from 18S rRNA gene sequencing (hereafter DNA sequencing) represented the species present. Compared to DNA, RNA is unstable in extracellular conditions, microbial community structures inferred from rRNA sequencing (hereafter RNA sequencing) can exclude sequences from dissolved extracellular pool, dormant cells and dead materials (Not et al., 2009). Thus, the RNA-based approach was used to identify the active species or groups in environmental samples (Massana et al., 2015; Hu et al., 2016; Wang et al., 2019). The RNA: DNA ratio (calculated by relative sequence abundance) has been used as an index for the relative metabolic activity in protist (Hu et al., 2016; Wu and Liu, 2018). However, sequences information derived from the rRNA indicates the possible ribosomal activity (i.e., protein synthesis), which is not a direct indicator of cell activity (Blazewicz et al., 2013). In addition, gene copy numbers, life strategies and histories are very different among species. The RNA: DNA ratio should be used with caution (Blazewicz et al., 2013). Comparison of RNA: DNA ratios usually used in the same species or group among different samples, but not for the comparison between different species or groups (Hu et al., 2016). A previous study showed that the RNA: DNA ratio could be a potential indicator of the upcoming *Phaeocystis globosa* bloom in the eastern English Chanel (Rachik et al., 2018). Xu et al. (2017) observed the varied metabolic activities of protist community at different sampling depths in the South China Sea. Wang et al. (2019) found the varied metabolic activities of picoeukaryotes at spatial scale in the Pacific Ocean.

The South China Sea is the largest marginal sea of the North Pacific (from the equator to 23°N, from 99 to 121°E), and its surface circulation is driven by monsoons (Liu et al., 2002). The North South China Sea (NSCS) exchanges water with the North Pacific through only the Luzon Strait channel. Kuroshio, the western boundary current of the North Pacific, is characterized by warm and saline waters and intrudes seasonally into the NSCS by passing through the Luzon Strait (Nan et al., 2015). Intrusion also generates mesoscale eddies in the NSCS (Wang et al., 2018). The mix of Kuroshio and NSCS waters dilutes nutrients (Du et al., 2013), but has been found to stimulate the activities of ammonia-oxidizing bacteria (Xu et al., 2018; Lu et al., 2019) as well as primary productivity (Huang et al., 2019). The diversity

and composition of picoeukaryotes in the NSCS have been previously explored by high-performance liquid chromatography (Xiao et al., 2018), fluorescence *in situ* hybridization (Wu et al., 2017c), and DNA sequencing (Wu et al., 2014). However, little is known about the diversity and composition of nano-eukaryotes in this area. Moreover, neutral processes have been overlooked in the past, but these processes could be important for Kuroshio-water-influenced areas because ocean currents are always related to the dispersal and colonization of species. This study examines the diversity and community composition of nano- and pico-eukaryotes in the NSCS using size-fractionated filtration and DNA/RNA high-throughput sequencing. The NSCS was sampled in late spring, when a significant proportion of the water mass is of Kuroshio origin, in order to evaluate the relative importance of environmental filtering and neutral processes in shaping communities. In particular, we assess how diversity and community composition of nano- and pico-eukaryotes are affected by deterministic processes by relating metabolic activity and environmental gradients.

MATERIALS AND METHODS

Cruise, Sampling, and Environmental Parameters

The research cruise was conducted in the NSCS from 114 to 119°E and 18 to 22.5°N from May 15th to June 5th, 2016 (**Supplementary Figure 1**). A total of 36 samples (18 picoeukaryotes and 18 nanoeukaryotes) were collected from the surface layer (Sur, 5 m) and deep chlorophyll maximum (DCM) layers at nine stations (**Supplementary Figure 1**). For each sample, 10–20 L of seawater was collected using Niskin bottles (12-L PVC) mounted on a conductivity, temperature, and depth (CTD) rosette (Sea-Bird Electronics, United States). The seawater was pre-filtered through a 20 μm Bolting Cloth to remove large organisms. Then the pre-filtered seawater was sequentially filtered through 3- and 0.2 μm pore size polycarbonate membranes (142 mm diameter, Millipore, United States) using a peristaltic pump. To reduce the loss of RNA samples, the filtration rate in our experiment was controlled at 0.5–1 L/min. The filters (nanoeukaryotic samples: 3–20 μm, picoeukaryotic samples: 0.2–3 μm) were stored in 5 mL cryotubes containing 4.6 mL RNA*later* (Thermo Fisher, Lithuania). The tubes were immediately frozen in liquid nitrogen. In this study, samples were named by the combination of sampling station and depth, for example, D2Sur means the sample was collected at the surface layer at Station D2. Seawater temperature and salinity at each sampling site were recorded using the SBE-911 CTD. Water samples (50 mL) were also collected at the sampling sites and preserved at −20°C for nutrient analysis. The nutrient concentrations (NO_2^-, $NO_2^- + NO_3^-$, PO_4^{3-}, and SiO_3^{2-}) were measured with an AutoAnalyzer using the SkalarSANplus model (Technicon AA3, Bran-Lube, GmbH). The analytical precision of NO_2^-, $NO_2^- + NO_3^-$, PO_4^{3-}, and SiO_3^{2-} were 0.1, 0.1, 0.05, and 0.2 μM. For chlorophyll *a* (Chl *a*) measurement, 1 L of seawater from each sampling depth were filtered onto 25 mm GF/F glass fiber filters (Whatman, United States) under 200 mm Hg pressure. The filters were stored in liquid nitrogen on board. In the laboratory, the filters were submersed in 90% acetone in the dark at −20°C for 24 h. The concentrations of Chl *a* extracted into the acetone were measured with a Trilogy fluorometer (Turner Design, United States) (Welschmeyer, 1994). A geostrophic current is the result of the horizontal pressure gradient and the Coriolis force. The direction of the geostrophic current is parallel to the contour of the sea surface height. To generate a synoptic view of how Kuroshio intrusion physically influences the SCS, sea level anomalies and geostrophic current vectors for the study area were downloaded from the US NOAA National Environmental Satellite, Data, and Information Service.[1]

Kuroshio Fraction at the HTS Sampling Stations

An isopycnal mixing model described by Du et al. (2013) was used to quantify the impact of the Kuroshio intrusion (KI) at our sampling stations. This model assumes that the different water masses are dominated by isopycnal mixing, and diapycnal mixing is comparatively negligible (Du et al., 2013). In this model, two end-members (representing the Kuroshio water and SCS water, respectively, in this study) are required for index estimation. The P4 station (122.959°E, 20.003°N) was used to represent the Kuroshio water mass end-member, and the South East Asian time-series (SEATS) station (116°E, 18°N) was selected to represent the proper South China Sea (SCS) water mass end-member (**Figure 1A**). Notably, the fractional contribution of the two end-members varies depending on the end-member selection. The proportion of the Kuroshio water (R_K) indicated the relative contribution from P4 instead of the "typical Kuroshio" water. Our HTS samples were all collected at the surface (5 m) and DCM layers (less than 100 m), and the average R_K values of the upper 100 m ($R_{Kave-100}$, 1 m interval) were used to represent the KI fraction. Hence, an index was used to indicate the degree of KI influence (KI index) at each sampling station (**Supplementary Table 1**). According to the assumption of this model, Xu et al. (2018) who participated in the same cruise have calculated and published the KI index at all sampling stations. In this study, KI index ≥0.35 was considered to indicate more KI (MKI) affected stations, and the D2, D6, A3, A7, and K4 stations belonged to this category. KI index <0.35, was considered to indicate less KI (LKI), and 2A1, A10, SEATS, and K8 stations belonged to this category (**Figure 1A**).

DNA and RNA Co-extraction, PCR Amplification, and Illumina High-Throughput Sequencing

For each sample, total DNA and RNA were extracted simultaneously using the AllPrep DNA/RNA Min Kit (Qiagen, #80204, Germany). The RNA extracts were purified using the gDNA wipeout buffer (Qiagen, #205311) to remove possible genomic DNA contamination, and then the purified RNA was reverse transcribed into cDNA using the QuantiTect

[1]https://oceanwatch.pifsc.noaa.gov/erddap/griddap/noaa_sla_dt.graph

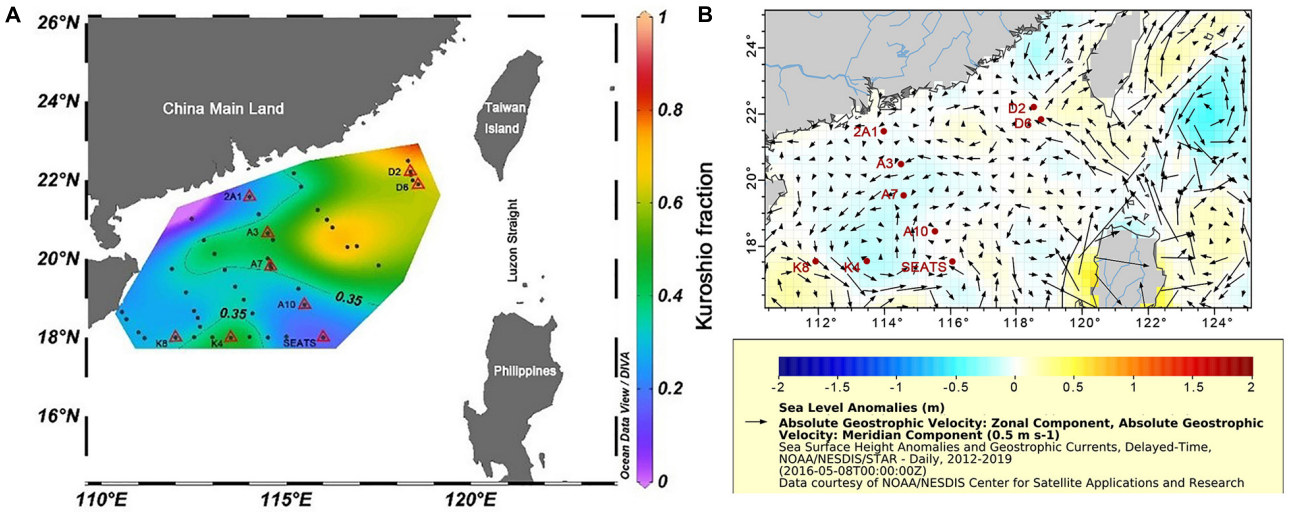

FIGURE 1 | The spatial distribution of **(A)** averaged Kuroshio fraction for upper 100 m (1 m resolution) at our HTS sampling sites (triangles) in the NSCS during the summer cruise conducted in 2016 and **(B)** geostrophic currents and sea level anomalies in a week before the cruise. The P4 station was the end-member used in our study for the Kuroshio water. The thin line stands for the isopleth of R_K (KI index) of 0.35. The color bar indicates the value $R_{kave-100}$ (from 0 to 1).

Reverse Transcription Kit (Qiagen, #205311, Germany). The V9 hypervariable region of the eukaryotic 18S rRNA gene was amplified using the 1380F (5-CCCTGCCHTTTGTACACAC-3) and 1510R (5-CCTTCYGCAGGTTCACCTAC-3) primers (Amaral-Zettler et al., 2009). For each polymerase chain reaction (PCR) reaction, 25 μL mixture contained 12.5 μL 2 × Taq PCR mix (Takara, China), ≤1 μg DNA or cDNA template, 0.1 μM forward primer, and 0.1 μM reverse primer. The PCR program consisted of a 5-min initial denaturation step at 95°C, followed by 34 cycles of denaturation at 94°C for 1 min, annealing at 57°C for 45 s, and elongation at 72°C for 1 min, and a final extension at 72°C for 10 min. Each PCR was performed in duplicates for each DNA and cDNA sample. The duplicate PCR products were pooled and purified using the QIAquick Gel Extraction Kit (Qiagen, #28704, Germany). Amplicons were sent with dry ice to the Novogene sequencing company (Beijing, China) where sequencing library, constructed using the TruSeq DNA PCR-Free Sample Preparation Kit, was prepared and sequenced on a single run using the Illumina HiSeq 2500 platform. High-throughput sequencing data from this study were deposited in the GenBank Sequence Read Archive database under the accession number PRJNA684778.

Sequencing Processing and Statistical Analysis

The raw tags were processed and checked using the Quantitative Insights Into Microbial Ecology (v.1.70) pipeline (Caporaso et al., 2010). Chimeras were identified and discarded after checking with the chimera search module (USEARCH, version 4.2) (Edgar et al., 2011) using the Silva 123 release (Quast et al., 2013) as a reference. The remaining filtered sequences were grouped into operational taxonomic units (OTUs) with 0.95 similarities using UPARSE (v. 7.0.100; Edgar, 2013). The most abundant sequence of each OTU was chosen as the representative sequence, and then taxonomically annotated against the V9_*PR2** database (de Vargas et al., 2015) using BLAST (E value = 10^{-6} and minimum percent query coverage = 0.9) (Altschul et al., 1990). The OTU taxonomy was determined from the top hit based on the BLAST score. OTUs occurring in a single sample, OTUs with only one read (singleton), and OTUs assigned to Metazoan, Bacteria, Archaea, and organelles were also discarded from the downstream analyses. To normalize the sampling effort, the nano- and pico-eukaryotic OTU tables were rarefied to 29,799 and 28,698 reads per sample, respectively (the lowest sequence reads numbers in these tables).

All statistical analyses in our study were performed using the R software (version 3.3.2) (R Core Team, 2014). To investigate whether the community structure of nano- and pico-eukaryotes in the NSCS was affected by the Kuroshio intrusion, principal coordinate analysis (PCoA) was conducted based on the Bray-Curtis distance matrix. Variation-partitioning analysis (VPA, Borcard et al., 1992) was performed to disentangle the relative effects of spatial and environmental factors on variation in nano- and pico-eukaryotic DNA/RNA-based communities using a 3-way PERMANOVA (McArdle and Anderson, 2001). One of the environmental factors was the data matrix consisting of water temperature, $NO_2^- + NO_3^-$, PO_4^{3-}, SiO_3^{2-}, and Chl *a*, and the other was the KI index. It might represent some unmeasured environmental variables that were related to the fraction of Kuroshio water or salinity. The spatial factor was computed as the principal coordinates of neighborhood matrix (PCNM) by the pcnm function of the "vegan" package in R, the second PCNM was used for the VPA analysis in this study. The neutral community model (NCM) was used to determine the potential contribution of neutral processes to the nano- and pico-eukaryotic communities by predicting the relationship between OTUs occurrence and their relative read

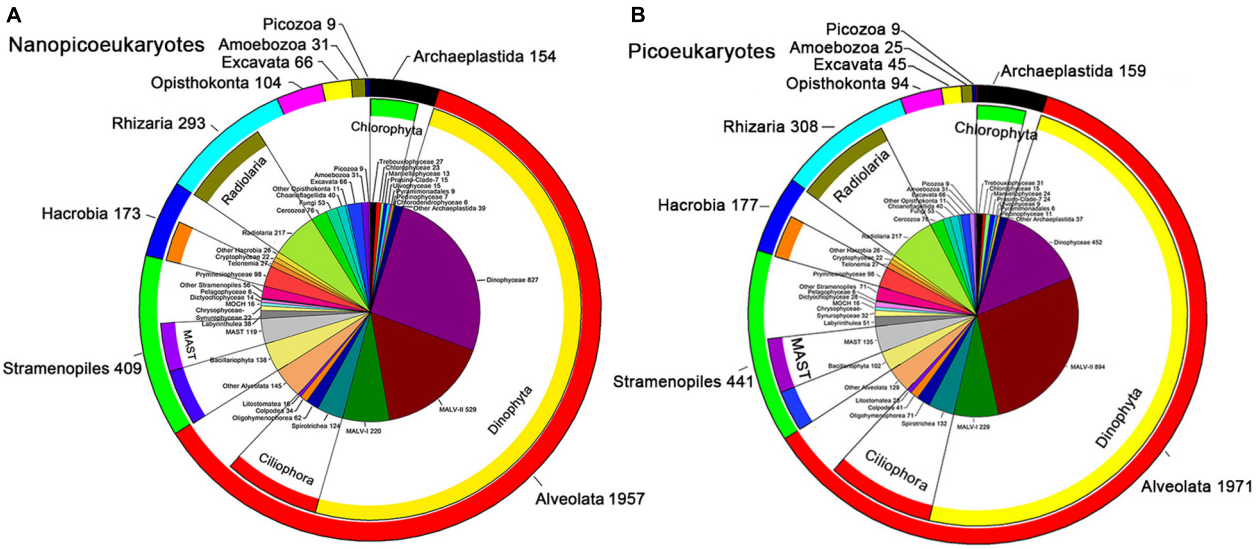

FIGURE 2 | Number of OTUs of nano- **(A)** and pico-eukaryotes **(B)** in the NSCS. The pie chart represents the numbers of OTUs mainly at class level; the inner ring indicates these classes affiliated to the phylum; the outer ring represented the OTUs numbers at super-group level.

abundance (Sloan et al., 2006). The normalized stochasticity test (NST) was used to further confirm the importance of neutral process during nano- and pico-eukaryotic community assembly. The NST was conducted using the function of the "*NST*" R package, which is based on the Ruzicka index (NSTruzicka). This index ranges from 0 to 100%, indicating an increase from more deterministic to more stochastic assembly (Ning et al., 2019). Principal component analysis (PCA) was performed using the "vegan" package in R to access the distribution pattern of eukaryotic assemblages among sampling sites. OTUs only occur in both DNA and RNA sequencing results and appeared in all samples were selected, and the RNA: DNA ratios of the selected OTUs were calculated based on their relative read abundance in the RNA and DNA results (Wu and Liu, 2018).

RESULTS

Environmental Setting

Stations D2 and D6 were close to the Luzon Strait and characterized by higher salinity (34.44–34.81) than other sampling stations. The two stations were greatly influenced by the Kuroshio intrusion, as indicated by KI indexes larger than 0.6 (**Figure 1A**). Kuroshio water affected stations A3 and A7 in the middle of the transect from 2A1 to SEATS (**Figure 1B**). Although station 2A1 is geographically close to the Pearl River Estuary, it was not affected by fresh water during our sampling period. Salinity at surface and DCM layers of 2A1 station were 34.28 and 34.33, respectively, which was close to those of SEATS station. The distinct temperature between surface and DCM (paired Mann-Whitney *U*-test, $p < 0.01$) indicated stratification in water columns (**Supplementary Table 2**). Nutrients at the surface were mostly below the detection limits but were abundant in the DCM. The lower concentrations of Chl *a* at the surface (average 0.08 mg m^{-3}) than at the DCM (average 0.37 mg m^{-3}) (paired Mann-Whitney *U*-test, $p < 0.01$) was consistent with the different nutrient regimes.

Richness of Nano- and Pico-Eukaryotes in the NSCS

In our study, 852,873 high-quality DNA sequences and 997,272 high-quality RNA sequences were obtained from the nanoeukaryotic samples (**Supplementary Tables 5, 6**), whereas 798,801 high-quality DNA sequences, and 787,383 high-quality RNA sequences were obtained from the picoeukaryotic samples (**Supplementary Tables 7, 8**). Note that picoeukaryotic DNA amplicons in A7Sur, SEATS-Sur, and cDNA amplicons in A7Sur and 2A1Sur were too low concentration for library preparation during high-throughput sequencing, and thus these samples were not included. In this study, 3,198 and 3,233 nanoeukaryotic and picoeukaryotic OTUs, respectively, were generated. All the OTUs were affiliated to ten super-groups: Alveolata, Stramenopiles, Hacrobia, Archaeplastida, Rhizaria, Opisthokonta, Picozoa, Amoebozoa, Excavata, and Apusozoa (**Figures 2A,B**).

Alveolata was the richest super-group (in terms of the number of OTUs) in both nano- and picoeukaryotes, accounting for 61.2 and 61.0% of total richness (observed OTU number), respectively (**Figure 2**); followed by Stramenopiles (12.8 and 13.6%) and Rhizaria (9.2 and 9.5%). The other seven super-groups contributed only a small proportion of total richness. Dinophyta and Ciliophora were the top two phyla of Alveolata, Dinophyceae was the richest class of nanoeukaryotes while it was MALV-II for picoeukaryotes.

Among the 3,198 nanoeukaryotic OTUs (3,233 picoeukaryotic OTUs), there were 292 (319) unique DNA OTUs in the MKI stations and 215 (215) in the LKI stations

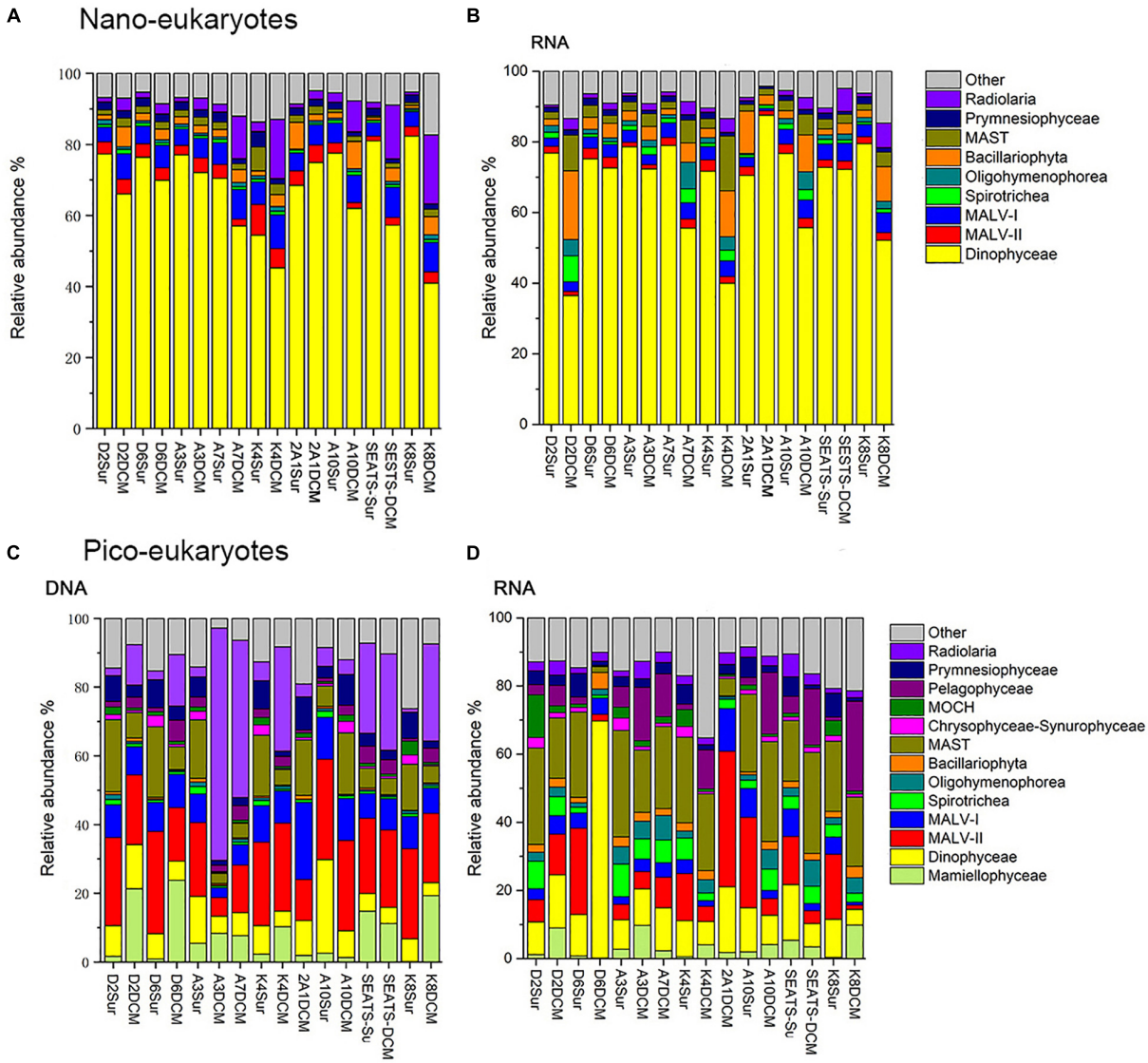

FIGURE 3 | Relative read abundance of nanoeukaryotes **(A,B)** and picoeukaryotes **(C,D)** mainly at class level based on the DNA-derived **(A,C)** and RNA-derived **(B,D)** approaches for each sample. The other category refers to groups with relatively lower sequence abundance.

(**Supplementary Figures 4A,C**); similar numbers were displayed for the RNA samples (**Supplementary Figures 4B,D**). In addition, there were more unique nanoeukaryotic DNA OTUs at the DCM than at the surface (466 vs. 192), similar to the unique picoeukaryotic DNA OTUs (397 vs. 228).

Relative Read Abundance of Nano- and Pico-Eukaryotes

Dinophyceae was the most sequenced nanoeukaryotic class (**Figures 3A,B** and **Table 1**). The most sequenced OTU was Dinophyceae *Gymnodinium_03 aureolum*, representing an average relative read abundance of 12.0 and 10.0% in DNA and RNA samples, respectively, and there was no significant difference between surface and DCM or between LKI and MKI stations. In contrast, MALV-II and MAST were the most sequenced picoeukaryotic classes in DNA and RNA samples, respectively (**Figures 3C,D** and **Table 1**). Radiolaria *Astrosphaera hexagonalis* (OTU5) which favored the DCM environments (Kruskal-Wallis test, $p < 0.05$) in MKI stations (Kruskal-Wallis test, $p < 0.05$) was the most sequenced OTU in picoeukaryotic DNA samples (averagely 8.2%), while Pelagophyceae *Pelagomonas calceolata* (OTU1) was the most sequenced in RNA samples (averagely 6.7%). The relative read abundance of the picoeukaryotic OTU1 was not significantly different between MKI and LKI stations (Kruskal-Wallis test, $p = 0.79$) but higher in DCM than in surface for some stations (Kruskal-Wallis test, $p = 0.06$).

In nanoeukaryotic samples, some of minor classes showed large variations in relative read abundance. For example,

TABLE 1 | Nano- and pico-eukaryotic taxonomic groups (mainly at class level) sequences and percentages across samples based on the DNA and RNA surveys.

Nano- and pico-eukaryotes	Taxonomic groups (mainly at class level)	DNA		RNA	
		Sequences	Percent	Sequences	Percent
Nanoeukaryotes	Dinophyceae	360,733	67.25	365,219	68.09
	MALV-I	33,332	6.21	19,645	3.66
	Radiolaria	29,576	5.51	12,435	2.32
	MALV-II	19,284	3.60	11,801	2.20
	Bacillariophyta	16,644	3.10	30,564	5.70
	Prymnesiophyceae	11,086	2.07	7,545	1.41
	MAST	11,059	2.06	22,038	4.11
	Oligohymenophorea	4,352	0.81	11,763	2.18
	Spirotrichea	4,165	0.78	10.130	1.89
	Others	46,151	8.60	45,332	8.45
Picoeukaryotes	MALV-II	97,736	21.29	55,159	12.01
	Radiolaria	80,770	17.59	13,944	3.04
	MAST	49,047	10.68	97,377	21.21
	MALV-I	43,806	9.54	21,033	4.58
	Dinophyceae	39,608	8.63	67,730	14.75
	Mamiellophyceae	38,181	8.32	16,474	3.59
	Pelagophyceae	23,078	5.03	16,245	3.54
	Chrysophyceae-Synurophyceae	6,204	1.35	7,008	1.53
	MOCH	5,631	1.23	10,805	2.35
	Spirotrichea	4,317	0.94	21,157	4.61
	Oligohymenophorea	3,012	0.66	16,198	3.53
	Bacillariophyta	2,362	0.51	10,505	2.29
	Others	52,378	11.41	68.805	14.98

The other category refers to groups with relatively lower sequence abundance.

Radiolaria was much more sequenced in DCM than in surface (Kruskal-Wallis test, $p < 0.001$) in DNA samples, increases of one order of magnitude occurred in DCM in stations such as A7, K4, SEATS, and K8 (**Figure 3A**). Increases of one order of magnitude in DCM relative to surface also occurred to RNA samples of Bacillariophyta and MAST in a few stations (**Figure 3B**). In picoeukaryotic samples, the distributions of relative read abundance among classes were not as uneven as in nanoeukaryotic samples, therefore some minor classes with large variations could dominate in a few stations. For example, the relative DNA abundance of Radiolaria was up to 67.6 and 45.8% in DCM of MKI stations A3 and A7; and the exceptional case for Dinophyceae was that it contributed 69.5% of RNA samples in DCM of the MKI station D6.

Beta Diversity of Nano- and Pico-Eukaryotic Communities and Controlling Factors

PCoA analysis showed that the beta diversity of both nano- and pico-eukaryotic communities was mainly shaped by sampling depths (**Figure 4**), and the surface and DCM samples were clearly separated on axis 1 while there was no apparent clustering on axis 2. Moreover, a 3-way PERMANOVA was used to assess the relative importance of environmental and spatial factors in shaping eukaryotic communities (**Table 2**). The combined effect of three components could explain 27.3-41.5% of variances in community structure. The unique environmental component [E| KI + S] (by excluding the effects of KI and spatial components) explained the largest proportions of variance for both nano- and pico-eukaryotic communities ($p < 0.05$) with numerically larger proportions for picoeukaryotes. The effect of the unique KI component [KI| E + S] was only significant for nanoeukaryotes ($p < 0.05$), and the effect of the unique spatial component [S| E + KI] was only significant for RNA samples of nanoeukaryotes ($p < 0.05$).

In contrast, NCM explained large fractions (71–81%) of variabilities in the occurrence of nanoeukaryotes and picoeukaryotes during the study period (**Figure 5**). The m value (immigration rate) was higher for nanoeukaryotes than for picoeukaryotes. The $NST_{ruzicka}$ index showed that both DNA and RNA samples of nanoeukaryotes were primarily controlled by stochastic processes (average $NST_{ruzicka}$ = 59 and 62%, respectively; there was no significant difference between DNA and RNA samples, Mann-Whitney U-test, $p = 0.17$), while the value of 38% for DNA samples of picoeukayotes indicated the dominance of deterministic processes (**Figure 6**; difference between nano- and pico-eukaryotes was significant, Mann-Whitney U-test, $p < 0.001$). However, for RNA samples of picoeukaryotes in the DCM, deterministic processes were only marginally stronger than stochastic processes (average $NST_{ruzicka}$ = 50.1%; difference between DNA and RNA samples was significant, Mann-Whitney U-test, $p < 0.001$). The above results indicated that neutral processes (stochastic processes)

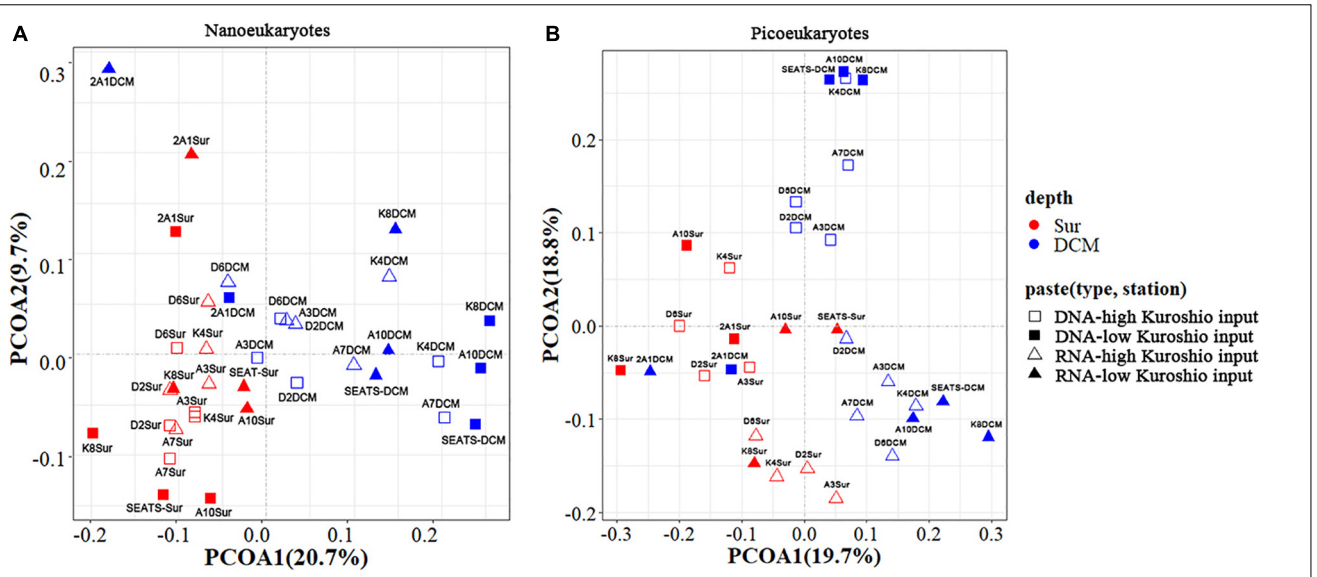

FIGURE 4 | Principal coordinate analysis (PCoA) of nanoeukaryotes **(A)** and picoeukaryotes **(B)** in all samples based on the Bray-Curtis distance matrix. Red color: the surface samples; Blue color: the DCM samples.

played a critical role in shaping the eukaryotic communities during the study period.

Variations in Relative Metabolic Activity of Nano- and Pico-Eukaryotes

PCA analysis was conducted on both the nano- and pico-eukaryotic groups. For nanoeukaryotes, four groups that showed large contributions to the total variation and RNA: DNA ratios different from 1 were identified: Dinophyceae, Radiolaria, MAST, and Bacillariophyta (**Figure 7A**). The average RNA: DNA ratios of Bacillariophyta, MAST, and Radiolaria were significantly higher for the DCM samples than for the surface samples (**Figure 7B**, Mann-Whitney *U*-test, $p < 0.05$, **Supplementary Table 4**). Following the same procedure, five groups of picoeukaryotes were identified: Dinophyceae, Radiolaria, MAST, Mamiellophyceae, and Pelagophyceae (**Figure 7C** and **Supplementary Table 3**, Mann-Whitney *U*-test, $p < 0.05$). The RNA: DNA ratios of four groups showed significant differences between the surface and DCM (**Figure 7D**). The average RNA: DNA ratio of Radiolaria was slightly higher for the surface than for DCM (Mann-Whitney *U*-test, $p < 0.05$). In contrast, Dinophyceae, MAST, and Pelagophyceae showed significantly higher average RNA: DNA ratios at the DCM than at the surface (Mann-Whitney *U*-test, $p < 0.05$).

The relationships between the RNA: DNA ratios and the measured environmental factors (KI, salinity, water temperature, $NO_2^- + NO_3^-$, PO_4^{3-}, SiO_3^{2-}, and Chl *a*) were assessed. The RNA: DNA ratios of the nanoeukaryotic groups Dinophyceae and Radiolaria showed positive correlations with nutrients but negative correlations with the Chl *a* concentration (**Figure 8A** and **Supplementary Figure 5**), although the correlation coefficients were small. The metabolic responses of picoeukaryotes to environmental factors had roughly two patterns (**Figure 8B** and **Supplementary Figure 6**). Dinophyceae, MAST, and Pelagophyceae increased RNA: DNA ratios with salinity, nutrients, and Chl *a* concentration but decreased with water temperature. Meanwhile, RNA: DNA ratios of Mamiellophyceae and Radiolaria correlated negatively with nutrients and salinity but positively with water temperature.

TABLE 2 | Variation partitioning results showing the contribution of unique environmental [E| KI + S], unique KI [KI| E + S], and unique spatial [S| E + KI], as well as combined environmental and KI [E∩KI], environmental and spatial [E∩S], KI and spatial [KI∩S], and all [ALL] component to the components of the nano- and pico-eukaryotic communities inferred from DNA and RNA approaches.

	Variance explained (%)						
	[E|KI + S]	**[KI|E + S]**	**[S|E + KI]**	**[E∩KI]**	**[E∩S]**	**[KI∩S]**	**[ALL]**
Nano-eukaryotes							
DNA	**29.6***	**7.9***	3.7	**32.6***	**28.5***	6.7	**36.3***
RNA	**17.9***	**4.5***	**6.9***	**20.4***	**22.8***	**9.4***	**27.3***
Pico-eukaryotes							
DNA	**32.0***	5.7	3.2	**38.3***	**35.8***	**9.5***	**41.5***
RNA	**25.6***	1.7	0.0	**33.6***	**31.4***	7.5	**33.1***

The bold font and asterisk indicate significant level at $p < 0.05$.

DISCUSSION

Nano- and Pico-Eukaryotic Community Structure in the NSCS During the Study Period

In our study, the high rate of assignment for nano- and pico-eukaryotes could be that many assignments have low taxonomic ranks (e.g., only to "Eukaryota"). Dinophyceae was

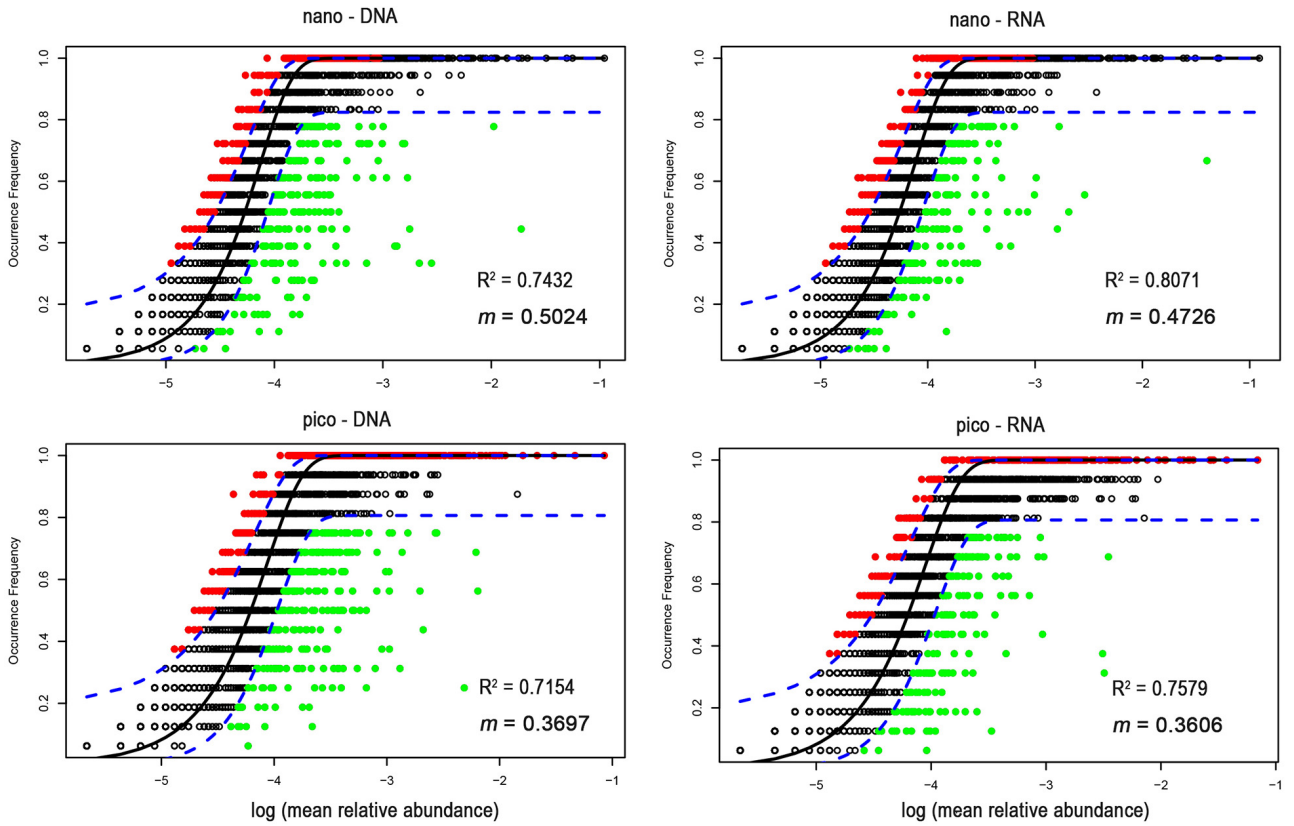

FIGURE 5 | The neutral community model based on the relationship between OTU occurrence and relative read abundance. OTUs with higher frequency than predicted by the model are shown in red, while those with lower frequency are shown in green. OTUs within the predicted range are displayed in black. The dotted line represents the 95% confidence interval (blue dotted line) around the model prediction.

the dominant nanoeukaryotic group and the most diverse picoeukaryotic group at all sampling sites (**Figures 2**, **3** and **Table 1**). Previous studies have revealed that many dinoflagellates were mixotrophic (Stoecker, 1999; Jeong et al., 2004), and the mixotrophic species could consume a wide variety of prey items (Seong et al., 2006; Park et al., 2006; Berge et al., 2008; Glibert et al., 2009). The most sequenced nanoeukaryotic OTU was *G. aureolum*, a common bloom-forming species in temperate waters that was first described by Hulburt (1957). *G. aureolum* contains a horseshoe-shaped apical groove, a nuclear fibrous connective (NFC), and nuclear chambers (Jeong et al., 2010). Jeong et al. (2010) have shown that *G. aureolum* is a mixotrophic dinoflagellate that feeds on *Synechococcus*, heterotrophic bacteria, and some algal species. The Dinophyceae *A. sanguinea* (OTU2) was the dominant nanoeukaryotic species in the DCM layer of station 2A1, which was located close to the Pearl River Estuary. *A. sanguinea* is also a common bloom-forming species with a wide distribution, including the Black Sea (Gómez and Boicenco, 2004), the coast of Hong Kong (Lu and Hodgkiss, 2004), the South Sea off the coast of South Korea (Lim et al., 2008), and the Ariake Sea off the coast of Japan (Katano et al., 2011). Large-scale blooms of *A. sanguinea* have been reported to be a significant threat to seabirds, fish, and shellfish (Jessup et al., 2009; Reis-Filho et al., 2012).

The MALV-I and II groups accounted for a significant proportion of the picoeukaryotic relative read abundance in the DNA survey. However, their relative read abundance

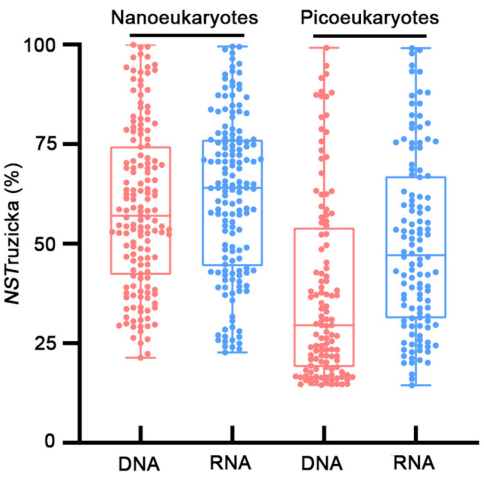

FIGURE 6 | Normalized stochasticity test values for the Ruzicka index ($NST_{ruzicka}$).

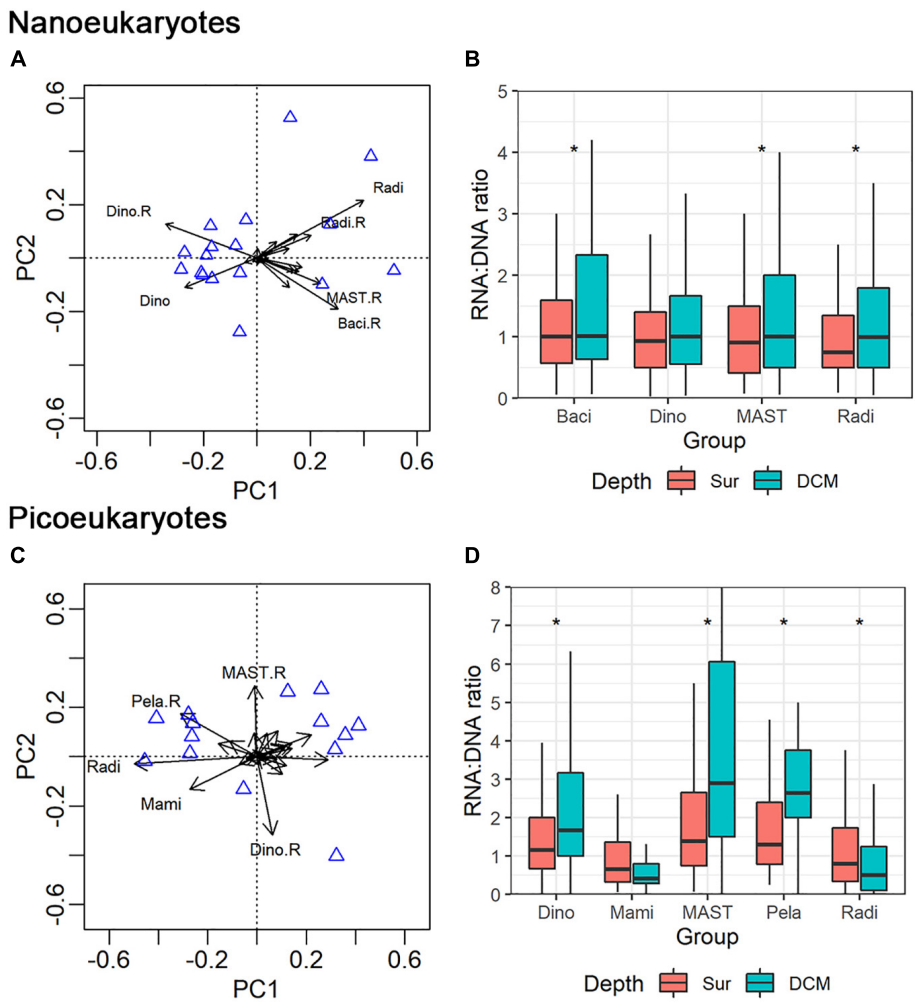

FIGURE 7 | Principal component analysis (PCA) showed the distribution pattern of nano- **(A)** and pico-eukaryotic **(C)** major groups (mainly at class level) in combined DNA and RNA samples. Range of RNA: DNA ratios of the major groups of nano- **(B)** and pico-eukaryotes **(D)** at surface and DCM layers. Mam: Mamiellophyceae; Pel: Pelagophyceae; Rad: Radiolaria; Dino: Dionophyceae; Baci: Bacillariophyta. The asterisk indicates significant level at $p < 0.05$.

decreased largely in the RNA survey. Most species in the MALV-I and II groups have been characterized as parasites in a range of hosts (Bachvaroff et al., 2012). Similarly, the most sequenced OTU of picoeukaryotes was Radiolaria *A. hexagonalis* (OTU_5), accounting for 8.5% of total DNA sequences, but decreased sharply to 0.5% in the RNA survey. The different results between DNA and RNA surveys and the underlying reasons have been extensively discussed. Sample collection by the size-fractionated filtration may introduce artifacts, for example, cell breakage and fragments may go through filters and be retained in smaller size fractions (Massana et al., 2015). The Radiolaria *A. hexagonalis* is supposed to be an organism with the diameter of 150 μm (Haeckel, 1887). Its DNA sequences appearing in a smaller fraction may represent dead individuals or swarmer cells for reproduction (Li and Endo, 2020). In addition, high rDNA gene copy numbers of some species may cause them to be overrepresented in DNA samples. Massana et al. (2015) also reported that the MALV-I and II groups were overrepresented in the DNA survey for all size fractions of eukaryotes in European coastal waters and they attributed this phenomenon to higher rDNA gene copy numbers of these two groups than other eukaryotes. Overall, it is likely that the DNA survey overestimated the relative read abundance of Radiolaria, MALV-I, and MALV-II, while underestimated that of MAST, Pelagophyceae, and Dinophyceae (**Figure 3D**). MAST is a remarkably diverse group of uncultured species (Massana et al., 2014). MASTs are heterotrophic flagellates preying on bacteria (Lin et al., 2012). They are widely distributed in the temperate and tropical oceans and supposed to play an important role in the microbial food web (Seeleuthner et al., 2018). The RNA survey found the average relative read abundance of 21.4% belonged to the MAST group relative to only 10.3% by the DNA survey (**Figure 3**). This large bias reinforced the argument that the RNA survey is a more reliable method than the DNA survey to investigate the eukaryotic community structure

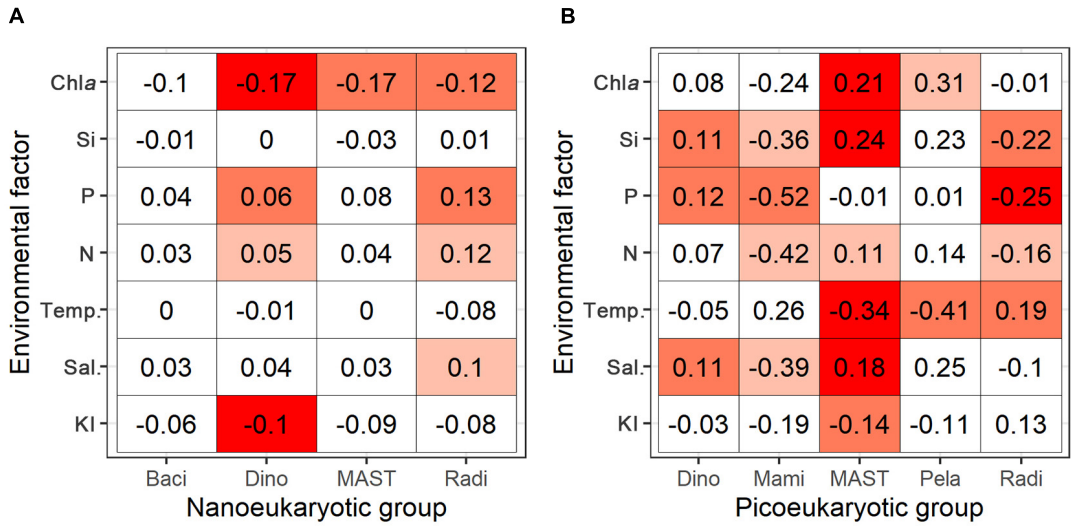

FIGURE 8 | Heatmaps of correlation matrix (spearman correlation) of the RNA: DNA ratio versus environmental factors for major groups of nanoeukaryotes **(A)** and picoeukaryotes **(B)**, including Bacillariophyta (Baci), Dinophyceae (Dino), Mamiellophyceae (Mami), MAST, Pelagophyceae (Pela), and Radiolaria (Radi). Environmental factors include Kuroshio intrusion (KI), salinity (Sal.), water temperature (Temp.), nitrate + nitrite (N), phosphate (P), silicate (Si), and chlorophyll *a* concentration (Chl *a*). Numbers are the correlation coefficients, background colors (from dark red to white) indicate significance levels associated to the *p* values (0.001, 0.01, 0.05) and no significance.

(Massana et al., 2015). The RNA-based results showing the abundant MAST reflected active functions of the microbial food web in the NSCS.

In contrast, the DNA and RNA surveys reported roughly the same community structure for nanoeukaryotes in this study (**Figure 3**). However, we should not interpret this consistency as an indication of that the DNA survey did not obscure the results with artifacts. The consistency between the DNA and RNA samples happened at the group level where Dinophyceae dominated supremely. But differences emerged at the OTU level, for example, *A. sanguinea* (OTU2) at the DCM layer of station 2A1 occupied 68.2% of RNA sequences relative to 32.7% of DNA sequences. The findings emphasized again the necessity to conduct the RNA survey to tackle with the technical issues of the DNA survey (Massana et al., 2015).

Filters may collect material belonging to species from other size fractions. We found many pairs of OTUs with identical sequences between the nano- and pico-eukaryotes. This phenomenon has long been an issue for analyzing plankton samples (de Vargas et al., 2015; Massana et al., 2015). de Vargas et al. (2015) reported that 64% of all OTUs spanned two or more size classes and Massana et al. (2015) even found 32–55% of picoeukaryotic OTUs and 20–41% of nanoeukaryotic OTUs in filtrate passed through a 0.8 μm-pore-size membrane filter. We found a significant proportion of shared OTUs were MALV-II and MALV-I (also known as Syndiniales). Syndiniales are marine parasites that infect hosts from protists to fish, they could be detected in the pico-sized fraction because they produce small, flagellated cells (dinospores) to infect new hosts (Guillou et al., 2008; Siano et al., 2011). Moreover, identical sequences do not essentially indicate identical species because OTUs are clusters. In spite of deficiencies, filtration is the most feasible way to study diversity for size characteristics of plankton, and the method did reveal distinctness of size classes in terms of relative abundance of OTUs (**Table 1** and **Figure 3**). Besides, BLAST identifies sequences with the top-hit taxon in the reference database which cannot guarantee the most accurate result because in fact there always have a series of hits with good scores; although BLAST is the common method, more robust methods for taxonomic annotation shall be further considered.

Differences in Mechanisms Shaping the Community Structure of Nano- and Pico-Eukaryotes in the NSCS

Environmental filtering played an important role in shaping the community structure of both nano- and pico-eukaryotes (**Table 2**). Phytoplankton growth in the NSCS is limited by nitrogen in the open water and phosphate and silicate in the river water influenced area (Yin et al., 2000, 2001). During the season when the study was conducted, the monsoon winds were too weak to break down water-column stratification, which prevents nutrients reentering the surface. Then, nutrients at the surface layer were depleted by light-saturated photosynthesis while nutrients at the DCM layer were abundant due to light limitation on nutrient uptake. Therefore, the community structure at the DCM layer was distinct from that at the surface layer because of the combined effects of photoadaptation and elevated nutrients, and decreased water temperature might play a role as well. Thus, it was not surprising that depth was the governing factor of the beta diversity (Countway et al., 2010; Wu et al., 2017a; Giner et al., 2020).

However, most of the variation in community structure were explained by neutral processes (**Figures 5, 6**), which was consistent with previous studies (Sloan et al., 2006). Furthermore, the $NST_{ruzicka}$ was higher for nanoeukaryotes than for picoeukaryotes, and the VPA results also indicated that nanoeukaryotes were subject to dispersal limitation while picoeukaryotes were not (**Table 2**). The latter was consistent with a previous study which suggested increasing dispersal limitation with cell size (de Vargas et al., 2015). Neutral community theory explains the species of a local community as a sample of the meta community regulated by immigration and extinction at the local level, therefore dissimilarities between local communities will be a function of the geographical distance (namely the dispersal limitation). The NCM displayed that the immigration rate for nanoeukaryotes was no less than that for picoeukaryotes (**Figure 5**). However, the number of individuals for the same amount of carbon biomass decreases with cell size, then the possibility of extinction at the local level will be higher for nanoeukaryotes than for picoeukaryotes, then the dispersal limitation might be explained. Ecological drift might be another mechanism accounting for the diversity of nanoeukaryotic community in this study. Ecological drift is stochastic changes in population resulted from equal chances of individuals to reproduce or die. Ecological drift drifts community composition from expectations of environmental filtering (Vellend, 2010). In this study, Dinophycease dominated the nanoeukaryotic communities by contributing two-thirds of the relative read abundance (**Figures 3A,B**), which might limit other taxa from establishing their population, leading to high similarity between local nanoeukaryotic communities.

The Kuroshio intrusion is supposed to mainly affect the eastern NSCS. However, **Figure 1B** shows the geostrophic currents in the NSCS in early May 2016 (a week before the cruise), which flowed into the NSCS through the northern Luzon Strait, and generated a westward branch at approximately 21°N. The current reached approximately 114°E and 20°N. Therefore, substantial fractions of Kuroshio water were found in the middle of the NSCS (**Figure 1A**). The VPA analysis showed that variations in the nanoeukaryotic community structure could be partially explained by the KI index. The reason could be different activities of archaea and bacteria that was reported by Xu et al. (2018). That study showed distinctly higher ammonia oxidation rates by archaea and bacteria in the MKI stations than in the LKI stations. Ammonia-oxidizing archaea and bacteria were dependent on dissolved organic matter, which was proportional to the faction of Kuroshio water.

Relative Metabolic Activities in Relation to Community Structure

Some argued that the discrepancy between the DNA and RNA surveys was mainly due to high rDNA copy numbers of some species or dead cells and did not reflect the metabolic activities, which, however, could be assessed by the relative changes of the RNA: DNA ratio between sampling sites (Hu et al., 2016). For example, a previous study in the northwestern Pacific Ocean reported different relative metabolic activities of Mamiellophyceae for different nutrient regimes (Wang et al., 2019). In this study, Mamiellophyceae also showed lower RNA: DNA ratios with increased nutrients (**Figure 8B**). Dinophyceae and MAST showed significantly higher RNA: DNA ratios at the DCM layers than at the surface layers (**Figure 7B**), which was consistent with a previous study in the South China Sea (Xu et al., 2017). That study reported that Dinophyceae, MALV-I, and MALV-II had the highest relative metabolic activities in middle layers (200, 300, and 500 m), followed by deep layers (1,000, 1,500, 2,000, and 3,900 m) and shallow layers (5, 25, and 75 m). Our analysis indicated that the relative metabolic activities of Dinophyceae and MAST increased with nutrients and the Chl *a* concentration (**Figure 8**).

In contrast, the correlations between the metabolic activities of nanoeukaryotes and environmental factors were not apparent (**Figure 8**). Nanophytoplankton were expected to have lower nutrient affinity than picophytoplankton, therefore nanophytoplankton would show larger changes of the relative metabolic activities than picophytoplankton for the ranges of nutrients in this study. However, our results contradicted this expectation. The metabolic activities of nanoeukaryotes might change parallelly, thus the changes were not reflected by the relative values. The relatively stable RNA: DNA ratios might account partially for the dominance of nanoeukaryotic Dinophyceae at all sampling sites (**Figure 7B**), but the underlying mechanism was not clear.

CONCLUSION

In the NSCS during the study period, Dinophyceae was the most diverse and sequenced nanoeukaryotic group revealed by both DNA and RNA surveys. In contrast, the relative read abundance of MAST, Pelagophyceae, and Dinophyceae in the size fraction of picoeukaryotes might be largely underestimated by the DNA survey. Environmental filtering played an important role in shaping the community structure, and the sampling depth became the governing factor of the beta diversity under the environmental setting of stratification during the study period. The spatial variations in the diversity of nanoeukaryotes were subject to the dispersal limitation under the size rule. The effects of the Kuroshio intrusion on the nanoeukaryotic community structure might also be explained by the dispersal limitation. Overall, neutral processes are critical in shaping the community structure of nanoeukaryotes. The relative metabolic activities of nanoeukaryotes were relatively stable in accordance with the high similarity of community structure between sampling sites. The responses of the relative metabolic activities of picoeukaryotes to environmental factors displayed two distinct patterns. Our

findings improved the understanding of the nano- and pico-eukaryotic communities in the NSCS and the mechanisms of their assembly.

DATA AVAILABILITY STATEMENT

The data presented in the study are deposited in the GenBank Sequence Read Archive repository, accession number PRJNA684778, https://www.ncbi.nlm.nih.gov/.

AUTHOR CONTRIBUTIONS

FW, YX, and BH designed the experiments. FW carried out the experiments and wrote the manuscript. SC helped analyze the data. YX and BH provided critical feedback and revised the manuscript. XW and JM helped analyze the data and revised the manuscript. All authors contributed to the article and approved the submitted version.

FUNDING

This work was supported by grants from the National Natural Science Foundation of China (Nos. U1805241 and 41776146), Monitoring and Protection of Ecology and Environment in the East Pacific Ocean (No. DY135-E2-5-5), and the study was also partially supported by NSFC (No. 41890803) and Xiamen University Presidential Fund (20720180102).

ACKNOWLEDGMENTS

We thank JianYu Hu for providing the CTD data and Minhan Dai for proving the nutrient data. The nutrients concentration data could be acquired from the supporting information of Xu et al. (2018). This study also benefited from the discussion with Wenxue Wu at Sun Yat-sen University, and Lizhen Lin, Jixin Chen, and Heng Zhu at Xiamen University for their assistances in phytoplankton sample collections and analyses. We thank NSFC Shiptime Sharing Project for supporting the cruises by R/V *Dongfanghong* 2 (No. NORC2015-05), and we also acknowledge captains and crew for their cooperation during the cruise. We truly thank two reviewers whose comments helped to improve and clarify this manuscript.

SUPPLEMENTARY MATERIAL

The Supplementary Material for this article can be found online at: https://www.frontiersin.org/articles/10.3389/fmars.2021.658233/full#supplementary-material

REFERENCES

Adl, S. M., Bass, D., Lane, C. E., Lukeš, J., Schoch, C. L., Smirnov, A., et al. (2019). Revisions to the classification, nomenclature, and diversity of eukaryotes. *J. Eukaryot. Microbiol.* 66, 4–119. doi: 10.1111/jeu.12691

Altschul, S. F., Gish, W., Miller, W., Myers, E. W., and Lipman, D. J. (1990). Basic local alignment search tool. *J. Mol. Biol.* 215, 403–410. doi: 10.1016/S0022-2836(05)80360-2

Amaral-Zettler, L. A., Mccliment, E. A., Ducklow, H. W., and Huse, S. M. (2009). A method for studying protistan diversity using massively parallel sequencing of v9 hypervariable regions of small-subunit ribosomal RNA genes. *PLoS One* 4:e6372. doi: 10.1371/journal.pone.0006372

Bachvaroff, T. R., Kim, S., Guillou, L., Delwiche, C. F., and Coats, D. W. (2012). Molecular diversity of the syndinean genus *Euduboscquella* based on single-cell PCR analysis. *Appl. Environ. Microbiol.* 78, 334–345. doi: 10.1128/aem.06678-11

Bahram, M., Kohout, P., Anslan, S., Harend, H., Abarenkov, K., and Tedersoo, L. (2016). Stochastic distribution of small soil eukaryotes resulting from high dispersal and drift in a local environment. *ISME J.* 10, 885–896. doi: 10.1038/ismej.2015.164

Barton, A. D., Pershing, A. J., Litchman, E., Record, N. R., Edwards, K. F., Kiørboe, T., et al. (2013). The biogeography of marine plankton traits. *Ecol. Lett.* 16, 522–534. doi: 10.1111/ele.12063

Berge, T., Hansen, P. J., and Moestrup, Ø (2008). Prey size spectrum and bioenergetics of the mixotrophic dinoflagellate *Karlodinium armiger*. *Aquat. Microb. Ecol.* 50, 289–299. doi: 10.3354/ame01166

Blazewicz, S. J., Barnard, R. L., Daly, R. A., and Firestone, M. K. (2013). Evaluating rRNA as an indicator of microbial activity in environmental communities: limitations and uses. *ISME J.* 7, 2061–2068. doi: 10.1038/ismej.2013.102

Borcard, D., Legendre, P., and Drapeau, P. (1992). Partialling out the spatial component of ecological variation. *Ecology* 73, 1045–1055. doi: 10.2307/1940179

Caporaso, J. G., Kuczynski, J., Stombaugh, J., Bittinger, K., Bushman, F. D., Costello, E. K., et al. (2010). QIIME allows analysis of high-throughput community sequencing data. *Nat. Methods* 7, 335–336. doi: 10.1038/nmeth.f.303

Caron, D. A., Alexander, H., Allen, A. E., Archibald, J. M., Armbrust, E. V., Bachy, C., et al. (2016). Probing the evolution, ecology and physiology of marine protists using transcriptomics. *Nat. Rev. Microbiol.* 15, 6–20. doi: 10.1038/nrmicro.2016.160

Caron, D. A., Countway, P. D., Jones, A. C., Kim, D. Y., and Schnetzer, A. (2012). Marine protistan diversity. *Annu. Rev. Mar. Sci.* 4, 467–493.

Chen, W. D., Pan, Y. B., Yu, L. Y., Yang, J., and Zhang, W. J. (2017). Patterns and processes in marine microeukaryotic community biogeography from Xiamen coastal waters and intertidal sediments, Southeast China. *Front. Microbiol.* 8:1912. doi: 10.3389/fmicb.2017.01912

Countway, P. D., Gast, R. J., Dennett, M. R., Savai, P., Rose, J. M., and Caron, D. A. (2010). Distinct protistan assemblages characterize the euphotic zone and deep sea (2500 m) of the western north Atlantic (Aargasso Sea and Gulf Stream). *Environ. Microbiol.* 9, 1219–1232. doi: 10.1111/j.1462-2920.2007.01243.x

de Vargas, C., Audic, S., Henry, N., Decelle, J., Mahé, F., Logares, R., et al. (2015). Eukaryotic plankton diversity in the sunlit ocean. *Science* 348:1261605. doi: 10.1126/science.1261605

Du, C., Liu, Z., Dai, M., Kao, S. J., and Li, Y. (2013). Impact of the Kuroshio intrusion on the nutrient inventory in the upper northern South China Sea: insights from an isopycnal mixing model. *Biogeosciences* 10, 6419–6432. doi: 10.5194/bg-10-6419-2013

Edgar, R. C. (2013). UPARSE: highly accurate OTU sequences from microbial amplicon reads. *Nat. Methods* 10, 996–998. doi: 10.1038/NMETH.2604

Edgar, R. C., Haas, B. J., Clemente, J. C., Quince, C., and Knight, R. (2011). UCHIME improves sensitivity and speed of chimera detection. *Bioinformatics* 27, 2194–2200. doi: 10.1093/bioinformatics/btr381

Edgcomb, V., Orsi, W., Bunge, J., Jeon, S., Christen, R., Leslin, C., et al. (2011). Protistan microbial observatory in the Cariaco Basin, Caribbean. I. Pyrosequencing *vs* Sanger insights into species richness. *ISME J.* 5, 1344–1356. doi: 10.1038/ismej.2011.6

Giner, C. R., Pernice, M. C., Balagué, V., Duarte, C. M., and Massana, R. (2020). Marked changes in diversity and relative activity of picoeukaryotes with depth in the world ocean. *ISME J.* 14, 437–449. doi: 10.1038/s41396-019-0506-9

Glibert, P. M., Burkholder, J. M., Kana, T. M., Alexander, J., Skelton, H., and Shilling, C. (2009). Grazing by Karenia brevis on *Synechococcus* enhances its growth rate and may help to sustain blooms. *Aquat. Microb. Ecol.* 55, 17–30. doi: 10.3354/ame01279

Gómez, F., and Boicenco, F. (2004). An annotated checklist of dinoflagellates in the Black Sea. *Hydrobiologia* 517, 43–59. doi: 10.1023/B:HYDR.0000027336.05452.07

Grob, C., Ulloa, O., Li, W., Alarcón, G., Fukasawa, M., and Watanabe, S. (2007). Picoplankton abundance and biomass across the eastern South Pacific Ocean along latitude 32.5°S. *Mar. Ecol. Prog. Ser.* 332, 53–62. doi: 10.3354/meps332053

Guillou, L., Viprey, M., Chambouvet, A., Welsh, R. M., Kirkham, A. R., Massana, R., et al. (2008). Widespread occurrence and genetic diversity of marine parasitoids belonging to *Syndiniales* (Alveolata). *Environ. Microbiol.* 10, 3349–3365. doi: 10.1111/j.1462-2920.2008.01731.x

Haeckel, E. (1887). "Report on the radiolaria collected by H.M.S. Challenger during the years 1873–1876. pp. i–viii [=1–8], i–clxxxviii [=1–188], 1–1803," in *Report of the Scientific Results of the Voyage of H.M.S. Challenger During the Years 1873–1876 Under the Com-mand of Captain George S. Nares and Captain Frank Tourle Thomson, Zoology. vol. XVIII [=18].*, eds Thomson, C. W. and J. Murray (London, Edinburgh, Dublin), 1–140.

Hartmann, M., Grob, C., Tarran, G. A., Martin, A. P., Burkill, P. H., Scanlan, D. J., et al. (2012). Mixotrophic basis of Atlantic oligotrophic ecosystems. *Proc. Natl. Acad. Sci. U. S. A.* 109, 5756–5760. doi: 10.1073/pnas.1118179109

Hu, S. K., Campbell, V., Connell, P., Gellene, A. G., Liu, Z., Terrado, R., et al. (2016). Protistan diversity and activity inferred from RNA and DNA at a coastal site in the eastern North Pacific. *FEMS Microbiol. Ecol.* 92:fiw050. doi: 10.1093/femsec/fiw050

Huang, Y., Laws, E., Chen, B., and Huang, B. (2019). Stimulation of heterotrophic and autotrophic metabolism in the mixing zone of the Kuroshio Current and northern South China Sea: implications for export production. *J. Geophys. Res. Biogeo.* 124, 2645–2661. doi: 10.1029/2018JG004833

Hubbell, S. P. (2011). *The Unified Neutral Theory of Biodiversity and Biogeography (MPB-32)*. Princeton: Princeton University Press.

Hulburt, E. M. (1957). The taxonomy of unarmored Dinophyceae of shallow embayments on Cape Cod, Massachusetts. *Biol. Bull.* 112, 196–219. doi: 10.2307/1539198

Jardillier, L., Zubkov, M. V., Pearman, J., and Scanlan, D. J. (2010). Significant CO_2 fixation by small prymnesiophytes in the subtropical and tropical northeast Atlantic Ocean. *ISME J.* 4, 1180–1192. doi: 10.1038/ismej.2010.36

Jeong, H. J., Yoo, Y. D., Kang, N. S., Rho, J. R., Seong, K. A., Park, J. W., et al. (2010). Feeding by red-tide dinoflagellate *Gymnodinium aureolum* from the western Korean waters. *Aquat. Microb. Ecol.* 59, 239–255.

Jeong, H. J., Yoo, Y. D., Kim, J. S., Kim, T. H., Kim, J. H., Kang, N. S., et al. (2004). Mixotrophy in the phototrophic harmful alga *Cochlodinium polykrikoides* (Dinophycean): prey species, the effects of prey concentration and grazing impact. *J. Eukaryot. Microbiol.* 51, 563–569. doi: 10.1111/j.1550-7408.2004.tb00292.x

Jessup, D. A., Miller, M. A., Ryan, J. P., Nevins, H. M., Kerkering, H. A., Mekebri, A., et al. (2009). Mass stranding of marine birds caused by a surfactant-producing red tide. *PLoS One* 4:e4550. doi: 10.1371/journal.pone.0004550

Katano, T., Yoshida, M., Yamaguchi, S., Hamada, T., Yoshino, K., and Hayami, Y. (2011). Diel vertical migration and cell division of bloom-forming dinoflagellate *Akashiwo sanguinea* in the Ariake Sea, Japan. *Plankton Benthos. Res.* 6, 92–100. doi: 10.3800/pbr.6.92

Leblanc, K., Quéguiner, B., Diaz, F., Cornet, V., Michel-Rodriguez, M., Xavier, D. D. M., et al. (2018). Nanoplanktonic diatoms are globally overlooked but play a role in spring blooms and carbon export. *Nat. Commun.* 9:953.

Li, L., and Endo, K. (2020). Phylogenetic positions of "pico-sized" radiolarians from middle layer waters of the tropical Pacific. *Prog. Earth. Planet. Sci.* 7:70. doi: 10.1186/s40645-020-00384-6

Li, P., Li, W., Dumbrell, A. J., Liu, M., Li, G., Wu, M., et al. (2020). Spatial variation in soil fungal communities across paddy fields in subtropical China. *mSystems* 5, e00704–19. doi: 10.1128/mSystems.00704-19

Lim, W. A., Lee, Y. S., and Lee, S. G. (2008). Characteristic of environmental factors related to outbreak and decline of *Cochlodinium polykrikoides* bloom in the southeast coastal waters of Korea, 2007. *J. Korean Soc. Oceanogr.* 13, 325–332.

Lin, Y., Campbell, T., Chung, C., Gong, G., Chiang, K., and Worden, A. (2012). Distribution patterns and phylogeny of marine stramenopiles in the north Pacific Ocean. *Appl. Environ. Microbiol.* 78, 3387–99. doi: 10.1128/AEM.06952-11

Liu, J., Meng, Z., Liu, X., and Zhang, X. (2019). Microbial assembly, interaction, functioning, activity and diversification: a review derived from community compositional data. *Mar. Life Sci. Technol.* 1, 112–128. doi: 10.1007/s42995-019-00004-3

Liu, K., Chao, S., Shaw, P., Gong, G., Chen, C., and Tang, T. (2002). Monsoon-forced chlorophyll distribution and primary production in the South China Sea: observations and a numerical study. *Deep-Sea Res. I Oceanogr.* 49, 1387–1412. doi: 10.1016/S0967-0637(02)00035-3

Logares, R., Lindström, E. S., Langenheder, S., Logue, J. B., Paterson, H., Laybourn-Parry, J., et al. (2013). Biogeography of bacterial communities exposed to progressive long-term environmental change. *ISME J.* 7, 937–948. doi: 10.1038/ismej.2012.168

Lu, S. H., and Hodgkiss, I. J. (2004). Harmful algal bloom causative collected from Hong Kong waters. *Hydrobiologia* 512, 231–238. doi: 10.1023/B:HYDR.0000020331.75003.18

Lu, Y., Wen, Z., Shi, D., Lin, W., Bonnet, S., Dai, M., et al. (2019). Biogeography of N_2 fixation influenced by the western boundary current intrusion in the South China Sea. *J Geophys. Res. Ocean* 124, 6983–6996. doi: 10.1029/2018JC014781

Massana, R., del Campo, J., Sieracki, M. E., Audic, S., and Logares, R. (2014). Exploring the uncultured microeukaryote majority in the oceans: reevaluation of ribogroups within stramenopiles. *ISME J.* 8, 854–866. doi: 10.1038/ismej.2013.204

Massana, R., Gobet, A., Audic, S., Bass, D., Bittner, L., Boutte, C., et al. (2015). Marine protist diversity in European coastal waters and sediments as revealed by high-throughput sequencing. *Environ. Microbiol.* 17, 4035–4049. doi: 10.1111/1462-2920.12955

Massana, R., Unrein, F., Rodriguez-Martinez, R., Forn, I., Lefort, T., Pinhassi, J., et al. (2009). Grazing rates and functional diversity of uncultured heterotrophic flagellates. *ISME. J.* 3, 588–596. doi: 10.1038/ismej.2008.130

McArdle, B. H., and Anderson, M. J. (2001). Fitting multivariate models to community data: a comment on distance-based redundancy analysis. *Ecology* 82, 290–297. doi: 10.2307/2680104

Nan, F., Xue, H., and Yu, F. (2015). Kuroshio intrusion into the South China Sea: a review. *Prog. Oceangr.* 137, 314–333. doi: 10.1016/j.pocean.2014.05.012

Ning, D., Deng, Y., Tiedje, J. M., and Zhou, J. (2019). A general framework for quantitatively assessing ecological stochasticity. *Proc. Natl. Acad. Sci. U. S. A.* 116, 16892–16898. doi: 10.1073/pnas.1904623116

Not, F., del Campo, J., Balagué, V., de Vargas, C., and Massana, R. (2009). New insights into the diversity of marine picoeukaryotes. *PLoS One* 4:e7143. doi: 10.1371/journal.pone.0007143

Park, M. G., Kim, S. J., Kim, H. S., Myung, G. O., Kang, Y. G., and Yih, W. H. (2006). First successful culture of the marine dinoflagellate *Dinophysis acuminata*. *Aquat. Microb. Ecol.* 45, 101–106. doi: 10.1007/BF00407285

Parris, D. J., Ganesh, S., Edgcomb, V. P., DeLong, E. F., and Stewart, F. J. (2014). Microbial eukaryote diversity in the marine oxygen minimum zone off northern Chile. *Front. Microbiol.* 5:543. doi: 10.3389/fmicb.2014.00543

Piwosz, K., Całkiewicz, J., Gołębiewski, M., and Creer, S. (2018). Diversity and community composition of pico- and nanoplanktonic protists in the Vistula River estuary (Gulf of Gdańsk, Baltic Sea). *Estuar. Coast. Shelf Sci.* 207, 242–249. doi: 10.1016/j.ecss.2018.04.013

Piwosz, K., Spich, K., Całkiewicz, J., Weydmann, A., Kubiszyn, A. M., and Wiktor, J. M. (2015). Distribution of small phytoflagellates along an Arctic fjord transect. *Environ. Microbiol.* 17, 2393–2406. doi: 10.1111/1462-2920.12705

Quast, C., Pruesse, E., Yilmaz, P., Gerken, J., Schweer, T., Yarza, P., et al. (2013). The SILVA ribosomal RNA gene database project: improved data processing and web-based tools. *Nucleic Acids Res.* 41, D590–D596. doi: 10.1093/nar/gks1219

R Core Team. (2014). *R: a Language and Environment For Statistical Computing*. Vienna: R Foundation for Statistical Computing.

Rachik, S., Christaki, U., Li, L. L., Genitsaris, S., Breton, E., and Monchy, S. (2018). Diversity and potential activity patterns of planktonic eukaryotic microbes in a mesoeutrophic coastal area (eastern English Channel). *PLoS One* 13:e0196987. doi: 10.1371/journal.pone.0196987

Ramond, P., Sourisseau, M., Simon, N., Romac, S., Schmitt, S., Rigaut-Jalabert, F., et al. (2019). Coupling between taxonomic and functional diversity in protistan

coastal communities: functional diversity of marine protists. *Environ. Microbiol.* 21, 730–749. doi: 10.1111/1462-2920.14537

Reis-Filho, J. A., da Silva, E. M., Nunes, J. A. C. C., and Barros, F. (2012). Effects of a red tide on the structure of estuarine fish assemblages in northeastern Brazil. *Internat. Rev. Hydrobiol.* 97, 389–404. doi: 10.1002/iroh.201101457

Sassenhagen, I., Irion, S., Jardillier, L., Moreira, D., and Christaki, U. (2019). Protist interactions and community structure during early autumn in the Kerguelen region (Southern Ocean). *Protist* 171:125709. doi: 10.1016/j.protis.2019.125709

Seeleuthner, Y., Mondy, S., Lombard, V., Carradec, Q., Pelletier, E., Wessner, M., et al. (2018). Single-cell genomics of multiple uncultured stramenopiles reveals underestimated functional diversity across oceans. *Nat. Commun.* 9:310. doi: 10.1038/s41467-017-02235-3

Seong, K. A., Jeong, H. J., Kim, S., Kim, G. H., and Kang, J. H. (2006). Bacterivory by co-occurring red-tide algae, heterotrophic nanoflagellates, and ciliates. *Mar. Ecol. Prog. Ser.* 322, 85–97. doi: 10.3354/meps322085

Siano, R., Alves-de-Souza, C., Foulon, E., Bendif, E. M., Simon, N., Guillou, L., et al. (2011). Distribution and host diversity of Amoebophryidae parasites across oligotrophic waters of the Mediterranean Sea. *Biogeosciences* 8, 267–278. doi: 10.5194/bg-8-267-2011

Sloan, W. T., Lunn, M., Woodcock, S., Head, I. M., Nee, S., and Curtis, T. P. (2006). Quantifying the roles of immigration and chance in shaping prokaryote community structure. *Environ. Microbiol.* 8, 732–740. doi: 10.1111/j.1462-2920.2005.00956.x

Stegen, J. C., Lin, X. J., Konopka, A. E., and Fredrickson, J. K. (2012). Stochastic and deterministic assembly processes in subsurface microbial communities. *ISME J.* 6, 1653–1664. doi: 10.1038/ismej.2012.22

Stoecker, D. K. (1999). Mixotrophy among dinoflagellates. *J. Eukaryot. Microbiol.* 46, 397–401. doi: 10.1111/j.1550-7408.1999.tb04619.x

Unrein, F., Gasol, J. M., Not, F., Forn, I., and Massana, R. (2014). Mixotrophic haptophytes are key bacterial grazers in oligotrophic coastal waters. *ISME J.* 8, 164–176. doi: 10.1038/ismej.2013.132

Vellend, M. (2010). Conceptual synthesis in community ecology. *Q. Rev. Biol.* 85, 183–206. doi: 10.1086/652373

Wang, F., Xie, Y., Wu, W., Sun, P., Wang, L., and Huang, B. (2019). Picoeukaryotic diversity and activity in the northwestern Pacific Ocean based on rDNA and rRNA high-throughput sequencing. *Front. Microbiol.* 9:3259. doi: 10.3389/fmicb.2018.03259

Wang, L., Huang, B., Laws, E. A., Zhou, K., Liu, X., Xie, Y., et al. (2018). Anticyclonic eddy edge effects on phytoplankton communities and particle export in the northern South China Sea. *J. Geophys. Res. Oceans* 123, 7632–7650. doi: 10.1029/2017JC013623

Ward, B. A., and Follows, M. J. (2016). Marine mixotrophy increases trophic transfer efficiency, mean organism size, and vertical carbon flux. *Proc. Natl. Acad. Sci. U. S. A.* 113, 2958–2963. doi: 10.1073/pnas.1517118113

Welschmeyer, N. A. (1994). Fluorometric analysis of chlorophyll a in the presence of chlorophyll b and pheopigments. *Limnol. Oceanogr.* 39, 1985–1992. doi: 10.4319/lo.1994.39.8.1985

Wu, W., Huang, B., and Zhong, C. (2014). Photosynthetic picoeukaryote assemblages in the South China Sea from the Pearl River estuary to the SEATS station. *Aquat. Microb. Ecol.* 71, 271–284. doi: 10.3354/ame01681

Wu, W., and Liu, H. (2018). Disentangling protist communities identified from DNA and RNA surveys in the Pearl River-South China Sea Continuum during the wet and dry seasons. *Mol. Ecol.* 27, 4627–4640. doi: 10.1111/mec.14867

Wu, W., Logares, R., Huang, B., and Hsieh, H. (2017a). Abundant and rare picoeukaryotic sub-communities present contrasting patterns in the epipelagic waters of marginal seas in the northwestern Pacific Ocean. *Environ. Microbiol.* 19, 287–300. doi: 10.1111/1462-2920.13606

Wu, W., Lu, H., Sastri, A., Yeh, Y., Gong, G., Chou, W., et al. (2017b). Contrasting the relative importance of species sorting and dispersal limitation in shaping marine bacterial versus protist communities. *ISME J.* 12, 485–494. doi: 10.1038/ismej.2017.183

Wu, W., Wang, L., Liao, Y., Xu, S., and Huang, B. (2017c). Spatial and seasonal distributions of photosynthetic picoeukaryotes along an estuary to basin transect in the northern South China Sea. *J. Plankton Res.* 3, 1–13. doi: 10.1093/plankt/fbx017

Xiao, W., Wang, L., Edward, L., Xie, Y., Chen, Y., Liu, X., et al. (2018). Realized niches explain spatial gradients in seasonal abundance of phytoplankton groups in the South China Sea. *Prog. Oceanogr.* 162, 223–239. doi: 10.1016/j.pocean.2018.03.008

Xu, D., Li, R., Hu, C., Sun, P., Jiao, N., and Warren, A. (2017). Microbial Eukaryote diversity and activity in the water column of the South China Sea based on DNA and RNA high-throughput sequencing. *Front. Microbiol.* 8:1121. doi: 10.3389/fmicb.2017.01121

Xu, M., Zhang, W., Zhu, Y., Liu, L., Zheng, Z., Wan, X. S., et al. (2018). Enhanced ammonia oxidation caused by lateral Kuroshio intrusion in the boundary zone of the northern South China Sea. *Geophys. Res. Lett.* 45, 6585–6593. doi: 10.1029/2018GL077896

Yin, K., Qian, P., Chen, J., Hsieh, D., and Harrison, P. J. (2000). Dynamics of nutrients and phytoplankton biomass in the pearl river estuary and adjacent waters of Hong Kong during summer: preliminary evidence for phosphorus and silicon limitation. *Mar. Ecol. Prog. Ser.* 194, 295–305. doi: 10.3354/meps194295

Yin, K., Qian, P., Wu, M., Chen, J., Huang, L., Song, X., et al. (2001). Shift from P to N limitation of phytoplankton growth across the pearl river estuarine plume during summer. *Mar. Ecol. Prog. Ser.* 221, 17–28. doi: 10.1038/s41467-018-03376-9

Yu, L., Zhang, W., Liu, L., and Yang, J. (2015). Determining microeukaryotic plankton community around Xiamen Island, southeast China, using Illumina MiSeq and PCR-DGGE techniques. *PLoS One* 10:e0127721. doi: 10.1371/journal.pone.0127721

Zhou, J. Z., and Ning, D. L. (2017). Stochastic community assembly: does it matter in microbial ecology? *Microbiol. Mol. Biol. Rev.* 81, e00002–17. doi: 10.1128/MMBR.00002-17

Conflict of Interest: The authors declare that the research was conducted in the absence of any commercial or financial relationships that could be construed as a potential conflict of interest.

Publisher's Note: All claims expressed in this article are solely those of the authors and do not necessarily represent those of their affiliated organizations, or those of the publisher, the editors and the reviewers. Any product that may be evaluated in this article, or claim that may be made by its manufacturer, is not guaranteed or endorsed by the publisher.

frontiers in Marine Science

ORIGINAL RESEARCH
published: 06 September 2021
doi: 10.3389/fmars.2021.678832

Eutrophication and Hypoxia in Tropical Negombo Lagoon, Sri Lanka

Hsueh-Han Hsieh[1], Ming-Hsiu Chuang[1], Yung-Yen Shih[1,2], W. Sanjaya Weerakkody[1,3], Wei-Jen Huang[1], Chin-Chang Hung[1], François L. L. Muller[1], R. R. M. K. P. Ranatunga[4] and D. S. Wijethunga[4]*

[1] Department of Oceanography, National Sun Yat-sen University, Kaohsiung, Taiwan, [2] Department of Applied Science, Republic of China Naval Academy, Kaohsiung, Taiwan, [3] Department of Fisheries and Aquaculture, Faculty of Fisheries and Marine Sciences & Technology, University of Ruhuna, Matara, Sri Lanka, [4] Center for Marine Science and Technology, University of Sri Jayewardenepura, Nugegoda, Sri Lanka

Hypoxic events are becoming frequent in some estuaries and coastal waters due to over-enrichment of anthropogenic nutrients, organic matter, and/or due to restricted water circulation. The coastal lagoons and estuaries of Sri Lanka are facing high population pressure and lacking sufficient infrastructure. Coastal lagoons may receive high anthropogenic inputs of natural or untreated nitrogen and phosphorus wastes, and consequently result in hypoxic conditions while sluggish circulation occurred. In this study, we examined the spatiotemporal variability of eutrophication and hypoxia in the Negombo Lagoon, one of the most productive and sensitive coastal ecosystems in Sri Lanka. Based on seasonal measurements of dissolved oxygen, nutrients, chlorophyll-*a* (Chl-*a*), particulate and dissolved organic carbon (POC and DOC), we concluded that eutrophication and hypoxia occurred in both the dry and wet seasons. The main contributing factors were high seawater temperature and poor water circulation in the dry season and high nutrient loading combined with elevated POC and DOC inputs in the wet season.

Keywords: hypoxia, eutrophication, organic pollution, nutrients pollution, Negombo Lagoon

OPEN ACCESS

Edited by:
Jesper H. Andersen, NIVA Denmark Water Research, Denmark

Reviewed by:
Helena Galvão, Universidade do Algarve, Portugal
Michelle Jillian Devlin, Centre for Environment, Fisheries and Aquaculture Science (CEFAS), United Kingdom

****Correspondence:***
Chin-Chang Hung
cchung@mail.nsysu.edu.tw

Specialty section:
This article was submitted to Marine Ecosystem Ecology, a section of the journal Frontiers in Marine Science

Received: *11 March 2021*
Accepted: *05 August 2021*
Published: *06 September 2021*

Citation:
Hsieh H-H, Chuang M-H, Shih Y-Y, Weerakkody WS, Huang W-J, Hung C-C, Muller FLL, Ranatunga RRMKP and Wijethunga DS (2021) Eutrophication and Hypoxia in Tropical Negombo Lagoon, Sri Lanka. Front. Mar. Sci. 8:678832. doi: 10.3389/fmars.2021.678832

INTRODUCTION

Sensitive coastal ecosystems such as wetlands, lagoons, and barrier-built estuaries are threatened by a combination of both marine and/or river discharge factors such as elevated seawater temperature, nutrient pollution, organic matter loading, and/or sediment inputs from turbid river waters (Hoegh-Guldberg and Smith, 1989; Hoegh-Guldberg et al., 2007; Mayfield et al., 2013; Breitburg et al., 2018; Cziesielski et al., 2019). Anthropogenic loading of nitrogen and phosphorus in particular has led to the proliferation of pelagic and benthic algal species that are not readily consumed and thus represent a burden in terms of their eutrophication potential (Andersen et al., 2006; Yan et al., 2021). In turn, the microbial respiration and decomposition of this biomass leads to increasing rates of oxygen consumption (Kemp et al., 2005) and oxygen concentrations decrease to less than 2 mg L^{-1}, the level not suitable for fish, shrimp, or crab (Renaud, 1986). In many of these ecosystems, hypoxia has indeed become a frequent seasonal or persistent feature.

Most hypoxic zones in coastal habitats can be directly linked to population growth and increasing industrial and tourism activity which generates industrial and municipal wastes and results in increased terrestrial fluxes of nutrients (Diaz and Rosenberg, 1995; Steckbauer et al., 2011). This type of eutrophication is most commonly seen in estuaries, coastal and marginal sea

areas such as the Changjiang estuary (Wei et al., 2007), the East China Sea (Chen, 2008; Chen and Guo, 2020; Chen et al., 2020, 2021), the Shenzhen Bay (Yan et al., 2021) and the Gulf of Mexico (Rabalais et al., 2001; Bianchi et al., 2010). In most of these regions, anthropogenic eutrophication has results in hypoxia.

The Negombo Lagoon is a shallow basin estuary running parallel to the west coast of Sri Lanka. It has an average water depth of less than 2 m and covers an area of approximately 32 km^2. At its northern end, it connects to the Indian Ocean through a narrow channel (**Figure 1**). At its southern end, it is connected to the Muthurajawela marsh (Samarakoon and Van Zon, 1991; IUCN, 2013). Negombo Lagoon receives freshwater from Attanagalu Oya as well as from Ja-Ela. In addition, the Hamilton canal brings freshwater from the Kelani River into the lagoon. The total freshwater discharge ranges from 20 to 225 $m^3\ s^{-1}$, with the Attanagalu Oya contributing over 70% (Rajapaksha, 1997; Amarasinghe et al., 1999). Negombo receives rainfall from the South-western monsoon from April to June and September to December (>200 mm/month, wet season) and there is little precipitation (less than 100 mm/month) during the remaining months (dry season) (Department of Meteorology, Sri Lanka and Devendra, 2002; **Figure 2A**).

Negombo Lagoon is a part of a larger coastal wetland along with Muthurajawela marsh. The lagoon and its associated sensitive habitats such as mangrove and sea grass beds provide an array of ecosystem services also serves as a shrimp and fish nursery and a nutrient source for the coastal waters. The Negombo lagoon has been one of the most productive coastal ecosystems which support important fishery (DFAR, 2012a). Negombo has an active fishery industry and it contributes 16% for Sri Lanka fish production with 80% of marine fish and 20% of lagoon fish (Urban Development Authority, 2019; **Figure 2B**). The Negombo fish market, situated in the lagoon, is a potential pollution source within the lagoon, but organic wastes from the fish market are discharged directly into the estuary and the data are not measured.

The population in Negombo area is continuously increasing from 60,000 in 1950 to 161,484 in 2020 (**Figure 2C**). The area around the Negombo Lagoon attracts nearly 350,000 tourists annually and concentrates 32% of all domestic tourist visits in Sri Lanka (Urban Development Authority, 2019; **Figure 2D**). Food waste and untreated human waste from heavily populated areas as well as from hotels situated in the Negombo Lagoon catchment (Malawaraaratchi, 2003) add up to very significant inputs of nutrients and organic matter which contribute to the overall degradation of water quality.

The presence of these pollutants and the subsequent eutrophic conditions may result in depletion of dissolved oxygen which is thought to be responsible for the fish kill events reported in the lagoon and surrounded waters (Dahanayaka et al., 2012; Narangoda et al., 2015; National Aquatic Resources Research and Development Agency, 2019). Dahanayaka et al. (2012) reported elevated chlorophyll-*a* (Chl-*a*) concentrations in the dry season as evidence for the above sequence of events, but nutrient and dissolved oxygen (DO) data were not available.

Here we report on the results of three seasonal surveys conducted along the main axis of the lagoon and extending into the adjacent coastal zone. We examined hydrodynamics, dissolved oxygen, nutrients, dissolved and particulate organic carbon across the full salinity mixing gradient between freshwater and seawater in order to investigate the eutrophication and hypoxia events in the dry and wet seasons. This study was focused on studying potential factors currently responsible for the development of eutrophication and hypoxia in the Negombo Lagoon and to assess the extent to which long-term, global changes may affect the lagoon in the future.

MATERIALS AND METHODS

Sampling Site and Hydrographic Parameter Analysis

Water samples were collected from 18 stations chosen to encompass the full salinity gradient from freshwater to coastal seawater. The only exception was Station 11, a private deck of a waterfront hotel (**Figure 1**) selected for real-time data recording purposes. Sampling took place in two dry seasons (February 2019 and 2020) and one wet season (October 2019). Precipitation was major in April to June and September to December, two rain seasons in southwest of Sri Lanka. The higher precipitation was shown in May in first rain season, and shown in October in second wet season. Dry season was regarded in inter wet season period, which monthly precipitation was lower than 100 mm day^{-1}. Sampling was conducted in the morning and repeated in the evening in the wet season. Salinity, pH, dissolved oxygen, and temperature were measured by conductivity meter (WTW Cond 3310, Germany), a pH meter (WTW pH 3110, Germany) and a dissolved oxygen meter (WTW Oxi 3310, Germany). Subsamples were filtered immediately in the shore-based laboratory and stored until analysis. Nitrite (NO_2), nitrate (NO_3), silicate (SiO_3), phosphate (PO_4), total suspended matter (TSM), chlorophyll-*a* (Chl-*a*), particulate organic carbon (POC), and dissolved organic carbon (DOC) were determined according to the methods described in Hung et al. (2000, 2013). The methods used for the determination of nutrients (nitrite, nitrate, phosphate, and silicate) were based on the standard dye methods which have been adapted for use with a flow injection analyzer by Gong et al. (1996). Chl-*a* concentrations were measured with a Turner Designed 10-AU-005 fluorometer using the non-acidification method (Gong et al., 1996; Shih et al., 2019). Concentrations of TSM and POC were measured following the methods of Hung et al. (2013) while DOC was measured by the method of Hung et al. (2016). The ecological water quality state (European Commission, 2000) was used to classify the conditions of water in Negombo lagoon. Different levels of nutrients were corresponded to different state from "very good" to "bad," the threshold of each category was presented in **Table 1**.

Statistical Analysis

A trophic state index (TSI) for brackish water lagoon (Kratzer and Brezonik, 1981) was used in this study to understand the

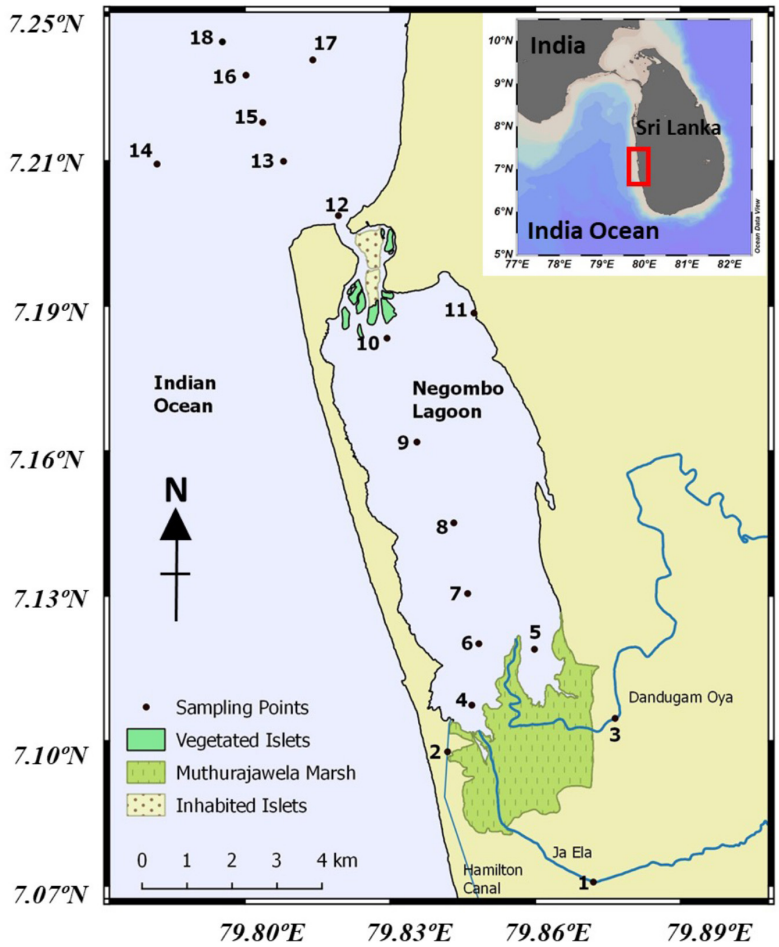

FIGURE 1 | Sampling locations in the Negombo Lagoon and the adjacent coastal waters.

trophic state in Negombo lagoon in dry and wet seasons. TSI of the lagoon water was calculated using TSI_{TP}, TSI_{TN}, and $TSI_{Chl\text{-}a}$. The equations are described as follows:

$$TSI_{TP} = 14.42 \ln(TP) + 4.15$$

$$TSI_{TN} = 14.43 \ln(TN) + 54.45$$

$$TSI_{Chl} = 9.81 \ln(Chl) + 30.6$$

The units of TP and Chl-*a* were in $\mu g\ L^{-1}$, and TN was in $mg\ L^{-1}$. According to Kratzer and Brezonik (1981), TSI below 40 represents to oligotrophic state, TSI between 40 and 50 represents to mesotrophic, TSI from 50 to 70 represents to eutrophic, TSI above 70 represents to hypereutrophic state of the water.

A principal components analysis (PCA) was used for identifying the data similarities and differences. For example, projections considered the principal components 1 and 2 for hydrographic parameters (temperature, salinity, DO, nutrients, Chl-*a*, DOC, and POC etc.) and sampling locations (located in river, lagoon, and ocean) in dry and wet seasons in the Negombo lagoon.

RESULTS

Hydrographic Settings, DO, DOC, and POC in the Dry Season

Sea surface temperatures showed a relatively uniform distribution along the entire transect and fell within the previously reported range of 27.5–31.7°C (Malawaraaratchi, 2003). Concentrations of dissolved and particulate chemicals measured in the surface waters are listed in **Table 1** and their distribution along the salinity gradient is shown in **Figure 2**. Surface salinity gradually increased from the southern part (stations 1–3) of the lagoon toward the lagoon inlet and the Indian Ocean (station 14) (**Table 1**) except one lower salinity (Sal = 28.5) at station 11 compared to station 10 (Sal = 30.0) in February 2019, suggesting an input of fresh water from hotels along the northeast lagoon. This depressed salinity at station 11 was associated with hypoxia (**Figure 2B**), even though DO concentrations at all other stations were above 4 mg l^{-1} (**Table 2**). In February 2020, however, DO values at stations 1–3 fell below 3 mg l^{-1} suggesting that oxygen deficient conditions

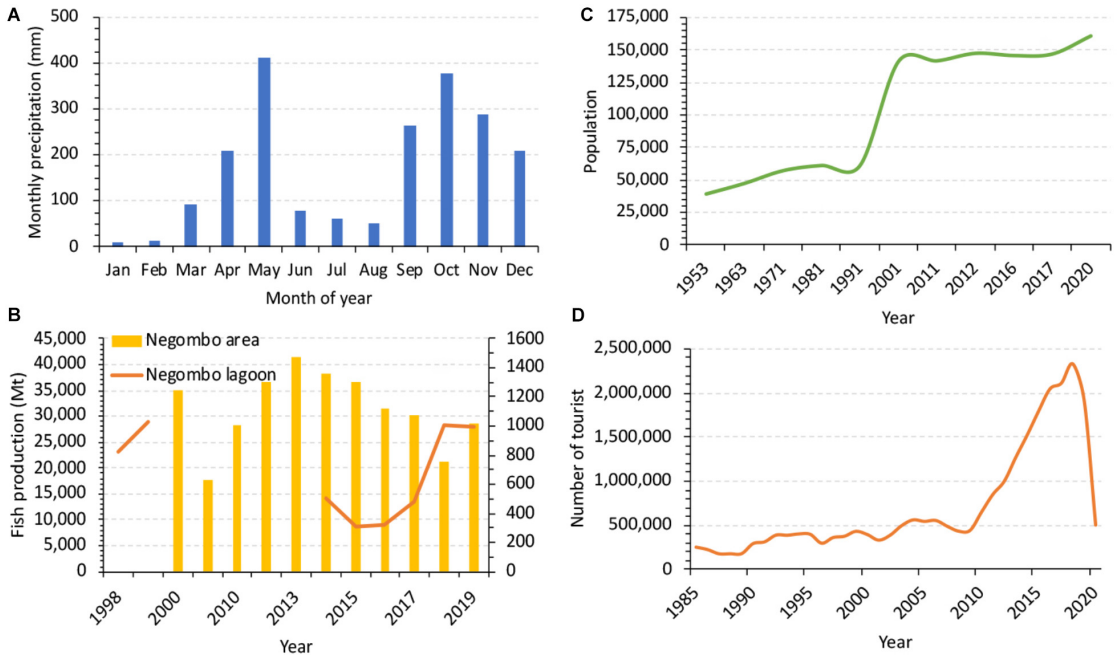

FIGURE 2 | Information of **(A)** monthly precipitation, **(B)** fish production, **(C)** population, and **(D)** tourists in the Negombo lagoon and the adjacent area.

were more widespread in February 2020 than in February 2019 (**Table 2**).

As with DO, pH values were lowest in the southern portion of the lagoon (inner lagoon, stations 1–3) and gradually increased to typical oceanic values (8.0–8.2) toward the lagoon inlet (**Figure 3C**), following a typical trend.

Concentrations of TSM and chlorophyll-*a* (Chl-*a*) were highest at low salinities as well as in freshwater, i.e., inner lagoon, Ja-Ela and Dandugam Oya rivers, and decreased steadily toward the lagoon inlet (**Figures 3D,E**). The elevated Chl-*a* concentrations (0.5–22.4 mg m^{-3}) were comparable to previously reported values in the same lagoon by Gammanpila (2010).

Concentrations of dissolved inorganic phosphate, silicate and nitrogen (=nitrite + nitrate) were elevated throughout the inner lagoon (**Figures 3H–J**). Some dissolved nitrogen with high concentration values (13–39 μM) were turn the water to "poor" in ecological water quality state, and this occurred in both 2019 and 2020.

The cumulative explanation of PCA variables in PC1 and PC2 axis was 69.9% in dry season (**Figure 4A**). Different characteristic of water was separated by PC1 and PC2 axis. For example, positive part of PC1 was related to high salinity, pH and DO in lagoon water. Nutrients and biogenic parameters (Chl-*a*, POC, PN, and DOC) were in negative part in lagoon water. On PC2 axis, nitrite, nitrate and silicate were predominate in positive part and phosphate, chlorophyll, POC, PN, and DOC were on the opposite side (**Figure 4A**).

The molar ratio (Si:N:P) in different waters was presented in dry season (**Figure 5A**). Highly biotic activity of phosphate in phytoplankton growth was evaluated as a P limitation in dry season in 2019 according to Redfield molar ratio, but it was N limitation in dry season in 2020 (**Table 1** and **Figure 5A**).

The TSI in Negombo lagoon was decreased from river mouth to lagoon mouth in both 2019 and 2020 (**Figure 6**). Overall, water nature was shown as the mesotrophic state overall in 2019, but the trophic state in some sampling stations turned into the eutrophic state in 2020 (**Figure 6**).

Hydrographic Settings, DO, DOC, and POC in the Wet Season

The distributions of surface temperature, DO, pH, TSM, Chl-*a*, POC, and DOC along the salinity gradient are shown in **Figures 3A–G** which combines data of the two surveys conducted in the wet season of 2019. Salinity values at all stations were generally lower than those recorded in the dry season due to seasonal precipitation. Sea surface temperature was relatively uniform and lower than in the dry season. In the first survey, DO

TABLE 1 | Classification of ecological water quality state by concentration inorganic nutrients, this table was modified from European Commission (2000).

Water quality state	NO_2 (μM)	NO_3 (μM)	PO_4 (μM)	O_2 (%)
Very good	<0	<0.81	<0.05	100
Good	0.02–0.11	0.81–8.06	0.05–0.32	80–100
Medium	0.11–0.43	8.06–24.19	0.32–1.06	60–80
Poor	0.46–2.17	24.19–40.32	1.06–3.19	30–60
Bad	>2.17	>40.32	>3.19	>30

TABLE 2 | Water temperature, salinity, dissolved oxygen (DO), pH, dissolved nitrogen (NO3+NO2), total suspended matter (TSM) and chlorophyll-*a* (Chl-*a*) in the Negombo Lagoon in the dry season 2019 and 2020.

Station	T (°C)	Salinity	DO (μM)	pH	DIN (μM)	PO4 (μM)	TSM (mg L^{-1})	Chl-*a* (mg m^{-3})
2019.02.27∼02.28								
1	32.0	1.6	143.7	6.9	39.00	0.09	7.80	7.2
3	31.9	4.1	125.3	6.8	22.85	0.11	9.20	8.6
5	32.7	19.2	202.1	7.8	0.57	0.03	13.60	8.7
6	31.9	20.5	206.1	8.0	2.21	0.04	8.60	7.2
8	31.2	23.2	203.0	8.0	0.89	0.04	7.10	6.7
10	30.8	30.0	176.0	8.0	1.09	0.04	6.40	5.5
11	29.6	28.5	27.5	7.3	0.96	0.12	7.70	5.3
12	30.4	31.7	146.5	8.0	3.99	0.22	15.20	4.9
13	29.7	32.6	169.7	8.2	0.85	0.19	1.73	1.3
14	29.6	32.9	185.0	8.2	0.42	0.17	2.00	0.7
15	29.9	32.5	175.1	8.2	1.68	0.18	1.44	1.1
16	29.9	32.4	171.0	8.2	0.32	0.18	1.25	1.3
17	30.4	32.7	175.8	8.2	0.40	0.18	1.70	1.1
18	29.9	32.5	177.1	8.2	0.56	0.19	1.20	1.3
2020.02.05∼02.06								
1	30.1	0.2	68.1	7.4	15.03	0.90	8.47	4.3
2	29.6	11.3	91.9	7.2	12.78	1.06	16.70	11.5
3	30.9	3.1	86.3	7.0	27.31	0.54	6.30	14.5
4	30.2	11.5	164.1	7.4	0.74	1.25	9.07	22.4
5	30.3	15.1	169.1	7.5	5.47	0.13	9.09	18.1
6	29.4	15.8	181.9	7.6	4.35	0.79	8.29	8.7
7	28.3	17.3	186.6	7.7	4.04	0.93	8.02	8.1
8	28.1	21.7	174.4	7.8	3.86	0.62	6.36	4.0
9	27.8	23.6	185.3	8.0	1.34	0.46	4.98	3.7
10	28.0	29.1	169.4	8.1	3.25	0.06	5.33	2.2
11	30.5	29.9	121.3	8.0	4.85	1.60	22.10	13.2
12	27.8	31.4	170.0	8.0	2.09	0.21	8.00	3.2
13	28.9	32.9	181.3	8.3	2.77	0.65	2.05	1.7
14	28.7	33.5	205.3	8.2	7.76	0.05	1.68	0.5
15	28.8	33.2	178.8	8.2	1.43	1.24	2.23	1.2
16	29.0	33.5	174.1	8.3	2.29	0.76	2.24	0.6
17	28.8	33.4	173.8	8.2	2.10	1.01	2.68	0.8
18	28.8	33.4	181.9	8.2	3.22	0.67	1.76	1.0

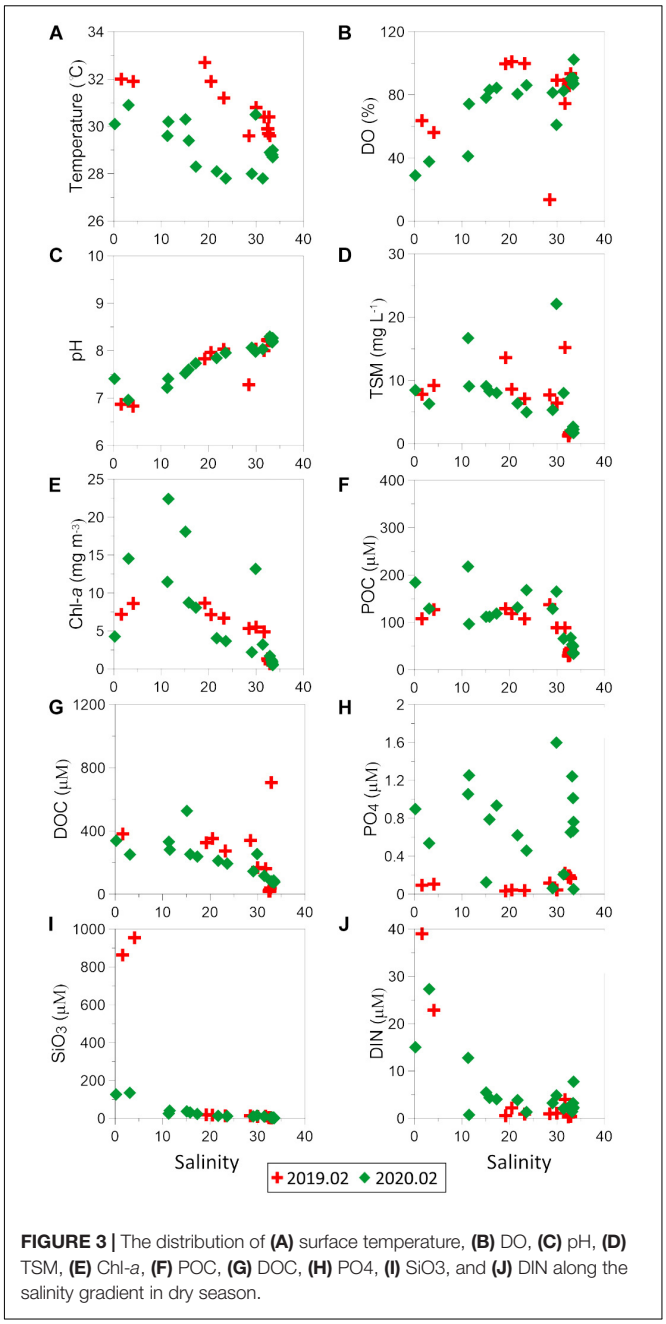

FIGURE 3 | The distribution of **(A)** surface temperature, **(B)** DO, **(C)** pH, **(D)** TSM, **(E)** Chl-*a*, **(F)** POC, **(G)** DOC, **(H)** PO4, **(I)** SiO3, and **(J)** DIN along the salinity gradient in dry season.

values were above 5 mg l^{-1} at most stations (**Table 3**) although lower values were recorded in the inner lagoon (0.7–3.8 mg l^{-1} at stations 1–4) and also at station 11 (4.8 mg l^{-1}). The same pattern was observed in the second survey, i.e., DO values were generally above 5 mg l^{-1}, but four lower values (<3.5 mg l^{-1}) were also recorded in the inner lagoon and at station 11 (**Table 3**). These results show that oxygen deficient conditions arise mainly in the inner lagoon but also along the periphery of the lagoon.

Surface pH values gradually increased from inner lagoon to lagoon inlet. Some anomalously high values (8.7–9.3) were recorded in the coastal waters outside the lagoon, shortly after a heavy rainfall event. Similar to the trend observed in the dry season, nitrogen concentrations decreased steadily from the inner to the outer part of the lagoon and beyond. However, the entire concentration gradient developed across the inlet itself whereas in the dry season the concentration gradient extended across the whole length of the lagoon. Dissolved nitrogen concentration values above the threshold level (24.6 μM) used to classify ecological water quality status as "poor" were recorded in nine stations. This suggests that flood water, storm water runoff and effluent discharge into the inner lagoon provided additional sources of biologically available nutrients and organic matter in the wet season.

As in the dry season, concentrations of TSM and chlorophyll-*a* (Chl-*a*) were highest in low salinity waters, i.e., inner lagoon, Ja-Ela and Dandugam Oya, and decreased toward the lagoon inlet (**Figures 7D,E**). POC and DOC followed a similar trend, but their values were higher than in the dry season, giving weight to

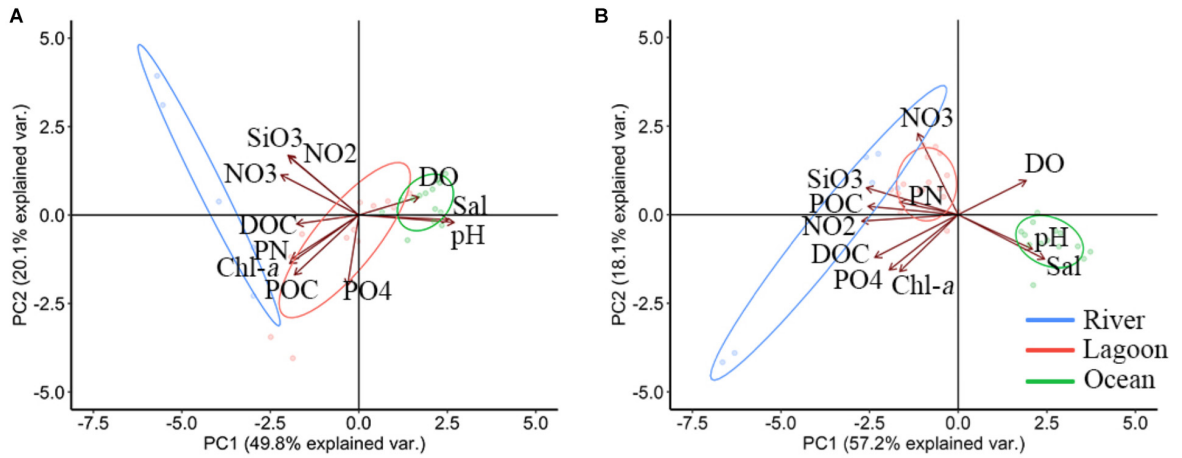

FIGURE 4 | Results from the principal component analysis (PCA) analysis, showing the principal components 1 and 2 for hydrographic parameters and sampling locations in dry season **(A)** and wet season **(B)** in Negombo lagoon from 2019 to 2020.

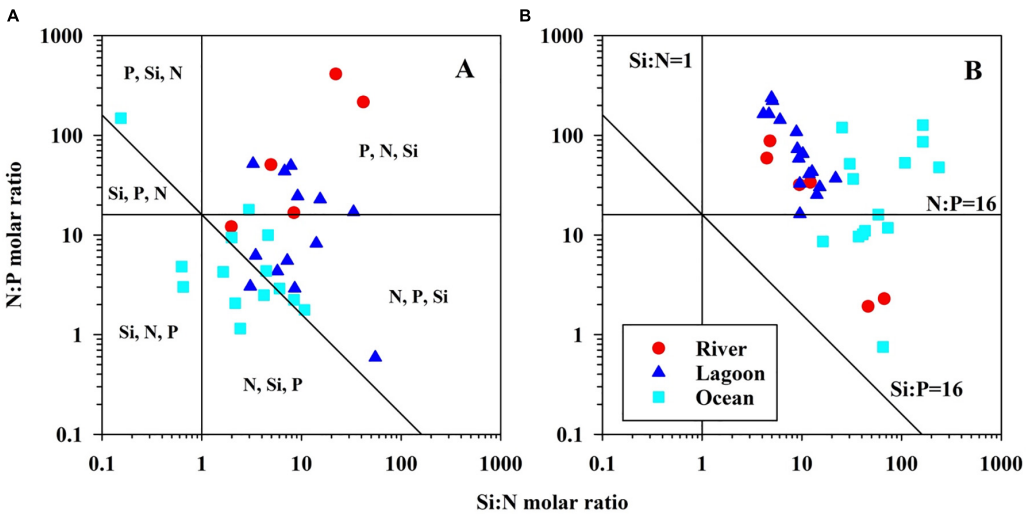

FIGURE 5 | Molar ratio of Si:N:P in Negombo lagoon in dry season **(A)** and wet season **(B)**. The potentially limited nutrients are divided from Redfield ratio (Si:N:P = 16:16:1). Different area in the plot was characterized by potentially limited nutrients in order of priority (Rocha et al., 2002).

the notion that they had been washed off the land by freshwater runoff, like the nutrients.

The cumulative explanation of variables of PCA in PC1 and PC2 axis in wet season was 75.3% (**Figure 4B**). PC1 and PC2 axes were similar to those at dry season. However, the POC and PN were shown in positive part of PC2, and they (POC and PN) were not related to observed Chl-*a* suggesting there was external source of particulate matters.

The molar ratio (Si:N:P) in different waters in wet season was presented in **Figure 5B**. Similar to in dry season, phosphate in both PCA result and Si:N:P plot was evaluated as a P limitation in wet season. One can easily see elevated N:P ratios in wet season (**Figure 5B**).

The TSI in Negombo lagoon in wet season was between mesotrophic and eutrophic conditions (**Figure 6**) and the trophic state suggesting that nutrient supply is quite sufficient for marine organisms in wet season as compared to in dry season.

DISCUSSION

Nutrient Dynamics the Negombo Lagoon

We observed a negative relationship between dissolved nitrogen and salinity (**Figures 3J, 7J**) during both the dry and wet seasons, which suggests that the sources of nitrogen were mainly from freshwater sources. This is consistent with previous work (Malawaraaratchi, 2003) indicating that Negombo Lagoon receives large quantities of wastewater containing high levels of nutrients and organic matter originating from its heavily populated catchment. At the same time, Negombo is rated as

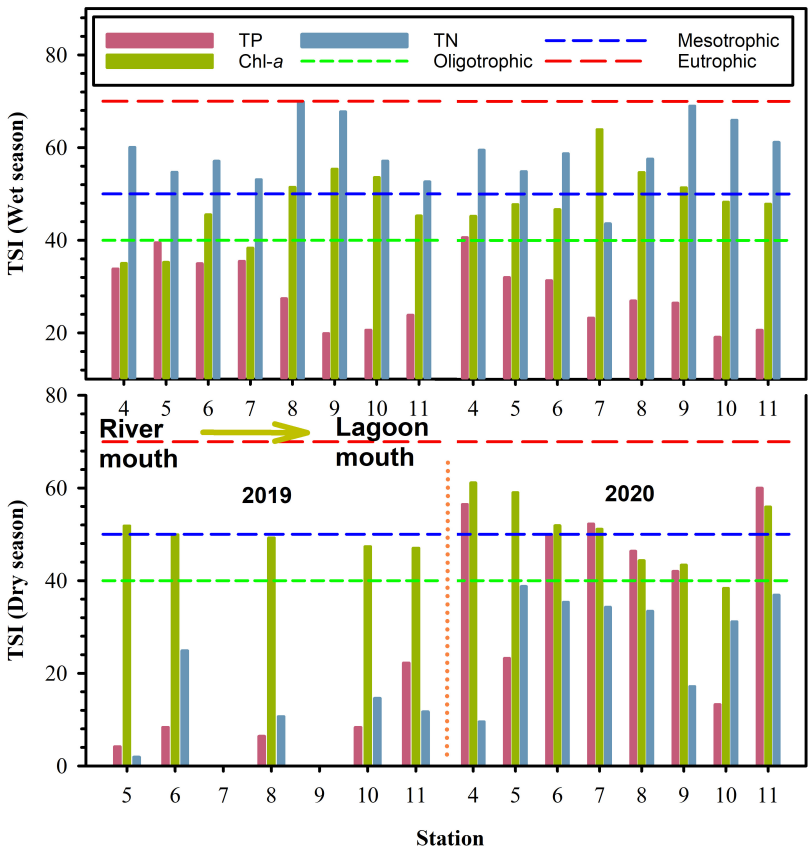

FIGURE 6 | Trophic state index from TP, TN, and Chl-*a* in dry season and wet season in Negombo lagoon. Short dash line represents oligotrophic, medium dash line represents transition from oligotrophic to mesotrophic, long dash line represents transition from mesotrophic to eutrophic.

the third most popular tourist destination in Sri Lanka due to its gorgeous lagoon, bountiful fishery resources and attractive coastal scenery. Nearly 32% of tourists from Sri Lanka visit the Negombo lagoon every year. Most of the hotels are located along the shore and the lagoon. Hotels may become point source if wastewater is discharged to the lagoon without advance treatment systems. This is a matter of great concern, not least because there is growing evidence (Halkos and Matsiori, 2018; Schuhmann et al., 2019) that water quality is the single most important factor contributing to the decision of tourists to revisit a particular seaside location.

Furthermore, it has been reported that unproper management planning, fecal pollution and solid waste pollution may be important problems in Negombo lagoon due to direct discharge of sewage, solid waste into water (Panagoda et al., 2016). Joseph (2011) estimated that nearly 250 kg/day of raw faces are released to the lagoon through channel segment and neatly 50 % uncollected solid waste are discharge to the surrounding environment illegally (Karunarathana et al., 2019). Therefore, the water quality of Negombo Lagoon is critical for the coastal communities and lagoon ecosystem.

Moreover, brackish water fishery is one of the major activity in the Negombo lagoon by using engine FRP boats which are anchored along the estuary bank (Joseph, 2011; DFAR, 2012b). Some of the pollutions are from these FRP boats and pollutants are directly released to the estuary or the lagoon. In addition, waste water discharge from the small scale shrimp farms, crab fattening in estuary and the waste from the dry fish production have estimated negative effect to the lagoon water quality (Pahalawattaarachchi and Siriwardena, 2003; Pathmi et al., 2003).

A negative relationship between phosphate and salinity was also observed within the lagoon (**Figures 3H, 7H**). However, phosphorus as a strong bioactive element, it usually depleted in the water. A remarkable difference of N:P ratio altered nitrogen become limited factor in dry season in 2020 (**Figure 5B**). High concentration of phosphate shown in Negombo lagoon in dry season in 2020, might result from remineralization of sediment or discharge of anthropogenic wastewater from coastal of lagoon. Besides, some elevated phosphate values were also found at high salinity stations revealing other sources of phosphate input, but it is difficult to trace their sources based on limited information.

It is worth noting that the main freshwater sources, i.e., the Dandugam Oya and Ja-Ela, brought enormous amounts of dissolved silicate and TSM to the lagoon in both seasons, while the Hamilton canal also brought large amounts of silicate in wet season only.

Nutrient supply to coastal lagoon habitats tends to play an important role in their primary production which in turn plays an

TABLE 3 | Water temperature, salinity, dissolved oxygen (DO), pH, dissolved nitrogen (NO3+NO2), total suspended matter (TSM) and chlorophyll-*a* (Chl-*a*) in the Negombo Lagoon in the wet season 2019.

Station	T (°C)	Salinity	DO (μM)	pH	DIN (μM)	PO4 (μM)	TSM (mg L^{-1})	Chl-*a* (mg m^{-3})
2019.10.15∼10.17								
(First Cruise)								
1	29.0	0.0	118.8	6.4	22.96	0.26	27.87	1.5
2	29.1	1.1	21.4	7.7	3.73	1.95	8.20	34.6
3	29.1	0.0	103.8	6.3	11.45	0.34	19.40	4.3
4	28.8	0.0	109.1	7.6	14.09	0.87	16.87	1.6
5	29.0	0.0	132.2	7.9	9.81	0.39	21.80	1.6
6	28.5	0.6	157.6	7.8	11.51	0.28	18.00	4.6
7	28.6	0.7	160.0	7.2	8.84	0.29	18.47	2.2
8	29.2	1.9	189.2	7.2	27.37	0.17	11.87	8.4
9	29.4	4.2	202.7	7.5	23.62	0.10	10.73	12.5
10	29.8	12.7	176.1	7.6	11.30	0.10	4.70	10.4
11	31.5	10.4	149.0	7.4	8.54	0.13	4.27	4.4
12	30.5	32.0	163.1	7.9	1.26	0.15	8.80	4.7
13	30.1	19.6	197.3	8.7	7.51	0.06	4.42	6.0
14	29.4	29.9	195.2	8.5	0.58	0.06	1.78	1.7
15	30.3	25.2	189.8	9.1	3.25	0.06	2.60	3.8
16	30.1	25.8	185.1	9.4	9.27	0.07	2.06	3.5
17	30.0	24.8	162.9	9.0	4.23	0.09	3.53	3.8
18	28.8	24.2	179.6	8.7	3.59	0.07	5.00	2.5
(Second Cruise)								
1	29.3	0.0	140.9	6.3	22.21	0.38	18.33	3.2
2	31.4	1.2	107.4	6.7	2.27	0.99	4.00	75.5
3	29.1	0.0	98.4	6.4	14.01	0.44	16.13	1.3
4	30.6	0.1	128.7	6.5	13.66	0.42	10.60	4.4
5	31.7	0.7	175.9	6.6	9.91	0.23	18.33	5.7
6	32.4	1.1	164.6	7.1	12.84	0.22	10.73	5.1
7	32.6	4.5	221.3	7.9	4.65	0.13	15.53	29.9
8	32.6	3.7	229.7	7.9	11.84	0.16	17.07	11.6
9	32.8	3.7	240.4	8.2	25.64	0.16	14.40	8.3
10	33.1	4.4	227.3	7.7	20.83	0.09	6.47	6.1
11	32.3	6.3	197.1	7.5	14.92	0.10	26.20	5.8
12	30.8	33.5	170.2	8.2	0.72	0.95	2.20	6.2
13	29.8	21.5	196.9	8.7	3.06	0.08	3.17	6.1
14	29.5	31.3	203.2	7.3	0.69	0.06	1.43	3.1
15	29.9	25.5	192.9	8.8	1.01	0.06	2.79	3.9
16	30.0	31.8	203.3	9.1	0.45	0.05	1.53	1.4
17	30.1	31.8	198.1	9.2	0.49	0.04	1.33	1.5
18	29.0	21.1	202.8	9.2	10.82	0.13	5.40	1.4

indirect role in providing a variety of habitats such as feeding and nursery ground for juvenile marine organisms (Vasconcelos et al., 2011). However, tropical lagoon worldwide has been damaged by human activity such as shoreline modifications and coastal works for tourists (Pérez-Ruzafa et al., 2019), sea salt extraction (Pérez-Ruzafa et al., 2011), fisheries and aquaculture, water sports etc. All of these factors affect nutrient and organic matter inputs as well as sediment resuspension in such a way as to shift the ecosystems and the lagoon waters toward eutrophication (Pérez-Ruzafa et al., 2019).

Eutrophication in the Negombo Lagoon

According to the European Commission (2000), nitrate concentrations in excess of 24.2 μM indicate bad quality water. Based on these criteria, the water quality status of the lagoon was "poor" in the wet season but switched to "good" in the dry season when concentrations were less than 8 μM. With respect to phosphorus concentrations, the status of lagoon waters was consistently "good" to "medium," with concentrations less than 1 μM. These findings are in agreement with those of Mendis et al. (2015). Only in the Hamilton canal could the phosphorus quality status be rated as "bad," with concentrations consistently higher than 1.7 μM.

In this study, Chl-*a* concentrations were persistently higher than 2 μg L^{-1} throughout the entire lagoon and Chl-*a* was always slightly higher in the dry season than that in the wet season (**Figures 3E, 7E**). These observations are likely the result of plankton blooms fueled by the abundance of nutrients coming from freshwater inputs. Negombo lagoon was between mesotrophic and eutrophic status in both dry and wet seasons based on the trophic index (**Figure 7**). In comparison our result to previous investigations, we observed that water quality in Negombo lagoon has been declined since 2009 (**Table 4**). We cannot give a real answer what mechanisms result in mesotrophic and eutrophic status in Negombo lagoon because previous sampling locations and time period might be different from this study. However, water quality in the wet season is more worsen than dry season based on current study. The observations may be affected by temporal-spatial variation in wet season. It is likely that flood water, storm water runoff and effluent discharge into the inner lagoon provided additional sources of biologically available nutrients and organic matter from watershed of main rivers. However, it needs further investigations to trace their sources of nutrients and organic matter at different time scales in the future.

Hypoxia and pH Variation in the Negombo Lagoon

The metabolic activity of all aquatic organisms increases exponentially with temperature. The main consequence of these elevated rates of physiological processes in the context of water quality is the consumption of oxygen by aerobic heterotrophs, mainly bacteria (Sokolova and Lannig, 2008). Another effect of increasing temperature is the decreasing solubility of oxygen in seawater (Garcia and Gordon, 1992). Higher sea surface temperatures also lead to density stratification which may severely reduce vertical mixing and hence prevent the transport of oxygen into the subsurface layer (Howarth et al., 2011). In the present study, surface water temperatures were in the range 27.8–33.1°C, with a mean value of 30.1 ± 1.0, i.e., similar to previously reported results for this lagoon (Gammanpila, 2010). Such high temperatures, coupled with the slow water circulation resulting from the very narrow connection to the Indian Ocean (Dahanayaka et al., 2012), mean that the Negombo Lagoon is at risk of experiencing hypoxic events (Hearn and Robson, 2001; Tyler et al., 2009). Moreover, the mean DO concentration we recorded in the Dandugam Oya river outflow (2.76 mg l^{-1}) was

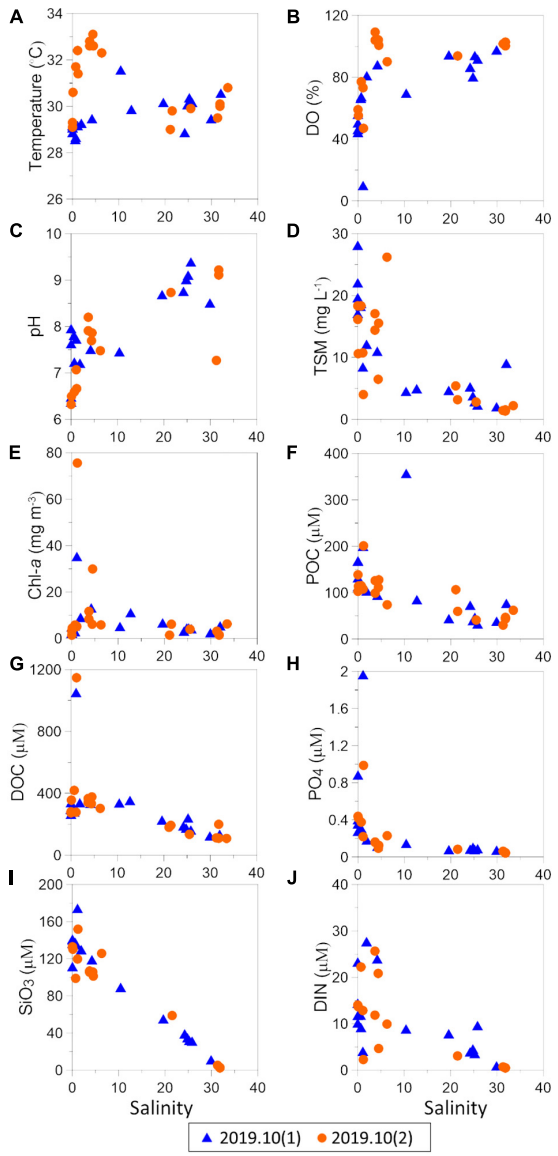

FIGURE 7 | The distribution of **(A)** surface temperature, **(B)** DO, **(C)** pH, **(D)** TSM, **(E)** Chl-*a*, **(F)** POC, **(G)** DOC, **(H)** PO4, **(I)** SiO3, and **(J)** DIN along the salinity gradient in wet season.

considerably lower than that recorded by Gammanpila (2010) 10 years earlier (6.7 ± 2.1 mg l^{-1}), which suggests that the lagoon is prone to hypoxic events in the near future. Likewise, the DO concentrations we recorded in the Hamilton canal, albeit a very small contributor to the total freshwater input to the lagoon, occasionally dropped below 1 mg l^{-1}.

Shallow coastal lagoons where the mean daily water temperature is above 26°C often exhibit a significant decrease in oxygen concentration with depth, coupled with intense dynamics of the daily cycle of oxygen concentration, with highest concentrations occurring in the late afternoon and lowest concentrations occurring around dawn. While our surface water measurements were all above 4 mg l^{-1}, the above considerations make it likely that some parts of the Negombo Lagoon must have been experiencing hypoxia in the waters immediately above the sediments on a daily or seasonal basis. Besides, the fish would avoid low DO water in usual (Claireaux and Chabot, 2016), however, shallow water restrict movement of fish in Negombo lagoon result in fish kill events.

High level of nutrients discharged into Negombo lagoon can trigger microorganism growth in both dry and wet seasons. During dry season, phytoplankton in Negombo lagoon produce large amounts of particulate organic carbon and consumed nutrients and oxygen in the water column. Oxygen depletion (<70% of saturated oxygen) in wet season was more remarkable. As mentioned above, heavy rainfall brought turbid water with high concentration nitrogenous nutrient to Negombo lagoon may stimulate phytoplankton growth, however, high concentration of POC and DOC were also discharged into the lagoon in wet season. Negative correlations between DO and DOC, and DO and POC can be observed in both seasons (**Figure 8**) suggesting that heterotrophic bacteria may largely use dissolved oxygen in the water column. Similar phenomenon about heterotrophic microorganism growth consumed more oxygen has been reported in the coastal water of the East China Sea (Chen et al., 2007, 2021).

Some unusually high pH values (8.5–9.3) were recorded in the coastal plume that formed off the lagoon's inlet in the wet season. The large freshwater outflow during the wet season meant that the mean salinity of the coastal water samples was only 27.0 ± 4.6 as compared to 32.8 ± 0.6 in the dry season. Therefore, it seems counterintuitive that seawater pH should be so much higher in the wet (pH = 8.5–9.3) than in the dry season (pH = 8.0–8.2). Two possible factors may account for the unusually high pH phenomenon: (1) photosynthetic activity by marine phytoplankton (2) discharge of septic wastewater effluents or industrial effluents through runoff or sea outfalls (Schneeberger et al., 2015). Photosynthetic activity has the potential to raise the pH of seawater significantly by fixing CO_2. Under high discharge conditions, plankton blooms are more likely to happen in the offshore waters than in the lagoon because of the short residence time and high turbidity of water inside the lagoon. Photosynthetic activity may thus explain in part the high pH values in the coastal zone. Chou et al. (2018) reported that large variation of pH in seagrass-dominated coastal region. On the other hand, the discharge of effluents cannot be discounted

TABLE 4 | Concentrations of dissolved inorganic nitrogen (DIN) and trophic state from previous studies and this study in Negombo lagoon.

References	Sampling time	DIN (mg L^{-1})	Trophic state
This study	February 2019	0.13	Oligotrophic
	October 2019	0.79	Eutrophic
	February 2021	0.34	Mesotrophic
Malawaraaratchi, 2003	September 2002	0.18	Oligotrophic
Gammanpila, 2010	June 2009	0.59	Mesotrophic
Mendis et al., 2015	2015 (N.A)	0.96	Eutrophic
National Aquatic Resources Research and Development Agency, 2019	April 2019	3.5	Hypertrophic

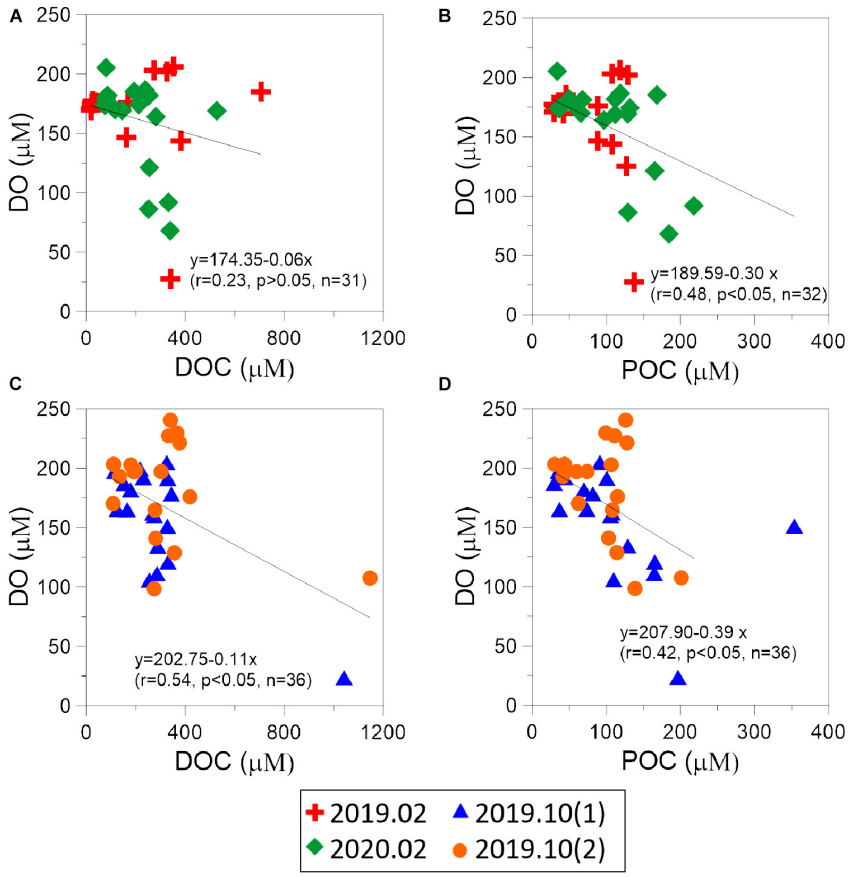

FIGURE 8 | The concentration of POC and DOC vs. DO in **(A,B)** dry season and **(C,D)** wet season.

as a contributing factor, especially in view of the documented evidence for unregulated and untreated waste discharge along the shore of the lagoon. The main sources of septic wastewater effluent to the Negombo lagoon are local settlements, municipal sewage carried with the freshwater inflows and tourist industry along its coastal area (Malawaraaratchi, 2003). Finally, the illegal dumping of solid wastes along the banks of the populated area and shoreline closer to the mouth (Malawaraaratchi, 2003) as well as waste from fish processing and fish landing sites may also be a contributing factor (DFAR, 2012a).

Driving Forces of Eutrophication in the Negombo Lagoon

Water exchange between the Negombo Lagoon and the Indian Ocean occurs through a channel which is 150 m wide and less than 2 m deep on average. The mean tidal range on the ocean side of the inlet is 30 cm and that inside the lagoon is only 10 cm. This decrease across the inlet is due to tidal choking (Rydberg and Wickbom, 1996; Rajapaksha and Jayasiri, 2000; Sivanantha et al., 2016). The extent to which choking occurs depends on the inlet structure, freshwater supply, size of the basin, and spring neap tidal ranges. For example, work conducted in another west coast lagoon (Wijeratne and Rydberg, 2007) suggests that tidal choking across the inlet is likely to be more pronounced during spring tides than during neap tides.

In recent years, mangroves have been planted around the lagoon by local residents for the purpose of subsequent landfill. The area of mangrove vegetation in some areas has increased to form new islets consequently narrowing the channels (Dahanayaka et al., 2012). This has also led to sediment deposition, further enhance choking the channels. If left unchecked, it will ultimately lead to the destruction of the Negombo estuarine lagoon as a productive ecosystem (IUCN, 2011). Besides encouraging sedimentation and restricting water exchange, mangrove forests can naturally lead to bottom water hypoxia during low tide (Dubuc et al., 2019). The major cause of hypoxia in mangrove swamps is the buildup of monosulfides and pyrites in the organic-rich sediment, creating a monosulfidic black ooze (Knight et al., 2013). Therefore, this may be another possible cause for very low DO concentrations in the Negombo lagoon, as it comprises several mangrove swamps and borders on the largest saline coastal salt marsh in Sri Lanka, called Muthurajawela, which is underlain by extensive peat deposits.

Dissolved oxygen recorded continuously for 24 h at station 11 (from the outdoor deck of a waterfront hotel) revealed that severe hypoxic episodes occurred at nighttime during the dry season

(personal communication, W-JH). This may be due to the poor circulation of water in that part of the lagoon, coupled with the long residence time of water in the central part of the lagoon in the dry season. In contrast, during the wet season, nighttime DO concentrations did not fall drastically as water replenished at much higher rates in the lagoon due to shorter residence time. Rajapaksha and Jayasiri (2000) calculated a mean residence time for the lagoon as a whole which ranged from 2 to 10 days, the shortest time corresponding to the highest recorded river flow (160 m^3 s^{-1}) and the longest time to the dry season (20 m^3 s^{-1}). Based on the above considerations and a case study from another tropical estuarine lagoon (Hearn and Robson, 2001), it can be anticipated that dredging the main channel of the Negombo Lagoon inlet, or a new channel, will a good option to increase ocean exchange and improve water quality in the lagoon.

High nutrient loading into the lagoon is a problem that also needs to be addressed. The anthropogenic sources are well identified and are associated with a range of intense activities around the lagoon such as local population, tourism, fishery activities, discharge of poorly treated water, pollution from both point sources and non-point sources. We provided investigations in both dry and wet seasons, but it indeed provides valuable data sets about eutrophication and hypoxia formation. It is worthy to note that such a short term study on this unique system may not be adequate to describe its whole scenario of Negombo lagoon and may still miss some considerations. For example, Sivanantha et al. (2016) reported that most of the water discharge to the lagoon does not go through a proper purification system to reduce nutrient pollution. This high nutrient loading has contributed to a 96% decline of the standing crop of the seagrass in northern, eastern, and western parts of the Negombo Lagoon between 1997 and 2004 (De Silva and Amarasinghe, 2007). In turn, the reduction of the seagrass may also contribute to the present-day low dissolved oxygen concentrations in certain parts of the lagoon.

In summary, elevated levels of nutrients, Chl-*a*, POC, and DOC were found in the water bodies emptying into the Negombo lagoon as well as in the inner lagoon, in both dry and wet seasons. The inner lagoon and probably some stretches of coast isolated from the main circulation (e.g., Station 11) is facing hypoxia, not only because of the in situ processes triggered by the abundance of nutrients and organic matter from sewage, but also because of the already low levels of dissolved oxygen in river discharge. Therefore, it would be good to significantly reduce nutrient loading while at the same time improving the existing mouth or new channel to improve water quality and water circulation. Going forward, regular hydrographic, biological oxygen demand, heterotrophic respiration, nutrient monitoring and phytoplankton assemblages will be essential for eutrophication and hypoxia trend analysis. If any modification to the lagoon's outline and physiography is to take place, it will be important to characterize the new estuarine mixing behavior of the lagoon as a function of river discharge variability in order to correctly interpret the monitoring data.

DATA AVAILABILITY STATEMENT

The original contributions presented in the study are included in the article/**Supplementary Material**, further inquiries can be directed to the corresponding author/s.

AUTHOR CONTRIBUTIONS

C-CH conceived the idea. C-CH, H-HH, and WW wrote the manuscript. H-HH, M-HC, Y-YS, WW, W-JH, C-CH, RR, and DW performed the experiments and created the figures. C-CH and H-HH revised the manuscript. All authors reviewed the manuscript.

FUNDING

This research was supported by Sun Yat-sen University and the Ministry of Sciences and Technology (MOST 107-2911-I-110-301, MOST 108-2911-I-110-301, and MOST 109-2911-I-110-301) of Taiwan.

ACKNOWLEDGMENTS

We appreciate the assistance of people of the Environmental Change Sciences and Technology Innovation Center at University of Sri Jayewardenepura in collaboration with National Sun Yat-sen University.

SUPPLEMENTARY MATERIAL

The Supplementary Material for this article can be found online at: https://www.frontiersin.org/articles/10.3389/fmars.2021.678832/full#supplementary-material

REFERENCES

Amarasinghe, U. A., Mutuwatta, L., and Sakthivadivel, R. (1999). *Water Scarcity Variations within a Country: A Case Study of Sri Lanka. IWMI Research Reports H024897*. Colombo: International Water Management Institute.

Andersen, J. H., Schlüter, L., and Ærtebjerg, G. (2006). Coastal eutrophication: recent developments in definitions and implications for monitoring strategies. *J. Plankton Res.* 28, 621–628. doi: 10.1093/plankt/fbl001

Bianchi, T. S., DiMarco, S. F., Cowan, J. H. Jr., Hetland, R. D., Chapman, P., Day, J. W., et al. (2010). The science of hypoxia in the Northern Gulf of Mexico: a review. *Sci. Total Environ.* 408, 1471–1484. doi: 10.1016/j.scitotenv.2009.11.047

Breitburg, D., Levin, L. A., Oschlies, A., Gregoire, M., Chavez, F. P., Conley, D. J., et al. (2018). Declining oxygen in the global ocean and coastal waters. *Science* 359:eaam7240. doi: 10.1126/science.aam7240

Chen, C.-C., Gong, G.-C., Chiang, K.-P., Shiah, F.-K., Chung, C.-C., and Hung, C.-C. (2021). Scaling effects of a eutrophic river plume on organic carbon consumption. *Limnol. Oceanogr.* 66, 1867–1881. doi: 10.1002/lno.11729

Chen, C.-C., Gong, G.-C., Chou, W.-C., and Shiah, F.-K. (2020). Hypoxia in autumn of the East China Sea. *Mar. Pollut. Bull.* 152:110875. doi: 10.1016/j.marpolbul.2019.110875

Chen, C.-C., Gong, G.-C., and Shiah, F.-K. (2007). Hypoxia in the East China Sea: one of the largest coastal low-oxygen areas in the world. *Mar. Environ. Res.* 64, 399–408. doi: 10.1016/j.marenvres.2007.01.007

Chen, C.-T. A. (2008). Distributions of nutrients in the East China Sea and the South China Sea connection. *J. Oceanogr.* 64, 737–751. doi: 10.1007/s10872-008-0062-9

Chen, C.-T. A., and Guo, X. (2020). *Changing Asia-Pacific Marginal Seas*. Singapore: Springer.

Chou, W.-C., Chu, H.-C., Chen, Y.-H., Syu, R.-W., Hung, C.-C., and Soong, K. (2018). Short-term variability of carbon chemistry in two contrasting seagrass meadows at Dongsha Island: implications for pH buffering and CO2 sequestration. *Estuar. Coast. Shelf Sci.* 210, 36–44. doi: 10.1016/j.ecss.2018.06.006

Claireaux, G., and Chabot, D. (2016). Responses by fishes to environmental hypoxia: integration through Fry's concept of aerobic metabolic scope. *J. Fish Biol.* 88, 232–251. doi: 10.1111/jfb.12833

Cziesielski, M. J., Schmidt-Roach, S., and Aranda, M. (2019). The past, present, and future of coral heat stress studies. *Ecol. Evol.* 9, 10055–10066. doi: 10.1002/ece3.5576

Dahanayaka, D., Tonooka, H., Wijeyaratne, M., Minato, A., and Ozawa, S. (2012). Monitoring land use changes and their impacts on the productivity of Negombo Estuary, Sri Lanka using time series satellite data. *Asian Fish. Sci.* 25, 97–112.

De Silva, K., and Amarasinghe, M. (2007). Substrate characteristics and species diversity of marine angiosperms in a micro tidal basin estuary on the west coast of Sri Lanka. *Sri Lanka J. Aquat. Sci.* 12, 103–114. doi: 10.4038/sljas.v12i0.2217

Devendra, A. (2002). *Hydrodynamics of Muthurajawela Marsh & Negombo lagoon coastal wetland ecosystem. Effective Management for Biodiversity Conservation in Sri Lankan Coastal Wetlands*. Portsmouth: University of Portsmouth, 9–10.

DFAR (2012a). *Fisheries Development and Management Plan of Negombo lagoon. Regional Fisheries Livelihoods Programme for South and Southeast Asia (GCP/RAS/237/SPA): Field Project Document 2012/LKA/CM/12*. Colombo: Department of Fisheries and Aquatic Resources.

DFAR (2012b). *Rapid Fisheries Frame Survey Report of Coastal and Brackish Water Fisheries in the Fisheries District of Negombo. Regional Fisheries Livelihoods Programme for South and Southeast Asia (GCP/RAS/237/SPA): Field Project Document 2012/LKA/CM/01*. Colombo: Department of Fisheries and Aquatic Resources.

Diaz, R. J., and Rosenberg, R. (1995). Marine benthic hypoxia: a review of its ecological effects and the behavioural responses of benthic macrofauna. *Oceanogr. Mar. Biol.* 33, 245–303.

Dubuc, A., Baker, R., Marchand, C., Waltham, N. J., and Sheaves, M. (2019). Hypoxia in mangroves: occurrence and impact on valuable tropical fish habitat. *Biogeosciences* 16, 3959–3976. doi: 10.5194/bg-16-3959-2019

European Commission (2000). Water framework directive, directive 2000/60/EEC of 22 December 2000 establishing a framework for community action in the field of water policy. *Off. J. Eur. Communities* 327, 1–72.

Gammanpila, M. (2010). Hydrography, nutrients and abundance and distribution of zooplankton in Negombo Lagoon, Sri Lanka. *Sri Lanka J. Aquat. Sci.* 15, 13–24. doi: 10.4038/sljas.v15i0.5447

Garcia, H. E., and Gordon, L. I. (1992). Oxygen solubility in seawater: better fitting equations. *Limnol. Oceanogr.* 37, 1307–1312. doi: 10.4319/lo.1992.37.6.1307

Gong, G.-C., Lee Chen, Y.-L., and Liu, K.-K. (1996). Chemical hydrography and chlorophyll a distribution in the East China Sea in summer: implications in nutrient dynamics. *Cont. Shelf Res.* 16, 1561–1590. doi: 10.1016/0278-4343(96)00005-2

Halkos, G., and Matsiori, S. (2018). Environmental attitudes and preferences for coastal zone improvements. *Econ. Anal. Policy* 58, 153–166. doi: 10.1016/j.eap.2017.10.002

Hearn, C. J., and Robson, B. J. (2001). Inter-annual variability of bottom hypoxia in shallow mediterranean estuaries. *Estuar. Coast. Shelf Sci.* 52, 643–657. doi: 10.1006/ecss.2001.0773

Hoegh-Guldberg, O., Mumby, P. J., Hooten, A. J., Steneck, R. S., Greenfield, P., Gomez, E., et al. (2007). Coral reefs under rapid climate change and ocean acidification. *Science* 318, 1737–1742. doi: 10.1126/science.1152509

Hoegh-Guldberg, O., and Smith, G. J. (1989). The effect of sudden changes in temperature, light and salinity on the population density and export of zooxanthellae from the reef corals *Stylophora pistillata* Esper and *Seriatopora hystrix* Dana. *J. Exp. Mar. Biol. Ecol.* 129, 279–303. doi: 10.1016/0022-0981(89)90109-3

Howarth, R., Chan, F., Conley, D. J., Garnier, J., Doney, S. C., Marino, R., et al. (2011). Coupled biogeochemical cycles: eutrophication and hypoxia in temperate estuaries and coastal marine ecosystems. *Front. Ecol. Environ.* 9, 18–26. doi: 10.1890/100008

Hung, C. C., Tseng, C. W., Gong, G. C., Chen, K. S., Chen, M. H., and Hsu, S. C. (2013). Fluxes of particulate organic carbon in the East China Sea in summer. *Biogeosciences* 10, 6469–6484. doi: 10.5194/bg-10-6469-2013

Hung, C. C., Wong, G. T., Liu, K. K., Fuh-Kwo, S., and Gwo-Ching, G. (2000). The effects of light and nitrate levels on the relationship between nitrate reductase activity and 15NO3− uptake: field observations in the East China Sea. *Limnol. Oceanogr.* 45, 836–848. doi: 10.4319/lo.2000.45.4.0836

Hung, C. W., Huang, K. H., Shih, Y. Y., Lin, Y. S., Chen, H. H., Wang, C. C., et al. (2016). Benthic fluxes of dissolved organic carbon from gas hydrate sediments in the northern South China Sea. *Sci. Rep.* 6:29597. doi: 10.1038/srep29597

IUCN (2011). *An Appraisal of Mangrove Management in Micro tidal Estuaries and Lagoons in Sri Lanka*, Vol. viii. Colombo: IUCN Sri Lanka Office, 116.

IUCN (2013). *Proceedings of the Workshop on Ecological Considerations in Coastal Development, Held at the Sequel, Cinnamon Grand, Colombo, Sri lanka, 22 November 2013*. Colombo: IUCN, xiv–80.

Joseph, L. (2011). *Fisheries and Environmental profile of Negombo lagoon, Sri Lanka: A Literature Review. Regional Fisheries Livelihoods Programme for South and Southeast Asia (GCP/RAS/237/SPA) Field Project Document 2011/LKA/CM/04*. Rome: FAO.

Karunarathana, A., Singh, R. K., Rajapaksha, T., Gamaralalage, D., Premakumara, J., Onogawa, K., et al. (2019). *State of Municipal Solid Waste Management in Negombo, Sri Lanka*. Hayama: Institute for Global Environmental Strategies.

Kemp, W. M., Boynton, W. R., Adolf, J. E., Boesch, D. F., Boicourt, W. C., Brush, G., et al. (2005). Eutrophication of Chesapeake Bay: historical trends and ecological interactions. *Mar. Ecol. Prog. Ser.* 303, 1–29. doi: 10.3354/meps303001

Knight, J. M., Griffin, L., Dale, P. E. R., and Sheaves, M. (2013). Short-term dissolved oxygen patterns in sub-tropical mangroves. *Estuar. Coast. Shelf Sci.* 131, 290–296. doi: 10.1016/j.ecss.2013.06.024

Kratzer, C. R., and Brezonik, P. L. (1981). A carlson-type trophic state index for nitrogen in florida lakes. *Water Resour. Bull.* 17, 713–715. doi: 10.1111/j.1752-1688.1981.tb01282.x

Malawaraaratchi, R. (2003). *A Study of the Negombo Lagoon with Respect to the Salinity Variation and Pollution of the Lagoon Water and Effects of Proposed Dredging Activities*. Moratuwa: University of Moratuwa.

Mayfield, A. B., Chen, M. N., Meng, P. J., Lin, H. J., Chen, C. S., and Liu, P. J. (2013). The physiological response of the reef coral *Pocillopora damicornis* to elevated temperature: results from coral reef mesocosm experiments in Southern Taiwan. *Mar. Environ. Res.* 86, 1–11. doi: 10.1016/j.marenvres.2013.01.004

Mendis, B., Najim, M., Kithsiri, H., and Azmy, S. (2015). "Assessment of water quality and identification of pollution status of Negombo estuary in Sri Lanka," in *Proceedings of the 21st Scientific Sessions of the Sri Lanka Association for Fisheries and Aquatic Resources, May, 2015. Sri Lanka Association for Fisheries and Aquatic Resources*, Colombo.

Narangoda, S. R. C., Maddumage, M. D. S. R., Wickramaarachchi, D. N., Weerasekara, K. A. W. S., Hettige, N. D., et al. (2015). "Water quality status of selected aquatic environments in Sri Lanka during fish kill incidents," in *Proceedings of 21st Annual Scientific Sessions of Sri Lanka Association for Fisheries and Aquatic Resources (SLAFAR), 22 May 2015*, Nara, 17.

National Aquatic Resources Research and Development Agency (2019). *Preliminary Report on Investigation of Fish in Hamilton Canal*. Nara: National Aquatic Resources Research and Development Agency.

Pahalawattaarachchi, V., and Siriwardena, P. (2003). "Effect of shrimp farm effluent on seagrass beds in Negombo Lagoon," in *Proceeding of the 1st Scientific Sessions on Inland Aquatic Resources and Aquaculture, National Aquatic Resources Research and Development Agency*, (Colombo).

Panagoda, P. A. B. G., Dissanayake, D. M. S. N., Nawalage, N. M. S. K., Silva, H. K. A. D., Tharaka, L. K. D. N., Weerasinghe, H. W. G. A. S., et al. (2016).

"Sustainable tourism development in Negombo coastline: an option for co-management," in *Proceedings of the International Research Symposium on Pure and Applied Sciences (IRSPAS 2016), Faculty of Science, University of Kelaniya*, Kelaniya, 106.

Pathmi, A., Jayamanne, S., Siriwardena, P., and Hirimuthugoda, Y. (2003). "Impact of crab fattening on the lagoon environment and the live hood of fishers in Negombo Lagoon," in *Proceeding of the 1st scientific sessions on Inland Aquatic Resources and Aquaculture, National Aquatic Resources Research and Development Agency*, Colombo.

Pérez-Ruzafa, A., Campillo, S., Fernández-Palacios, J. M., García-Lacunza, A., García-Oliva, M., Ibañez, H., et al. (2019). Long-term dynamic in nutrients, chlorophyll a, and water quality parameters in a coastal Lagoon during a process of eutrophication for decades, a sudden break and a relatively rapid recovery. *Front. Mar. Sci.* 6:26. doi: 10.3389/fmars.2019.00026

Pérez-Ruzafa, A., Marcos, C., Pérez-Ruzafa, I. M., and Pérez-Marcos, M. (2011). Coastal lagoons:"transitional ecosystems" between transitional and coastal waters. *J. Coast. Conserv.* 15, 369–392. doi: 10.1007/s11852-010-0095-2

Rabalais, N. N., Turner, R. E., and Wiseman, W. J. Jr. (2001). Hypoxia in the Gulf of Mexico. *J. Environ. Qual.* 30, 320–329. doi: 10.2134/jeq2001.302320x

Rajapaksha, J. K. (1997). *Low Frequency Tidal Response and Water Exchange in a Restricted Lagoon: The Negombo Lagoon, Sri Lanka.* M.Sc. thesis. Gothenburg: University of Gothenburg.

Rajapaksha, J. K., and Jayasiri, H. B. (2000). Restricted water exchange in the Negombo Lagoon on the west coast of Sri Lanka. *J. Natl. Aquat. Resour. Res. Dev. Agency* 36, 35–46.

Renaud, M. L. (1986). Detecting and avoiding oxygen deficient sea water by brown shrimp, *Penaeus aztecus* (*Ives*), and white shrimp *Penaeus setiferus* (*Linnaeus*). *J. Exp. Mar. Biol. Ecol.* 98, 283–292. doi: 10.1016/0022-0981(86)90218-2

Rocha, C., Galvao, H., and Barbosa, A. (2002). Role of transient silicon limitation in the development of cyanobacteria blooms in the Guadiana estuary, south-western Iberia. *Mar. Eco. Prog. Ser.* 228, 35–45. doi: 10.3354/meps228035

Rydberg, L., and Wickbom, L. (1996). Tidal choking and bed friction in Negombo Lagoon, Sri Lanka. *Estuaries* 19, 540–547. doi: 10.2307/1352516

Samarakoon, J., and Van Zon, H. (1991). *Environmental Profile of Muthurajawela and Negombo Lagoon*. Colombo: Euroconsult/Greater Colombo Economic Commission.

Schneeberger, C. L., O'Driscoll, M., Humphrey, C., Henry, K., Deal, N., Seiber, K., et al. (2015). Fate and transport of enteric microbes from septic systems in a coastal watershed. *J. Environ. Health* 77, 22–30.

Schuhmann, P., Skeete, R., Waite, R., Bangwayo-Skeete, P., Casey, J., Oxenford, H. A., et al. (2019). Coastal and marine quality and tourists' stated intention to return to Barbados. *Water* 11:1265. doi: 10.3390/w11061265

Shih, Y.-Y., Lin, H.-H., Li, D., Hsieh, H.-H., Hung, C.-C., and Chen, C. T. A. (2019). Elevated carbon flux in deep waters of the South China Sea. *Sci. Rep.* 9:1496. doi: 10.1038/s41598-018-37726-w

Sivanantha, N., Wijesinghe, M., and Wijesekara, R. (2016). Distribution of five toxic heavy metals in biotic and abiotic constituents of the Negombo Lagoon, Sri Lanka. *Sri Lankan J. Biol.* 1, 1–14. doi: 10.4038/sljb.v1i1.1

Sokolova, I. M., and Lannig, G. (2008). Interactive effects of metal pollution and temperature on metabolism in aquatic ectotherms: implications of global climate change. *Clim. Res.* 37, 181–201. doi: 10.3354/cr00764

Steckbauer, A., Duarte, C. M., Carstensen, J., Vaquer-Sunyer, R., and Conley, D. J. (2011). Ecosystem impacts of hypoxia: thresholds of hypoxia and pathways to recovery. *Environ. Res. Lett.* 6:025003. doi: 10.1088/1748-9326/6/2/025003

Tyler, R. M., Brady, D. C., and Targett, T. E. (2009). Temporal and spatial dynamics of biel-cycling hypoxia in estuarine tributaries. *Estuar. Coast* 32, 123–145. doi: 10.1007/s12237-008-9108-x

Urban Development Authority (2019). *Negombo Development Plan – 2019 - 2030*, Vol. I. Colombo: Urban Development Authority.

Vasconcelos, R. P., Reis-Santos, P., Costa, M. J., and Cabral, H. N. (2011). Connectivity between estuaries and marine environment: integrating metrics to assess estuarine nursery function. *Ecol. Indic.* 11, 1123–1133. doi: 10.1016/j.ecolind.2010.12.012

Wei, H., He, Y., Li, Q., Liu, Z., and Wang, H. (2007). Summer hypoxia adjacent to the Changjiang Estuary. *J. Mar. Syst.* 67, 292–303. doi: 10.1016/j.jmarsys.2006.04.014

Wijeratne, E. M. S., and Rydberg, L. (2007). Modelling and observations of tidal wave propagation, circulation and residence times in Puttalam Lagoon, Sri Lanka. *Estuar. Coast. Shelf Sci.* 74, 697–708. doi: 10.1016/j.ecss.2007.05.012

Yan, Q., Cheng, T. T., Song, J., Zhou, J., Hung, C.-C., and Cai, Z. (2021). Internal nutrient loading is a potential source of eutrophication in Shenzhen Bay, China. *Ecol. Indic.* 127:107736. doi: 10.1016/j.ecolind.2021.107736

Conflict of Interest: The authors declare that the research was conducted in the absence of any commercial or financial relationships that could be construed as a potential conflict of interest.

Publisher's Note: All claims expressed in this article are solely those of the authors and do not necessarily represent those of their affiliated organizations, or those of the publisher, the editors and the reviewers. Any product that may be evaluated in this article, or claim that may be made by its manufacturer, is not guaranteed or endorsed by the publisher.

frontiers in Marine Science

ORIGINAL RESEARCH
published: 16 September 2021
doi: 10.3389/fmars.2021.709783

Biological CO_2 Uptake and Upwelling Regulate the Air-Sea CO_2 Flux in the Changjiang Plume Under South Winds in Summer

*Dewang Li[1,2,3], Xiaobo Ni[2,3,4], Kui Wang[5], Dingyong Zeng[2,3,4], Bin Wang[1,2,3], Haiyan Jin[1,2,6], Hongliang Li[1,2,3], Feng Zhou[2,3,4], Daji Huang[6] and Jianfang Chen[1,2,4]**

[1] Key Laboratory of Marine Ecosystem Dynamics, Ministry of Natural Resources, Hangzhou, China, [2] Second Institute of Oceanography, Ministry of Natural Resources, Hangzhou, China, [3] Observation and Research Station of Yangtze River Delta Marine Ecosystems, Ministry of Natural Resources, Zhoushan, China, [4] State Key Laboratory of Satellite Ocean Environment Dynamics, Second Institute of Oceanography, Ministry of Natural Resources, Hangzhou, China, [5] Ocean College, Zhejiang University, Zhoushan, China, [6] Key Laboratory of Tropical Marine Ecosystem and Bioresources, Fourth Institute of Oceanography, Ministry of Natural Resources, Beihai, China

OPEN ACCESS

Edited by:
Bangqin Huang, Xiamen University, China

Reviewed by:
Chen-Tung Chen, National Sun Yat-sen University, Taiwan
Xuegang Li, Institute of Oceanology, Chinese Academy of Sciences, China

***Correspondence:**
Jianfang Chen
jfchen@sio.org.cn

Specialty section:
This article was submitted to Marine Ecosystem Ecology, a section of the journal Frontiers in Marine Science

Received: *14 May 2021*
Accepted: *04 August 2021*
Published: *16 September 2021*

Citation:
Li D, Ni X, Wang K, Zeng D, Wang B, Jin H, Li H, Zhou F, Huang D and Chen J (2021) Biological CO_2 Uptake and Upwelling Regulate the Air-Sea CO_2 Flux in the Changjiang Plume Under South Winds in Summer. Front. Mar. Sci. 8:709783. doi: 10.3389/fmars.2021.709783

The partial pressure of CO_2 (pCO_2) in the sea and the air-sea CO_2 flux in plume waters are subject to interactions among biological production, horizontal advection, and upwelling under wind events. In this study, time series of pCO_2 and other biogeochemical parameters in the dynamic Changjiang plume were presented to illuminate the controlling factors of pCO_2 and the air-sea CO_2 flux after a strong south wind event (July 23–24, maximum of 11.2 ms^{-1}). The surface pCO_2 decreased by 310 μatm (to 184 μatm) from July 24 to 26. Low-pCO_2 waters (<200 μatm) were observed in the following 2 days. Corresponding chlorophyll *a* and dissolved oxygen (DO) increase, and a significant relationship between DO and npCO_2 indicated that biological uptake drove the pCO_2 decrease. The salinity of undersaturated-CO_2 waters decreased by 3.57 (from 25.03 to 21.46) within 2 days (July 27–28), suggesting the offshore advection of plume waters in which CO_2 had been biologically reduced. Four days after the wind event, the upwelling of high-CO_2 waters was observed, which increased the pCO_2 by 428 μatm (up to 584 μatm) within 6 days. Eight days after the onset of upwelling, the surface pCO_2 started to decrease (from 661 to 346 μatm within 3 days), which was probably associated with biological production. Regarding the air-sea CO_2 flux, the carbon sink of the plume was enhanced as the low-pCO_2 plume waters were pushed offshore under the south winds. In its initial stage, the subsequent upwelling made the surface waters act as a carbon source to the atmosphere. However, the surface waters became a carbon sink again after a week of upwelling. Such short-term air-sea carbon fluxes driven by wind have likely occurred in other dynamic coastal waters and have probably induced significant uncertainties in flux estimations.

Keywords: CO_2, Changjiang plume, biological uptake, wind, upwelling, plume advection, air-sea CO_2 flux

INTRODUCTION

The carbon cycles in shelf seas are important components of global carbon cycles. With 7% of the global ocean surface area, shelf seas take up to 0.05–0.4 Pg C a^{-1} (Borges et al., 2005; Cai et al., 2006; Chen et al., 2013; Dai et al., 2013; Laruelle et al., 2014), accounting for more than 10% of the global ocean carbon sink. The carbon sink is typically strong in river-dominated margins where large river plumes, such as the Changjiang plume (Zhai and Dai, 2009; Tseng et al., 2014; Guo et al., 2015), Pearl River plume (Zhai et al., 2005; Guo et al., 2009), and Amazon River plume (Ternon et al., 2000), induce significant biological uptake of carbon (Dai et al., 2013; Cao et al., 2020). Biological CO_2 uptake and the air-sea CO_2 flux in large river plumes have large spatial and temporal variations (Chen C.-T. A. et al., 2008; Guo et al., 2015) due to the influences of plume dynamics (Huang et al., 2013; Tseng et al., 2014), physical mixing, and the advection of water masses (Li et al., 2019), nutrient supply, temperature, etc. Wind forcing is one of the main factors impacting plume dynamics and biogeochemical cycles, as it has been revealed in field observations (Yin et al., 1997; Huang et al., 2013) and model studies (Fong and Geyer, 2001; Xuan et al., 2012; Lachkar and Gruber, 2013). However, the responses of CO_2 in plume waters to wind are largely unknown.

Alongshore wind drives offshore transport *via* Ekman transport of surface waters, leading to the upwelling of subsurface waters. Such well-known physical processes transport carbon and nutrients horizontally and vertically. The wind-driven upwelling of acidified and hypoxic bottom waters in the Chesapeake Bay contributes to large spatial variations in the surface partial pressure of carbon dioxide (pCO_2), pH, and aragonite saturation state (Li et al., 2020). In the eastern boundary of the Pacific Ocean, equatorward winds drive surface Ekman transport and the upwelling of nutrient-laden subsurface waters into the euphotic zone (Lachkar and Gruber, 2013). Such a nutrient supply stimulates phytoplankton blooms, which partially reduce CO_2 in upwelling waters. In the Mississippi River plume, upwelling-favorable winds transport the low-pCO_2 surface water offshore, enhancing the carbon sink (Huang et al., 2013).

Similar to the Mississippi River plume, the Changjiang plume is a strong carbon sink in summer due to intense biological production. The biological uptake of CO_2 and the air-sea CO_2 flux in the Changjiang plume have large temporal variations associated with episodic wind events (Li et al., 2018, 2019; Wu et al., 2020). Typhoon winds cause Changjiang plume waters to become a strong carbon source through the upward transport of high-CO_2 bottom waters (Li et al., 2019) or cause the waters to become carbon sinks by *in situ* biological production or the advection of undersaturated-CO_2 waters (Zhang et al., 2018; Wu et al., 2020). Unlike typhoons, southerly or southwesterly winds prevail in summer in the East China Sea and are associated with offshore advection and even the detachment of Changjiang plume waters (Lie et al., 2003; Xuan et al., 2012). Such plume dynamics affect the surface biological activity (Wei et al., 2017; Zhang et al., 2018) and likely also impact the air-sea carbon flux.

The offshore transport of buoyant plumes typically favors upwelling. In the outer Changjiang Estuary, upwelling is also modulated by the bottom topography and tidal mixing (Zhao, 1993; Lü et al., 2006; Hu and Wang, 2016). Cold surface waters with high surface pCO_2 have been identified along the Zhejiang coast (Chou et al., 2009a) due to the upwelling of high-CO_2 bottom waters. In contrast, the nutrients supplied by upwelling lead to a complex response of phytoplankton growth, which takes up CO_2. To our knowledge, few studies have reported how upwelling-favorable winds influence the pCO_2 of the Changjiang plume due to their transient nature.

In this study, we presented time-series buoy data in the Changjiang plume. High-temporal-resolution variations in temperature, salinity, pCO_2, dissolved oxygen (DO), and chlorophyll *a* (Chl *a*) after a wind event were analyzed to illuminate the response of pCO_2 to upwelling-favorable winds. The transient responses of the air-sea CO_2 flux to winds during the advection period, upwelling period, and post-upwelling period of the plume were also discussed.

MATERIALS AND METHODS

Buoy Deployment and Sample Measurements

The variations of sea surface temperature (SST), salinity, pCO_2, DO, Chl *a*, and 2-m winds were obtained using a moored buoy (July 20–August 11, 2015). The buoy was deployed at a Changjiang plume site (water depth ~45 m, 122.8°E, 30.6°N, **Figure 1**), which is located at the track of typhoon "Chan-Hom" (July 11, 2015). The details of the buoy observations were explained by Li et al. (2018). In brief, a mounted SAMI-CO_2

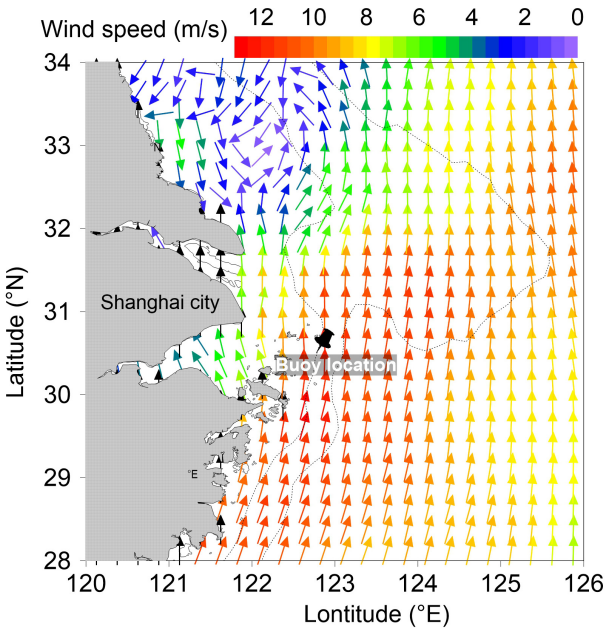

FIGURE 1 | Advanced Scatterometer winds over the East China Sea on July 24. The black pin denotes the buoy location. The colors represent the wind speed.

sensor (Sunburst Sensors, LLC) was used to measure sea surface pCO_2. This sensor has been previously used to measure pCO_2 at many locations worldwide (DeGrandpre et al., 1998; Körtzinger et al., 2008; Moore et al., 2011; Moralespineda et al., 2014; Li et al., 2019). The performances of the instrument were evaluated in a laboratory before deployment. Salinity, temperature, DO, and Chl *a* were measured with Water Quality Monitor meters (WET Labs, currently belonging to Sea-Bird Scientific). In addition, the bottom water temperature was also measured using an RBR *Maestro* data logger (RBR Ltd.) mounted on a trawl-resistant bottom mount (Ni et al., 2016). The wind speeds were recorded with a Young sensor attached to the top of the buoy (∼2 m above the sea surface). We also collected wind direction data from the NCEP/NCAR reanalysis 10-m wind dataset (124°E, 31.3°N). All sensors collected data every 15 min, except for the pCO_2 sensor, which collected data at 30-min intervals.

A Multi-Water Sampler (Hydro-Bios) was used to collect discrete water samples and measure salinity, temperature profiles on July 15, July 17, August 30, and September 1–2, 2015. The DO concentrations in the samples were determined using the Winkler titration method, and the discrete DO data were used to calibrate our buoy DO data. The Chl *a* concentrations in the samples were measured with a 10-AU Field Fluorometer (Turner Designs) after extraction with 90% of acetone.

Satellite-Retrieved SSTs and Winds

We collected remotely sensed SST data in the Changjiang Estuary from the Remote Sensing Systems[1]. This system comprises microwave optimally interpolated daily SST data products that combine the through-cloud capability of microwave data with the high spatial resolution and near-coastal capability of infrared SST data.

The wind data (**Figure 1**) were obtained from the Advanced Scatterometer wind products, which are processed by National Oceanic and Atmospheric Administration and National Environmental Satellite, Data, and Information Service[2]. The scatterometer instrument aboard the European Organization for the Exploitation of Meteorological Satellites Metop satellites uses radar to measure backscatter to determine the speed and direction of winds over the surface of the oceans.

Data Processing

The dissolved inorganic carbon (DIC) data at the buoy were calculated from the total alkalinity values, *in situ* temperature, salinity, and pCO_2 using the program CO2SYS (Pierrot et al., 2006) with the equilibrium constants of Mehrbach et al. (1973) as refined by Dickson and Millero (1987). The total alkalinity values were calculated using the buoy-recorded salinity data and the regression results of the total alkalinity and salinity data recorded during a cruise conducted from July 9 to 20, 2015 in the Changjiang estuary (Xiong et al., 2019).

The thermodynamic effect on pCO_2 was eliminated by normalizing it to a constant temperature, namely normalized pCO_2 ($npCO_2$) (Takahashi et al., 1993): $npCO_2 = pCO_2 \times \exp[0.0423 \times (25.04 - \mathrm{SST})]$. In the expression, 25.04 is the average SST during our record. The air-sea CO_2 fluxes were estimated using $F_{gas} = k \times s \times \Delta pCO_2$, where k is the gas transfer velocity, s is the carbon dioxide solubility (Weiss, 1974), and ΔpCO_2 is the difference between the sea surface pCO_2 and air pCO_2, which is assumed to be a constant of 396 μatm (calculated from the monthly air pCO_2 in July 2015 at Korea's Tae-ahn Peninsula site[3]. The gas transfer velocity (cm h^{-1}) was calculated according to *Wanninkhof* [2014].

RESULTS

Surface Salinity, Temperature, pCO_2, DO, and Chl *a* Variations

The wind speeds were generally less than 8 m s^{-1} in our record, except on July 23 and 24, when strong south winds prevailed with a maximum wind speed of 11.2 m s^{-1} (**Figures 1**, **2E**). Nine days before the presented buoy data (July 11), typhoon "Chan-Hom" passed the buoy, likely setting the baseline water property values. The SST and salinity fluctuated sharply within 23 days (July 20–August 11, **Figures 2A,B**). In this study, we divided the record into three periods according to the variations in salinity and temperature.

From July 20 to 26, the daily surface salinity values were relatively stable (25.03–26.32), while a steady surface Chl *a* increase and a pCO_2 decrease (494–184 μatm) were observed from July 24 to 26. During these 3 days, the surface oxygen was also supersaturated with respect to the atmosphere (7.75–10.32 mg L^{-1}). A sharp salinity decrease was observed from July 26 to 28, during which the daily salinity decreased by 3.57 (from 25.03 to 21.46). The surface CO_2 was undersaturated with respect to the atmosphere. The DO in the waters was supersaturated during the period of decreasing salinity. We assigned July 20–28 as period I, which witness strong south wind (**Figure 2E**).

Period II (July 28–August 3) was characterized by a continuous increase in salinity (21.46–29.72) and a decrease in temperature (26.91–23.46). Meanwhile, DO decreased from 9.85 to 6.59 mg L^{-1}. In addition, pCO_2 increased sharply from below 156 to 584 μatm. The surface Chl *a* decreased sharply during period II.

During period III (August 3–11), the temperature increased from 23.46 to 26.68 (August 9) and then decreased to 25.39 on August 11. The salinity decreased and then increased within 9 days. By comparison, the change in salinity in period III was much smaller than those during periods I and II. The surface pCO_2 continuously increased at the start of period III (from 156 to 584 μatm). However, it decreased sharply from August 5 to 9 (from 661 to 346 μatm). We also observed increases in Chl *a* and DO during this period.

Air-Sea CO_2 Flux

The air-sea CO_2 fluxes in the surface waters around our buoy showed significant short-term variations (**Figure 2F**). The surface waters served as weak CO_2 sources to the atmosphere at the

[1] http://www.remss.com/

[2] https://oceanwatch.pifsc.noaa.gov

[3] ftp://aftp.cmdl.noaa.gov

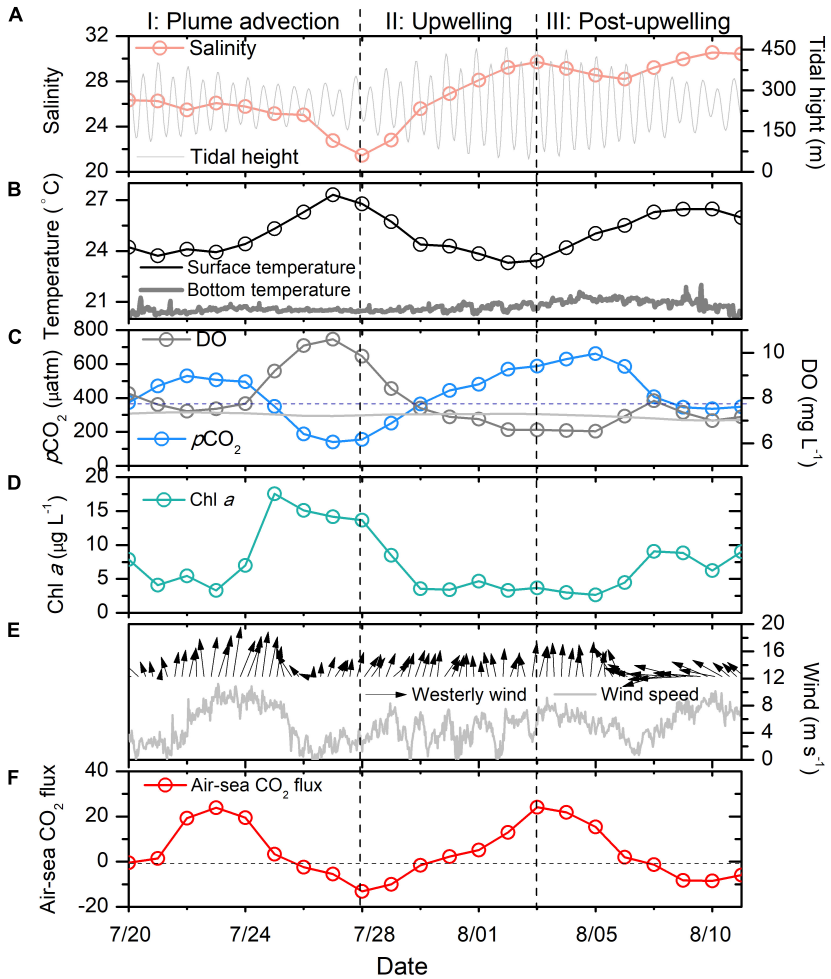

FIGURE 2 | Salinity **(A)**, temperature **(B)**, pCO_2 and DO **(C)**, Chl *a* **(D)**, wind **(E)** and air-sea CO_2 flux **(F)** variations during 20 July–11 August in the Changjiang plume waters. The gray dashed line in **(C)** is the atmospheric CO_2, while the gray line is the saturated oxygen in surface waters. In **(F)**, the gray dashed line shows the position where the air-sea CO_2 flux is zero. The two vertical dashed lines indicate the dates used to divide our time series data into three periods.

beginning of period I. The CO_2 source was enhanced from July 22 to 24 (maximum of +23.9 mmol m^{-2} day^{-1}), accompanied by a strong south wind. Starting on July 26, the surface waters became a strong CO_2 sink (−13.09 mmol m^{-2} day^{-1}).

During period II, the surface waters around our buoy gradually turned from a CO_2 sink to a CO_2 source (+24.1 mmol m^{-2} day^{-1}). However, the waters changed from a CO_2 source to a CO_2 sink again during period III (−8.45 mmol m^{-2} day^{-1}).

DISCUSSION

Advection of Plume Waters Influenced by the Biological Uptake of CO_2

A sharp increase in oxygen and a significant decrease in pCO_2 occurred on July 24–26 (from 494 to 184 μatm), at which time the maximum surface Chl *a* concentration was three times than that measured on July 23 (**Figure 2D**). The salinity varied by only 0.75, which was relatively minor in the dynamic coastal environment. Thus, it seemed that the advection of plume waters was not the driver of such significant biogeochemical responses around the buoy. The increasing Chl *a* concentration suggested that biological activity probably caused the coupled variations in pCO_2 and DO. Surface heating and low tides favor stratification, which is suitable for phytoplankton blooms. It is hard to know if the high biological production was directly associated with the strong south wind event (July 23) that may have made the plume thinner (Fong and Geyer, 2001). The high pCO_2 measured at the beginning of period I was probably related to the influence of the typhoon that occurred 9 days before period I (July 11) (Li et al., 2019).

The surface pCO_2 did not decrease gradually, as shown in the high temporal-resolution record: it decreased by 360 μatm within 16 h (**Figure 3B**). Such a sharp decrease did not necessarily indicate that CO_2 uptake occurred within such a short period, as it is an Euler observation. Generally, the biological uptake of DIC should be the sum of biological production uptake

within the transit time of plume, which is approximately 1 week for the Changjiang plume (Zhang et al., 2020). However, a considerable portion of CO_2 should have recently been consumed for the following reasons: first, the salinity was relatively constant within the 16 h (25.11–25.73, **Figure 3A**). Horizontal mixing should homogenize Chl *a* and pCO_2, as observed for salinity if the biological production occurred a week earlier. Second, the supersaturated oxygen indicated that the biological signals, or at least part of the signals, were probably created more recently, as the air-sea oxygen exchange equilibrates the surface water oxygen within approximately 1 week (Zeebe and Wolf-Gladrow, 2001). If biological production occurred a week earlier, the air-sea exchange should have largely modified the npCO_2–DO relationship (Zhai and Dai, 2009), which was not supported by our results (**Figure 4B**).

If the total alkalinity (calculated from the total alkalinity–salinity relationship) and pCO_2 were used to calculate the buoy DIC (details are shown in the "Materials and Methods" section) (Pierrot et al., 2006; Xiong et al., 2019), the DIC decrease from July 25 to 27 was 207 μmol kg^{-1}. Similar magnitudes of DIC drawdown have been reported in the Changjiang plume and Mississippi River plume (Guo et al., 2012; Wang et al., 2017). If we use 7 days as the plume residence time (Wang et al., 2014; Zhang et al., 2020), the net community production would be 346 mg m^{-3} day^{-1}. It is difficult to compare our results with previously reported results, as we did not measure DIC uptake data within the whole euphotic zone. In this study, we simply assumed no DIC uptake at the bottom of the euphotic zone. If a euphotic zone of 5 m was adopted (Ning, 1988), the net community production would be estimated as (346 mg m^{-3} day^{-1}+0)/2*5 *m* = 865 mg m^{-2} day^{-1}, which is well within the reported net community production and exported particulate organic carbon flux in the Changjiang plume waters (0.4–1.8 g m^{-2} day^{-1}) (Gong et al., 2003; Hung et al., 2013b; Wang et al., 2014, 2017). Such intense phytoplankton blooms could have a significant influence on bottom hypoxia, which is frequently observed outer of the Changjiang Estuary (Zhu et al., 2011; Wang et al., 2017). Moreover, we likely underestimated the biological production rate, as CO_2 uptake could happen within fewer days than the residence time. Such an underestimation was possible, as the hypoxic water volume in the Changjiang Estuary is larger than that in the Gulf of Mexico (Rabalais et al., 2003; Wang et al., 2017; Zhou et al., 2017), and in the Mississippi River plume, the net community production rate can be even larger than 7 g m^{-2} day^{-1} (Guo et al., 2012).

On July 27 and 28, we observed low-salinity waters (daily salinity = 21.46, **Figure 3A**) that were probably driven by the eastward expansion of the low-salinity Changjiang plume waters. The mixing of the low-salinity Changjiang plume waters and cold subsurface waters was verified by the salinity–temperature

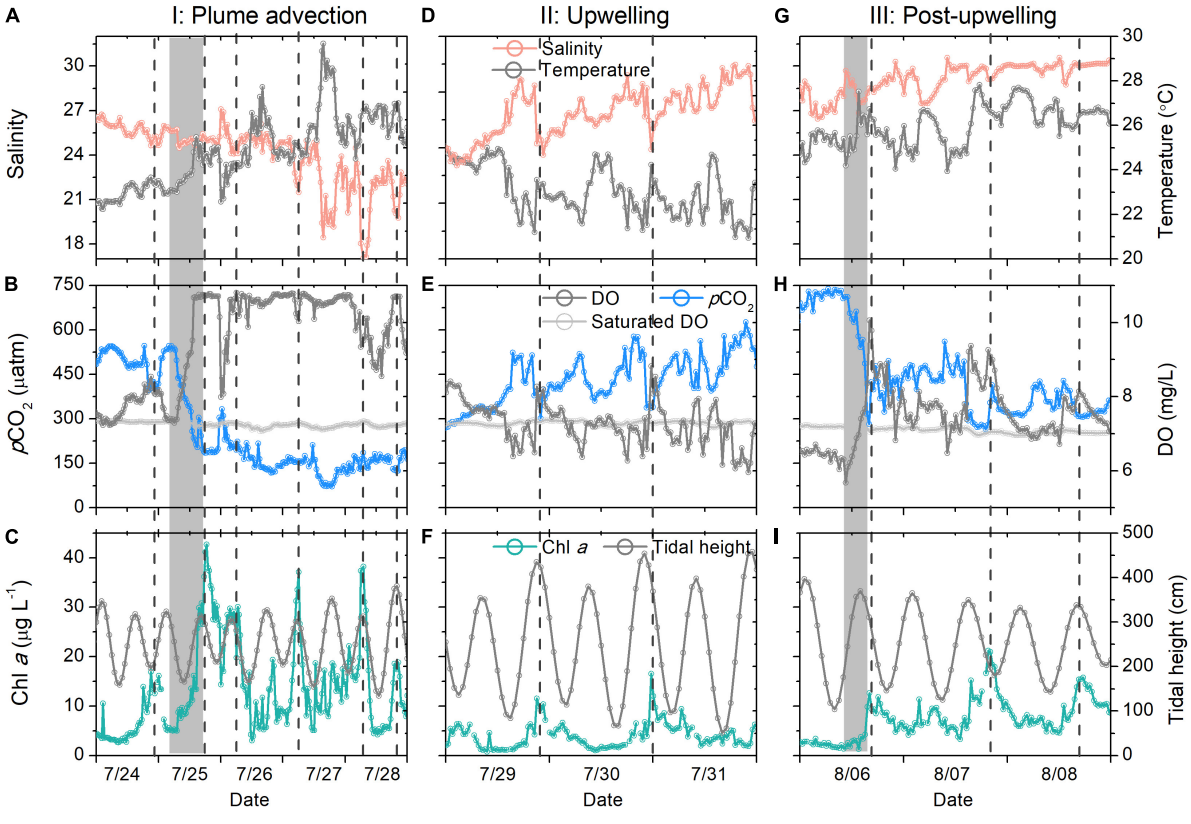

FIGURE 3 | High-temporal-resolution salinity and temperature **(A,D,G)**, pCO_2 and DO **(B,E,H)**, Chl *a* and tidal height **(C,F,I)** data during the three studied periods. The gray bars in **(C,I)** denote the sharp pCO_2 decrease. All vertical dashed lines denote the Chl *a* peaks.

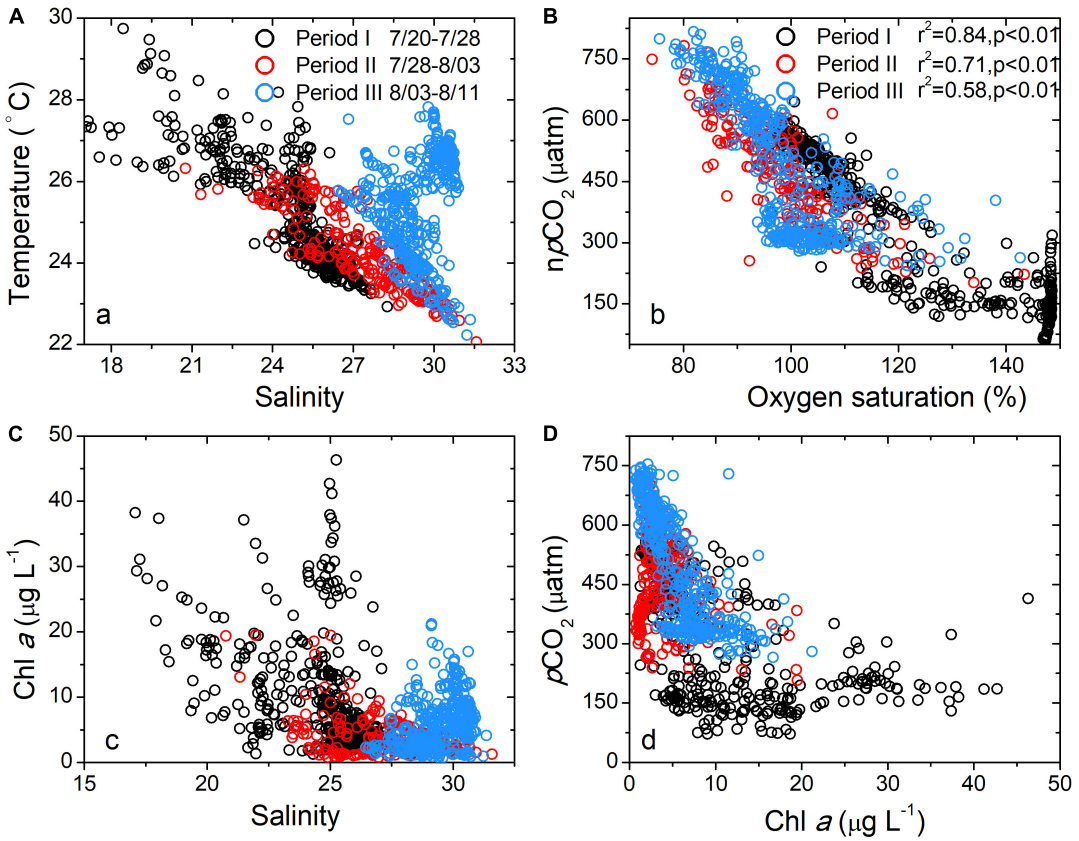

FIGURE 4 | Relationships among buoy-measured salinity and temperature **(A)**, oxygen saturation and npCO_2 **(B)**, Chl *a* and pCO_2 **(C)**, salinity and Chl *a* **(D)**.

relationship (**Figure 4A**). Such an extension was also verified by remotely sensed SST images, in which the plume water temperature was found to be higher than that of the ambient water (**Figure 5**). The extension of plume waters and even the detachment of the Changjiang plume from the main body have been frequently observed (Chen C. et al., 2008; Moon et al., 2010) and are probably driven by strong winds and tide mixing (Moon et al., 2010; Wu et al., 2011; Xuan et al., 2012). During period I, we observed strong south winds (>11 m s^{-1}, **Figure 2E**), which agreed with previous observations (Xuan et al., 2012).

The advection signal appeared 2 days after the end of the strong south winds (strong winds prevailed from July 23 to 24), while the plume extension seemed to start on July 24, as inferred from the satellite-derived results (**Figures 5a–e**). This delay was likely due to the plume largely extending northeast (**Figures 5c–e**), while our buoy was located east of the warm plume waters. On July 27 and 28, the salinity decreased by ∼5 within 12 h and increased by ∼3 within the next 12 h (**Figure 3A**), indicating that the plume core with a strong horizontal salinity gradient was probably located close to our buoy. That is, our buoy was located at the periphery of the plume. Our time-series and remote sensing results suggested strong temporal and spatial variations in the wind-induced plume dynamics. Wind-driven plume advection was also observed in the Mississippi River plume (Huang et al., 2013) and was found to enhance the carbon sink.

During the advection of plume waters, we observed a pulse of maximum Chl *a* (**Figure 3C**) that corresponded to extremely low salinity (salinity minimum of 17.07, **Figure 3A**). In addition, pCO_2 was lower than 200 μatm during this period. Low-salinity waters in inner estuaries typically have supersaturated pCO_2 (>600 μatm) (Zhai et al., 2007). In addition, the temperature increase observed during period I should accompany elevated pCO_2. The significant relationship between npCO_2 and DO observed during period I (**Figure 4B**) demonstrated that the pCO_2 decrease was probably dominated by biological production (Li et al., 2018).

In the Changjiang estuary, blooms are typically found in waters within a salinity range of 25–30 due to their high nutrient concentrations and suitable light conditions (Ning, 1988; Tseng et al., 2013; Wang et al., 2014). High Chl *a* concentrations at salinities of 17–22 are not frequently reported due to the high turbidity of these waters (**Figures 3C**, **4C**) (suspended matter typically >200 mg L^{-1}), as turbidity limits phytoplankton growth (Cloern, 1999). It is likely that the advection of the plume carried the low-salinity waters (minimum of 17.07) out of the maximum-turbidity zone (Shen et al., 2008). Thus, the biological production of the plume water was less limited by light.

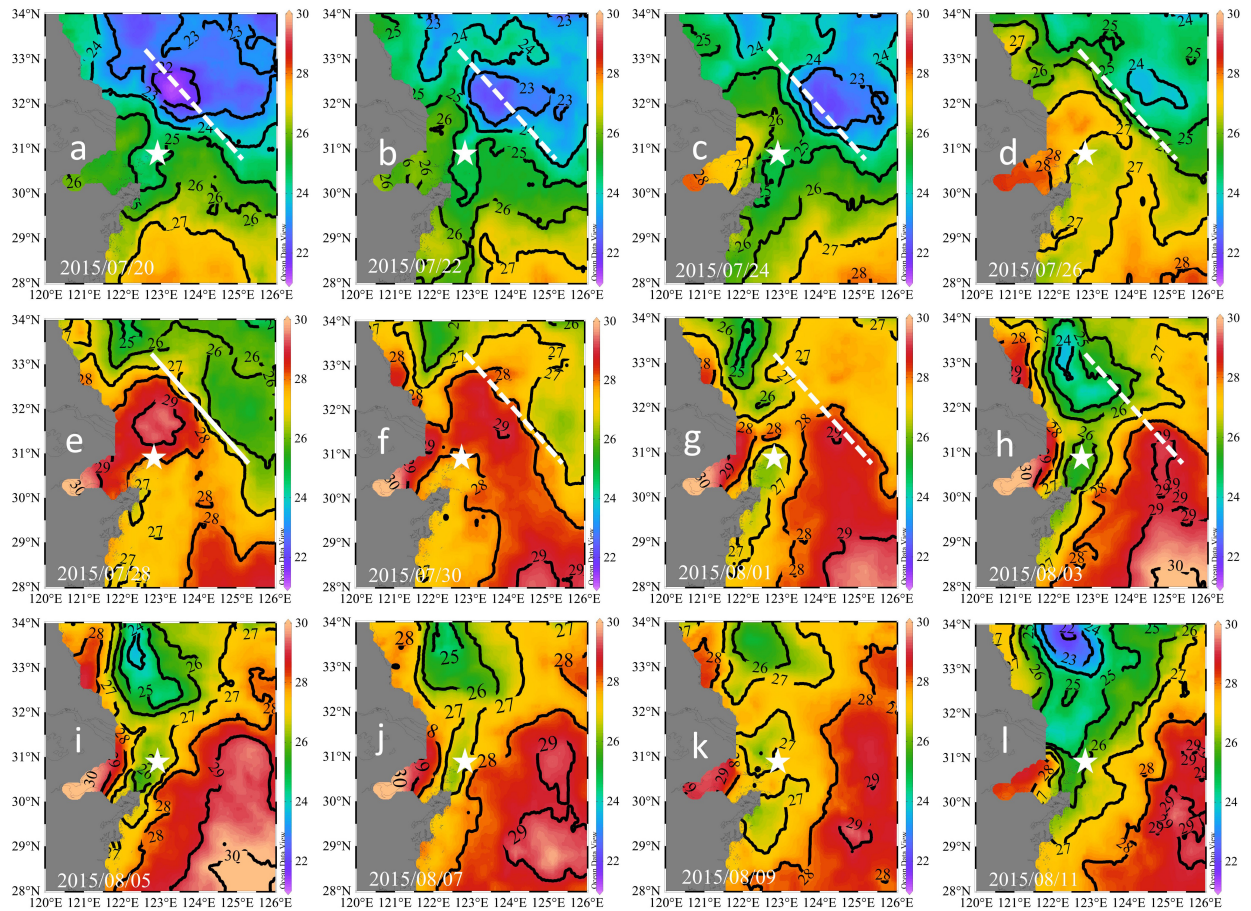

FIGURE 5 | Remotely-sensed sea surface temperatures during July 20 to August 11, 2015: 07/20 **(a)**, 07/22 **(b)**, 07/24 **(c)**, 07/26 **(d)**, 07/28 **(e)**, 07/30 **(f)**, 08/01 **(g)**, 08/03 **(h)**, 08/05 **(i)**, 08/07 **(j)**, 08/09 **(k)**, and 08/11 **(l)**. The white lines denote the location of the thermal front on July 28. The buoy location is shown by stars.

An extreme Chl *a* peak occurred from July 25 to 28 (**Figures 2D**, **3C**). Undersaturated CO_2 conditions lasted for 4 days, revealing the influence of an intense phytoplankton bloom. As high-Chl *a* plume waters were transported eastward under south winds, the low-pCO_2 signals could occupy a larger area. The cross-shelf transport of high-Chl *a* waters by frontal processes has been identified in the East China Sea (Yuan et al., 2005). In the Gulf of Mexico, the cross-shelf transport of low-salinity and low-pCO_2 waters under the influence of winds has also been reported previously (Huang et al., 2013). In this study, we showed that the advection of biological signals occurred within a few days, which makes it hard to capture these signals by traditional ship-based observations.

Although Chl *a* fluctuated considerably, pCO_2 remained low (**Figure 3B**). It is reasonable that the biological CO_2 signal lasted for a month due to the slow air-sea CO_2 exchange (Zeebe and Wolf-Gladrow, 2001), while Chl *a* has diel variations. Moreover, the surface pCO_2 and Chl *a* have a non-linear relationship (**Figure 4D**), which results from the non-linear pCO_2–DIC relationship and from Chl *a*–carbon ratio variations (Chang et al., 2003). The results also demonstrated that we should be cautious when using Chl *a* concentrations to retrieve biological-induced CO_2 uptake (Bai et al., 2015; Le et al., 2019).

Contrasting CO_2 During and After Upwelling

Four days after the wind event (July 29), the surface temperature decreased continuously (**Figure 2B**), verifying the upwelling of bottom waters. Upwelling was also revealed in the satellite results (**Figure 5g**). The upwelling signal overtook the horizontal advection signal, as inferred from the variations in salinity and temperature. It is reasonable to infer that the subsurface water upwelled to compensate for the offshore transport of surface waters. In addition, tidal mixing could also contribute to the observed upwelling, as discussed by Lü et al. (2006). Wu et al. (2011) also showed through simulations that subsurface waters under plumes upwell to the surface during spring tides. The daily salinity and temperature increased and decreased by 7.76°C (21.46–29.22°C) and 3.42°C (26.91–23.49°C) within 5 days, respectively (**Figure 3D**). The salinity profile of the water column around the buoy on July 17 showed waters with a salinity of 29.22 located at a depth of 22.5 m (**Figure 6**), which was adopted

as the depth of the upwelled water. Thus, the upwelling speed was calculated as 22.5 m per 5 days = 4.5 m day^{-1}, which is comparable with that reported in the upwelling area of northeast Taiwan (5.4 m day^{-1}) (Liu et al., 1992). The cold water patches (defined as areas with SSTs < 26°C) had double cores with a spatial scale of approximately 45,000 km^2 (**Figure 5i**), which is of similar magnitude to that measured in the southern East China Sea (32,000 km^2) (Hung et al., 2013a). As the subsurface waters upwelled, the high-temperature plume waters seemed to separate into two parts (**Figures 5f–h**), similar to the reported plume-detachment process (Xuan et al., 2012). The decreasing temperature in our buoy record ended on August 3. The cold core outside the Changjiang estuary lasted for at least a week after August 3, as revealed in the satellite results (**Figures 5g–k**).

We observed a continuous increase in pCO_2 during upwelling (increased by 428 μatm, **Figure 2C**). Supersaturated and undersaturated CO_2 have both been reported in other upwelling areas (Borges et al., 2005; Cai et al., 2006). It is typically accepted that the upwelling of nutrient-rich subsurface waters favors biological production, increasing Chl *a* and lowering pCO_2 (Fassbender et al., 2011). However, the Chl *a* concentration decreased rapidly at the onset of upwelling in this study (**Figure 3E**), probably because the upward transport of bottom waters diluted the surface Chl *a*. During 4 days of upwelling, an episodic Chl *a* peak was observed; this peak was always associated with a low-salinity spike (**Figure 3F**). The cold waters, however, did not have high Chl *a* signals. This result is reasonable, as the spring tides in period II did not favor the accumulation of Chl *a*. Additionally, phytoplankton growth requires time (their growth rates range from 0.3 to 3 day^{-1}) (Laws, 2013). The waters below the thermocline in the Changjiang Estuary are hypoxic and rich in CO_2 in summer (Chou et al., 2009b). The upwelling of hypoxic and high-CO_2 waters overtook the biological utilization of CO_2 (Li et al., 2019), inducing extremely high pCO_2 in surface waters during the initial period of upwelling. The extremely high pCO_2 (~600 μatm) observed in spring tides indicates that tidal mixing could be an important factor involved in carrying the high-CO_2 waters below the thermocline to the surface (August 2–3, **Figure 2C**).

Eight days after the onset of upwelling, a pCO_2 decrease of 353 μatm (from 635 to 282 μatm, **Figure 3H**) was observed within 8 h, accompanied by high Chl *a*. However, the salinity only changed by 1.59 within 8 h (**Figures 3G,I**). Additionally, the observed Chl *a* peaks were not necessarily related to low-salinity spikes, suggesting that they were probably not caused by the advection of the water mass. *In situ* CO_2 uptake by phytoplankton could be the reason for such a sharp pCO_2 decrease. Phytoplankton blooms occurred approximately 1 week after the onset of upwelling. Time delays have also been reported for blooms after typhoon events (Li et al., 2019). Phosphate supplies induced by upwelling are crucial for biological production in the Changjiang plume waters (Tseng et al., 2013), as these waters typically lack phosphate after strong biological production (Harrison et al., 1990; Wang et al., 2014). While the major nutrient supplying occurs during upwelling, the delay of blooms could possibly be attributed to hydrological factors, as the relaxation of upwelling and the neap tide favor the accumulation of Chl *a*.

Dynamic Air-Sea CO_2 Flux of Plume Waters Under South Winds

The turbid waters in the inner shelf served as a carbon source to the atmosphere (Zhai et al., 2007; **Figure 7**), while the role of the mid-salinity plume waters as either a carbon sink or source was temporally variable under the south winds (**Figures 2F**, **6**).

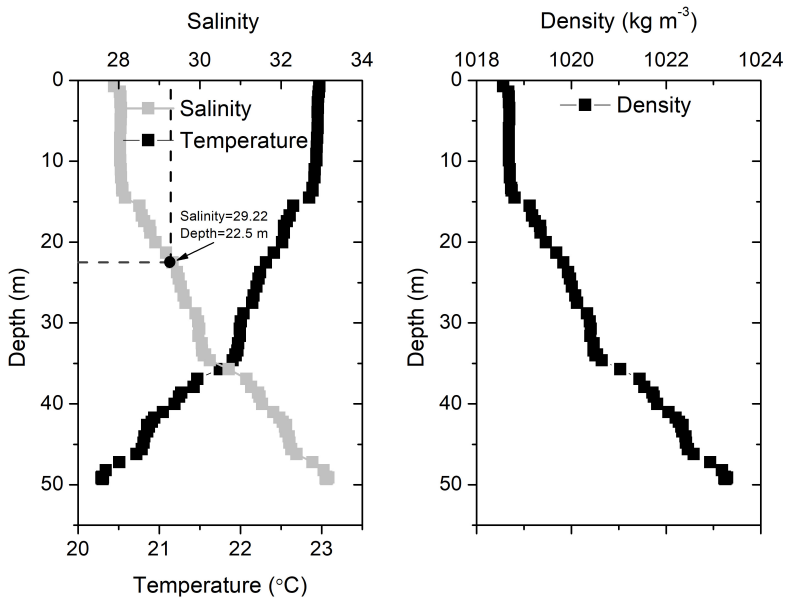

FIGURE 6 | Vertical salinity, temperature, and water density profiles around the buoy on July 17, 2015.

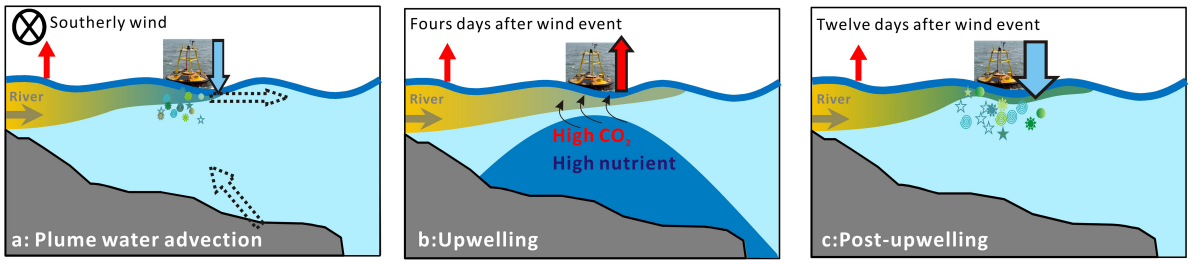

FIGURE 7 | Schematic of carbon flux variations in the Changjiang plume under south winds at plume water advection **(a)**, upwelling **(b)**, and post-upwelling **(c)** stages. The arrows on the right side of the buoy show the air-sea CO_2 fluxes in our results (blue arrow denotes carbon sink, while red arrow denotes carbon source). The horizontal and tilt dash arrows in panel **(a)** denote horizontal extension of plume waters and upwelling after the wind event, respectively. Upwelling of subsurface waters in panel **(b)** is marked by dark blue.

The surface waters turned from a carbon source to a carbon sink during the advection period (**Figure 7a**), accompanied by extremely high Chl *a* and supersaturated oxygen (**Figures 2C,D**). Previous study has validated the role of Changjiang plume waters as a significant carbon sink in summer (Zhai and Dai, 2009; Tseng et al., 2014). In this study, the carbon sink was estimated to be approximately −12 mmol m^{-2} day^{-1} (**Figure 2F**), which agreed with the values reported in previous study (Guo et al., 2015). As plume waters were transported offshore during upwelling-favorable wind, the carbon sink area likely expanded (**Figure 7a**), enhancing the carbon sink of the coastal waters. A similar mechanism has been revealed in the Mississippi River plume (Huang et al., 2013). In the Changjiang plume waters, the carbon sink area was probably larger than that reported for the Mississippi River plume.

Upwelling is frequently observed in the coastal waters of Zhejiang and the outer Changjiang Estuary (Lü et al., 2006; Hu and Wang, 2016). In our study, upwelling occurred 4 days after the wind event. Our observations showed that wind-driven upwelling first made the area a carbon source (**Figures 2F**, **7b**), which lasted for 5 days in our record. A previous study also suggested that the upwelling center along the Zhejiang coast had high surface DIC and supersaturated CO_2 (Chou et al., 2009a). Twelve days after the wind event, the waters around the buoy turned into a strong carbon sink with high Chl *a* (**Figure 7c**). There are intense debates about whether upwelling areas should be carbon sources or carbon sinks. As inferred from our results, it could be strongly dependent on the timing of observations (**Figures 7a–c**). The overall effects of upwelling on the air-sea CO_2 flux rely on nutrients and the CO_2 concentrations of source waters during upwelling and should be evaluated on larger spatial and temporal scales.

The offshore advection of water parcels and cold upwelling water have been frequently observed in the outer Changjiang estuary and along the Zhejiang coast in summer (Zhao, 1993; Yuan et al., 2005; Lü et al., 2006; Chen C. et al., 2008; Moon et al., 2010). The interactions of biogeochemical and physical processes occur on multiple time scales of days to a week under the influence of winds. Thus, the surface carbon systems and the air-sea CO_2 flux of coastal waters could be extremely dynamic, as inferred from our time-series study. A combination of mooring observations, transect surveys, numerical simulations, and satellite observations is needed to fully understand the response of carbon dynamics to wind events.

DATA AVAILABILITY STATEMENT

The raw data supporting the conclusions of this article will be made available by the authors, without undue reservation, to any qualified researcher.

AUTHOR CONTRIBUTIONS

JC and DL conceived the idea. DL collected the data and wrote the manuscript. XN, KW, and DZ collected and processed the data. BW, HJ, HL, FZ, and DH discussed and revised the manuscript. All authors reviewed the manuscript.

FUNDING

This study was jointly supported by the National Natural Science Foundation of China (U1709201, 41806095, 41706120, and 41976154), Long-Term Observation and Research Plan in the Changjiang Estuary and the Adjacent East China Sea Project I and II (LORCE I&II), Hypoxia and Acidification Monitoring and Warning Project in the Changjiang Estuary, and Scientific Research Fund of the Second Institute of Oceanography, MNR (JG1715).

ACKNOWLEDGMENTS

We would like to thank the crew of Zheshengyu 06145 for their support in collecting water samples and deploying the buoy. We would also like to thank Minhui Zheng for his help in the calibration of the SAMI-pCO_2 sensor before and after the field deployment. Data are available by contacting the corresponding author. The remotely sensed SST data were obtained from the Remote Sensing Systems (www.remss.com), which is sponsored by NASA.

REFERENCES

Bai, Y., Cai, W. J., He, X. Q., Zhai, W. D., Pan, D. L., Dai, M. H., et al. (2015). A mechanistic semi-analytical method for remotely sensing sea surface pCO_2 in river-dominated coastal oceans: a case study from the East China Sea. *J. Geophys. Res.* 120, 2331–2349. doi: 10.1002/2014JC010632

Borges, A., Delille, B., and Frankignoulle, M. (2005). Budgeting sinks and sources of CO_2 in the coastal ocean: diversity of ecosystems counts. *Geophys. Res. Lett.* 32:L14601.

Cai, W.-J., Dai, M. H., and Wang, Y. C. (2006). Air-sea exchange of carbon dioxide in ocean margins: a province-based synthesis. *Geophys. Res. Lett.* 33:L12603.

Cao, Z., Yang, W., Zhao, Y., Guo, X., Yin, Z., Du, C., et al. (2020). Diagnosis of CO_2 dynamics and fluxes in global coastal oceans. *Nat. Sci. Rev.* 7, 786–797. doi: 10.1093/NSR/NWZ105

Chang, J., Shiah, F.-K., Gong, G.-C., and Chiang, K. P. (2003). Cross-shelf variation in carbon to chlorophyll *a* ratios in the East China Sea, summer 1998. *Deep Sea Res. Part II* 50, 1237–1247.

Chen, C., Xue, P., Ding, P., Beardsley, R. C., Xu, Q., Mao, X., et al. (2008). Physical mechanisms for the offshore detachment of the Changjiang diluted water in the East China Sea. *J. Geophys. Res.* 113:C02002.

Chen, C. T. A., Huang, T., Chen, Y. C., Bai, Y., He, X., and Kang, Y. (2013). Air-sea exchanges of CO_2 in the world's coastal seas. *Biogeosciences* 10, 6509–6544. doi: 10.5194/bg-10-6509-2013

Chen, C.-T. A., Zhai, W. D., and Dai, M. H. (2008). Riverine input and air–sea CO_2 exchanges near the Changjiang (Yangtze River) Estuary: status quo and implication on possible future changes in metabolic status. *Cont. Shelf Res.* 28, 1476–1482. doi: 10.1016/j.csr.2007.10.013

Chou, W. C., Gong, G. C., Sheu, D. D., Hung, C., and Tseng, T. (2009a). Surface distributions of carbon chemistry parameters in the East China Sea in summer 2007. *J. Geophys. Res.* 114:C07026. doi: 10.1029/2008JC005128

Chou, W. C., Gong, G. C., Sheu, D. D., Jan, S., Hung, C. C., and Chen, C. C. (2009b). Reconciling the paradox that the heterotrophic waters of the East China Sea shelf act as a significant CO_2 sink during the summertime: evidence and implications. *Geophys. Res. Lett.* 36:L15607. doi: 10.1029/2009GL038475

Cloern, J. E. (1999). The relative importance of light and nutrient limitation of phytoplankton growth: a simple index of coastal ecosystem sensitivity to nutrient enrichment. *Aquat. Ecol.* 33, 3–15. doi: 10.1023/A:1009952125558

Dai, M. H., Cao, Z. M., Guo, X. H., Zhai, W. D., Liu, Z., Yin, Z., et al. (2013). Why are some marginal seas sources of atmospheric CO_2? *Geophys. Res. Lett.* 40, 2154–2158. doi: 10.1002/grl.50390

DeGrandpre, M. D., Hammar, T. R., and Wirick, C. D. (1998). Short-term pCO_2 and O_2 dynamics in California coastal waters. *Deep Sea Res. Part II* 45, 1557–1575. doi: 10.1016/s0967-0645(98)80006-4

Dickson, A. G., and Millero, F. J. (1987). A comparison of the equilibrium constants for the dissociation of carbonic acid in seawater media. *Deep Sea Res. A Oceanogr. Res. Pap.* 34, 1733–1743. doi: 10.1016/0198-0149(87)90021-5

Fassbender, A. J., Sabine, C. L., Feely, R. A., Langdon, C., and Mordy, C. W. (2011). Inorganic carbon dynamics during northern California coastal upwelling. *Cont. Shelf Res.* 31, 1180–1192. doi: 10.1016/j.csr.2011.04.006

Fong, D. A., and Geyer, W. R. (2001). Response of a river plume during an upwelling favorable wind event. *J. Geophys. Res.* 106, 1067–1084. doi: 10.1029/2000JC900134

Gong, G.-C., Wen, Y.-H., Wang, B.-W., and Liu, G.-J. (2003). Seasonal variation of chlorophyll *a* concentration, primary production and environmental conditions in the subtropical East China Sea. *Deep Sea Res. Part II* 50, 1219–1236. doi: 10.1016/s0967-0645(03)00019-5

Guo, X., Dai, M., Zhai, W., Cai, W.-J., and Chen, B. (2009). CO_2 flux and seasonal variability in a large subtropical estuarine system, the Pearl River Estuary, China. *J. Geophys. Res.* 114:G03013. doi: 10.1029/2008JG000905

Guo, X. H., Cai, W.-J., Huang, W.-J., Wang, Y., Chen, F., Murrell, M. C., et al. (2012). Carbon dynamics and community production in the Mississippi River plume. *Limnol. Oceanogr.* 57, 1–17. doi: 10.4319/lo.2012.57.1.0001

Guo, X.-H., Zhai, W.-D., Dai, M.-H., Zhang, C., Bai, Y., Xu, Y., et al. (2015). Air–sea CO_2 fluxes in the East China Sea based on multiple-year underway observations. *Biogeosciences* 12, 5495–5514. doi: 10.5194/bg-12-5495-2015

Harrison, P., Hu, M., Yang, Y., and Lu, X. (1990). Phosphate limitation in estuarine and coastal waters of China. *J. Exp. Mar. Biol. Ecol.* 140, 79–87. doi: 10.1016/0022-0981(90)90083-o

Hu, J., and Wang, X. H. (2016). Progress on upwelling studies in the China seas. *Rev. Geophys.* 54, 653–673. doi: 10.1002/2015RG000505

Huang, W., Cai, W. J., Castelao, R. M., Wang, Y., and Lohrenz, S. E. (2013). Effects of a wind-driven cross-shelf large river plume on biological production and CO_2 uptake on the Gulf of Mexico during spring. *Limnol. Oceanogr.* 58, 1727–1735. doi: 10.4319/lo.2013.58.5.1727

Hung, C. C., Chung, C., Gong, G., Jan, S., Tsai, Y., Chen, K., et al. (2013a). Nutrient supply in the Southern East China Sea after Typhoon Morakot. *J. Mar. Res.* 71, 133–149. doi: 10.1357/002224013807343425

Hung, C. C., Tseng, C. W., Gong, G. C., Chen, K. S., Chen, M. H., and Hsu, S. C. (2013b). Fluxes of particulate organic carbon in the East China Sea in summer. *Biogeosciences* 10, 6469–6484. doi: 10.5194/bg-10-6469-2013

Körtzinger, A., Send, U., Lampitt, R., Hartman, S., Wallace, D. W., Karstensen, J., et al. (2008). The seasonal pCO_2 cycle at 49 N/16.5 W in the northeastern Atlantic Ocean and what it tells us about biological productivity. *J. Geophys. Res. Oceans* 113:C04020.

Lachkar, Z., and Gruber, N. (2013). Response of biological production and air–sea CO_2 fluxes to upwelling intensification in the California and Canary Current Systems. *J. Mar. Res.* 109, 149–160. doi: 10.1016/J.JMARSYS.2012.04.003

Laruelle, G. G., Lauerwald, R., Pfeil, B., and Regnier, P. (2014). Regionalized global budget of the CO_2 exchange at the air-water interface in continental shelf seas. *Glob. Biogeochem. Cycle* 28, 1199–1214. doi: 10.1002/2014gb004832

Laws, E. A. (2013). Evaluation of *In Situ* Phytoplankton Growth Rates: a Synthesis of Data from Varied Approaches. *Annu. Rev. Mar. Sci.* 5, 247–268. doi: 10.1146/annurev-marine-121211-172258

Le, C. F., Gao, Y., Cai, W.-J., Lehrter, J. C., Bai, Y., and Jiang, Z.-P. (2019). Estimating summer sea surface pCO_2 on a river-dominated continental shelf using a satellite-based semi-mechanistic model. *Remote Sens. Environ.* 225, 115–126. doi: 10.1016/J.RSE.2019.02.023

Li, D. W., Chen, J. F., Ni, X. B., Wang, K., Zeng, D. Y., Wang, B., et al. (2018). Effects of biological production and vertical mixing on sea surface pCO_2 variations in the Changjiang River plume during early autumn: a buoy-based time series study. *J. Geophys. Res. Oceans* 123, 6156–6173. doi: 10.1029/2017JC013740

Li, D. W., Chen, J. F., Ni, X. B., Wang, K., Zeng, D. Y., Wang, B., et al. (2019). Hypoxic bottom waters as a carbon source to atmosphere during a typhoon passage over the East China Sea. *Geophys. Res. Lett.* 46, 11329–11337. doi: 10.1029/2019gl083933

Li, M., Li, R., Cai, W.-J., Testa, J. M., and Shen, C. (2020). Effects of wind-criven lateral upwelling on estuarine carbonate chemistry. *Front. Mar. Sci.* 7:588465. doi: 10.3389/FMARS.2020.588465

Lie, H. J., Cho, C. H., Lee, J. H., and Lee, S. (2003). Structure and eastward extension of the Changjiang River plume in the East China Sea. *J. Geophys. Res.* 108:3077.

Liu, K.-K., Gong, G.-C., Lin, S., Yang, C.-Y., Wei, C.-L., Pai, S.-C., et al. (1992). The year-round upwelling at the shelf break near the northern tip of Taiwan as evidenced by chemical hydrography. *Terr. Atmos. Ocean. Sci.* 3, 243–275. doi: 10.3319/tao.1992.3.3.243(keep)

Lü, X., Qiao, F., Xia, C., Zhu, J., and Yuan, Y. (2006). Upwelling off Yangtze River estuary in summer. *J. Geophys. Res. Oceans* 111:C11S08.

Mehrbach, C., Culberson, C. H., Hawley, J. E., and Pytkowicx, R. M. (1973). Measurement of the apparent dissociation constants of carbonic acid in seawater at atmospheric pressure. *Limnol. Oceanogr.* 18, 897–907. doi: 10.4319/lo.1973.18.6.0897

Moon, J.-H., Hirose, N., Yoon, J.-H., and Pang, I.-C. (2010). Offshore detachment process of the low-salinity water around Changjiang bank in the East China Sea. *J. Phys. Oceanogr.* 40, 1035–1051. doi: 10.1175/2010jpo4167.1

Moore, T. S., Degrandpre, M. D., Sabine, C. L., Hamme, R. C., Zappa, C. J., Mcgillis, W. R., et al. (2011). Sea surface pCO_2 and O_2 in the Southern Ocean during the austral fall, 2008. *J. Geophys. Res.* 116:C00F11. doi: 10.1029/2010JC006560

Moralespineda, M., Cozar, A., Laiz, I., Ubeda, B., and Galvez, J. A. (2014). Daily, biweekly, and seasonal temporal scales of pCO_2 variability in two stratified Mediterranean reservoirs. *J. Geophys. Res.* 119, 509–520. doi: 10.1002/2013JG002317

Ni, X. B., Huang, D. H., Zeng, D. Y., Zhang, T., Li, H. L., and Chen, J. F. (2016). The impact of wind mixing on the variation of bottom dissolved oxygen off the Changjiang Estuary during summer. *J. Mar. Res.* 154, 122–130. doi: 10.1016/j.jmarsys.2014.11.010

Ning, X. R. (1988). Standing stock and production of phytoplankton in the estuary of the Changjiang (Yangtze River) and the adjacent East China Sea. *Mar. Ecol. Prog. Ser.* 49, 141–150. doi: 10.3354/meps049141

Pierrot, D., Lewis, E., and Wallace, D. (2006). *MS Excel program developed for CO_2 system calculations ORNL/CDIAC-105a*. Oak Ridge, Tennessee: Carbon Dioxide Information Analysis Center, Oak Ridge National Laboratory, US Department of Energy.

Rabalais, N. N., Turner, R. E., and Wiseman, J. W. (2003). Gulf of Mexico hypoxia, A.K.A. "The dead zone". *Annu. Rev. Ecol. Syst.* 33, 235–263. doi: 10.1146/annurev.ecolsys.33.010802.150513

Shen, Z., Zhou, S., and Pei, S. (2008). Transfer and transport of phosphorus and silica in the turbidity maximum zone of the Changjiang estuary. *Estuar. Coast. Shelf Sci.* 78, 481–492. doi: 10.1016/j.ecss.2008.01.010

Takahashi, T., Olafsson, J., Goddard, J. G., Chipman, D. W., and Sutherland, S. (1993). Seasonal variation of CO_2 and nutrients in the high-latitude surface oceans: a comparative study. *Glob. Biogeochem. Cycle* 7, 843–878. doi: 10.1029/93GB02263

Ternon, J.-F., Oudot, C., Dessier, A., and Diverrès, D. (2000). A seasonal tropical sink for atmospheric CO_2 in the Atlantic ocean : the role of the Amazon river discharge. *Mar. Chem.* 68, 183–201. doi: 10.1016/S0304-4203(99)00077-8

Tseng, C. M., Shen, P. Y., and Liu, K. K. (2014). Synthesis of observed air-sea CO_2 exchange fluxes in the river-dominated East China Sea and improved estimates of annual and seasonal net mean fluxes. *Biogeosciences* 11, 3855–3870. doi: 10.5194/bg-11-3855-2014

Tseng, Y.-F., Lin, J., Dai, M., and Kao, S.-J. (2013). Joint effect of freshwater plume and coastal upwelling on phytoplankton growth off the Changjiang River. *Biogeosciences* 10, 10363–10397.

Wang, B., Chen, J. F., Jin, H. Y., Li, H. L., Huang, D. J., and Cai, W.-J. (2017). Diatom bloom-derived bottom water hypoxia off the Changjiang estuary, with and without typhoon influence. *Limnol. Oceanogr.* 62, 1552–1569. doi: 10.1002/lno.10517

Wang, K., Chen, J. F., Jin, H. Y., Li, H. L., Gao, S. Q., Xu, J., et al. (2014). Summer nutrient dynamics and biological carbon uptake rate in the Changjiang River plume inferred using a three end-member mixing model. *Cont. Shelf Res.* 91, 192–200. doi: 10.1016/j.csr.2014.09.013

Wei, Q. S., Yu, Z., Wang, B., Wu, H., Sun, J., Zhang, X., et al. (2017). Offshore detachment of the Changjiang River plume and its ecological impacts in summer. *J. Oceanogr.* 73, 277–294. doi: 10.1007/s10872-016-0402-0

Weiss, R. F. (1974). Carbon dioxide in water and seawater: the solubility of a non-ideal gas. *Mar. Chem.* 2, 203–215. doi: 10.1016/0304-4203(74)90015-2

Wu, H., Zhu, J., Shen, J., and Wang, H. V. (2011). Tidal modulation on the Changjiang River plume in summer. *J. Geophys. Res.* 116:C08017. doi: 10.1029/2011JC007209

Wu, Y. X., Dai, M. H., Guo, X. H., Chen, J., Xu, Y., Dong, X., et al. (2020). High-frequency time-series autonomous observations of sea surface pCO_2 and pH. *Limnol. Oceanogr.* 66, 588–606. doi: 10.1002/LNO.11625

Xiong, T. Q., Liu, P. F., Zhai, W. D., Bai, Y., Liu, D., Qi, D., et al. (2019). Export Flux, biogeochemical effects, and the fate of a terrestrial carbonate system: from Changjiang (Yangtze River) estuary to the East China Sea. *Earth Space Sci.* 6, 2115–2141. doi: 10.1029/2019EA000679

Xuan, J. L., Huang, D. J., Zhou, F., Zhu, X., and Fan, X. (2012). The role of wind on the detachment of low salinity water in the Changjiang Estuary in summer. *J. Geophys. Res.* 117:C10004. doi: 10.1029/2012JC008121

Yin, K. D., Goldblatt, R. H., Harrison, P. J., John, M. S., Clifford, P. J., and Beamish, R. J. (1997). Importance of wind and river discharge in influencing nutrient dynamics and phytoplankton production in summer in the central Strait of Georgia. *Mar. Ecol. Prog. Ser.* 161, 173–183. doi: 10.3354/meps161173

Yuan, D. L., Qiao, F. L., and Su, J. (2005). Cross-shelf penetrating fronts off the southeast coast of China observed by MODIS. *Geophys. Res. Lett.* 32:L19603.

Zeebe, R. E., and Wolf-Gladrow, D. (2001). *CO_2 in Seawater: Equilibrium, Kinetics, Isotopes*. Amsterdam: Elsevier Oceanography Book Series.

Zhai, W. D., and Dai, M. H. (2009). On the seasonal variation of air–sea CO_2 fluxes in the outer Changjiang (Yangtze River) Estuary, East China Sea. *Mar. Chem.* 117, 2–10. doi: 10.1016/j.marchem.2009.02.008

Zhai, W. D., Dai, M. H., Cai, W.-J., Wang, Y., and Hong, H. (2005). The partial pressure of carbon dioxide and air–sea fluxes in the northern South China Sea in spring, summer and autumn. *Mar. Chem.* 96, 87–97. doi: 10.1016/j.marchem.2004.12.002

Zhai, W. D., Dai, M. H., and Guo, X. H. (2007). Carbonate system and CO_2 degassing fluxes in the inner estuary of Changjiang (Yangtze) River, China. *Mar. Chem.* 107, 342–356. doi: 10.1016/j.marchem.2007.02.011

Zhang, Z. R., Zhou, M., Zhong, Y. S., Zhang, G. S., Jiang, S., Gao, Y. H., et al. (2020). Spatial variations of phytoplankton biomass controlled by river plume dynamics over the lower Changjiang Estuary and adjacent shelf based on high-resolution observations. *Front. Mar. Sci.* 7:587539. doi: 10.3389/FMARS.2020.587539

Zhang, Z. W., Wu, H., Yin, X. Q., and Qiao, F. L. (2018). Dynamical response of Changjiang River plume to a severe typhoon with the surface wave-induced mixing. *J. Geophys. Res.* 123, 9369–9388. doi: 10.1029/2018jc014266

Zhao, B. R. (1993). Upwelling phenomenon off Changjiang estuary. *Acta Oceanol. Sin.* 15, 106–114.

Zhou, F., Chai, F., Huang, D. J., Xue, H. J., Chen, J. F., Xiu, P., et al. (2017). Investigation of hypoxia off the Changjiang Estuary using a coupled model of ROMS-CoSiNE. *Prog. Oceanogr.* 159, 237–254. doi: 10.1016/J.POCEAN.2017.10.008

Zhu, Z.-Y., Zhang, J., Wu, Y., Zhang, Y.-Y., Lin, J., and Liu, S.-M. (2011). Hypoxia off the Changjiang (Yangtze River) Estuary: oxygen depletion and organic matter decomposition. *Mar. Chem.* 125, 108–116. doi: 10.1016/j.marchem.2011.03.005

Conflict of Interest: The authors declare that the research was conducted in the absence of any commercial or financial relationships that could be construed as a potential conflict of interest.

Publisher's Note: All claims expressed in this article are solely those of the authors and do not necessarily represent those of their affiliated organizations, or those of the publisher, the editors and the reviewers. Any product that may be evaluated in this article, or claim that may be made by its manufacturer, is not guaranteed or endorsed by the publisher.

frontiers in Marine Science

ORIGINAL RESEARCH
published: 04 October 2021
doi: 10.3389/fmars.2021.747763

Comparison of Primary Production Using *in situ* and Satellite-Derived Values at the SEATS Station in the South China Sea

*Yung-Yen Shih[1,2], Fuh-Kwo Shiah[3], Chao-Chen Lai[3], Wen-Chen Chou[4,5], Jen-Hua Tai[3], Yu-Shun Wu[1], Cheng-Yang Lai[1], Chia-Ying Ko[6] and Chin-Chang Hung[2]**

[1] Department of Applied Science, R.O.C. Naval Academy, Kaohsiung, Taiwan, [2] Department of Oceanography, National Sun Yat-sen University, Kaohsiung, Taiwan, [3] Research Center for Environmental Changes, Academia Sinica, Taipei, Taiwan, [4] Institute of Marine Environment and Ecology, National Taiwan Ocean University, Keelung, Taiwan, [5] Center of Excellence for the Oceans, National Taiwan Ocean University, Keelung, Taiwan, [6] Institute of Fisheries Science, National Taiwan University, Taipei, Taiwan

OPEN ACCESS

Edited by:
Bernardo Antonio Perez Da Gama, Fluminense Federal University, Brazil

Reviewed by:
Hartmut Schulz, University of Tuebingen, Germany
David Michael Karl, University of Hawaii, United States

***Correspondence:**
Chin-Chang Hung
cchung@mail.nsysu.edu.tw

Specialty section:
This article was submitted to Marine Ecosystem Ecology, a section of the journal Frontiers in Marine Science

Received: *26 July 2021*
Accepted: *02 September 2021*
Published: *04 October 2021*

Citation:
Shih Y-Y, Shiah F-K, Lai C-C, Chou W-C, Tai J-H, Wu Y-S, Lai C-Y, Ko C-Y and Hung C-C (2021) Comparison of Primary Production Using in situ and Satellite-Derived Values at the SEATS Station in the South China Sea. Front. Mar. Sci. 8:747763. doi: 10.3389/fmars.2021.747763

Satellite-based observations of primary production (PP) are broadly used to assess carbon fixation rate of phytoplankton in the global ocean with small spatiotemporal limitations. However, the remote sensing can only reach the ocean surface, the assumption of a PP vertically exponential decrease with increasing depth from the surface to the bottom of euphotic zone may cause a substantial and potential discrepancy between *in situ* measurements and satellite-based observations of PP. This study compared euphotic zone integrated PP derived from measurements based on ship-based *in situ* incubation (i.e., $PP_{in\ situ}$) and those derived from the satellite-based vertically generalized production model (VGPM; PP_{VGPM}) for the period 2003∼2016 at the South East Asian Time-series Study (SEATS) station. PP values obtained during the NE-monsoon (NEM: Nov∼Mar; $PP_{in\ situ}$ = 323 ± 134; PP_{VGPM} = 443 ± 142 mg-C m^{-2} d^{-1}) were ∼2-fold higher than those recorded during the SW-monsoon (SWM: Apr∼Oct; $PP_{in\ situ}$ = 159 ± 58; PP_{VGPM} = 250 ± 36 mg-C m^{-2} d^{-1}), regardless of the method used for derivation. The main reason for the higher PP values during the NEM appears to have been a greater abundance of inorganic nutrients were made available by vertical advection. Note that on average, $PP_{in\ situ}$ estimates were ∼50% lower than PP_{VGPM} estimates, regardless of the monsoon. These discrepancies can be mainly attributed to differences from the euphotic zone depth between satellite-based and *in situ* measurements. The significantly negative relationship between PP measurements obtained *in situ* and sea surface temperatures observed throughout this study demonstrates that both methods are effective indicators in estimating PP. Overall, our $PP_{in\ situ}$ analysis indicates that a warming climate is unfavorable for primary production in low-latitude open ocean ecosystems.

Keywords: carbon fixation rate, remote sensing, time-series study, global warming, low-latitude ocean, VGPM

INTRODUCTION

Primary production at the bottom of the marine food web plays a key role in the ocean ecosystem (Pauly and Christensen, 1995) and represents a major pathway for sequestration and/or cycling of atmospheric CO_2 by the oceans. However, this process is highly susceptible to environmental and climatic changes (Buitenhuis et al., 2013; Hung et al., 2013, 2016; Liu et al., 2021; Zhong et al., 2021). It is important for oceanographers to gain a comprehensive understanding of the spatiotemporal characteristics of primary production (Field et al., 1998; Campbell et al., 2002; Tang et al., 2008; Tilstone et al., 2015).

The quantification of oceanic primary production is generally based on *in situ* measurements pertaining to incubation wherein the euphotic zone integrated primary production (PP) is calculated *via* trapezoidal integration (i.e., the PP inventory is evaluated by integrating PP divided into small trapezoids from the surface to the bottom of the euphotic zone). Measurements of PP by the radiolabeled carbon (C-14) uptake method has been extensively used in marine environments since the introduction of this method to determine the carbon uptake rate of phytoplankton (Nielsen, 1952; Hama et al., 1983; Gong, 1993; Shiah et al., 2000). Despite considerable research in the western North Pacific (WNP), i.e., East China Sea, South China Sea (SCS), and Taiwan Strait, to establish phytoplankton carbon fixation rates, researchers continue to debate whether phytoplankton growth conditions at the surface are indicative of conditions in deeper waters. Obtaining measurements of temperature at depth is straightforward; however, the *in situ* observation of PP ($PP_{in\ situ}$) requires considerable effort in terms of manpower and time. Specifically, seawater samples collected at discrete depths must be incubated on deck within an incubator using running surface water for cooling (Shiah et al., 2000, 2003, 2005; Chen, 2005; Lai et al., 2014; Chen et al., 2016). Note also that gaps in $PP_{in\ situ}$ coverage inevitably lead to discrepancies in corresponding estimates. The first empirical algorithm for PP predictions based on remote sensing was proposed by Balch et al. (1989). Behrenfeld and Falkowski (1997) developed an attractive alternative approach to estimating global PP using a small number of inputs. Their vertically generalized production model (VGPM; PP_{VGPM}) is widely regarded as the most highly optimized yet usable methods for PP estimation (Kameda and Ishizaka, 2005; Yamada et al., 2005; Ishizaka et al., 2007; Hill and Zimmerman, 2010).

The semi-analytical VGPM uses satellite-based data as an input to calculate PP. Thus, it is conceivable that data measured *in situ* could be used as an alternative to satellite-based input data, and vice versa (Behrenfeld and Falkowski, 1997; Hill and Zimmerman, 2010). The VGPM can be used to derive PP using satellite-based observations, such as remote passive ocean color, sea surface temperature (SST), surface optimal carbon fixation rate (P^B_{opt}) per unit chlorophyll *a* (Chl) of the euphotic zone (Z_{eu}), surface Chl concentration (Chl_s), surface light intensity (E_0), and the surface light diffuse attenuation coefficient (K_d) (Yamada et al., 2005; Ishizaka et al., 2007). Nonetheless, it is still problematic whether the assumption based on peak values of PP and Chl_s occur at the surface and decrease exponentially with depth until reaching the bottom of the Z_{eu} is true (Hill and Zimmerman, 2010; Buitenhuis et al., 2013). Furthermore, the reliability of VGPM in evaluating PP diminishes when geographic features, vertical hydrographic distributions, regional characteristics, extreme weather events, and climate change are taken into consideration (Dierssen, 2010; Friedland et al., 2012; Hung et al., 2013, 2016; Chen et al., 2015; Shih et al., 2015, 2020b). In the absence of a robust estimation method, the results derived from PP_{VGPM} cannot be relied upon to reflect the actual situation throughout the oceans. Empirical models developed by Dunne et al. (2005); Laws et al. (2011), and Henson et al. (2011) are widely used by oceanographers to estimate particulate organic carbon (POC) export flux; however, reliance on PP_{VGPM} also calls into question all corresponding estimates pertaining to global carbon export flux and oceanic carbon sequestration.

The South East Asian Time-series Study (SEATS) conducted in the South China Sea (SCS) was the lowest latitude time-series program implemented during the Joint Global Ocean Flux Study era (Karl et al., 2003; Wong et al., 2007). Numerous studies have characterized the upper ocean of the SCS as stratified and oligotrophic (Chen et al., 2004; Chen, 2005; Wong et al., 2007). Thus, biological activity and regulation of biogeochemical responses depend heavily on dynamic perturbations, including the yearly monsoon, typhoons, storms, internal waves, Kuroshio intrusion, and atmospheric deposition as well as nutrient supply in the form of phytoplankton nitrogen fixation (Liu et al., 2002; Chou et al., 2006; Chen et al., 2008, 2020; Du et al., 2013; Yang et al., 2014; Li et al., 2018; Shih et al., 2020a).

Throughout the SCS basin, the annual modeled PP ranges from 280 to 343 and PP_{VGPM} ranges from 308 to 354 mg-C m^{-2} d^{-1} (**Table 1**; Liu et al., 2002; Tan and Shi, 2009; Ma et al., 2014). High PP values are generally associated with the strong NE-monsoon (NEM) system during the cold season, whereas low PP values are associated with a relative weak SW-monsoon (SWM) during the warm season (**Table 1**). Based on long-term satellite-based SST records, Chen et al. (2020) reported that declining PP can be attributed at least in part to rising SST ($0.012°C\ y^{-1}$). Their and several selected researches in our study went a long way toward establishing a connection between monsoons and PP; however, all of the suppositions are based on indirect measurements; i.e., remote sensing (Liu et al., 2002; Hao et al., 2007; Zhao et al., 2008; Tan and Shi, 2009; Pan et al., 2012; Ma et al., 2014; Chen et al., 2020), rather than direct *in situ* incubation, such as the C^{13} and C^{14} methods (Liu et al., 2002; Chen et al., 2004, 2007; Ning et al., 2004). Note also that even PP research based on *in situ* oceanographic analysis is limited to short-term observations rather than long-term time-series (Chen, 2005; Chen et al., 1998, 2006; Liu et al., 2002; Tseng et al., 2005).

Remote sensing has made it possible to conduct large-scale PP monitoring over extended durations; however, most existing sensing technology is limited to the upper ocean and there is little evidence supporting the assumption of an exponential decrease in PP as a function of depth (Buitenhuis et al., 2013; Shih et al., 2020b). In the current study, we employed data obtained in the SEATS time-series study to elucidate long-term variations in $PP_{in\ situ}$ under the prevailing monsoon system. We also looked

TABLE 1 | Integrated primary production in the euphotic zone (PP) based on selected studies conducted in the South China Sea.

Region	Location		Month/period	PP	Method	References
	(°N)	(°E)		(mg-C m^{-2} d^{-1})		
NSCS	18.5	116.0	Nov–Feb	207	POC flux-estimate*	Chen et al., 1998
NSCS	18.5	116.0	Mar–May, Oct	59	POC flux-estimate*	Chen et al., 1998
NSCS	18.5	116.0	Jun–Sep	149	POC flux-estimate*	Chen et al., 1998
CSCS	14.6	115.1	Nov–Feb	196	POC flux-estimate*	Chen et al., 1998
CSCS	14.6	115.1	Mar–May, Oct	159	POC flux-estimate*	Chen et al., 1998
CSCS	14.6	115.1	Jun–Sep	203	POC flux-estimate*	Chen et al., 1998
NSCS	17.9–22.3	115.5–119.8	Mar	313	C^{14} incubation	Liu et al., 2002
NSCS	17.9–22.3	115.5–119.8	Mar	363	Model	Liu et al., 2002
SCS	2.0–24.8	99.0–124.6	Jan–Dec	354	VGPM	Liu et al., 2002
SCS	2.0–24.8	99.0–124.6	Jan–Dec	280	Model	Liu et al., 2002
NSCS	18.0	115.5	Mar	180–330	C^{13} incubation	Chen et al., 2004
NSCS	18.0	115.0	Jun–Jul	228	C^{14} incubation	Ning et al., 2004
NSCS	17.5	114.5	Nov–Dec	509	C^{14} incubation	Ning et al., 2004
NSCS	18.0	115.5	Mar	190–350	C^{13} incubation	Chen, 2005
NSCS	18.0	115.5	Jul	190	C^{13} incubation	Chen, 2005
NSCS	18.0	115.5	Oct	270–280	C^{13} incubation	Chen, 2005
NSCS	18.0	115.5	Jan	550	C^{13} incubation	Chen, 2005
NSCS	18.0	116.0	Jan	300	C^{14} incubation	Tseng et al., 2005
NSCS	18.0	116.0	Feb–Nov	110	C^{14} incubation	Tseng et al., 2005
NSCS	19.0	118.5	Jan	684	Chl function	Chen et al., 2006
NSCS	19.0	118.5	Mar	148	Chl function	Chen et al., 2006
NSCS	19.0	118.5	May	275	Chl function	Chen et al., 2006
NSCS	19.0	118.5	Jul	86	Chl function	Chen et al., 2006
NSCS	18.0	116.0	Mar–May	310	C^{13} incubation	Chen et al., 2007
NSCS	18.0	116.0	Jul–Aug	250	C^{13} incubation	Chen et al., 2007
NSCS	18.0	116.0	Oct–Nov	400	C^{13} incubation	Chen et al., 2007
NSCS	18.0	116.0	Dec–Feb	550	C^{13} incubation	Chen et al., 2007
NSCS	18.0–23.0	110.0–117.0	Apr–Oct	340	VGPM	Hao et al., 2007
NSCS	18.0–23.0	110.0–117.0	Nov–Mar	573	VGPM	Hao et al., 2007
NSCS	18.3	115.5	Jan–Dec	329–466	Overview	Wong et al., 2007
CSCS	12.5–16.5	112.5–116.0	Nov	274	VGPM	Zhao et al., 2008
WSCS	13.0–16.0	110.0–113.0	Oct–Nov	312	VGPM	Zhao et al., 2008
SCS	5.0–18.0	103.0–120.0	Mar–May	281	VGPM	Tan and Shi, 2009
SCS	5.0–18.0	103.0–120.0	Jun–Aug	267	VGPM	Tan and Shi, 2009
SCS	5.0–18.0	103.0–120.0	Sep–Nov	280	VGPM	Tan and Shi, 2009
SCS	5.0–18.0	103.0–120.0	Dec–Feb	374	VGPM	Tan and Shi, 2009
NSCS	17.5–18.5	115.5–116.5	May–Oct	214	VGPM	Pan et al., 2012
SCS	9.0–16.5	110.0–119.0	Jan–Dec	343	Model	Ma et al., 2014
SCS	9.0–16.5	110.0–119.0	Jan–Dec	351	VGPM	Ma et al., 2014
NSCS	18.0	116.0	Apr–Oct	159 (76–247)	C^{14} incubation	This study
NSCS	18.0	116.0	Nov–Mar	323 (117–528)	C^{14} incubation	This study
NSCS	18.0	116.0	Apr–Oct	250 (154–771)	VGPM	This study
NSCS	18.0	116.0	Nov–Mar	443 (190–1193)	VGPM	This study

*NSCS, northern South China Sea; CSCS, central South China Sea; WSCS, western South China Sea. *PP = POC flux / (17/Z + 1/100), where Z is the specific depth of the POC flux, units of POC flux and Z are (g-C m^{-2} y^{-1}) and (m) (Chen et al., 1998).*

for discrepancies between satellite-based and *in situ* observations, which could potentially influence PP estimates derived using the VGPM algorithm.

MATERIALS AND METHODS

In situ Observation

A total of 44 *in situ* observations were conducted at the SEATS site (18 °N, 116 °E) at regular intervals between 1998 and 2016. These expeditions involved hydrographic seawater sampling and biogeochemical field experiments using research vessels (*RV*; *Ocean Researcher I*, *Ocean Researcher III*, and *Fishery Researcher I*) (Karl et al., 2003; Wong et al., 2007). On-deck incubation of PP in accordance with ^{14}C protocols was also conducted during 20 of 25 expeditions between 2003 and 2016 (**Figure 1**). Conductivity–temperature–depth (CTD) (SBE9/11, SeaBird) and quantum scalar irradiance (QSP-200L, Biospherical) were, respectively, used to obtain vertical profiles of temperature and underwater photosynthetically available

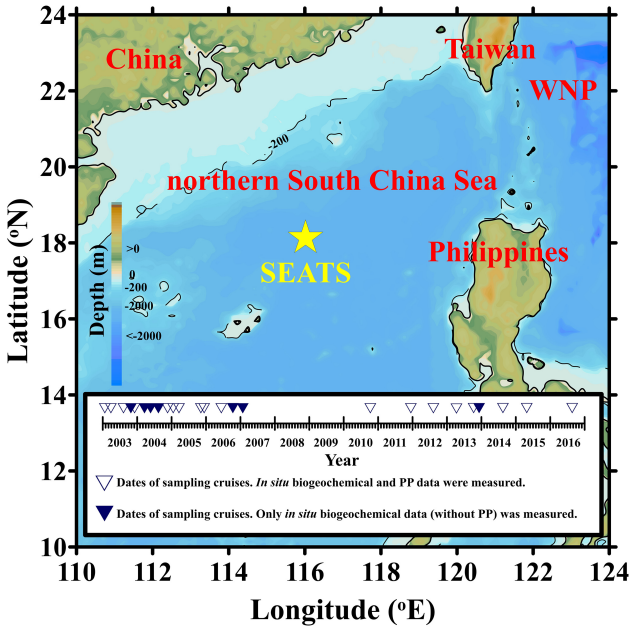

FIGURE 1 | Location of the South East Asian Time-series Study (SEATS) site. Inner box represents the date of cruises conducted at the SEATS site. Major and minor ticks, respectively, exhibit intervals of years and months. WNP refers to the western North Pacific.

radiation (PAR). A Biospherical instrument (QSR-240) was used to obtain daily PAR measurements (i.e., daily surface light intensity). In that study, Z_{eu} was defined as the depth at which underwater PAR reached 1%. The mixed layer depth (MLD) was defined as the deepest depth at which the temperature was 0.8°C lower than at the surface (Kara et al., 2000; Chou et al., 2006).

Seawater samples were collected at discrete depths to determine Chl concentrations and PP values. Briefly, 2L seawater samples were filtered using 47-mm GF/F filters before obtaining Chl concentrations (*via* acidification) using a Turner 10-AU-005 fluorometer (Gong et al., 2003; Shiah et al., 2003). PP was measured using the ^{14}C assimilation method (Parsons et al., 1984) following incubation under an artificial light source (2,000 μE m^{-2} s^{-1} with full spectrum from 350 to 2450 nm, similar to sunlight) for ∼3 h in a proprietary isolation container using flowing surface seawater for cooling. Following incubation and acidification (0.5 N HCl), radioactive substances collected in 25-mm GF/F filters were transported to a lab for quantification using a scintillation counter (Packard 2200) (Gong et al., 2003; Shiah et al., 2003; Lai et al., 2014). Finally, PP was calculated *via* trapezoidal integration (i.e. integrated from surface to 1% PAR). Note that SST, Chl and PP measurements from the Ocean Data Bank (Ministry of Science and Technology, Taiwan[1]) were used to compensate for deficiencies in *in situ* observations. Some of the hydrographic records (i.e., SST) and biogeochemical parameters (i.e., PP, Chl_s) of May–October from 2003 to 2006 have been present by Pan et al. (2012).

Remote Sensing Observation

Between 2003 and 2016, the daily data of level-3 products were obtained using a passive ocean color MODerate resolution Imaging Spectroradiometer (Aqua sensor; MODIS-Aqua) with spatial resolution of 4 km for the region covering 17.5–18.5°N and 115.5–116.5°E. We also collected PP_{VGPM}, SST, E_0, K_d, and Chl_s values from the Environmental Research Division's Data Access Program (ERDDAP), National Oceanic and Atmospheric Administration, Department of Commerce, U. S.[2]. Note that 8-day composite data were applied in situations where daily observations were missing. Note also that PP_{VGPM} values obtained from ERDDAP were estimated using VGPM developed by Behrenfeld and Falkowski (1997).

Plausible deviations between PP_{VGPM} and $PP_{in\ situ}$ were examined by comparing data obtained from satellites vs. data obtained *in situ*, including i.e., SST_{sate}, $(P^B_{opt})_{sate}$, E_{0-sate}, $[E_0/(E_0+4.1)]_{sate}$, K_{d-sate}, $Z_{eu-sate}$, Chl_{s-sate}; $SST_{in\ situ}$, $(P^B_{opt})_{in\ situ}$, $E_{0-in\ situ}$, $[E_0/(E_0+4.1)]_{in\ situ}$, $K_{d-in\ situ}$, $Z_{eu-in\ situ}$, $Chl_{s-in\ situ}$. Note that this analysis was conducted using the VGPM algorithm proposed by Behrenfeld and Falkowski (1997) (with far fewer input variables), as Equation 2–1:

$$PP = 0.66125 \times P^B_{opt} \times [E_0/(E_0+4.1)] \times Z_{eu} \times Chl_s \times D_{irr} \quad (2\text{-}1)$$

where the D_{irr} refers to the photoperiod. Z_{eu} was estimated from the average K_d of the water column (Behrenfeld and Falkowski, 1997 and references therein).

P^B_{opt} was computed using the empirical equation proposed by Behrenfeld and Falkowski (1997), as Equation 2–2, where T refers to the incubation temperature measured in the deck incubator as $SST_{in\ situ}$ or SST_{sate}. In cases where SST exceeded 28.5°C, a constant value of 4.0 mg-C mg-Chl^{-1} h^{-1} was taken as P^B_{opt} (Behrenfeld and Falkowski, 1997; Hu et al., 2014).

$$P^B_{opt} = -3.27 \times 10^{-8}T^7 + 3.4132 \times 10^{-6}T^6 - 1.348 \times 10^{-4}T^5 + 2.462 \times 10^{-3}T^4 - 0.0205T^3 + 0.0617T^2 + 0.2749T + 1.2956 \quad (2\text{-}2)$$

To evaluate the impact of monsoonal force on time-series variations, all data sets were divided into two groups: SW-monsoon (SWM, Apr. to Oct., including inter-monsoons of Apr and Oct) and NE-monsoon (NEM, Nov. to Mar). Variations between satellite-based observations and *in situ* measurements were examined by averaging all relevant values and reporting them as mean ± standard deviation (SD). Linear regression was used to assess relationships between any two of the variables. The *t*-tests were used to compare sets of observations with the significance level set at $p = 0.10$.

[1]http://www.odb.ntu.edu.tw/

[2]https://coastwatch.pfeg.noaa.gov/erddap/index.html

RESULTS

Time-Series Distributions: PP, SST, E_0, K_d, and Chl_s

As shown in **Figure 2A**, $PP_{in\ situ}$ was ∼2.0 times higher during the NEM (117–528, average = 323 ± 134 mg-C m^{-2} d^{-}) than during the SWM (76–247, average = 159 ± 58 mg-C m^{-2} d^{-1}) (**Table 2**). PP_{VGPM} values between 2003 and 2016 were as follows: SWM was 250 ± 36; 154–771 mg-C m^{-2} d^{-1} and NEM was 443 ± 142; 190–1,153 mg-C m^{-2} d^{-1} (**Figure 2A**). Note that PP_{VGPM} during the NEM was ∼1.8 times higher than during the SWM ($p < 0.01$) (**Table 2**). The differences in $PP_{in\ situ}$ and PP_{VGPM} between the NEM and SWM are in line with those reported by Ning et al. (2004); Chen (2005), and Hao et al. (2007), all of which were obtained from the same area of the SCS using different methods (**Table 1**). PP_{VGPM} exhibited monsoonal variations resembling the curve derived from $PP_{in\ situ}$; however, the magnitudes were 37% higher during the NEM and 57% higher during the SWM. On average, $PP_{in\ situ}$ estimates were ∼50% lower than PP_{VGPM} estimates, regardless of monsoon.

The lowest $SST_{in\ situ}$ (25.0 ± 1.4°C) and SST_{sate} (25.1 ± 1.2°C) values were obtained under the prevailing NEM during the cold season. The highest $SST_{in\ situ}$ (28.9 ± 0.9°C) and SST_{sate} (28.8 ± 1.0°C) values were obtained under the prevailing SWM during the warm season (**Table 2**). The low SST values recorded during the NEM can be attributed to the combined dynamics of NEM-driven vertical mixing of seawater and reduced solar radiation (Tseng et al., 2005; Zhou et al., 2020). By contrast, the P^B_{opt} showed a synchronous but opposite distribution (**Figures 2B,C**). The $(P^B_{opt})_{in\ situ}$ and $(P^B_{opt})_{sate}$ values computed from SST for the NEM, respectively, ranged from 4.4 to 6.1 and 4.0 to 6.6 mg-C mg-Chl^{-1} h^{-1}, and the average value was the same (5.4 ± 0.5 mg-C mg-Chl^{-1} h^{-1}). The $(P^B_{opt})_{in\ situ}$ and $(P^B_{opt})_{sate}$ values for the SWM, respectively, ranged from 4.0 to 4.4 and 4.0 to 6.0 mg-C mg-Chl^{-1} h^{-1}, with mean P^B_{opt} values of 4.1 ± 0.2 and 4.2 ± 0.2 mg-C mg-Chl^{-1} h^{-1} (**Table 2**).

$E_{0-in\ situ}$ and E_{0-sate} values in the SWM (50 ± 11 and 47 ± 6 Eins m^{-2} d^{-1}) were higher than those in the NEM (33 ± 14 and 36 ± 8 Eins m^{-2} d^{-1}) (see **Figures 2D,E** and **Table 2**). From the perspective of variables in the VGPM algorithm, $E_0/(E_0+4.1)$ ratios varied little between the *in situ* measurement and satellite-based observation. The variable of $[E_0/(E_0+4.1)]$ thereby seemed not an important parameter to influence the PP level. Z_{eu} was estimated using the expression of $-\ln(0.01)/K_d$ (Kirk, 1994; Behrenfeld and Falkowski, 1997), which led to a reversal of monsoonal K_d and Z_{eu} distributions (see **Figures 2F,G**). The mean $Z_{eu-in\ situ}$ was deeper during the SWM than during the NEM (87 ± 10 and 75 ± 14 m, respectively). The $Z_{eu-sate}$ as well as the $Z_{eu-in\ situ}$ presented similar trends between SWM and NEM (156 ± 17 and 120 ± 30 m, respectively) (**Table 2**). Z_{eu} values were shallower in the NEM than in the SWM, due perhaps to reduced light penetration resulting from more abundant biomass in the water column (Chen, 2005; Tseng et al., 2005; Chen et al., 2008).

Figure 2H presents long-term temporal variations in Chl_s. *In situ* measurements and satellite-based observations revealed a distinct NEM maximum (0.24 ± 0.16 and 0.20 ± 0.08 mg m^{-3}, respectively) and a SWM minimum (0.08 ± 0.02 and 0.10 ± 0.02 mg m^{-3}, respectively). $Chl_{s-in\ situ}$ and Chl_{s-sate} concentrations were, respectively, 0.07 to 0.58 and 0.09 to 0.71 mg m^{-3} during the NEM, and were, respectively, 0.04 to 0.11 and 0.05 to 0.43 mg m^{-3} during the SWM. For the same location, our observations were close to the data reported by Chen (2005) and Tseng et al. (2005). The SWM minimum Chl_s values in the

TABLE 2 | Summary of euphotic zone PP (PP) and its relevant variables in the current study conducted at the SEATS: SST, P^B_{opt}, E_0, $E_0/(E_0+4.1)$, K_d, Z_{eu}, Chl_s and Z_{ML}.

Variables	NE-monsoon (n)	SW-monsoon (n)	*p* value
$PP_{in\ situ}$ (mg-C m^{-2} d^{-1})	323 ± 134(10)	159 ± 58(10)	$p < 0.01$
PP_{VGPM} (mg-C m^{-2} d^{-1})	443 ± 142(66)	250 ± 36(96)	$p < 0.01$
$SST_{in\ situ}$ (°C)	25.0 ± 1.4(12)	28.9 ± 0.9(13)	$p < 0.01$
SST_{sate} (°C)	25.1 ± 1.2(70)	28.8 ± 1.0(98)	$p < 0.01$
$(P^B_{opt})_{in\ situ}$ (mg-C mg-Chl^{-1} h^{-1})	5.4 ± 0.5(12)	4.1 ± 0.2(13)	$p < 0.01$
$(P^B_{opt})_{sate}$ (mg-C mg-Chl^{-1} h^{-1})	5.4 ± 0.5(70)	4.2 ± 0.2(98)	$p < 0.01$
$E_{0-in\ situ}$ (Eins m^{-2} d^{-1})	33 ± 14(5)	50 ± 11(11)	$p < 0.01$
E_{0-sate} (Eins m^{-2} d^{-1})	36 ± 8(70)	47 ± 6(98)	$p < 0.01$
$(E_0/(E_0+4.1))_{in\ situ}$	0.88 ± 0.05(5)	0.92 ± 0.02(11)	$p < 0.10$
$(E_0/(E_0+4.1))_{sate}$	0.89 ± 0.02(70)	0.92 ± 0.01(98)	$p < 0.01$
$K_{d-in\ situ}$ (×10^{-3} m^{-1})	63 ± 11(12)	54 ± 6(13)	$p < 0.05$
K_{d-sate} (×10^{-3} m^{-1})	40 ± 10(69)	30 ± 3(94)	$p < 0.01$
$Z_{eu-in\ situ}$ (m)	75 ± 14(12)	87 ± 10(13)	$p < 0.05$
$Z_{eu-sate}$ (m)	123 ± 30(69)	156 ± 17(94)	$p < 0.01$
$Chl_{s-in\ situ}$ (mg m^{-3})	0.24 ± 0.16(12)	0.08 ± 0.02(13)	$p < 0.01$
Chl_{s-sate} (mg m^{-3})	0.20 ± 0.08(68)	0.10 ± 0.02(96)	$p < 0.01$
Z_{ML} (m)	66 ± 20(31)	35 ± 11(29)	$p < 0.01$

Values obtained during the NEM and SWM are presented as means and SD, where n indicates the number of observations and p values indicate the level of significance in the t test. In situ, in situ measured; VGPM, VGPM estimate; sate, satellite-base.

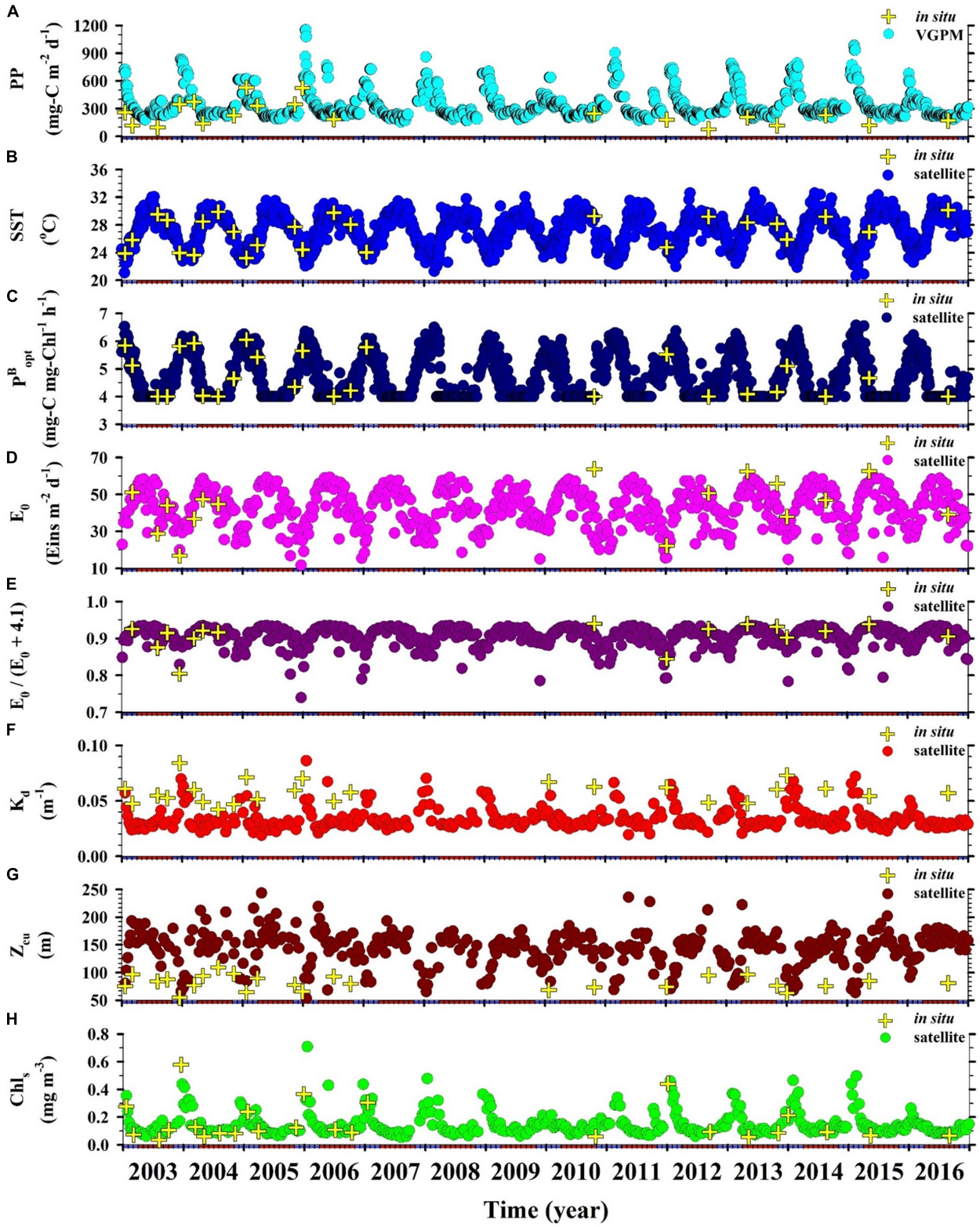

FIGURE 2 | Time-series distributions of satellite-based (circles) and *in situ* measurements obtained at the SEATS site (crosses): **(A)** Euphotic zone integrated primary production, PP; **(B)** sea surface temperature, SST; **(C)** optimal carbon fixation rate, P^B_{opt}; **(D)** sea surface daily light intensity, E_0; **(E)** $E_0/(E_0+4.1)$ ratio; **(F)** light diffuse attenuation coefficient, K_d; **(G)** depth of euphotic zone, Z_{eu}; **(H)** sea surface Chl, Chl_s. Red and blue colors on the horizontal axis, respectively, indicate SWM (Apr–Oct) and NEM (Nov–Mar).

current study were nearly the same as those reported in the oligotrophic ocean time-series studies at HOT (Hawaii Ocean Time-Series) and BATS (Bermuda Atlantic Time-Series Study) during the summer (0.05 mg m^{-3}); however, NEM values at SEATS exceeded the winter maximum at HOT and BATS (0.1 and 0.3 mg m^{-3}, respectively) (Karl et al., 2003). The high NEM maximum at SEATS may perhaps be explained by an increase in phytoplankton biomass (particularly larger sizes of >3 μm), which was stimulated by the deepening Z_{ML} (**Table 2**). The deeper nutrient-rich water was then efficiently transported to the upper surface water under the influence of NEM given that the nutrient-cline depth was shallower in SCS than in other oceans (Chen, 2005; Tseng et al., 2005).

Monthly Variations in PP, SST, E_0, K_d and Chl_s

The PP_{VGPM} values in this study are in good agreement with $PP_{in\ situ}$ in terms of amplitude as well as phase. Overall, we observed a maximum $PP_{in\ situ}$ of 394 ± 190 in January (NEM) and a minimum of 143 ± 70 mg-C m^{-2} d^{-1} in August (SWM) (**Figure 3A**). The magnitude of PP_{VGPM} was higher than the values obtained using *in situ* measurements; however, the trend over a span of 12 months was similar, with a pronounced NEM peak 619 ± 113 mg-C m^{-2} d^{-1} in January and the lowest SWM value of 230 ± 28 mg-C m^{-2} d^{-1} in September. These results are similar to those reported by other researchers for same area using different methods, such as the particulate organic carbon flux re-calculation (NEM: 207, SWM: 149 mg-C m^{-2} d^{-1}) (Chen et al., 1998); on-deck C^{14} incubation (NEM: 300–509, SWM: 110–228 mg-C m^{-2} d^{-1}) (Ning et al., 2004; Tseng et al., 2005); on-deck C^{13} incubation (NEM: 190–550, SWM: 190–280 mg-C m^{-2} d^{-1}) (Chen, 2005; Chen et al., 2007), and Chl empirical function (NEM: 148–684, SWM: 86–275 mg-C m^{-2} d^{-1}) (Chen et al., 2006; **Table 1**).

We observed opposing trends between monthly SST and the corresponding P^B_{opt}. The highest $(P^B_{opt})_{in\ situ}$ values (5.9 mg-C mg-Chl^{-1} h^{-1}) were observed in January and the lowest (4.0 mg-C mg-Chl^{-1} h^{-1}) were observed in August. The $(P^B_{opt})_{sate}$ values converted from SST_{sate} (5.8 and 4.0 mg-C mg-Chl^{-1} h^{-1} in January and June, respectively) were nearly identical to those for the same time slots obtained *via in situ* measurements (**Figures 3B,C**). The highest mean monthly $E_{0-in\ situ}$ in April (63 ± 0 Eins m^{-2} d^{-1}) was higher than the highest mean monthly E_{0-sate} (53 ± 3 Eins m^{-2} d^{-1}). Overall, $E_{0-in\ situ}$ and E_{0-sate} levels in December were very similar (∼26 and ∼27 Eins m^{-2} d^{-1}, respectively). Based on $E_{0-in\ situ}$, the highest $E_0/(E_0+4.1)_{in\ situ}$ ratio (0.94) occurred in April and the lowest $E_0/(E_0+4.1)_{in\ situ}$ ratio (0.85) occurred in December. $E_0/(E_0+4.1)_{sate}$ values of 0.93 in April and 0.86 in December were similar with the $E_0/(E_0+4.1)_{in\ situ}$ values (**Figures 3D,E**). As for parameterization, it appears that P^B_{opt} and $E_0/(E_0+4.1)$ values had little influence on VGPM results (PP), regardless of whether the values were obtained from *in situ* measurements or satellite-based observation.

We did not observe large monsoonal variations in $K_{d-in\ situ}$ and K_{d-sate}; however, the highest $K_{d-in\ situ}$ (0.072 ± 0.009 m^{-1}) was obtained in December and the highest K_{d-sate} (0.052 ± 0.009 m^{-1}) was obtained in January. These high K_d values resulted in a shallower $Z_{eu-in\ situ}$ (64 ± 8 m) and $Z_{eu-sate}$ (92 ± 19 m), compared to the values converted from the $K_{d-in\ situ}$ (0.053 ± 0.007 m^{-1}) for August ($Z_{eu-in\ situ}$ = 89 ± 13 m) and the K_{d-sate} (0.029 ± 0.003 m^{-1}) for September ($Z_{eu-sate}$ = 162 ± 22 m) (**Figures 3F,G**). The shallow Z_{eu} observed in December and January can be attributed mainly to an increase in phytoplankton biomass that reduces the light penetration in that region during the NEM (Chen, 2005; Tseng et al., 2005; Chen et al., 2008).

Figure 3H presents temporal variations in $Chl_{s-in\ situ}$ and Chl_{s-sate}. Conspicuously high $Chl_{s-in\ situ}$ values were observed in December (0.40 ± 0.15 mg m^{-3}) and high Chl_{s-sate} values were observed in January (0.29 ± 0.09 mg m^{-3}). The high Chl_s values observed throughout the NEM were triggered by the monsoonal force, which stimulated phytoplankton photosynthesis, thereby increasing the phytoplankton abundance or enriching the area with Chl_s from subsurface waters (Liu et al., 2002; Tseng et al., 2005). The drop in $Chl_{s-in\ situ}$ and Chl_{s-sate} values to nearly < 0.10 mg m^{-3} during the SWM has previously been reported in studies focusing on the same region of the SCS (Liu et al., 2002; Chen, 2005; Tseng et al., 2005; Shih et al., 2020a). Similar findings were also recorded in oligotrophic time-series studies, such as HOT and BATS (Karl et al., 2003).

Relationships Among of PP, SST, E_0, K_d and Chl_s in *in situ* Measurements and Satellite-Based Observations

$PP_{in\ situ}$ was generally lower than PP_{VGPM}; however, we observed a significantly positive correlation between these two parameters; i.e., slope = 0.70, r^2 = 0.42, $p < 0.01$ (**Figure 4A**). This clearly indicates the feasibility of the VGPM for predictions; however, tuning would be required for the study area. As shown in **Figure 4**, we identified significantly positive correlations between $PP_{in\ situ}$ and PP_{VGPM} as well as their respective variables SST, E_0, K_d and Chl_s. As indicated by high r^2 and low p values with slopes close to 1, the most significant correlations were found in SST and E_0 (**Figures 4C–F**) : SST (slope = 0.92, r^2 = 0.92, $p < 0.01$) and E_0 (slope = 0.62, r^2 = 0.58, $p < 0.01$). Taken together, these results indicate that SST_{sate} and E_{0-sate} were the variables most strongly correlated with $SST_{in\ situ}$ and $E_{0-in\ situ}$, providing the most accurate estimates of PP when using the VGPM. As indicated by the 1:1 lines in **Figures 4B,G,H**, the parameters with the greatest variability in terms of slope were Chl_s (slope = 0.41, r^2 = 0.74, $p < 0.01$) and K_d (slope = 0.59, r^2 = 0.50, $p < 0.01$). This suggests Chl_{s-sate} and K_{d-sate} could potentially bias PP estimates obtained using the VGPM.

The fact that the regression line between PP_{VGPM} and $PP_{in\ situ}$ lies above the 1:1 line indicates that PP_{VGPM} estimates exceeded $PP_{in\ situ}$. When using the VGPM to estimate PP, the two main variables are P^B_{opt} and $E_0/(E_0+4.1)$, derived from *in situ* measurements and satellite-based observations of SST ($SST_{in\ situ}$ and SST_{sate}) and E_0 ($E_{0-in\ situ}$ and E_{0-sate}). Between $SST_{in\ situ}$ and SST_{sate} as well as between $E_{0-in\ situ}$ and E_{0-sate}, we observed nearly linear relationships (i.e., close

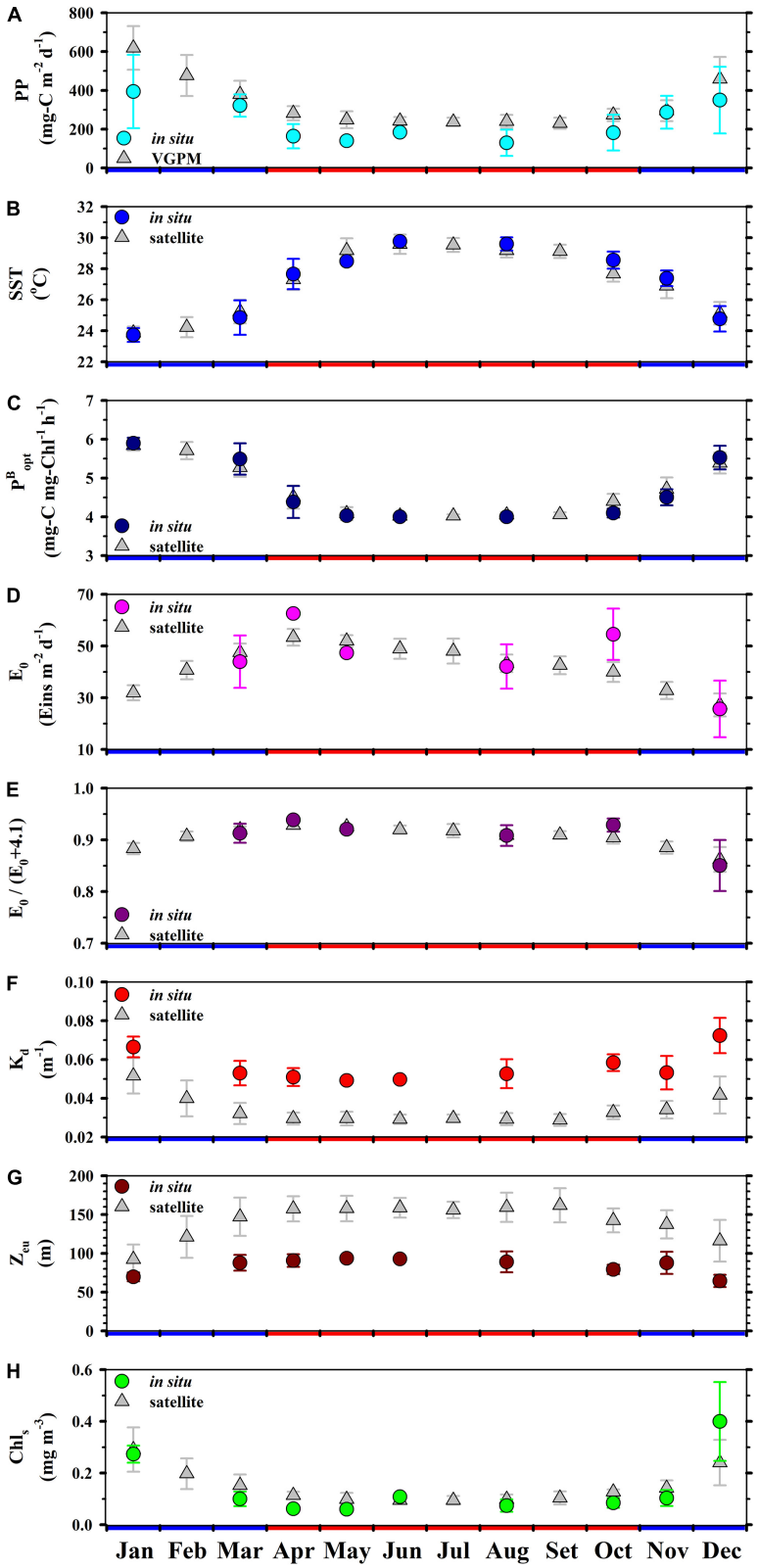

FIGURE 3 | Monthly averages (±1 SD) of **(A)** PP, **(B)** SST, **(C)** P^B_{opt}, **(D)** E_0, **(E)** $E_0/(E_0+4.1)$, **(F)** K_d, **(G)** Z_{eu}, **(H)** Chl_s at the SEATS site. Circles and triangles, respectively, represent *in situ* measurements and satellite-based observations. Red and blue colors on the horizontal axis, respectively, indicate SWM (Apr–Oct) and NEM (Nov–Mar).

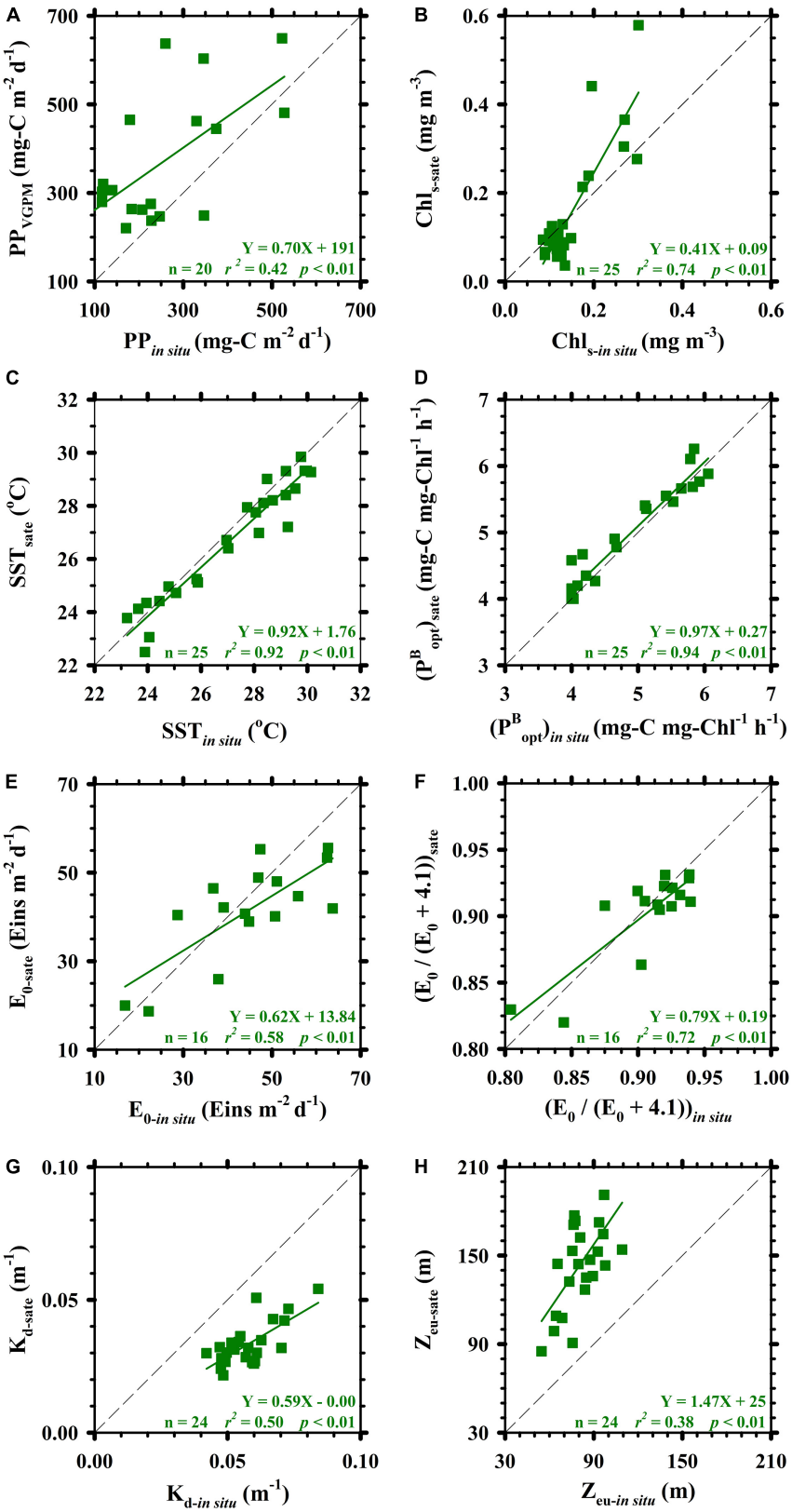

FIGURE 4 | Linear relationships among satellite-based observations and *in situ* measurements. Panels **(A–H)** are PP, Chl_s, SST, P^B_{opt} (estimated from SST), E_0, $E_0/(E_0+4.1)$ ratio, K_d, and Z_{eu} (estimated from K_d), respectively. Diagonals in panels **(A–H)** are 1:1 lines.

to the 1:1 diagonal). This suggests that P^{B}_{opt} and $E_0/(E_0+4.1)$ were not scaling variables governing the magnitude of PP in this study. Influences derived from these two variables [P^{B}_{opt}, $E_0/(E_0+4.1)$] of the both methods on calculated results were less than 1%. By contrast, the correlations between $Chl_{s-in\ situ}$ and Chl_{s-sate}, and $Z_{eu-in\ situ}$ and $Z_{eu-sate}$ (converted from $K_{d-in\ situ}$ and K_{d-sate}, respectively) had a pronounced impact on VGPM PP estimates. If we considered only the difference between $Chl_{s-in\ situ}$ and Chl_{s-sate}, then PP values estimated using VGPM would be slightly higher (~ 5%, depended on the given case) than those obtained using *in situ* measurements. If we considered only the difference between $Z_{eu-in\ situ}$ and $Z_{eu-sate}$, then PP values estimated using VGPM would be apparently 1.72-fold higher than those obtained using *in situ* measurements.

The mean PP in the euphotic zone (PP/Z_{eu}, mg-C m^{-3} d^{-1}) presented a positive linear relationship between ($PP_{VGPM}/Z_{eu-sate}$) and ($PP_{in\ situ}/Z_{eu-in\ situ}$); i.e., slope: 0.51, $r^2 = 0.39$, $p < 0.01$ (**Figure 5A**). Higher values were observed during the NEM (4.7 ± 2.4 and 3.8 ± 2.2 mg-C m^{-3} d^{-1} of $PP_{in\ situ}/Z_{eu-in\ situ}$ and $PP_{VGPM}/Z_{eu-sate}$, respectively) and lower values were observed during the SWM (1.9 ± 0.8 and 1.7 ± 0.4 mg-C m^{-3} d^{-1} of $PP_{in\ situ}/Z_{eu-in\ situ}$ and $PP_{VGPM}/Z_{eu-sate}$, respectively). The slope of 0.51 for $PP_{VGPM}/Z_{eu-sate}$ and $PP_{in\ situ}/Z_{eu-in\ situ}$ was lower than that of PP_{VGPM} and $PP_{in\ situ}$ (slope = 0.70), such that most data fell on

DISCUSSION

Uncertainty in Estimating PP Due to Differences Between $Chl_{s-in\ situ}$ and Chl_{s-sate} as Well as $Z_{eu-in\ situ}$ and $Z_{eu-sate}$: Implications

Our analysis of revealed a number of potential uncertainties pertaining to PP estimation using the VGPM algorithm. Most of the discrepancies were due primarily to differences between $Z_{eu-in\ situ}$ and $Z_{eu-sate}$ as well as between $Chl_{s-in\ situ}$ and Chl_{s-sate}. Overall, the product of Z_{eu} and Chl_s (i.e., the phytoplankton inventory in the euphotic zone), suggests that the base assumption of vertically distributed standing stock biomass in low latitude waters (SCS) may perhaps be erroneous. If so, then it will be necessary to reformulate methods for the prediction of biomass standing stocks when implementing the VGPM algorithm (Ning et al., 2004; Hill and Zimmerman, 2010).

The fundamental structure of the VGPM is based on a relationship between integrated phytoplankton biomass in the euphotic zone and Chl_s (Behrenfeld and Falkowski, 1997; Hill and Zimmerman, 2010). Thus, obtaining accurate estimates of PP by comparing $PP_{in\ situ}$ and PP_{VGPM} results depends on reliable estimates of the integrated phytoplankton biomass in the euphotic zone. However, passive satellites recording the color of the ocean surface are unable to elucidate the situation at arbitrary depths below the surface (Hill and Zimmerman, 2010; Shih et al., 2020b). Contrary to the assumption that Chl decreases exponentially with depth, most observations in the SCS revealed that the subsurface Chl maximum (SCM) was often found at great depths (Liu et al., 2002; Chen, 2005; Shih et al., 2020a,b). This makes it very difficult or even impossible to estimate the integrated biomass in the euphotic zone simply as a product of Z_{eu} and Chl_s. Enhancing the reliability of the VGPM requires that we increase the number of $PP_{in\ situ}$ observations and the corresponding variables in order to improve the correlation between our assumptions pertaining to phytoplankton integrated biomass and actual measurements obtained in the field. This is particularly important in phytoplankton populations, dynamics and assemblages in specific locations under specific conditions (Hill and Zimmerman, 2010; Shih et al., 2015, 2020b). Only by increasing the number of observations and enhancing our analysis of water composition will it be possible to reduce the uncertainty associated with Z_{eu} and Chl_s in estimating PP using the VGPM.

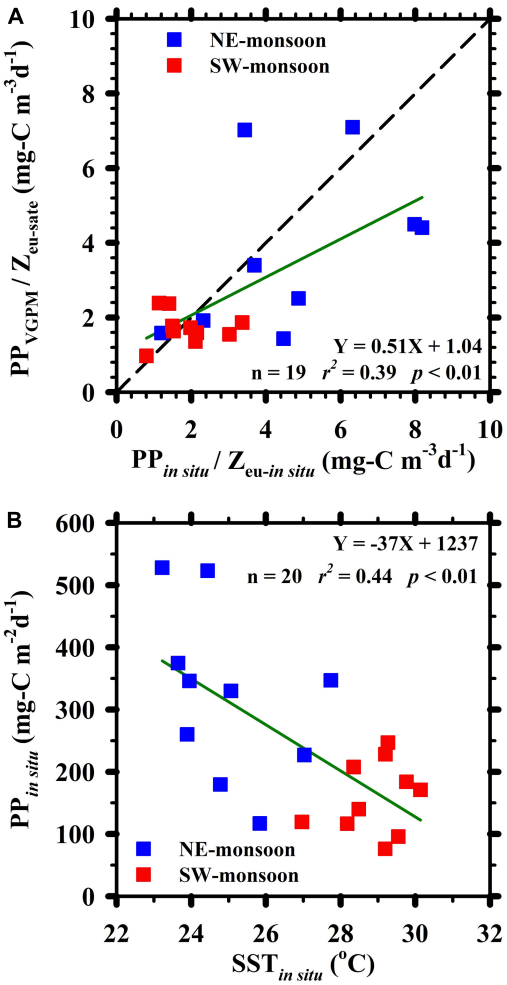

FIGURE 5 | (A) Relationship between satellite-based observations of (PP_{VGPM} / $Z_{eu-sate}$) and *in situ* measurements of ($PP_{in\ situ}$ / $Z_{eu-in\ situ}$) ratios; **(B)** relationship between $PP_{in\ situ}$ and $SST_{in\ situ}$. Red and blue symbols, respectively, indicate observations made during the SW-monsoon and NE-monsoon. The diagonal in panel **(A)** is 1:1 line.

the right side of the 1:1 line. Ratios of $PP_{VGPM}/Z_{eu-sate}$ were nearly 20% lower than those of $PP_{in\ situ}/Z_{eu-in\ situ}$, indicating that $Z_{eu-sate}$ was deeper than $Z_{eu-in\ situ}$, particularly during the SWM. This also indicates that the VGPM parameter $Z_{eu-sate}$ indeed substantially affected PP estimates in this study. It has been proposed that satellite-based K_d values have to be calibrated against the zenith solar angle during the data processing in accordance with the methods outlined by Lee et al. (2005) and Li et al. (2015). However, users may not to confirm the processing from the downloaded or retrieved satellite-based products of PP and its relevant variables.

The significant linear correlation between $(P^B_{opt})_{sate}$ and $(P^B_{opt})_{in\ situ}$ (slope = 0.97, r^2 = 0.94, $p < 0.01$; **Figure 4D**) is simply a reflection of the relationship between the two SST records, resulting from the fact that P^B_{opt} is computed as a function of SST (i.e., a seventh-order polynomial, Equation 2–2) (Behrenfeld and Falkowski, 1997). Thus, any potential deviations between SST and P^B_{opt} had only a negligible influence on PP estimates obtained using VGPM. Many studies have nevertheless concluded that the accuracy of VGPM-based estimates of PP are poor, when using the 7th order polynomial of SST (Equation 2–2) to calculate the input of P^B_{opt} (Mizobata and Saitoh, 2004; Kameda and Ishizaka, 2005; Yamada et al., 2005; Siswanto et al., 2006; Ishizaka et al., 2007; Tang et al., 2008; Tang and Chen, 2016).

Researchers have reported that much of the uncertainty in estimating PP_{VGPM} is related to the computation of P^B_{opt} under the effects of phytoplankton physiology, growth conditions, abundance, size, and productivity (Gong and Liu, 2003; Kameda and Ishizaka, 2005; Yamada et al., 2005). It has been suggested that P^B_{opt} is influenced by SST as well as E_0 and various biological parameters, such as Chl concentration. P^B_{opt} represents an optimal daily carbon fixation rate in the water column previously described as a 7th order polynomial of SST, however, when SST exceeds 28.5°C, P^B_{opt} remains fixed at a constant 4 mg-C mg-Chl^{-1} h^{-1} (Behrenfeld and Falkowski, 1997; Mizobata and Saitoh, 2004), indicating that P^B_{opt} tends to be underestimated when SST exceeds 28.5°C. In low-latitude regions of the SCS, the constant P^B_{opt} mentioned above usually occurred in late spring, summer, and early fall, during which $SST_{in\ situ}$ and SST_{sate} both exceeded 28.5°C. This increased the margin between actual PP values and the estimates obtained by inputting P^B_{opt} derived using $SST_{in\ situ}$ or SST_{sate}. The reliability of P^B_{opt} estimates obtained using the VGPM seventh-order polynomial SST algorithm is not universally applicable (temporally or spatially). This has prompted oceanographers to tune existing methods or devise new methods for the precise estimation of P^B_{opt}, especially for ocean water at low latitudes.

Our results reveal that the satellite-derived primary production (e.g., PP_{VGPM}) may significantly affect global carbon export flux to deep waters, but what is the overall significance and impact of these PP values on POC fluxes? For example, Dunne et al. (2005) used the empirical model expression (Equation 4–1) to estimate carbon flux (or sequestration) in oceans. PP (mg-C m^{-2} d^{-1}), Z_{eu} (m) and SST (°C) are three major factors affecting the estimated values of POC flux which is almost linearly proportional to PP.

$$\text{POC flux} = PP \times \left[-0.0101^{\circ}\text{C}^{-1} \times SST + 0.0582 \times \ln\left(\frac{PP}{Z_{eu}}\right) + 0.419\right] \quad (4\text{-}1)$$

According to the expression 4–1, the POC fluxes estimated from *in situ* measurements ($PP_{in\ situ}$, $SST_{in\ situ}$ and $Z_{eu-in\ situ}$) of Hung et al. (2000); Hung and Gong (2007), and Shih et al. (2015) were from 12 to 319 mg-C m^{-2} d^{-1}, an average of 20% less than the trap POC fluxes (25–274 mg-C m^{-2} d^{-1}) (**Figure 6**). As described above, the inputs of $SST_{in\ situ}$ and $Z_{eu-in\ situ}$ to the expression were fixed, the $PP_{in\ situ}$ was replaced by the PP_{VGPM}, an average difference between estimated and trap POC fluxes (estimated POC flux: 16–781 mg-C m^{-2} d^{-1}) was a factor of 2. It has been suggested that the uncertainty of these POC fluxes is quite large if satellite-based PP is used to estimate carbon sequestrations in oceans. If the discrepancy between *in situ* measurements and satellite-based observations of PP can be diminished and the reliance on them (e.g., PP_{VGPM}) can be increased, it is to dedicate the potential importance and goal of the present study.

Impact of Global Warming on *in situ* Observations

In both the Atlantic and Pacific oceans, increased phytoplankton biomass is observed at low latitudes during the boreal

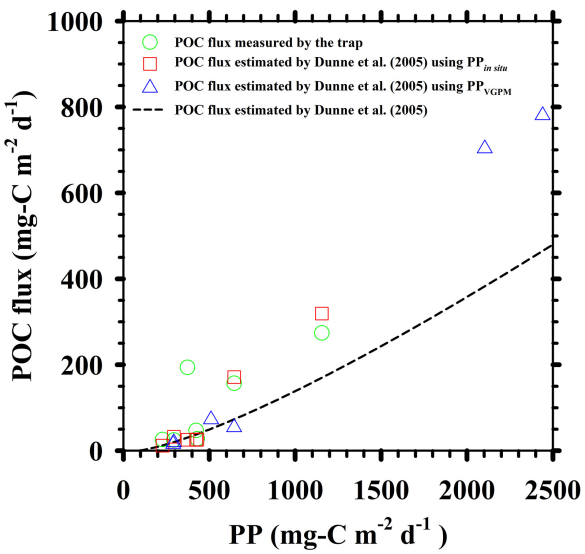

FIGURE 6 | A comparison of the difference between *in situ* trap measured and estimated POC fluxes. The estimated POC fluxes were computed according to the empirical model expression revealed by Dunne et al. (2005). The dashed line represented the proportional relationship of estimated POC flux and PP. The $PP_{in\ situ}$ and PP_{VGPM} were also exerted on the expression to estimate POC fluxes (red square and blue triangle, respectively). *In situ* measurements of $PP_{in\ situ}$ and trap measured POC fluxes (green circle) were based on Hung et al. (2000); Hung and Gong (2007), and Shih et al. (2015).

warm season. Other than equatorial upwelling, there are no other conspicuous seasonal trends in biogeochemical activities (Dandonneau et al., 2004). In the Arabian Sea, enhanced biogeochemical responses are also observed at low latitudes during the SWM (Banse and English, 2000). In this study, long-term and monthly variations in $PP_{in\ situ}$ and PP_{VGPM} demonstrated influential monsoonal system at the SEATS (**Figures 2**, **3** and **Table 2**). The concurrence of low SST, deep Z_{ML}, high Chl_s, shallow Z_{eu}, and increased PP suggest that increased phytoplankton biomass or specific phytoplankton communities dominating were triggered during the NEM. It has been reported that the average nitrate+nitrite (N+N) concentration, one of the key nutrients for phytoplankton growth in the SCS, in the MLD in the seasons of NEM (0.1–0.3 μM) is ∼10 times higher than of SWM (∼0.03 μM) (Tseng et al., 2005). Moreover, the inventory of N+N and the depth of nitracline in the NEM (30 ± 19 mmol m^{-2} and 28–62 m, respectively) have been observed a ∼ 4.5 fold higher and a ∼ 25–50% shallower than those reported in the SWM (7 ± 4 mmol m^{-2} and 52–82 m, respectively) (Chen, 2005; Shih et al., 2020a). Evidences of abundant nutrient (e.g., N+N) and shallow nitracline depth favoring biological activities, imply that the growth of phytoplankton communities and associated photosynthesis were affected mainly by vertical advection providing inorganic nutrients from deeper waters, under the NEM system prevailing in the SCS (Liu et al., 2002; Bai et al., 2018; Chen et al., 2020; Zhou et al., 2020).

The global decrease in PP is particularly pronounced in high-latitude waters, which lose roughly 2,000 Mt-C y^{-1} (Mt = 10^{12} g), accounting for a 70% decline in carbon fixation *via* photosynthesis (Gregg et al., 2003). To compare annually reductions in $PP_{in\ situ}$ (−11 mg-C m^{-2} d^{-1} y^{-1}) vs. the annual $PP_{in\ situ}$ (241 mg-C m^{-2} d^{-1}; mean $PP_{in\ situ}$ of NEM and SWM; **Table 1**), it indicated that the annual reduction in carbon fixation *via* photosynthesis was ∼ -5% y^{-1}. Based on the 200 m isobath boundary of oligotrophic waters in the SCS (2.76×10^{12} m^2; Lin et al., 2003), the e-ratios were 5–16% in the SCS (Hung and Gong, 2010; Shih et al., 2019) and the decreased in carbon fixation was roughly 11 Mt-C, thereby accounting for 30–90% of the export production. This suggests a gradual decrease in the efficiency of photosynthetic carbon fixation by phytoplankton. Nevertheless, satellite-based observations do not show the signs of global warming on carbon fixation and sequestration.

Figure 5B illustrates the significantly negative relationship between $PP_{in\ situ}$ and $SST_{in\ situ}$ at the SEATS site. The slope of −37 mg-C m^{-2} d^{-1}°C $^{-1}$ was exceptionally close to the −36 mg-C m^{-2} d^{-1}°C $^{-1}$ reported in previous studies (Chen and Chen, 2006; Chen et al., 2007, 2008). Scaling factors related to the increase in $SST_{in\ situ}$ caused by global changes are extremely complex (Sarmiento et al., 1998; Hung et al., 2010; Bai et al., 2018). Notwithstanding the complexity of factors governing $SST_{in\ situ}$, they can still be used to estimate PP values. The differences between daytime and nighttime $SST_{in\ situ}$ values were statistically insignificant, during the NEM as well as the SWM (one-tail t test: p = 0.15 and 0.24, respectively (**Figure 6**). We therefore surmise that SST sampling schedules had no effect on the overall results. Furthermore, we observed a strong statistically significant correlation between SST_{sate} and $SST_{in\ situ}$ (**Figure 4C**), indicating the efficacy of SST in estimating PP distributions over a broad horizontal area, regardless of the method used for derivation.

The straightforward relationship between $PP_{in\ situ}$ and $SST_{in\ situ}$ is important when seeking to predict PP values and estimate new or export production in euphotic zones. Under the environmental conditions described above, the reduction in carbon fixation due to photosynthesis would be ∼ −15% °C^{-1}, and the decrease in carbon fixation would be roughly 37 Mt-C, thereby accounting for a 1- to 3-fold quantity of export production. The negative correlation between $PP_{in\ situ}$ and $SST_{in\ situ}$ in the current study matched the findings observed in mid-latitude tropical/subtropical regions of the Pacific and Atlantic oceans (Chen, 2000; Tilstone et al., 2009), but differed drastically from those reported in high-latitude regions (Kudryavtseva et al., 2018).

Generally speaking, the sampling resolution of *in situ* time-series is too low to eliminate temporal uncertainty over all timespans. Fortunately, we can use SST_{sate} to compensate for deficiencies in $SST_{in\ situ}$ coverage (Bai et al., 2018; Chen et al., 2020). Only one daily SST_{sate} reading can be obtained at any given location; however, it would be perfectly reasonable to substitute that value with one obtained $SST_{in\ situ}$. We observed a statistically significant linear relationship between SST_{sate} with $SST_{in\ situ}$ (**Figure 4C**); however, differences between daytime and nighttime $SST_{in\ situ}$ measurements did not reach the level of significance (**Figure 7**). This suggests that SST estimates obtained using either method could be used to assess the influence of temperature on biogeochemical phenomena, such as PP.

Asynchronous variations between $PP_{in\ situ}$ and PP_{VGPM} and their related variables in the VGPM algorithm indicate the following: (1) Satellite-based evaluations depend primarily on the assumption of an exponential decrease in the vertical distribution of PP from the surface to the euphotic zone base. Nonetheless, remote sensing cannot penetrate beyond the surface, and therefore cannot reflect the true vertical distribution of PP at depth (Hung et al., 2010; Buitenhuis et al., 2013; Shih et al., 2013, 2020b). This assumption is the primary cause for uncertainty between PP values obtained from satellite-based observations (i.e., PP_{VGPM}) and those derived from *in situ* measurements (i.e., $PP_{in\ situ}$). (2) When using satellite-based observations to estimate horizontal PP distributions, mathematical extrapolation/interpolation is commonly used to compensate for gaps in data coverage resulting from cloud coverage, heavy rains, rough seas, extreme weather events, natural episodes, suspended particles, and/or chromophoric dissolved organic matter. Thus, this approach cannot reflect "true" or "*in situ*" biogeochemistry responses to PP in the oceans. (Boyd and Trull, 2007; Shang et al., 2008; Tang et al., 2008; Hung et al., 2009, 2010; Shih et al., 2020a). For decades, SEATS has been used as a natural laboratory for studies of prolonged environmental changes and reciprocal biogeochemical responses. It is time to tune existing models or develop more reliable models if we are to gain meaningful estimates of biogeochemical phenomena in the oceans. The proposed calibration method

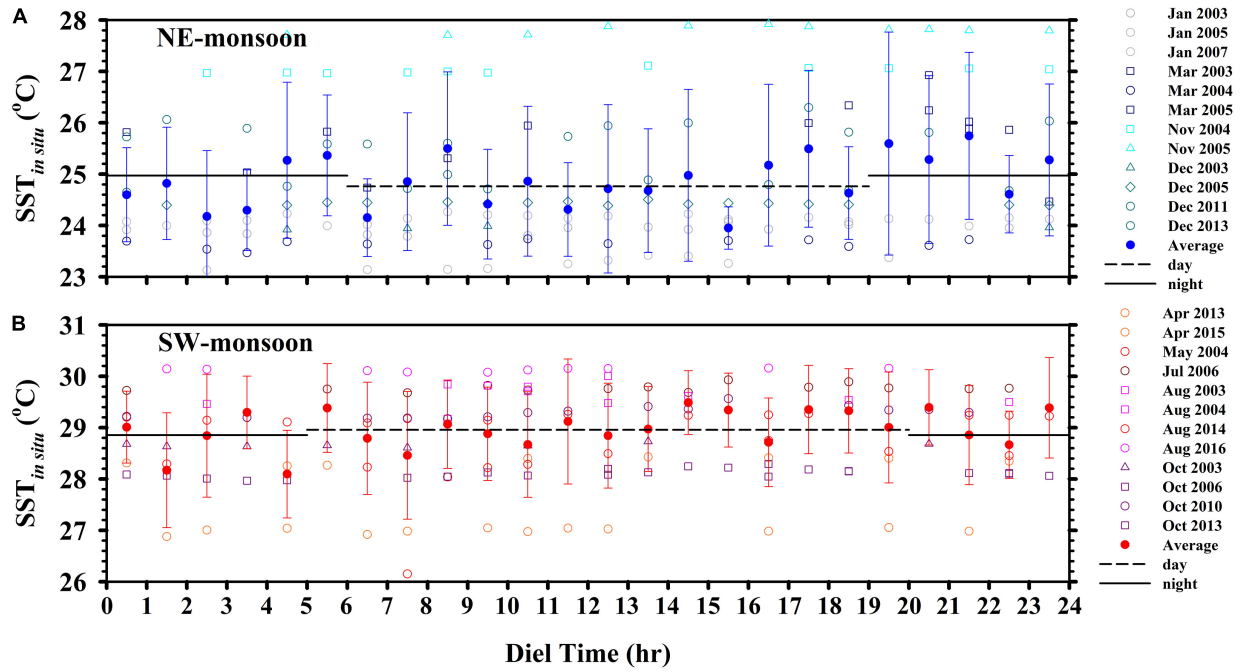

FIGURE 7 | Averaged diel records (±1 SD) of SST during the **(A)** NE-monsoon and **(B)** SW-monsoon. Horizontal dashed and solid lines indicate the mean daytime measurements (GMT+8: 06–18 and 05–19 h, NE- and SW-monsoons, respectively) and nighttime measurements (GMT+8: 19–05 and 20–04 h, NE- and SW-monsoons, respectively).

aimed at improving PP estimates for the VGPM is expected to enhance our understanding of changes in the SCS.

SUMMARY

Our time-series study (2003 ∼ 2016) at SEATS compared PP estimates based on *in situ* measurements and those based on the VGPM in the SCS during the NEM and SWM. PP values obtained during the NEM exceeded those obtained during the SWM, which appears to indicate that weather conditions during the cold season are conducive to high PP values. $PP_{in\ situ}$ values were roughly 50% lower than PP_{VGPM} values, regardless of the season (NEM or SWM). These discrepancies can be attributed to the satellite-based integrated phytoplankton biomass in the euphotic zone. The discrepancies can be derived as the product of Z_{eu} and Chl_s, which are two main variables in the VGPM algorithm, especially the impact of difference between *in situ* and satellite-based Z_{eu} on the magnitude of PP.

The observed overall decrease in $PP_{in\ situ}$ can be partially explained by an increase in $SST_{in\ situ}$. Our results also showed that SST_{sate} could be used to predict horizontal PP distributions over extended time scales, based on our observation of a statistically significant relationship between SST_{sate} with $SST_{in\ situ}$. A significantly negative relationship between $PP_{in\ situ}$ and $SST_{in\ situ}$ appears to indicate that global changes, such as oceanic warming, could have a negative impact on ocean biogeochemistry in low-latitude regions of the SCS. Nonetheless, further research will be required to assess the influence of global changes on biogeochemical phenomena, particularly in low-latitude waters. The SEATS has been used for decades to assess the sensitivity and resilience of low-latitude oceans to environmental fluctuations. Our analysis of discrepancies between *in situ* measurements and satellite-based observations could help to guide revisions aimed at enhancing the robustness and reliability of the VGPM in estimating biogeochemical responses. Satellite-based data could be used to expand the spatiotemporal scale of observations and thereby shed light on the actual biogeochemical effects of global environmental changes in low-latitude regions of the SCS.

DATA AVAILABILITY STATEMENT

The original contributions presented in the study are included in the article/supplementary material, further inquiries can be directed to the corresponding author.

AUTHOR CONTRIBUTIONS

Y-YS, F-KS, and C-CH wrote the manuscript with contributions from W-CC. C-YL, J-HT, Y-SW, and C-CL performed the experiments and created the tables and figures. Y-YS, F-KS, C-CH, W-CC, C-YL, J-HT, Y-SW, C-CL and C-YK reviewed and revised the manuscript. All authors listed have made substantial, direct, and intellectual contribution to the work and approved it for publication.

FUNDING

This research was supported by the MOST (Ministry of Sciences and Technology, Taiwan) under grant numbers 108-2611-M-012-001, 108-2611-M-110-019-MY3, 109-2611-M-012-001, 109-2740-M-110-001, 110-2611-M-012-002, 110-2740-M-110-001, and 110-2611-M-019-005.

ACKNOWLEDGMENTS

We would like to thank the assistance given us by the crews of R/V *Ocean Researcher I* and R/V *Fishery Researcher I*. We would also like to thank the unsung heroes and contributors who have contributed to the SEATS program.

REFERENCES

Bai, Y., He, X. Q., Yu, S. J., and Chen, C. T. A. (2018). Changes in the ecological environment of the marginal seas along the Eurasian Continent from 2003 to 2014. *Sustainability* 10:635. doi: 10.3390/su10030635

Balch, W. M., Abbott, M. R., and Eppley, R. W. (1989). Remote sensing of primary production—I. A comparison of empirical and semi-analytical algorithms. *Deep Sea Res. A* 36, 281–295. doi: 10.1016/0198-0149(89)90139-8

Banse, K., and English, D. C. (2000). Geographical differences in seasonality of CZCS-derived phytoplankton pigment in the Arabian Sea for 1978–1986. *Deep Sea Res. II* 47, 1623–1677. doi: 10.1016/S0967-0645(99)00157-5

Behrenfeld, M. J., and Falkowski, P. G. (1997). Photosynthetic rates derived from satellite-based chlorophyll concentration. *Limnol. Oceanogr.* 42, 1–20. doi: 10.4319/lo.1997.42.1.0001

Boyd, P. W., and Trull, T. W. (2007). Understanding the export of biogenic particles in oceanic waters: is there consensus? *Prog. Oceanogr.* 72, 276–312. doi: 10.1016/j.pocean.2006.10.007

Buitenhuis, E. T., Hashioka, T., and Le Quéré, C. (2013). Combined constraints on global ocean primary production using observations and models. *Glob. Biogeochem. Cycles* 27, 847–858. doi: 10.1002/gbc.20074

Campbell, J., Antoine, D., Armstrong, R., Arrigo, K., Balch, W., Barber, R., et al. (2002). Comparison of algorithms for estimating ocean primary production from surface chlorophyll, temperature, and irradiance. *Glob. Biogeochem. Cycles* 16:1035. doi: 10.1029/2001GB001444

Chen, C. C., Shiah, F. K., Chung, S. W., and Liu, K. K. (2006). Winter phytoplankton blooms in the shallow mixed layer of the South China Sea enhanced by upwelling. *J. Mar. Syst.* 59, 97–110. doi: 10.1016/j.jmarsys.2005.09.002

Chen, X., Pan, D., Bai, Y., He X., Chen, C. T. A., Kang, Y., et al. (2015). Estimation of typhoon-enhanced primary production in the South China Sea: a comparison with the Western North Pacific. *Cont. Shelf Res.* 111, 286–293. doi: 10.1016/j.csr.2015.10.003

Chen, C. T. A., Yu, S., Huang, T. H., Lui, H. K., Bai, Y., and He, X. (2020). "Changing biogeochemistry in the South China Sea," in *Changing Asia-Pacific Marginal Seas. Atmosphere, Earth, Ocean & Space*, eds C. T. A. Chen, and X. Guo (Singapore: Springer), doi: 10.1007/978-981-15-4886-4_12

Chen, J., Zheng, L., Wiesner, M. G., Chen, R., Zheng, Y., and Wong, H. K. (1998). Estimations of primary production and export production in the South China Sea based on sediment trap experiments. *Chin. Sci. Bull.* 43, 583–586. doi: 10.1007/BF02883645

Chen, T. Y., Tai, J. H., Ko, C. Y., Hsieh, C., Chen, C. C., Jiao, N., et al. (2016). Nutrient pulses driven by internal solitary waves enhance heterotrophic bacterial growth in the South China Sea. *Environ. Microbiol.* 18, 4312–4323. doi: 10.1111/1462-2920.13273

Chen, Y. L. L. (2000). Comparisons of primary productivity and phytoplankton size structure in the marginal regions of southern East China Sea. *Cont. Shelf Res.* 20, 437–458. doi: 10.1016/S0278-4343(99)00080-1

Chen, Y. L. L. (2005). Spatial and seasonal variations of nitrate-based new production and primary production in the South China Sea. *Deep Sea Res. I* 52, 319–340. doi: 10.1016/j.dsr.2004.11.001

Chen, Y. L. L., and Chen, H. Y. (2006). Seasonal dynamics of primary and new production in the northern South China Sea: the significance of river discharge and nutrient advection. *Deep Sea Res. I* 53, 971–986. doi: 10.1016/j.dsr.2006.02.005

Chen, Y. L. L., Chen, H. Y., Karl, D. M., and Takahashi, M. (2004). Nitrogen modulates phytoplankton growth in spring in the South China Sea. *Cont. Shelf Res.* 24, 527–541. doi: 10.1016/j.csr.2003.12.006

Chen, Y. L. L., Chen, H. Y., Lin, I. I., Lee, M. A., and Chang, J. (2007). Effects of cold eddy on phytoplankton production and assemblages in Luzon strait bordering the South China Sea. *J. Oceanogr.* 63, 671–683. doi: 10.1007/s10872-007-0059-9

Chen, Y. L. L., Chen, H. Y., Tuo, S. H., and Ohki, K. (2008). Seasonal dynamics of new production from *Trichodesmium* N_2 fixation and nitrate uptake in the upstream Kuroshio and South China Sea basin. *Limnol. Oceanogr.* 53, 1705–1721. doi: 10.4319/LO.2008.53.5.1705

Chou, W. C., Chen, Y. L. L., Sheu, D. D., Shih, Y. Y., Han, C. A., Cho, C. L., et al. (2006). Estimated net community production during the summertime at the SEATS time-series study site, northern South China Sea: implications for nitrogen fixation. *Geophys. Res. Lett.* 33:L22610. doi: 10.1029/2005gl025365

Dandonneau, Y., Deschamps, P. Y., Nicolas, J. M., Loisel, H., Blanchot, J., Montel, Y., et al. (2004). Seasonal and interannual variability of ocean color and composition of phytoplankton communities in the North Atlantic, equatorial Pacific and South Pacific. *Deep Sea Res. II* 51, 303–318. doi: 10.1016/j.dsr2.2003.07.018

Dierssen, H. M. (2010). Perspectives on empirical approaches for ocean color remote sensing of chlorophyll in a changing climate. *Proc. Natl. Acad. Sci. U.S.A.* 107, 17073–17078. doi: 10.1073/pnas.0913800107

Du, C., Liu, Z., Dai, M., Kao, S. J., Cao, Z., Zhang, Y., et al. (2013). Impact of the Kuroshio intrusion on the nutrient inventory in the upper northern South China Sea: insights from an isopycnal mixing model. *Biogeosciences* 10, 6419–6432. doi: 10.5194/bg-10-6419-2013

Dunne, J. P., Armstrong, R. A., Gnanadesikan, A., and Sarmiento, J. L. (2005). Empirical and mechanistic models for the particle export ratio. *Glob. Biogeochem. Cycles* 19:GB4026. doi: 10.1029/2004GB002390

Field, C. B., Behrenfeld, M. J., Randerson, J. T., and Falkowski, P. (1998). Primary production of the biosphere: integrating terrestrial and oceanic components. *Science* 281, 237–240. doi: 10.1126/science.281.5374.237

Friedland, K. D., Stock, C., Drinkwater, K. F., Link, J. S., Leaf, R. T., Shank, B. V., et al. (2012). Pathways between primary production and fisheries yields of large marine ecosystems. *PLoS One* 7:e28945. doi: 10.1371/journal.pone.0028945

Gong, G. C. (1993). Correlation of chlorophyll *a* concentration and sea tech fluorometer fluorescence in seawater. *Acta Oceanogr. Taiwan.* 31, 117–126.

Gong, G. C., and Liu, G. J. (2003). An empirical primary production model for the East China Sea. *Cont. Shelf Res.* 23, 213–224. doi: 10.1016/S0278-4343(02)00166-8

Gong, G. C., Wen, Y. H., Wang, B. W., and Liu, G. J. (2003). Seasonal variation of chlorophyll a concentration, primary production and environmental conditions in the subtropical East China Sea. *Deep Sea Res. II* 50, 1219–1236. doi: 10.1016/s0967-0645(03)00019-5

Gregg, W. W., Conkright, M. E., Ginoux, P., O'Reilly, J. E., and Casey, N. W. (2003). Ocean primary production and climate: global decadal changes. *Geophys. Res. Lett.* 30:1809. doi: 10.1029/2003GL016889

Hama, T., Miyazaki, T., Ogawa, Y., Iwakuma, T., Takahashi, M., Otsuki, A., et al. (1983). Measurement of photosynthetic production of a marine phytoplankton population using a stable ^{13}C isotope. *Mar. Biol.* 73, 31–36. doi: 10.1007/BF00396282

Hao, Q., Ning, X., Liu, Y., Cai, Y., and Le, F. (2007). Satellite and in situ observations of primary production in the northern South China Sea. *Acta Oceanol. Sin.* 29, 58–68. (in Chinese with English abstract)

Henson, S. A., Sanders, R., Madsen, E., Morris, P. J., Le Moigne, F., and Quartly, G. D. (2011). A reduced estimate of the strength of the ocean's biological carbon pump. *Geophys. Res. Lett.* 38:L04606. doi: 10.1029/2011GL046735

Hill, V. J., and Zimmerman, R. C. (2010). Estimates of primary production by remote sensing in the Arctic Ocean: assessment of accuracy with passive and active sensors. *Deep Sea Res. I* 57, 1243–1254. doi: 10.1016/j.dsr.2010.06.011

Hu, Z., Tan, Y., Song, X., Zhou, L., Lian, X., Huang, L., et al. (2014). Influence of mesoscale eddies on primary production in the South China Sea during spring inter-monsoon period. *Acta Oceanol. Sin.* 33, 118–128. doi: 10.1007/s13131-014-0431-8

Hung, C. C., Chen, Y. F., Hsu, S. C., Wang, K., Chen, J. F., and Burdige, D. J. (2016). Using rare earth elements to constrain particulate organic carbon flux in the East China Sea. *Sci. Rep.* 6:33880. doi: 10.1038/srep33880

Hung, C. C., and Gong, G. C. (2007). Export flux of POC in the main stream of the Kuroshio. *Geophys. Res. Lett.* 34:L18606. doi: 10.1029/2007GL030236

Hung, C. C., and Gong, G. C. (2010). POC/^{234}Th ratios in particles collected in sediment traps in the northern South China Sea. *Estuar. Coast Shelf Sci.* 88, 303–310. doi: 10.1016/j.ecss.2010.04.008

Hung, C. C., Gong, G. C., Chou, W. C., Chung, C. C., Lee, M. A., Chang, Y., et al. (2010). The effect of typhoon on particulate organic carbon flux in the southern East China Sea. *Biogeosciences* 7, 3007–3018. doi: 10.5194/bg-7-3007-2010

Hung, C. C., Gong, G. C., Chung, W. C., Kuo, W. T., and Lin, F. C. (2009). Enhancement of particulate organic carbon export flux induced by atmospheric forcing in the subtropical oligotrophic northwest Pacific Ocean. *Mar. Chem.* 113, 19–24. doi: 10.1016/j.marchem.2008.11.004

Hung, C. C., Tseng, C. W., Gong, G. C., Chen, K. S., Chen, M. H., and Hsu, S. C. (2013). Fluxes of particulate organic carbon in the East China Sea in summer. *Biogeosciences* 10, 6469–6484. doi: 10.5194/bg-10-6469-2013

Hung, C. C., Wong, G. T. F., Liu, K. K., Shiah, F. K., and Gong, G. C. (2000). The effects of light and nitrate levels on the relationship between nitrate reductase activity and $^{15}NO_3$- uptake: field observations in the East China Sea. *Limnol. Oceanogr.* 45, 836–848. doi: 10.4319/lo.2000.45.4.0836

Ishizaka, J., Siswanto, E., Itoh, T., Murakami, H., Yamaguchi, Y., Horimoto, N., et al. (2007). Verification of vertically generalized production model and estimation of primary production in Sagami Bay, Japan. *J. Oceanogr.* 63, 517–524. doi: 10.1007/s10872-007-0046-1

Kameda, T., and Ishizaka, J. (2005). Size-fractionated primary production estimated by a two-phytoplankton community model applicable to ocean color remote sensing. *J. Oceanogr.* 61, 663–672. doi: 10.1007/s10872-005-0074-7

Kara, A. B., Rochford, P. A., and Hurlburt, H. E. (2000). An optimal definition for ocean mixed layer depth. *J. Geophys. Res.* 105, 16803–16821. doi: 10.1029/2000jc900072

Karl, D. M., Bates, N. R., Emerson, S., Harrison, P. J., Jeandel, C., Llinâs, O., et al. (2003). "temporal studies of biogeochemical processes determined from ocean time-series observations during the JGOFS era," in *Ocean Biogeochemistry: The Role of the Ocean Carbon Cycle in Global Change*, ed. M. J. R. Fasham (New York, NY: Springer), 239–267. doi: 10.1007/978-3-642-55844-3_11

Kirk, J. T. O. (1994). *Light and Photosynthesis in Aquatic Ecosystems*. Cambridge: Cambridge University Press, 509.

Kudryavtseva, E., Bukanova, T., and Bubnova, E. (2018). "Primary productivity estimates based on the remote sea surface temperature data in the Baltic Sea," in *Proceedings of the 2018 IEEE/OES Baltic International Symposium (BALTIC)*, Klaipeda, 1–4. doi: 10.1109/BALTIC.2018.8634855

Lai, C. C., Fu, Y. W., Liu, H. B., Kuo, H. Y., Wang, K. W., Lin, C. H., et al. (2014). Distinct bacterial-production–DOC–primary-production relationships and implications for biogenic C cycling in the South China Sea shelf. *Biogeosciences* 11, 147–156. doi: 10.5194/bg-11-147-2014

Laws, E. A., D'Sa, E., and Naik, P. (2011). Simple equations to estimate ratios of new or export production to total production from satellite-derived estimates of sea surface temperature and primary production. *Limnol. Oceanogr.* 9, 593–601. doi: 10.4319/lom.2011.9.593

Lee, Z. P., Darecki, M., Carder, K. L., Davis, C. O., Stramski, D., and Rhea, W. J. (2005). Diffuse attenuation coefficient of downwelling irradiance: an evaluation of remote sensing methods. *J. Geophys. Res.* 110:C02017. doi: 10.1029/2004JC002573

Li, D., Chou, W. C., Shih, Y. Y., Chen, G. Y., Chang, Y., Chow, C. H., et al. (2018). Elevated particulate organic carbon export flux induced by internal waves in the oligotrophic northern South China Sea. *Sci. Rep.* 8:2042. doi: 10.1038/s41598-018-20184-9

Li, T., Bai, Y., Li, G., He, X., Chen, C.-T. A., Gao, K., et al. (2015). Effects of ultraviolet radiation on marine primary production with reference to satellite remote sensing. *Front. Earth Sci.* 9:237–247. doi: 10.1007/s11707-014-0477-0

Lin, I., Liu, W. T., Wu, C. C., Wong, G. T. F., Hu, C. M., Chen, Z. Q., et al. (2003). New evidence for enhanced ocean primary production triggered by tropical cyclone. *Geophys. Res. Lett.* 30:1718. doi: 10.1029/2003gl017141

Liu, K. K., Chao, S. Y., Shaw, P. T., Gong, G. C., Chen, C. C., and Tang, T. Y. (2002). Monsoon-forced chlorophyll distribution and primary production in the South China Sea: observations and a numerical study. *Deep Sea Res. I* 49, 1387–1412. doi: 10.1016/S0967-0637(02)00035-3

Liu, L., Bai, Y., Sun, R., and Niu, Z. (2021). Stereo observation and inversion of the key parameters of global carbon cycle: project overview and mid-term progressess. *Remote Sens. Technol. Appl.* 36, 11–24. doi: 10.11873/j.issn.1004-0323.2021.1.0011 (in Chinese with English abstract)

Ma, W., Chai, F., Xiu, P., Xue, H., and Tian, J. (2014). Simulation of export production and biological pump structure in the South China Sea. *Geo-Mar. Lett.* 34, 541–554. doi: 10.1007/s00367-014-0384-0

Mizobata, K., and Saitoh, S. (2004). Variability of Bering Sea eddies and primary productivity along the shelf edge during 1998–2000 using satellite multisensor remote sensing. *J. Mar. Syst.* 50, 101–111. doi: 10.1016/j.jmarsys.2003.09.014

Nielsen, E. S. (1952). The use of radio-active carbon (C14) for measuring organic production in the sea. *ICES J. Mar. Sci.* 18, 117–140. doi: 10.1093/icesjms/18.2.117

Ning, X., Chai, F., Xue, H., Cai, Y., Liu, C., and Shi, J. (2004). Physical-biological oceanographic coupling influencing phytoplankton and primary production in the South China Sea. *J. Geophys. Res.* 109:C10005. doi: 10.1029/2004JC002365

Pan, X., Wong, G. T. F., Shiah, F. K., and Ho, T. Y. (2012). Enhancement of biological productivity by internal waves: observations in the summertime in the northern South China Sea. *J. Oceanogr.* 68, 427–437. doi: 10.1007/s10872-012-0107-y

Parsons, T. R., Maita, Y., and Lalli, C. M. (1984). *A Manual of Chemical and Biological Methods for Seawater Analysis*. New York, NY: Pergamon, 173.

Pauly, D., and Christensen, V. (1995). Primary production required to sustain global fisheries. *Nature* 374, 255–257. doi: 10.1038/374255a0

Sarmiento, J. L., Hughes, T. M. C., Stouffer, R. J., and Manabe, S. (1998). Simulated response of the ocean carbon cycle to anthropogenic climate warming. *Nature* 393, 245–249. doi: 10.1038/30455

Shang, S., Li, L., Sun, F., Wu, J., Hu, C., Chen, D., et al. (2008). Changes of temperature and bio-optical properties in the South China Sea in response to Typhoon Lingling, 2001. *Geophys. Res. Lett.* 35:L10602. doi: 10.1029/2008GL033502

Shiah, F. K., Chung, S. W., Kao, S. J., Gong, G. C., and Liu, K. K. (2000). Biological and hydrographical responses to tropical cyclones (typhoons) in the continental shelf of the Taiwan Strait. *Cont. Shelf Res.* 20, 2029–2044. doi: 10.1016/s0278-4343(00)00055-8

Shiah, F. K., Gong, G. C., and Chen, C. C. (2003). Seasonal and spatial variation of bacterial production in the continental shelf of the East China Sea: possible controlling mechanisms and potential roles in carbon cycling. *Deep Sea Res. II* 50, 1295–1309. doi: 10.1016/S0967-0645(03)00024-9

Shiah, F. K., Tu, Y. Y., Tsai, H. S., Kao, S. J., and Jan, S. (2005). A case study of system and planktonic responses in a subtropical warm plume receiving thermal effluents from a power plant. *Terr. Atmos. Ocean. Sci.* 16, 513–528. doi: 10.3319/TAO.2005.16.2.513(O)

Shih, Y. Y., Hsieh, J. S., Gong, G. C., Chou, W. C., Lee, M. A., Hung, C. C., et al. (2013). Field observations of changes in SST, chlorophyll and POC flux in the southern East China Sea before and after the passage of typhoon Jangmi. *Terr. Atmos. Ocean. Sci.* 24, 899–910. doi: 10.3319/TAO.2013.05.23.01(Oc)

Shih, Y. Y., Hung, C. C., Gong, G. C., Chung, W. C., Wang, Y. H., Lee, I. H., et al. (2015). Enhanced particulate organic carbon export at eddy edges in the oligotrophic western North Pacific ocean. *PLoS One* 10:e0131538. doi: 10.1371/journal.pone.0131538

Shih, Y. Y., Hung, C. C., Huang, S. Y., Muller, F. L. L., and Chen, Y. H. (2020a). Biogeochemical variability of the upper ocean response to typhoons and storms in the northern South China Sea. *Front. Mar. Sci.* 7:151. doi: 10.3389/fmars.2020.00151

Shih, Y. Y., Hung, C. C., Tuo, S., Shao, H. J., Chow, C. H., Muller, F. L. L., et al. (2020b). The impact of eddies on nutrient supply, diatom biomass and carbon export in the northern South China Sea. *Front. Earth Sci.* 8:537332. doi: 10.3389/feart.2020.537332

Shih, Y. Y., Lin, H. H., Li, D., Hsieh, H. H., Hung, C. C., and Chen, C. T. A. (2019). Elevated carbon flux in deep waters of the South China Sea. *Sci. Rep.* 9:1496. doi: 10.1038/s41598-018-37726-w

Siswanto, E., Ishizaka, J., and Yokouchi, K. (2006). Optimal primary production model and parameterization in the eastern East China Sea. *J. Oceanogr.* 62, 361–372. doi: 10.1007/s10872-006-0061-7

Tan, S. C., and Shi, G. Y. (2009). Spatiotemporal variability of satellite-derived primary production in the South China Sea, 1998–2006. *J. Geophys. Res.* 114:G03015. doi: 10.1029/2008JG000854

Tang, S., and Chen, C. (2016). Novel maximum carbon fixation rate algorithms for remote sensing of oceanic primary productivity. *IEEE J. Sel. Top. Appl. Earth Obs. Remote Sens.* 9, 5202–5208. doi: 10.1109/JSTARS.2016.2574898

Tang, S., Chen, C., Zhan, H., Zhang, J., and Yang, J. (2008). An appraisal of surface chlorophyll estimation by satellite remote sensing in the South China Sea. *Int. J. Remote Sens.* 29, 6217–6226. doi: 10.1080/01431160802175579

Tilstone, G., Smyth, T., Poulton, A., and Hutson, R. (2009). Measured and remotely sensed estimates of primary production in the Atlantic Ocean from 1998 to 2005. *Deep Sea Res. II* 56, 918–930. doi: 10.1016/j.dsr2.2008.10.034

Tilstone, G. H., Taylor, B. H., Blondeau-Patissier, D., Powell, T., Groom, S. B., and Rees, A. P. (2015). Comparison of new and primary production models using SeaWiFS data in contrasting hydrographic zones of the northern North Atlantic. *Remote Sens. Environ.* 156, 473–489. doi: 10.1016/j.rse.2014.10.013

Tseng, C. M., Wong, G. T. F., Lin, I. I., Wu, C. R., and Liu, K. K. (2005). A unique seasonal pattern in phytoplankton biomass in low-latitude waters in the South China Sea. *Geophys. Res. Lett.* 32:L086080. doi: 10.1029/2004gl022111

Wong, G. T. F., Ku, T. L., Mulholland, M., Tseng, C. M., and Wang, D. P. (2007). The SouthEast Asian time-series study (SEATS) and the biogeochemistry of the South China Sea-an overview. *Deep Sea Res. II* 54, 1434–1447. doi: 10.1016/J.DSR2.2007.05.012

Yamada, K., Ishizaka, J., and Nagata, H. (2005). Spatial and temporal variability of satellite primary production in the Japan Sea from 1998 to 2002. *J. Oceanogr.* 61, 857–869. doi: 10.1007/s10872-006-0005-2

Yang, J. Y. T., Hsu, S. C., Dai, M., Hsiao, S. S. Y., and Kao, S. J. (2014). Isotopic composition of water-soluble nitrate in bulk atmospheric deposition at Dongsha Island: sources and implications of external N supply to the northern South China Sea. *Biogeosciences* 11, 1833–1846. doi: 10.5194/bg-11-1833-2014

Zhao, H., Tang, D., and Wang, Y. (2008). Comparison of phytoplankton blooms triggered by two typhoons with different intensities and translation speeds in the South China Sea. *Mar. Ecol. Prog. Ser.* 365, 57–65. doi: 10.3354/meps0741838

Zhong, J., Wallin, M. B., Wang, W., Li, S.-L., Guo, L., Dong, K., et al. (2021). Synchronous evaporation and aquatic primary production in tropical river networks. *Water Res.* 200:117272. doi: 10.1016/j.watres.2021.117272

Zhou, K., Dai, M., Maiti, K., Chen, W., Chen, J., Hong, Q., et al. (2020). Impact of physical and biogeochemical forcing on particle export in the South China Sea. *Prog. Oceanogr.* 187:102403. doi: 10.1016/j.pocean.2020.102403

Conflict of Interest: The authors declare that the research was conducted in the absence of any commercial or financial relationships that could be construed as a potential conflict of interest.

frontiers in Marine Science

ORIGINAL RESEARCH
published: 20 October 2021
doi: 10.3389/fmars.2021.729269

Simultaneous Occurrence of Tropical Cyclones in the Northern Indian Ocean: Differential Response and Triggering Mechanisms

Riyanka Roy Chowdhury[1], *S. Prasanna Kumar*[2]* *and Arun Chakraborty*[1]

[1] Centre for Oceans, Rivers, Atmosphere and Land Sciences, Indian Institute of Technology Kharagpur, Kharagpur, India,
[2] CSIR-National Institute of Oceanography, Dona Paula, India

OPEN ACCESS

Edited by:
Francois L. L. Muller,
National Sun Yat-sen University, Taiwan

Reviewed by:
Kusum Komal Karati,
Centre for Marine Living Resources and Ecology (CMLRE), India
C. Gnanaseelan,
Indian Institute of Tropical Meteorology (IITM), India

***Correspondence:**
S. Prasanna Kumar
prasanna.ocean@gmail.com

Specialty section:
This article was submitted to Marine Ecosystem Ecology, a section of the journal Frontiers in Marine Science

Received: 22 June 2021
Accepted: 10 September 2021
Published: 20 October 2021

Citation:
Roy Chowdhury R, Prasanna Kumar S and Chakraborty A (2021) Simultaneous Occurrence of Tropical Cyclones in the Northern Indian Ocean: Differential Response and Triggering Mechanisms. Front. Mar. Sci. 8:729269. doi: 10.3389/fmars.2021.729269

The northern Indian Ocean, comprising of two marginal seas, the Arabian Sea (AS) and the Bay of Bengal (BoB), is known for the occurrence of tropical cyclones. The simultaneous occurrence of the cyclones Luban in the AS and Titli in the BoB is a rare phenomenon, and, in the present study, we examined their contrasting upper ocean responses and what led to their formation in October 2018. Being a category-2 cyclone, the maximum cooling of sea surface temperature associated with Titli was 1°C higher than that of Luban, a category-1 cyclone. The higher tropical cyclone heat potential in the BoB compared with the AS was one of the reasons why Titli was more intense than Luban. The enhancement of chlorophyll *a* (Chl-*a*) and net primary productivity (NPP) by Luban was 2- and 3.7-fold, respectively, while that by Titli was 3- and 5-fold, respectively. Despite this, the magnitudes of both Chl-*a* and NPP were higher in the AS compared with the BoB. Consistent with physical and biological responses, the CO_2 outgassing flux associated with Titli was 12-fold higher in comparison to the pre-cyclone value, while that associated with Luban was 10-fold higher. Unlike the Chl-*a* and NPP, the magnitude of CO_2 flux in the BoB was higher than that in the AS. Although the cyclones Luban and Titli originated simultaneously, their generating mechanisms were quite different. What was common for the genesis of both cyclones was the pre-conditioning of the upper ocean in 2018 by the co-occurrence of El Niño and the positive phase of Indian Ocean dipole along with the cold phase of the Pacific decadal oscillation, all of which worked in tandem and warmed the AS and parts of the BoB. What triggered the genesis of Luban in the AS was the arrival of the Madden–Julian oscillation (MJO) and the mixed Rossby-gravity wave during the first week of October. The genesis of Titli in the BoB was triggered by the eastward propagation of the MJO and the associated enhanced convection from the AS into the region of origin of Titli along with the arrival of the downwelling oceanic Rossby wave.

Keywords: tropical cyclone, SST cooling, chlorophyll *a*, net primary productivity, CO_2 efflux, Madden-Julian oscillation, mixed Rossby-gravity wave, tropical cyclone heat potential

INTRODUCTION

The North Indian Ocean (NIO), consisting of the Arabian Sea (AS) and the Bay of Bengal (BoB), is one of the warmest tropical oceans and accounts for ∼7% of the global tropical cyclones that occur annually (Gray, 1985). Although the BoB and the AS are situated in similar latitudinal belts, the occurrence of tropical cyclones over the BoB is four times higher than that in the AS (Dube et al., 1997). In the NIO, cyclones form every year during the pre-monsoon (April–May) and the post-monsoon (October–December) seasons. Although the occurrences of tropical cyclones in the NIO are relatively less compared with the global tropics, it has a disastrous impact during landfall due to the shallow bathymetry, low-lying coastal terrain, and funnel-shaped coastline. As NIO-rim countries house one-third of the global population and their coastal regions are densely populated, there is an urgent need for a better prediction of the track and intensity of cyclones, and their landfall. There is also a growing concern that the rapid warming of the NIO (e.g., RupaKumar et al., 2002; Prasanna Kumar et al., 2009a; Roxy et al., 2014) may alter the number and intensity of cyclones (e.g., Singh et al., 2001; Prasanna Kumar et al., 2009a; Knutson et al., 2010; Rajeevan et al., 2013). All this has led to several studies in recent decades aimed at understanding the various aspects of cyclones in the NIO. Studies on cyclone-induced changes can be broadly classified as physical changes associated with the cooling of sea surface temperature (SST) and upper ocean dynamics (e.g., Rao, 1987; Gopalakrishna et al., 1993; Subrahmanyam et al., 2005; Neetu et al., 2012; Pothapakula et al., 2017; Balaji et al., 2018; Shengyan et al., 2019; Singh et al., 2020) and as biological changes associated with the enhancement of chlorophyll and net primary production (e.g., Latha et al., 2015; Chacko, 2018, 2019; Maneesha et al., 2019; Singh and Roxy, 2020 and references therein). The least explored aspect in this field of study is the cyclone-induced changes in the CO_2 flux (Byju and Prasanna Kumar, 2011; Ye et al., 2019; Chowdhury et al., 2020a,b). A review of the recent work on cyclone-induced changes in the BoB and the AS can be found in Chowdhury et al. (2020a,b).

It is evident from the above mentioned studies that various researchers attempted to gain insight into the characteristics of the cyclone-induced variability of the upper ocean either in the BoB or in the AS. However, there are no studies to date that address the simultaneous occurrence of cyclones in the AS and the BoB and the resulting differential responses. One of the reasons could be that it is a rare phenomenon and, to the best of our knowledge, apart from the simultaneous occurrence of cyclones over the AS and the BoB in 2018, the only other occurrence was recorded in 1960. Hence, it provided a unique opportunity to study the differential response of the two tropical seas with contrastingly different physical and biogeochemical characteristics and regional oceanography. This is the motivation of the present study. Before attempting to understand the differential response, it is necessary that the contrasting characteristics of the AS and the BoB be examined first.

The AS and the BoB, although are tropical seas situated between similar latitudes and driven by the same semi-annually reversing monsoonal winds, both have distinctly different regional oceanography. A detailed account of the contrasting physical and biogeochemical characteristics of both seas can be found in Prasanna Kumar et al. (2009b) and Narvekar et al. (2017). The salient differences are that, in the AS, evaporation exceeds precipitation with very little contribution from river discharge to the freshwater flux, while, in the BoB, precipitation exceeds evaporation, and river runoff contributes dominantly to the freshwater flux (Prasad, 1997). This makes the basin-averaged surface salinity of the AS at least 3 units higher than that of the BoB, while the SST of the BoB is 1°C colder than the AS. In terms of the basin-averaged winds, although they show a similar semi-annual variability over both the seas, the wind speeds in the AS are about 3 m/s higher compared with those in the BoB. Biologically, considering the productivity of its surface waters, the AS is one of the most productive regions in the oceans of the world (Ryther et al., 1966), while the BoB is a region of low productivity (Qasim, 1977; Madhupratap et al., 2003). Apart from this, the annual cycle of the basin-averaged surface chlorophyll pigment concentrations in both seas are very different. In the AS, the annual cycle shows a bimodal distribution with primary (1.2 mg/m^3) and secondary (0.7 mg/m^3) peaks, coinciding with the phytoplankton blooms during summer (June–September) and winter monsoons (November–February), respectively. In contrast, the BoB does not exhibit any strong seasonality, and the chlorophyll pigment concentration remains almost the same over the year with a value of 0.5 mg/m^3. Despite such strong differences in the surface chlorophyll pigment concentrations and associated primary productivity, the annual mean flux of organic carbon (26 g m^{-2} $year^{-1}$) collected at mid-depths (nominally at 1,000 m) by sediment traps shows a comparable value in both seas (Ramaswamy and Nair, 1994). Subsequent studies attributed the mismatch between the surface chlorophyll biomass and the sinking flux of organic carbon into the mesopelagic layer in the BoB to mesoscale cold-core eddies that enhance the chlorophyll biomass in the subsurface layers and are not captured by the satellite remote sensing (Prasanna Kumar et al., 2004; Vidya and Prasanna Kumar, 2013; Sridevi et al., 2019). In addition, the tropical cyclones that occur regularly in the BoB also contribute toward the enhancement of chlorophyll (Maneesha et al., 2011; Chacko, 2017; Chowdhury et al., 2020b), although for much shorter periods compared with upwelling or mesoscale eddies. The high-sinking flux of organic carbon combined with the poor ventilation of the waters of the NIO due to its land-locked nature leads to the formation of an intense mid-depth oxygen minimum zone (OMZ) and associated denitrification (Naqvi et al., 1990) in both seas. However, its intensity and spatiotemporal variability are more in the AS compared with the BoB. This has large implications for the ecosystem structure in both the basins and its fishery. For example, an increase in the sinking flux of organic carbon would lead to an intensification of the OMZ, and the resulting hypoxic/anoxic conditions would impact the marine organisms that live in the mesopelagic zone. Similarly, increased denitrification would also impact the ecosystem apart from the imminent danger of the production of nitrous oxide, a potent greenhouse gas.

It is the above-stated differential characteristics of the two seas and the simultaneous occurrence of cyclones in both the seas that motivated the present study, providing a unique opportunity to study the differential response. The rest of the study is organized as follows: The second section describes the data and methodology used. The third section describes the physical and biogeochemical responses due to the passage of cyclones Luban and Titli and the probable mechanisms for the formation of twin cyclones over the NIO. Section four summarizes the findings of the study.

DATA AND METHODS

Data

In the present study, the cyclone intensities and track information for Luban and Titli were taken from Indian Meteorological Department (IMD) (http://www.rsmcnewdelhi.imd.gov.in/report.php?internal_menu=MzM=). The daily SSTs for October 2018 were extracted from the National Oceanic and Atmospheric Organization (NOAA) high-resolution blended analysis of SST (Reynolds et al., 2007), having a spatial resolution of 0.25 degrees (https://www.esrl.noaa.gov/psd/cgibin/db_search/DBListFiles.pl?did=132andtid=68603andvid=2423), while the extended reconstructed SST, SST anomalies, and Nino-3.4 index from 1979 to 2020 were downloaded from the Asia Pacific Data Research Center (http://apdrc.soest.hawaii.edu/las/v6/dataset?catitem=1261). The Dipole Mode Index (DMI) was calculated using reconstructed SST data (Saji et al., 1999) for the identification of Indian Ocean Dipole (IOD) years. Daily sea level anomaly (SLA), having a spatial resolution of 0.25 degrees latitude by longitude, was taken from Copernicus Marine Services (CMMES) (https://resources.marine.copernicus.eu/?option=com_cswandview=orderandrecord_id=bd5a176b-350e-4d5f-8683-da457637bdcb). The daily temperature and salinity data were taken from Hybrid Coordinate Ocean Model (HYCOM) with a spatial resolution of 1/12 degree and used for the calculation of potential density (sigma-theta), mixed layer depth (MLD), and the depth of the 26°C isotherm (D_{26}). The MLD is defined as the depth at which density exceeds 0.2 kg/m^3 from its surface value (Narvekar and Prasanna Kumar, 2006). The daily salinity data required for the calculation of the solubility of CO_2 in seawater were taken from the HYCOM global 1/12 degree Global Ocean Forecasting System (GOFS) 3.1 reanalysis (http://apdrc.soest.hawaii.edu/las_ofes/v6/constrain?var=234).

The tropical cyclone heat potential (TCHP) was calculated using Equation (1).

$$\mathrm{TCHP} = \rho c_p \int_0^{D_{26}} [T(z) - 26]\, dz \tag{1}$$

where "ρ" is the density of seawater, "c_p" is the specific heat capacity of seawater taken as 4 kJ kg^{-1} K^{-1}, $T(z)$ is the daily temperature profile taken from HYCOM, and D_{26} is the depth of the 26°C isotherm.

The relative humidity at 500 hPa and the zonal and meridional components of wind at 850 and 200 hPa having a horizontal resolution of 25 km were extracted from the National Center for Medium Range Weather Forecast (NCMRWF) NGFS 6-h reanalysis data product (https://rds.ncmrwf.gov.in/dashboard/download) (Prasad et al., 2011; Sandeep and Prasad, 2018). Daily values were calculated from the hourly dataset. The winds at 850 and 200 hPa were further used for the calculation of vertical wind shear, using Equation (2) (Evan and Camargo, 2011).

$$\text{Vertical wind shear} = \sqrt{(U_{200hPa} - U_{850hPa})^2 + (V_{200hPa} - V_{850hPa})^2} \tag{2}$$

The relative vorticity at 850 hPa has been calculated using Equation (3)

$$\text{Relative vorticity} = \frac{\partial v}{\partial x} - \frac{\partial u}{\partial y} \tag{3}$$

The daily outgoing longwave radiation (OLR) data for October 2018 were obtained from the NOAA (Liebmann and Smith, 1996) (http://www.esrl.noaa.gov). The daily OLR data and the data on the zonal wind at 850 hPa were subjected to 30- to 90-day bandpass filters to decipher the presence of Madden–Julian Oscillation (MJO) signal (intraseasonal variability) during the period of both cyclones (Shoup et al., 2019; Roman-Stork et al., 2020). The real-time multivariate MJO (RMM) index was taken from the Australian Bureau of Meteorology (http://www.bom.gov.au/climate/mjo/graphics/rmm.74toRealtime.txt) to identify the phase and amplitude of the MJO and its role in the cyclogenesis of Luban and Titli. The RMM index is calculated using the first two empirical orthogonal functions (RMM1 and RMM2), using 15°S−15°N averaged OLR and lower (850 hPa) and upper level (200 hPa) zonal wind data following Wheeler and Hendon (2004).

To identify the presence of the mixed Rossby-gravity (MRG) wave signal, a continuous wavelet transforms analysis (Torrence and Compo, 1998; Grinsted et al., 2004) was carried out using the 6-h meridional wind data of the lower (850 hPa) and upper (200 hPa) troposphere. Furthermore, a wavelet power spectrum analysis of the meridional wind in the region of origin of cyclones Luban and Titli was carried out to confirm the periodicity of the MRG wave.

The Data Processing Method of Chlorophyll *a*, Net Primary Production, and CO_2 Flux

The satellite-derived daily chlorophyll *a* (Chl-a) pigment concentration data and net primary production (NPP) were estimated based on a vertically generalized productivity model (VGPM) (Behrenfeld and Falkowski, 1997) were obtained from Moderate Resolution Imaging Spectro-radiometer (MODIS) Aqua Ocean color (https://oceandata.sci.gsfc.nasa.gov/MODISA/). The Level 3 Chl-*a* dataset has a spatial resolution of 4 km. From the daily data, 3-day composites were calculated for further analysis.

To determine the net CO_2 flux over the AS and the BoB before, during, and after the passage of the cyclones Luban and Titli, pCO_2 air data were taken from the NOAA Earth System Research Laboratories (ESRL) (https://gml.noaa.gov/webdata/ccgg/trends/co2/co2_mm_mlo.txt). Since the daily pCO_2^{sea} values are not available, the value of climatological pCO_2^{sea} was taken from Takahashi et al. (2009), and the net flux was calculated using the following formula:

$$F = k.a.(pCO_2{}^{sea} - pCO_2{}^{air}) \tag{4}$$

where k denotes the gas transfer velocity and a is the solubility of CO_2 in seawater, which is dependent on sea surface temperature and salinity (Weiss, 1974) as per the following equations:

$$\ln a = A_1 + A_2\left(\frac{100}{T}\right) + A_3 \ln\left(\frac{T}{100}\right) + S\left[B_1 + B_2\left(\frac{T}{100}\right) + B_3\left(\frac{T}{100}\right)^2\right] \tag{5}$$

A1, A2, A3, B1, B2, and B3 are solubility constants, and the values were taken from Weiss (1974). The values of the solubility constants are −60.24, 93.45, 23.35, 0.023517, −0.023656, and 0.0047036 mol/kg.atm, respectively.

The gas-transfer velocity "k" is calculated using wind speed following Wanninkhof (1992) using the formula:

$$k\left(cm\,h^{-1}\right) = \Gamma \cup^2 \left(\frac{S_c}{660}\right)^{-1/2} \tag{6}$$

where Γ is the scaling factor, and its value of 0.26 is taken from Takahashi et al. (2009), while $\cup$ is the wind speed. S_c is the Schmidt number (kinematic viscosity of water/diffusion coefficient of CO_2 in water), the value of which is 660 for CO_2 in seawater at 20°C and is a function of temperature and is computed as

$$S_c = A - BT + CT^2 - DT^3 \tag{7}$$

where A, B, C, and D are constants, and, for their values, we referred to Wanninkhof (1992). The values of A, B, C, and D are 2,073.1, 125.62, 3.6276, and 0.043219, respectively.

Computation of Mixed Layer Heat Budget

Variability in SSTs is driven by the heat balance in the surface-mixed layer of the ocean, which is governed by the surface air-sea fluxes, horizontal advection, and entrainment processes in the mixed layer. To understand the contribution of each term on the mixed layer heat budget, we have analyzed the simplified version of the mixed layer heat balance followed by Vialard et al. (2008) and Foltz and McPhaden (2009), as shown in the following equation. For this calculation, we have taken temperature, salinity, and zonal and meridional water velocity data from HYCOM. Surface net heat flux and shortwave radiation were taken from TropFlux (https://www.incois.gov.in/tropflux/tf_products.jsp), having a spatial resolution of 1 degree (Praveen Kumar et al., 2013).

$$\underset{(a)}{\frac{\partial T}{\partial t}} = \underset{(b)}{\frac{Q_{net}-Q_{pen}}{\rho C_p h}} \underset{(c)}{-\left[u\frac{\partial T}{\partial x} + v\frac{\partial T}{\partial y}\right]} \underset{(d)}{-\frac{w\Delta T}{h}} \underset{(e)}{+residual} \tag{8}$$

The terms in Equation (8) represent (a) the temperature tendency, (b) the net heat flux, (c) the horizontal advection, (d) the vertical entrainment, and (e) the residual term in units of °C/day. T is the vertically averaged mixed layer temperature, ρ is the density of the seawater with a value of 1,026 kg/m^3, C_p is the specific heat capacity of seawater at constant pressure, t is the time, h is the mixed layer depth, Q_{net} is the net heat flux (W/m^2) at the surface, and Q_{pen} is the penetrating shortwave radiation below the mixed layer and is calculated as follows:

$$Q_{pen} = Q_{sw} \times 0.47 \times exp(-z/h\nu) \tag{9}$$

where Q_{sw} is the net shortwave radiation received at the surface and $h\nu = 1/0.027 + 0.518\ \mathrm{Chl}^{428}$. The value of $h\nu$ is estimated from the moderate resolution imaging spectroradiometer (MODIS) daily composite of Chl-a (in mg/m^3) (Morel and Antoine, 1994; Sweeney et al., 2005). u, v, and w are the eastward, northward, and vertical velocities. The residual term represents the exchanges with the subsurface (upwelling and vertical turbulent processes at the base of the ML and diffusion).

All the parameters were analyzed for pre-, during, and post-cyclone periods. The pre-, during, and post-Luban periods were September 26–October 5, October 6–15, and October 16–25, 2018, respectively. The pre-, during, and post-Titli periods were October 3–7, October 8–12, and October 13–17, 2018, respectively. We have selected two box regions in the AS and the BoB for further analysis. Box A in the AS (11–16.5°N; 52.2–67.2°E) and Box B in the BoB (13.7–18.7°N; 84.4–88.9°E) encompassed the tracks of cyclones Luban and Titli, respectively (see **Figure 1**).

RESULTS AND DISCUSSIONS

Genesis and Evolution of Cyclones Luban and Titli

The simultaneous occurrence of the cyclones Luban (October 6–15, 2018) in the AS and Titli (October 8–12, 2018) in the BoB being an unusual phenomenon, it is important to track their origin and evolution. The daily-mean values of the translation speed, estimated central pressure, and maximum sustained wind speed for Luban and Titli are given in **Tables 1**, **2**, respectively, along with the category of disturbance. Luban was a category-1 (wind speed between 119 and 153 km/h) cyclone, whereas Titli was a category-2 (wind speed between 154 and 177 km/h) cyclone as per the Saffir–Simpson Scale (https://www.nhc.noaa.gov/pdf/sshws_2012rev.pdf). The maximum sustained wind speed of Luban was 75 knots (38.58 m/s; 138.9 km/h), and that for Titli was 80 knots (41.15 m/s; 148.16 km/h), which occurred at 06:00 UTC and 12:00 UTC, respectively on October 10. However,

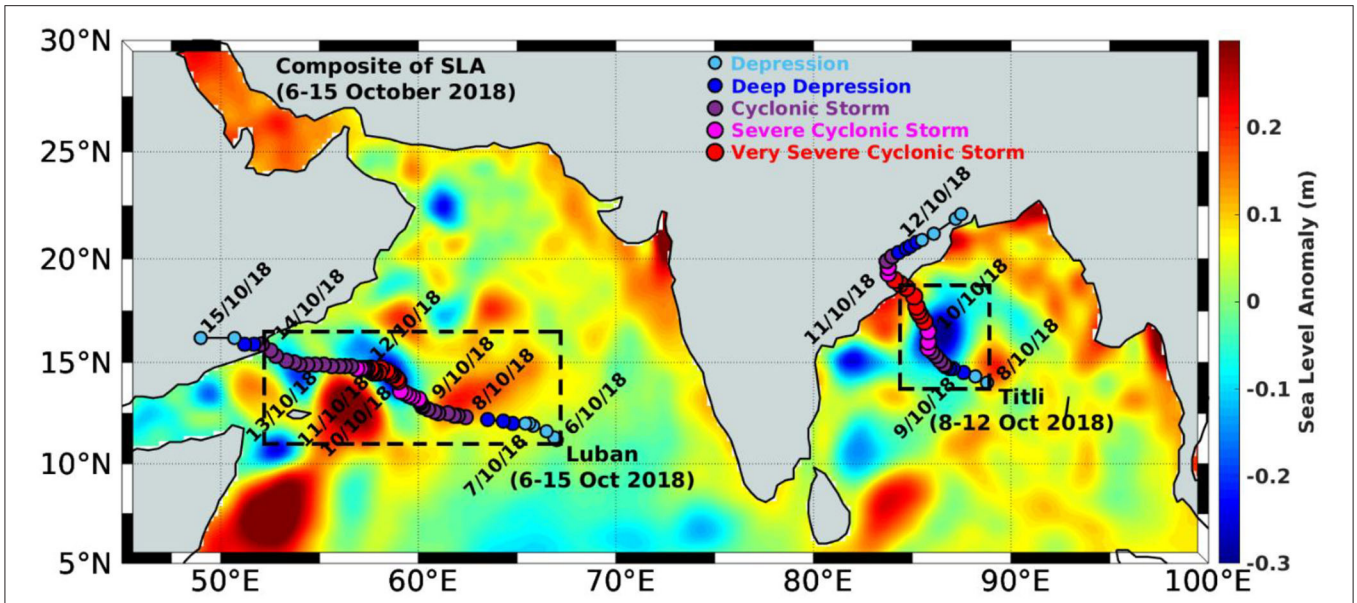

FIGURE 1 | A map showing the North Indian Ocean comprising of the Arabian Sea (AS) and the Bay of Bengal (BoB) with tracks of the cyclones Luban and Titli denoted by the filled circles with different color markers to show the different stages of the cyclone (a cyan circle for depression, a blue circle for deep depression, a purple circle for cyclonic storm, a magenta circle for severe cyclonic storm, and a red circle for very severe cyclonic storm). Shading is the sea level anomaly (SLA) (m). The boxes with broken black lines are the regions that were used for the computation of various parameters. See text for details.

TABLE 1 | Daily mean characteristics of the cyclone Luban in the Arabian Sea (AS) during its genesis and evolution.

Date	Translation speed (m/s)	Category of cyclonic disturbance	Estimated central pressure (hPa)	Maximum sustained surface wind speed in kt (km/h) m/s
06/10/2018	1.34	D	1002.33	25.0 (46.30) 12.86
07/10/2018	3.87	D to DD	1001.33	27.5 (50.93) 14.15
08/10/2018	3.54	CS	996.25	42.5 (78.71) 21.86
09/10/2018	1.84	CS to SCS	991.50	51.2 (94.82) 26.34
10/10/2018	1.66	VSCS	979.62	72.5 (134.27) 37.30
11/10/2018	1.36	VSCS	979.75	70.0 (129.64) 36.01
12/10/2018	1.62	VSCS to SCS	990.25	50.6 (93.71) 26.03
13/10/2018	3.77	CS	994.50	40.6 (75.19) 20.89
14/10/2018	5.92	CS to DD	999.66	33.3 (61.67) 17.13
15/10/2018	8.37	D	1003.00	25.0 (46.30) 12.86

L, low pressure; DD, deep depression; CS, cyclonic storm; SCS, severe cyclonic storm; VSCS, very severe cyclonic storm.

TABLE 2 | Daily mean characteristics of the cyclone Titli in the Bay of Bengal (BoB) during its genesis and evolution.

Date	Translation speed (m/s)	Category of cyclonic disturbance	Estimated central pressure (hPa)	Maximum sustained surface wind speed in kt (km/h) m/s
08/10/2018	1.62	D	1001.5	26.2 (48.52) 13.48
09/10/2018	2.46	DD to CS	996.87	38.1 (70.56) 19.60
10/10/2018	4.11	SCS to VSCS	978.0	72.5 (134.27) 37.30
11/10/2018	3.54	VSCS to SCS to CS	960.28	52.8 (107.79) 29.94
12/10/2018	3.96	DD	1001.85	26.4 (48.89) 13.58

L, low pressure; DD, deep depression; CS, cyclonic storm; SCS, severe cyclonic storm; VSCS, very severe cyclonic storm.

cyclone Titli had an estimated surface wind speed of 140–150 km/h, gusting to 165 km/h during the period 23:00 UTC of October 10 and 00:00 UTC of October 11 when it crossed the coast near Palasa (18.8°N; 84.4°E) of Andhra Pradesh, making it a category-2 cyclone. According to the IMD classification, both were very severe cyclonic storms (VSCS) (as shown in **Tables 1**, **2**). Luban formed as a depression on October 6 over the east-central AS (11.2°N, 67°E, **Figure 1**) and gradually moved west-northwestwards. It intensified into a deep depression on October 7 at 09:00 UTC, became a cyclonic storm (CS) on October 8 at 03:00 UTC, and then into a severe cyclonic storm (SCS) on October 9 at 09:00 UTC (**Figure 1**). While moving northwestward on October 10 at 00:00 UTC, it further intensified into a VSCS. The translation speed of the system initially showed a rapid increase from 1.34 m/s on October 6 to 3.87 m/s on October 7, which was 2.9-times higher than the initial value (**Table 1**). However, the translation speed showed a steady decrease as the system was intensifying and became 1.36 m/s on October 10 when it strengthened into a VSCS. At this time, the system attained a maximum wind speed of 75 kt (38.6 m/s; 138.90 km/h) and the lowest pressure of 978 hPa at 06:00 UTC of October 10 and then continued its west-northwestward

movement as a VSCS until 00:00 UTC of October 12. Note that the daily mean of the maximum sustained wind speed on October 10 was lower (72.5 kt, 134.27 km/h, **Table 1**) than the highest value recorded at 06:00 UTC. At 03:00 UTC of October 10, the system weakened to an SCS, and a CS at 18:00 UTC while moving further northwestward. On October 13, the system continued moving northwestward as a CS and then crossed Yemen and the adjoining Oman coast near 15.8°N and 52.2°E during 05:30 to 06:00 UTC on October 14. On October 15 at 03:00 UTC, the system weakened into a well-marked low pressure area over Yemen and adjoining Saudi Arabia. Interestingly, as the system started dissipating from October 12 to 15, the translation speed showed a rapid increase once again, attaining the highest value of 8.37 m/s (**Table 1**).

Cyclone Titli, on the other hand, was formed as a depression in the central BoB (14°N and 88.8°E) on October 8, at 03:00 UTC, and moved in a northwestward direction (**Figure 1**). On October 9, it became a CS at 06:00 UTC and further intensified into a VSCS on October 10 at 06:00 UTC while moving in a north-northwestward direction. The system was further intensified with a maximum sustained wind speed of 80 kt and the lowest pressure of 972 hPa at 12:00 UTC, while the daily mean of the maximum sustained wind speed was 72.5 kt (**Table 2**). Contrary to the translation speed of Luban, that of Titli showed a steady increase from October 8 to 10 when the system was intensifying into a VSCS (**Table 2**). The increase was 2.5 times the initial value of 1.62 m/s. On the same day, during 23:00 UTC, the cyclone crossed the north Andhra Pradesh and south Odisha coast near 18.8°N and 84°E with an estimated surface wind speed of 140–150 km/h, gusting to 165 km/h (**Figure 1**). As the system gradually reduced its intensity from a VSCS to an SCS on October 11, its translation speed also decreased (**Table 2**) unlike that of Luban. On October 12, the system weakened into a well-marked low pressure area over Gangetic West Bengal and adjoining Bangladesh.

SST Response

The time evolution of SST before the cyclones Luban (**Figure 2A**) and Titli (**Figure 2D**) showed that the eastern and central parts of the AS were at least 2°C warmer than the western part (**Figure 2A**). In contrast, the SST in most of the BoB was almost the same with values above 29°C (**Figure 2D**). The colder SST in the western part of the AS was due to the prevailing coastal upwelling during the summer monsoon (Smith and Bottero, 1977; Smith and Codispoti, 1980). Before the formation of cyclone Luban, the SST was 29°C at the location where the cyclone originated and 28°C where the cyclone gained its maximum intensity (**Figure 2A**). During the period of cyclone Luban, a reduction in SST was noticed along the track (**Figure 2B**), and after the passage of the cyclone, a cooling of 1.5–2°C was observed at the right side of the track (**Figure 2C**). Before the formation of cyclone Titli, the SST was 30°C at the location of its origin and 31°C where the cyclone attained its maximum intensity (**Figure 2D**). During (**Figure 2E**) and after (**Figure 2F**) the passage of cyclone Titli, a cooling of 1 and 3°C, respectively, was observed at the right side of the track where the cyclone attained its maximum intensity (**Figure 2F**).

TCHP Response

The TCHP is a measure of the integrated vertical temperature of the ocean from the surface to the depth of the 26°C isotherm (D_{26}). Being a measure of the heat energy of the ocean, it plays a significant role in the formation and intensification of tropical cyclones. The characteristic feature of the spatial distribution of TCHP was that, although it was higher in the central and eastern regions of both basins, the values prior to the cyclones in the BoB were 20 kJ/cm^2 higher compared with the AS (**Figures 3A,D**). In the AS, there was a strong zonal gradient with the lowest values occurring in the western region and close to the southeastern region (**Figure 3A**). These lowest values were associated with coastal upwelling that occurs along the western boundary and southeastern boundary of the AS, which was also discernible in the spatial distribution of SST in **Figure 2A**. The cyclone Luban originated from a region in the central AS where TCHP was close to 60 kJ/cm^2 (**Figure 3A**). During the cyclone period (**Figure 3B**), the TCHP values showed a reduction of 20 kJ/cm^2 toward the west along the track, which was associated with the intensification of Luban into a VSCS on October 10. When Luban moved further westward, it was passing through the region of the lowest TCHP, and that resulted in the weakening of the cyclone. After the passage of Luban, the reduction in the values of TCHP along the track persisted, and the magnitude of reduction was more toward the right side of the track (**Figure 3C**), consistent with the maximum cooling noticed in the SST (**Figure 2C**). As the TCHP in the BoB was higher than the AS, the formation of cyclone Titli took place in a region where the TCHP was close to 80 kJ/cm^2 prior to its formation (**Figure 3D**). During the active phase of Titli, the TCHP along the cyclone track showed a decrease of nearly 20 kJ/cm^2 (**Figure 3E**), a reduction similar to that of Luban. However, unlike Luban, the northwestward track of Titli was through the region of high TCHP. This may be the reason why cyclone Titli was much more intense (**Table 2**) compared with Luban (**Table 1**). Similar to Luban, the TCHP values along the track of Titli were also low, with a maximum reduction to the right of the track (**Figure 3F**).

SLA Response

The spatial pattern of SLA overlaid with the geostrophic current before, during, and after the passage of cyclones Luban and Titli (**Figure 4**) has been analyzed to understand the differences in the life cycle of both cyclones. The blue-colored region with negative SLA indicates the cold-core eddy, and the red-colored region with positive SLA indicates the warm core eddy region (Prasanna Kumar et al., 2004). Prominent circulation features seen prior to the formation of cyclones were the Great Whirl located between 5 and 10°N off the Somali coast and Socotra Gyre (Fischer et al., 1996) and north of the Great Whirl in the AS, with both cold and warm-core eddies located close to the western boundary (**Figures 4A,D**). In the BoB, three cold-core eddies were present near the western boundary and two warm-core eddies in the offshore region. The origin of cyclone Luban was in a region of positive SLA, and it intensified into a VSCS, while the track was over the edge of Socotra Gyre, a warm core region, and a cold-core eddy (**Figure 4B**). Its further westward track was over a prominent cold-core eddy region, which may

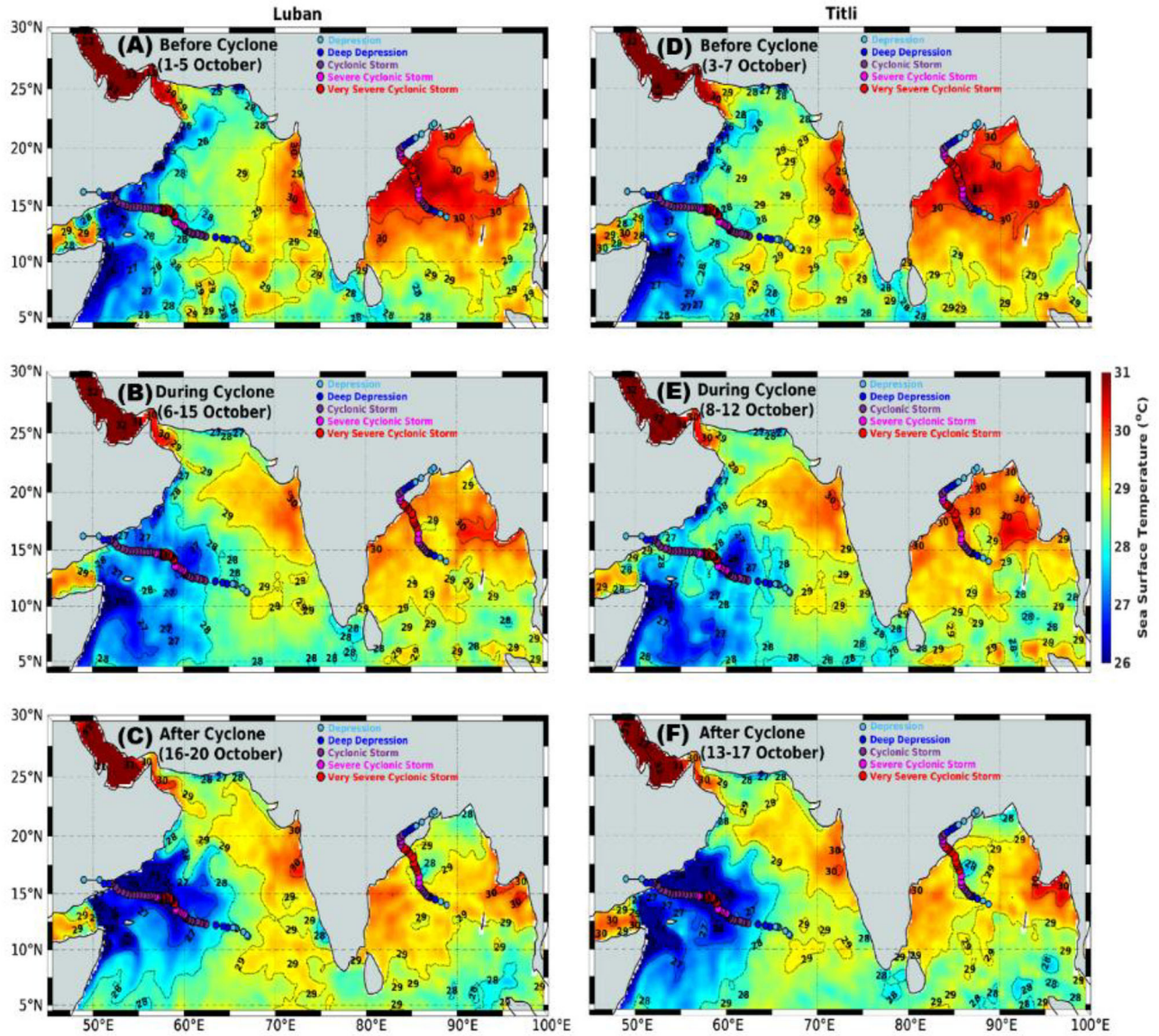

FIGURE 2 | Spatial distribution of the sea surface temperature (SST, °C) before **(A,D)**, during **(B,E)**, and after **(C,F)** cyclones Luban **(A–C)** and Titli **(D–F)**, superposed with cyclone tracks.

be the reason why the system weakened to an SCS and then to a CS, finally crossing over to Yemen. Notice the change in the circulation pattern by way of the intensification of the cold-core eddy region with a much lower SLA and the reduction in the size of the Socotra Gyre after the passage of Luban (**Figure 4C**). Unlike Luban, the origin of cyclone Titli was in the region of a warm core eddy (**Figure 4D**). As it moved northwestward, its track entered into a cold-core eddy region where it intensified from an SCS into a VSCS (**Figure 4E**). This is an anomaly, as the cyclone is expected to weaken while it is over a cold-core eddy region (Chowdhury et al., 2020b) as it encompasses colder waters compared with its surrounding region. An examination of the SST (**Figure 2E**) did not show colder waters in the eddy region; instead, the SST was 30°C. This is because, in the BoB, cold-core eddies are usually subsurface, lying just below the warm and thin surface-mixed layer (Prasanna Kumar et al., 2007). Hence, this warm surface water would have helped in the intensification of Titli from an SCS to a VSCS. During its further northward movement, it crossed over a warm core eddy region; after which, the estimated surface wind speed increased to 140–150 km/h, with gusting to 165 km/h. Again, unlike Luban, cyclone Titli crossed the coast as a VSCS and subsequently weakened. The circulation pattern of the western BoB was impacted by the passage of Titli, which resulted in the intensification and expansion of the cold core eddy region over which it passed through (**Figure 4F**).

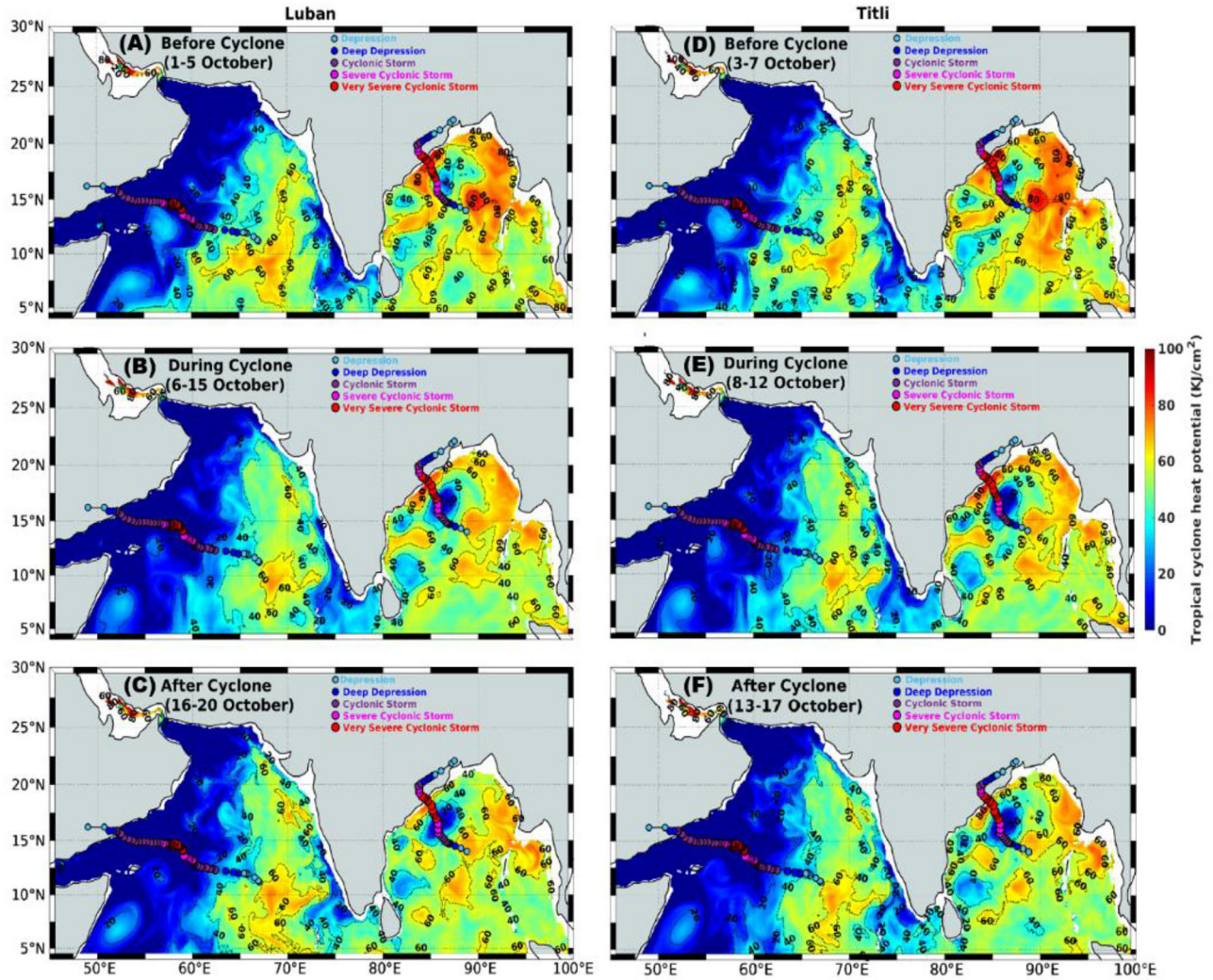

FIGURE 3 | Spatial distribution of the tropical cyclone heat potential (TCHP, kJ/cm^2) before **(A,D)**, during **(B,E)**, and after **(C,F)** cyclones Luban **(A–C)** and Titli **(D–F)**, superposed with cyclone tracks.

Response of Mixed Layer Heat Budget

The dominant response of the upper ocean to both cyclones was the cooling of the sea surface. To understand the roles of different oceanic processes in regulating cyclone-induced upper ocean cooling, the mixed layer heat budget over the box regions (as shown in **Figure 1**) was computed based on methods described in Section Computation of mixed layer heat budget. The temporal evolution of various terms of the mixed layer heat budget, such as temperature tendency, horizontal advection, net heat flux, and vertical entrainment computed in units of °C/day before, during, and after the passage of cyclone Luban and Titli, was presented in **Figure 5**. Note that the residual term denotes any processes other than those listed above. The residual term represents unresolved processes, such as turbulent mixing and diffusion. The maximum cooling for Luban was −0.57°C/day (**Figure 5A**), while that for Titli was −0.44°C/day (**Figure 5B**), which occurred on October 9 for both cyclones but persisted until October 10 in the case of Titli. The cooling was the combined contributions from the horizontal advection, vertical entrainment, and net heat flux at the sea surface where the cyclones intensified from a CS to an SCS/VSCS. Note that the contribution of vertical entrainment was very small for both Luban and Titli during the study period. During the peak cooling, the horizontal advection contributed 0.10 and −1.77°C/day, respectively, for Luban and Titli. In the case of Luban, the net heat flux showed a rapid decrease from the pre-cyclone value of 0.2°C/day to almost zero when the temperature tendency showed the lowest value (highest cooling). This indicated that the rapid decline in the temperature tendency was contributed by horizontal advection and residual. However, after the passage of cyclone Luban, the net heat flux showed a rapid increase in its pre-cyclone value, while the temperature tendency more or less maintained its pre-cyclone value. This indicated that the temperature tendency was controlled by the balance between the

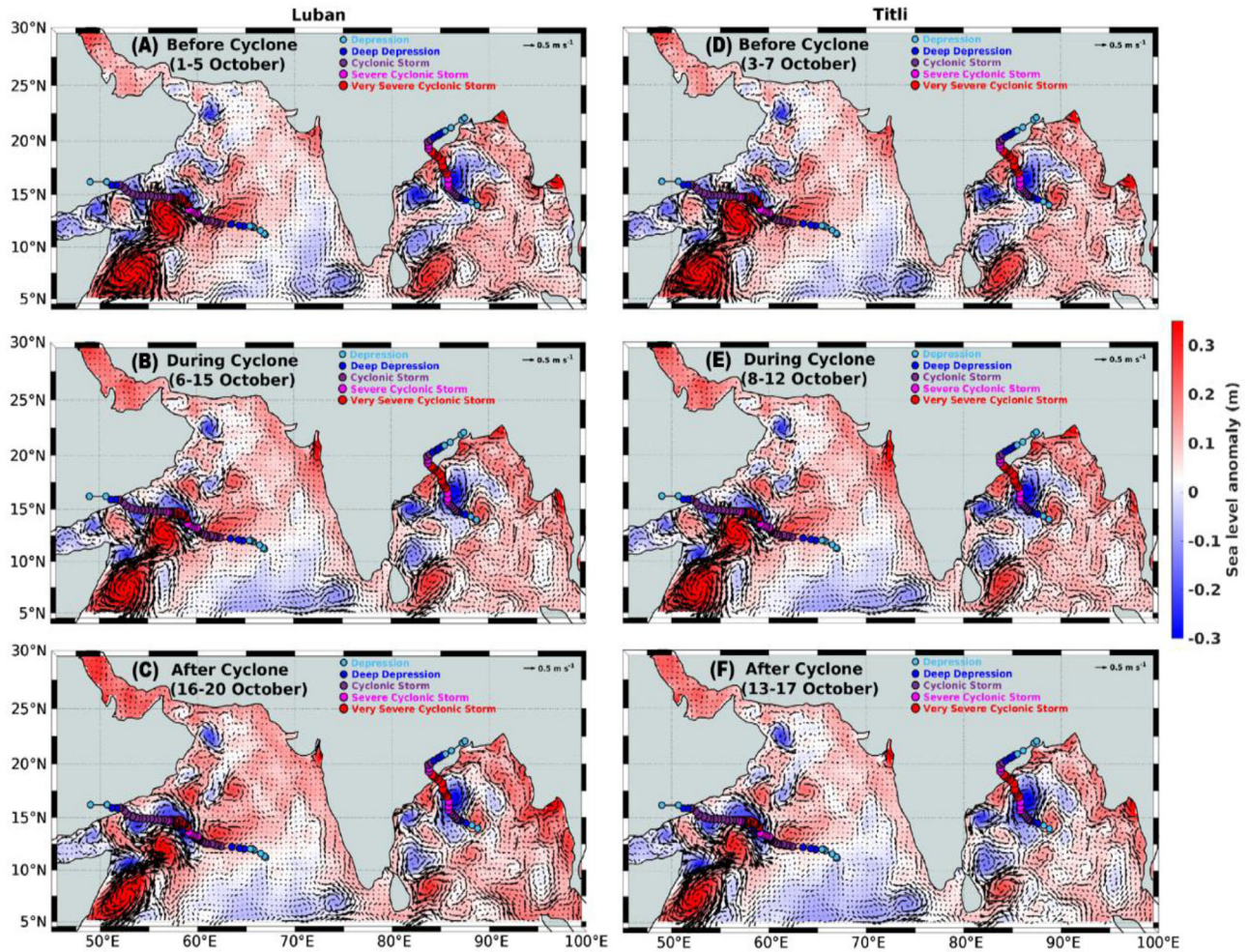

FIGURE 4 | A spatial map of sea level anomaly (m) overlaid with the geostrophic current (m/s) before **(A,D)**, during **(B,E)**, and after **(C,F)** cyclones Luban **(A–C)** and Titli **(D–F)**, superposed with cyclone tracks.

increasing net heat flux and the declining horizontal advection along with the residual.

The time evolution of the response of the mixed layer heat budget under the influence of cyclone Titli (**Figure 5B**) was somewhat different in comparison to Luban. Although the magnitude of the variation of temperature tendency and net heat flux associated with Titli were similar to that of Luban, the horizontal advection and residual showed a much higher magnitude of variation. In fact, during the period of cyclone Titli, horizontal advection and residual showed the highest negative value (∼-2.5°C/day) on October 8/9, when the cyclone was intensifying, while the highest positive value (∼1.5°C/day) was on October 11, when the cyclone was weakening (**Figure 5B**). However, in spite of these large variations in the horizontal advection and residual, the temperature tendency (peak cooling) during Titli was comparable to that of Luban. This implies a large modification to the surface currents under Titli compared with Luban, which is corroborated by a comparison of the geostrophic flow fields before and after the passage of cyclones (**Figures 4D,F**). Note that the pattern of variability of the horizontal advection and residual before and after the passage of cyclone Titli was similar and worked in tandem with net heat flux to maintain the temperature tendency. It is important to state the limitation in the present study in deciphering the possible causes for the high values of the residual term. In the mixed layer heat budget equation (Equation 8), the residual term is the estimation of error that comes along with the horizontal and vertical eddy diffusion. As all the terms of the equation are calculated based on different sets of data, having different horizontal and vertical resolutions, there is a possibility of error accumulation during the interpolation of such heterogeneous data as indicated in Liang et al. (2019), in addition to unresolved ocean dynamic processes. Although we do not have any information on the unresolved processes that contributed to the residual, it is worth mentioning that the cyclone-induced enhanced evaporative cooling and upward Ekman pumping of cold subsurface waters would influence the mixed layer temperature tendencies under a cyclone. After the

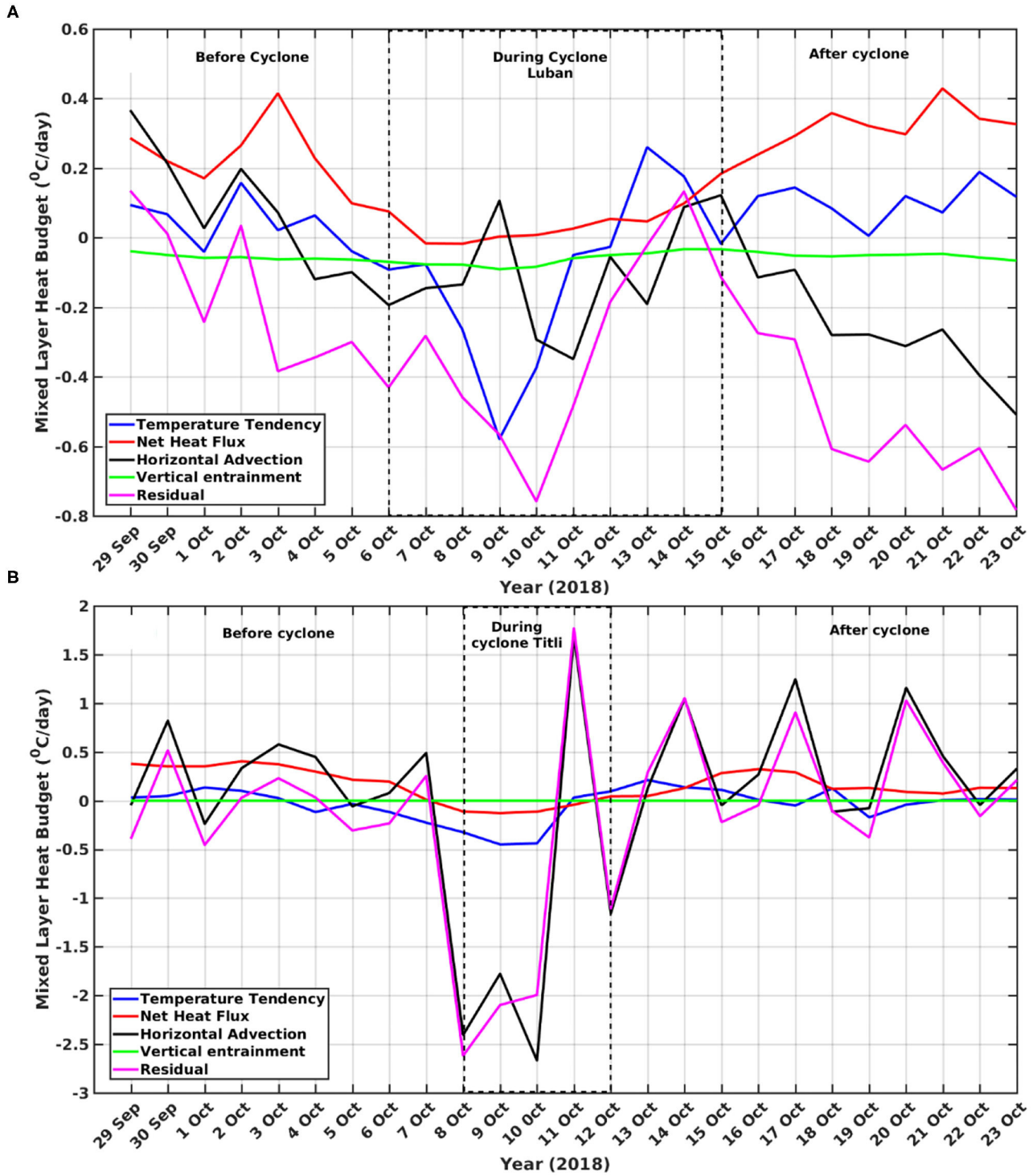

FIGURE 5 | Variation of mixed layer heat budget terms (°C/day) before, during, and after the passage of the Luban **(A)** and Titli **(B)** cyclones. The box with a black broken line over the curve indicates the period of the cyclone.

passage of cyclones, temperature tendencies were dominated by net heat flux, horizontal advection, and the residual terms of the mixed layer.

Response of Water Mass Characteristics

The characteristics of the water masses present in the upper 200 m of the water columns in the AS and the BoB are different.

To understand the upper ocean water mass variability due to the passage of cyclones Luban and Titli, potential temperature vs. salinity was plotted (θ-S diagram) at the location where both the cyclones attain their maximum intensity, following Chowdhury et al. (2020b). The location of the cyclones on October 10 at 12:00 UTC (14.7°N; 51.7°E for Luban and 17.5°N; 85.3°E for Titli; as shown in **Figure 1**) was taken as a center, and a 0.5°latitude × 0.5°longitude box around it was considered for computing the box-averaged potential temperature (θ) and salinity. The HYCOM temperature and salinity profiles up to the 200-m depth of October 5 and 16 were used as before and after the cyclone, respectively, for computing the θ-S diagram for Luban (**Figure 6A**). Similarly, the temperature and salinity profiles of October 7 and 13 were used as before and after the cyclone, respectively, for computing the θ-S diagram for Titli (**Figure 6B**). Two water masses were identified from the θ-S diagram in the AS, such as the Arabian Sea High Salinity Watermass (ASHSW) and the Persian Gulf Water mass (PGW), having sigma-θ values of 22.8–24 and 26.2–26.8 kg/m^3, respectively. Before the formation of cyclone Luban, the θ-S diagram on October 5 (blue line in **Figure 6A**) showed the presence of ASHSW in the upper 20 m with salinity maxima at 10 m, while the PGW was located between 150 and 250 m with a high-salinity core at 200 m (**Figure 6C**). After the passage of cyclone Luban (green line in **Figure 6A**), the ASHSW deepened to a ∼25-m depth, while the PGW deepened to a below 350-m depth (**Figure 6C**). Apart

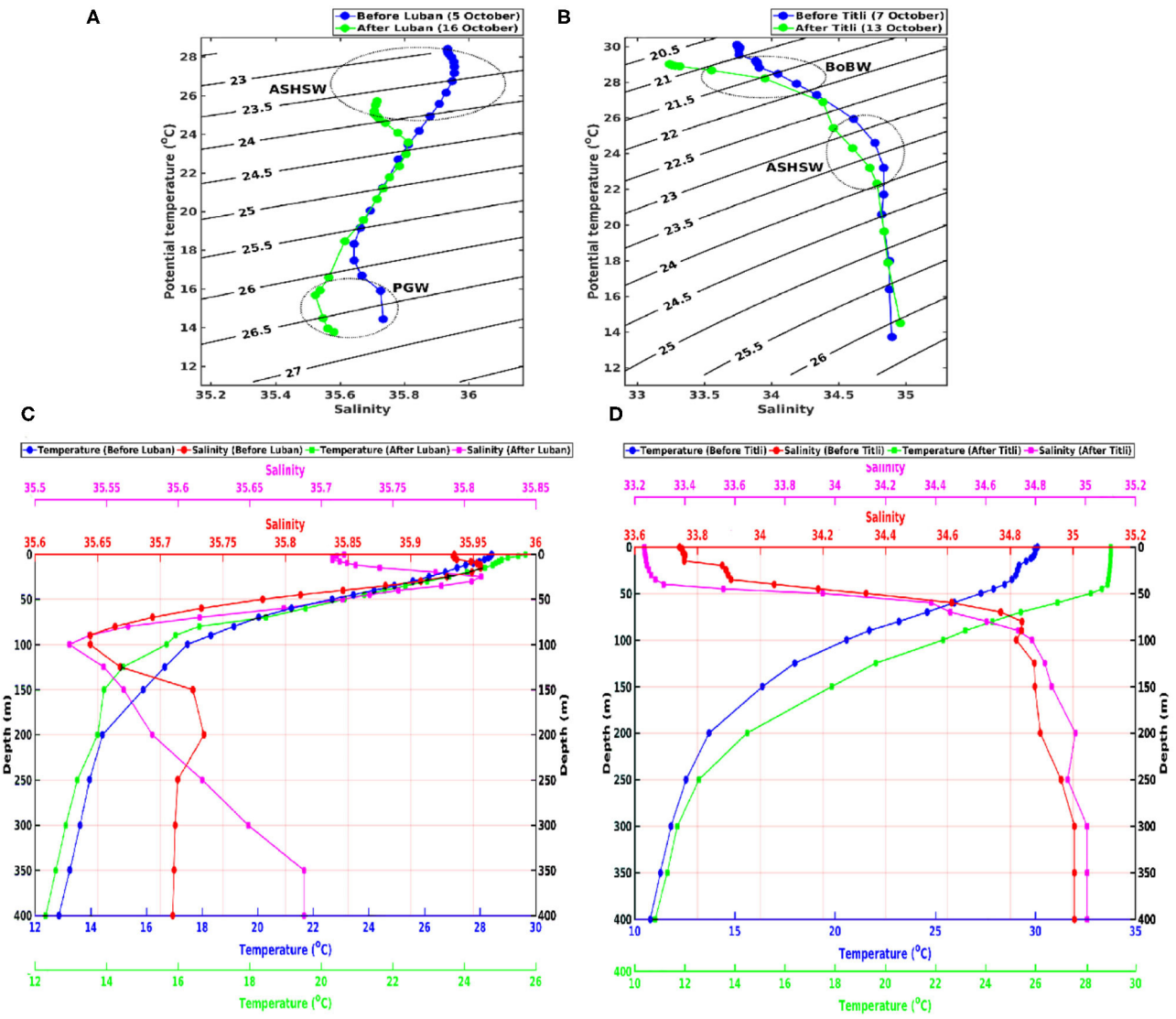

FIGURE 6 | θ-S diagram (0–200 m depth) for Luban (October 5 and 16) **(A)**, Titli (October 7 and 13) **(B)** before (blue line), and after (green line) cyclones. A black solid line indicates the sigma-θ line. ASHSW, Arabian Sea High Salinity Water mass; PGW, Persian Gulf Water mass. The vertical profiles of temperature and salinity (0–400 m) before and after Luban **(C)** and Titli **(D)**. Blue and green lines show the temperature profile, while red and magenta lines show the salinity profiles before and after the cyclones, respectively.

from deepening due to intense mixing, both water masses were subjected to cooling and freshening as could be inferred from the vertical profiles of the temperature and salinity in the upper 400 m (**Figure 6C**). In the case of ASHSW, it was cooled by 2.7°C, and salinity was lowered by 0.22 units. In the case of PGW, it was cooled by 1.8°C, and salinity was lowered by 0.12 units.

In the BoB, two water masses were also identified such as the Bay of Bengal water mass (BoBW) and the ASHSW (**Figure 6B**). Before the cyclone, the Titli, θ-S diagram (blue line) showed the presence of BoBW and ASHSW, having sigma- θ values of 21–23 and 22.8–24 kg/m^3, respectively. Prior to the formation of cyclone Titli, the θ-S curve on October 7 (blue line in **Figure 6B**) showed the presence of low-salinity BoBW in the depth range of 20–30 m, while the ASHSW was located in the depth range of 70–80 m (**Figure 6D**). After the passage of cyclone Titli, the BoBW deepened and occupied the depth range of 20–40 m, and the ASHSW was deepened to a 100-m depth. The entrainment and mixing in the case of Titli (**Figure 6B**) were much less intense compared with Luban (**Figure 6A**) as could be inferred from the shift of the θ-S curves before (blue) and after (green) the cyclones. Under the entrainment and mixing, the BoBW cooled by 1.09°C, and the salinity was decreased by 0.51 units (**Figure 6D**).

Cyclone-Induced Biological Response

Having examined the physical and dynamic responses of the upper ocean due to the passage of cyclones Luban and Titli, we now analyze the biogeochemical response in this section. To understand the biological response, the 3-day composites of the Chl-*a* and NPP before, during, and after cyclone were analyzed within the boxes (as shown in **Figure 1**). While plotting the 3-day composite figures, the average values of Chl-*a* and NPP were assigned to the day between the beginning and the end when the 3-day composite was calculated. For example, the 3-day averaged values computed for Chl-*a* and NPP during the period from September 29 to October 1 were assigned to September 30 in the plot.

The average Chl-*a* before the origin of cyclone Luban was 0.61 ± 0.11 mg/m^3, and it increased to a maximum value of 1.22 ± 0.11 mg/m^3, which occurred in the 3-day composite period between October 17 and 19 after the passage of the cyclone

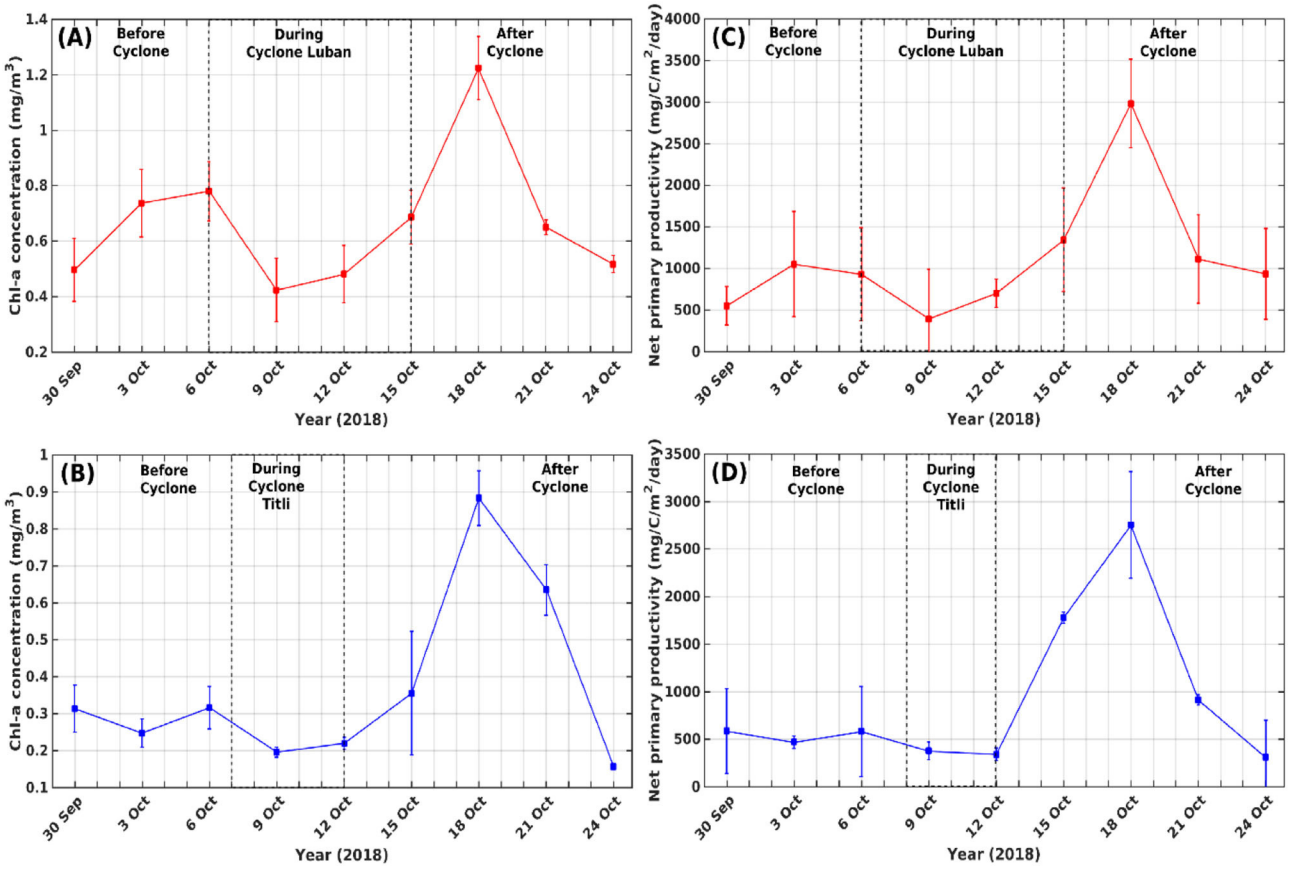

FIGURE 7 | Box-averaged 3-day mean chlorophyll *a* (Chl-*a*) concentration (mg/m^3) and net primary productivity (mg/C/m^2/day) before, during, and after the passage of cyclone Luban **(A,C)** and cyclone Titli **(B,D)** from September 29 to October 25, 2018. The box with a black broken line over the curve indicates the period of the cyclone.

(**Figure 7A**). Note that the initial decline in Chl-*a* concentration during the cyclone must be due to the thick cloud cover that cuts off the visible radiation from the ocean. A similar situation was reported by Byju and Prasanna Kumar (2011) in the case of cyclone Phyan in the AS, and they showed that the initial decline in Chl-*a* was due to a decrease in the number of data pixels in the study region due to cloud cover associated with the cyclone. Once the cyclone moves out of the study region, the sky clears off, and the pixel count increases and captures well the variability in Chl-*a*. Note also that the peak Chl-*a*, which was 2-fold higher than the pre-cyclone value, occurred 3 days after the dissipation of the cyclone. Within a week after the passage of cyclone, the enhancement of Chl-*a* declines and attains its pre-cyclone values. The Chl-*a* response of the BoB to cyclone Titli (**Figure 7B**) was similar to that of the AS to cyclone Luban, except for the magnitude. The average Chl-*a* before cyclone Titli was 0.29 ± 0.05 mg/m^3, which showed a 3-fold increase after the passage of a cyclone. Similarly, during the initial phase of Titli, the Chl-*a* showed a decline, and it peaked at 0.88 ± 0.07 mg/m^3 after 5 days of its dissipation.

The time variation of NPP under the influence of both cyclones (**Figures 7C,D**) showed a pattern that was very similar to that of the Chl-*a* variation. Before the passage of cyclone Luban, the average value of NPP was 799.77 ± 431.58 mg C/m^2/day (**Figure 7C**). Consistent with the Chl-*a*, the value of NPP showed a small decline during the initial period of the cyclone and then increased to a maximum value of 2,980.90 mg C/m^2/day after the passage of the cyclone. The NPP enhancement after the cyclone Luban was 3.7-times its pre-cyclone value. Unlike Luban, the NPP did not show much variation before the cyclone Titli (**Figure 7D**). The average NPP value before Luban was 544.94 ± 327.93 mg C m^2/day, and it showed a small decline during the period of the cyclone. The maximum value of $2{,}752.00 \pm 560.66$ mg C m^2/day occurred in the 3-day composite period between October 17 and 19 after the passage of the cyclone. The NPP enhancement after the cyclone Titli was five times its pre-cyclone value. A pertinent question would be why there is a lag between the passage of a cyclone and the peaking of Chl-*a* and NPP. This is the biological response time for the photosynthesis to start (NPP) and, eventually, to build up the chlorophyll biomass (Chl-*a*). This can be understood in the following manner. The anti-clockwise winds associated with the cyclone will create a divergence of the surface water and initiate upward Ekman pumping (Subrahmanyam et al., 2002; Lin et al., 2003). This will bring subsurface nutrient-rich colder waters to the surface. Although there is a build-up of surface nutrient concentration, the phytoplankton present in the water column is unable to carry out photosynthesis due to the light limitation because of cloud cover. Once the cyclone moves away from the region, the sky is cleared of clouds, allowing the sunlight to reach the upper ocean, which will kick-start the biological production through photosynthesis. Hence, there is always a lag between the cyclone-induced nutrient supply to the oligotrophic upper ocean and its response by way of the enhancement of Chl-*a* and NPP (Byju and Prasanna Kumar, 2011; Chowdhury et al., 2020a,b).

Thus, there was a striking similarity between the time evolution of Chl-*a* and NPP in response to cyclones in both the AS and the BoB. Although the pattern of variability was similar, the magnitudes of both were higher in the AS than in the BoB. The pre-cyclone Chl-*a* concentration in the AS was three times higher than that in the BoB, while NPP was 1.5 times higher than that in the BoB. However, the maximum NPP did not show much difference between the AS and the BoB, although the maximum enhancement of Chl-*a* in the AS was 1.4 times higher than that in the BoB. The AS is also known for its high values of Chl-*a* and NPP compared with the BoB, which is linked to the differences in the regional oceanographic processes between the AS and the BoB (Prasanna Kumar et al., 2009b). With October being the period of secondary heating, the thermal stratification is high in both the AS and the BoB (Prasanna Kumar and Narvekar, 2005; Narvekar and Prasanna Kumar, 2006). In addition, in the BoB, the freshwater flux due to the precipitation and river runoff peaks in October leads to the strongest haline stratification (Narvekar and Prasanna Kumar, 2014). Strong upper ocean stratification in the BoB in comparison to the AS curtails the vertical mixing due to wind, thereby limiting the availability of nutrients in the upper ocean. This is the reason for the lower pre-cyclone Chl-*a* and NPP in the BoB compared with the AS. However, being a category-2 cyclone, Titli could potentially initiate stronger vertical transport of cold and nutrient-rich waters to the upper ocean compared with the category-1 Luban. The 5-fold increase of NPP by Titli in comparison to the 3.7-fold increase by Luban lends support to this.

Response of CO_2 Flux

The air-sea CO_2 flux at the sea surface has an impact on the storage of anthropogenic CO_2 in the ocean (Takahashi et al., 2009). Air-sea CO_2 flux depends on the difference between the partial pressure of CO_2 at the surface and in the atmosphere, wind speed, SST, and sea surface salinity (Wanninkhof, 1992). Wind speed plays the most important role in the variability of CO_2 flux due to the quadratic functional dependence of gas transfer velocity and wind speed. Studies have suggested that strong winds associated with tropical cyclones increase the CO_2 flux from the ocean to the atmosphere (Bates et al., 1998; Bates and Peters, 2007; Nemoto et al., 2009). To understand the changes in the CO_2 flux from the ocean to the atmosphere under the influence of Luban and Titli, we have analyzed the cyclone-induced CO_2 flux in the box region (see **Figure 1**). Before cyclone Luban, the average CO_2 flux value was 0.65 ± 0.11 mmol/m^2/day (**Figure 8A**). During the cyclone, the values showed a rapid increase, and the maximum value of 6.41 ± 1.01 mmol/m^2/day was on October 9, which was almost approximately a 10-fold increase compared with the pre-cyclone value. Note that the intensification of Luban to an SCS occurred on October 9, when the box-averaged CO_2 flux showed a maximum value. However, the CO_2 flux value on October 10 was only marginally low, which was when Luban further intensified to become a VSCS. The upward Ekman pumping velocity (EKV) (not shown) was maximum on October 9, and the value was 0.55 m/day. During a cyclone, an upward EKV brings subsurface waters with high CO_2 to the surface and causes CO_2 efflux or/outgassing. Positive values of CO_2 flux indicate the release of CO_2 from the ocean to the atmosphere. The value of CO_2 flux on October 10 during

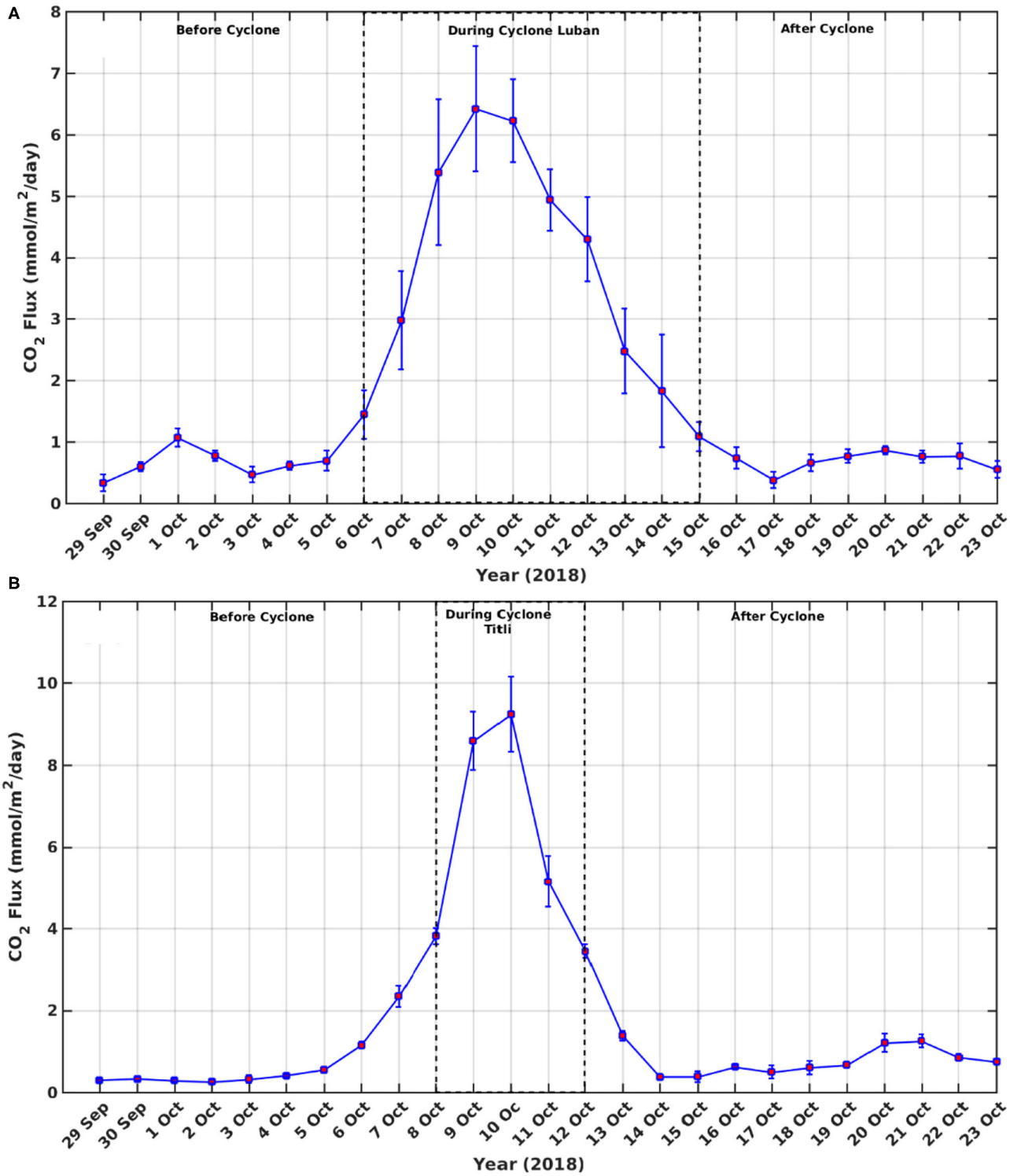

FIGURE 8 | Box-averaged daily CO_2 flux (mmol/m^2/day) over the box region before, during, and after the passage of cyclones Luban **(A)** and Titli **(B)** from September 29 to October 23, 2018. The box with a black broken line over the curve indicates the period of the cyclone.

cyclone Luban was 6.22 ± 0.67 mmol/m^2/day (**Figure 8A**). As the cyclone started reducing its intensity after October 10, the CO_2 flux values also showed a rapid decline and attained the pre-cyclone values after the passage of the cyclone. In the case of Titli, the CO_2 flux before the cyclone was 0.76 ± 0.08 mmol/m^2/day (**Figure 8B**). During the cyclone, the maximum

CO_2 flux was observed on October 10, and the value was 9.23 ± 0.91 mmol/m^2/day. Recall that Titli attained its maximum intensity as a VSCS on October 10. The upward EKV (not shown) was maximum on the October 10, and the value was 0.8 m/day. Like cyclone Luban, the CO_2 flux values showed a rapid decline after the passage of Titli from the box region. The maximum CO_2 flux associated with Titli was a 12-fold increase compared with its pre-cyclone value.

Atmospheric Conditions Before, During, and After Cyclone

Having deciphered the physical and biogeochemical response of the upper ocean to the passage of cyclones Luban and Titli, in this section, the atmospheric variables related to cyclone genesis and intensification, namely, low-level wind convergence, low-level relative vorticity, vertical wind shear, and mid-tropospheric relative humidity, were examined. It is well-known that, for the generation of a tropical cyclone, the necessary conditions of the above variables are strong low-level wind convergence, high-relative vorticity, weak vertical wind shear, and high-relative humidity (Evan and Camargo, 2011). Strong low-level wind convergence is associated with strong convection, and OLR is a proxy for convection. Hence, the spatial maps of OLR (**Figure 9**), the relative vorticity at 850 hPa (**Supplementary Figure 1**), the vertical wind shear between 850 and 200 hPa (**Figure 10**), and the relative humidity at 500 hPa (**Figure 11**) were prepared and presented below.

The OLR, in general, showed low values in the southern part of the study region and increased toward the north (**Figure 9**). Prior to the formation of both cyclones, the OLR values were low and close to 200 and 220 W/m^2 in the region of origin of Luban (**Figure 9A**) and Titli (**Figure 9D**), respectively. The large-scale easterly and northeasterly winds showed convergence in the region of origin of Luban and Titli (**Figures 9A,D**). The low OLR along with wind convergence indicated strong convection, a condition that is favorable for the formation of cyclones. The spatial distribution of relative vorticity showed high positive values in the region of origin of Luban (**Supplementary Figure 1A**) and Titli (**Supplementary Figure 1D**), while the vertical wind shear was the least, 5 m/s, at the origins of Luban (**Figure 10A**) and Titli (**Figure 10D**) prior to the formation of both the cyclones. The mid-tropospheric relative humidity, on the other hand, was high with values of 80 and 70%, respectively, in the region of Luban (**Figure 11A**) and Titli (**Figure 11D**). Thus, the atmospheric condition by way of the low OLR, high-positive-relative vorticity, low-vertical wind shear, and high-relative humidity set the stage for the formation of cyclones Luban and Titli.

During both the cyclones, the OLR along the track and in its vicinity was low with strong cyclonic circulation (**Figures 9B,E**), while the wind shear increased to ∼15 m/s (**Figures 10B,E**). The vorticity showed a general increase along the track for both Luban (**Supplementary Figure 1B**) and Titli (**Supplementary Figure 1E**). The relative humidity, however, decreased to 40–50% in the case of Luban (**Figure 11B**) and 50–70% for Titli (**Figure 11D**). After the passage of the cyclones, the values of all the atmospheric parameters showed a recovery toward the pre-cyclone values.

POTENTIAL MECHANISM FOR THE SIMULTANEOUS GENERATION OF CYCLONES

The formation of tropical cyclones requires a large amount of thermal energy to be available in the upper ocean in the form of TCHP. However, the mere availability of TCHP alone will not lead to the formation of a cyclone. Cyclogenesis would need the pre-conditioning of several ocean-atmospheric parameters, as indicated in the previous section, followed by a triggering mechanism. To gain insight into the ocean-atmospheric dynamics that lead to the simultaneous formation of cyclones Luban in the AS and Titli in the BoB, we examined the interannual and intraseasonal variability that could potentially suggest such mechanism/s.

Role of Climate Modes

Climate modes, such as the Pacific decadal oscillation (PDO), El Niño Southern Oscillation (ENSO), and IOD, influence the tropical Indian ocean on an interannual time scale. Recently, Girishkumar and Ravichandran (2012) and Sreenivas et al. (2012) studied the role of ENSO in the formation of tropical cyclones in the BoB during the October–December period. To understand how the above modes influence the AS and the BoB, the indices associated with these modes was analyzed from 1979 to 2020 and presented in **Supplementary Figure 2**. The indices are the Pacific decadal oscillation index for PDO (**Supplementary Figure 2A**), Nino-3.4 index for ENSO (**Supplementary Figure 2B**), and dipole mode index for IOD (**Supplementary Figure 2C**). The year 2018 showed the presence of moderate El Niño and positive IOD, while the PDO was in the cold phase. The co-occurrence of El Niño and positive IOD in 2018 (**Supplementary Figures 2B,C**) made the waters of the eastern Indian Ocean colder than normal, along with the prevalence of the descending branch of Walker circulation (Walker and Bliss, 1932), while the waters of the western Indian Ocean become warmer than normal, along with the prevalence of the ascending branch of Walker circulation (as shown in Chowdhury et al., 2020a). This would make the AS and part of the BoB warmer than normal. The negative values of the PDO index (**Supplementary Figure 2A**), which indicated that 2018 was in the cold phase, were associated with warm SST anomalies in the north, west, and southern Pacific (Mantua et al., 1997; Mantua and Hare, 2002). Thus, all three climate modes in 2018 were congenial for creating warmer than the normal upper ocean. The SST anomaly for the year 2018 clearly showed a warm anomaly of 0.5°C in the region where cyclones Luban and Titli originated (**Supplementary Figure 3**), which corroborates the fact that all the three climate modes acted in tandem to make 2018 a warmer than normal year. Although a warm SST is one of the necessary conditions for cyclogenesis, other conditions also need to be met. So, next, we examined the intraseasonal variability to see what

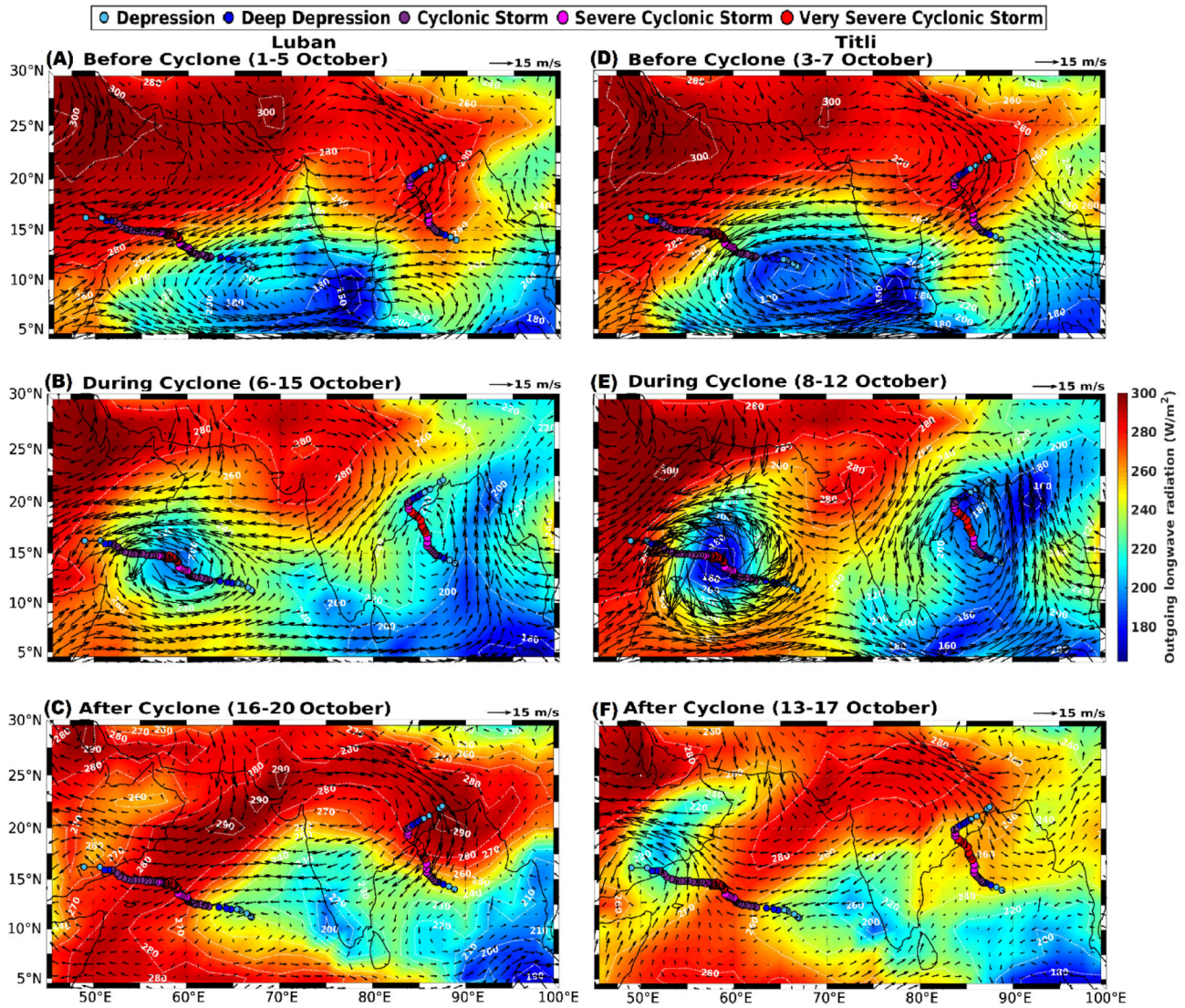

FIGURE 9 | A spatial map of outgoing longwave radiation (W/m^2), overlaid with 850 hPa wind (m/s) before **(A,D)**, during **(B,E)**, and after **(C,F)** cyclones Luban **(A–C)** and Titli **(D–F)**. The color-filled circles denote the cyclone tracks.

was unique in 2018 that would have supported the generation of cyclones simultaneously.

Role of Intraseasonal Variability

We examined two types of intraseasonal variability associated with the atmospheric phenomena, such as the mixed Rossby-gravity wave and the MJO, and the oceanic Rossby wave.

Mixed Rossby-Gravity Wave

Mixed Rossby-gravity waves (Hayashi, 1974; Hayashi and Golder, 1978) are equatorially trapped planetary waves that form an integral part of the tropical atmospheric circulation (Matsuno, 1966). They are generated in the troposphere, having a wavelength of 9,000 km and a period of 4–5 days, and form an integral part of the tropical atmospheric circulation (Matsuno, 1966). These waves originate from the lower troposphere and propagate vertically. The energy propagation of Mixed Rossby-gravity (MRG) waves is in an eastward and downward direction, while their phase propagation is westward and upward. The asymmetric warming pattern on either side of the equator during October, associated with the period of secondary heating (Prasanna Kumar and Narvekar, 2005), triggers an MRG wave-type disturbance. To assess the presence of such a disturbance, the time-longitude Hovmöller diagram using a high-frequency (2–10 days) bandpass filtered meridional wind component at the lower (850 hPa) and upper (200 hPa) troposphere was prepared and is presented in **Figure 12**. The Hovmöller diagram of the meridional wind at 850 hPa revealed the presence of the westward propagation of high positive values of the meridional wind at the lower troposphere, starting from September 1 in

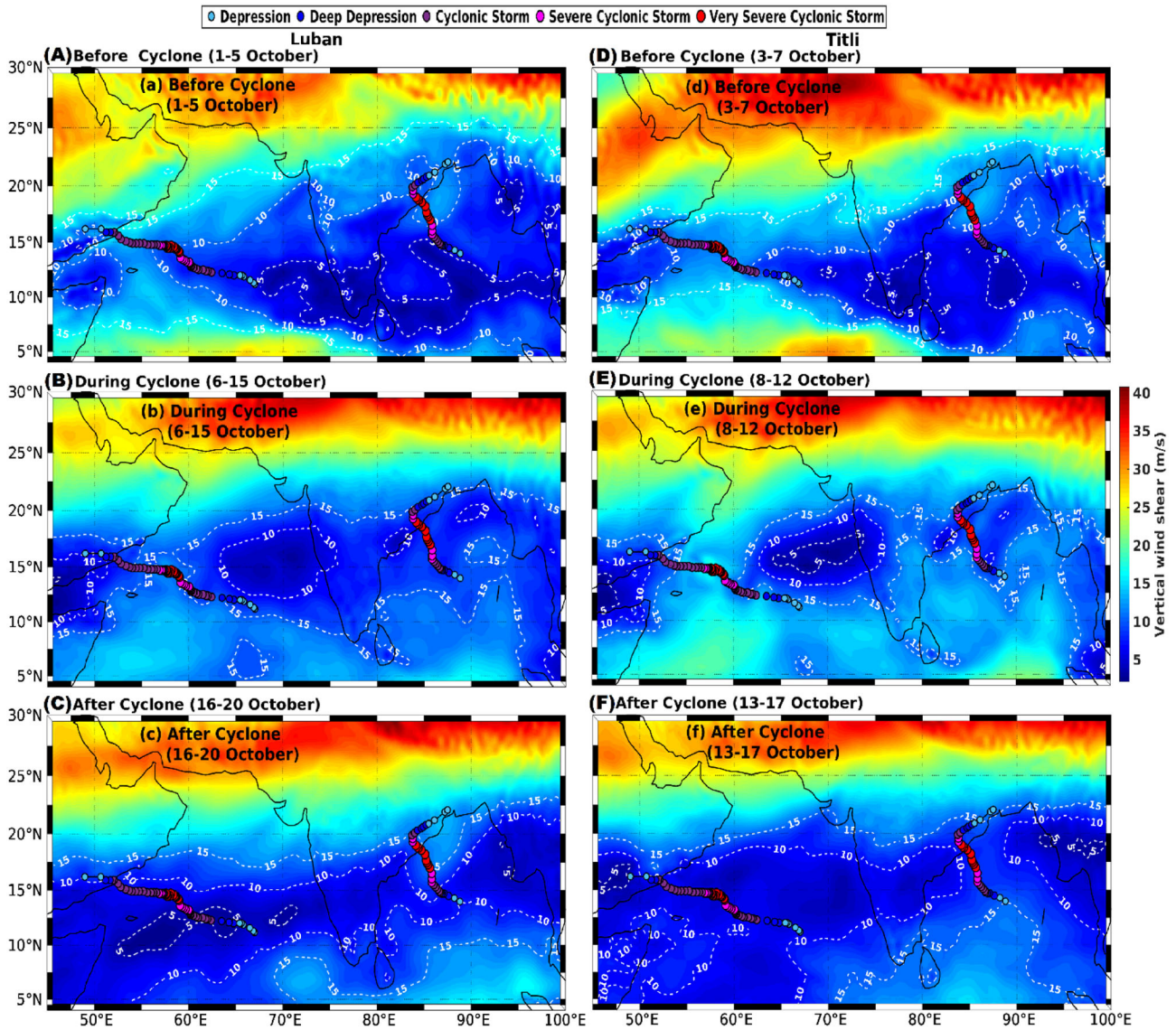

FIGURE 10 | A spatial map of vertical wind shear (difference between 200 and 850 hPa) (m/s) before **(A,D)**, during **(B,E)**, and after **(C,F)** cyclones Luban **(A–C)** and Titli **(D–F)**. The color-filled circles denote the track of the cyclone.

the eastern Indian Ocean and reaching the site of origin of Luban by October 6, the day when the depression was formed (**Figure 12A**). A similar eastward propagation feature could be noticed in the Hovmöller diagram of the meridional wind at 200 hPa (**Figure 12B**). This was the signature of the MRG wave. However, no such prominent propagation feature was noticed in the vicinity of the site of origin of Titli.

To further ascertain the presence of the MRG wave, we have carried out the continuous wavelet transform analysis using the 6-h meridional wind data of the lower and upper troposphere in the vicinity of Luban (**Figures 12C,D**) and Titli (**Figures 12E,F**) by taking a 1-degree-longitude by a 1-degree-latitude box with the origin of the cyclone as the center. The wavelet power spectrum analysis in the region of origin of cyclone Luban confirmed the presence of a 5- to 8-day periodicity in the lower (**Figure 12C**) and upper (**Figure 12D**) troposphere. The 5- to 8-day periodicity noticed in the meridional wind at the lower and upper troposphere was significant at the 95% confidence level; however, no such periodicity was noticed in the case of Titli (**Figures 12E,F**). Thus, the wavelet analysis confirms the presence of MRG waves of 5- to 8-day periodicity in the vicinity of Luban during the period of the cyclone. The MRG waves originate at the lower troposphere and are forced to propagate vertically, and the associated surface convection is responsible for ascending moisture to the middle troposphere. The mid-tropospheric-relative humidity makes the layer convectively unstable, leading to the formation of deep convection, which is conducive for the initiation of MJO and propagation (Muraleedharan et al., 2015). To determine the presence of MJO, we have analyzed the MJO phase space diagram.

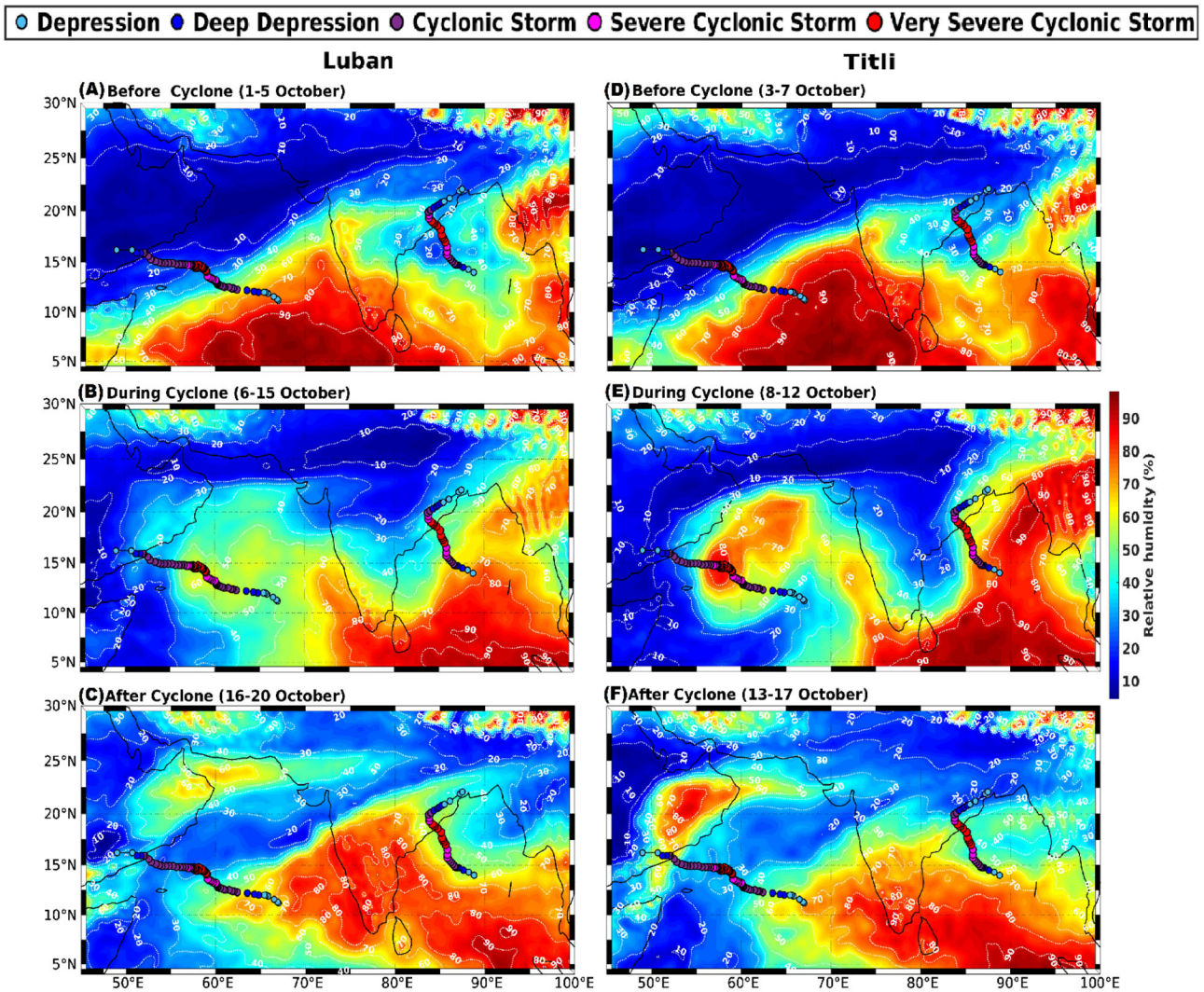

FIGURE 11 | A spatial map of mid-tropospheric (500 hPa) relative humidity (%) before **(A,D)**, during **(B,E)**, and after **(C,F)** cyclones Luban **(A–C)** and Titli **(D–F)**. The color-filled circles denote the cyclone.

Madden–Julian Oscillation

The MJO is a dominant mode of atmospheric variability in the tropical region in the intraseasonal time scale, which has a periodicity of 30–90 days (Madden and Julian, 1971). The MJO propagates eastward in boreal winter and northward in boreal summer (Zhang, 2005). Camargo et al. (2009) showed that MJO plays an important role in the genesis of cyclones in the Indian Ocean. To determine the role of MJO in initiating the cyclone, we have calculated the real-time multivariate MJO principal component time series 1 and 2 (RMM1 and RMM2) using the first two empirical orthogonal functions of equatorially averaged OLR and lower-level (850 hPa, and upper-level (200 hPa) wind data. See Wheeler and Hendon (2004) for computation details.

Prior to the formation of cyclone Luban, MJO was in active Phase 1 (**Figure 13A**). On October 6, cyclone Luban originates in the AS when MJO was in Phase 1, and it started to move toward the Indian Ocean region. The dissipation of cyclone Luban occurred on October 15, when MJO was in Phase 3 and activity was strong. Similarly, cyclone Titli was formed in the active MJO phase. The genesis and dissipation of cyclone Titli were formed in Phase 2. To understand MJO propagation, we have analyzed the time-longitude section of the 30- to 90-day bandpass-filtered OLR (**Figure 13B**) and the zonal wind at 850 hPa averaged over 10°S to 10°N (**Figure 13C**). The blue region in OLR having negative values (**Figure 13B**) showed the enhanced convection, whereas the positive value in the red region indicated the suppressed convection. The zonal wind with positive values with the red color (**Figure 13C**) indicated the westerly wind, and the blue color having negative values indicated the easterly wind. The eastward propagation of MJO is seen from the time-longitude plots of zonal wind. The OLR showed the presence of enhanced convection on October 6, while zonal wind showed the

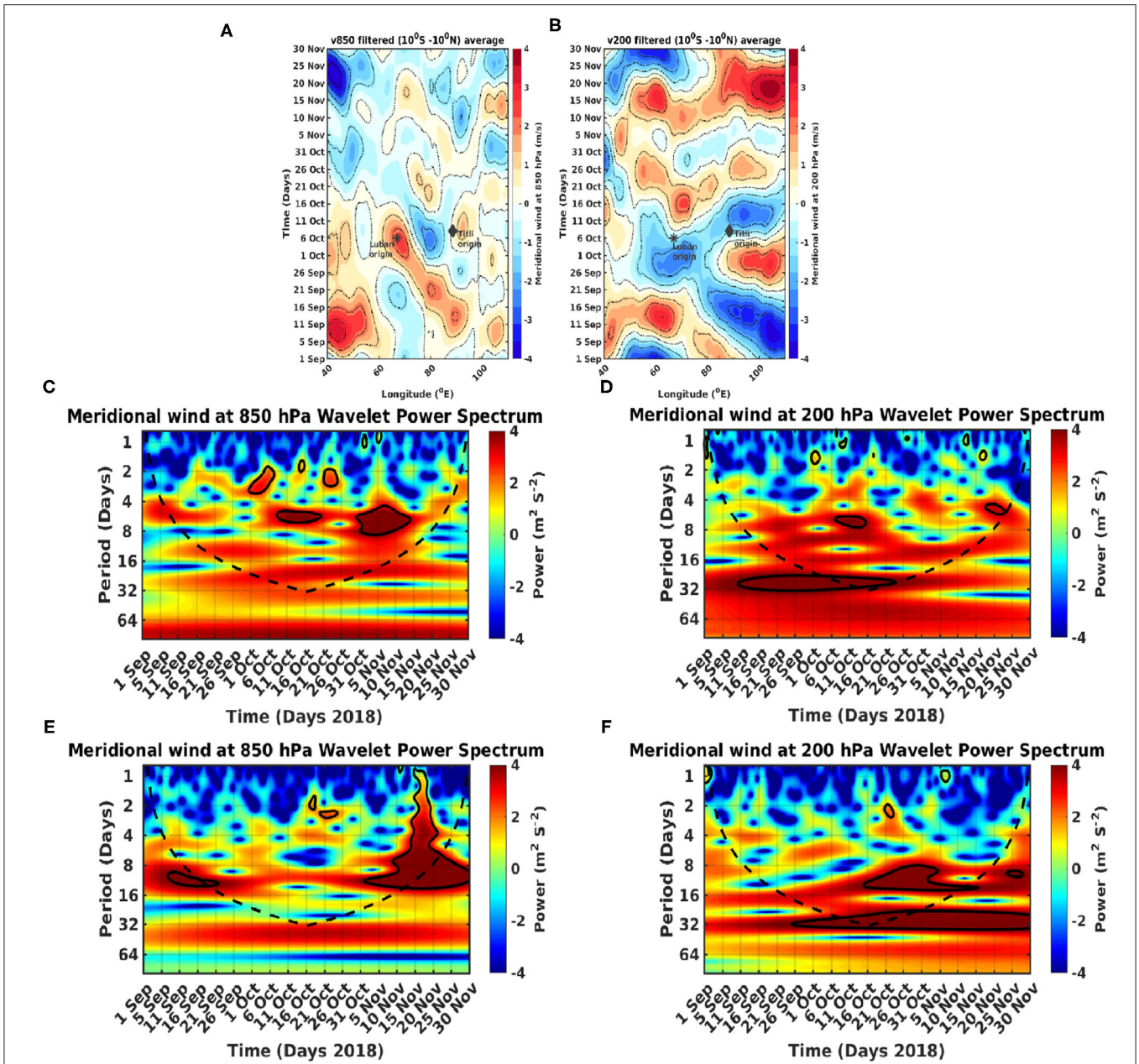

FIGURE 12 | A time-longitude Hovmöller diagram of filtered meridional wind (m/s) at 850 hPa **(A)** and 200 hPa **(B)** averaged over 10°S to 10°N from September 1 to November 30, 2018. Black asterisk and diamond symbols show the origin of cyclones Luban and Titli, respectively. Wavelet power spectrum analysis of meridional wind (m^2 s^{-2}) at 850 hPa **(C,E)** and 200 hPa **(D,F)** at the origin of cyclones Luban and Titli from September 1 to November 30, 2018. The black broken line represents the cone of influence, and, beyond that line, wavelet power can be distorted (less reliable). The black solid contoured regions show the power, which is 95% significant.

presence of an active phase of MJO at the location of Luban. After the formation of Luban, the convection associated with MJO moved eastward. The MJO associated with easterly wind and enhanced convection reached the BoB on October 8. The enhanced convection associated with anomalous easterlies was conducive for the formation of the second cyclone, Titli.

It is, thus, amply clear that, while PDO, ENSO, and IOD pre-conditioned the upper waters in the vicinity of the origin of Luban and Titli by providing excess heat, the atmospheric MRG waves along with MJO provided the trigger for the initiation of Luban. To understand what could be the trigger for Titli, we analyzed the oceanic Rossby waves as a potential remote force.

Oceanic Rossby Wave

The oceanic Rossby wave excited by the coastally trapped Kelvin wave plays an important role in the dynamics and circulation in

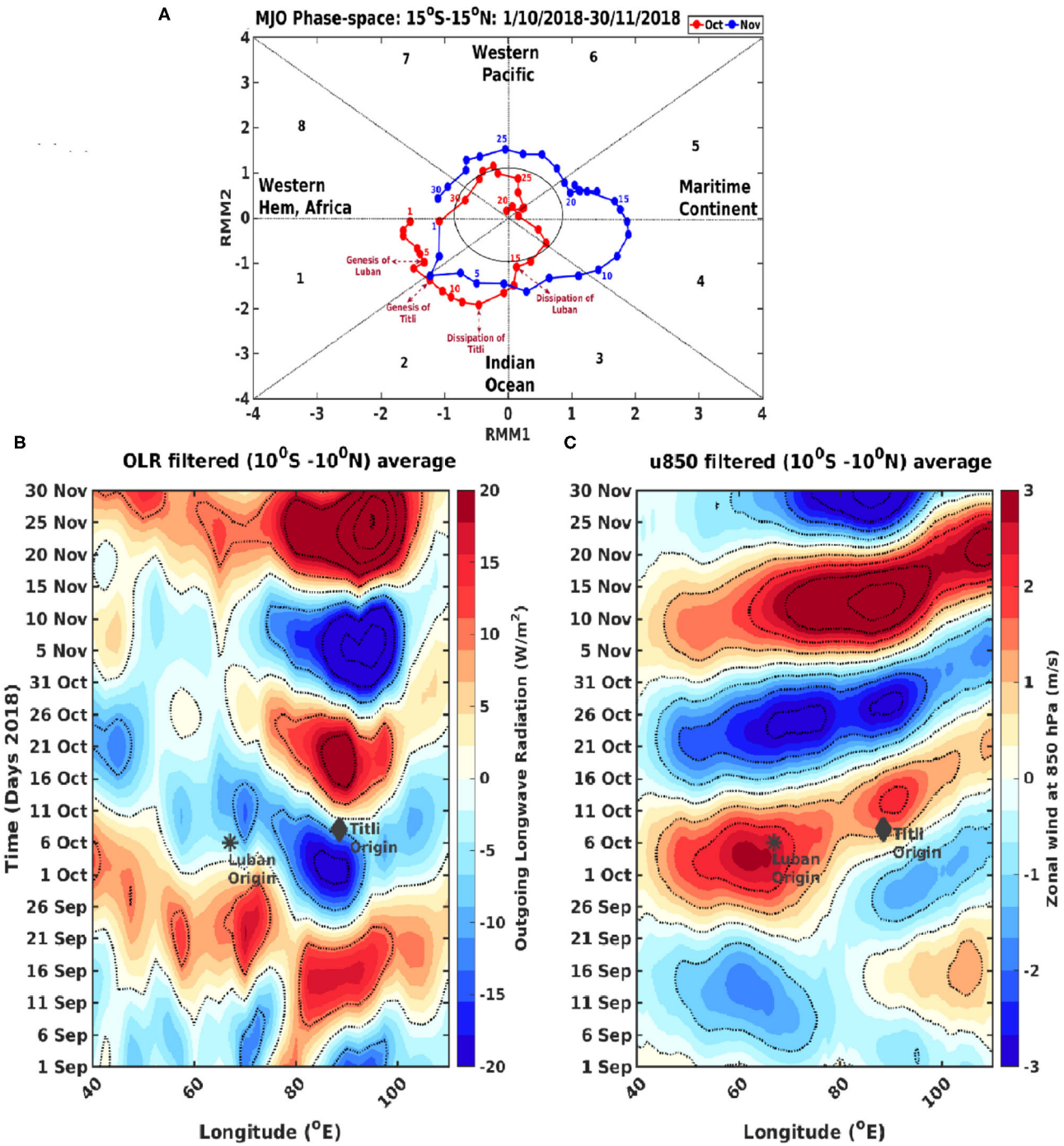

FIGURE 13 | (A) A phase diagram of the Madden-Julian oscillation (MJO) from September 1 to November 30, 2018. The red and blue colors denote the propagation in October and November, respectively. MJO activity is weak (strong) when the index is within (outside) the circle, **(B)** a time-longitude Hovmöller diagram of 30- to 90-day band-pass-filtered outgoing longwave radiation (W/m^2), and **(C)** zonal wind (m/s) at 850 hPa **(C)**, averaged over 10°S to 10°N from September 1 to November 30, 2018. Black asterisk and diamond symbols show the origin of cyclones Luban and Titli, respectively.

the BoB (Potemra et al., 1991; Yu et al., 1991). It also modulates the upper ocean through thermocline variations. Recall that the TCHP in the BoB, especially in the region of the formation of Titli, was 20 kJ/cm^2 higher than that in the AS prior to the formation of the cyclone. We examined the role of the Rossby wave in altering the TCHP in the BoB by analyzing

the time-longitude Hovmöller plots of SLA, D_{26}, and TCHP along 14°N by averaging values between the 13.5 and 14.5°N (**Figure 14**). The Hovmöller plot of SLA (**Figure 14A**) showed the westward propagation of a high positive SLA in the vicinity of the origin of Titli, which was the signature of a downwelling Rossby wave. The downwelling Rossby wave reached the location of the origin of Titli in the first week of October. Consistent with this, the Hovmöller plot of D_{26} showed the deepening of the ocean surface layer up to the 80-m SLA (**Figure 14B**), while the Hovmöller plot of TCHP enhanced to 60 kJ/cm^2 (**Figure 14C**). Thus, the downwelling Rossby wave leads to an enhancement of TCHP in the location of the origin of Titli in the first week of October by deepening the thermocline.

SUMMARY AND CONCLUSION

The simultaneous occurrence of cyclones over the AS and the BoB in the NIO is an unusual phenomenon that happened in October 2018 for the first time since the reliable record became available in 1960. The physical and biogeochemical responses due to the passage of category-1 cyclone Luban (6–15 October) in the AS and category-2 cyclone Titli (8–12 October) in the BoB have been analyzed using various ocean and atmosphere datasets. The higher TCHP in the BoB compared with the AS was one of the reasons why Titli was more intense than Luban. Another reason was that, while moving westward/northwestward, Luban encountered regions with waters colder by 2°C and TCHP lower by 20 kJ/cm^2 in comparison to Titli. This is because the western AS was colder due to the upwelling along the western boundary, while no such upwelling occurs in the BoB. In response to the passage of Luban, the surface water showed a maximum cooling of 2°C, while that by Titli was 3°C. The contrast in the cyclone-induced changes was more pronounced in the biogeochemical parameters. The Chl-*a* and NPP enhancements by Luban were 2 and 3.7-fold, respectively, compared with the pre-cyclone values, while that by Titli were 3 and 5-fold, respectively. Although there were strong similarities between the time evolution of Chl-*a* and NPP in the AS and the BoB, their values were higher in the AS compared with the BoB. This is because the upper ocean stratification in the BoB was stronger compared with that in the AS. Similar to the biological parameters, the CO_2 flux under Luban showed a 10-fold increase in comparison to the pre-cyclone value, while that under Titli was 12-fold. Based on the data analysis, it was found that the cyclone in the BoB had more influence on the enhancement of phytoplankton biomass and primary production compared with the AS. However, unlike the Chl-*a* and NPP, the magnitude of CO_2 outgassing in the BoB was higher than that in the AS. This is because of the warmer SST in the BoB and the stronger wind speed associated with Titli, both of which control the magnitude of the CO_2 outgassing.

The most intriguing question is: What triggered the simultaneous occurrence of Luban and Titli? Being an energy-intensive process, the genesis of cyclones requires a large amount of thermal energy close to the upper ocean with a high SST. The year 2018 was an unusual year when both El Niño and IOD

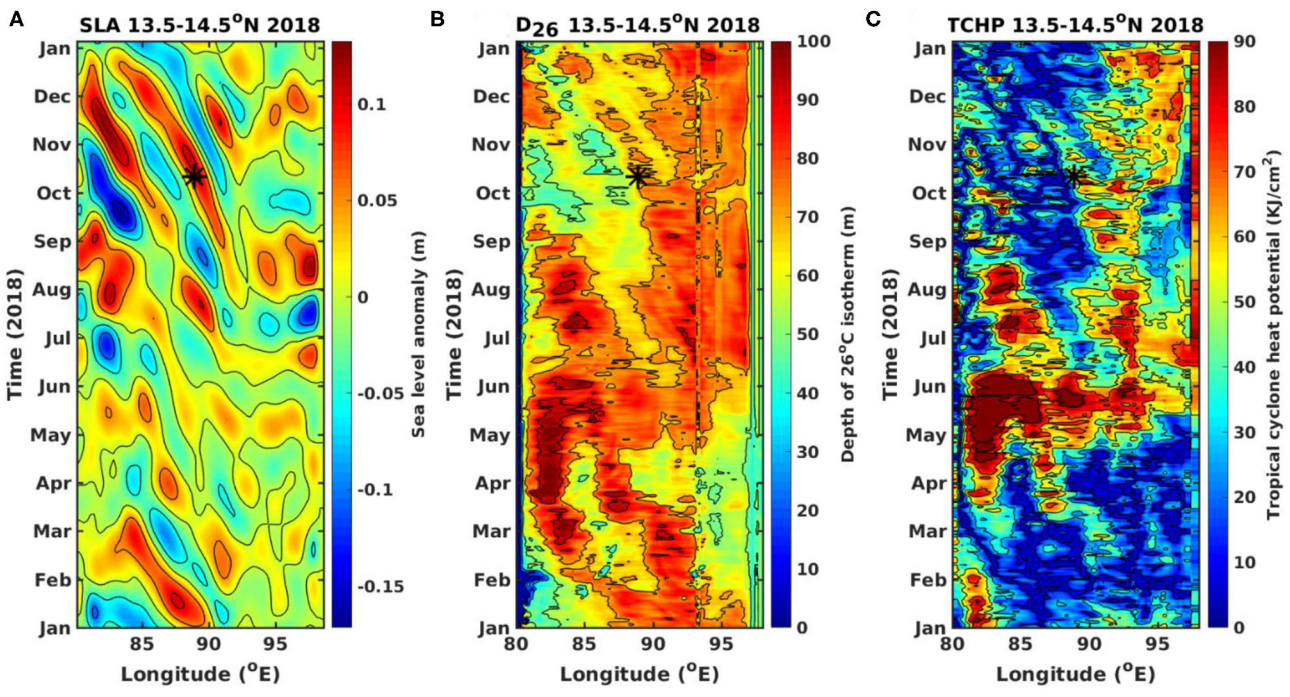

FIGURE 14 | A time-longitude Hovmöller diagram of **(A)** SLA (m), **(B)** D_{26} (m), and **(C)** TCHP (kJ/cm^2) from January 1 to December 31, 2018, averaged over 13.5–14.5°N latitude. A black asterisk denotes the location of the origin of the cyclone Titli.

co-occurred and PDO was in the cold phase. All three climate modes acting in tandem led to the warming of the upper ocean in the AS and part of the BoB by 0.5°C compared with the climatological mean value. This excess warming pre-conditioned the upper ocean by making higher-than-normal thermal energy available for the formation of cyclones by way of TCHP. It is the arrival of MJO and the MRG wave in the first week of October in the vicinity of the origin of cyclone Luban in the AS that initiated a basin-wide air-sea interaction, which acted as a trigger for the generation of Luban on October 6. In the case of Titli, the triggering mechanism was the arrival of MJO and the oceanic Rossby wave in the vicinity of the origin of Titli on October 8. The eastward propagation of enhanced convection associated with MJO and the shifting of low vertical wind shear and high mid-tropospheric humidity created a favorable condition for cyclogenesis. Along with this, the westward propagating downwelling Rossby wave depressed the thermocline, which increased TCHP and augmented the genesis of cyclones. The above mechanisms explaining the simultaneous occurrence of Luban and Titli in the NIO are schematically shown in **Figure 15**.

The complex dynamics of tropical cyclones involve mixed layer dynamics, planetary waves, intraseasonal variability, and climate modes. An intuitive mechanistic understanding of such interactions, although possible through extensive data analysis as done in the present study, still needs high-resolution coupled-model studies and near real-time observations for a quantitative understanding and better prediction of cyclones. As climate models continue to project the rapid warming of the NIO (Ogata et al., 2014), more studies are required using sophisticated coupled models.

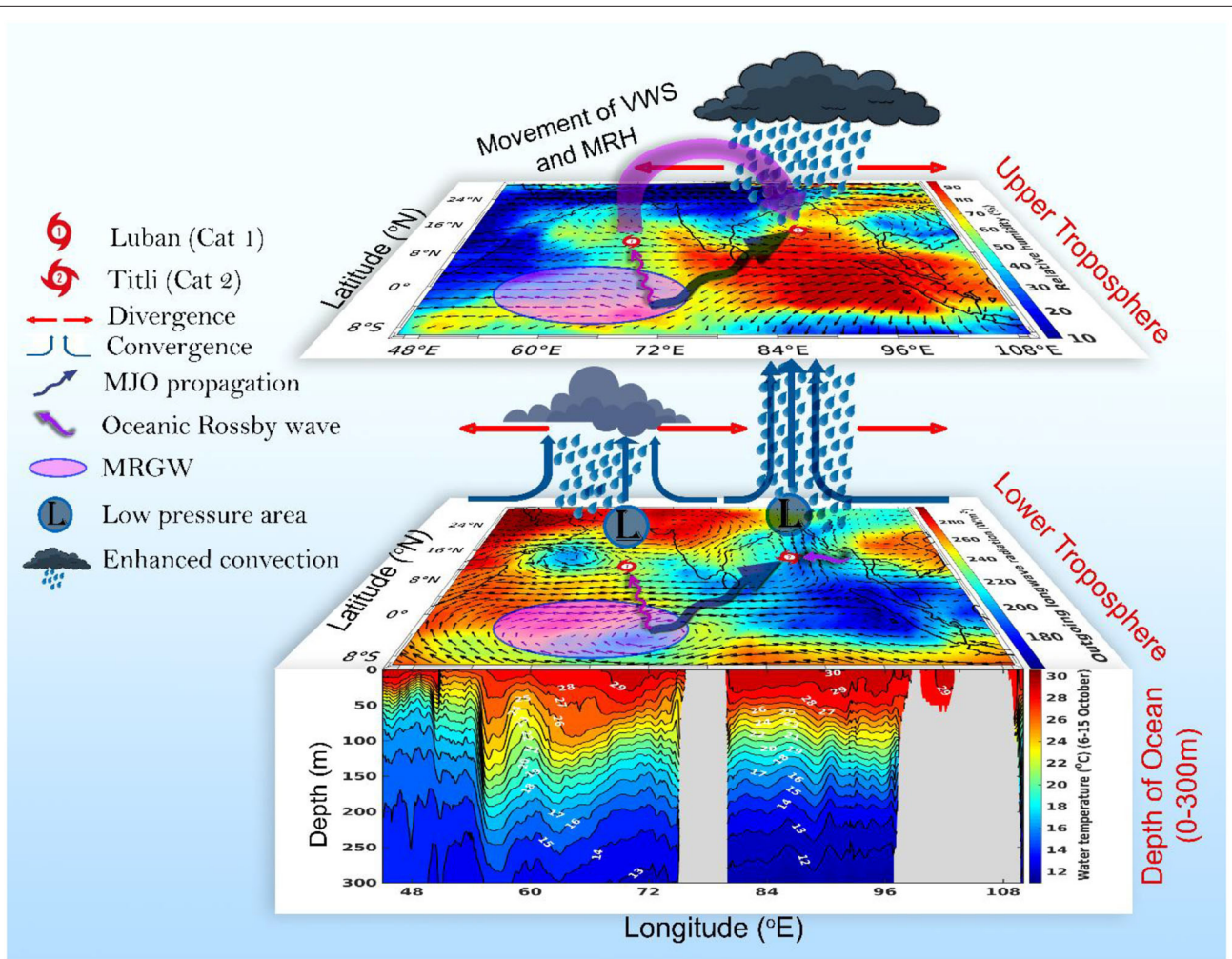

FIGURE 15 | A schematic diagram represents the ocean-atmosphere dynamics associated with the simultaneous genesis of cyclone Luban in the AS and Titli in the BoB over the North Indian Ocean. The lower (vertical) panel depicts the vertical temperature structure during October 6–15, 2018 (the cyclone period) in the upper 300-m depth. The middle (horizontal) panel depicts the outgoing longwave radiation (W/m^2, shading), superposed with the lower tropospheric wind (m/s) at 850 hPa, and the upper (horizontal) panel depicts mid-tropospheric-relative humidity (%, shading) at 500 hPa, superposed with the upper tropospheric wind (m/s) at 200 hPa. VWS and MRH denote vertical wind shear and mid-tropospheric-relative humidity, respectively, moving from the AS to the BoB, indicated by the curved thick magenta arrow. MJO and MRGW stand for Madden–Julian oscillation and mixed Rossby-gravity wave. Refer to text for details.

DATA AVAILABILITY STATEMENT

The original contributions presented in the study are included in the article/**Supplementary Material**, further inquiries can be directed to the corresponding author/s.

AUTHOR CONTRIBUTIONS

RRC and SPK formulated the objective after discussing with AC. RRC carried out the data analysis and graphics preparation. SPK and RRC interpreted the results and wrote the manuscript. All authors reviewed the manuscript.

ACKNOWLEDGMENTS

The authors thank the directors of the Indian Institute of Technology (IIT), Kharagpur, and Council of Scientific and Industrial Research (CSIR)-National Institute of Oceanography (CSIR-NIO), Goa for all the support and encouragement for this research. RRC acknowledges the Ministry of Human Resources Development (MHRD), Government of India for providing the research fellowship. The authors would like to thank the handling editor and the two reviewers for their constructive criticism and suggestions that helped to improve the quality of the manuscript. The figures are generated using MATLAB. SPK would like to acknowledge CSIR Emeritus Scientist project ES84091 (RIO-CC-AMEF) and CSIR-NIO Goa (NIO contribution).

SUPPLEMENTARY MATERIAL

The Supplementary Material for this article can be found online at: https://www.frontiersin.org/articles/10.3389/fmars.2021.729269/full#supplementary-material

REFERENCES

Balaji, M., Chakraborty, A., and Mandal, M. (2018). Changes in tropical cyclone activity in north Indian ocean during satellite era (1981–2014). *Int. J. Climatol.* 38, 2819–2837. doi: 10.1002/joc.5463

Bates, N. R., Knap, A. H., and Michaels, A. F. (1998). Contribution of hurricanes to local and global estimates of air-sea exchange of CO_2. *Nature* 395, 58–61. doi: 10.1038/25703

Bates, N. R., and Peters, A. J. (2007). The contribution of atmospheric acid deposition to ocean acidification in the subtropical North Atlantic ocean. *Mar. Chem.* 107, 547–558. doi: 10.1016/j.marchem.2007.08.002

Behrenfeld, M. J., and Falkowski, P. G. (1997). Photosynthetic rates derived from satellite-based chlorophyll concentration. *Limnol. Oceanogr.* 42, 1–20. doi: 10.4319/lo.1997.42.1.0001

Byju, P., and Prasanna Kumar, S. (2011). Physical and biological response of the Arabian sea to tropical cyclone phyan and its implications. *Mar. Environ. Res.* 71, 325–330. doi: 10.1016/j.marenvres.2011.02.008

Camargo, S. J., Wheeler, M. C., and Sobel, A. H. (2009). Diagnosis of the MJO modulation of tropical cyclogenesis using an empirical index. *J. Atmosph. Sci.* 66, 3061–3074. doi: 10.1175/2009JAS3101.1

Chacko, N. (2017). Chlorophyll bloom in response to tropical cyclone Hudhud in the Bay of Bengal: bio-argo subsurface observations. *Deep Sea Res. Part Oceanogr. Res.* 124, 66–72. doi: 10.1016/j.dsr.2017.04.010

Chacko, N. (2018). Effects of cyclone Thane in the Bay of Bengal explored using moored buoy observations and multiplatform satellite data. *J. Indian Soc. Remote Sens.* 46, 821–828. doi: 10.1007/s12524-017-0748-9

Chacko, N. (2019). Differential chlorophyll blooms induced by tropical cyclones and their relation to cyclone characteristics and ocean pre-conditions in the Indian ocean. *J. Earth Syst. Sci.* 128, 1–11. doi: 10.1007/s12040-019-1207-5

Chowdhury, R. R., Prasanna Kumar, S., and Chakraborty, A. (2020b). A study on the physical and biogeochemical responses of the Bay of Bengal due to cyclone Madi. *J. Operat. Oceanogr.* 1–22. doi: 10.1080/1755876X.2020.1817659

Chowdhury, R. R., Prasanna Kumar, S., Narvekar, J., and Chakraborty, A. (2020a). Back-to-back occurrence of tropical cyclones in the Arabian sea during October-November 2015: causes and responses. *J. Geophys. Res. Oceans* 125:e2019JC015836. doi: 10.1029/2019JC015836

Dube, S. K., Rao, D., Sinha, P. C., Murty, T. S., and Bahuluyan, N. (1997). Storm surge in the Bay of Bengal and Arabian sea: the problem and its prediction. *Mausam* 48, 283–304.

Evan, A. T., and Camargo, S. J. (2011). A climatology of Arabian Sea cyclonic storms. *J. Clim.* 24, 140–158. doi: 10.1175/2010JCLI3611.1

Fischer, J., Schott, F., and Stramma, L. (1996). Currents and transports of the Great Whirl-Socotra Gyre system during the summer monsoon, August 1993. *J. Geophys. Res. Oceans* 101, 3573–3587. doi: 10.1029/95JC03617

Foltz, G. R., and McPhaden, M. J. (2009). Impact of barrier layer thickness on SST in the Central Tropical North Atlantic. *J. Clim.* 22, 285–299. doi: 10.1175/2008JCLI2308.1

Girishkumar, M. S., and Ravichandran, M. (2012). The influences of ENSO on tropical cyclone activity in the Bay of Bengal during October-December. *J. Geophys. Res. Oceans* 117:C02033. doi: 10.1029/2011JC007417

Gopalakrishna, V., Murty, V. S. N., Sarma, M. S. S., and Sastry, J. S. (1993). Thermal response of upper layers of Bay of Bengal to forcing of a severe cyclonic storm: a case study. *Indian J. Mar.Sci.* 22, 8–11.

Gray, W. M. (1985). *Technical Document WMO/TD No. 72, Vol. I.* Geneva: WMO, 3-19.

Grinsted, A., Moore, J. C., and Jevrejeva, S. (2004). Application of the cross wavelet transform and wavelet coherence to geophysical time series. *Nonlin. Process. Geophys.* 11, 561–566. doi: 10.5194/npg-11-561-2004

Hayashi, Y. (1974). Spectral analysis of tropical disturbances appearing in a GFDL general circulation model. *J. Atmos. Sci.* 31, 180–218. doi: 10.1175/1520-0469(1974)031<0180:SAOTDA>2.0.CO;2

Hayashi, Y., and Golder, D. G. (1978). The generations of equatorial transient planetary waves: control experiments with a GFDL general circulation model. *J. Atmos. Sci.* 35, 2068–2082. doi: 10.1175/1520-0469(1978)035<2068:TGOETP>2.0.CO;2

Knutson, T. R., McBride, J. L., Chan, J., Emanuel, K., Holland, G., Landsea, C., et al. (2010). Tropical cyclones and climate change. *Nat. Geosci.* 3, 157–163. doi: 10.1038/ngeo779

Latha, T. P., Rao, K. H., Nagamani, P. V., Amminedu, E., Choudhury, S. B., Dutt, C. B. S., et al. (2015). Impact of cyclone phailin on chlorophyll-a concentration and productivity in the Bay of Bengal. *Int. J. Geosci.* 6, 473–480. doi: 10.4236/ijg.2015.65037

Liang, Z., Xing, T., Wang, Y., and Zeng, L. (2019). Mixed layer heat variations in the South China sea observed by argo float and reanalysis data during 2012-2015. *Sustainability* 11:5429. doi: 10.3390/su11195429

Liebmann, B., and Smith, C. A. (1996). Description of a complete (Interpolated) outgoing longwave radiation dataset. *Bull. Am. Meteorol. Soc.* 77, 1275–1277.

Lin, I. I., Liu, W. T., Wu, C. C., Wong, G. T. F., Hu, C., Chen, Z., Liang, W. D., et al. (2003). New evidence for enhanced ocean primary production triggered by tropical cyclone. *Geophys. Res. Lett.* 30:1718. doi: 10.1029/2003GL017141

Madden, R. A., and Julian, P. R. (1971). Detection of a 40–50 Day Oscillation in the Zonal Wind in the Tropical Pacific. *J. Atmos. Sci.* 28, 702–708. doi: 10.1175/1520-0469(1971)028<0702:DOADOI>2.0.CO;2

Madhupratap, M., Gauns, M., Ramaiah, N., Prasanna Kumar, S., Muraleedharan, P. M., de Sousa, S. N., et al. (2003). Biogeochemistry of the Bay of Bengal: physical, chemical and primary productivity characteristics of the

central and western Bay of Bengal during summer monsoon 2001. *Deep Sea Res. Part Trop. Stud. Oceanogr.* 50, 881–896. doi: 10.1016/S0967-0645(02)00611-2

Maneesha, K., Prasad, D. H., and Patnaik, K. V. K. R.K. (2019). Biophysical responses to tropical cyclone Hudhud over the Bay of Bengal. *J. Oper. Oceanogr.* 14, 87–97. doi: 10.1080/1755876X.2019.1684135

Maneesha, K., Sarma, V. V. S. S., Reddy, N. P. C., Sadhuram, Y., RamanaMurty, T. V., Sarma, V. V., et al. (2011). Meso-scale atmospheric events promote phytoplankton blooms in the coastal Bay of Bengal. *J. Earth Syst. Sci.* 120, 773–782. doi: 10.1007/s12040-011-0089-y

Mantua, N. J., and Hare, S. R. (2002). The Pacific decadal oscillation. *J. Oceanogr.* 58, 35–44. doi: 10.1023/A:1015820616384

Mantua, N. J., Hare, S. R., Zhang, Y., Wallace, J. M., and Francis, R. C. (1997). A Pacific interdecadal climate oscillation with impacts on salmon production. *Bull. Am. Meteor. Sock.* 78, 1069–1080. doi: 10.1175/1520-0477(1997)078<1069:APICOW>2.0.CO;2

Matsuno, T. (1966). Quasi-geostrophic motion in the equatorial area. *J. Meteor. Soc. Japan* 44, 25–43. doi: 10.2151/jmsj1965.44.1_25

Morel, A., and Antoine, D. (1994). Heating rate within the upper ocean in relation to its bio-optical state. *J. Phys. Oceanogr.* 24, 1652–1665. doi: 10.1175/1520-0485(1994)024<1652:HRWTUO>2.0.CO;2

Muraleedharan, P. M., Kumar, S. P., Sijikumar, S., Sivakumar, K. U., and Mathew, T. (2015). Observational evidence of mixed rossby gravity waves at the central equatorial Indian ocean. *Meteorol. Atmos. Phys.* 127, 407–417. doi: 10.1007/s00703-015-0376-2

Naqvi, S. W. A., Noronha, R. J., Somasundar, K., and Sen Gupta, R. (1990). Seasonal changes in the denitrification regime of the Arabian sea. *Deep Sea Res. Part Oceanogr. Res. Pap.* 37, 593–611. doi: 10.1016/0198-0149(90)90092-A

Narvekar, J., D'Mello, J. R., Prasanna Kumar, S., Banerjee, P., Sharma, V., and Shenai-Tirodkar, P. (2017). Winter-time variability of the eastern Arabian sea: a comparison between 2003 and 2013. *Geophys. Res. Lett.* 42, 6269–6277. doi: 10.1002/2017GL072965

Narvekar, J., and Prasanna Kumar, S. (2006). Seasonal variability of the mixed layer in the central Bay of Bengal and associated changes in nutrients and chlorophyll. *Deep Sea Res. I* 53, 820–835. doi: 10.1016/j.dsr.2006.01.012

Narvekar, J., and Prasanna Kumar, S. (2014). Mixed layer variability and chlorophyll a biomass in the Bay of Bengal. *Biogeosciences* 11, 3819–3843. doi: 10.5194/bg-11-3819-2014

Neetu, S., Lengaigne, M., Vincent, E. M., Vialard, J., Madec, G., Samson, G., et al. (2012). Influence of oceanic stratification on tropical cyclones-induced surface cooling in the Bay of Bengal. *J. Geophys. Res.* 117:C12020. doi: 10.1029/2012JC008433

Nemoto, K., Midorikawa, T., Wada, A., Ogawa, K., Takatani, S., Kimoto, H., et al. (2009). Continuous observations of atmospheric and oceanic CO2 using a moored buoy in the East China sea: variations during the passage of typhoons. *Deep Sea Res. Part II Top. Stud. Oceanogr.* 56, 542–553. doi: 10.1016/j.dsr2.2008.12.015

Ogata, T., Ueda, H., Inoue, T., Hayasaki, M., Yoshida, A., Watanabe, S., et al. (2014). Projected future changes of the Asian Monsoon: a comparison of CMIP3 and CMIP5 model results. *J. Meteorol. Soc. Japan* 92, 207–225. doi: 10.2151/jmsj.2014-302

Potemra, J. T., Luther, M. E., and O'Brien, J. J. (1991). The seasonal circulation of the upper ocean in the Bay of Bengal. *J. Geophys. Res. Oceans* 96, 12667–12683. doi: 10.1029/91JC01045

Pothapakula, P. K., Osuri, K. K., Pattanayak, S., Mohanty, U. C., Sil, S., and Nadimpalli. (2017). Observational perspective of SST changes during life cycle of tropical cyclone over Bay of Bengal. *Nat. Hazards* 88, 1769–1787. doi: 10.1007/s11069-017-2945-9

Prasad, T. G. (1997). Annual and seasonal mean buoyancy fluxes for the tropical Indian Ocean. *Curr. Sci.* 73, 667–674.

Prasad, V. S., Mohandas, S., Das Gupta, M., and Rajagopal, E. N. (2011). *Implementation of Upgraded Global Forecasting Systems (T382L64 and T574L64) at NCMRWF*. Technical Report, National Centre for Medium Range Weather Forecasting (NCMRWF); Ministry of Earth Science (MoES); Government of India. Available online at: http://www.ncmrwf.gov.in/ncmrwf/gfs_report_final.pdf

Prasanna Kumar, S., and Narvekar, J. (2005). Seasonal variability of the mixed layer in the central Arabian sea and its implication on nutrients and primary productivity. *Deep Sea Res. Part II* 52, 1848–1861. doi: 10.1016/j.dsr2.2005.06.002

Prasanna Kumar, S., Narvekar, J., Nuncio, M., Gauns, M., and Sardesai, S. (2009b). "What drives the biological productivity of the northern Indian Ocean?," in *Indian Ocean Biogeochemical Processes and Ecological Variability, Vol. 185,* eds J. D. Wiggert, W. R. Hood, S. W. A. Naqvi, K. H. Brink, S. L. Smith (Washington, DC: AGU), 33–56. doi: 10.1029/2008GM000757

Prasanna Kumar, S., Nuncio, M., Narvekar, J., Kumar, A., Sardesai, D. S., De Souza, S. N., et al. (2004). Intrusion of the Bay of Bengal water into the Arabian sea during winter monsoon and associated chemical and biological response. *Geophys. Res. Lett.* 31:L15304. doi: 10.1029/2004GL020247

Prasanna Kumar, S., Nuncio, M., Ramaiah, N., Sardesai, S., Narvekar, J., Fernandes, V., et al. (2007). Eddy-mediated biological productivity in the Bay of Bengal during fall and spring intermonsoons. *Deep Sea Res. Part I* 54, 1619–1640. doi: 10.1016/j.dsr.2007.06.002

Prasanna Kumar, S., Roshin, R. P., Narvekar, J., Kumar, P. K. D., and Vivekanandan, E. (2009a). Response of the Arabian sea to global warming and associated regional climate shift. *Mar. Environ. Res.* 68, 217–222. doi: 10.1016/j.marenvres.2009.06.010

Praveen Kumar, B., Vialard, J., Lengaigne, M., Murty, V. S. N., McPhaden, M. J., Cronin, M. F., et al. (2013). TropFlux wind stresses over the tropical oceans: evaluation and comparison with other products. *Clim. Dyn.* 40, 2049–2071. doi: 10.1007/s00382-012-1455-4

Qasim, S. Z. (1977). Biological productivity of the Indian ocean. *Indian J. Mar. Sci.* 6, 122–137.

Rajeevan, M., Srinivasan, J., Niranjan Kumar, K., Gnanaseelan, C., and Ali, M. M. (2013). On the epochal variation of intensity of tropical cyclones in the Arabian sea. *Atmos. Sci. Lett.* 14, 249–255. doi: 10.1002/asl2.447

Ramaswamy, V., and Nair, R. R. (1994). Fluxes of material in the Arabian sea and Bay of Bengal-sediment trap studies. *Proc. Indian Acad. Sci. Earth Planet Sci.* 103, 189–210.

Rao, R. (1987). Further analysis on the thermal response of the upper Bay of Bengal to the forcing of pre-monsoon cyclonic storm and summer monsoonal onset during MONEX-79. *Mausam* 38, 147–156. doi: 10.1007/BF00868098

Reynolds, R. W., Smith, T. M., Liu, C., Chelton, D. B., Casey, K. S., and Schlax, M. G. (2007). Daily high-resolution-blended analyses for sea surface temperature. *J. Clim.* 20, 5473–5496. doi: 10.1175/2007JCLI1824.1

Roman-Stork, H. L., Subrahmanyam, B., and Trott, C. B. (2020). Monitoring intraseasonal oscillations in the Indian Ocean using satellite observations. *J. Geophys. Res. Oceans* 125:e2019JC015891. doi: 10.1029/2019JC015891

Roxy, M. K., Ritika, K., Terray, P., and Masson, S. (2014). The curious case of Indian ocean warming. *J. Clim.* 27, 8501–8509. doi: 10.1175/JCLI-D-14-00471.1

RupaKumar, R., KrishnaKumar, K., Ashrit, R. G., Patwardhan, S. K., and Pant, G. B. (2002). "Climate change in India: observations and model projections," in *Climate Change and India: Issues, Concerns and Opportunities*, eds P. R. Shukla, S. K. Sharma, P. Venkata Ramana (New Delhi: Tata McGraw-Hill Ltd), 24–75.

Ryther, J. H., Hall, J. R., Pease, A. K., Bakun, A., and Jones, M. M. (1966). Primary organic production in relation to the chemistry and hydrography of the western Indian ocean. *Limnol. Oceanogr.* 11, 371–380. doi: 10.4319/lo.1966.11.3.0371

Saji, N. H., Goswami, B. N., Vinayachandran, P. N., and Yamagata, T. (1999). A dipole mode in the tropical Indian ocean. *Nature* 401, 360–363. doi: 10.1038/43854

Sandeep, A., and Prasad, V. S. (2018). Intra-annual variability of heat wave episodes over the east coast of India. *Int. J. Climatol.* 38. e617–e628. doi: 10.1002/joc.5395

Shengyan, Y., Juncheng, Z., and Subrahmanyam, M. V. (2019). Sea surface temperature cooling induced by tropical cyclone Hudhud over Bay of Bengal. *Indian J. Geo Mar. Sci.* 48, 9–17.

Shoup, C. G., Subrahmanyam, B., and Roman-Stork, H. L. (2019). Madden-Julian oscillation-induced sea surface salinity variability as detected in satellite-derived salinity. *Geophys. Res. Lett.* 46, 9748–9756. doi: 10.1029/2019GL083694

Singh, O. P., Masood, T., Khan, A., and Rahman, M. S. (2001). Has the frequency of intense tropical cyclones increased in the north Indian Ocean? *Curr. Sci.* 80, 575–580.

Singh, V. K., and Roxy, M. K. (2020). A review of the ocean-atmosphere interactions during tropical cyclones in the North Indian Ocean. *Preprint*. Available online at: http://arxiv.org/abs/2012.04384

Singh, V. K., Roxy, M. K., and Deshpande, M. (2020). The unusual long track and rapid intensification of very severe cyclone Ockhi. *Curr. Sci.*119, 771–779.

Smith, R. L., and Bottero, J. S. (1977). "On upwelling in the Arabian Sea," in *A Voyage of Discovery,* ed M. Angel (New York, NY: Pergamon), 291–304.

Smith, S. L., and Codispoti, L. A. (1980). Southwest monsoon of 1979: chemical and biological response of somali coastal waters. *Science* 209, 597–600. doi: 10.1126/science.209.4456.597

Sreenivas, P., Gnanaseelan, C., and Prasad, K. V. S. R. (2012). Influence of El Niño and Indian ocean dipole on sea level variability in the Bay of Bengal. *Glob. Planet. Change* 80–81, 215–225. doi: 10.1016/j.gloplacha.2011.11.001

Sridevi, B. K., Srinivasu, T. S., and Bhavani, D., Prasad, K. V. S. R. (2019). Extreme events enhance phytoplankton bloom in the South-Western Bay of Bengal. *Indian J. Mar. Sci.* 48, 253–258.

Subrahmanyam, B., Murty, V. S. N., Sharp, R. J., and O'Brien, J. J. (2005). Air-sea coupling during the tropical cyclones in the Indian Ocean: a case study using satellite observations. *Pure Appl. Geophys.* 162, 1643–1672. doi: 10.1007/s00024-005-2687-6

Subrahmanyam, B., Rao, K. H., Srinivasa Rao, N., Murty, V. S. N., and Sharp, R. J. (2002). Influence of a tropical cyclone on chlorophyll-a concentration in the Arabian Sea. *Geophys. Res. Lett.* 29, 22–31. doi: 10.1029/2002GL015892

Sweeney, C., Gnanadesikan, A., Griffies, S., Harrison, M., Rosati, A., and Samuels, B. (2005). Impacts of shortwave penetration depth on large-scale ocean circulation heat transport. *J. Phys. Oceanogr.* 35, 1103–1119. doi: 10.1175/JPO2740.1

Takahashi, T., Sutherland, S. C., Wanninkhof, R., Sweeney, C., Feely, R. A., Chipman, D. W., et al. (2009). Climatological mean and decadal change in surface ocean pCO2, and net sea-air CO2 flux over the global oceans. *Deep Sea Res. Part II Top. Stud. Oceanogr.* 56, 554–577. doi: 10.1016/j.dsr2.2008.12.009

Torrence, C., and Compo, G. P. (1998). A practical guide to wavelet analysis. *Bull. Am. Meteorol. Soc.* 79, 61–78. doi: 10.1175/1520-0477(1998)079<0061:APGTWA>2.0.CO;2

Vialard, J., Foltz, G. R., McPhaden, M. J., Duvel, J. P., and Montegut, C. B. (2008). Strong Indian Ocean sea surface temperature signals associated with the Madden-Julian oscillation in late 2007 and early 2008. *Geophys. Res. Lett.* 35:L19608. doi: 10.1029/2008GL035238

Vidya, P. J., and Prasanna Kumar, S. (2013). Role of mesoscale eddies on the variability of biogenic flux in the northern and central Bay of Bengal. *J. Geophys. Res. Oceans.* 118, 5760–5771. doi: 10.1002/jgrc.20423

Walker, G. T., and Bliss, E. W. (1932). World weather. *V. Mem. Roy. Meteor. Soc.* 4, 53–84.

Wanninkhof, R. (1992). Relationship between wind-speed and gas exchange over the ocean. *J. Geophys. Res.* 97, 7373–7382. doi: 10.1029/92JC00188

Weiss, R. F. (1974). Carbon dioxide in water and seawater: the solubility of a non-ideal gas. *Mar. Chem.* 2, 203–215. doi: 10.1016/0304-4203(74)90015-2

Wheeler, M. C., and Hendon, H. H. (2004). An all-season real-time multivariate MJO index: development of an index for monitoring and prediction. *Mon. Weather Rev.* 132, 1917–1932. doi: 10.1175/1520-0493(2004)132<1917:AARMMI>2.0.CO;2

Ye, H., Sheng, J., Tang, D., Morozov, E., Kalhoro, M. A., Wang, S., et al. (2019). Examining the impact of tropical cyclones on air-sea CO2 exchanges in the Bay of Bengal based on satellite data and in situ observations. *J. Geophys. Res. Oceans* 124, 555–576. doi: 10.1029/2018JC014533

Yu, L., O'Brien, J. J., and Yang, J. (1991). On the remote forcing of the circulation in the Bay of Bengal. *J. Geophys. Res.* 96, 20449–20454. doi: 10.1029/91JC02424

Zhang, C. (2005). Madden-Julian oscillation. *Rev. Geophys.* 43:RG2003. doi: 10.1029/2004RG000158

Conflict of Interest: The authors declare that the research was conducted in the absence of any commercial or financial relationships that could be construed as a potential conflict of interest.

frontiers in Marine Science

ORIGINAL RESEARCH
published: 21 October 2021
doi: 10.3389/fmars.2021.732017

Diel to Seasonal Variation of Picoplankton in the Tropical South China Sea

Tzong-Yueh Chen [1,2], Chao-Chen Lai [3], Jen-Hua Tai [3], Chia-Ying Ko [4] and Fuh-Kwo Shiah [1,3,5]**

[1] Institute of Marine Environment and Ecology, National Taiwan Ocean University, Keelung, Taiwan, [2] Center of Excellence for the Oceans, National Taiwan Ocean University, Keelung, Taiwan, [3] Research Center for Environmental Changes, Academia Sinica, Taipei, Taiwan, [4] Institute of Fisheries Science, National Taiwan University, Taipei, Taiwan, [5] Institute of Oceanography, National Taiwan University, Taipei, Taiwan

Eight diel surveys on picoplankton (*Prochlorococcus*, *Synechococcus*, picoeukaryotes, and heterotrophic bacteria) abundance at the South East Asian Time-Series Station (SEATS; 18°N; 116°E) were conducted during the period of 2010 to 2014. The results indicated that *Prochlorococcus* and picoeukaryotes showed a subsurface maximum in warm seasons (spring, summer, and fall) and were abundant at the surface in the cold season (winter). *Synechococcus* and heterotrophic bacteria exhibited higher cell numbers at the surface and decreased with depth throughout the year. Although not all, some clear diel patterns for picoplankton were observed. Picophytoplankton usually peaked in the nighttime; picoeukaryotes peaked at ∼7 to 8 p.m., followed by Synechococcus (peaking at 1 a.m.) and Prochlorococcus (peaking at 2 a.m.). Unlike these picoautotrophs, heterotrophic bacteria could peak either at dusk (i.e., 7 p.m.) or at noon. Seasonally, *Prochlorococcus* was more abundant in the warm than the cold seasons, while *Synechococcus* and picoeukaryotes showed blooms in the winter of 2013 and 2011, respectively. Heterotrophic bacteria showed no significant seasonality. Regression analysis indicated that ∼73% of the diel-to-seasonal variation of the euphotic zone depth-integrated picophytoplankton biomass (i.e., $PicoB_{eu}$) could be explained by the changes of the mixed-layer depth (MLD), and this suggested that inorganic nutrient supply could be the major controlling factor in their growth. The strong linear relationship (coefficient of determination, R^2 of 0.83, $p < 0.01$) between sea surface temperature (SST) and $PicoB_{eu}$ implied, for the first time, a potential of using satellite-based SST to trace the biomass of picophytoplankton in the pelagic areas of the northern South China Sea.

Keywords: picoplankton, *Prochlorococcus*, *Synechococcus*, picoeukaryotes, heterotrophic bacteria, SEATS, South China Sea

OPEN ACCESS

Edited by:
Chin-Chang Hung, National Sun Yat-sen University, Taiwan

Reviewed by:
Jun Sun, China University of Geosciences Wuhan, China
Sarat Chandra Tripathy, National Center for Polar and Ocean Research (NCPOR), India

****Correspondence:***
Tzong-Yueh Chen
tzongyueh.chen@gmail.com
Fuh-Kwo Shiah
fkshiah@rcec.sinica.edu.tw

Specialty section:
This article was submitted to Marine Ecosystem Ecology, a section of the journal Frontiers in Marine Science

Received: *28 June 2021*
Accepted: *17 September 2021*
Published: *21 October 2021*

Citation:
Chen T-Y, Lai C-C, Tai J-H, Ko C-Y and Shiah F-K (2021) Diel to Seasonal Variation of Picoplankton in the Tropical South China Sea. Front. Mar. Sci. 8:732017. doi: 10.3389/fmars.2021.732017

INTRODUCTION

Marine picoplankton, 0.2 to 2 μm in size, consists of autotrophic and heterotrophic unicellular microorganisms. These tiny microbes play crucial roles in global biogeochemical cycles (Azam et al., 1983; Azam and Malfatti, 2007; Richardson, 2017). Picoautotrophs, including *Prochlorococcus* (*Pro*), *Synechococcus* (*Syn*), and picoeukaryotes (Peuk) contribute a substantial fraction to both total

phytoplankton biomass and production in marine ecosystems, especially in oligotrophic waters (Li et al., 1983; Campbell et al., 1994; Buitenhuis et al., 2012), while picoheterotrophs, mostly bacteria, consume photosynthetically fixed carbon and drive the microbial loop (Azam and Malfatti, 2007; Chen et al., 2020). Because of its significance to pelagic food webs, picoplankton community structure has been widely investigated in the world's oceans, such as the Atlantic Ocean (Zubkov et al., 1998; Durand et al., 2001), Pacific Ocean (Blanchot et al., 1997; Vaulot and Marie, 1999), Indian Ocean (Garrison et al., 2000), marginal seas of the Mediterranean Sea (Jacquet et al., 1998), and South China Sea (SCS; Liu et al., 2007).

Prochlorococcus is usually more abundant than *Synechococcus* in stratified, low-nutrient waters (e.g., Vaulot and Marie, 1999; Durand et al., 2001). Picoeukaryotes are less abundant than autotrophic cyanobacteria, especially in tropical and subtropical oceans (e.g., Vaulot and Marie, 1999; Durand et al., 2001). Seasonal variations in picoplankton abundance are well understood in temperate (e.g., Morán, 2007) and polar regions (e.g., Iversen and Seuthe, 2011). However, the seasonal variability in picoplankton in tropical and subtropical oceans is more complicated. For example, the maximum abundance of *Synechococcus* occurs during spring blooms in the subtropical Atlantic Ocean (Durand et al., 2001) but in the winter in the North Pacific Subtropical Gyre (Campbell et al., 1997). One of the objectives of this study is to present the seasonal variability in picoplankton in the tropical SCS.

Many oceanic phenomena exhibit a diel (i.e., a 24-h periodicity) cycle. The Earth's rotation leads to a rhythm of light and darkness, which is probably the most obvious diel setting in the world. The daily cycle of solar heating induces a temporary thermocline in the equatorial Pacific, which disappears at night (Moum et al., 1989). Solar insolation could affect not only diel ocean physics but also subsequent biogeochemical processes. A clear diel pattern of *in vivo* chlorophyll fluorescence has been observed in the equatorial Pacific (Dandonneau and Neveux, 1997). The diel variation in chlorophyll, then, may affect the diel pattern of zooplankton grazing rates (Neveux et al., 2003). Marked diel variability in picoplankton was observed in the equatorial Pacific (Vaulot and Marie, 1999) and the Mediterranean Sea (Jacquet et al., 1998). However, there is a lack of studies on the diel cycles of picophytoplankton in the SCS. In addition to a study of variable fluorescence (Xie et al., 2018), the only report of diel pattern in heterotrophic bacteria was to investigate the effect of nutrient pulses on heterotrophic bacterial growth in the SCS (Chen et al., 2016). The second objective of this study is to, for the first time, present the diel variability in picophytoplankton in the SCS.

The SCS is one of the largest marginal seas in the world, with an area of 3.5×10^6 km^2 and a volume of 4.7×10^6 km^3 (Wong et al., 2007). The SCS is a tropical semi-enclosed basin lying in a northeast-southwest direction from 23°N to 3°S and 102°E to 121°E (**Figure 1**). Most of the major rivers, including the Pearl River and Mekong River, discharge nutrient-rich freshwater into the northwestern boundary of the SCS. Although major rivers bring large amounts of terrestrial material to the SCS, basin-wide circulations effectively isolate the SCS from the influence of high amounts of runoff, ensuring the SCS remains similar to major oligotrophic oceans (Wong et al., 2007). In terms of climate, the SCS is strongly affected by the East Asian Monsoon (Shaw and Chao, 1994) and is also recognized to have frequent internal waves propagating westward from the Luzon Strait (Alford et al., 2010). On the one hand, the SCS is large and deep enough to have characteristics similar to those of major ocean basins; on the other hand, it is relatively confined to specific climatic and oceanic events. Therefore, research in the SCS has long been the focus of scientific interest. A multidisciplinary multi-institutional time-series project, the SouthEast Asian Time-Series Study (SEATS), was initiated in 1998. The primary station is located at 18°N, 116°E in the tropical northern South China Sea, more than 450 km away from land. The SEATS station has been routinely investigated for more than 20 years. In this study, we performed eight diel surveys of picoplankton abundance and environmental variables during the four seasons. With such sampling strategies, we were able to show the distribution of picoplankton on two timescales of diel and seasonal variability and the controlling factors.

MATERIALS AND METHODS

Study Area and Sampling

From 2010 to 2014, eight anchored diel studies were conducted at the SEATS station (18°N, 116°E; **Figure 1**) in the northern SCS. Eight diel studies were categorized as representatives of the four seasons (**Table 1**). Seawater was collected from 4 to 8 depths within the upper 100 m every 3–6 h (see **Supplementary Figures** for detailed sampling information) for at least 24 h using a rosette sampler with 20-L Teflon-coated X-Niskin bottles (General Oceanics, Miami, FL, USA) and a mounted CTD (Seabird, Bellevue, WA, USA). In addition to temperature and salinity, depth profiles of underwater PAR (Chelsea Technologies, UK), fluorescence, and transmission were also recorded. The mixed layer depth (MLD) was defined at which a density (sigma-*t*) change of 0.125 kg m^{-3} from the surface occurred (Vaulot and Marie, 1999).

Chemical Determinations

Nutrient (nitrate, nitrite, phosphate, and silicate) samples were collected in acid-washed polypropylene bottles, immediately frozen in liquid nitrogen on board, transferred, and kept at −20°C in the laboratory until analysis. Nitrate was reduced to nitrite using cadmium-copper filings, and concentrations were determined by the diazo-pink method (Parsons et al., 1984). Nitrite concentrations were determined the same way as nitrate concentration but excluding the reduction process. Phosphate concentrations were determined by the molybdenum-blue method (Parsons et al., 1984), and silicate concentrations were determined by the molybdate-blue method (Parsons et al., 1984). The dissolved organic carbon (DOC) concentrations were determined by the high-temperature catalytic oxidation (HTCO) method on a Shimadzu TOC-V (Japan) analyzer (Wurl, 2009). Samples (2 L) for chlorophyll-a (Chl-a) were collected on GF/F filters (Whatman, Marlborough, MA, USA)

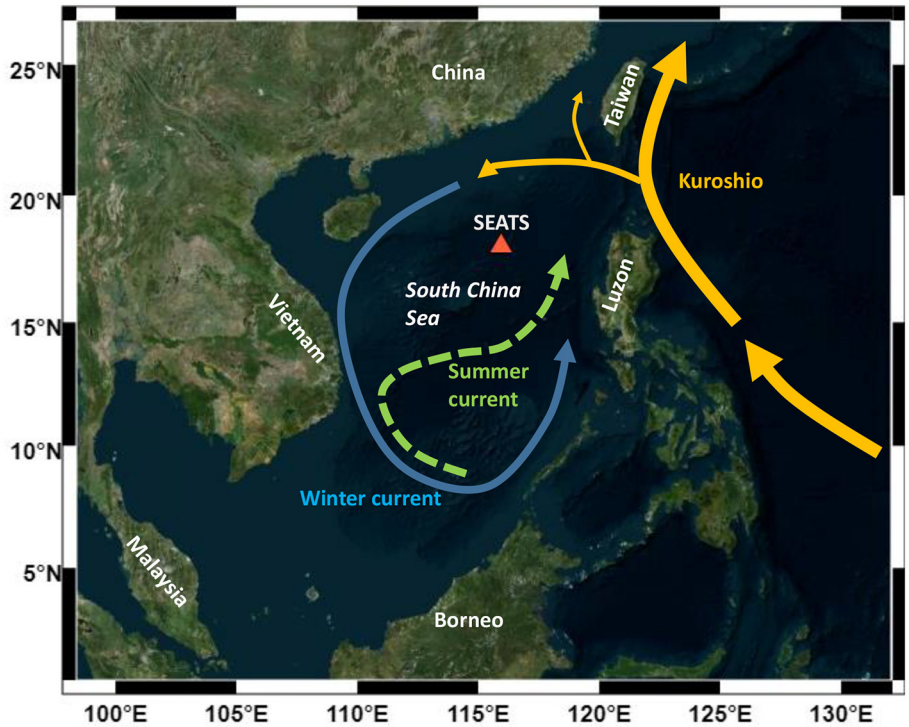

FIGURE 1 | A sampling site of the SEATS station (116°E, 18°N) in the South China Sea. The blue solid line represents the winter counterclockwise current, while the green dashed line represents the summer clockwise current (adapted from Wong et al., 2007).

TABLE 1 | Picoplankton abundance and hydrological parameters.

Cruise	Season	SST (°C)	MLD (m)	Chl-a (mg m^{-3})	*Prochlorococcus* (× 10^4 cells mL^{-1})	*Synechococcus* (× 10^3 cells mL^{-1})	Picoeukaryotes (× 10^3 cells mL^{-1})	Bacteria (× 10^5 cells mL^{-1})
OR1_1034	Spring (Apr. 2013)	28.37 ± 0.07 (28.27–28.43)	21.7 ± 3.7 (18–27)	0.19 ± 0.02 (0.17–0.22)	5.88 ± 1.43 (3.84–7.35)	4.48 ± 0.67 (3.57–5.39)	1.40 ± 0.90 (0.39–5.39)	4.86 ± 1.20 (3.11–6.67)
OR1_1103	Spring (Apr. 2014)	26.99 ± 0.05 (26.90–27.05)	24.3 ± 2.0 (21–27)	0.21 ± 0.04 (0.15–0.29)	6.25 ± 0.56 (5.46–7.20)	4.86 ± 1.62 (3.62–8.51)	2.53 ± 0.22 (2.15–2.76)	2.97 ± 0.20 (2.84–3.43)
OR1_1010	Summer (Aug. 2012)	29.20 ± 0.17 (28.85–29.35)	28.3 ± 15.1 (8–48)	0.21 ± 0.05 (0.14–0.29)	6.68 ± 1.57 (3.50–8.21)	3.80 ± 0.88 (2.81–5.07)	1.08 ± 0.38 (0.42–1.66)	4.12 ± 0.39 (3.63–4.87)
OR1_1084	Summer (Aug. 2014)	29.22 ± 0.05 (29.14–29.27)	22.7 ± 2.3 (19–25)	0.19 ± 0.02 (0.17–0.23)	6.38 ± 1.27 (4.53–8.70)	3.14 ± 0.62 (2.07–4.00)	1.54 ± 0.38 (1.19–2.22)	1.77 ± 0.58 (1.27–2.90)
OR1_0944	Fall (Oct., 2010)	29.26 ± 0.09 (29.18–29.39)	24.9 ± 7.3 (11–35)	0.18 ± 0.05 (0.11–0.26)	9.43 ± 1.89 (7.13–13.48)	3.91 ± 1.47 (2.43–6.99)	1.79 ± 0.33 (1.32–2.33)	6.50 ± 1.12 (4.55–8.43)
OR1_1053	Fall (Oct., 2013)	28.16 ± 0.09 (28.06–28.29)	37.8 ± 3.2 (34–42)	0.21 ± 0.07 (0.11–0.30)	6.07 ± 1.49 (4.62–8.31)	3.50 ± 1.27 (2.39–5.29)	2.08 ± 1.11 (1.25–4.02)	4.63 ± 0.69 (3.89–5.57)
OR1_0988	Winter (Dec. 2011)	24.78 ± 0.16 (24.55–25.03)	55.6 ± 5.6 (46–62)	0.32 ± 0.09 (0.21–0.46)	1.85 ± 0.56 (1.17–2.51)	6.01 ± 1.71 (3.46–8.00)	6.18 ± 1.75 (4.34–8.92)	6.37 ± 0.57 (5.67–7.13)
OR1_1060	Winter (Dec. 2013)	25.71 ± 0.08 (25.59–25.80)	45.6 ± 28.5 (6–76)	Not available	4.61 ± 1.12 (2.90–6.47)	57.13 ± 11.25 (44.81–72.23)	2.41 ± 0.36 (1.84–2.86)	5.02 ± 0.53 (4.07–5.72)

Data are shown as the mean ± SD and the range in parentheses in a given diel survey. Sea surface temperature (SST), mixed layer depth (MLD), 1 and chlorophyll-a (Chl-a). Picoplankton abundance and Chl-a are presented as depth averages.

and kept at −20°C until analysis. Chl-a was extracted with 90% acetone, and concentrations were determined using a fluorometer (Turner Designs, San Jose, CA, USA) (Parsons et al., 1984).

Biological Determinations

Picoplankton abundance was determined by flow cytometric counting. Subsamples of 2 ml for flow cytometry were preserved with paraformaldehyde (0.2%, final concentration), placed in

liquid nitrogen, and stored at −80°C until analysis (Campbell et al., 1997). A flow cytometer (PARTEC, Germany) equipped with a 488-nm laser was used to count picoplankton (Marie et al., 1999). Forward and side light scatters and green, red, and orange fluorescence were collected and analyzed using FlowMax software to identify three major groups of picophytoplankton (*Prochlorococcus*, *Synechococcus*, and picoeukaryotes) and heterotrophic bacteria. Fluoresbrite yellow-green beads (1 μm; Polysciences, Warrington, PA, USA) were used as internal standards. Heterotrophic bacteria were counted in separate subsamples stained with SYBR Green I (Molecular Probes, Eugene, OR, USA) (Marie et al., 1999). Carbon conversion factors were adopted from previous studies. The carbon conversion factors for *Prochlorococcus*, *Synechococcus*, and picoeukaryotes were 32, 100, and 1,500 fg C cell^{-1} (Zubkov et al., 1998), respectively, while a cellular carbon content of 20 fg C cell^{-1} was used for heterotrophic bacteria (Lee and Fuhrman, 1987).

Data Analysis

JMP software (SAS Institute, USA) was used for statistical analysis. Unless otherwise indicated, variation around each mean is presented as +/− one standard deviation. All depth averages were calculated as the integrations down to 100 m divided by 100.

RESULTS

Hydrological Parameters

The sea surface temperature (SST) and the mixed layer depth (MLD) are presented in **Table 1**. The SST showed obvious seasonal differences with small diel changes (**Table 1**; **Supplementary Figure 1**). The SSTs of 24.78 ± 0.16 and 25.71 ± 0.08°C in the winter (December 2011 and 2013, respectively) were significantly lower than those in the other seasons (mean SST ranged from 26.99 to 29.26°C) with very small diel variations (coefficient of variance, CV%, ranging from 0.2 to 0.7%). On the other hand, the seawater temperature at a depth of 100 m had a relatively narrow range (see **Supplementary Figure 1**; mean temperature ranged from 18.34 to 21.62°C) with a diel CV% of 1.2 to 4.4%. The MLD displayed a similar pattern to that of SST but with larger diel variations (**Table 1**; **Supplementary Figure 1**). The MLD values of 55.6 ± 5.6 and 45.6 ± 28.5 m in the winter (December 2011 and 2013, respectively) were deeper than those in the other seasons (mean MLD ranged from 21.7 to 37.8 m) with relatively large diel variations (CV% ranged from 8.2 to 62.4% and a maximum/minimum factor of 1.29 to 12.7). The large diel variability in the MLD indicated a dynamic physical environment in the interior of the water column during a 24-h period. Nitrate concentrations were homogeneous under the detection limit in the upper ocean (see **Supplementary Figure 2**) and were high at depths of 100 m (>5 μm). Nitracline depth (defined as the depth where nitrate concentration equals 1 μm) was fairly consistent at depths of ∼60 m (see **Supplementary Figure 2**). Phosphate and silicate concentrations exhibited vertical and temporal distributions similar to those of nitrate, showing depleted or low concentrations at the surface (**Supplementary Figures 3, 4**). Dissolved organic carbon (DOC) concentrations exhibited typical vertical distributions in the open ocean, ranging from 70 to 100 μm at the surface and decreased to 50–60 μm at a depth of 100 m (**Supplementary Figure 5**).

The Chl-a concentration generally displayed a subsurface chlorophyll maximum (SCM) except in the winter of 2011 (see **Supplementary Figure 6**). The SCM was consistently located at a depth of ∼50 m except in the spring of 2013 (∼80 m). In the winter of 2011, Chl-a appeared high at the surface and decreased with depth. Generally, Chl-a concentration was <0.7 mg m^{-3}. For seasonal variation, the depth-averaged Chl-a concentration showed high values of 0.32 ± 0.09 mg m^{-3} in the winter and a range of 0.18 to 0.21 mg m^{-3} in the other seasons (**Table 1**). The CV% of Chl-a diel variability ranged from 9.7 to 32.1% with an average of 22 ± 9%, while the maximum/minimum factor ranged from 1.3 to 2.6 with an average of 2 ± 0.5.

Vertical Distribution of Picoplankton

Prochlorococcus abundance was generally low at the surface and displayed a subsurface maximum in warm seasons (spring, summer, and fall; see **Supplementary Figure 7**), ranging from 3.1 to 9.9 × 10^4 cells ml^{-1} at the surface and reaching up to 13.9 × 10^4 cells ml^{-1} in the mid-layer except in the fall of 2010. *Prochlorococcus* was the most abundant in the fall of 2010, with 24.1 × 10^4 cells ml^{-1} as the subsurface maximum. The subsurface maximum of *Prochlorococcus* disappeared in the winter with decreasing depth-averaged cell numbers (1.8 ± 0.6 and 4.6 ± 1.1 × 10^4 cells ml^{-1} in the winter of 2011 and 2013, respectively). *Synechococcus* abundance was generally high at the surface and decreased with depth (see **Supplementary Figure 8**). The depth-averaged abundance of *Synechococcus* in the upper 50 m ranging from 4.2 to 8.4 × 10^3 cells ml^{-1} was higher than those of 1.8 to 3.6 × 10^3 cells ml^{-1} in the depth between 50 and 100 m except in the winter of 2013. *Synechococcus* abundance in the winter of 2013 was 10 times more abundant than that of other investigated seasons, at 90.9 ± 17.3 × 10^3 cells ml^{-1} in the upper 50 m of the ocean. The vertical distribution of picoeukaryotes was similar to that of *Prochlorococcus*, which displayed a subsurface maximum in the warm seasons and was relatively homogeneous in the winter (see **Supplementary Figure 9**). Generally, the subsurface maximum of picoeukaryotes ranged between 4 and 8 × 10^3 cells ml^{-1}, located mostly at depths of 40 to 60 m. In the winter of 2011, picoeukaryotes abundance was approximately double that of the other seasons and reached 13.9 × 10^3 cells ml^{-1}.

Heterotrophic bacteria accounted for the major component of the picoplankton community. Heterotrophic bacteria were ubiquitous in the water column and slightly more abundant at the surface (see **Supplementary Figure 10**). The heterotrophic bacterial abundance ranged from 1.2 to 11 × 10^5 cells ml^{-1} at the surface and from 0.7 to 3.9 × 10^5 cells ml^{-1} at a depth of 100 m.

Seasonal Variability in Picoplankton

Despite the existence of the vertical variability in picoplankton, depth-averaged abundance better described the seasonal variability. *Prochlorococcus* occurred at high-abundance levels in

the warm seasons (i.e., spring, summer, and fall; ranging from 5.88 to 9.43 $\times$ 10^4 cells ml^{-1}) and at low-abundance levels of 1.85 $\pm$ 0.56 and 4.61 $\pm$ 1.12 $\times$ 10^4 cells ml^{-1} in the winter of 2011 and 2013, respectively (**Table 1**). *Synechococcus*, by contrast, occurred at low-abundance levels in the warm seasons (ranging from 3.14 to 4.86 $\times 10^3$ cells ml^{-1}) and at high-abundance levels of 6.01 $\pm$ 1.71 $\times$ 10^3 cells ml^{-1} and an extremely high abundance of 57.13 $\pm$ 11.25 $\times$ 10^3 cells ml^{-1} in the winter of 2011 and 2013, respectively (**Table 1**), at approximately an orderly less abundant than that of *Prochlorococcus* in terms of cell numbers. Similar to *Synechococcus*, the seasonal pattern of picoeukaryotes showed low values of 1.08 to 2.53 $\times$ 10^3 cells ml^{-1} in the warm seasons and high values of 6.18 $\pm$ 1.75 and 2.41 $\pm$ 0.36 $\times$ 10^3 cells ml^{-1} in the winters of 2011 and 2013, respectively (**Table 1**). *Prochlorococcus* was the most abundant autotrophic picoplankton in the warm seasons, accounting for 92.1 $\pm$ 1.8% of the total picophytoplankton cell numbers. The picophytoplankton community structure substantially changed in the winters. In the winter of 2011, *Prochlorococcus* was still the most abundant with a smaller fraction of 59.8 $\pm$ 6.3%, followed by picoeukaryotes (20.2 $\pm$ 2.1%) and *Synechococcus* (20 $\pm$ 5.1%). In the winter of 2013, *Synechococcus* became the most abundant picophytoplankton (54.1 $\pm$ 9.8%), followed by *Prochlorococcus* (43.6 $\pm$ 9.8%) and picoeukaryotes (2.3 $\pm$ 0.3%).

Integrated autotrophic picoplankton carbon biomass in the upper 100 m showed high values in the winter (1.046 $\pm$ 0.289 and 1.080 $\pm$ 0.114 g m^{-2} for 2011 and 2013, respectively) and ranged from 0.414 to 0.628 gm^{-2} in the warm seasons (**Figure 2**). Picoeukaryotes and *Prochlorococcus* were the major components of autotrophic picoplankton biomass in the warm seasons, accounting for 48.7 $\pm$ 8.6 and 43.3 $\pm$ 7.7% of the biomass, respectively. However, contributions to picophytoplankton carbon biomass were variable in the winter. In the winter of 2011, picoeukaryotes dominated the autotrophic picoplankton biomass (accounting for 88.5 $\pm$ 1.2%), followed by *Synechococcus* (5.8 $\pm$ 1.3%) and *Prochlorococcus* (5.7 $\pm$ 1.3%). In the winter of 2013, *Synechococcus* became the dominant group of picophytoplankton (contributing 52.6 $\pm$ 6.7%), followed by picoeukaryotes (33.5 $\pm$ 3.9%) and *Prochlorococcus* (13.9 $\pm$ 4.2%).

Heterotrophic bacteria were the major component of the picoplankton community in terms of both abundance and biomass. Heterotrophic bacterial abundance ranged from 1.77 to 6.37 $\times$ 10^5 cells ml^{-1}, showing an insignificant seasonality (**Table 1**). Heterotrophic bacterial biomass generally exceeded or equaled the total picophytoplankton biomass, ranging from 0.353 to 1.300 gm^{-2} in warm seasons and 1.274 $\pm$ 0.113 and 1.003 $\pm$ 0.106 gm^{-2} in the winters of 2011 and 2013, respectively (**Figure 2**).

Diel Variability in Picoplankton

Picoplankton abundance in some investigations showed clear diel cycles (**Figure 3**; see more detail in Section 4.3). *Synechococcus* abundance (data from OR1_1103, OR1_944, and OR1_1053) peaked at 1 a.m. (**Figure 3B**), followed by *Prochlorococcus* (peaking at 2 a.m.) based on data from OR1_944, OR1_1053, and OR1_1060 (**Figure 3A**). Picoeukaryotes peaked at ~7 to 8 p.m. based on data from OR1_1034, OR1_1010, OR1_944, and OR1_988 (**Figure 3C**). Diel variation occurred in two types for heterotrophic bacteria: the night-peak group, including OR1_944 and OR1_1053, which peaked at 7 p.m. (**Figure 3D**), and the day-peak group, including OR1_1034, OR1_1010, OR1_1084, and OR1_1060, which peaked at noon (**Figure 3E**). In addition to diel patterns, the results also showed large variations among frequent samplings (**Table 1**). The CV% of depth-averaged *Prochlorococcus* abundance ranged from 9 to 30.3% with an average of 22 $\pm$ 6.2%, while the maximum/minimum factor ranged from 1.3 to 2.3 with an average of 1.9 $\pm$ 0.3. Diel variation in *Synechococcus* abundance was larger than that in *Prochlorococcus* abundance. The CV% of *Synechococcus* ranged from 14.9 to 37.6% with an average of 26.6 $\pm$ 8.5%, while the factor ranged from 1.5 to 2.9 with an average of 2.1 $\pm$ 0.4. Picoeukaryotes showed the largest diel variation in abundance. The CV% of picoeukaryotes ranged from 8.8 to 64.5% with an average of 30.9 $\pm$ 19.2%, while its factor ranged from 1.3 to 6.6 with an average of 2.8 $\pm$ 1.8. Heterotrophic bacteria seemed to have the least diel variation. The CV% of heterotrophic bacterial abundance ranged from 6.6 to 33% with an average of 15.7 $\pm$ 9%, while the factor ranged from 1.2 to 2.3 with an average of 1.6 $\pm$ 0.4.

DISCUSSION

Vertical Distribution in Picoplankton

Picophytoplankton was mostly observed within the upper 100 m and had insignificant numbers below a depth of 150 m at SEATS station in the South China Sea (Liu et al., 2007). *Prochlorococcus* and picoeukaryotes tended to accumulate at subsurface depths of mostly ca. 40 to 60 m in the warm seasons (**Supplementary Figures 7, 9**), while *Synechococcus* tended to peak at the surface (**Supplementary Figure 8**). Such a difference in vertical distribution between *Prochlorococcus* and *Synechococcus* is well recognized (Campbell et al., 1997; Durand et al., 2001), indicating different light adaptation strategies (Ting et al., 2002). *Prochlorococcus* seemed to be well adapted to low light (Partensky et al., 1993) and had higher absorption efficiency for blue light, which is predominant in deep waters (Morel et al., 1993), favoring the formation of subsurface maxima. Moreover, *Prochlorococcus* was also ultraviolet sensitive, which could induce DNA damage (Boelen et al., 2000) and, therefore, restrict *Prochlorococcus* growth at the surface. On the other hand, *Synechococcus* developed a phycobilisome antenna system, which contained phycobiliproteins (for example, phycoerythrin and phycocyanin) and had a high capability for light-harvesting at the surface (Biller et al., 2015). Boelen et al. (2000) also found that, in comparison to *Prochlorococcus*, *Synechococcus* was more resistant to UVB damage. These factors helped to form the difference in the vertical distributions between *Prochlorococcus* and *Synechococcus*. Picoeukaryotes peaked at subsurface depths in the warm seasons along with the subsurface chlorophyll maximum. The subsurface maximum of *Prochlorococcus*, picoeukaryotes, and Chl-a disappeared during the winter, which was also observed in Liu et al. (2007). Winter mixing broke water column stability and the subsurface maximum. After strong mixing, the stratification and then the subsurface maximum were

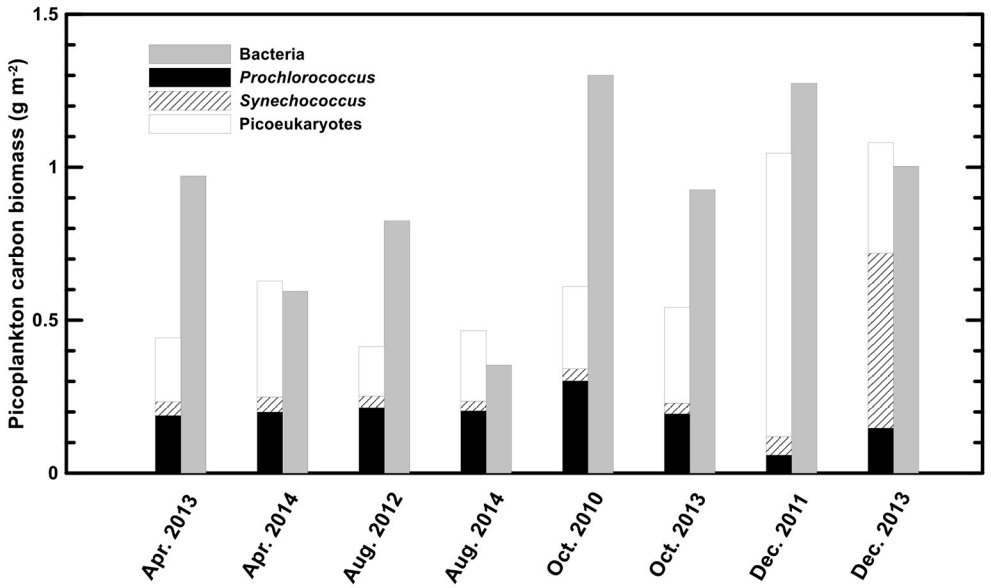

FIGURE 2 | Integrated picoplankton carbon biomass at the SEATS station.

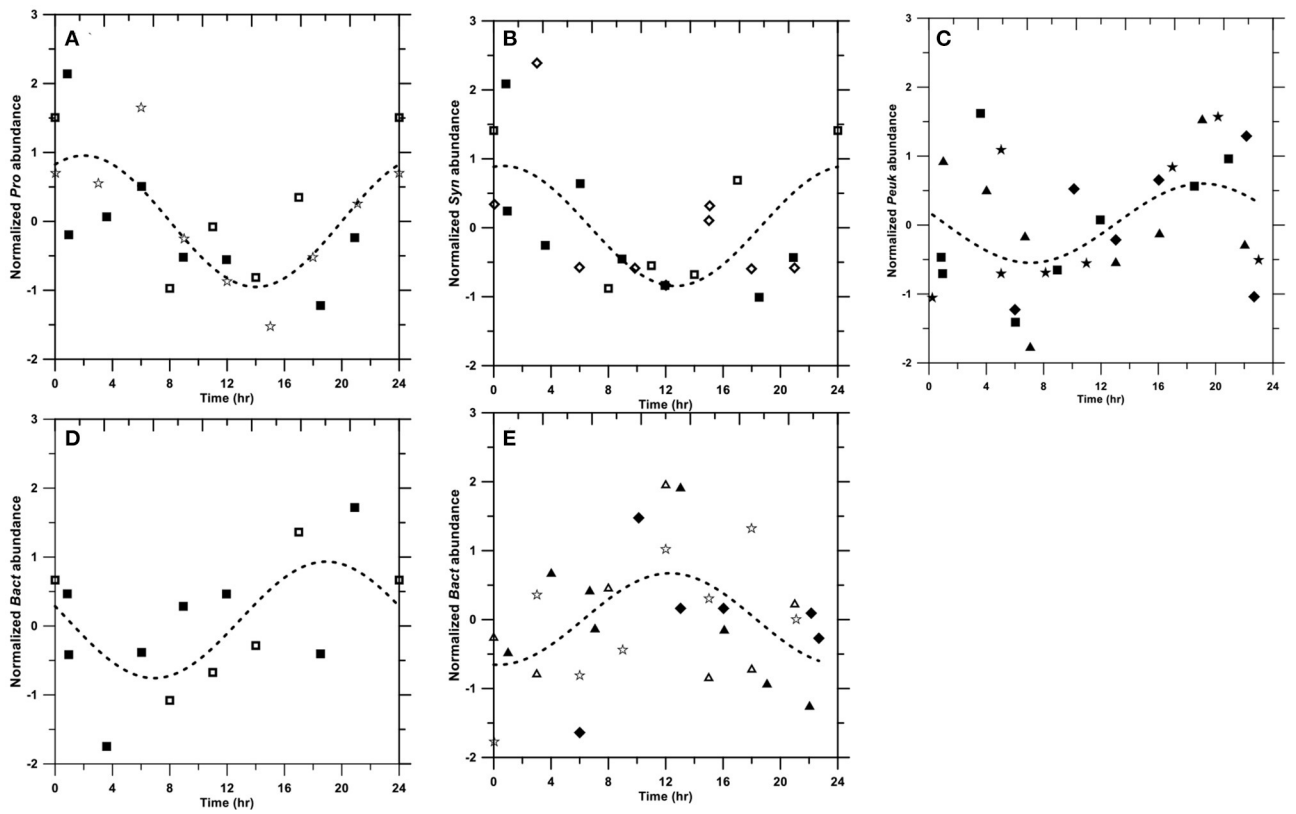

FIGURE 3 | Diel patterns of *Prochlorococcus* **(A)**, *Synechococcus* **(B)**, picoeukaryotes **(C)**, heterotrophic bacterial night-peak type **(D)**, and heterotrophic bacterial day-peak type **(E)**. Symbols: OR1_1034 (◆); OR1_1103 (◇); OR1_1010 (▲); OR1_1084 (Δ); OR1_944 (■); OR1_1053 (□); OR1_988 (★); and OR1_1060 (☆). The dashed line denotes the fitting curve as $Y = A_o \bullet sin\left(2\pi\left(\frac{X+A_1}{24}\right)\right) + A_2$.

TABLE 2 | Comparison of picophytoplankton abundance in major tropical and subtropical oceans.

Location	*Prochlorococcus* ($\times 10^4$ cells mL^{-1})	*Synechococcus* ($\times 10^3$ cells mL^{-1})	Picoeukaryotes ($\times 10^3$ cells mL^{-1})	References
South China Sea	1.85–9.43	3.14–6.01	1.08–6.18	This study
South China Sea	15–28	<1–100	0.5–15	Liu et al., 2007
North Atlantic	18.3 ± 11.1	9.3 ± 13	1.2 ± 1.9	Buck et al., 1996
North Pacific	17.6 (median)	1.4 (median)	1.0 (median)	Campbell et al., 1997
Global	12.7 ± 4.4	7.7 ± 0.8	1.7 ± 0.1	Agusti et al., 2019

reestablished in the following warm seasons (Olson et al., 1990; Li, 1995). The vertical distribution of heterotrophic bacterial abundance appeared high at the surface and gradually decreased with depth (**Supplementary Figure 10**), corresponding to the DOC concentrations (**Supplementary Figure 5**). Heterotrophic bacteria accompanied with total DOC were also reported in the Mediterranean Sea, indicating a tight coupling with photosynthetically released DOC (Gasol et al., 1998). Overall, the vertical distributions of picoplankton were affected by the depths associated with surrounding environmental parameters (including light, temperature, and substrate/nutrient supply).

Seasonal Variability in Picoplankton

Seasonal variation in picophytoplankton communities has been recorded in tropical and subtropical oceans (Campbell et al., 1997; Durand et al., 2001; Liu et al., 2007). Our results showed that *Prochlorococcus* abundance appeared low in the winter and higher with insignificant differences among the warm seasons. *Synechococcus* abundance peaked in the winter and decreased but was relatively constant in the warm seasons. Picoeukaryotes abundance did not have a clear seasonal pattern with exceptionally high values in the winter of 2011. These observations were slightly different from those in the report at the subtropical Bermuda Atlantic Time-Series Study (BATS) station, where *Prochlorococcus* abundance peaked in the summer and fall and had low cell numbers in the winter, while *Synechococcus* and picoeukaryotes abundance peaked during the spring bloom and decreased in the summer (Durand et al., 2001). Compared to a previous survey at the SEATS station, Liu et al. (2007) observed similar seasonal patterns as those of BATS, showing that *Prochlorococcus* peaked in the summer and appeared low in the winter, whereas *Synechococcus* and picoeukaryotes peaked in the winter and decreased in the summer. However, more complicated seasonal patterns were observed at the Hawaiian Ocean Time-Series (HOT) station ALOHA (Campbell et al., 1997). At the HOT station, *Prochlorococcus* showed a minimum abundance in the winter but an unclear seasonal pattern in the warm seasons. *Synechococcus* and picoeukaryotes usually peaked in the winter and early spring. However, such peaks did not appear every year. In this study, we found that the seasonal variation in picophytoplankton at the SEATS station was more similar to that at the HOT station than to previous observations. In summary, picophytoplankton at the SEATS station could be distinguished between warm and cold seasons. This phenomenon could be partially explained by Bunse and Pinhassi (2017), who suggest that the seasonality of picoplankton could become less obvious when approaching the equator. However, the different results from those of previous observations at the SEATS station indicated that the seasonal succession dynamics of the picoplankton community structure in the South China Sea might be more complicated than previously thought.

Heterotrophic bacterial abundance was high in the winter and spring based on a previous study at the SEATS station (Liu et al., 2007). However, we observed an unclear seasonal pattern of heterotrophic bacterial abundance (**Table 1**). Heterotrophic bacterial abundance has been reported to peak in the summer at the BATS station (Carlson and Ducklow, 1996), while high abundance appeared in summer and fall at the HOT station (Campbell et al., 1997). However, undetectable seasonality in heterotrophic bacterial abundance has also been reported in the subtropical Red Sea (Al-Otaibi et al., 2020).

In terms of cell numbers, *Prochlorococcus* was the most abundant picophytoplankton. Our *Prochlorococcus* abundance (depth-averaged mean ranging from 1.85 to 9.43 $\times$ 10^4 cells ml^{-1}) was at the lower end of the tropical and subtropical reports, at 18.3 $\pm$ 11.1 $\times$ 10^4 cells ml^{-1} in the North Atlantic Ocean (Buck et al., 1996) and 17.6 $\times$ 10^4 cells ml^{-1} at the HOT station (**Table 2**, Campbell et al., 1997). *Synechococcus* abundance (depth-averaged mean ranging from 3.14 to 6.01 $\times$ 10^3 cells ml^{-1}), on the other hand, was comparable to 9.3 $\pm$ 13 $\times$ 10^3 and 1.4 $\times$ 10^3 cells ml^{-1} in the North Atlantic and the North Pacific Subtropical Gyre, respectively (**Table 2**, Buck et al., 1996; Campbell et al., 1997). Mann et al. (2002) found that *Prochlorococcus* is inhibited by free copper, whereas *Synechococcus* is resistant to copper. However, whether the low abundance of *Prochlorococcus* at the SEATS station is due to copper toxicity needs further investigation. The abundance of picoeukaryotes (depth-averaged mean ranging from 1.08 to 6.18 $\times$ 10^3 cells ml^{-1}) was at the higher end of the global subtropical and tropical values (1.7 $\pm$ 0.1 $\times$ 10^3 cells ml^{-1}; **Table 2**) (Agusti et al., 2019). The different picophytoplankton community structures reflected biomass carbon composition at the SEATS station.

The integrated biomass of total picophytoplankton ranged from 0.414 to 1.080 g C m^{-2} in this study, which is comparable to previous investigations (Liu et al., 2007). However, the contributions from the three picophytoplankton groups were quite different from the previous study from the same station and other subtropical reports. *Prochlorococcus* has been recognized as the major component of biomass in tropical and subtropical

regions. At the HOT station, *Prochlorococcus* accounted for 72.6 ± 16.6% of the total picophytoplankton biomass, followed by picoeukaryotes (24.2 ± 11.5%) and *Synechococcus* (3.2 ± 1.9%) (Campbell et al., 1997). In the investigation at the STEATS station by Liu et al. (2007), *Prochlorococcus* constituted 70 to 80% of the picophytoplankton biomass in the summer and fall and decreased to less than 40% in the winter, whereas *Synechococcus* became more important in the winter. In our results, picoeukaryotes and *Prochlorococcus* displayed equal importance in the warm seasons (accounting for 48.7 ± 8.6% and 43.3 ± 7.7% of the total picophytoplankton biomass, respectively). Picophytoplankton community dynamics during the winter in the SCS appear complicated. Liu et al. (2007) found a "winter bloom" of *Synechococcus* and picoeukaryotes in 2001 and 2002, respectively. Similar phenomena appeared in this study, with a "winter picoeukaryotes bloom" (88.5 ± 1.2% of picophytoplankton biomass) in 2011 and a "winter *Synechococcus* bloom" (52.6 ± 6.7% of picophytoplankton biomass) in 2013, while *Prochlorococcus* decreased to less than 15% of the total picophytoplankton biomass. The strong winter mixing (deeper MLD) accompanied by more available nutrients could possibly drive the winter bloom of relatively larger-sized groups of picoeukaryotes and *Synechococcus*.

Heterotrophic bacteria had undetectable seasonality in this study. Their abundance of 1.77 to 6.50 × 10^5 cells ml^{-1} was slightly less but still comparable to that in the North Atlantic Ocean (6.59 ± 3.42 × 10^5 cells ml^{-1}) (Buck et al., 1996), the HOT station (7.10 ± 0.16 × 10^5 cells ml^{-1}) (Campbell et al., 1997), and the previous SEATS station (2.5 to 12 × 10^5 cells ml^{-1}) (Liu et al., 2007). The integrated biomass of heterotrophic bacteria generally exceeded that of autotrophic picoplankton (six out of eight; **Figure 2**), ranging from 0.353 to 1.300 g m^{-2}. In contrast, autotrophic picoplankton-exceeding heterotrophic bacteria have been previously reported at the SEATS station (Liu et al., 2007). This was basically due to the choice of bacterial carbon conversion factors. The cellular carbon content of 11 fg $cell^{-1}$ in Liu et al. (2007) led to approximately a half of bacterial biomass compared with a commonly used estimate of 20 fg $cell^{-1}$. In fact, heterotrophic bacteria are more important in terms of biomass in tropical and subtropical oceans than in other oceans. For example, a basin-wide investigation from the equator to 20°N in the North Atlantic Ocean suggested that the overall integrated biomass of heterotrophic bacteria slightly surpassed that of autotrophic picoplankton (Buck et al., 1996).

Diel Variability in Picoplankton

During the eight diel surveys, diel patterns of picoplankton were not clear from an individual data set. Therefore, we transformed the depth-averaged abundance as follows and superimposed it on a 24-h scale.

$$A_{n,t} = (A_t - \overline{A_t}) \cdot \sigma(A_t)^{-1}$$

where $A_{n,t}$ and A_t denote the normalized and original depth-averaged abundance at the time t during a given cruise, respectively; $\overline{A_t}$ denotes the arithmetic mean of the depth-averaged abundance during the given cruise; and $\sigma(A_t)$ denotes the standard deviation of the depth-averaged abundance during the given cruise. After normalization, a non-linear fitting was conducted.

$$Y = A_o \bullet sin\left(2\pi\left(\frac{X + A_1}{24}\right)\right) + A_2$$

where X and Y denote the time in 24 h and the predicted $A_{n,t}$, respectively. A_0, A_1, and A_2 denote fitting coefficients. The results showed that three out of eight cruises for *Synechococcus* peaked at 1 a.m. (**Figure 3B**), followed by *Prochlorococcus* (also three out of eight cruises), peaking at ∼2 a.m. (**Figure 3A**). These diel patterns were similar to those in the equatorial Pacific, where *Synechococcus* peaked at 12 a.m., followed by *Prochlorococcus* peaking at 2 a.m. (Vaulot and Marie, 1999). Our picoeukaryotes (four out of eight cruises), on the other hand, peaked at ∼7 to 8 p.m., which was similar to observations in the equatorial Pacific (Blanchot et al., 1997). In fact, the timing of division from various strains in a given picophytoplankton group could be variable (Jacquet et al., 2001). Generally, phytoplankton tends to photosynthesize and grow during the daytime, followed by division during the night (Durand and Olson, 1998). In addition to intrinsic genetics (Jacquet et al., 2001), the phasing of cell division in natural environments could be regulated by light intensities (Vaulot et al., 1995) and nutrient conditions (Vaulot et al., 1996), possibly causing different diel patterns.

Heterotrophic bacteria exhibited two different diel patterns. The night-peak type had a high abundance at 7 p.m. (**Figure 3D**), whereas the day-peak type exhibited a high abundance at noon (**Figure 3E**). These two opposite diel patterns were also observed in the Mediterranean Sea (Gasol et al., 1998). Bacteria peaking during the daytime are usually subjected to high-bacterial production associated with the release of photosynthetically fixed carbon (Gasol et al., 1998). On the other hand, bacterial abundance peaking at night usually corresponds with picophytoplankton increases (e.g., Lefort and Gasol, 2014).

Although we expected to see diel patterns in picoplankton, many of the cruises in this study did not present a clear 24-h periodicity. Previous studies have also shown a lack of diel periodicity in picoplankton (Jacquet et al., 1998; Lefort and Gasol, 2014). In fact, cell abundance tightly reflects the combination of gain and loss terms. Cell division, as the major gain term, usually exhibits its intrinsic "biological clock"(Johnson et al., 1996). However, the lost terms, including viral lysis, predator grazing, and physical processes, such as disturbance or advection, could play an important role in shaping the diel patterns. Viral lysis may account for daily losses of up to 20% of picoplankton (Suttle, 1994; Mojica et al., 2016), while grazing could be equivalent or more important than cell lysis (Pernthaler, 2005). Sherr et al. (1992) found preferential protozoa grazing on dividing prokaryotes. Peters (1994) further estimated that the protozoan ingestion rate increases by ∼70% when prey is divided at 100%. Moreover, the diel pattern of heterotrophic nanoflagellates (HNF) directly affects picoplankton diel cycles. HNF has been observed as high-grazing rates during either day (Ng and Liu, 2016) or night (Christoffersen, 1994). Physical processes

TABLE 3 | A linear relationship between picoplankton biomass and environmental variables of sea surface temperature (SST) and mixed layer depth (MLD).

	Picoplankton biomass (mg C m^{-2}; *Y*)			
X	**Slope ± SD**	**Intercept ± SD**	**R^2**	***p*-value**
Prochlorococcus				
SST	33.487 ± 8.579	−739.33 ± 238.11	0.7175	0.0080**
MLD	−4.3134 ± 1.3513	329.21 ± 46.80	0.6293	0.0188*
Synechococcus[a]				
SST	−5.3736 ± 1.1087	192.88 ± 31.08	0.8245	0.0047**
MLD	0.4938 ± 0.2767	27.258 ± 9.063	0.3892	0.1343
Picoeukaryotes				
SST	−117.57 ± 31.73	3614.24 ± 880.58	0.6959	0.0100*
MLD	15.687 ± 4.647	−155.07 ± 160.95	0.6551	0.0149*
ΣPicophytoplankton				
SST	−139.54 ± 26.21	4520.10 ± 727.37	0.8253	0.0018**
MLD	18.085 ± 4.456	63.89 ± 154.33	0.7330	0.0067**
Bacteria				
SST	−64.989 ± 71.100	2706.74 ± 1973.49	0.1222	0.3959
MLD	13.269 ± 8.921	473.34 ± 308.96	0.2694	0.1875

*, $p < 0.05$; **, $p < 0.01$.
[a]*Linear regression excluded the extremely high Synechococcus abundance in the winter of 2013.*

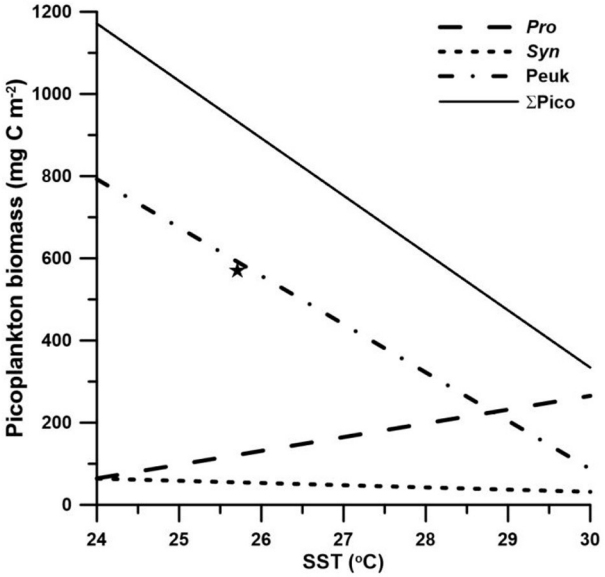

FIGURE 4 | Linear regressions between the sea surface temperature (SST) and picoplankton biomass. The star (★) denoted the winter bloom of *Synechococcus* in 2013, which is excluded from the linear regression model.

could have both positive and negative effects on picoplankton abundance, essentially due to the mixing of different water masses. Generally, mixing and turbulence increase nutrient fluxes for picoplankton growth. However, Peters and Gross (1994) observed that turbulence enhanced protozoan grazing rates on picoplankton-sized particles. Lefort and Gasol (2014) further suggested that a climate event with increased turbulence potentially disrupts the diel pattern of picoplankton. All loss terms may shape, weaken, or even dissipate the diel patterns.

Whether picoplankton displayed diel patterns, large diel variabilities were clearly observed. Picoeukaryotes had the largest CV% at 30.9 ± 19.2%, followed by *Synechococcus* (26.6 ± 8.5%), *Prochlorococcus* (22. ± 6.2%), and heterotrophic bacteria (15.7 ± 9.1%). The results were similar to, although slightly higher than, those in the Mediterranean, which also showed the highest CV% of picoeukaryotes (30%), followed by *Synechococcus* (16.5%), *Prochlorococcus* (16.5%), and heterotrophic bacteria (10.5%) (Lefort and Gasol, 2014). However, the maximum/minimum factor for picophytoplankton, ranging from 1.9 to 2.8, is apparently larger than that of ∼1.5 in the equatorial Pacific (André et al., 1999).

Environmental Controls on Picoplankton Community Structure

Prochlorococcus has usually been observed in high temperature and low-nutrient waters, while *Synechococcus* and picoeukaryotes are frequently dominant in relatively low-temperature waters with higher nutrient concentrations (Partensky et al., 1999). Among the factors that may regulate picoplankton distribution, temperature and nutrient concentration have been recognized to potentially affect picoplankton community size structure (Morán et al., 2010; Marañón et al., 2012). Morán et al. (2010) suggested that a temperature rise could lead to a shift toward smaller primary producers. From a geographical point of view, the contribution of picophytoplankton to total phytoplankton biomass increases when moving from temperate regions to the equator (Marañón et al., 2001). However, Marañón et al. (2012) suggested that temperature is independent of the picoplankton community structure. On the other hand, nutrient availability controls the partitioning of biomass between different picoplankton groups. A geographical distribution where a higher fraction of picoplankton biomass appeared in oligotrophic oceans than in coastal-nutrient-replete waters supports the resource control hypothesis (Marañón et al., 2001). We found that the contribution of picophytoplankton to total phytoplankton biomass appeared to not be significantly affected by temperature or nutrient supply (represented as the MLD). The MLD has long been considered an indicator of the nutrient supply and was used for the estimate of phytoplankton growth (e.g., Sverdrup, 1953; Yentsch, 1990). Although temperature and nutrient supply hypotheses were rejected in this study, we observed that the sea surface temperature (SST) and the MLD could both well predict the seasonal fluctuations in picophytoplankton biomass (**Table 3**), with better correlations with SST (**Table 3**; **Figure 4**). Unfortunately, none of the SST or MLD presented suitable predictions for heterotrophic bacterial biomass. *Prochlorococcus* biomass was positively correlated with SST ($p < 0.01$) and negatively correlated with MLD ($p < 0.05$). On the other hand, *Synechococcus* biomass was negatively correlated with SST ($p < 0.01$). Picoeukaryotes were similar to *Synechococcus*, showing a negative correlation with SST and a positive correlation with MLD (both $p < 0.05$). Total picophytoplankton biomass behaved as larger-size

groups of picoeukaryotes and *Synechococcus*, showing a negative correlation with SST and a positive correlation with MLD (both $p < 0.01$). The positive correlation with temperature and negative correlation with nutrient supply in *Prochlorococcus* biomass were consistent with global regressions in tropical and subtropical oceans (Agusti et al., 2019). However, the negative correlation between temperature and *Synechococcus* (and picoeukaryotes) was opposite to the projection by Agusti et al. (2019). In fact, the temperature usually changes concurrently with nutrient availability. The higher temperature, the less nutrients are available. Boyd et al. (2010) summarized that nutrient supply is likely to be the most important factor controlling the abundance and distribution of *Synechococcus*. In this study, the SST here in the regression possibly reflected the index of nutrient supply rather than the temperature effect itself. In brief, inorganic nutrient supply and temperature (for *Prochlorococcus*) were the major factors controlling picophytoplankton distribution at the SEATS station in the South China Sea. Since the nutrient supply is likely the controlling factor in the distribution of picophytoplankton biomass, other sources of nutrients should be considered. Previous studies showed that large-scale eddies and internal waves could bring extra nutrients to the surface and enhance phytoplankton growth in the SCS (Li et al., 2018; Shih et al., 2020). The SST and the MLD were both demonstrated to appropriately predict the distribution of picophytoplankton. This is the first time showing a good relationship between SST and the depth-integrated picophytoplankton biomass in the South China Sea (coefficient of determination, $R^2 = 0.83$). The models projected that *Prochlorococcus* became dominant when the SST reaches 28.8°C or more, while picoeukaryotes dominated in the rest of the temperature regimes (**Figure 4**). It is widely known that picophytoplankton contributes a significant fraction of primary production and carbon exports in the open ocean (Richardson and Jackson, 2007). In the future warmer SCS, *Prochlorococcus* could become more and more important regulating the carbon cycles. With small diel variabilities and ease to obtain from the satellite, the SST was a powerful parameter to quickly predict picophytoplankton biomass, as well as the abundance, at the SEATS station in the South China Sea.

CONCLUSION

Through eight diel surveys in all four seasons, we improved knowledge of the diel and seasonal variability, as well as vertical distribution, in the picoplankton community at the SEATS station in the South China Sea. The results displayed different vertical distributions in the picoplanktonic groups. *Prochlorococcus* and picoeukaryotes tended to accumulate at subsurface depths in the warm seasons, while *Synechococcus* and heterotrophic bacteria were abundant at the surface and decreased with depth. Vertical segregation in the warm seasons was broken in the winter, showing high cell numbers at the surface for all picoplanktonic groups. Light, substrate, and physical mixing seemed to jointly regulate the vertical distribution of picoplankton. Although not all 24-h periodicities were observed in this study, we did observe some clear diel cycles in picoplankton abundance. These observed diel variabilities showed that picoeukaryotes peaked at ∼7 to 8 p.m., followed by *Synechococcus* (1 a.m.) and *Prochlorococcus* (2 a.m.). Heterotrophic bacteria exhibited two types of diel cycles. The night-peak group peaked at 7 p.m., while the day-peak group peaked at noon. Seasonality in picophytoplankton was also clearly observed. *Prochlorococcus* abundance was low in the winter, while *Synechococcus* and picoeukaryotes abundance peaked in the winter. However, seasonality in heterotrophic bacteria was undetectable. The inorganic nutrient supply seemed to be the major controlling factor in picophytoplankton biomass. The sea surface temperature (SST) and mixed layer depth (MLD) both demonstrated good predictions of the variation in picophytoplankton biomass, as well as abundance. The regression model predicted that picoeukaryotes would be generally the most abundant picophytoplankton in terms of biomass. Once the temperature reached 28.8°C, *Prochlorococcus* would become the dominant picoautotrophs. In the future warmer ocean, *Prochlorococcus* could become more and more important in regulating carbon exports. The strong correlation between the SST and picophytoplankton biomass indicated the potential use of the satellite SST to trace the pelagic picophytoplankton biomass in the northern South China Sea. Our picoplankton abundance results showed, to some extent, differences from those in a previous report (Liu et al., 2007), indicating that picoplankton community dynamics at the SEATS station might be more complicated than we previously thought, and further continuous investigations will improve our understanding of the tropical South China Sea.

DATA AVAILABILITY STATEMENT

Data used in this study are available upon the request to corresponding authors.

AUTHOR CONTRIBUTIONS

F-KS designed and managed the project. T-YC wrote the manuscript. T-YC, C-CL, J-HT, and C-YK analyzed data. All authors reviewed and approved the final manuscript.

FUNDING

Funding was provided by the Ministry of Science and Technology of Taiwan (Grants #109-2611-M-019-012-) awarded to T-YC.

ACKNOWLEDGMENTS

We deeply thank the crew of the R/V Ocean Researcher I for shipboard operations and water sampling.

SUPPLEMENTARY MATERIAL

The Supplementary Material for this article can be found online at: https://www.frontiersin.org/articles/10.3389/fmars.2021.732017/full#supplementary-material

REFERENCES

Agusti, S., Lubián, L. M., Moreno-Ostos, E., Estrada, M., and Duarte, C. M. (2019). Projected changes in photosynthetic picoplankton in a warmer subtropical ocean. *Front. Mar. Sci.* 5:506. doi: 10.3389/fmars.2018.00506

Alford, M. H., Lien, R.-C., Simmons, H., Klymak, J., Ramo, S., Yang, Y. J., et al. (2010). Speed and evolution of non-linear internal waves transiting the South China Sea. *J. Phys. Oceanogr.* 40, 1338–1355. doi: 10.1175/2010JPO4388.1

Al-Otaibi, N., Huete-Stauffer, T. M., Calleja, M. L., Irigoien, X., and Morán, X. (2020). Seasonal variability and vertical distribution of autotrophic and heterotrophic picoplankton in the Central Red Sea. *PeerJ.* 8:e8612. doi: 10.7717/peerj.8612

André, J.-M., Navarette, C., Blanchot, J., and Radenac, M.-H. (1999). Picophytoplankton dynamics in the equatorial Pacific: growth and grazing rates from cytometric counts. *J. Geophys. Res.* 104, 3369–3380. doi: 10.1029/1998JC900005

Azam, F., Fenchel, T., Field, J. G., Gray, J. S., Mayer-Reil, L. A., and Thingstad, F. (1983). The ecological role of water-columnmicrobes in the sea. *Mar. Ecol. Prog. Ser.* 10, 257–263. doi: 10.3354/meps010257

Azam, F., and Malfatti, F. (2007). Microbial structuring of marine ecosystems. *Nat. Rev. Microbiol.* 5, 782–791. doi: 10.1038/nrmicro1747

Biller, S. J., Berube, P. M., Lindell, D., and Chisholm, S. W. (2015). *Prochlorococcus*: the structure and function of collective diversity. *Nat. Rev. Microbiol.* 13, 13–27. doi: 10.1038/nrmicro3378

Blanchot, J., Andrb, J.-M., Navarette, C., and Neveux, J. (1997). Picophytoplankton dynamics in the equatorial Pacific: diel cycling from flow-cytometer observations. *C. R. Acad. Sci.* 320, 925–931. doi: 10.1016/S0764-4469(97)80878-5

Boelen, P., De Boer, M. K., Kraay, G. W., Veldhuis, M. J. W., and Buma, A. G. J. (2000). UVBR-induced DNA damage in natural marine picoplankton assemblages in the tropical Atlantic Ocean. *Mar. Ecol. Prog. Ser.* 193, 1–9. doi: 10.3354/meps193001

Boyd, P. W., Strzepek, R., Fu, F., and Hutchins, D. A. (2010). Environmental control of open-ocean phytoplankton groups: now and in the future. *Limnol. Oceanogr.* 55, 1353–1376. doi: 10.4319/lo.2010.55.3.1353

Buck, K. R., Chavez, F. P., and Campbell, L. (1996). Basin-wide distributions of living carbon components and the inverted trophic pyramid of the central gyre of the North Atlantic Ocean, summer 1993. *Aquat. Microb. Ecol.* 10, 283–298. doi: 10.3354/ame010283

Buitenhuis, E. T., Li, W. K. W., Vaulot, D., Lomas, M. W., Landry, M. R., Partensky, F., et al. (2012). Picophytoplankton biomass distribution in the global ocean. *Earth Syst. Sci. Data* 4, 37–46. doi: 10.5194/essd-4-37-2012

Bunse, C., and Pinhassi, J. (2017). Marine bacterioplankton seasonal succession dynamics. *Trends Microbiol.* 25, 494–505. doi: 10.1016/j.tim.2016.12.013

Campbell, L., Liu, H., Nolla, H. A., and Vaulot, D. (1997). Annual variability of phytoplankton and bacteria in the subtropical North Pacific Ocean at Station ALOHA during the 1991-1994 ENSO event. *Deep-Sea Res. I* 44, 167–192. doi: 10.1016/S0967-0637(96)00102-1

Campbell, L., Nolla, H. A., and Vaulot, D. (1994). The importance of *Prochlorococcus* to community structure in the central North Pacific Ocean. *Limnol. Oceanogr.* 39, 954–961. doi: 10.4319/lo.1994.39.4.0954

Carlson, C. A., and Ducklow, H. W. (1996). Growth of bacterioplankton and consumption of dissolved organic ncarbon in the Sargasso Sea. *Aquat. Microb. Ecol.* 10, 69–85. doi: 10.3354/ame010069

Chen, T.-Y., Lai, C.-C., Shiah, F.-K., and Gong, G.-C. (2020). Dissolved and particulate primary production and subsequent bacterial C consumption in the southern East China Sea. *Front. Mar. Sci.* 7:713. doi: 10.3389/fmars.2020.00713

Chen, T.-Y., Tai, J.-H., Ko, C.-Y., Hsieh, C.-H., Chen, C.-C., Jiao, N., et al. (2016). Nutrient pulses driven by internal solitary waves enhance heterotrophic bacterial growth in the South China Sea. *Environ. Microbiol.* 18, 4312–4323. doi: 10.1111/1462-2920.13273

Christoffersen, K. (1994). Variations of feeding activities of heterotrophic nanoflagellates on picoplankton. *Mar. Microb. Food Webs* 8, 111–123.

Dandonneau, Y., and Neveux, J. (1997). Diel variations of *in vivo* fluorescence in the eastern equatorial Pacific: an unvarying pattern. *Deep-Sea Res. II* 44, 1869–1880. doi: 10.1016/S0967-0645(97)00020-9

Durand, M. D., and Olson, R. J. (1998). Diel patterns in optical properties of the chlorophyte *Nannochloris* sp.: relating individual-cell to bulk measurements. *Limnol. Oceanogr.* 43, 1107–1118. doi: 10.4319/lo.1998.43.6.1107

Durand, M. D., Olson, R. J., and Chisholm, S. W. (2001). Phytoplankton population dynamics at the Bermuda Atlantic Time-series station in the Sargasso Sea. *Deep-Sea Res. II* 48, 1983–2003. doi: 10.1016/S0967-0645(00)00166-1

Garrison, D. L., Gowing, M. M., Hughes, M. P., Campbell, L., Caron, D. A., Dennett, M. R., et al. (2000). Microbial food web structure in the Arabian Sea: a US JGOFS study. *Deep-Sea Res. II* 47, 1387–1422. doi: 10.1016/S0967-0645(99)00148-4

Gasol, J. M., Doval, M. D., Pinhassi, J., Calderón-Paz, J. I., Guixa-Boixareu, N., Vaqu,é, D., et al. (1998). Diel variations in bacterial heterotrophic activity and growth in the northwestern Mediterranean Sea. *Mar. Ecol. Prog. Ser.* 164, 107–124. doi: 10.3354/meps164107

Iversen, K. R., and Seuthe, L. (2011). Seasonal microbial processes in a high-latitude fjord (Kongsfjorden, Svalbard): I. Heterotrophic bacteria, picoplankton and nanoflagellates. *Polar Biol.* 34, 731–749. doi: 10.1007/s00300-010-0929-2

Jacquet, S., Lennon, J.-F., Marie, D., and Vaulot, D. (1998). Picoplankton population dynamics in coastal waters of the northwestern Mediterranean Sea. *Limnol. Oceanogr.* 43, 1916–1931. doi: 10.4319/lo.1998.43.8.1916

Jacquet, S., Partensky, F., Lennon, J.-F., and Vaulot, D. (2001). Diel patterns of growth and division in marine picoplankton in culture. *J. Phycol.* 37, 357–369. doi: 10.1046/j.1529-8817.2001.037003357.x

Johnson, C. H., Golden, S. S., Ishiura, M., and Kondo, T. (1996). Circadian clocks in prokaryotes. *Mol. Microbiol.* 21, 5–11. doi: 10.1046/j.1365-2958.1996.00613.x

Lee, S., and Fuhrman, J. A. (1987). Relationships between biovolume and biomass of naturally derived marine bacterioplankton. *Appl. Environ. Microb.* 53, 1298–1303. doi: 10.1128/aem.53.6.1298-1303.1987

Lefort, T., and Gasol, J. M. (2014). Short-time scale coupling of picoplankton community structure and single-cell heterotrophic activity in winter in coastal NW Mediterranean Sea waters. *J. Plankton Res.* 36, 243–258. doi: 10.1093/plankt/fbt073

Li, D., Chou, W.-C., Shih, Y.-Y., Chen, G.-Y., Chang, Y., Chow, C. H., et al. (2018). Elevated particulate organic carbon export flux induced by internal waves in the oligotrophic northern South China Sea. *Sci. Rep.* 8:2042. doi: 10.1038/s41598-018-20184-9

Li, W. K. W. (1995). Composition of ultraphytoplankton in the central North Atlantic. *Mar. Ecol. Prog. Ser.* 122, 1–8. doi: 10.3354/meps122001

Li, W. K. W., Subba Rao, D. V., Harrison, W. G., Smith, J. C., Cullen, J. J., Irwin, B., et al. (1983). Autotrophic picoplankton in the tropical ocean. *Science* 219, 292–295. doi: 10.1126/science.219.4582.292

Liu, H., Chang, J., Tseng, C.-M., Wen, L.-S., and Liu, K.-K. (2007). Seasonal variability of picoplankton in the Northern South China Sea at the SEATS station. *Deep-Sea Res. II* 54, 1602–1616. doi: 10.1016/j.dsr2.2007.05.004

Mann, E. L., Ahlgren, N., Moffett, J. W., and Chisholm, S. W. (2002). Copper toxicity and cyanobacteria ecology in the Sargasso Sea. *Limnol. Oceanogr.* 47, 976–988. doi: 10.4319/lo.2002.47.4.0976

Marañón, E., Cermeño, P., Latasa, M., and Tadonlék,é, R. D. (2012). Temperature, resources, and phytoplankton size structure in the ocean. *Limnol. Oceanogr.* 57, 1266–1278. doi: 10.4319/lo.2012.57.5.1266

Marañón, E., Holligan, P. M., Barciela, R., González, N., Mouriño, B., Paz,ó, M. J., et al. (2001). Patterns of phytoplankton size structure and productivity in contrasting open-ocean environments. *Mar. Ecol. Prog. Ser.* 216, 43–56. doi: 10.3354/meps216043

Marie, D., Partensky, F., Vaulot, D., and Brussaard, C. (1999). Enumeration of phytoplankton, bacteria, and viruses in marine samples. *Curr. Protocols Cytometr.* 10:1111s10. doi: 10.1002/0471142956.cy1111s10

Mojica, K. D. A., Huisman, J., Wilhelm, S. W., and Brussaard, C. P. D. (2016). Latitudinal variation in virus-induced mortality of phytoplankton across the North Atlantic Ocean. *ISME J.* 10, 500–513. doi: 10.1038/ismej.2015.130

Morán, X. (2007). Annual cycle of picophytoplankton photosynthesis and growth rates in a temperate coastal ecosystem: a major contribution to carbon fluxes. *Aquat. Microb. Ecol.* 49, 267–279. doi: 10.3354/ame01151

Morán, X.,a,.G., López-Urrutia, A., Calvo-Díaz, A., and Li, W.K.W. (2010). Increasing importance of small phytoplankton in a warmer ocean. *Global Change Biol.* 16, 1137–1144. doi: 10.1111/j.1365-2486.2009.01960.x

Morel, A., Ahn, Y.-H., Partensky, F., Vaulot, D., and Claustre, H. (1993). *Prochlorococcus* and *Synechococcus*: a comparative study of their optical properties in relation to their size and pigmentation. *J. Mar. Res.* 51, 617–649. doi: 10.1357/0022240933223963

Moum, J., Caldwell, D. R., and Paulson, C. A. (1989). Mixing in the equatorial surface layer and thermocline. *J. Geophys. Res.* 94, 2005–2021. doi: 10.1029/JC094iC02p02005

Neveux, J., Dupouy, C., Blanchot, J., Le Bouteiller, A., Landry, M. R., and Brown, S. L. (2003). Diel dynamics of chlorophylls in high-nutrient, low-chlorophyll waters of the equatorial Pacific (180°): interactions of growth, grazing, physiological responses, and mixing. *J. Geophys. Res.* 108:8140. doi: 10.1029/2000JC000747

Ng, W. H., and Liu, H. (2016). Diel periodicity of grazing by heterotrophic nanoflagellates influenced by prey cell properties and intrinsic grazing rhythm. *J. Plankton Res.* 38, 636–651. doi: 10.1093/plankt/fbw014

Olson, R. J., Chisholm, S. W., Zettler, E. R., Altabet, M. A., and Dusenberry, J. A. (1990). Spatial and temporal distributions of prochlorophyte picoplankton in the North Atlantic Ocean. *Deep-Sea Res.* 37, 1033–1051. doi: 10.1016/0198-0149(90)90109-9

Parsons, T. R., Maita, Y., and Lalli, C. M. (1984). *A Manual of Chemical and Biological Methods for Seawater Analysis.* New York, NY: Pergamon Press.

Partensky, F., Blanchot, J., and Vaulot, D. (1999). Differential distribution and ecology of *Prochlorococcus* and *Synechococcus* in oceanic waters: a review. *Bull. Inst. Oceanogr.* 19, 457–475.

Partensky, F., Hoepffner, N., Li, W. K. W., Ulloa, O., and Vaulot, D. (1993). Photoacclimation of *Prochlorococcus* sp. *(Prochlorophyta)* strains isolated from the North Atlantic and the Mediterranean Sea. *Plant Physiol.* 101, 285–296. doi: 10.1104/pp.101.1.285

Pernthaler, J. (2005). Predation on prokaryotes in the water column and its ecological implications. *Nat. Rev. Microbiol.* 3, 537–546. doi: 10.1038/nrmicro1180

Peters, F. (1994). Prediction of planktonic protistan grazing rates. *Limnol. Oceanogr.* 39, 195–206. doi: 10.4319/lo.1994.39.1.0195

Peters, F., and Gross, T. (1994). Increased grazing rates of microplankton in response to small-scale turbulence. *Mar. Ecol. Prog. Ser.* 115, 299–307. doi: 10.3354/meps115299

Richardson, T. L. (2017). Mechanisms and pathways of small-phytoplankton export from the surface ocean. *Ann. Rev. Mar. Sci.* 11:18. doi: 10.1146/annurev-marine-121916-063627

Richardson, T. L., and Jackson, G. A. (2007). Small phytoplankton and carbon export from the surface ocean. *Science* 315, 838–840. doi: 10.1126/science.1133471

Shaw, P.-T., and Chao, S.-Y. (1994). Surface circulation in the South China Sea. *Deep-Sea Res. I* 41, 1663–1683. doi: 10.1016/0967-0637(94)90067-1

Sherr, B. F., Sherr, E. B., and Mcdaniel, J. (1992). Effect of protistan grazing on the frequency of dividing cells in bacterioplankton assemblages. *Appl. Environ. Microb.* 58, 2381–2385. doi: 10.1128/aem.58.8.2381-2385.1992

Shih, Y.-Y., Chin-Chang, H., Tuo, S.-H., Shao, H.-J., Chow, C. H., Muller, F. L. L., et al. (2020). The impact of eddies on nutrient supply, diatom biomass and carbon export in the northern South China Sea. *Front. Earth Sci.* 8:537332. doi: 10.3389/feart.2020.537332

Suttle, C. A. (1994). The significance of viruses to mortality in aquatic microbial communities. *Microbial Ecol.* 28, 237–243. doi: 10.1007/BF00166813

Sverdrup, H. U. (1953). On conditions for the vernal blooming of phytoplankton. *ICES J. Mar. Sci.* 18, 287–295. doi: 10.1093/icesjms/18.3.287

Ting, C. S., Rocap, G., King, J., and Chisholm, S. W. (2002). Cyanobacterial photosynthesis in the oceans: the origins and significance of divergent light-harvesting strategies. *Trends Microbiol.* 10, 134–142. doi: 10.1016/S0966-842X(02)02319-3

Vaulot, D., Lebot, N., Marie, D., and Fukai, E. (1996). Effect of phosphorus on the *Synechococcus* cell cycle in surface Mediterranean waters during summer. *Appl. Environ. Microb.* 62, 2527–2533. doi: 10.1128/aem.62.7.2527-2533.1996

Vaulot, D., and Marie, D. (1999). Diel variability of photosynthetic picoplankton in the equatorial Pacific. *J. Geophys. Res.* 104, 3297–3310. doi: 10.1029/98JC01333

Vaulot, D., Marie, D., Olson, R. J., and Chisholm, S. W. (1995). Growth of *Prochlorococcus*, a photosynthetic prokaryote, in the equatorial Pacific Ocean. *Science* 268, 1480–1482. doi: 10.1126/science.268.5216.1480

Wong, G. T. F., Ku, T.-L., Mulholland, M., Tseng, C.-M., and Wang, D.-P. (2007). The SouthEast Asian Time-series Study (SEATS) and the biogeochemistry of the South China Sea—an overview. *Deep-Sea Res. II* 54, 1434–1447. doi: 10.1016/j.dsr2.2007.05.012

Wurl, O. (2009). *Practical Guidelines for the Analysis of Seawater*. Boca Raton, FL: CRC Press.

Xie, Y., Laws, E., Yang, L., and Huang, B. (2018). Diel patterns of variable fluorescence and carbon fixation of picocyanobacteria *Prochlorococcus*-dominated phytoplankton in the South China Sea basin. *Front. Mar. Sci.* 9:1589. doi: 10.3389/fmicb.2018.01589

Yentsch, C. S. (1990). Estimates of 'new production' in the Mid-North Atlantic. *J. Plankton Res.* 12, 717–734. doi: 10.1093/plankt/12.4.717

Zubkov, M. V., Sleigh, M. A., Tarran, G. A., Burkill, P. H., and Leaky, R. J. G. (1998). Picoplanktonic community structure on an Atlantic transect from 50°N to 50°S. *Deep-Sea Res. I* 45, 1339–1355. doi: 10.1016/S0967-0637(98)00015-6

Conflict of Interest: The authors declare that the research was conducted in the absence of any commercial or financial relationships that could be construed as a potential conflict of interest.

Publisher's Note: All claims expressed in this article are solely those of the authors and do not necessarily represent those of their affiliated organizations, or those of the publisher, the editors and the reviewers. Any product that may be evaluated in this article, or claim that may be made by its manufacturer, is not guaranteed or endorsed by the publisher.

frontiers in Marine Science

ORIGINAL RESEARCH
published: 11 November 2021
doi: 10.3389/fmars.2021.717685

A Unique Diel Pattern in Carbonate Chemistry in the Seagrass Meadows of Dongsha Island: The Enhancement of Metabolic Carbonate Dissolution in a Semienclosed Lagoon

Wen-Chen Chou[1,2], Lan-Feng Fan[1], Chang-Chang Yang[1], Ying-Hsuan Chen[1], Chin-Chang Hung[3], Wei-Jen Huang[3], Yung-Yen Shih[3,4], Keryea Soong[3], Hsiao-Chun Tseng[1], Gwo-Ching Gong[1,2], Hung-Yu Chen[5] and Cheng-Kuan Su[6]*

[1] Institute of Marine Environment and Ecology, National Taiwan Ocean University, Keelung, Taiwan, [2] Center of Excellence for the Oceans, National Taiwan Ocean University, Keelung, Taiwan, [3] Department of Oceanography, National Sun Yat-sen University, Kaohsiung, Taiwan, [4] Department of Applied Science, R.O.C. Naval Academy, Kaohsiung, Taiwan, [5] Department of Marine Environmental Informatics, National Taiwan Ocean University, Keelung, Taiwan, [6] Department of Chemistry, National Chung Hsing University, Taichung, Taiwan

OPEN ACCESS

Edited by:
Christian Grenz,
UMR 7294 Institut Méditerranéen d'océanographie (MIO), France

Reviewed by:
Kimberlee Baldry,
University of Tasmania, Australia
Jennifer Joan Verduin,
Murdoch University, Australia

***Correspondence:**
Wen-Chen Chou
wcchou@mail.ntou.edu.tw

Specialty section:
This article was submitted to Marine Ecosystem Ecology, a section of the journal Frontiers in Marine Science

Received: 31 May 2021
Accepted: 11 October 2021
Published: 11 November 2021

Citation:
Chou W-C, Fan L-F, Yang C-C, Chen Y-H, Hung C-C, Huang W-J, Shih Y-Y, Soong K, Tseng H-C, Gong G-C, Chen H-Y and Su C-K (2021) A Unique Diel Pattern in Carbonate Chemistry in the Seagrass Meadows of Dongsha Island: The Enhancement of Metabolic Carbonate Dissolution in a Semienclosed Lagoon. Front. Mar. Sci. 8:717685. doi: 10.3389/fmars.2021.717685

In contrast to other seagrass meadows where seawater carbonate chemistry generally shows strong diel variations with higher pH but lower partial pressure of CO_2 (pCO_2) during the daytime and lower pH but higher pCO_2 during nighttime due to the alternation in photosynthesis and respiration, the seagrass meadows of the inner lagoon (IL) on Dongsha Island had a unique diel pattern with extremely high pH and low pCO_2 across a diel cycle. We suggest that this distinct diel pattern in pH and pCO_2 could be associated with the enhancement of total alkalinity (TA) production coupled to carbonate sediment dissolution in a semienclosed lagoon. The confinement of the IL may hamper water exchange and seagrass detritus export to the adjacent open ocean, which may result in higher organic matter loading to the sediments, and longer residence time of the water in the IL, accompanied by microbial respiration (both aerobic and anaerobic) that may reduce carbonate saturation level to drive carbonate dissolution and thus TA elevation, thereby forming such a unique diel pattern in carbonate chemistry. This finding further highlights the importance of considering TA production through metabolic carbonate dissolution when evaluating the potential of coastal blue carbon ecosystems to buffer ocean acidification and to absorb atmospheric CO_2, in particular in a semienclosed setting.

Keywords: alkalinity production, carbonate dissolution, seagrass, Dongsha Island, blue carbon, ocean acidification

INTRODUCTION

As one of the most productive ecosystems on Earth, seagrass meadows have been recognized for their important role in "blue carbon" storage (Duarte et al., 2010; Fourqurean et al., 2012). In addition to the significant carbon sequestration potential of seagrass meadows, previous studies have shown that the high level of seagrass primary productivity may alter seawater carbonate

chemistry by taking up a large amount of carbon dioxide (Frankignoulle and Distèche, 1984; Gattuso et al., 1998), and some recent studies have further proposed that seagrass meadows have the potential to mitigate ocean acidification (OA) induced by rising atmospheric CO_2 (Manzello et al., 2012; Unsworth et al., 2012; Pacella et al., 2018).

Carbonate chemistry dynamics in the water column of seagrass meadows is well known to be driven by a variety of metabolic activities, including plant photosynthesis/respiration (Gattuso et al., 1998; Semesi et al., 2009), carbonate formation/dissolution (Barrón et al., 2006; Burdige et al., 2008; Howard et al., 2018; Saderne et al., 2019b), benthic metabolism (Berg et al., 2019), and hydrodynamic processes (Ruesink et al., 2015; Baldry et al., 2020). As a result, the carbonate system in the overlying water column of seagrass meadows generally shows large variabilities at diel and tidal time scales as well as seasonal variations (Frankignoulle and Distèche, 1984; Waldbusser and Salisbury, 2014; Cyronak et al., 2018; Saderne et al., 2019a). In fact, several *in situ* investigations have revealed conflicting evidence as to whether seagrass meadows can buffer against OA. For instance, Challener et al. (2016) found significant diel and seasonal variability in seawater pH and the saturation state of aragonite (Ω_a) in a Florida seagrass meadow; the high pH and Ω_a values, which would alleviate OA, were observed during the daytime/growing season due to dissolved inorganic carbon (DIC) uptake, while the low pH and Ω_a values, which would exacerbate OA, occurred during the nighttime/decay season due to DIC release. Furthermore, Hendriks et al. (2014) also reported diel pH changes in Mediterranean seagrass meadows, where the pH during 47% of the observation time was lower than the source seawater pH, suggesting a certain period of time when the seagrass meadows could not mitigate OA but exacerbated OA. These surveys clearly demonstrate that the OA buffering potential of seagrass meadows may have considerable temporal variability.

Our previous study documented the divergent behaviors in carbonate chemistry in two hydrodynamically contrasting seagrass meadows at Dongsha Island in the northern South China Sea (NSCS) during a 6-day survey in August 2015 (**Figure 1**), in which higher pH and total alkalinity (TA) but lower partial pressure of CO_2 (pCO_2) were observed in the semi-enclosed inner lagoon (IL) than on the open north shore, and a unexpected diel pattern with an extremely high pH and pCO_2 across a diurnal cycle was found in the sheltered IL (Chou et al., 2018). In this study, we revisited the same sites to examine whether the divergent behaviors in carbonate chemistry between two sites and the distinct diel pattern in the sheltered IL would occur repeatedly in all seasons. More importantly, recent studies have suggested that sedimentary TA production and export may represent an important but overlooked sink in blue carbon ecosystems (Sippo et al., 2016; Maher et al., 2018; Saderne et al., 2020; Reithmaier et al., 2021). Thus, we also collected sediment cores and porewater samples to examine the potential role of TA production coupled to carbonate dissolution in regulating the carbonate dynamics in the overlying waters. We found that the confinement of the semienclosed IL may provide an ideal scenario for metabolic carbonate dissolution in sediments and thus TA production, including high organic matter (OM) content, low sediment permeability and a long porewater residence time, thus distinguishing the seagrass meadows in the IL on Dongsha Island from those in the open environment.

MATERIALS AND METHODS

Study Sites

The study sites were the same as those in our previous work and have been comprehensively described in Chou et al. (2018). Briefly, the Dongsha Atoll is a circular coral reef located in the NSCS, and Dongsha Island is situated on the western margin of the atoll. A semienclosed IL occupies the central part of Dongsha Island (**Figure 1**). Two hydrodynamically contrasting seagrass meadows were chosen so that their characteristics in seawater carbonate chemistry could be compared. One meadow is located on the northern shore (NS), where water can freely exchange with the adjacent open ocean; the other is situated in the IL, where water exchange is largely hampered due to confinement by a sand barrier. Both sites are multispecies seagrass meadows with the same dominant species (*Thalassia hemprichii* and *Cymodocea rotundata*). Previous study have revealed that the average total seagrass biomass, seagrass cover, canopy height, and shoot density were 949.4 ± 62.1 and 827.4 ± 74.8 (g DW m^{-2}), 81.91 ± 2.13 and 85.14 ± 6.33 (%), 22.36 ± 1.22 and 20.62 ± 1.52 (cm), and 2677 ± 485 and 2920 ± 639 (shoots $m^{-2)}$ on the NS and in the IL, respectively, based on four surveys conducted in April, August, October 2010, and February 2011 (Lee et al., 2015).

Sampling and Carbonate Chemistry Analysis

This study was conducted in four different seasons between 2016 and 2019. During each investigation, a multiparameter sonde (Ocean Seven 316 Plus CTD; Idronaut S.r.I, Brugherio, Italy) attached to a frame was deployed within the seagrass canopy 0.1 m above the sediment at each site to record temperature, salinity, water depth, and dissolved oxygen (DO). The CTD mooring were from January 2 to 7 and from January 7 to 12, 2016 in winter, and from November 16 to 19 and from November 11 to 19 with an interruption between November 14 and 16, 2016 in autumn at the NS and IL sites, respectively. In spring, the CTD mooring was from April 6 to 18, 2018 at the both sites, and with an interruption between April 7 and 10 at the NS site. Furthermore, probably due to the low water level with periods of emersions, a malfunction of the CTD caused a missing of temperature and salinity data at the IL site during the spring deployment. And so, the temperature, salinity and DO data were disregarded for the NS site when water level less than 15 cm. In summer, the CTD mooring was from June 28 to July 3, 2019 at the two sites.

Discrete seawater samplings were conducted in January 2016 (1/1–12; winter), November 2016 (11/11–13; autumn), April 2018 (4/12–18; spring), and June–July 2019 (6/28–7/3; summer). The water depth at the IL and NS sampling sites was approximately 0.5 to 1 m. During these sampling periods, discrete surface seawater samples for carbonate chemistry analysis were

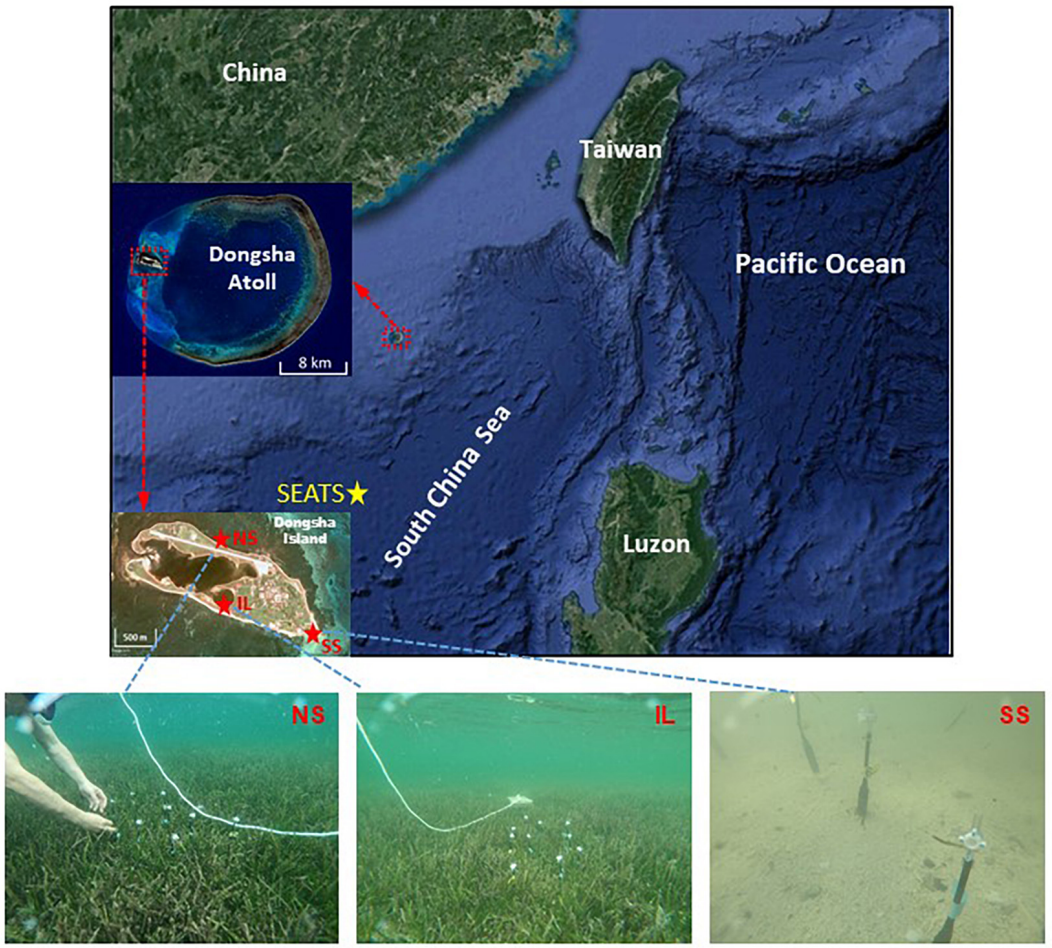

FIGURE 1 | Map showing the locations of Dongsha Atoll, Dongsha Island, and the sampling sites around Dongsha Island (upper panels) and photos showing the porewater sampling sites on the northern shore (NS), in the inner lagoon (IL), and on the southern shore (SS) (lower panels). The yellow asterisk indicating the location of the SouthEast Asian Time-series Study (SEATS).

taken at approximately 6:00 a.m., 12:00 a.m., and 18:00 p.m. every day, using a 9-L Nalgene^{TM} HDPE carboy. The water samples were first passed through a 100-μM nylon mesh, and then transferred into 350-mL pre-cleaned borosilicate bottles thoroughly flushed with sample with extensive overflow (>200 mL). These samples were subsequently injected with 100 μL of saturated $HgCl_2$ solution and stored at room temperature in darkness until they were analyzed in a shore-based laboratory. Measurements of TA, DIC, and pH followed the standard operating procedures described in Dickson et al. (2007), and the procedures were consistent with those used in our previous studies (Chou et al., 2018, 2020). Briefly, DIC and TA were determined using the non-dispersive infrared method on a DIC analyzer (AS-C3, Apollo SciTech) and Gran titration on an automatic TA titrator (AS-ALK2, Apollo SciTech), respectively, and both measurements had accuracies and precisions of 0.2% or better. The pH was spectrophotometrically measured at 25°C with a precision of 0.005 (Chou et al., 2016). The pCO_2 and Ω_a were calculated from the measured DIC and TA data using the Excel macro CO2SYS version 2.1 (Pelletier et al., 2011). Furthermore, in order to examine the effect of temperature on pH and pCO_2 variations, the measured pH at 25°C (pH_{25}) was corrected to *in situ* temperature ($pH_{in\ situ}$), and the pCO_2 was calculated at both *in situ* temperature ($pCO_{2in\ situ}$) and the average temperature of 26.2°C ($TpCO_2$). Similarly, TA and DIC were normalized to the average salinity of 35.6 (NTA (NDIC) = TA (DIC) × 35.6/salinity) to remove the effect of evaporation/precipitation on their variations (Chou et al., 2018).

Sediment Cores and Porewater Samplings and Grain Size, Total Carbon and Nitrogen, and Calcium Ion Analyses

Sediment cores and porewater samples were collected in the summer of 2019 at the IL, NS, and another unvegetated site located on the southern shore (SS; **Figure 1**), which served as a reference site. Because of the difficulty inherent in collecting a core of sandy sediments (Drupp et al., 2016), only one 25-cm

push core from the IL, one 16.5-cm push core from the NS and one 18-cm push core from the SS were collected. The IL, NS, and SS cores were sectioned into 5, 3, and 3 layers ∼5 to 6 cm thick, respectively, which were stored in a −20°C freezer until subsequent analysis. Grain size distribution was determined via wet-sieving through the Wentworth series of screens with mesh openings from 1.0 mm to 63 μm (Folk, 1966). Median grain size was calculated using the GRADISTAT software (Blott and Pye, 2001). Each core section was measured for total carbon (TC) and total nitrogen (TN) contents using an elemental analyzer (Elementar, Vario EL-III, Germany), according to Hung and Gong (2010).

Porewater samples were collected using porewater wells and modified from Falter and Sansone (2000). A total volume of 25 ml porewater was extracted from each well at 2, 4, 6, 8, 12, 16, and 20 cm sediment depths using a Luer-Lok syringe. The sampling procedure and sample preservation of porewater followed the methods in Kindeberg et al. (2020). In addition to carbon chemistry parameters (TA, DIC, and pH), the calcium ion concentration of the porewater was determined using an ICP-MS system (Agilent 7700×, Agilent Technologies) based on that in Su and Ho (2019).

Statistical Analysis

Due to the variance changes across seasons and sites, a Wilcox's robust ANOVA (WR-ANOVA) was chosen to account for heteroscedasticity among habitat groups. Tests between medians were chosen rather than between means, as seagrass habitats displayed skewed carbonate chemistry observations (Baldry et al., 2020). Differences in the medians of pH_{25}, $pH_{in\ situ}$, $pCO_{2\ in\ situ}$, $TpCO_2$, DIC, normalized DIC (NDIC), TA, and normalized TA (NTA) between the IL and NS sites in each season were assessed using a WR-ANOVA that was implemented by the function "med1way" of the R package "WRS2" (Mair and Wilcox, 2020). All statistical tests were performed using R software v4.1.1 (R Core Team, 2021) with a 95% confidence level.

RESULTS

Temporal Variations in Temperature, Salinity, Water Depth, and Dissolved Oxygen

The mean (±SD) temperature during the sampling period was 23.6 ± 1.8, 27.1 ± 0.8, 26.4 ± 2.1, and 31.1 ± 1.1°C at the NS site (red symbols in **Figures 2A–D**), and 21.7 ± 1.4, 26.3 ± 1.1, not determined (n.d.), and 31.4 ± 1.7°C at the IL site (blue symbols in **Figures 2A–D**) in winter, autumn, spring and summer, respectively. Not surprisingly, the highest average temperature was in summer, and the lowest was in winter, and the average temperature in spring and autumn was in the intermediate range. The mean (±SD) salinity was 34.6 ± 0.3, 33.8 ± 0.5, 33.8 ± 0.4, and 33.8 ± 0.5 at the NS site (red symbols in **Figures 2E–H**), and 36.8 ± 0.3, 34.7 ± 0.3, n.d., and 34.9 ± 0.6 at the IL site (blue symbols in **Figures 2E–H**) in winter, autumn, spring, and summer, respectively. The highest average salinity was in winter, but the average salinity did not display remarkable difference among the other seasons at the both sites. Generally, the average salinity at the IL site was higher than the NS site in all seasons. The mean (±SD) water depth was 0.71 ± 0.17, 0.62 ± 0.37, 0.37 ± 0.18, and 1.07 ± 0.29 at the NS site (red symbols in **Figures 2I–L**), and 0.48 ± 0.11, 0.70 ± 0.20, 0.24 ± 0.10, and 0.50 ± 0.20 at the IL site (blue symbols in **Figures 2I–L**) in winter, autumn, spring and summer, respectively. The lowest average water depth was in spring at the both sites, and the highest average water depth was in autumn and summer at the IL and NS sites, respectively. Overall, the water depth showed a larger daily variation range at the NS site than the IL site in all seasons. The mean (±SD) DO saturation during the complete recording period was 93 ± 33, 112 ± 37, 83 ± 42, and 66 ± 33 at the NS site (red symbols in **Figures 2M–P**), and 77 ± 12, 82 ± 13, 69 ± 21, and 59 ± 19 at the IL site (blue symbols in **Figures 2M–P**) in winter, autumn, spring, and summer, respectively. The highest and lowest average DO saturation was in autumn and summer, respectively, at the both sites. Similar to the water depth, DO saturation generally showed a larger daily variation range at the NS site than the IL site in all seasons.

Temporal Variations in Carbonate Chemistry

The seasonal daily variations in pH_{25}, $pH_{in\ situ}$, $pCO_{2\ in\ situ}$, $TpCO_2$, TA, NTA, DIC, and NDIC at the NS and IL sites are shown in **Figure 3**, and the means (±SD) and the statistical analysis results on the difference in the medians of these parameters between the two sites are given in **Table 1**. Despite the notable daily variations in temperature and salinity, the temperature corrected pH (pH_{25}) and pCO_2 ($TpCO_2$) generally displayed the similar daily variation pattern as those in *in situ* condition. Likewise, the salinity normalized NTA and NDIC also showed the parallel daily variation pattern as those in *in situ* condition.

At the NS site (red squares), pH_{25}, $TpCO_2$ and NDIC showed distinct daily excursions in all seasons, which generally followed the daily pattern of photosynthesis and respiration, as evidenced by the DO data shown in **Figures 2M–P**: pH_{25} increased, but $TpCO_2$ and NDIC decreased during the day; and pH_{25} decreased, but $TpCO_2$ and NDIC increased during the night due to the daytime photosynthetic CO_2 uptake and nighttime respiratory CO_2 release. In contrast, NTA did not show a clear daily cycle in all seasons, except that a weak daily pattern occurred in winter, with an increase at night but a decrease during the day (**Figure 3M**). At the IL site (blue circle), similar daily variability was found for pH_{25}, $TpCO_2$, and NDIC; however, the amplitudes of variation were generally much smaller than those at the NS site: the mean (±SD) daily variation ranges in pH_{25} (pH_{25} at 18:00–pH_{25} at 06:00) for NS vs. IL were 0.58 ± 0.18 vs. 0.13 ± 0.07, 0.56 ± 0.03 vs. 0.11 ± 0.04, 0.42 ± 0.16 vs. 0.05 ± 0.06, and 0.30 ± 0.19 vs. 0.05 ± 0.15; the mean (±SD) daily variation ranges in $TpCO_2$ ($TpCO_2$ at 18:00–$TpCO_2$ at 06:00) were −765 ± 406 vs. −34 ± 13 μatm, −518 ± 77 vs. −58 ± 12 μatm, −249 ± 164 vs. −10 ± 13 μatm, and −313 ± 272 vs. −5 ± 36 μatm; and the mean (±SD) daily variation range

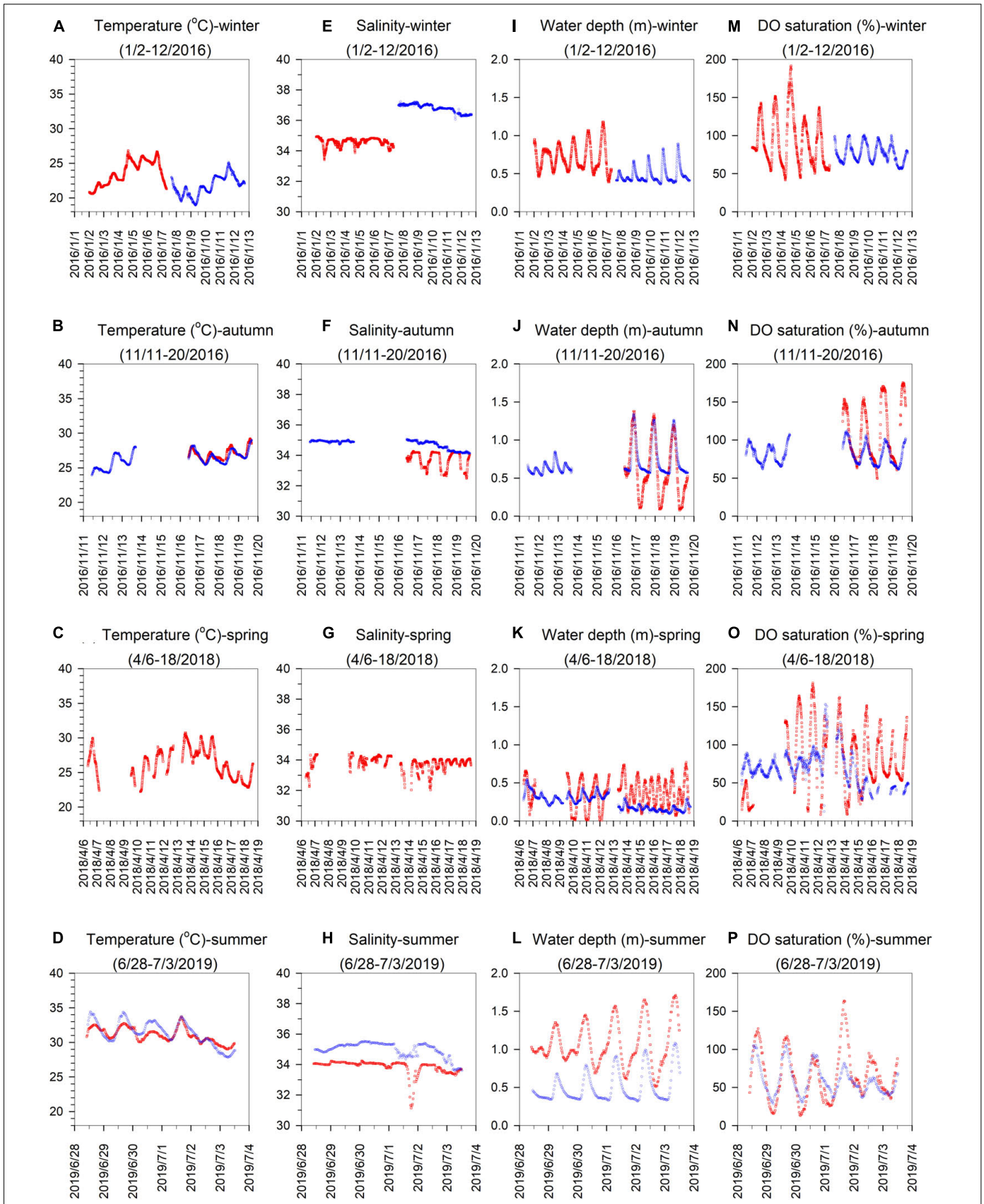

FIGURE 2 | Seasonal time-series observations of **(A–D)** temperature, **(E–H)** salinity, **(I–L)** water depth, and **(M–P)** DO saturation in the inner lagoon (IL, blue circles) and on the northern shore (NS, red squares) of Dongsha Island.

in NDIC (NDIC at 18:00–NDIC at 06:00) were -503 ± 191 vs. -144 ± 63 μmol kg^{-1}, -390 ± 7 vs. -122 ± 32 μmol kg^{-1}, -257 ± 255 vs. -141 ± 118 μmol kg^{-1}, and -115 ± 154 vs. -107 ± 181 μmol kg^{-1} in winter, autumn, spring and summer, respectively. The potential mechanism causing the smaller amplitudes of daily variations in pH_{25}, TpCO_2 and NDIC will be further examined in "Discussion" section.

The horizontal bands superimposed on **Figures 3A–D,I–P** represent the typical seasonal variation ranges of pH, DIC, and TA, respectively, in the adjacent NSCS, which were collected from the SouthEast Asian Time-series Study (SEATS) station at 18°N and 116°E (**Figure 1**) during 19 cruises between 1999 and 2003 (Chou et al., 2005; Tseng et al., 2007). The horizontal dashed lines shown in Figures E–H denote the atmospheric pCO_2 (400 μatm). As shown, at the NS site, the pH_{25} was generally higher than the typical ranges in the adjacent NSCS from midday to midnight; however, the pH_{25} was lower from midnight to midday in all seasons, and the opposite pattern was found for NDIC. Similarly, TpCO_2 was lower than the atmospheric pCO_2 from midday to midnight, while it was higher from midnight to midday in all seasons, except in spring, when TpCO_2 across a daily cycle was almost always lower than the atmospheric pCO_2. NTA across a daily cycle was generally higher than the typical range in the adjacent NSCS, except in summer, when NTA varied within the typical range. In contrast, at the IL site, the pH_{25} across a daily cycle was higher than the typical range in the adjacent NSCS, while the TpCO_2 across a daily cycle was lower than the atmospheric pCO_2 in all seasons, suggesting that OA buffering and atmospheric CO_2 absorbing capacities for the seagrass meadows in the IL on Dongsha Island existed in all seasons. Furthermore, NDIC across a daily cycle was generally lower than the typical range in the adjacent NSCS, except in fall when NDIC was higher. In contrast, NTA across a daily cycle was almost always higher than the typical TA range in the adjacent NSCS in all seasons.

Porewater Carbonate Chemistry and Calcium Ion Concentration

The vertical porewater profiles of the carbonate parameters and calcium ion concentrations at the SS, NS, and IL sites are shown in **Figures 4A–F**. Overall, porewater DIC, TA, and pCO_2 profiles showed an increasing trend with sediment depth, and values were generally greater in the porewater than in the overlying water column at all sites. In contrast, pH and Ω_a revealed a decreasing trend, and values were lower in the porewater than in the overlying water column. Nevertheless, the vertical gradients of the carbonate parameters differed strikingly among the different sites. The sharpest vertical gradients of porewater carbonate parameters were found at the IL site, where the average depth-integrated changes in DIC, TA, pCO_2, pH, and Ω_a relative to the sediment-water interface (SWI) were $+3502 \pm 1218$ μM, $+1791 \pm 865$ μM, $+27457 \pm 15775$ μatm, -2.31 ± 0.18 pH units, and -12.29 ± 0.73, respectively, and the smallest vertical gradients of carbonate parameters were observed at the unvegetated SS site, where the average depth-integrated changes in DIC, TA, pCO_2, pH, and Ω_a were $+77 \pm 23$ μM, $+27 \pm 28$ μM, $+151 \pm 75$ μatm, -0.18 ± 0.15 pH units, and -0.51 ± 0.31, respectively. The vertical profiles of the carbonate parameters at the NS site were closer in magnitude to those at the unvegetated SS site than those at the IL site, where the average depth-integrated changes in DIC, TA, pCO_2, pH, and Ω_a were $+386 \pm 114$ μM, $+91 \pm 67$ μM, $+1456 \pm 627$ μatm, -0.44 ± 0.09 pH units, and -2.90 ± 0.57, respectively. Furthermore, it is worth noting that porewater below 2 cm at the IL site was generally undersaturated with respect to aragonite ($\Omega_a < 1$; except at 12 cm), while porewater remained supersaturated ($\Omega_a > 1$) throughout the entire profiles at the NS and SS sites (**Figure 4E**).

The vertical profiles of calcium ion concentration in porewaters also differed markedly among the different sites. The calcium ion concentration remained fairly constant at 9.5–10 mM throughout the entire profile at the SS and NS sites, while it gradually increased from the SWI to a maximum of 13.1 mM at 12 cm and then decreased to 20 cm at the IL site. Similar to those of the carbonate parameters, the average depth-integrated change in calcium ion concentration at the IL site ($+0.76 \pm 0.84$ mM) was noticeably higher than those at the NS ($+0.23 \pm 0.06$ mM) and SS ($+0.17 \pm 0.17$ mM) sites.

Median Grain Size, Total Carbon, and Total Nitrogen in Sediments

The vertical distributions of MGS, TC, and TN in the sediments at the SS, NS, and IL sites are shown in **Figures 4G–I**. Similar to the results of the porewater, the MGS, TC, and TN in the sediments also revealed considerable difference among the different sites. The coarsest grain size was found at the unvegetated SS site (MGS ranging from 800 to 1000 μm), followed by that at the NS site (MGS ranging from 400 to 600 μm), and the finest grain size was observed in the top 12.5 cm layer at the IL site (MGS ranging from 200 to 400 μm). TC and TN showed the highest contents at the IL site, with a mean of 17.1 and 0.82 wt%, respectively. At the unvegetated SS site, TC and TN remained relatively constant throughout the core and had the lowest contents, with a mean of 12.8 and 0.01%, respectively. The TC and TN contents at the NS site were closer in magnitude to those at the SS site than those at the IL site, with a mean of 14.1 and 0.04 wt%, respectively.

DISCUSSION

The Differences in pH and Partial Pressure of CO_2 Between the Northern Shore and Inner Lagoon Sites

In terms of carbonate chemistry, two striking differences between the NS and IL sites can be clearly seen in **Figures 3A–H**. First, pH was generally higher, while pCO_2 was lower at the IL sites than those at the NS site (noting that due to the smaller sampling numbers and larger variations, the medians of pH in autumn and the medians of pCO_2 in winter and autumn did not show significant difference between the two sites according to a WR-ANOVA analysis, **Table 1**). Second, the amplitude of daily variations in pH and pCO_2 at the IL site were smaller than the NS site. Because the temperature-corrected pH and pCO_2 (pH_{25} and TpCO_2) displayed the similar patterns (**Figures 3A–H**) and

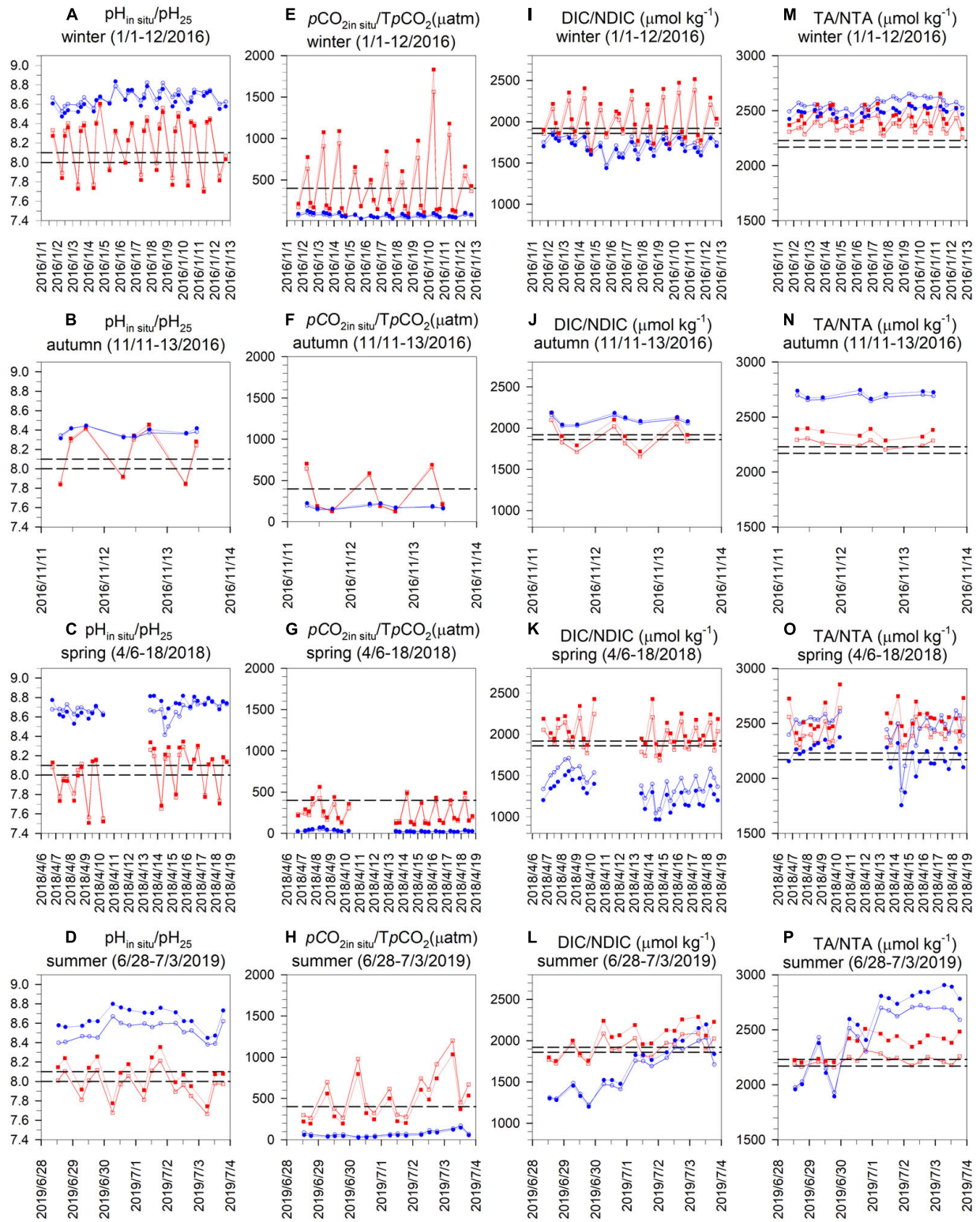

FIGURE 3 | Seasonal daily variations in **(A–D)** pH at *in situ* temperature ($pH_{in\ situ}$, open symbols) and pH at 25°C (pH_{25}, solid symbols), **(E–H)** pCO_2*in situ* ($pCO_{2in\ situ}$, open symbols) and temperature normalized pCO_2 ($TpCO_2$, solid symbols), **(I–L)** DIC (open symbols) and salinity normalized DIC (NDIC, solid symbols), and **(M–P)** TA (open symbols) and salinity normalized TA (NTA, solid symbols) in the inner lagoon (IL, blue circles) and on the northern shore (NS, red squares) of Dongsha Island. The horizontal bands superimposed on Panels **(A–D,I–L,M–P)** represent the typical seasonal variation ranges in pH, DIC, and TA, respectively, in the open northern South China Sea. The horizontal dashed lines shown in panels **(E–H)** denote atmospheric pCO_2 (400 μatm).

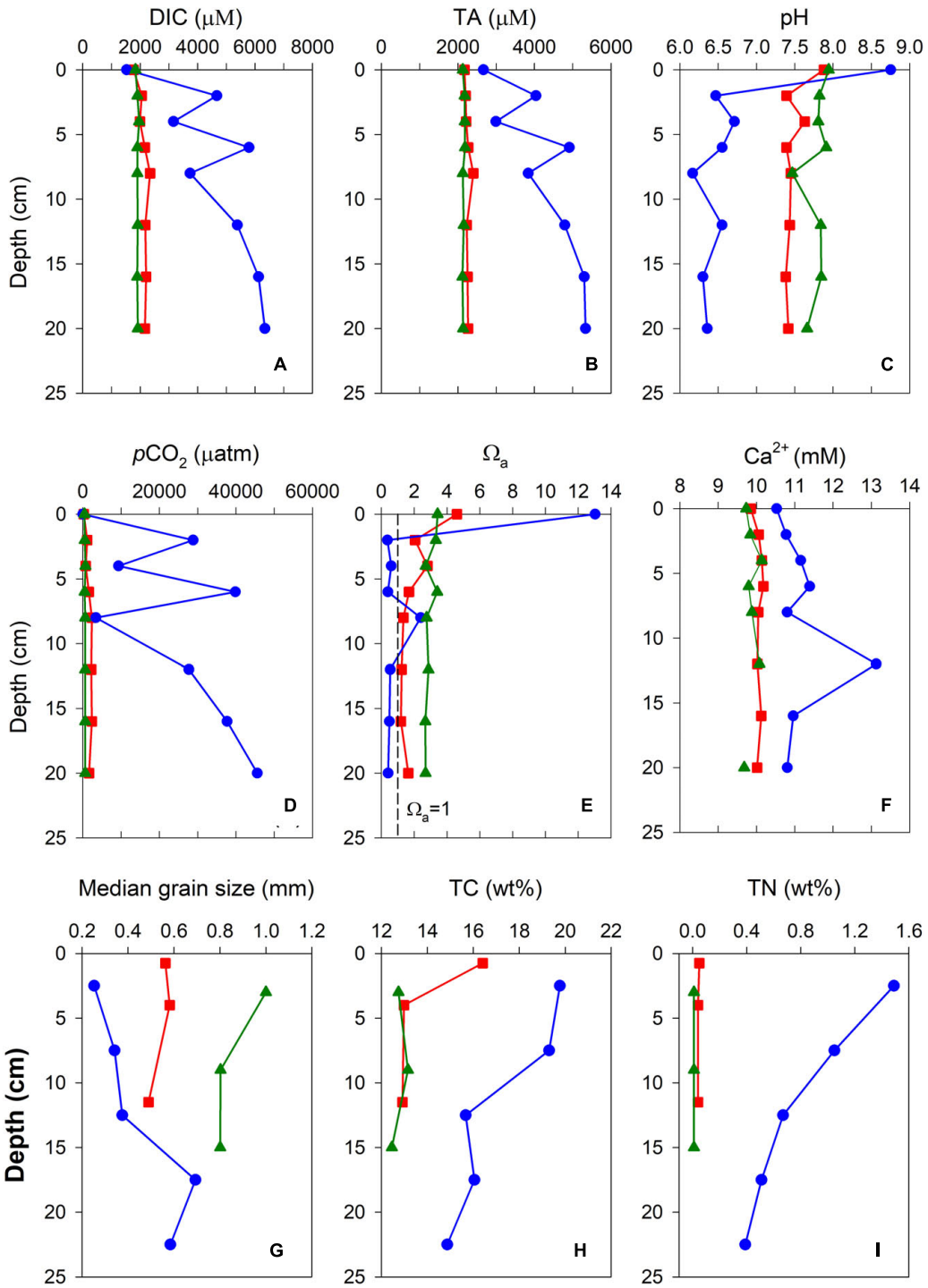

FIGURE 4 | Vertical porewater profiles of **(A)** DIC, **(B)** TA, **(C)** pCO_2, **(D)** pH, **(E)** Ω_a, and **(F)** Ca^{2+}, and vertical distributions of **(G)** median grain size, **(H)** total carbon, and **(I)** total nitrogen in the sediment cores collected on the northern shore (NS, red squares), on the southern shore (SS, green triangles), and in the inner lagoon (IL, blue circles) of Dongsha Island.

the NS and IL sites exhibited similar temperatures in both autumn and summer (**Figures 2B,D**), temperature effect could not explain the observed different behaviors in pH and pCO_2 between the two sites.

Previous studies have indicated that hydrodynamics is of major importance in seagrass biology, ecology, and ecophysiology (Koch, 1994; Koch et al., 2006). Unfortunately, with the present dataset we cannot clearly quantify the influence

TABLE 1 | A summary of the mean ± standard deviation of surface seawater $pH_{in\ situ}$, pH_{25}, $pCO_{2in\ situ}$, $TpCO_2$, TA, NTA, DIC, and NDIC along with number of samples (n) at the inner lagoon (IL) and the northern shore (NS) sites in four different seasons.

	Season	IL	NS	*n*	*p*-value
$pH_{in\ situ}$	Winter	8.67 ± 0.07	8.21 ± 0.27	64	<0.01
	Autumn	8.37 ± 0.04	8.16 ± 0.25	16	=0.25
	Spring	8.68 ± 0.08	8.02 ± 0.22	56	<0.01
	Summer	8.52 ± 0.09	7.95 ± 0.15	34	<0.01
pH_{25}	Winter	8.63 ± 0.09	8.18 ± 0.28	64	<0.01
	Autumn	8.38 ± 0.05	8.18 ± 0.26	16	=0.34
	Spring	8.70 ± 0.08	8.03 ± 0.25	56	<0.01
	Summer	8.65 ± 0.10	8.07 ± 0.17	34	<0.01
$pCO_{2in\ situ}$ (μatm)	Winter	62 ± 17	374 ± 357	64	=0.12
	Autumn	178 ± 24	343 ± 238	16	=0.63
	Spring	27 ± 10	238 ± 115	56	<0.01
	Summer	76 ± 36	553 ± 284	34	<0.01
$TpCO_2$ (μatm)	Winter	75 ± 23	436 ± 423	64	=0.14
	Autumn	187 ± 30	354 ± 258	16	=0.77
	Spring	29 ± 16	260 ± 139	56	<0.01
	Summer	59 ± 33	443 ± 247	34	<0.01
DIC (μmol kg^{-1})	Winter	1741 ± 96	1962 ± 221	64	<0.05
	Autumn	2088 ± 52	1877 ± 161	16	<0.01
	Spring	1417 ± 165	1946 ± 163	56	<0.01
	Summer	1621 ± 262	1916 ± 124	34	<0.05
NDIC (μmol kg^{-1})	Winter	1689 ± 94	2037 ± 241	64	<0.01
	Autumn	2109 ± 57	1955 ± 167	16	<0.05
	Spring	1265 ± 153	2060 ± 179	56	<0.01
	Summer	1679 ± 317	2042 ± 176	34	<0.05
TA (μmol kg^{-1})	Winter	2567 ± 51	2365 ± 64	64	<0.01
	Autumn	2681 ± 24	2265 ± 34	16	<0.01
	Spring	2458 ± 152	2405 ± 95	56	<0.01
	Summer	2461 ± 281	2219 ± 43	34	<0.01
NTA (μmol kg^{-1})	Winter	2490 ± 37	2455 ± 83	64	=0.12
	Autumn	2709 ± 32	2359 ± 41	16	<0.01
	Spring	2192 ± 139	2546 ± 121	56	<0.01
	Summer	2545 ± 355	2363 ± 105	34	<0.05

Differences in the medians of these parameters between the IL and NS were assessed using a Wilcox's robust ANOVA. A significance level of 0.05 was used to determine significant statistical differences.

of physical mixing processes on the dynamics of pH and pCO_2. Nonetheless, the water depth revealed smaller variation ranges at the IL site than the NS site in all seasons (**Figures 2I–L**), suggesting a weaker water exchange process and thus a potential higher control of metabolic activities in carbonate chemistry at the sheltered IL site. Additionally, as shown in **Figure 5**, the variations of DO saturation (green symbols) were generally in phase with temperature (red symbols) but out of phase with water depth (blue symbols) at the both sites, implying that factor(s) other than water exchange could also play an important role in regulating the variations of biogeochemical characteristics in the study area. From these lines of evidence, we suggest that the physical mixing processes and the diverse biogeochemical processes deriving from the different hydrodynamic regimes between the two sites could altogether cause the observed different behaviors in pH and pCO_2 between the NS and IL sites.

The Enhancement of Metabolic Carbonate Dissolution in the Inner Lagoon

As revealed in the results, the CO_2 dynamics at the NS site showed strong diel variation in all seasons (red squares in **Figure 3**), which was similar to the common pattern found in other seagrass meadows (Frankignoulle and Distèche, 1984; Gattuso et al., 1998; Bouillon et al., 2007; Turk et al., 2015; Ganguly et al., 2017; Cyronak et al., 2018; Berg et al., 2019; McCutcheon et al., 2019). In contrast, the unexpected high pH and low pCO_2 values across a diel cycle were found repeatedly at the IL site (blue circles in **Figure 3**) in four different seasons. We suggest that the semienclosed setting of the IL may provide an ideal circumstance for sedimentary TA production through enhanced carbonate dissolution that could represent an important driver to form the observed unique diel pattern in carbonate chemistry at the IL site.

Previous studies have shown that seagrasses may induce carbonate sediment dissolution by the combined effect of OM being supplied and oxygen pumping via their roots and rhizomes, which may fuel OM respiration and thus CO_2 release and a lower carbonate saturation state (**Ω**), consequently leading to carbonate mineral dissolution (Burdige and Zimmerman, 2002; Burdige et al., 2008). This process is often referred to as "metabolic carbonate dissolution" (Kindeberg et al., 2020), as represented in the following equations:

$$CH_2O + O_2 \rightarrow CO_2 + H_2O \rightarrow H_2CO_3 \quad (1)$$

$$CaCO_3 + H_2CO_3 \rightarrow Ca^{2+} + 2HCO_3^- \quad (2)$$

where CH_2O represents a simplified formula for OM undergoing remineralization. The net reaction can therefore be described stoichiometrically as:

$$CH_2O + O_2 + CaCO_3 \rightarrow Ca^{2+} + 2HCO_3^- \quad (3)$$

which increases both the TA and DIC of the porewater with a ratio of 1:1.

We suggest that the "metabolic carbonate dissolution" can be stimulated in the seagrass meadows of the IL, due to several auspicious conditions. First, the confinement of the semienclosed IL may hamper seagrass detritus export to the adjacent open ocean and thus cause more OM to accumulate in the reef sediments at the IL site, as evidenced by the elevated TC and TN contents shown in **Figures 4H,I**. More OMs may fuel stronger aerobic and/or anaerobic respiration that can decrease carbonate saturation level, and thus drive carbonate dissolution. This explanation is further supported by the undersaturated values of Ω_a (<1) and elevated levels of Ca^{2+} in the porewater at the IL site (**Figures 4E,F**). Second, the relatively calm hydrodynamic environment at the IL site could also be favorable for fine-grained sediment accumulation as shown in **Figure 4G**, which may facilitate DIC and TA production

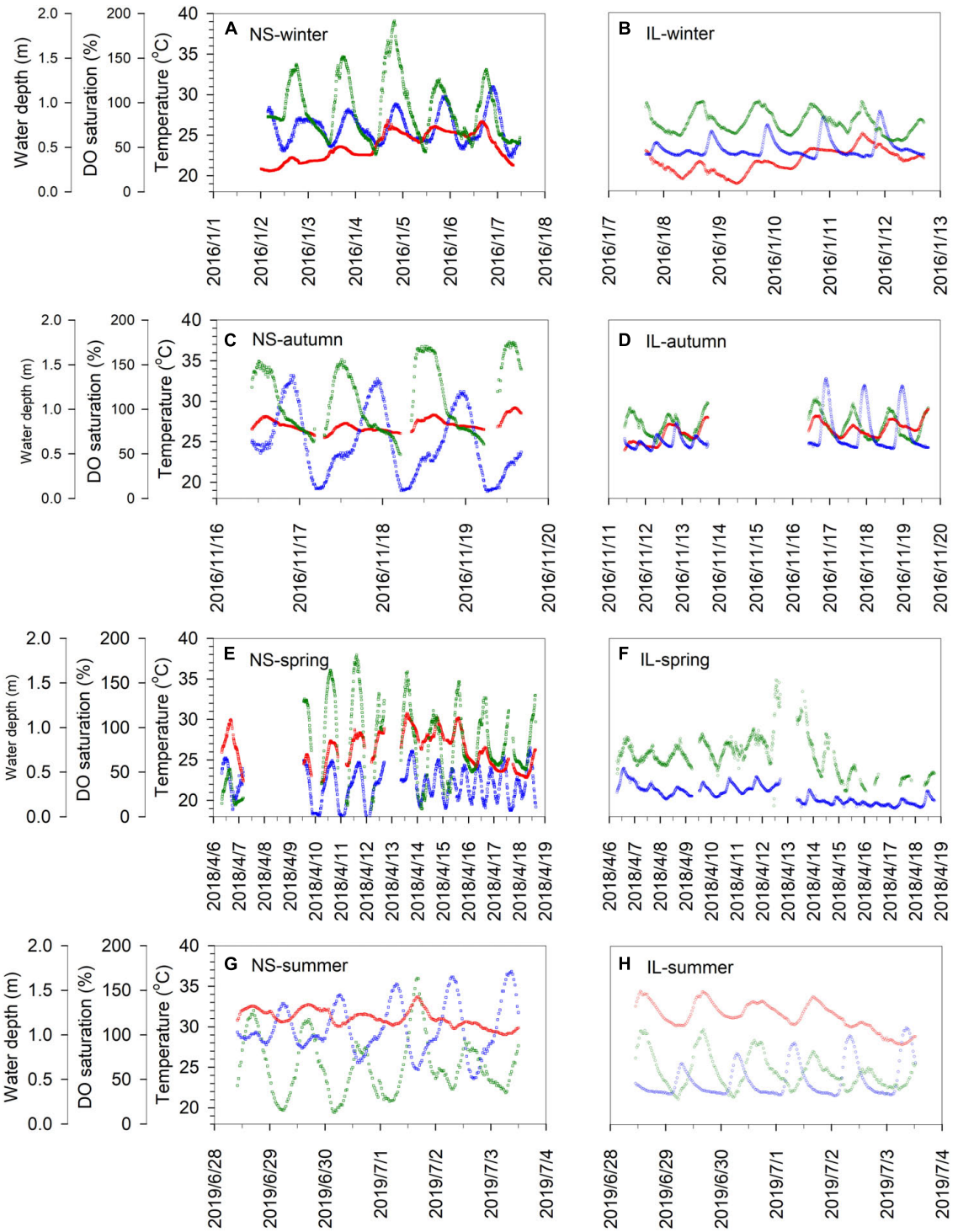

FIGURE 5 | Seasonal time-series observations of temperature (red symbols), water depth (red symbols), and DO saturation (red symbols) in the inner lagoon (IL, right panels; **B,D,F,H**) and on the northern shore (NS, left panels; **A,C,E,G**) of Dongsha Island.

in various ways. For instance, fine-grained sediments can provide greater available reactive surface area for all of the metabolic processes. Moreover, the overall finer-grained sediments may result in a lower permeability that may reduce oxygen penetration and thus favor the occurrence of anaerobic OM remineralization, which could also contribute to DIC and TA production (Hu and Cai, 2011; Reithmaier et al., 2021). Finally, the less-energetic hydrodynamic and low sediment permeability may collectively

result in a longer porewater residence time and thus allow for the buildup of DIC and TA in the porewater at the IL site as shown in **Figures 4A,B**. Besides, previous studies have indicated the occurrence of carbonate mineral reprecipitation along with dissolution in sediments at dense seagrass site (Hover et al., 2001; Hu and Burdige, 2007). Though we cannot be sure whether the coupled carbonate dissolution and reprecipitation occurred at our study sites due to the limitation of data, we think that carbonate mineral reprecipitation could be more likely to take place in the porewater at the NS site compared to the Il site, because the former was supersaturated but the latter was undersaturated with respect to aragonite (**Figure 4E**), and this could also partially explain why TA and DIC in the porewater at the NS site were lower than the IL site. Nevertheless, we suggest that the role of coupled carbonate dissolution and reprecipitation in regulating CO_2 system in porewater of seagrass meadows remains to be further examined.

Although the "metabolic carbonate dissolution" can simultaneously release DIC and TA in the porewater (reaction 3), which can then be exported to the overlying water column via the advection induced by tide, current, and wave actions and/or the diffusion driven by the chemical gradient between the SWI. The exported DIC can be taken up again through the high productivity of the seagrasses, whereas photosynthesis cannot consume TA. Consequently, the TA exported from porewater can remain in the overlying water column. The confinement of the IL site may also hinder water exchange with the adjacent open ocean, thus providing another favorable circumstance for the accumulation of the sedimentary generated TA in the overlying water column. Thermodynamically, TA increases with a constant DIC may not only drive pH increases and pCO_2 decreases in seawater but also enhance their buffer capacities, which could at least partially explain why a weak diel pattern with an extremely high pH and low pCO_2 across a diurnal cycle was seasonally observed within the seagrass meadows at the IL site.

It is worth noting that the studied seagrass meadows are not totally isolated from the Dongsha Atoll, where the living coral reef flat encircles the lagoon (**Figure 1**). Depending on the direction and strength of water exchange, the CO_2 system in individual ecosystem can affect each other (Sippo et al., 2016; Saderne et al., 2019a). In fact, a recent study has shown that TA in the Dongsha Atoll lagoon is depleted relative to the offshore water due to calcification therein (Fan et al., 2021). Thus, if the produced TA through the aforementioned processes in seagrass meadows can be exported to the adjacent Dongsha Atoll lagoon, it could at least partially offset the TA depletion from calcification, and thus could be beneficial for the associated coral reefs facing future OA. However, quantifying the export of TA by benthic ecosystems requires hydrological and bathymetrical data, and models (Saderne et al., 2019a), which are not available for us now. Nevertheless, we highlight the importance of quantifying the hydrodynamics-induced TA and DIC exchanges between coastal ecosystems, which could be crucial to better understand how costal blue carbon ecosystems could contribute to the growth of downstream reefs (Sippo et al., 2016; Saderne et al., 2019a).

Relationship Between Normalized Total Alkalinity and Normalized Dissolved Inorganic Carbon

Besides organic and $CaCO_3$ metabolisms associated to the plant themselves, and the related flora and fauna, aerobic and anaerobic processes in sediments may also affect seawater carbonate chemistry in seagrass meadows (Chou et al., 2018; Saderne et al., 2019a). Generally, the stoichiometry of the relationship between

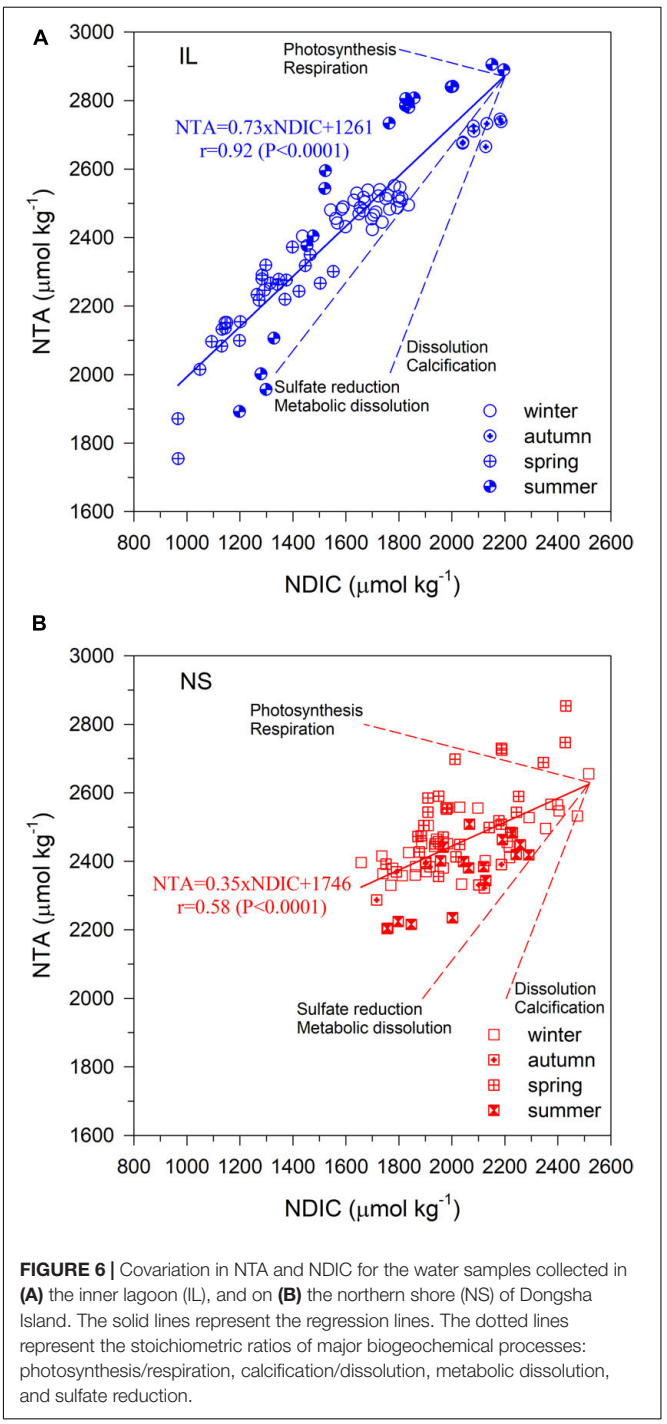

FIGURE 6 | Covariation in NTA and NDIC for the water samples collected in **(A)** the inner lagoon (IL), and on **(B)** the northern shore (NS) of Dongsha Island. The solid lines represent the regression lines. The dotted lines represent the stoichiometric ratios of major biogeochemical processes: photosynthesis/respiration, calcification/dissolution, metabolic dissolution, and sulfate reduction.

NTA and NDIC is used to interpret the dominant processes driving the carbonate system because the relative variation in TA and DIC follows a well-established stoichiometric ratio that is specific to the respective processes, where the ratios for organic metabolism (photosynthesis/respiration), carbonate metabolism (calcification/carbonate dissolution), and net "metabolic carbonate dissolution" (reaction 3) are 0/1, 2/1, and 1/1, respectively (Hu and Cai, 2011; Rassmann et al., 2020). In addition to organic and $CaCO_3$ metabolisms, a series of redox reactions in sediments, including denitrification, manganese reduction, iron reduction, and sulfate reduction (SR), may also play an important role in regulating the carbonate system. As sulfate is far more abundant than other oxidant in seawater, SR is often the dominant redox reaction in sediment with a relative variation ratio in TA and DIC of 1/1 (Burdige, 2011), as denoted in the following equation:

$$2CH_2O + SO_4^{2-} \rightarrow 2HCO_3^- + H_2S \quad (4)$$

Figure 6 shows the covariation in NTA and NDIC for the water samples collected at the IL (**Figure 6A**) and NS (**Figure 6B**) sites. As shown, the slopes of NTA vs. NDIC of the regression lines for the IL and NS are 0.73 and 0.35, respectively. Neither slope follows the specific ratio of any single process, implying that organic and $CaCO_3$ metabolisms, and SR may collectively control TA and DIC variations at the IL and NS sites (Drupp et al., 2016). Though partitioning between the causes of the observed CO_2 system variation is difficult, the higher slope suggests that the "metabolic carbonate dissolution" and/or SR could play a more

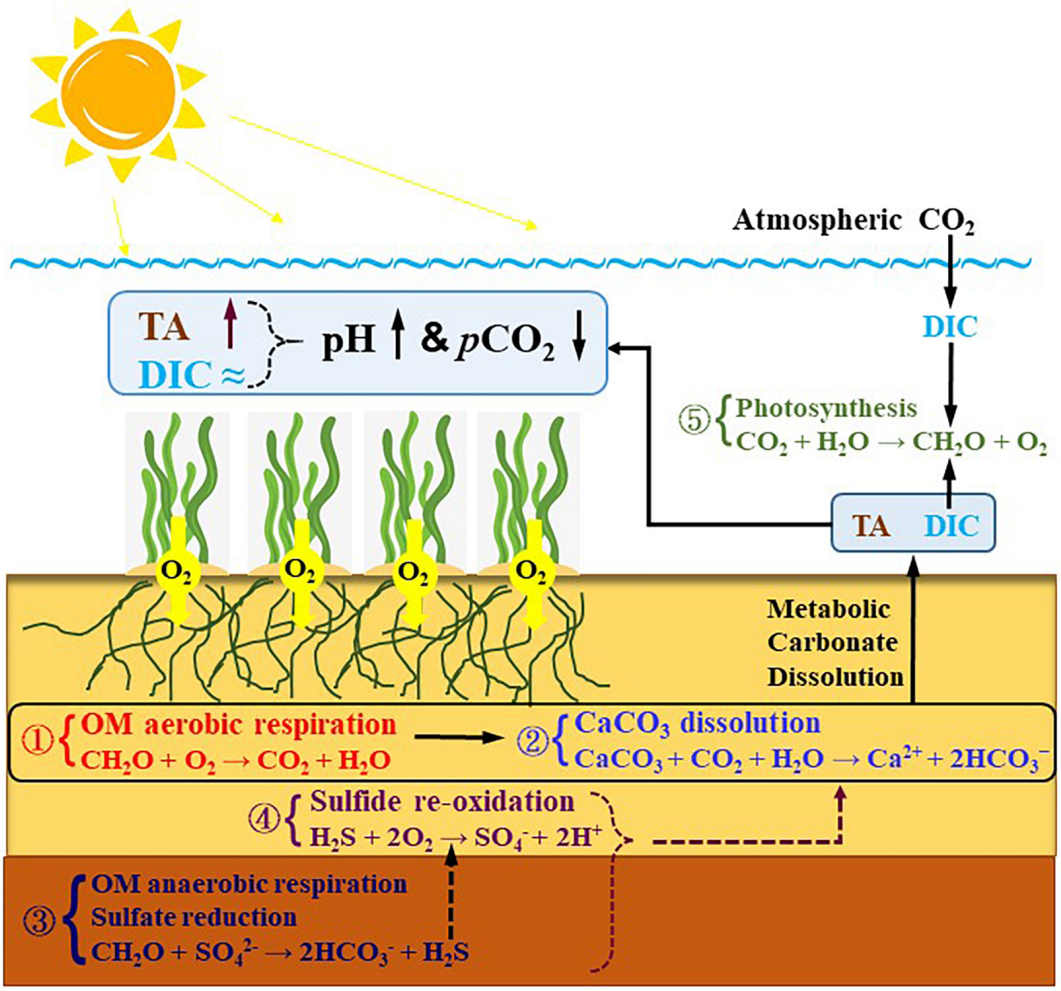

FIGURE 7 | A tentative conceptual model explaining the enhancement of metabolic carbonate dissolution in the seagrass meadows of the inner lagoon on Dongsha Island. First, the elevated OM loading may fuel aerobic respiration (reaction 1) that can produce DIC and reduce carbonate saturation level leading to carbonate dissolution (reaction 2) and thus TA and DIC production, i.e., the "metabolic carbonate dissolution." Secondly, presuming that sulfate reduction (reaction 3) would take place in the deeper anoxic layer and the resulting sulfide subsequently re-oxide to sulfate (reaction 4) in the shallow oxic layer, the whole process can serve as a proton shuttle that can also facilitate carbonate dissolution. Finally, the sedimentary exported DIC can be taken up again by the high productivity of the seagrasses, whereas photosynthesis (reaction 5) cannot consume TA. Consequently, the sedimentary exported TA can remain in the overlying seawater, and thereby forming a unique diel pattern with extremely high pH and low pCO_2 values across a diel cycle.

important role in regulating carbonate chemistry at the IL site compared to the NS site.

Besides, it is worth noting that although we did not measure sulfate and sulfide in this study, the presence of SR in the sediments at the IL site is to be expected, providing that the favorable conditions of elevated OM loading and finer MGS were observed. If SR takes place, the resulting H_2S in iron-poor carbonate sediments could easily re-oxidize to sulfate within the shallow oxic layer. This process can serve as a proton shuttle to facilitate carbonate dissolution (Ku et al., 1999; Burdige et al., 2008; Drupp et al., 2016), as represented in the following equations:

$$H_2S + 2O_2 \rightarrow SO_4^{2-} + 2H^+ \quad (5)$$

$$CaCO_3 + H^+ \rightarrow Ca^{2+} + HCO_3^- \quad (6)$$

Therefore, SR coupled to sulfide re-oxidation may represent another potential pathway to stimulate carbonate dissolution at the IL site. Nonetheless, the net impact of reactions 4–6 on carbonate system are indistinguishable from "metabolic carbonate dissolution" denoted by reaction 3. Thus, more studies of detailed porewater chemistry in sulfate and sulfide as well as pyrite formation in sediments will be needed to further clarify the potential contribution of SR to TA production (Reithmaier et al., 2021). In fact, the partitioning between the sources of TA from CD and SR remains a scientific and analytical challenge to date in blue carbon studies (Saderne et al., 2020).

In summary, based on these discussions, we tentatively proposed a conceptual model summarizing the potential processes controlling TA and DIC dynamics in the IL in **Figure 7**, which may collectively enhance sedimentary $CaCO_3$ dissolution and thus TA production.

The Potential Role of Organic Alkalinity

In seawater dissolved organic acids produced by organic metabolism dissociate into conjugate bases, which may react with protons during seawater titration and thereby contribute to the titration alkalinity (i.e., organic alkalinity, TA^{org}; Ko et al., 2016). A number of studies have shown that TA^{org} can be significant in productive coastal environments (Cai et al., 1998; Kulinski et al., 2014). Therefore, TA^{org} could also play a non-ignorable role in regulating carbonate chemistry in seagrass meadows. TA^{org} has been measured indirectly as a difference between TA measured by direct titration (TA^{meas}) and TA calculated (TA^{cal}) from the measured DIC and pH (i.e., $\Delta TA = TA^{meas} - TA^{cal}$; Yang et al., 2015). Since the CO_2 system was overdetermined in the present study, we can determine TA^{org} by calculating ΔTA.

Figure 8 shows the comparison of the TA^{meas} and TA^{cal} at the NS and IL site, in which the difference between the data points and the 1:1 line (ΔTA) denotes TA^{org}. As shown, the TA^{meas} and TA^{cal} generally follow the 1:1 line in winter, autumn and summer at the NS site, and in winter and autumn at the IL site, suggesting no significant TA^{org} production during these periods. In contrast, the TA^{meas} are apparently higher than TA^{cal} in spring at the NS site, and in spring and summer at the IL site, indicating substantial TA^{org} production during these periods. The higher TA^{org} production in spring and summer at the IL site could be associated with the more active organic metabolism in seagrass meadows during the warm seasons (Huang et al., 2015). Moreover, it is worth noting that spring and summer are also the only two seasons when the median of $TpCO_2$ is significant lower at the IL site compared to the NS site according to a W-R ANOVA analysis (**Table 1**). Also, at the NS site, when TA^{org} production was higher in spring, the amplitudes of daily variations in pH and pCO_2 appear to be smaller than the other seasons (**Figures 3A–H**). These results imply that in addition to the aforementioned processes in Sections "The Enhancement of Metabolic Carbonate Dissolution in the Inner Lagoon" and "Relationship Between Normalized Total Alkalinity and Normalized Dissolved Inorganic Carbon," TA^{org} production could also play a non-ignorable role in regulating carbonate chemistry in seagrass meadows, especially during the warm seasons. Therefore, we suggest that TA^{org} production could be a potentially interesting and relevant research topic in studying CO_2 system in costal blue carbon ecosystems, which needs more research.

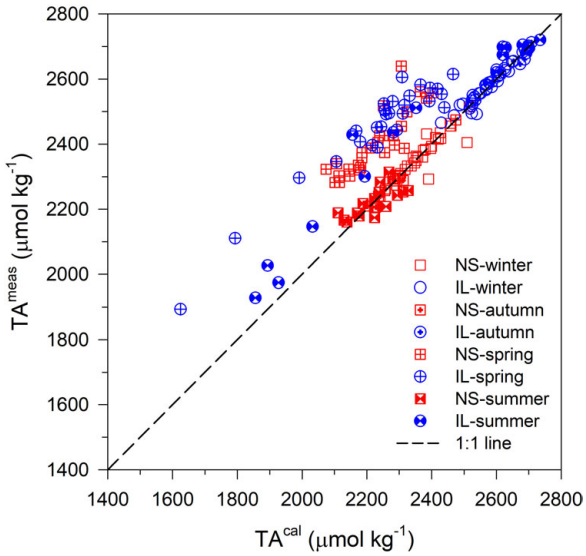

FIGURE 8 | Comparison of the measured TA (TA^{meas}) by direct titration and the TA calculated (TA^{cal}) from the measured DIC and pH in the inner lagoon (IL; circles), and on the northern shore (NS; squares). The difference between TA^{meas} and TA^{meas} (ΔTA) denotes organic TA (TA^{org}; see text for definition).

CONCLUDING REMARKS

To the best of our knowledge, the seasonal recurrence of high pH and low pCO_2 values across a diel cycle within seagrass meadows, such as those at the IL site on Dongsha Island, has never been reported in other marine ecosystems. We suggest that this unique diel pattern in carbonate chemistry could be associated with the semienclosed nature of the IL site, including, higher OM loading, finer-grained sediment, smaller sediment permeability and longer residence time of the porewater, that may stimulate both aerobic and anaerobic respiration leading to $CaCO_3$ dissolution and thus TA production. Overall, our

results demonstrate that $CaCO_3$ dissolution in vegetated reef sediments can be enhanced in a semienclosed environmental setting. Most importantly, the present study provides the first observational evidence showing that the intense mechanistic coupling between metabolic processes and carbonate dissolution in seagrass meadows in reef sediment with a confinement setting may create a localized buffering effect against OA and a strong CO_2 sink, and thus may provide a valuable theoretical proposition for conserving and restoring seagrass meadows as a promising strategy for climate change mitigation. We also highlight the importance in quantifying the hydrodynamics-induced TA and DIC exchanges between coastal ecosystems, which could be crucial to better understand how costal blue carbon ecosystems could contribute to the growth of downstream reefs. Furthermore, we find that TA^{org} could play a non-ignorable role in regulating carbonate chemistry in seagrass meadows, and thus may be a potentially interesting and relevant research topic in studying CO_2 system in costal blue carbon ecosystems. Finally, since the present work was not conducted over a single year, the observed seasonal variation could be also affected by inter-annual variability, more studies with better temporal coverage are still needed to further elucidate the potential impact of inter-annual variability in our findings.

DATA AVAILABILITY STATEMENT

The datasets presented in this study can be found in online repositories. The names of the repository/repositories and accession number(s) can be found below: The data used for this study are available at PANGEA (https://doi.org/10.1594/PANGEA.928748).

AUTHOR CONTRIBUTIONS

W-CC conceived the study, performed the field work, and wrote the manuscript. C-CY, Y-HC, and H-CT performed the field work and contributed to data collection and analysis. L-FF, C-CH, W-JH, Y-YS, and KS conceived the study and contributed to data interpretation. G-CG, H-YC, and C-KS contributed to the data collection and interpretation. All authors read and approved the final manuscript.

FUNDING

Funding was provided by the Ministry of Science and Technology of Taiwan grants #107-2611-M-019-001-MY3 awarded to W-CC.

ACKNOWLEDGMENTS

We are grateful to the Dongsha Atoll Research Station, Dongsha Atoll National Park, and Coast Guard Administration for assistance in field sampling. We thank Rong-Wei Syu, Hui-Chuan Chu, and Kuan-Chieh Wu for their help with the field and laboratory work.

REFERENCES

Baldry, K., Saderne, V., McCorkle, D. C., Churchill, J. H., Agusti, S., and Duarte, C. M. (2020). Anomalies in the carbonate system of Red Sea coastal habitats. *Biogeosciences* 17, 423–439. doi: 10.5194/bg-17-423-2020

Barrón, C., Duarte, C. M., Frankignoulle, M., and Borges, A. V. (2006). Organic carbon metabolism and carbonate dynamics in a Mediterranean seagrass (Posidonia oceanica) meadow. *Estuaries Coast.* 29, 417–426. doi: 10.1007/bf02784990

Berg, P., Delgard, M. L., Polsenaere, P., McGlathery, K. J., Doney, S. C., and Berger, A. C. (2019). Dynamics of benthic metabolism, O2, and pCO2 in a temperate seagrass meadow. *Limnol. Oceanogr.* 64, 2586–2604. doi: 10.1002/lno.11236

Blott, S. J., and Pye, K. (2001). GRADISTAT: a grain size distribution and statistics package for the analysis of unconsolidated sediments. *Earth Surf. Process Landf.* 26, 1237–1248. doi: 10.1002/esp.261

Bouillon, S., Dehairs, F., Velimirov, B., Abril, G., and Borges, A. V. (2007). Dynamics of organic and inorganic carbon across contiguous mangrove and seagrass systems (Gazi Bay, Kenya). *J. Geophys. Res. Biogeosci.* 112:G02018.

Burdige, D. J. (2011). "Estuarine and coastal sediments–coupled biogeochemical cycling," in *Treatise on Estuarine and Coastal Science*, eds R. Laane and J. J. Middelburg (Amsterdam: Elsevier Inc.), 279–316. doi: 10.1016/b978-0-12-374711-2.00511-8

Burdige, D. J., and Zimmerman, R. C. (2002). Impact of sea grass density on carbonate dissolution in Bahamian sediments. *Limnol. Oceanogr.* 47, 1751–1763.

Burdige, D. J., Zimmerman, R. C., and Hu, X. P. (2008). Rates of carbonate dissolution in permeable sediments estimated from pore-water profiles: the role of sea grasses. *Limnol. Oceanogr.* 53, 549–565.

Cai, W.-J., Wang, Y., and Hodson, R. E. (1998). Acid-base properties of dissolved organic matter in the estuarine waters of Georgia, USA. *Geochim. Cosmochim. Acta* 62:4732483.

Challener, R. C., Robbins, L. L., and McClintock, J. B. (2016). Variability of the carbonate chemistry in a shallow, seagrass-dominated ecosystem: implications for ocean acidification experiments. *Mar. Freshw. Res.* 67, 163–172. doi: 10.1071/mf14219

Chou, W.-C., Chu, H.-C., Chen, Y.-H., Syu, R.-W., Hung, C.-C., and Soong, K. (2018). Short-term variability of carbon chemistry in two contrasting seagrass meadows at Dongsha island: implications for pH buffering and CO_2 sequestration. *Estuar. Coast. Shelf Sci.* 210, 36–44. doi: 10.1016/j.ecss.2018.06.006

Chou, W.-C., Gong, G.-C., Yang, C.-Y., and Chuang, K.-Y. (2016). A comparison between field and laboratory pH measurements for seawater on the East China Sea shelf. *Limnol. Oceanogr. Methods* 14, 315–322. doi: 10.1002/lom3.10091

Chou, W.-C., Liu, P.-J., Chen, Y.-H., and Huang, W.-J. (2020). Contrasting changes in diel variations of net community calcification support that carbonate dissolution can be more sensitive to ocean acidification than coral calcification. *Front. Mar. Sci.* 7:3. doi: 10.3389/fmars.2020.00003

Chou, W.-C., Sheu, D.-D., Chen, C.-T. A., Wang, S.-L., and Tseng, C.-M. (2005). Seasonal variability of carbon chemistry at the SEATS time-series site, northern South China Sea between 2002 and 2003. *Terr. Atmospheric Ocean. Sci.* 16, 445–465. doi: 10.3319/tao.2005.16.2.445(o)

Cyronak, T., Andersson, A. J., D'Angelo, S., Bresnahan, P., Davidson, C., Griffin, A., et al. (2018). Short-term spatial and temporal carbonate chemistry variability in two contrasting seagrass meadows: implications for pH buffering capacities. *Estuaries Coast.* 41, 1282–1296. doi: 10.1007/s12237-017-0356-5

Dickson, A. G., Sabine, C. L., and Christian, J. R. (2007). *Guide to Best Practices for Ocean CO_2 Measurements*. Patricia Bay: North Pacific Marine Science Organization.

Drupp, P. S., De Carlo, E. H., and Mackenzie, F. T. (2016). Porewater CO_2-carbonic acid system chemistry in permeable carbonate reef sands. *Mar. Chem.* 185, 48–64. doi: 10.1016/j.marchem.2016.04.004

Duarte, C. M., Marba, N., Gacia, E., Fourqurean, J. W., Beggins, J., Barron, C., et al. (2010). Seagrass community metabolism: assessing the carbon sink capacity of seagrass meadows. *Global Biogeochem. Cycles* 24:GB4032.

Falter, J., and Sansone, F. (2000). Shallow pore water sampling in reef sediments. *Coral Reefs* 19, 93–97. doi: 10.1007/s003380050233

Fan, L.-F., Qiu, S.-Q., and Chou, W.-C. (2021). Carbonate chemistry of the Dongsha Atoll Lagoon in the northern South China Sea. *Terr. Atmos. Ocean. Sci.* 32, 399–409. doi: 10.3319/tao.2021.05.15.02

Folk, R. L. (1966). A review of grain-size parameters. *Sedimentology* 6, 73–93. doi: 10.1111/j.1365-3091.1966.tb01572.x

Fourqurean, J. W., Duarte, C. M., Kennedy, H., Marbà, N., Holmer, M., Mateo, M. A., et al. (2012). Seagrass ecosystems as a globally significant carbon stock. *Nat. Geosci.* 5, 505–509.

Frankignoulle, M., and Distèche, A. (1984). CO2 chemistry in the water column above a Posidonia seagrass bed and related air-sea exchanges. *Oceanol. Acta* 7, 209–219.

Ganguly, D., Singh, G., Ramachandran, P., Selvam, A. P., Banerjee, K., and Ramachandran, R. (2017). Seagrass metabolism and carbon dynamics in a tropical coastal embayment. *Ambio* 46, 667–679. doi: 10.1007/s13280-017-0916-8

Gattuso, J.-P., Frankignoulle, M., and Wollast, R. (1998). Carbon and carbonate metabolism in coastal aquatic ecosystems. *Annu. Rev. Ecol. Evol. Syst.* 29, 405–434.

Hendriks, I. E., Olsen, Y. S., Ramajo, L., Basso, L., Steckbauer, A., Moore, T. S., et al. (2014). Photosynthetic activity buffers ocean acidification in seagrass meadows. *Biogeosciences* 11, 333–346. doi: 10.1111/gcb.15594

Hover, V. C., Walter, L. M., and Peacor, D. R. (2001). Early marine diagenesis of biogenic aragonite and Mg-calcite: new constrains from high-resolution STEM and AEM analysis of modern platform carbonate. *Chem. Geol.* 175, 221–248. doi: 10.1016/s0009-2541(00)00326-0

Howard, J. L., Creed, J. C., Aguiar, M. V. P., and Fouqurean, J. W. (2018). CO_2 released by carbonate sediment production in some coastal areas may offset the benefits of seagrass "blue carbon" storage. *Limnol. Oceanogr.* 63, 160–172. doi: 10.1002/lno.10621

Hu, X., and Burdige, D. J. (2007). Enriched stable carbon isotopes in the pore waters of carbonate sediments dominated by seagrasses: evidence for coupled carbonate dissolution and reprecipitation. *Geochim. Cosmochim. Acta* 71, 129–144. doi: 10.1016/j.gca.2006.08.043

Hu, X., and Cai, W. J. (2011). An assessment of ocean margin anaerobic processes on oceanic alkalinity budget. *Global Biogeochem. Cycles* 25:GB3003.

Huang, Y.-H., Lee, C.-L., Chung, C.-Y., Hsiao, S.-C., and Lin, H.-J. (2015). Carbon budgets of multispecies seagrass beds at Dongsha Island in the South China Sea. *Mar. Environ. Res.* 106, 92–102. doi: 10.1016/j.marenvres.2015.03.004

Hung, C.-C., and Gong, G.-C. (2010). POC/^{234}Th ratios in particles collected in sediment traps in the northern South China Sea. *Estuar. Coast. Shelf Sci.* 88, 303–310.

Kindeberg, T., Bates, N. R., Courtney, T. A., Cyronak, T., Griffin, A., Mackenzie, F. T., et al. (2020). Porewater carbonate chemistry dynamics in a temperate and a subtropical seagrass system. *Aquat. Geochem.* 26, 375–399. doi: 10.1007/s10498-020-09378-8

Ko, Y. H., Lee, K., Eom, K. H., and Han, I.-S. (2016). Organic alkalinity produced by phytoplankton and its effect on the computation of ocean carbon parameters. *Limnol. Oceanogr.* 61, 1462–1471. doi: 10.1002/lno.10309

Koch, E. W. (1994). Hydrodynamics, diffusion boundary layers and photosynthesis of the seagrasses *Thalassia testudinum* and *Cymodocea nodosa*. *Mar. Biol.* 118, 767–776. doi: 10.1007/bf00347527

Koch, E. W., Ackerman, J., van Keulen, M., and Verduin, J. (2006). "Fluid dynamics in seagrass ecology: from molecules to ecosystems," in *Seagrasses: Biology, Ecology and conservation*, eds A. W. D. Larkum, R. J. Orth, and C. M. Duarte (Berlin: Springer Verlag), 193–225. doi: 10.1007/1-4020-2983-7_8

Ku, T. C. W., Walter, L. M., Coleman, M. L., Blake, R. E., and Martini, A. M. (1999). Coupling between sulfur recycling and syndepositional carbonate dissolution: evidence from oxygen and sulfur isotope composition of pore water sulfate, South Florida Platform, USA. *Geochim. Cosmochim. Acta* 63, 2529–2546.

Kulinski, K., Schneider, B., Hammer, K., Machulik, U., and Schulz-Bull, D. (2014). The influence of dissolved organic matter on the acid–base system of the Baltic Sea. *J. Mar. Syst.* 132:1062115.

Lee, C.-L., Huang, Y.-H., Chung, C.-Y., Hsiao, S.-C., and Lin, H.-J. (2015). Herbivory in multi-species, tropical seagrass beds. *Mar. Ecol. Prog. Ser.* 525, 65–80. doi: 10.3354/meps11220

Maher, D. T., Call, M., Santos, I. R., and Sanders, C. J. (2018). Beyond burial: lateral exchange is a significant atmospheric carbon sink in mangrove forests. *Biol. Lett.* 14:20180200. doi: 10.1098/rsbl.2018.0200

Mair, P., and Wilcox, R. (2020). Robust statistical methods in R using the WRS2 package. *Behav. Res. Methods* 52, 464–488. doi: 10.3758/s13428-019-01246-w

Manzello, D. P., Enochs, I. C., Melo, N., Gledhill, D. K., and Johns, E. M. (2012). Ocean acidification refugia of the Florida reef tract. *PLoS One* 7:e41715. doi: 10.1371/journal.pone.0041715

McCutcheon, M. R., Staryk, C. J., and Hu, X. P. (2019). Characteristics of the carbonate system in a semiarid estuary that experiences summertime hypoxia. *Estuaries Coasts.* 42, 1509–1523. doi: 10.1007/s12237-019-00588-0

Pacella, S. R., Brown, C. A., Waldbusser, G. G., Labiosa, R. G., and Hales, B. (2018). Seagrass habitat metabolism increases short-term extremes and long-term offset of CO_2 under future ocean acidification. *Proc. Natl. Acad. Sci. U.S.A.* 115, 3870–3875. doi: 10.1073/pnas.1703445115

Pelletier, G., Lewis, E., and Wallace, D. (2011). *CO2SYS. XLS: A Calculator for the CO_2 System in Seawater for Microsoft Excel/VBA. Version 16*. Washington, DC: Washington State Department of Ecology.

R Core Team (2021). *R v4.1.1, Vienna, Austria*. Available online at: https://www.R-project.org/, (accessed August 10, 2021).

Rassmann, J., Eitel, E. M., Lansard, B., Cathalot, C., Brandily, C., Taillefert, M., et al. (2020). Benthic alkalinity and dissolved inorganic carbon fluxes in the Rhone River prodelta generated by decoupled aerobic and anaerobic processes. *Biogeosciences* 17, 13–33.

Reithmaier, G. M. S., Johnston, S. G., Junginger, T., Goddard, M. M., Sanders, C. J., Hutley, L. B., et al. (2021). Alkalinity production coupled to pyrite formation represents an unaccounted blue carbon sink. *Global Biogeochem. Cycles* 35:e2020GB006785.

Ruesink, J. L., Yang, S., and Trimble, A. C. (2015). Variability in carbon availability and eelgrass (Zostera marina) biometrics along an estuarine gradient in Willapa Bay, WA, USA. *Estuaries Coasts.* 38, 1908–1917. doi: 10.1007/s12237-014-9933-z

Saderne, V., Fusi, M., Thomson, T., Dunne, A., Mahmud, F., Roth, F., et al. (2020). Total alkalinity production in a mangrove ecosystem reveals an overlooked Blue Carbon component. *Limnol. Oceanogr. Lett.* 6, 61–67.

Saderne, V., Geraldi, N. R., Macreadie, P. I., Maher, D. T., Middelburg, J. J., Serrano, O., et al. (2019b). Role of carbonate burial in blue carbon budgets. *Nat. Commun.* 10:1106.

Saderne, V., Baldry, K., Anton, A., Agustí, S., and Duarte, C. M. (2019a). Characterization of the CO2 system in a coral reef, a seagrass meadow, and a mangrove forest in the central Red Sea. *J. Geophys. Res. Oceans* 2, 1–16.

Semesi, I. S., Beer, S., and Bjork, M. (2009). Seagrass photosynthesis controls rates of calcification and photosynthesis of calcareous macroalgae in a tropical seagrass meadow. *Mar. Ecol. Prog. Ser.* 382, 41–47.

Sippo, J. Z., Maher, D. T., Tait, D. R., Holloway, C., and Santos, I. R. (2016). Are mangroves drivers or buffers of coastal acidification? Insights from alkalinity and dissolved inorganic carbon export estimates across a latitudinal transect. *Global Biogeochem. Cycles* 30, 753–766. doi: 10.1002/2015gb005324

Su, C.-K., and Ho, C.-C. (2019). Online profiling of living rat brain extracellular pH using a pH-dependent solid phase extraction scheme coupled with microdialysis sampling and inductively coupled plasma mass spectrometry. *Anal. Chim. Acta* 1055, 36–43. doi: 10.1016/j.aca.2018.12.020

Tseng, C. M., Wong, G. T. F., Chou, W. C., Lee, B. S., Sheu, D. D., and Liu, K. K. (2007). Temporal variations in the carbonate system in the upper layer at the SEATS station. *Deep-Sea Res. II* 54, 1448–1468. doi: 10.1016/j.dsr2.2007.05.003

Turk, D., Yates, K. K., Vega-Rodriguez, M., Toro-Farmer, G., L'Esperance, C., Melo, N., et al. (2015). Community metabolism in shallow coral reef and seagrass ecosystems, lower Florida Keys. *Mar. Ecol. Prog. Ser.* 538, 35–52. doi: 10.3354/meps11385

Unsworth, R. K. F., Collier, C. J., Henderson, G. M., and McKenzie, L. J. (2012). Tropical seagrass meadows modify seawater carbon chemistry: implications

for coral reefs impacted by ocean acidification. *Environ. Res. Lett.* 7:024026. doi: 10.1088/1748-9326/7/2/024026

Waldbusser, G. G., and Salisbury, J. E. (2014). Ocean acidification in the coastal zone from an organism's perspective: multiple system parameters, frequency domains, and habitats. *Ann. Rev. Mar. Sci.* 6, 221–247. doi: 10.1146/annurev-marine-121211-172238

Yang, B., Byrne, R. H., and Lindemuth, M. (2015). Contributions of organic alkalinity to total alkalinity in coastal waters: a spectrophotometric approach. *Mar. Chem.* 176, 199–207. doi: 10.1016/j.marchem.2015.09.008

Conflict of Interest: The authors declare that the research was conducted in the absence of any commercial or financial relationships that could be construed as a potential conflict of interest.

Publisher's Note: All claims expressed in this article are solely those of the authors and do not necessarily represent those of their affiliated organizations, or those of the publisher, the editors and the reviewers. Any product that may be evaluated in this article, or claim that may be made by its manufacturer, is not guaranteed or endorsed by the publisher.

frontiers | Frontiers in Marine Science

ORIGINAL RESEARCH
published: 22 July 2022
doi: 10.3389/fmars.2022.735702

Variation of Carbon–Nitrogen Contents and Allelopathic Disruption of Renieramycin M–Producing Sponge *Xestospongia* sp. in the Gulf of Thailand

Udomsak Darumas[1†], *Gad Elsayed Mohamed Salem*[2†], *Khanit Suwanborirux*[3], *Voranop Viyakarn*[2,4] and *Suchana Chavanich*[2,4,5*]

[1]School of Science, Walailak University, Nakhon Si Thammarat, Thailand, [2]Reef Biology Research Group, Department of Marine Science, Faculty of Science, Chulalongkorn University, Bangkok, Thailand, [3]Department of Pharmacognosy, Faculty of Pharmaceutical Sciences, Chulalongkorn University, Bangkok, Thailand, [4]Aquatic Resources Research Institute, Chulalongkorn University, Bangkok, Thailand, [5]Center of Excellence for Marine Biotechnology, Department of Marine Science, Faculty of Science, Chulalongkorn University, Bangkok, Thailand

OPEN ACCESS

Edited by:
Keryea Soong,
National Sun Yat-sen University, Taiwan

Reviewed by:
Perumal Karthick,
Sea6 Energy Pvt Ltd., India
Sing-how Tuo,
Dalhousie University, Canada

***Correspondence:**
Suchana Chavanich
suchana.c@chula.ac.th

[†]These authors have contributed equally to this work and share first authorship

Specialty section:
This article was submitted to Marine Ecosystem Ecology, a section of the journal Frontiers in Marine Science

Received: 03 July 2021
Accepted: 21 June 2022
Published: 22 July 2022

Citation:
Darumas U, Salem GEM, Suwanborirux K, Viyakarn V and Chavanich S (2022) Variation of Carbon–Nitrogen Contents and Allelopathic Disruption of Renieramycin M–Producing Sponge Xestospongia sp. in the Gulf of Thailand. Front. Mar. Sci. 9:735702. doi: 10.3389/fmars.2022.735702

Allelopathy is commonly found in marine sponges. However, information on allelopathic activities of sponge extracts is limited. In this study, variations of nutritional values of *Xestospongia* sp. were investigated. *Xestospongia* did not unequally distribute its nutritional values for predatory defense. Carbon–nitrogen contents and renieramycin M concentrations were not significantly different among the areas of *Xestospongia* sp. (edge, inner, and outer). However, carbon–nitrogen contents and renieramycin M concentrations of *Xestospongia* sp. coexisting with different organisms were not significantly different. In the laboratory, bleaching and necrosis of coral nubbins were not observed in every treatment, and renieramycin M did not show any allelopathic effect on its coexisting organisms (Porites lutea and Palythoa caesia). However, renieramycin M inhibited settlement of acorn barnacle (Semibalanus balanoides) but did not inhibit the settlement of pelecypods. When testing for antimicrobial effect, renieramycin M did not inhibit the growth of aerobic bacteria in any treatments. This study provides evidence that renieramycin M found in *Xestospongia* was uniform; however, it can possess strong inhibitory activities against some marine organisms.

Keywords: ***Xestospongia*** **sp., renieramycin M, sponge, allelopathy, Gulf of Thailand, bioactive compounds, coral**

INTRODUCTION

Sponges are one of the common marine organisms in tropical areas and are known to produce diverse secondary metabolites (Faulkner, 1984). Some secondary metabolites and chemical compounds produced by sponges have been intensively screened as marine natural products (Frincke and Faulkner, 1982; Nakao et al., 2004). They are also known as inhibitors of bacteria and antileishmania (Frincke and Faulkner, 1982; Nakao et al., 2004). The blue sponge, *Xestospongia* sp., can be found worldwide (Pulitzer-Finali, 1996; Kritsanapuntu et al., 2001; Darumas et al., 2007). In Thailand, *Xestospongia* sp. is found commonly in both the Gulf of Thailand and the Andaman Sea coexisting

with other reef organisms (e.g., corals, algae, and other sponges) and settling on rock beds and dead coral rubble (Darumas et al., 2007). This sponge differs from renierid, cribrochalinid, and neopetrosid sponges by its ectosomal skeleton with a tangential disordered network and no specialized structure (Darumas et al., 2007). In coral reef communities, sponge species have been found to successfully compete with corals (Vicente, 1990). They are also well-known space competitors in the reefs (Aerts and Van Soest, 1997). Factors influencing the outcomes of the competitive interactions include distances between species and chemical defense mechanisms (Lang and Chornesky, 1990; Nakao et al., 2004). The chemical defense of secondary metabolites can serve as antipredatory, antimicrobial, antifouling, and allelopathy agents (Wang et al., 2008).

Allelopathy is the beneficial or harmful effect of one organism on another organism by the release of chemicals from body part(s) by leaching, root exudation (in plants), volatilization, residue decomposition, and other processes (Folt and Goldman, 1981; Willis, 2007). The term "allelopathy" has been borrowed by zoologists to describe chemical-based interactions among invertebrates, especially sponges and corals (Willis, 2007). Allelopathy is also common in marine habitats. Some cyanobacteria produce chemicals to inhibit the growth of algae (Suikkanen et al., 2004). The same multifunctional roles of allelopathic chemicals were observed in marine habitats as well (Kubanek et al., 2002). For example, hexanic extracted from soft coral, *Stereonephthya* aff. *curvata*, caused serious necrosis on gorgonians and deterred fish feeding (Lages et al., 2006). The allelochemicals that prevented space settlement of either intra or interspecific larva were known as antifouling agents. These inhibited larval settlement (pre-settlement allelopathic) or killed the new settlers (post-settlement allelopathic) (Sears et al., 1990; Hirota et al., 1998). However, more complex antifouling activity was reported. Some chemicals prevent settlement of specific species, while some species benefit from settlement of others on them, thus producing the chemicals promotes settlement of specific species (Henrikson and Pawlik, 1995).

One of chemical compounds that *Xestospongia* produced is renieramycin (Suwanborirux et al., 2003). Renieramycins are also produced by several species of sponge such as *Reniera* sp., *Haliclona cribricutis cribricutis*, *Cribrochalina* sp., and *Neopetrosia* sp./spp. (Frincke and Faulkner, 1982; Parameswaran et al., 1998; Pettit et al., 2000; Oku et al., 2003; Nakao et al., 2004; Van Soest et al., 2005). They have potent cytotoxicities against cancer cell lines (Suwanborirux et al., 2003; Amnuoypol et al., 2004). Structures (Types) of renieramycins have been modified and documented (Amnuoypol et al., 2004). However, the natural structure, but easily degraded, was renieramycin E because the hydroxyl function group causes this compound to be unstable (Suwanborirux et al., 2003). The protocol to make renieramycin E more stable is to replace the hydroxyl function group with a cyanide functional group to become renieramycin M (Suwanborirux et al., 2003). This protocol allowed the high-yield extraction of renieramycin (Suwanborirux et al., 2003). However, the ecological roles of these compounds are less well understood.

The present study aimed to investigate the variation of nutritional values [carbon (C), hydrogen (H), and nitrogen (N)] and renieramycin M concentrations in different areas within the individuals of *Xestospongia* coexisting with *Porites* and *Palythoa*. *Xestospongia* was expected to face intensive predatory and competitive pressures because of the high diversity in the coral reef community. Thus, nutritional values that are essential sources of energy and growth of *Xestospongia* may exhibit differently in different parts of *Xestospongia*. In addition, the necrotic effect of renieramycin M on *Xestospongia*'s coexisting species, *Porites*, and its effect on settlement of fouling organisms were investigated.

MATERIALS AND METHODS

In this study, C, H, and N contents and renieramycin M concentrations were investigated in different areas within the individuals of *Xestospongia*. The allelopathic effects of renieramycin M on *Portes* bleaching, larval settlement, and aerobic bacteria were examined.

Carbon, Hydrogen, Nitrogen Contents and Allocations of Renieramycin M in *Xestospongia*

Sample Collection

Fifteen specimens of *Xestospongia* coexisting with *Porites lutea* (thereafter *Porites*) (Phylum Cnidaria; Class Anthozoa; Family Poritidae) and 15 sponge specimens coexisting with *Palythoa caesia* (thereafter *Palythoa*) (Phylum Cnidaria; Class Anthozoa; Family Zoanthidae) were collected from Ran Dok Mai Island (13°09′05.35″N, 100°50′01.41″E) by scuba diving. Each sponge specimen was separated into three areas: the outer area (blue color); the inner area (yellowish-gray color), and the edge of the sponge. The definition of each area was as follows: the outer area was about 1 mm thick of the sponge's upper surface that was totally blue in color; the inner area was about 1 mm thick of the sponge's surface attached to the substrate that was totally yellowish-gray; the edge was about 1 mm thick of the sponge's surface attached to the living tissue of the coexisting organisms (herein were *Porites* and *Palythoa*) that was located at the edge of the sponges and mostly were bluish-gray in color (**Figure 1**). To reduce the amount of saltwater, each specimen was cut into 2-cm^2-sized pieces and dried with tissue paper for a minute, twice. The semidried specimens were placed in plastic bags in an icebox during transportation to the lab. The specimens were then stored at -20°C until extraction.

Elemental Analysis

The samples were analyzed for C, H, and N contents (percent of dry weight) by Dynamic Flash Combustion Technique. The instrument used was the CE Instruments Flash 1112 Series EA CHNS-O Analyzer at the Scientific Equipment Center, Prince of Songkla University. The analyzing condition was as follows: furnace temperature: 900°C; oven temperature: 65°C; carrier flow: 130 ml/min; reference flow: 100 ml/min; oxygen flow: 250

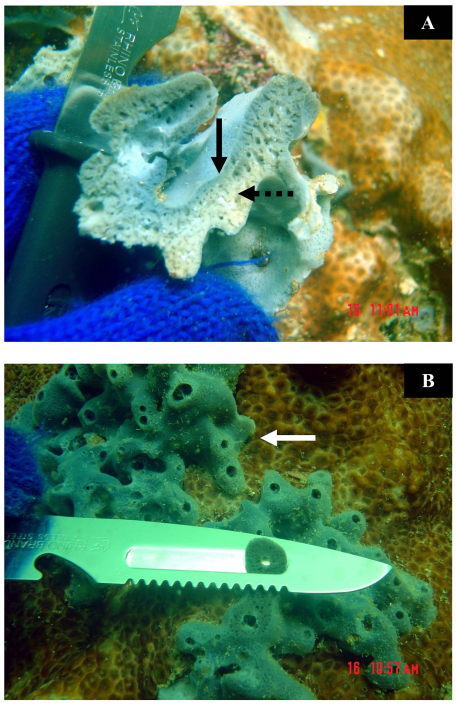

FIGURE 1 | (A) The outer area (solid arrow) and the inner area (dot arrow) of *Xestospongia*. **(B)** The edge (solid arrow) of *Xestospongia* and the cutting method.

ml/min. Before the analysis, the samples were freeze-dried and then fumed with hydrochloric acid to remove inorganic C.

Renieramycin M Measurement

For crude extract preparation, all samples were lyophilized for 12 h using a freeze dryer. Each sample was accurately weighed at 100.0 mg for extraction. The sample was macerated with 10 mM potassium cyanide in phosphate buffer solution (6 ml, pH 7.0) for 5 h. Then, the suspension was extracted with methanol (24 ml) for 1 h. After centrifugation at 5,000 rpm for 5 min, the supernatant (3 ml) was partitioned with ethyl acetate (9 ml) and a brine solution (6 ml). The ethyl acetate layer (3 ml) was evaporated until dry. The dried residue was dissolved in methanol (1 ml) containing 300 ng acenapthene as an internal standard. The sample solutions were filtered through 0.45-nm nylon syringe tip filters before the high-performance liquid chromatographic (HPLC) analysis. All procedures were conducted by following the university safety protocol.

To calibrate the standard solution, standard renieramycin M derived from *Xestospongia* sp. in the Gulf of Thailand was obtained from Dr. Khanit Suwanborirux, Center of Bioactive Natural Products from Marine Organisms and Endophytic Fungi (BNPME). A stock standard solution of renieramycin M at a concentration of 1 mg/ml was prepared in methanol. Calibration solutions containing 2.4, 4.8, 9.0, 180, 375, 750, and 1,500 ng/ml were prepared by appropriate dilutions of the stock solution with methanol containing 800 ng acetonaphthone as an internal standard.

For HPLC conditions, a Waters 2690 Controller was used with a Waters 996 Photodiode Array (PDA) Detector operating at 270 nm. The separation was performed on a LiChrospher®100RP-18 reversed phase column (5 μm, spherical, 4 mm × 125 mm) with methanol–water (7:3) as the mobile phase at a flow rate of 1.00 ml/min.

Bleaching and Necrotic Effects of Renieramycin M on *Porites*

A colony of live massive coral, *Porites*, was collected from the intertidal zone of Sichon (9°00′16″N, 99°55′20″E). It was then broken into small pieces. There were about 10–15 corallites in each piece (nubbins). A nubbin was attached on top of a plastic rod using a very small amount of ethyl-2-cyanoacrylate glue and then left in the air for several seconds for the hardening of the glue. All coral nubbins were vertically set onto the plastic net (approximate mesh size 5 mm). The plastic net (culture frame) with coral nubbins was hung in the ocean for 2 months. The survival rate was monitored weekly.

Thirty coral nubbins were collected from the culture frame and then were acclimatized in the lab for a week prior to the experiment. There were five treatments of different renieramycin M concentrations: 0.00 ppm (control), 0.02 ppm, 0.20 ppm (natural concentration), 1.00 ppm, and 10.00 ppm. One hundred microliters of dimethyl sulfoxide (DMSO), which was preliminarily tested and showed no effects on *Porites*, was used as a solvent for each treatment, including the control. The total volume was made to be 50.0 ml by 30 ppt of filtered seawater with natural salinity. For each treatment, 5 coral nubbins were submerged in the solution with air bubbles for 8 h. After that, coral nubbins from each treatment were separately placed into transparent containers, each of them containing 500 ml of seawater. To control the growth of algae during the experiment, every container was left under approximately 40% of natural light. Bleaching and necrosis were observed daily for 2 weeks.

Antifouling Effect of Renieramycin M on Larval Settlement

This method was modified from Maida et al. (2006). Several dead coral rocks of *Porites* sp. with approximately 20 × 30 × 20 cm^3 (W × L × H) were collected from an intertidal zone of Sichon (9°00′16″N, 99°55′20″E). They were then cut into approximately 4 × 4 × 1 cm^3 (W × L × H) cubes. Each coral cube was desalinated by submerging it in distilled water several times. After that, the coral cubes were dried in an oven at 50°C for 2 days. In all of the cubes, a hole (6.35 mm in diameter) was made at the center by a drilling machine.

Five experiments were prepared with 0.00 ppm (control), 0.05 ppm (natural concentration), 0.10 ppm, 0.20 ppm, and 2.00 ppm renieramycin M in 500 ml of methanol. Three cubes were randomly assigned for each experimental unit. The cubes were submerged into the methanolic solutions for 24 h. Then, they were hung and dried at room temperature (28°C). The experiment contained four experimental sets. Each set

consisted of a control unit and four treatment units with different renieramycin M concentrations as described above. There were three replicates of each unit. All experimental sets were then hung in the sea (approximately 1 m below the low tide level) at the same coral reef habitat where the dead coral rocks were collected (**Figure 2**). Each replicate was approximately 10 cm deep apart from each other. Thus, the depths did not have any effects. The first experimental set was collected from the sea 5 days after the experiment started and the second, third, and fourth experimental sets on days 10, 15, and 20, respectively. Only the upper and lower surfaces of every cube were investigated for fouling organisms under a binocular stereoscope. The number of sessile organisms was counted and grouped into class taxa level. Species diversity index (H') was used to determine the fouling effect of renieramycin M as well.

Antimicrobial Effect of Renieramycin M on Aerobic Bacteria

Fresh seawater, collected from a coral reef habitat from Sichon (9°00′16″N, 99°55′20″E), was aerated 24 h prior to the experiment. Then, 1.00 ml of this water was pipetted using a micropipette and was poured onto an aerobic count plate (petrifilm sheet) (3M Petrifilm Aerobic Count Plate, 3M) for each treatment. A petrifilm sheet was unmoved for a couple of minutes to let the gel solidify. Paper disks (5.0-mm diameter) (MF-Millipore Membrane Filter, Merck) have 200, 100, 10, or 1 μg of renieramycin M. As a control, paper disks bearing 0.0 μg of renieramycin M were prepared (**Figure 3**). The petrifilm sheets were placed and incubated at 30°C for 24 h. In one plate, both a control disk and a treatment disk (a single concentration of renieramycin M in each plate) were placed. After 24 h, the diameter of the zone of inhibition in each paper disk was recorded. The number of bacterial colonies growing on the grid areas containing the paper disks was also counted by using an illuminated magnifier and a hand tally counter.

Statistical Analyses

The differences on C, H, and N contents and renieramycin M concentrations with *Porites* or *Palythoa* were examined using the nested analysis of variance (ANOVA) to examine both differences between coexisting species and among the areas, as the factor of the areas is nested in the factor of the coral species. In addition, the numbers of bacterial colonies on paper disks (3 disks for control and 3 disks for treatment) of each treatment petrifilm sheet were statistically compared using t-test. A significant level applied in this study was 0.05.

RESULTS

Carbon, Hydrogen, and Nitrogen Contents and Allocations of Renieramycin M in *Xestospongia*

The results showed that C, H, N contents and renieramycin M concentration were not significantly different ($P > 0.05$) among areas of *Xestospongia* coexisting with *Porites* and *Palythoa* (**Table 1**). The nutrition values (C/N ratio) at different areas of *Xestospongia* coexisting with *Porites* and of those coexisting with *Palythoa* were also not significant ($P > 0.05$) (**Table 1**). However, 8 out of 15 *Xestospongia* individuals that coexisted with *Porites* had their highest renieramycin M concentrations in the edge area, whereas 7 out of 15 *Xestospongia* individuals coexisting with *Palythoa* had the highest concentrations in the outer area (**Table 2**).

Bleaching and Necrosis Effects of Renieramycin M on *Porites*

Bleaching and necrosis of coral nubbins were not observed during 2 weeks in every treatment. Coral nubbins were still brown in color in both control and treatments and sometimes covered by a mucous sheet. During nighttime or low light intensity, corallites

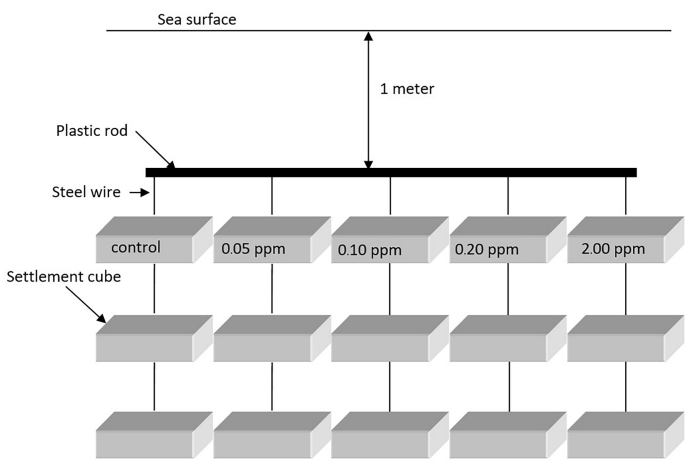

FIGURE 2 | Diagram of the experimental setup of an antifouling experiment.

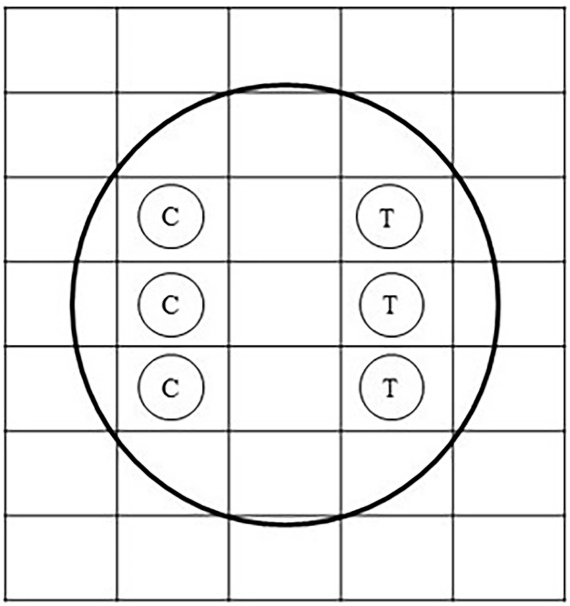

FIGURE 3 | Diagram of the paper disk technique on an aerobic count plate. C stands for the control bearing only 3 µl of dimethyl sulfoxide (DMSO). T stands for the treatment bearing renieramycin M at 200, 100, 10, or 1 µg with 3 µl of DMSO.

of some coral nubbins protruded and waved their trunks and their tentacles into the water column.

Antifouling Effect of Renieramycin M on Larval Settlement

Renieramycin M was found to inhibit the settlement of some sessile organisms. However, the duration of the antifouling effect could be found on the first 5 days (**Figure 4**). There were three groups of sessile organisms found on the control plates, pelecypoda, polychaeta, and barnacle (*Semibalanus balanoides*), whereas only pelecypoda was found on the treatment plates during the 5-day period. After 10 days, pelecypods were the major group of sessile organisms on control and treatment plates. Polychaeta was found settled on the treatment plates of 0.05–2.0 ppm concentrations (**Figure 4**). After a 15-day period, *S. balanoides* was found again on the settlement plates (control, 0.05 ppm, 0.1 ppm, and 2.0 ppm), whereas at the 5-day period, *S. balanoides* was found only on the control plates (**Figure 4**). The composition of sessile organisms on every treatment was the same as the composition of sessile organisms on the control after 20 days (**Figure 4**). The diversity index also supported the effect on antifouling of renieramycin M (**Figure 5**). After 5 days, the highest diversity index was for the control plates, whereas other treatment plates had a zero diversity index. After longer periods (days 15 and 20), the diversity index values were high in all treatments.

Antimicrobial Effect of Renieramycin M on Aerobic Bacteria

There was no significant difference ($P > 0.05$) in the number of aerobic bacterial colonies in all contents of renieramycin M (**Figure 6**). The average number of bacterial colonies on the control paper disks ranged from 30 to 62 colonies per 50 µl, whereas the average number of colonies on treatment paper disks ranged from 45 to 61 colonies per 50 µl (**Figure 6**). The zone of colonial growth inhibition was not observed on any control or any treatment paper disks. The statistical analysis of antimicrobial effects between different concentrations of renieramycin M compared with control was shown in **Table S1**.

DISCUSSION

Allocations of Carbon and Nitrogen Contents and Renieramycin M in *Xestospongia*

In this study, the C, H, and N contents were uniformly allocated in the body of *Xestospongia* coexisting with *Porites*, even though there were no significant differences on C, H, or N contents in same areas of *Xestospongia* when it coexisted with different competitors (*Porites* or *Palythoa*) (**Table 1**). However, the varieties of nutrition, chemical contents, and morphological and physiological changes were commonly found in plants, sponges, and other sessile organisms (Haukioja et al., 1998; Swearingen

TABLE 1 | The percentage (mean ± SE) of carbon (C), hydrogen (H), and nitrogen (N) contents, C:N ratio, and renieramycin M concentration in different areas of *Xestospongia* coexisting with different organisms.

	Porites			***Palythoa***			**$F_{1,4}$(between the coexisting coral species)***	**$F_{4,84}$(among the areas nested in coral species)***
	Edge	**Inner**	**Outer**	**Edge**	**Inner**	**Outer**		
C (% dry weight)	8.64 ± 1.66	9.44 ± 1.99	9.86 ± 1.56	9.88 ± 0.77	10.55 ± 1.04	10.41 ± 1.17	2.13	1.33
H (% dry weight)	1.74 ± 0.16	1.94 ± 0.19	2.07 ± 0.14	1.89 ± 0.12	2.02 ± 0.15	2.07 ± 0.15	1.85	1.20
N (% dry weight)	1.53 ± 0.36	1.77 ± 0.40	1.96 ± 0.41	1.93 ± 0.25	2.00 ± 0.27	2.08 ± 0.28	1.90	1.17
C:N ratio	5.92 ± 1.15	5.41 ± 0.95	5.01 ± 0.89	5.32 ± 0.35	5.51 ± 0.47	5.03 ± 0.51	1.21	0.30
Renieramycin M Concentration (µg/g)	0.075 ± 0.060	0.066 ± 0.051	0.060 ± 0.053	0.050 ± 0.049	0.068 ± 0.047	0.050 ± 0.054	0.84	0.68

** All of the F values are not significant (P > 0.05).*

TABLE 2 | The proportions of *Xestospongia* individuals that contain the highest renieramycin M concentrations at different areas when they coexist with *Porites* and *Palythoa*.

Areas	With *Porites*	With *Palythoa*
Outer	5/15	7/15
Inner	2/15	3/15
Edge	8/15	5/15

There were no significant distributions of renieramycin M concentrations along the body parts of *Xestospongia* (**Table 1**). On the other hand, other sponge species, *Oceanapia* spp. and *Crambe crambe*, have been proven to significantly distribute their toxicity and secondary metabolites within specimens such as at fistule, capitum, basal, or even different cell types (Uriz et al., 1996; Schupp et al., 1999; Salomon et al., 2001). By

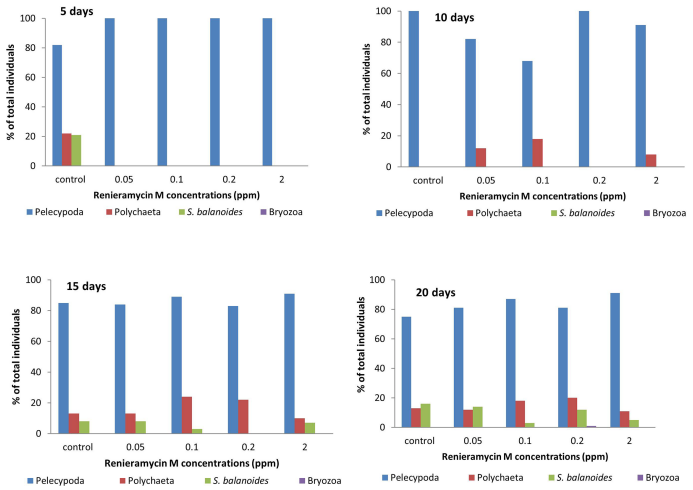

FIGURE 4 | The percentage of total individuals of sessile organisms on different experimental plates after 5, 10, 15, and 20 days.

and Pawlik, 1998; Puglisi et al., 2000; Furrow et al., 2003; Meroz-Fine et al., 2005). For example, for plant species in boreal forests, plants balance their C/N utilizations to survive in the intensely competitive and herbivory pressured habitats (Bryant et al., 1983). In addition, some N-based chemicals, produced by organisms, were varied by N-limited habitats (Bryant et al., 1983).

comparison, renieramycin M concentrations at the edges were higher in *Porites*-coexisted *Xestospongia* than *Palythoa*-coexisted ones. These results might be due to the allocation of chemicals on different spatial competitors of *Xestospongia*. Although there were a number of studies on the effects of allelochemicals and secondary metabolites of marine sponges on potential spatial competitors, particularly

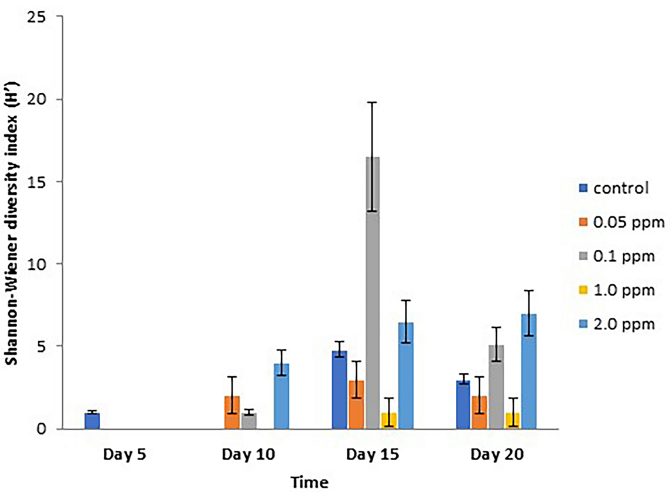

FIGURE 5 | Shannon–Wiener diversity index (H') (mean ± SE) on different experimental plates at different concentrations of renieramycin M and different periods.

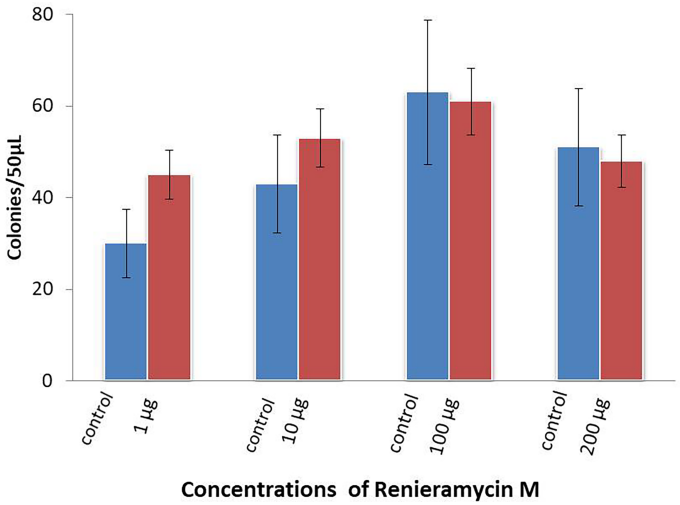

FIGURE 6 | Numbers of colonies (mean ± SE) of aerobic bacteria growing on aerobic count plates.

corals, the comparison of chemicals produced by sponges when they coexist with different potential spatial competitors was less available (see examples in Porter and Targett, 1988; Aerts and Van Soest, 1997; Aerts, 1998; Nishiyama and Bakus, 1999; Engel and Pawlik, 2000; Pawlik et al., 2007).

Allelopathic Effects of Renieramycin M

The effects of allelochemicals of sponges on corals and on other sponge species were necrotic effects, bleaching, and the effect on the photosynthetic ability of coral's symbionts (Porter and Targett, 1988; Engel and Pawlik, 2000; Pawlik et al., 2007). However, renieramycin M exhibited neither bleaching nor necrosis effects on *Porites*.

During the surveys, the necrotic scars or the dead zones of *Porites* were observed only on the tissue that contacted *Xestospongia* (in this study; Darumas et al., 2007). Therefore, the dead zones or necrotic areas might be caused by the synergy of physical damage (by spicules) and other allelochemicals. In addition, sessile organisms were known to compete for space. The strategies to compete with their competitors include overgrowth, physical damage, allelochemicals, and waterborne substances (Porter and Targett, 1988; Paul, 1992; Aerts, 1998; Nishiyama and Bakus, 1999). According to the field surveys of this study, the interactions between *Xestospongia* and the massive coral, *Porites*, were of the single category, sponge overgrowing coral. The sponge/coral interactions were classified into four categories: overgrowth, peripheral contact, tissue contact, and non-contact (Aerts and Van Soest, 1997). Their study showed that 46.6% of *Xestospongia* spp. (*X. caminata*, *X. muta*, *X. proxima*) had tissue contact with corals, and 32.6% had non-contact with corals, while 2.5% of *Xestospongia* overgrew corals. On the other hand, just 2.2%, 14.3%, and 33.8% of massive coral, *Porites astreoides*, had overgrown, peripheral contact, and tissue contact by sponges, respectively. In addition, the major proportion of the interaction (49.7%) of this coral was non-contact to sponges (Aerts and Van Soest, 1997). Although, the effect of overgrowth by sponges on corals was not directly documented, one study showed that the overgrowth of sponge on introduced mussels in the Great Lakes (USA) caused mortality or at least loss in the mussels (Ricciardi et al., 1995).

Renieramycin M had no antifouling effect on pelecypods but on polychaetes and barnacles (*S. balanoides*) during the first 5 days of the experiments. The antifouling chemicals produced by pre-settlement organisms were not universally against newcomers (Porter and Targett, 1988; Paul, 1992; Nishiyama and Bakus, 1999). Antifouling was the active competitive defense of sessile organisms. This strategy prevented interspecific larva from settling on surfaces of the previous one (Jackson and Buss, 1975; Nishiyama and Bakus, 1999; Kubanek et al., 2002). The antifouling process operates through mechanical and chemical mechanisms. Some soft corals were swept out and were damaged by sweeper tentacles and nematocysts of hard corals (Paul, 1992). Some sessile organisms used at least two mechanisms to inhibit interspecific larval settlement (Bak and Borsboom, 1984; Coll et al., 1987; Sears et al., 1990; Henrikson and Pawlik, 1995; Hirota et al., 1998; Nishiyama and Bakus, 1999). First was a waterborne substance production, which was released into the water column to affect the competitor's fitness. Second was the allelochemical that affected the competitors when the tissues were in contact.

Renieramycins were tested to inhibit *Staphylococcus aureus*, *Bacillus subtilis*, and *Vibrio angularium* but not *Escherichia coli*, *Candida albicans*, *Pseudomonas aeruginosa*, and *Enterobacter aerogenes* (Frincke and Faulkner, 1982; Kelman et al., 2001). In this study, renieramycin M did not inhibit the growth of aerobic bacteria in any treatment. However, antibiotic chemicals produced by sessile organisms or the symbionts were effective against specific bacteria rather than a broad spectrum (Frincke and Faulkner, 1982; Kelman et al., 2001). A number of studies elaborated more about the interaction between bacteria vs. sponge and bacteria vs. macroalgae such as anti-non-symbiotic species and antifouling (Imhoff and Trüper, 1976; Wilkinson, 1978; Lemos et al., 1985; Althoff et al., 1998; Webster and Hill, 2001; Thacker and Starnes, 2003; Armstrong et al., 2006). Sponges

of the genus *Dysidea* were a specific host of cyanobacterium (Thacker and Starnes, 2003). Sometimes, the chemicals produced by microsymbionts were beneficial to the host (Lemos et al., 1985; Webster and Hill, 2001). Epiphytic bacteria attached to seaweed produced antimicrobial chemicals for the host (Lemos et al., 1985). α-Proteobacteria, surrounding the choanocyte chamber of *Rhopaloeides* sponge, was expected to play the role of nutrient uptake in the host sponge (Webster and Hill, 2001). In some cases, microorganisms may be harmful to sessile organisms. This can be inferred by the varieties of antibiotic substances produced by sessile organisms or their symbionts (Frincke and Faulkner, 1982; Lemos et al., 1985; Kelman et al., 2001; Kubanek et al., 2002; Müller et al., 2004).

CONCLUSION

This study provides evidence that renieramycin M found in *Xestospongia* was uniform; however, it can possess strong inhibitory activities against some marine organisms. From our study, there were variations of nutritional values of *Xestospongia*. *Xestospongia* did not unequally distribute its nutritional values for predatory defense. The overall contents of C, H, and N in every area of *Xestospongia* coexisting with *Porites* were not different from those of *Xestospongia* coexisting with *Palythoa*. In the laboratory, renieramycin M did not show any allelopathic effect on its coexisting organisms (*Porites*). Furthermore, it did not inhibit the growth of aerobic bacteria. However, renieramycin M inhibited the settlement of acorn barnacle. However, it did not inhibit the settlement of pelecypods.

DATA AVAILABILITY STATEMENT

The original contributions presented in the study are included in the article/**Supplementary Material**. Further inquiries can be directed to the corresponding author.

AUTHOR CONTRIBUTIONS

UD, KS, and SC conceived the ideas and designed the study. UD and SC carried out the field work and sampling quantification. US, KS, VV, and SC contributed to the data analysis and interpretation. UD, GS, VV, and SC drafted the manuscript. All authors contributed to the article and approved the submitted version.

FUNDING

This work was supported by Second Century Fund (C2F) Postdoctoral Scholarship of Chulalongkorn University, NRCT-JSPS Core to Core Program, CREPSUM JPJSCCB20200009, Thailand Science research and Innovation Fund Chulalongkorn University (CU_FRB65_dis (3)_091_23_21)), National Research Council of Thailand and Chulalongkorn University (N42A650257), and Mubadala Petroleum (Thailand) Limited. Mubadal Petrolem (Thailand) was not involved in the study design, collection analysis, interpretation of data, the writing of this article or the decision to submit it for publication.

ACKNOWLEDGMENTS

We acknowledged Dr. John Hooper, Dr. Larry Harris, Dr. Pitiwong Tantichodok, editor and reviewers for their valuable comments and suggestions. We also thank UNESCO/IOC-WESTPAC for the support.

SUPPLEMENTARY MATERIAL

The Supplementary Material for this article can be found online at: https://www.frontiersin.org/articles/10.3389/fmars.2022.735702/full#supplementary-material

REFERENCES

Aerts, L. A. M. (1998). Sponge/coral Interactions in Caribbean Reefs: Analysis of Overgrowth Patterns in Relation to Species Identity and Cover. *Mar. Ecol. Prog. Ser.* 175, 241–249. doi: 10.3354/meps175241

Aerts, L. A. M. and Van Soest, R. W. M. (1997). Quantification of Sponge/Coral Interactions in a Physically Stressed Reef Community, NE Colombia. *Mar. Ecol. Prog. Ser.* 148, 125–134. doi: 10.3354/meps148125

Althoff, K., Schütt, C., Steffen, R., Batel, R. and Müller, W. E. G. (1998). Evidence for a Symbiosis Between Bacteria of the Genus Rhodobacter and the Marine Sponge Halichondria Panacea: Harbor Also for Putatively Toxic Bacteria? *Mar. Biol.* 130, 529–536. doi: 10.1007/s002270050273

Amnuoypol, S., Suwanborirux, K., Pummangura, S., Kubo, A., Tanaka, C. and Saito, N. (2004). Chemistry of Renieramycins. Part 5. Structure Elucidation of Renieramycin-Type Derivatives O, Q, R, and S From Thai Marine Sponge Xestospongia Species Pretreated With Potassium Cyanide. *J. Nat. Prod.* 67, 1023–1028. doi: 10.1021/np030534o

Armstrong, R. A., Singh, H., Torres, J., Nemeth, R. S., Can, A., Roman, C., et al. (2006). Characterizing the Deep Insular Shelf Coral Reef Habitat of the Hind Bank Marine Conservation District (US Virgin Islands) Using the Seabed Autonomous Underwater Vehicle. *Continent. Shelf. Res.* 26, 194–205. doi: 10.1016/j.csr.2005.10.004

Bak, R. P. M. and Borsboom, J. L. A. (1984). Allelopathic Interaction Between a Reef Coelenterate and Benthic Algae. *Oecologia.* 63, 194–198. doi: 10.1007/BF00379877

Bryant, J. P., Chapin, F.S.III. and Klein, D. R. (1983). Carbon/nutrient Balance of Boreal Plants in Relation to Vertebrate Herbivory. *Oikos.* 40, 357–368. doi: 10.2307/3544308

Coll, J. C., Price, I. R., König, G. M. and Bowden, B. F. (1987). Algal Overgrowth Alcyonacean Soft Corals. *Mar. Biol.* 96, 129–135. doi: 10.1007/BF00394846

Darumas, U., Chavanich, S. and Suwanborirux, K. (2007). Distribution Patterns of the Renieramycin-Producing Sponge, Xestospongia Sp., and its Association With Other Reef Organisms in the Gulf of Thailand. *Zoological Stud.* 46 (6), 695–704.

Engel, S. and Pawlik, J. R. (2000). Alleopathic Activities of Sponge Extracts. *Mar. Ecol. Prog. Ser.* 207, 273–281. doi: 10.3354/meps207273

Faulkner, D. J. (1984). Marine Natural Products: Metabolites of Marine Invertebrates. *Nat.Prod. Rep.* 1, 551–598. doi: 10.1039/np9840100551

Folt, C. and Goldman, C. (1981). Allelopathy Between Zooplankton: A Mechanism for Interference Competition. *Science* 213, 1133–1135. doi: 10.1126/science.213.4512.1133

Frincke, J. M. and Faulkner, D. J. (1982). Antimicrobial Metabolites of the Sponge Reniera Sp. *J. Am. Chem. Soc* 104, 265–269. doi: 10.1021/ja00365a048

Furrow, F. B., Amsler, C. D., McClintock, J. B. and Baker, B. J. (2003). Surface Sequestration of Chemical Feeding Deterrents in the Antarctic Sponge Latrunculia Apicalis as an Optimal Defense Against Sea Star Spongivory. *Mar. Biol.* 143, 443–449. doi: 10.1007/s00227-003-1109-5

Haukioja, E., Ossipov, V., Koricheva, J., Honkanen, T., Larsson, S. and Lempa, K. (1998). Biosynthetic Origin of Carbon-Based Secondary Compounds: Cause of Variable Responses of Woody Plants to Fertilization? *Chemoecol.* 8, 133–139. doi: 10.1007/s000490050018

Henrikson, A. A. and Pawlik, J. R. (1995). A New Antifouling Assay Method: Results From Field Experiments Using Extracts of Four Marine Organisms. *J. Exp. Mar. Biol. Ecol.* 194, 157–165. doi: 10.1016/0022-0981(95)00088-7

Hirota, H., Okino, T., Yoshimora, E. and Fusetani, N. (1998). Five New Antifouling Sesquiterpenes From Two Marine Sponges of the Genus Axinyssa and the Nudibranch Phyllidia Pustulosa. *Tetrahedron.* 54, 13971–13980. doi: 10.1016/S0040-4020(98)00867-9

Imhoff, J. F. and Trüper, H. G. (1976). Marine Sponges as Habitats of Anarobic Phototrophic Bacteria. *Microb. Ecol.* 3, 1–9. doi: 10.1007/BF02011449

Jackson, J. B. C. and Buss, L. (1975). Allelopathy and Spatial Competition Among Coral Reef Invertebrates. *Proc. Nat. Acad. Sci.* 72 (12), 5160–5163. doi: 10.1073/pnas.72.12.5160

Kelman, D., Kashman, Y., Rosenberg, E., Ilan, M., Ifrach, I. and Loya, Y. (2001). Antimicrobial Activity of the Reef Sponge Amphimedon Viridis From the Red Sea: Evidence for Selective Toxicity. *Aquat. Microb.* 24, 9–16. doi: 10.3354/ame024009

Kritsanapuntu, S., Chaitanawisuti, N., Yeemin, T. and Putchakan, S. (2001). First Investigation on Biodiversity of Marine Sponges Associated With Reef Coral Habitats in the Eastern Gulf of Thailand. *Asian Mar. Biol.* 18, 105–115.

Kubanek, J., Whalen, K. E., Engle, S., Kelly, S. R., Henkel, T. P., Fenical, W., et al. (2002). Multiple Defensive Roles for Triterpene Glycosides From Two Caribbean Sponges. *Oecologia.* 131, 125–136. doi: 10.1007/s00442-001-0853-9

Lages, B. G., Fleury, B. G., Ferreira, C. E. L. and Pereira, R. C. (2006). Chemical Defense of an Exotic Coral as Invasion Strategy. *J. Exp. Mar. Biol. Ecol.* 328, 127–135. doi: 10.1016/j.jembe.2005.07.011

Lang, J. C. and Chornesky, E. A. (1990). "Competition Between Scleractinian Reef Corals: A Review of Mechanisms and Effects," in *Ecosystems of the World: Coral Reefs*. Ed. Dubinsky, Z. (Amsterdam: Elsevier Press).

Lemos, M. L., Toranzo, A. E. and Barja, J. L. (1985). Antibiotic Activity of Epiphytic Isolated From Intertidal Seaweeds. *Microb. Ecol.* 11, 149–163. doi: 10.1007/BF02010487

Maida, M., Sammarco, P. W. and Coll, J. C. (2006). A Diffusion Chamber for Assessing Efficacy of Natural Anti-Fouling Defenses in Marine Organisms. *J. Exp. Mar. Biol. Ecol.* 337, 59–64. doi: 10.1016/j.jembe.2006.06.008

Meroz-Fine, E., Shefer, S. and Ilan, M. (2005). Changes in Morphology and Physiology of an East Mediterranean Sponge in Different Habitats. *Mar. Biol.* 147, 243–250. doi: 10.1007/s00227-004-1532-2

Müller, W. E. G., Klemt, M., Thakur, N. L., Schröder, H. C., Aiello, A., D'Esposito, M., et al. (2004). Molecular/chemical Ecology in Sponges: Evidence for an Adaptive Antibacterial Response in Suberites Domancula. *Mar. Biol.* 144 (1), 19–29. doi: 10.1007/s00227-003-1184-7

Nakao, Y., Shiroiwa, T., Murayama, S., Matsunaga, S., Goto, Y., Masumoto, Y., et al. (2004). Identification of Renieramycin A as an Antileishmanial Substance in Marine Sponge Neopetrosia Sp. *Mar. Drugs* 2, 55–62. doi: 10.3390/md202055

Nishiyama, G. K. and Bakus, G. J. (1999). Release of Allelochemicals by Three Tropical Sponges (Demospongiae) and Their Toxic Effects on Coral Substrate Competitors. *Memoirs Queensland Museum.* 44, 411–417.

Oku, N., Matsunaga, S., van Soest, R. W. M. and Fusetani, N. (2003). Renieramycin J, a Highly Cytotoxic Tetrahydroisoquinoline Alkaloid, From a Marine Sponge Neopetrosia Sp. *J. Nat. Prod.* 66, 1136–1139. doi: 10.1021/np030092g.

Parameswaran, P. S., Naik, C. G. and Kamat, S. Y. (1998). Renieramycins H and I, Two Novel Alkaloids From the Sponge Haliclona Cribricutis Dany. *Indian J. Chem.*, 37B. 1258–1263.

Paul, V. J. (1992). "Chemical Defenses of Benthic Marine Invertebrates," in *Ecological Roles of Marine Natural Products*. Ed. Paul, V. J. (London: Comstock Publishing Associates), 164–188. doi: 10.7591/9781501737435-009

Pawlik, J. R., Steindler, L., Henkel, T. P., Beer, S. and Ilan, M. (2007). Chemical Warfare on Coral Reefs: Sponge Metabolites Differently Affect Coral Symbiosis in Situ. *Limnol. Oceanogr.* 52 (2), 907–911. doi: 10.4319/lo.2007.52.2.0907

Pettit, G. R., Knight, J. C., Collin, J. C., Herald, D. L., Pettit, R. K., Boyd, M. R., et al. (2000). Antineoplastic Agent 430. Isolation and Structure of Cribrostatins 3, 4 and 5 From the Republic of Maldives Cribrochalina Species. *J. Nat. Prod.* 63, 793–798. doi: 10.1021/np990618q

Porter, J. W. and Targett, N. M. (1988). Allelochemical Interactions Between Sponges and Corals. *Biol. Bull.* 175, 230–239. doi: 10.2307/1541563

Puglisi, M. P., Paul, V. J. and Slattery, M. (2000). Biogeographic Compositions of Chemical and Structural Defenses of the Pacific Gorgonians Annella Mollis and A. Reticulate. *Mar. Ecol. Prog. Ser.* 207, 263–272. doi: 10.3354/meps207263

Pulitzer—Finali, G. (1996) *Sponges from the Bismarck Sea*. Bollettino dei Musei e degli Istituti Biologici della (R.) Università di Genova, 60–61, 101–138.

Ricciardi, A., Snyder, F. L., Kelch, D. O. and Reiswig, H. M. (1995). Lethal and Sublethal Effects of Sponge Overgrowth on Introduced Dreissenid Mussels in the Great Lakes-St. Lawrence River System. *Can. J. Fish. Aqua. Sci.* 52, 2695–2703. doi: 10.1139/f95-858

Salomon, C. E., Deerinck, T., Ellisman, M. H. and Faulkner, D. J. (2001). The Cellular Location of Dercitimide in the Palauan Sponge Oceanapia Sagittaria. *Mar. Biol.* 139, 313–319. doi: 10.1007/s002270100493

Schupp, P., Eder, C., Paul, V. and Proksch, P. (1999). Distribution of Secondary Metabolites in Sponge Oceanapia Sp. And its Ecological Implications. *Mar. Biol.* 135, 573–580. doi: 10.1007/s002270050658

Sears, M. A., Gerhart, D. J. and Rittschof, D. (1990). Antifouling Agents From Marine Sponge Lissodendroxyx Isodictylis Carter. *J. Chem. Ecol.* 16 (3), 791–799. doi: 10.1007/BF01016489

Suikkanen, S., Fistarol, G. O. and Granéli, E. (2004). Allelopathic Effects of the Baltic Cyanobacteria Nodularia Spumigena, Aphanizomanon Flos-Aquae and Anabaena Lemmermannii on Algal Monocultures. *J. Exp. Mar. Biol. Ecol.* 308, 85–101. doi: 10.1016/j.jembe.2004.02.012

Suwanborirux, K., Amnuoypol, S., Plubrukarn, A., Pummangura, S., Kubo, A., Tanaka, C., et al. (2003). Chemistry of Renieramycins. Part 3. Isolation and Structure of Stabilized Renieramycin Type Derivatives Possessing Antitumor Activity From Thai Sponge Xestospongia Species, Pretreated With Potassium Cyanide. *J. Nat. Prod.* 66, 1441–1446. doi: 10.1021/np030262p

Swearingen, D. C. and Pawlik, J. R. (1998). Variability in the Chemical Defense of the Sponge Chondrilla Nucula Against Predatory Reef Fishes. *Mar. Biol.* 131, 619–627. doi: 10.1007/s002270050354

Thacker, R. W. and Starnes, S. (2003). Host Specificity of the Symbiotic Cyanobacterium Oscillatoria Spongiliae in Marine Sponges Dysidea Spp. *Mar. Biol.* 142, 643–648. doi: 10.1007/s00227-002-0971-x

Uriz, M. J., Becerro, M. A., Tur, J. M. and Turon, X. (1996). Location of Toxicity Within the Mediterranean Sponge Crambe Crambe (Demospongiae: Poecilosclerida). *Mar. Biol.* 124, 583–590. doi: 10.1007/BF00351039

Van Soest, R. W. M., Boury-Esnault, N., Janussen, D. and Hooper, J. (2005) *World Porifera Database*. Available at: http://www.vliz.be/vmdcdata/porifera.

Vicente, V. P. (1990). Response of Sponges With Autotrophic Endosymbionts During the Coral-Bleaching Episode in Puerto Rico. *Coral Reefs* 8, 199–202. doi: 10.1007/BF00265011

Wang, C. Y., Liu, H. Y., Shao, C. L., Wang, Y., Li, L. and Guan, H. S. (2008). Chemical Defensive Substances of Soft Corals and Gorgonians. *Acta Ecologica Sin.* 28, 2320–2328. doi: 10.1016/S1872-2032(08)60048-7

Webster, N. S. and Hill, R. T. (2001). The Culturable Microbial Community of the Great Barrier Reef Sponge Rhopaloeides Odorabile is Dominated by an α-Proteobacterium. *Mar. Biol.* 138, 843–851. doi: 10.1007/s002270000503

Wilkinson, C. R. (1978). Microbial Associations in Sponges. I. Ecology, Physiology and Microbial Populations of Coral Reef Sponges. *Mar. Biol.* 49, 161–167. doi: 10.1007/BF00387115

Willis, R. J. (2007). *The History of Allelopathy* (Amsterdam: Springer).

Conflict of Interest: The authors declare that the research was conducted in the absence of any commercial or financial relationships that could be construed as a potential conflict of interest.

Publisher's Note: All claims expressed in this article are solely those of the authors and do not necessarily represent those of their affiliated organizations, or those of the publisher, the editors and the reviewers. Any product that may be evaluated in this article, or claim that may be made by its manufacturer, is not guaranteed or endorsed by the publisher.

Advantages of publishing in Frontiers

OPEN ACCESS
Articles are free to read for greatest visibility and readership

FAST PUBLICATION
Around 90 days from submission to decision

HIGH QUALITY PEER-REVIEW
Rigorous, collaborative, and constructive peer-review

TRANSPARENT PEER-REVIEW
Editors and reviewers acknowledged by name on published articles

Frontiers
Avenue du Tribunal-Fédéral 34
1005 Lausanne | Switzerland

Visit us: www.frontiersin.org
Contact us: frontiersin.org/about/contact

REPRODUCIBILITY OF RESEARCH
Support open data and methods to enhance research reproducibility

DIGITAL PUBLISHING
Articles designed for optimal readership across devices

FOLLOW US
@frontiersin

IMPACT METRICS
Advanced article metrics track visibility across digital media

EXTENSIVE PROMOTION
Marketing and promotion of impactful research

LOOP RESEARCH NETWORK
Our network increases your article's readership